ADVANCED SURVEILLANCE, DIAGNOSTICS, AND PROGNOSTICS TECHNIQUES USED FOR HEALTH MONITORING OF SYSTEMS, STRUCTURES, AND COMPONENTS IN NUCLEAR POWER PLANTS

APPENDIX TO THE CRP MAIN REPORT

CONTENTS

1. REACTOR AND SIGNAL NOISE ANALYSIS (TO CHAPTER 2 OF THE MAIN REPORT)

This chapter contains a number of supplementary papers which describe in further details the following topics introduced in the CRP main report:

- The Paks autonomous noise data acquisition system from KFKI, called PAZAR;
- Some general guidelines about the design and the implementation of process information and reactor diagnostics systems;
- The multi-purpose neutronic tool CORE SIM;
- The MTC theory;
- The theory of coolant velocity determination;
- The high speed noise analysis data logger from AECL, called HSDL.

1.1. PAZAR

By: Sándor Kiss, Sándor Lipcsei and János Végh
KFKI Atomic Energy Research Institute

In the following sections the requirements applied for the hardware and software components of the PAZAR reactor noise data acquisition system and the coupled PAZAR-K noise signal evaluation system are outlined. Both systems are in operation at the four VVER-440/V213 type reactors of the Hungarian Paks nuclear power plant.

Basic requirements related to hardware and signal coupling were given in detail in the requirements specification issued by the nuclear power plant with the bid invitation letter (see [1]). These items were complemented by applicable requirements outlined for similar process information systems (see [2]). In Hungary the basic regulation document to be applied is the Nuclear Safety Regulations (see [3]), issued and periodically updated by the Hungarian Atomic Energy Authority.

In addition, requirements from Nuclear Regulatory Commission (NRC) Regulatory Guides and International Atomic Energy Agency (IAEA) draft Safety Standards were reviewed and used, whenever they were appropriate and applicable (see e.g. [4] and [5]). KFKI AEKI, as an organization involved in the development of process information and reactor data acquisition systems for a long time, has its own quality assurance handbook related to hardware and software procurement, development, installation, testing and maintenance activities carried out for nuclear installations (see [6]). This section summarizes the principles of application software and human-machine interface development procedure according to this quality assurance (QA) handbook. (See also [7] to [9].)

1.1.1. Requirements for hardware equipment and signal coupling

1.1.1.1. Safety classification

The PAZAR system belongs to safety class #4. According to regulations [3] this is the class for "systems not related to safety", or more exactly "systems not belonging to any of the higher safety classes numbered #1 through #3". This classification is justified by the fact that the reactor noise data acquisition and signal evaluation system is performing purely monitoring tasks, i.e. it does not influence either the safety of the plant or the electricity production process.

1.1.1.2. Seismic classification

The input signal coupling part of the PAZAR system is connected to the in-core data acquisition system cabinets; therefore it belongs to seismic class #3. According to regulations [3] this is the class

for those systems which do not belong to seismic class #1 or #2, but their degradation during an earthquake event may potentially endanger the functionality of systems belonging to seismic class #1 or #2 (the in-core data acquisition system itself belongs to seismic class #1). Due to this requirement the height of the rack containing PAZAR equipment is only 2/3 of the height of the in-core data acquisition system cabinets in order to avoid damage.

1.1.1.3. Environmental qualification

Special environmental qualification is required only for that plant equipment that must survive extreme conditions during design basis accident (DBA) transients. Data acquisition cabinets and the signal processing unit of the PAZAR system are located in the unit computer room; therefore no extreme environmental requirements must be prescribed for any part of the system. System operating temperature and relative air humidity limits are as follows:

- Operating temperature limits: between 16°C and 26°C (the optimal value is 23°C);
- Relative air humidity limits: between 40% and 60 % (the optimal value is 45%).

The system must not be operated if the above given limits are exceeded for a longer time period (at least for 5 hours continuously). Otherwise the standard environmental requirements corresponding to digital equipment placed in the unit computer rooms are valid for the PAZAR system, as well.

1.1.1.4. Signal coupling requirements

Coupling of In-Core Thermocouple Signals:
The most demanding signal connection part is the coupling of in-core thermocouple (TC) signals. Extremely strict isolation requirements are imposed by the fact that the modules measuring in-core TC signals in the VERONA in-core data acquisition system (abbreviated as PDA) are very sensitive to external loads. Therefore, the PAZAR system may receive TC signals from the PDA system only through well-isolated signal coupling modules (these are called Isolated Signal Coupling = ISC modules). An ISC module consists of 8 independent channels, complete signal isolation is achieved by using a transformer-based coupling. The common-mode input impedance of the ISC must be at least 2.0 GOhms (maximum 4.5 pF).
Coupling of Self-Powered Neutron Detector (SPND) Signals:
The PDA in-core data acquisition system has special modules for measuring the SPN detector currents in the microAmpere range. These special modules have a dedicated output channel called DIAG, specially tailored for safe connections to external modules. It means that PAZAR self-powered neutron detectors (SPND) input channels are simply connected to these DIAG outputs and no special isolation is required.

1.1.1.5. Electrical interference, grounding

There are no special requirements with respect to electrical interference and grounding protection: standards and requirements for instrumentation and control (I&C) equipment belonging to safety class #4 are applicable.

1.1.1.6. Data acquisition

General Requirements:
General data acquisition requirements must be taken into account during system design, to be able to satisfy the demands listed below, when sizing system hardware and data acquisition equipment:

- The system must be able to access and process all plugged-in input signals by using software control (at this moment there are 352 permanent input signals connected at the plant);
- All measured input signals must be digitized simultaneously;

2

− The alternating current (AC) and direct current (DC) components of all measured input signals must be separated and stored;

Signal Conditioning:

− The signal conditioning module should be able to receive an adjustable (controllable) test signal for performing automatic or user-initiated measurement channel checks;
− The module should be able to suppress common mode electrical interference on the input and it should be equipped with appropriate protection circuits on the input side;
− It should support the required 100 Hz sampling frequency and should provide appropriate pre-amplifying / amplifying, as well as adjustable low-pass and high-pass filtering functions.

As far as data acquisition hardware modules are concerned, standardized commercial off-the-shelf (COTS) products are preferred. Application of special measurement cards or other hardware equipment developed only for a certain system should be avoided as much is possible, in order to facilitate hardware maintenance and effective spare part stockpiling policy.

1.1.2. Requirements for software and human-machine interface components

1.1.2.1. Programming requirements

Application programs should be developed to be as much portable as possible, therefore common, widely used programming languages should be used (preferably C or C++). Application programs should be developed by using a commercial Rapid Application Development (RAD) environment, such as Borland C++ Builder, Microsoft Visual Studio or similar. Application programs responsible for measurement control and data acquisition should be developed by using the standard application programmer's interface (API) delivered with the data acquisition hardware modules.

1.1.2.2. Reliability, availability and system security

Program self-diagnostics and comprehensive error reporting should be embedded in all software components, in order to facilitate system health monitoring and effective error recovery.

Cyber security issues (e.g. local/network access control, data protection, computer virus or spy ware detection etc.) should be addressed, wherever it is appropriate. Possibilities for interference with other plant network sections should be eliminated during the design phase.

The system belongs to safety class #4; therefore no special reliability or availability requirements are imposed. However, the system should be able to carry out long-term noise measurements lasting for several days in an uninterrupted manner. Minimum 8 days of uninterrupted operation is required, during this time period all measured data should be preserved on disk in a safe (redundant) manner.

Measured data should be stored on the local disk, preferably in a compressed ("disk-space saving") format. The contents and format of the data files should be standardized, as much as possible. In case of system failure the program system should be able to continue the previously recorded data.

In case of thermocouple noise measurements the high-precision is of primary importance, therefore 16 bit analog-to-digital converter (ADC) cards should be applied for these measurement channels.

1.1.2.3. User interface

Graphical user interface should be provided to support at least the following tasks:

- Input signal selection and definition of measurement parameter settings (e.g. gain, filtering);
- Measurement control (manual start/stop, scheduled automatic start) and progress monitoring;
- Visualization of measured data stored in local disk resident data files;
- Measured signal selection and definition of evaluation parameters;
- Visualization of results given by the spectral evaluation tools (e.g. spectra, phases etc.);
- Displaying signal evaluation results on color-coded core maps;
- Providing "task-oriented" displays specially tailored to carry out dedicated core-parameter evaluation tasks (e.g. coolant velocity determination, in-core vibration detection).

The above listed graphical elements should be organized into a user-friendly environment ("shell"), in order to facilitate easy data access for standard users and experts.

1.1.3. Testing, verification and validation

Verification and Validation (V&V) of a process data acquisition and measurement analysis system is of primary importance, therefore appropriate procedures and resources should be assigned to this activity. V&V investigations and other tests (e.g. checking the robustness and long-term operation of a system) should be carried out according to a predefined test (V&V) plan and all findings should be documented in order to facilitate tracing of error correction activities. All tests should have clearly defined and unambiguous acceptance criteria, derived from the functional specification. At least the following main items should be included in the test procedures:

- Module tests for qualifying individual software components. Here preferably a "test bed" approach should be used, where the modules can be driven with predetermined input sets and the obtained output sets can be recorded and later analyzed off-line.
- Factory Acceptance Tests (FAT) for testing the integrated hardware and software system at the premises of the system integrator organization. FAT tests should use realistic input data sets; simulated input signals with high process-fidelity should be preferred, where applicable. During these tests the performance limits of the system (as defined in the functional specification) should be checked, as well. These tests may include artificial input data sets resulting in high data processing loads, thus checking the performance of the system under extreme, but still realistic conditions.
- Site Acceptance Tests (SAT) for testing the system at the final location of its utilization. During SAT tests the data acquisition cabinets receive "real" process input signals and all other connections of the system (e.g. network connections to other plant systems) should be operated as described in the System Design Document and Site Installation Plan. SAT tests should concentrate on the qualification of the system under realistic (i.e. "as planned") conditions, in order to determine its behaviour during normal usage. However, SAT may include some tests for checking the system's response to abnormal conditions, e.g. its response to network problems, hardware degradation and power supply failures. Cyber security issues should be addressed here, as well, if malicious activity can be expected.
- In certain cases the customer may demand a trial period. The trial period normally lasts for some weeks and it is started after the commissioning of the system (after the completion of the SAT procedure). During the trial period generally no specific "forced" tests are carried out, but the system is used by its intended regular users for measurements etc. In this period the system's state and its behaviour is regularly registered by the staff responsible for its operation at the site. Daily and weekly logs are analyzed by the O&M staff together with the software developers in order to reveal possible errors or suggest further enhancements.

1.1.4. Documentation

At least the following documentation should be issued for the system during its complete life-cycle:

- Feasibility study (conceptual plan of system implementation);
- Functional specification (detailed description of system requirements);
- Quality assurance plan;
- System design document (description of system implementation, including hardware and software specification);
- Site installation plan (detailed description of hardware mounting, power supply, network components and rack positioning on the final site);
- User's Manual;
- Hardware and software operation and maintenance manual;
- Software development documentation (including software generation procedures).

The above listed documentation should be reviewed, approved and maintained according to the procedures outlined in the Quality Assurance Plan.

1.1.5. Description of PAZAR

In its present configuration the PAZAR system measures and processes 352 in-core noise signals simultaneously (without multiplexing). The number of inputs can be expanded to 512 channels by adding new measurement modules. The input signals taken from the reactor are as follows:

- 252 SPND currents;
- 36 SPND compensation cable signals;
- 31 thermocouple signals (these can be selected from the 210 in-core and 24 loop TCs);
- 1 reference signal (it can be used for test and measurement validation purposes);
- 32 reserve signals (for such sensors as ionization chambers, and vibration detectors).

Inputs are led to PAZAR through a special noise signal coupling system connected to the cabinets of the in-core data acquisition system. The signal coupling ensures that inputs for the noise measurements are extracted prior to passing through the standard in-core signal processing algorithms, therefore signals preserve their noise contents. Input signals are connected to special conditioning modules, where after pre-amplification, each input line is split and filtered to obtain the AC and DC parts. FIG. 1-1 shows the signal conditioning actions for a single data channel. Both AC and DC parts are digitized with 100 Hz sampling frequency, but DC is down-sampled to 3.125 Hz. Two time series are created in each measurement: both AC and DC parts of the signals are stored. Signal conditioning and measurement modules are standard, high-precision industrial devices; the majority of the measurement hardware is made by National Instruments (NI) Company of Texas, USA.
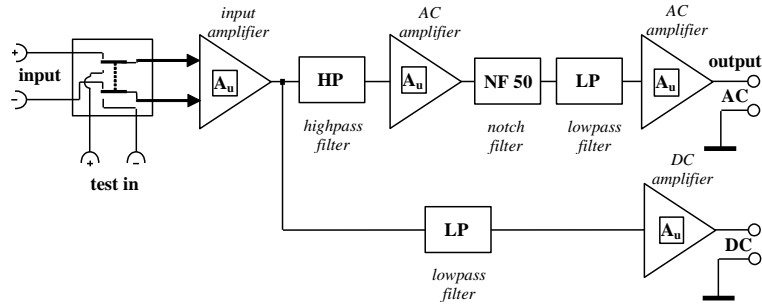
FIG. 1-1. Scheme of the signal conditioning for one data channel.

The architecture of the system uses the latest developments in computer and network technology. The basic design features of the architecture are as follows:

− It is designed to work as a distributed system, using a client-server model;
− Each reactor unit has an autonomous data acquisition system consisting of:

  • signal conditioning modules,
  • fast multiplexer modules for input extension,
  • an industrial PC with fast A/D converter modules.

− Data acquisition at the units can be remote controlled from a central client workstation:

  • the standard TCP/IP interface is used for communication,
  • data evaluation and data storage is performed on the client machine after data transfer.

Measurement sessions are organized according to the client-server model: measurement servers run on dedicated Windows server machines located in every unit computer room, close to the noise signal coupling system. Clients run on Windows computers that can be connected to the measurement server through the plant's standard IT network. Data acquisition is performed by the server in an autonomous manner, but measurement sessions can be remotely controlled, monitored from the client computers. All digitized data are stored locally on the server machine, but selected binary files can be transferred to the client computer via the network. Detailed data evaluation can be performed on the client node. FIG. 1-2 shows the scheme of a PAZAR installation.

The system has some unique features: it can measure all connected noise signals simultaneously and it is able to make long measurements for up to 512 channels, the time span can be as much as several days.
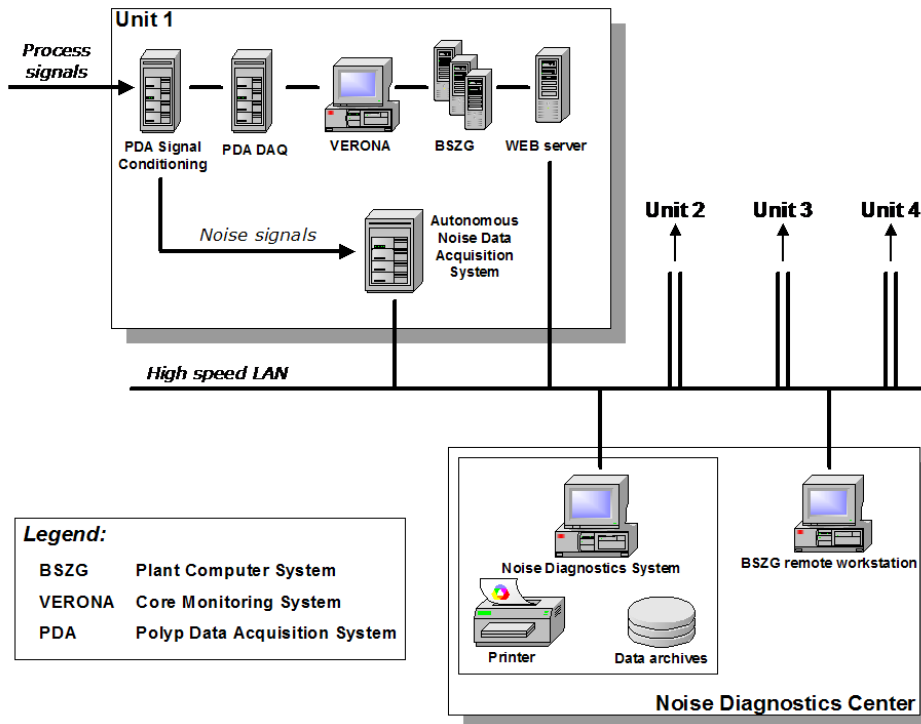
FIG. 1-2. Schematic view of the PAZAR system installed at a Paks unit.

Basic principles of the autonomous data acquisition are as follows (see FIG. 1-3):
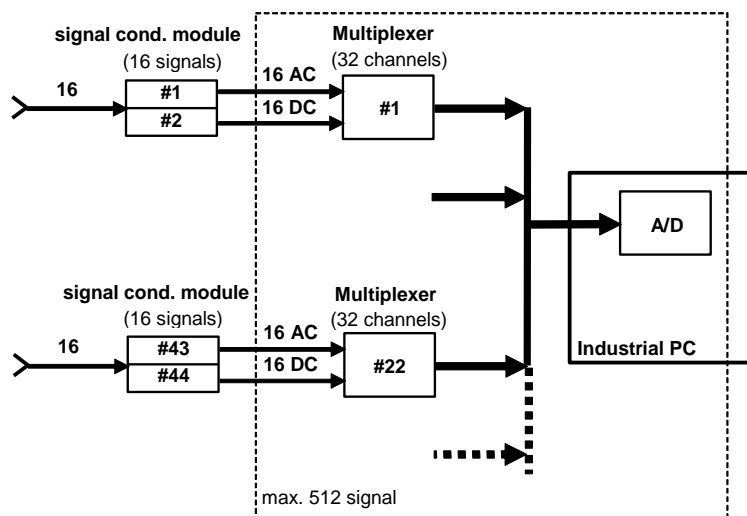
FIG. 1-3. Scheme of the noise data acquisition system.

- − Quasi-simultaneous digitization of the signals;
- − DC and AC parts of the signals are separated;
- − Both DC and AC signals are sampled together;
- − Real-time down-sampling of the DC signals is performed;
- − Two A/D cards work parallel.

Multiplexers are fast NI SCXI multiplexers to extend the number of input signals received by the A/D converters. They work up to 333 kHz and handle 32 channels per module (16 AC and 16 DC signals). A/D converters are high speed NI cards that work up to 1 MSample/sec and have built in

amplifiers (with gain factors from 0.5× to 100×) handling maximum 2047 AC and maximum 2047 DC signals.

FIG. 1-4 shows the rack of the Unit 4 data acquisition server and the signal conditioning cabinet.

FIG. 1-4. PAZAR Configuration at Unit 4: system computer and multiplexers are placed in the smaller rack; signal conditioning modules are installed in the larger cabinet.

Basic services available in the measurement software are as follows:

− Signal selection, setting measurement parameters and gains;
− Performing measurements and monitoring measurement sessions;
− Performing basic ("raw") signal validation functions automatically;
− Providing additional services, such as setting of optimal gains, self-testing, data maintenance, on-line help, version control, computer clock synchronization.

The PAZAR architecture was designed to facilitate the creation of a "noise diagnostics centre" at the Paks NPP. The centre is used to control the four server configurations located at the four units and it is the central workplace for measurement evaluation, visualization of results and report generation. It has a sufficiently large disk capacity to store primary measured data and analysis results. It also serves as a tool for producing long-term noise parameter trends. It is believed that long term noise trend analysis is an excellent tool for state change detection and to locate the first occurrence of a specific anomaly.

1.2. DESIGN AND IMPLEMENTATION OF PROCESS INFORMATION AND REACTOR DIAGNOSTICS SYSTEMS – GENERAL GUIDELINES

By: Sándor Kiss, Sándor Lipcsei and János Végh
KFKI Atomic Energy Research Institute

When designing a computerized operator support or data collection system to be applied in a nuclear power plant it is essential to define the services of the future system properly: the required functions of the system in various reactor operation states must be identified and clearly defined.

Information systems monitoring the status of the reactor and the coupled technology can be classified e.g. according to the operation states of the reactor. Generally three basic categories are distinguished in order to characterize the operation state of a reactor, namely: normal, emergency and accident operation states are defined. During normal reactor operation the control room staff routinely uses the basic functions of the plant computer and the core monitoring system. Standard diagnostics systems are also applied during normal operation (such as noise, vibration, acoustic leakage detection or loose part monitoring systems).

When an emergency situation occurs operators turn to the application of the safety parameter display system (SPDS) or to the critical safety functions monitoring (CSFM) system. Generally there is no sharp transition between emergency and accident states; therefore in the early stage of an accident it is sufficient to use the SPD or the CSFM systems only. Later, if the accident develops into a severe accident, operators and Technical Support Centre (TSC) personnel change over to the application of a special system supporting the effective management and mitigation of severe accidents. In most nuclear power plants the so called Severe Accident Management Guidance (SAMG) documents were already prepared and introduced. These procedures are generally "paper based" and computerized support of SAMG execution is not often applied.

1.2.1. Functional specification, conceptual and system design documents

Development of process information and operator support systems is a complex, multidisciplinary activity: in order to create a reliable system which is trusted by its users one must possess a fairly deep knowledge of the process to be monitored, must have an expert developer's level in handling the computer technology to be applied (i.e. hardware, network and software), and must master on-line programming techniques. The design of a proper human-machine interface requires the knowledge of the various activities carried out by the control room staff, a detailed analysis of ergonomic and functional requirements, and the programming tools applicable to create an optimal user interface.

The basic design phase is probably the most important period during the creation process of a data acquisition, a computerized operator support or diagnostics system. In principle the design phase consists of three basic activities: in the first phase tasks of the new system must be determined. System functions during various reactor operation states must be defined, together with the scope and access methods of relevant process measurements. The scope of calculated signals (i.e. variables derived from input measurements) must be determined and the requirements for the user interface must be clearly outlined.

In this phase important system parameters are quantified, as well: e.g. measurement cycle time, maximum data flux, expected display update time, reliability and availability requirements, maximum size of the process database, etc. In the preparation of specifications the potential users of the new system play a very important role, their involvement is indispensable. The result of this work is the Functional Specification of the new system, which later serves as the basic document for detailed system design.

The next milestone in the design process is the creation of the Conceptual Plan (a detailed feasibility study). In this document the development teams outline their proposals to fulfil the requirements given in the Functional Specification: e.g. what kind of hardware architecture and software tools should be used, what kind of algorithms (models) should be applied.

The preparation of a Conceptual Plan is generally preceded by a complex analysis; the most important questions to be analyzed are as follows:

– Analysis of measurements corresponding to the process to be monitored

Characteristic process parameters must be carefully selected and the corresponding measurement points must be identified in the technology. Proper functioning of the selected measurements must be clarified in those reactor operation states, where the planned system is to be used by the personnel (e.g. identification of those parameter ranges which are not covered by the available measurements, analysis of transducer behaviour in extreme temperature, pressure and radiation conditions, availability of redundant sensors). The result of this analysis determines a minimum measured input signal set, which is required and sufficient to fulfil all system tasks.

– Analysis of calculations required for process monitoring

In this procedure those algorithms are defined which are necessary to determine all calculated signals required for process monitoring (e.g. non-measurable in-core parameters). The selected algorithms must fulfil the accuracy requirements given in the Functional Specification document, as well. Obviously this analysis may lead to a conclusion that a significant model improvement is required in order to achieve the prescribed accuracy targets.

– Analysis of fulfilment of quantitative requirements

It must be outlined how reliability, availability and data processing (e.g. speed) requirements (detailed in the Functional Specification) will be satisfied by the new system: e.g. what kind of hardware and network architecture will be applied, what kind of operating system and application software will be used, etc. In case of important systems, where continuous, uninterrupted operation is expected one must also define solutions applicable to avoid potential data losses or to perform automatic reconfiguration procedures of system resources (e.g. continuous self-diagnostics and performance supervision). Distribution of redundant measurements to independent data acquisition units must be analyzed and a suitable reservation strategy for the network communication routes should be worked out. This analysis finally results practical information for the sizing of the new system: based on this information experts can design server and workstation resources (e.g. processor speed, memory size, disk capacity, etc.), as well as the necessary bandwidth and redundancy of network communication devices. Generally this analysis requires a lot of experiments (assessment and testing of hardware devices and software tools); it may even happen that some application software modules must be programmed in their final form in order to carry out more or less realistic tests.

– Analysis of human-machine interface functions and outlay

Generally the design of a new human-machine interface (HMI) begins with the establishment of a so called user model. This model identifies potential system users and their tasks, determines what kind of user interface elements are used by them during their routine work. A well-established user model facilitates the creation of a proper authorization system and the adjustment of HMI services to special user needs. This analysis supplies information for the detailed design of HMI tools, display formats and functions dedicated to serve special user groups. The information used for the creation of a user model generally originates from the evaluation of questionnaires and from personal interviews with the future users of the system. Results from local inspections and walk-rounds are utilized, as well.

In the final phase of the design process the System Design Document is issued. This document outlines the proposals of the Conceptual Plan is such a detailed manner that it can form the base of programming of the whole operator support system. In case of information systems to be installed at the nuclear power plant (NPP) the System Design Document is the main document in the licensing

procedure, therefore descriptions must be accurate and deep enough, in order to minimize changes during the realization process. In these cases the System Design Document is complemented by a safety analysis. It describes safety functions realized by the new system and analyses the effects of potential system failures or degradations on the safe operation of the reactor unit.

1.2.2. Implementation and testing (verification & validation) phase

In the first part of the implementation phase all functional modules are programmed according to the contents of the System Design Document. The applicable software development environment depends on the tasks to be solved, as well as on the selected platform and operating system. FORTRAN is the traditional "language" applied for coding various algorithms (e.g. thermal-hydraulic, reactor physical calculations). Interactive, "Visual" FORTRAN versions are also available on the market. Parallel with the expansion of PC-based software development tools the application of Visual C and C++ languages becomes more and more widespread. These tools were originally applied mainly for PC user interface programming, but gradually they became dominant in other application areas (e.g. creation of network communication programs), as well.

For a very long time the X Window/Motif graphic standard (and the associated software development environment) was the only applicable tool under VMS and UNIX operating systems if programming of user interfaces was considered. The X Windows represents a robust client-server model, generating low network traffic, but it is being gradually ousted due to the rapid development of the PC-based graphics. Presently the Windows graphical user interface (GUI) is a widely used and very efficient tool for developing user interfaces, ensuring a highly competitive price/performance ratio. This leading role is not influenced even by some disadvantages: e.g. the network traffic required for information display was increased dramatically, because process data must be transferred to the PC through the network (in the X client-server model only graphic commands are sent through the network, process data are handled in the mainframe). Increased network traffic was compensated by dramatic developments in the network hardware and software components: high-speed 100 Mbps networks are routinely used in industrial applications. The DECnet network transfer protocol (which was earlier very popular due to its reliability and transparent programming features) was everywhere replaced by TCP/IP (this protocol became practically dominant due to the Internet). The rapid development of Internet technology initiated important changes in document (i.e. textual information) handling: the application of HTML and XML documents viewable in a standard hypertext browser (e.g. MS Internet Explorer) for electronic handling and visualization of industrial systems' operational documents represents a real breakthrough. The perspectives of these changes are not predictable today: e.g. the complete omission of paper based procedures is a valid option in the near future. Java, the language supporting the animated display of HTML pages is spreading rapidly due to the fact that it can be used for the creation of platform-independent applications.

A new approach must be mentioned here, as well: this is the use of Supervisory Control and Data Acquisition (SCADA) systems, spreading in industrial applications. In principle a SCADA is a general-purpose software shell, which contains the most common industrial data acquisition interfaces, the basic data processing and display functions and a simple database. By using such a system plant experts are able to create small-scale data acquisition or process monitoring systems, without being experts in programming. Its definite advantage is the efficient creation of applications; on the other hand it has some drawbacks: generally the shells are quite "closed", i.e. the implementation of new or special functions is not an easy task. In spite of these problems the number of industrial SCADA applications is growing rapidly, mainly due to their standardized features.

The next part of the realization phase contains V&V tests, when programs are first tested at module level, then integrally. In case of operator support systems the most important test procedure is the integral test; therefore applicable methods will be discussed in more detail. In order to perform a comprehensive test for an operator support system it is essential to supply consistent technological data corresponding to all reactor operation states "covered" by the information system.

The best tool to create such consistent data is a full-scope simulator; therefore a simulator should be extensively used for the qualification of most process information systems. During the V&V tests the new system (or its functional equivalent) must be installed at the simulator, but measured signals coming from the plant's data acquisition units have to be replaced by appropriate simulated signals.

These "measured" signals are collected by special programs running in the simulator computer and then transferred through the network to the information system. Here the signal processing should take place exactly in the same manner as in the configuration running at the plant. In order to test various functions of an operator support system, appropriate simulated scenarios (so called transients) must be designed in co-operation with the simulator instructors. Then these transients are executed during a simulator training session, where operators use the human-machine interface of the new system to retrieve and display process information. During the sessions observers register operator's actions, the functioning of the new system, and analyze the correctness and consistency of the information displayed. Interviews with the operators can be very useful: they fill in questionnaires inquiring usability, ergonomics and weak points of the system under investigation. The experience obtained during the tests then must be analyzed and errors detected in the man-machine interface and algorithms must be duly corrected. Active involvement of future system users into the V&V tests may produce very positive results: the final system (installed at the plant) can be "cleaned" from disturbing errors and awkward interface behaviour; it can function in a manner fully accepted by the operators.

A different but rather frequently used test method is the so called parallel operation, and the remote data feeding. In the first case the full plant configuration of a new information system is installed at its final operation site. All measured data are fed into the new system, parallel to the old one which serves control room staff with process information in a fully undisturbed manner. During the parallel operation those quantities, which are determined in both systems can be compared conveniently and tests with real data acquisition units can be performed in the real plant environment. The drawback of this test method is that the parallel feeding of two systems from the same data acquisition unit sometimes can be achieved only by rather expensive modifications (sometimes it is even impossible).

This drawback is eliminated by the remote data feeding method, when measured data are taken not directly from the data acquisition units, but from the data processing computers and then transferred to a "remote" test configuration through the network. The hardware and software of this remote configuration is the same as for the plant configuration, but it does not contain data acquisition units. Generally this method is applied to perform comprehensive tests of software modifications carried out in already existing systems. In these tests the results given by the original (i.e. licensed) and the modified software can be compared very well and the new software can be thoroughly qualified.

The application of artificial signals must be mentioned, as well, this test method is quite frequently used in Factory Acceptance Test procedures. These signals are generated by appropriate, so called "stimulator" programs: these programs can simulate the behaviour of the data acquisition units, but they can produce extremely high data fluxes, as well. This method is mainly used to create very high loads on the input side, when the systems' response to the maximum specified data flux can be investigated (e.g. proper functioning of data communication, no data loss in the archives, delays in information display, etc.). This method is frequently used to test a new process information system under extreme load conditions.

The final stage of the realization phase is the installation (mounting), site acceptance tests, commissioning tests and the preparation of system documentation for the users and developers (programmers). Tests performed during the installation phase generally use a combination of the above outlined test methods, usually they are based on the V&V Plan prepared for the Factory Acceptance Test. Acceptance criteria are defined by using requirements given in the Functional Specification and the System Design.

An operator support system can be considered as a large software system, therefore its life-cycle is obviously not over when it is installed and successfully commissioned. In the further stages of the software life cycle mainly software configuration management, tracing of software modifications methods and such activities are required.

1.3. OVERVIEW OF THE MULTI-PURPOSE NEUTRONIC TOOL CORE SIM

By: Christophe Demazière
Chalmers University of Technology

1.3.1. Abstract

In the following, the development of a neutronic core simulator, called CORE SIM, is reported. Although the tool was primarily meant to estimate the transfer function of any heterogeneous nuclear core for noise analysis applications, the tool can actually performed other types of calculations as well. Both critical systems and subcritical systems with an external neutron source can be studied, and static and dynamic cases in the frequency domain (i.e. for stationary fluctuations) can be considered. In addition, the tool has the ability to determine the different eigenfunctions of any nuclear core. For each situation, the static neutron flux, the different eigenmodes and eigenvalues, the first-order neutron noise, and their adjoint functions are estimated, as well as the effective multiplication factor of the system. The main advantages of the tool, which is entirely MatLab based, lie with the robustness of the implemented numerical algorithms, its high portability between different computer platforms and operative systems, and finally its ease of use since no input deck writing is required. The present version of the tool, which is based on two-group diffusion theory, is mostly suited to investigate thermal systems. Although the tool cannot be compared in terms of accuracy to existing core simulators, the definition of both the static and dynamic core configurations directly from the static macroscopic cross-sections and their fluctuations, respectively, makes the tool particularly well suited for research and education. The tool was also successfully validated against analytical, semi-analytical, and numerical reference solutions.

1.3.2. Introduction

The deterministic modelling of Light Water Reactors (LWRs) requires special techniques due to the multi-physics and multi-scale aspects of such systems. The fact that water is used both as a neutron moderator and a coolant makes the modelling of such system particularly challenging.

Complementing state-of-the-art modelling techniques by simpler computational tools that can still catch the main physical phenomena and at the same time provide some physical insight is the purpose of the work reported hereafter. More specifically, a computational tool, called CORE SIM and which exclusively focuses on the determination of the neutron density field in any heterogeneous core, was developed. From a neutron kinetic point of view, the thermal-hydraulic variables (i.e. density/velocity/enthalpy fields of the coolant/temperature field of the fuel) directly affect the macroscopic cross-sections. As a result, the neutronic computational tool presented hereafter uses sets of macroscopic cross-sections as input parameters. This is equivalent to saying that the implicit coupling between the neutron kinetics and the thermal-hydraulics is disabled and artificially reintroduced by the user via the macroscopic cross-sections. This way of defining the input parameters allows a high degree of flexibility in the use of the tool compared to coupled neutron kinetics/thermal-hydraulics tools, where the only parameters that the user can modify are mostly related to core power, control rod positions, and inlet flow conditions. In the present tool, the user can freely define configurations representative of any actual core and most importantly can perturb the system by directly defining perturbations of the macroscopic cross-sections. Such perturbations can be of an artificial nature or can represent actual cases (such as perturbations travelling with the core flow, core barrel vibrations, fuel assembly vibrations, etc.).

In addition to the flexibility in the definition of the problems to be investigated by the tool, another main novelty is its multi-purpose character. Namely, the tool can consider both critical systems and subcritical systems with an external neutron source, static cases and dynamic cases in the frequency domain (i.e. for stationary fluctuations). In addition, the tool has the ability to determine the different eigenfunctions of a nuclear core. For each situation, the static neutron flux, the different eigenmodes and eigenvalues, the first-order neutron noise, and their adjoint functions can be determined, as well as the effective multiplication factor of the system.

The calculations performed by the tool rely on the two-group diffusion approximation, while the spatial discretization is based on finite differences. The coding was implemented in *MatLab*, which makes the pre- and post-processing of data easy, as well as the code highly portable between different operative systems and computer platforms. Two types of equations are solved within the tool: homogeneous or eigenvalue equations, and non-homogeneous or source equations. For the former, the explicitly-restarted Arnoldi method was implemented, so that the calculation of different eigenmodes is possible. In case of convergence problem, the user has also the possibility of choosing the power iteration method, which was implemented using Wielandt's shift technique. The initial guess of the eigenvalues required for the application of Wielandt's shift technique is provided by an Arnoldi run without restart. For the latter, Gaussian elimination is used. In all cases, the matrix operations are based on an LU factorization of the matrices with full pivoting, in order to preserve the sparsity of the matrices. A Graphical User Interface (GUI) allowing easily plotting both the input and output data was also developed. Although the accuracy of this tool cannot be compared to commercial core simulators, the tool offers several advantages such as: its ease of use, the robustness of the algorithms, and the fact that non-conventional systems can be easily investigated. Another main strength of the tool is that no input deck writing is required since only few data are required.

The structure of this section is as follows. First, the neutronic models on which the tool relies are presented, both for the static and dynamic cases. Thereafter, the numerical algorithms used for the spatial discretization of the implemented equations, as well as for solving the different types of equations, are touched upon. In the third part of the paper, various validation cases for one-dimensional, two-dimensional, and three-dimensional systems are briefly reported, where the results of the calculations performed by the tool are benchmarked against analytical or semi-analytical cases, and in some occurrences against the results of commercial high-fidelity core simulators. Finally, the tool is demonstrated and some explanations on its use are given.

1.3.3. Description of the neutronic models

In this section, the neutronic models implemented in the tool are presented. The tool has the ability to calculate the solution to static problems with or without any external neutron source, as well as the solution to dynamic problems in linear theory and in the frequency-domain. The equations thus solved in these different cases are presented.

1.3.3.1. Introduction

The tool is based on diffusion theory with two energy groups and one group of delayed neutrons. In this formalism, the time- and space-dependent fast neutron flux, thermal neutron flux, and precursor density, can be expressed, respectively, as:

$$\frac{1}{v_1}\frac{\partial}{\partial t}\phi_1(\boldsymbol{r},t)$$
$$= \nabla \cdot [D_{1,0}(\boldsymbol{r})\nabla\phi_1(\boldsymbol{r},t)] + [(1-\beta)\upsilon\Sigma_{f,1}(\boldsymbol{r},t) - \Sigma_{a,1}(\boldsymbol{r},t) - \Sigma_r(\boldsymbol{r},t)]\phi_1(\boldsymbol{r},t) \qquad (1)$$
$$+ (1-\beta)\upsilon\Sigma_{f,2}(\boldsymbol{r},t)\phi_2(\boldsymbol{r},t) + \lambda C(\boldsymbol{r},t) + S_1(\boldsymbol{r},t)$$

$$\frac{1}{v_2}\frac{\partial}{\partial t}\phi_2(\boldsymbol{r},t) = \nabla \cdot [D_{2,0}(\boldsymbol{r})\nabla\phi_2(\boldsymbol{r},t)] + \Sigma_r(\boldsymbol{r},t)\phi_1(\boldsymbol{r},t) - \Sigma_{a,2}(\boldsymbol{r},t)\phi_2(\boldsymbol{r},t) + S_2(\boldsymbol{r},t) \qquad (2)$$

$$\frac{\partial}{\partial t}C(\boldsymbol{r},t) = \beta\upsilon\Sigma_{f,1}(\boldsymbol{r},t)\phi_1(\boldsymbol{r},t) + \beta\upsilon\Sigma_{f,2}(\boldsymbol{r},t)\phi_2(\boldsymbol{r},t) - \lambda C(\boldsymbol{r},t) \qquad (3)$$

and where the macroscopic removal cross-section is defined as:

$$\Sigma_r(\boldsymbol{r}, t) = \Sigma_{s0, 1 \to 2}(\boldsymbol{r}, t) - \frac{\Sigma_{s0, 2 \to 1}(\boldsymbol{r}, t)\phi_2(\boldsymbol{r}, t)}{\phi_1(\boldsymbol{r}, t)} \tag{4}$$

In the previous equations, all the symbols have their usual meaning. The equations were obtained by assuming that both the prompt and delayed neutrons only contribute to the fast energy group. $S_1(\boldsymbol{r}, t)$ and $S_2(\boldsymbol{r}, t)$ represent possible external neutron sources in the fast and thermal groups, respectively, and as such, the tool has the ability to model both critical systems, for which $S_1(\boldsymbol{r}, t) = 0, \forall(\boldsymbol{r}, t)$ and $S_2(\boldsymbol{r}, t) = 0, \forall(\boldsymbol{r}, t)$, or subcritical systems with external sources. All the macroscopic cross-sections and possible external neutron sources might be time-dependent. It was earlier demonstrated in [10] that allowing the diffusion coefficients to be time-dependent lead to dynamical results essentially identical to keeping such diffusion coefficients time-independent. Since the computational burden introduced by letting the diffusion coefficients vary with time increases drastically, the diffusion coefficients are kept time-independent in the tool reported hereafter.

1.3.3.2. Derivation of the static equations

If the system contains an external neutron source (case of a subcritical system driven by an external neutron source), Eqs. (1) - (3) written in steady-state conditions reduce to the following matrix equation:

$$[\nabla \cdot \bar{\bar{D}}(\boldsymbol{r})\nabla + \bar{\bar{\Sigma}}_{sta}(\boldsymbol{r}) - \bar{\bar{F}}(\boldsymbol{r})] \times \begin{bmatrix} \phi_{1, 0}(\boldsymbol{r}) \\ \phi_{2, 0}(\boldsymbol{r}) \end{bmatrix} = -\begin{bmatrix} S_{1, 0}(\boldsymbol{r}) \\ S_{2, 0}(\boldsymbol{r}) \end{bmatrix} \tag{5}$$

with

$$\bar{\bar{D}}(\boldsymbol{r}) = \begin{bmatrix} D_{1, 0}(\boldsymbol{r}) & 0 \\ 0 & D_{2, 0}(\boldsymbol{r}) \end{bmatrix} \tag{6}$$

$$\bar{\bar{\Sigma}}_{sta}(\boldsymbol{r}) = \begin{bmatrix} -\Sigma_{a, 1, 0}(\boldsymbol{r}) - \Sigma_{r, 0}(\boldsymbol{r}) & 0 \\ \Sigma_{r, 0}(\boldsymbol{r}) & -\Sigma_{a, 2, 0}(\boldsymbol{r}) \end{bmatrix} \tag{7}$$

$$\bar{\bar{F}}(\boldsymbol{r}) = \begin{bmatrix} -\nu\Sigma_{f, 1, 0}(\boldsymbol{r}) & -\nu\Sigma_{f, 2, 0}(\boldsymbol{r}) \\ 0 & 0 \end{bmatrix} \tag{8}$$

and where the subscript 0 refers to the static values of the different variables.

In many occurrences, the determination of the solution to the adjoint problem associated to the direct or forward problem given by Eq. (5) is of high interest. In order to properly define the concept of adjoint, the space on which Eq. (5) is defined needs to be given an inner product. In two-group theory, any space-dependent function can be represented as a column vector, where the first component corresponds to the fast energy group, and the second component corresponds to the thermal energy group. One can then define the inner product of two space-dependent functions $\bar{\psi}(\boldsymbol{r}) = \begin{bmatrix} \psi_1(\boldsymbol{r}) & \psi_2(\boldsymbol{r}) \end{bmatrix}^T$ and $\bar{\varphi}(\boldsymbol{r}) = \begin{bmatrix} \varphi_1(\boldsymbol{r}) & \varphi_2(\boldsymbol{r}) \end{bmatrix}^T$, where the superscript T represents the transpose operator, as the integral of the scalar product between the two vectors $\bar{\psi}(\boldsymbol{r})$ and $\bar{\varphi}(\boldsymbol{r})$ on the whole volume V of the system. This reads as:

$$(\overline{\psi}, \overline{\varphi}) = \int_V \overline{\psi}^T(\boldsymbol{r}) \cdot \overline{\varphi}(\boldsymbol{r}) d\boldsymbol{r} = \int_V [\psi_1(\boldsymbol{r})\varphi_1(\boldsymbol{r}) + \psi_2(\boldsymbol{r})\varphi_2(\boldsymbol{r})] d\boldsymbol{r} \tag{9}$$

Operators to any function defined on the previous space can be formally considered as 2x2 matrices, and the application of such operators on any space-dependent function (considered as a vector), can be regarded as the multiplication of a matrix and a vector. The adjoint $\overline{\overline{L}}^+$ of any operator $\overline{\overline{L}}$ can then be defined as the one which satisfies the following relationship:

$$(\overline{\psi}^+, \overline{\overline{L}} \times \overline{\varphi}) = \left(\overline{\overline{L}}^+ \times \overline{\psi}^+, \overline{\varphi}\right) \tag{10}$$

where $\overline{\psi}^+$ and $\overline{\varphi}$, which are the adjoint and forward or direct functions respectively, satisfy certain boundary and continuity conditions. In two-group diffusion theory, it could be further demonstrated that the adjoint operator is the transposed of the direct operator [11], that is:

$$\overline{\overline{L}}^+ = \overline{\overline{L}}^T \tag{11}$$

The adjoint problem corresponding to the forward problem as given by Eq. (5) can then be formally written as:

$$[\nabla \cdot \overline{\overline{D}}(\boldsymbol{r})\nabla + \overline{\overline{\Sigma}}_{sta}^T(\boldsymbol{r}) - \overline{\overline{F}}^T(\boldsymbol{r})] \times \begin{bmatrix} \phi_{1,0}^{\dagger}(\boldsymbol{r}) \\ \phi_{2,0}^{\dagger}(\boldsymbol{r}) \end{bmatrix} = -\begin{bmatrix} S_{1,0}^{\dagger}(\boldsymbol{r}) \\ S_{2,0}^{\dagger}(\boldsymbol{r}) \end{bmatrix} \tag{12}$$

It has to be noted that the source in the adjoint problem [i.e. the right-hand side of Eq. (12)] can be different from the source in the forward problem [i.e. the right-hand side of Eq. (5)]. This also means that Eq. (12) can be used for investigating any type of system (not necessarily restricted to subcritical systems driven by an external neutron source).

From a mathematical viewpoint, the static forward problem of a subcritical source-driven system as given by Eq. (5) is represented by a non-homogeneous equation. Likewise, the corresponding adjoint problem as given by Eq. (12) is also represented by a non-homogeneous equation.

If the system does not contain any external neutron source, a steady-state solution to Eqs. (1) - (3) only exists if the system is critical. Equations (1) - (3) written in steady-state conditions then reduce to the following matrix equation:

$$[\nabla \cdot \overline{\overline{D}}(\boldsymbol{r})\nabla + \overline{\overline{\Sigma}}_{sta}(\boldsymbol{r})] \times \begin{bmatrix} \phi_{1,0}(\boldsymbol{r}) \\ \phi_{2,0}(\boldsymbol{r}) \end{bmatrix} = \overline{\overline{F}}(\boldsymbol{r}) \times \begin{bmatrix} \phi_{1,0}(\boldsymbol{r}) \\ \phi_{2,0}(\boldsymbol{r}) \end{bmatrix} \tag{13}$$

If the system is not critical, a steady-state solution can still be obtained by renormalizing the fission source terms by a factor k_m, and thus Eqs. (1) - (3) reduce to:

$$[\nabla \cdot \overline{\overline{D}}(\boldsymbol{r})\nabla + \overline{\overline{\Sigma}}_{sta}(\boldsymbol{r})] \times \begin{bmatrix} \phi_{1,m}(\boldsymbol{r}) \\ \phi_{2,m}(\boldsymbol{r}) \end{bmatrix} = \frac{1}{k_m}\overline{\overline{F}}(\boldsymbol{r}) \times \begin{bmatrix} \phi_{1,m}(\boldsymbol{r}) \\ \phi_{2,m}(\boldsymbol{r}) \end{bmatrix} \tag{14}$$

From a mathematical viewpoint, the static problem without source as given by Eq. (14) corresponds to an eigenvalue problem, where both the eigenfunctions $\phi_{1,m}(r)$ and $\phi_{2,m}(r)$ and the corresponding eigenvalue $1/k_m$ have to be determined. There is an infinite number of solutions, i.e. an infinite number of pairs of solutions $\left[\phi_{1,m}(r) \; \phi_{2,m}(r)\right]$ and k_m, where the index m represents the mode number. The eigenfunctions having the same sign throughout the entire system corresponds to the static fluxes denoted as $\left[\phi_{1,0}(r) \; \phi_{2,0}(r)\right]$ (fundamental mode) and the associated factor k_0 is then the effective multiplication factor of the system, i.e.

$$k_0 = k_{eff} \tag{15}$$

All other eigenfunctions change sign throughout the system, and their associated factor k_m is strictly smaller than k_{eff}. It is customary to order the eigenmodes in increasing order of their eigenvalue $1/k_m$ (thus in decreasing order of the factor k_m):

$$k_{eff} = k_0 > k_1 > k_2 > ... > k_m \tag{16}$$

It has to be noted that Eq. (13) is a sub-case of Eq. (14) obtained with $k_0 = k_{eff} = 1$.

As before, an adjoint problem corresponding to the forward problem as given by Eq. (14) can be formally written as:

$$[\nabla \cdot \overline{\overline{D}}(r)\nabla + \overline{\overline{\Sigma}}_{sta}^{T}(r)] \times \begin{bmatrix} \phi_{1,m}^{\dagger}(r) \\ \phi_{2,m}^{\dagger}(r) \end{bmatrix} = \frac{1}{k_m^{\dagger}} \overline{\overline{F}}^{T}(r) \times \begin{bmatrix} \phi_{1,m}^{\dagger}(r) \\ \phi_{2,m}^{\dagger}(r) \end{bmatrix} \tag{17}$$

It could be demonstrated that in two-group diffusion theory [11]:

$$k_m^{\dagger} = k_m \tag{18}$$

As for the forward problem, the adjoint problem as given by Eq. (17) corresponds to an eigenvalue problem from a mathematical viewpoint.

Depending on whether the system is subcritical with an external neutron source, or critical without neutron source, one notices that two types of equations need to be solved:

- A non-homogeneous type of equation for the subcritical system, in both the forward and adjoint problems;
- An eigenvalue type equation for the critical system, in both the forward and adjoint problems.

It has to be noted here that the eigenmodes can also be calculated for the subcritical system with an external neutron source. Nevertheless, the static flux is given by the fundamental mode only in the case of a critical system, since the static flux in the case of a subcritical system with an external neutron source is given by solving a non-homogeneous equation as represented by Eq. (5).

1.3.3.3. Derivation of the dynamic equations

In case of non-steady-state conditions, the time-dependent terms, generically expressed as $X(r, t)$, can be split into a mean value $X_0(r)$ (corresponding to the steady-state configuration of the system) and a fluctuating part $\delta X(r, t)$ around the mean value as:

$$X(r, t) = X_0(r) + \delta X(r, t) \tag{19}$$

If the system is subcritical and driven by an external neutron source, using Eq. (19) for all time-dependent terms in Eqs. (1) - (3), removing the static equations [i.e. Eq. (5)], performing a temporal Fourier-transform, and neglecting second-order terms (linear theory), the following matrix equation is obtained:

$$[\nabla \cdot \overline{\overline{D}}(r)\nabla + \overline{\overline{\Sigma}}_{dyn}^{sub}(r, \omega)] \times \begin{bmatrix} \delta\phi_1(r, \omega) \\ \delta\phi_2(r, \omega) \end{bmatrix}$$

$$= - \begin{bmatrix} \delta S_1(r, \omega) \\ \delta S_2(r, \omega) \end{bmatrix} + \bar{\phi}_r(r)\delta\Sigma_r(r, \omega) + \overline{\overline{\phi}}_a(r) \begin{bmatrix} \delta\Sigma_{a,1}(r, \omega) \\ \delta\Sigma_{a,2}(r, \omega) \end{bmatrix} + \overline{\overline{\phi}}_f^{sub}(r, \omega) \begin{bmatrix} \delta\upsilon\Sigma_{f,1}(r, \omega) \\ \delta\upsilon\Sigma_{f,2}(r, \omega) \end{bmatrix} \tag{20}$$

with

$$\overline{\overline{\Sigma}}_{dyn}^{sub}(r, \omega) = \begin{bmatrix} -\Sigma_1^{sub}(r, \omega) & \upsilon\Sigma_{f,2,0}(r)\left(1 - \dfrac{i\omega\beta}{i\omega + \lambda}\right) \\ \Sigma_{r,0}(r) & -\left(\Sigma_{a,2,0}(r) + \dfrac{i\omega}{v_2}\right) \end{bmatrix} \tag{21}$$

$$\bar{\phi}_r(r) = \begin{bmatrix} \phi_{1,0}(r) \\ -\phi_{1,0}(r) \end{bmatrix} \tag{22}$$

$$\overline{\overline{\phi}}_a(r) = \begin{bmatrix} \phi_{1,0}(r) & 0 \\ 0 & \phi_{2,0}(r) \end{bmatrix} \tag{23}$$

$$\overline{\overline{\phi}}_f^{sub}(r, \omega) = \begin{bmatrix} -\phi_{1,0}(r)\left(1 - \dfrac{i\omega\beta}{i\omega + \lambda}\right) & -\phi_{2,0}(r)\left(1 - \dfrac{i\omega\beta}{i\omega + \lambda}\right) \\ 0 & 0 \end{bmatrix} \tag{24}$$

and with

$$\Sigma_1^{sub}(r, \omega) = \Sigma_{a,1,0}(r) + \frac{i\omega}{v_1} + \Sigma_{r,0}(r) - \upsilon\Sigma_{f,1,0}(r) \times \left(1 - \frac{i\omega\beta}{i\omega + \lambda}\right) \tag{25}$$

The right-hand side of Eq. (20) gives the neutron noise source, resulting from either the fluctuations of the external neutron source around its mean value, or from the fluctuations of the

macroscopic cross-sections (removal, absorption, and fission) around their mean value. Although the effect of the fluctuations of the macroscopic fission cross-sections and of the macroscopic absorption cross-sections are given by two separate terms in Eq. (20), any fluctuation in the macroscopic fission cross-section has also an impact on the macroscopic absorption cross-section (since fission is a special type of absorption).

An adjoint problem corresponding to the forward problem as given by Eq. (20) can then be formally written as:

$$
\left[\nabla \cdot \bar{\bar{D}}(r)\nabla + \bar{\bar{\Sigma}}_{dyn}^{sub\dagger}(r, \omega) \right] \times \begin{bmatrix} \delta\phi_1^{\dagger}(r, \omega) \\ \delta\phi_2^{\dagger}(r, \omega) \end{bmatrix} = - \begin{bmatrix} \delta S_1^{\dagger}(r, \omega) \\ \delta S_2^{\dagger}(r, \omega) \end{bmatrix} \tag{26}
$$

where

$$
\bar{\bar{\Sigma}}_{dyn}^{sub\dagger}(r, \omega) = \bar{\bar{\Sigma}}_{dyn}^{sub, T}(r, \omega) \tag{27}
$$

If the neutron noise is induced by perturbations of the macroscopic cross-sections and if there is no external neutron source, then splitting the time-dependent parameters into mean values and fluctuations according to Eq. (19), removing the static equations [i.e. Eq. (14) taken with $n = 0$], performing a temporal Fourier-transform, and neglecting second-order terms (linear theory), the following matrix equation is obtained:

$$
\begin{aligned}
& [\nabla \cdot \bar{\bar{D}}(r)\nabla + \bar{\bar{\Sigma}}_{dyn}^{crit}(r, \omega)] \times \begin{bmatrix} \delta\phi_1(r, \omega) \\ \delta\phi_2(r, \omega) \end{bmatrix} \\
& = \bar{\phi}_r(r)\delta\Sigma_r(r, \omega) + \bar{\bar{\phi}}_a(r) \begin{bmatrix} \delta\Sigma_{a,1}(r, \omega) \\ \delta\Sigma_{a,2}(r, \omega) \end{bmatrix} + \bar{\bar{\phi}}_f^{crit}(r, \omega) \begin{bmatrix} \delta\upsilon\Sigma_{f,1}(r, \omega) \\ \delta\upsilon\Sigma_{f,2}(r, \omega) \end{bmatrix}
\end{aligned} \tag{28}
$$

When deriving this equation for the neutron noise, the system is assumed to be critical without source, since the system is supposed to be stationary. This means that Eq. (14) is assumed to be verified with $k_0 = k_{eff} = 1$ for $m = 0$. In reality, it is very unlikely that the eigenvalue of the first eigenmode is exactly equal to unity. Furthermore, Eq. (28) has to be spatially discretized (see Section 1.3.4.1), and such a spatial discretization might also lead to a discretized system deviating from criticality, even if the non-discretized system was exactly critical. One way to cope with this difficulty is to renormalize the macroscopic fission cross-sections with k_{eff}, i.e. to replace in all equations $\upsilon\Sigma_{f,g}(r, t)$ by $\upsilon\Sigma_{f,g}(r, t)/k_{eff}$. This re-normalization guarantees that the discretized system is stationary. Therefore, the matrix $\bar{\bar{\Sigma}}_{dyn}^{crit}$ is defined as:

$$
\bar{\bar{\Sigma}}_{dyn}^{crit}(r, \omega) = \begin{bmatrix} -\Sigma_1^{crit}(r, \omega) & \dfrac{\upsilon\Sigma_{f,2,0}(r)}{k_{eff}}\left(1 - \dfrac{i\omega\beta}{i\omega + \lambda}\right) \\[3mm] \Sigma_{r,0}(r) & -\left(\Sigma_{a,2,0}(r) + \dfrac{i\omega}{v_2}\right) \end{bmatrix} \tag{29}
$$

with

19

$$\Sigma_1^{crit}(\boldsymbol{r}, \omega) = \Sigma_{a,1,0}(\boldsymbol{r}) + \frac{i\omega}{v_1} + \Sigma_{r,0}(\boldsymbol{r}) - \frac{\upsilon\Sigma_{f,1,0}(\boldsymbol{r})}{k_{eff}}\left(1 - \frac{i\omega\beta}{i\omega + \lambda}\right) \tag{30}$$

and the matrix $\overset{=}{\phi}_f^{crit}$ is given as:

$$\overset{=}{\phi}_f^{crit}(\boldsymbol{r}, \omega) = \begin{bmatrix} -\dfrac{\phi_{1,0}(\boldsymbol{r})}{k_{eff}}\left(1 - \dfrac{i\omega\beta}{i\omega + \lambda}\right) & -\dfrac{\phi_{2,0}(\boldsymbol{r})}{k_{eff}}\left(1 - \dfrac{i\omega\beta}{i\omega + \lambda}\right) \\ 0 & 0 \end{bmatrix} \tag{31}$$

The expressions for $\overset{-}{\phi}_r(\boldsymbol{r})$ and $\overset{=}{\phi}_a(\boldsymbol{r})$ are identical to the ones given by Eqs. (22) and (23), respectively. The right-hand side of Eq. (28) gives the neutron noise source, resulting from the fluctuations of the macroscopic cross-sections (removal, absorption, and fission) around their mean value. Although the effect of the fluctuations of the macroscopic fission cross-sections and of the macroscopic absorption cross-sections are given by two separate terms in Eq. (28), any fluctuation in the macroscopic fission cross-section has also an impact on the macroscopic absorption cross-section (since fission is a special type of absorption).

An adjoint problem corresponding to the forward problem as given by Eq. (28) can then be formally written as:

$$\left[\nabla \cdot \overset{=}{\overline{D}}(\boldsymbol{r})\nabla + \overset{=}{\Sigma}_{dyn}^{crit\dagger}(\boldsymbol{r}, \omega)\right] \times \begin{bmatrix} \delta\phi_1^{\dagger}(\boldsymbol{r}, \omega) \\ \delta\phi_2^{\dagger}(\boldsymbol{r}, \omega) \end{bmatrix} = -\begin{bmatrix} \delta S_1^{\dagger}(\boldsymbol{r}, \omega) \\ \delta S_2^{\dagger}(\boldsymbol{r}, \omega) \end{bmatrix} \tag{32}$$

where

$$\overset{=}{\Sigma}_{dyn}^{crit\dagger}(\boldsymbol{r}, \omega) = \overset{=}{\Sigma}_{dyn}^{crit,T}(\boldsymbol{r}, \omega) \tag{33}$$

1.3.4. Description of the numerical algorithms

In this section, the numerical algorithms developed and implemented into the tool are touched upon. First, the numerical scheme used for spatially discretizing the equations introduced in the previous section is presented. Thereafter, the numerical algorithms allowing solving the different types of equations (i.e. non-homogeneous equations and eigenvalue equations, respectively) are reported in detail.

1.3.4.1.   Algorithm used for the spatial discretisation

In the developed tool, any three-dimensional system is assumed to be made of adjacent volumes or nodes. In a Cartesian coordinate system, a given node n can be represented by the triplet of indexes (I, J, K), where the indexes I, J, and K refer to the x-, y-, and z-directions, respectively.

The equations derived in Section 1.3.3.2 and Section 1.3.3.3 will be spatially-averaged on each of these nodes. For the sake of simplicity, the possible dependence on frequency of the different terms appearing in these equations is dropped. The different notations and conventions used throughout this section are highlighted in FIG. 1-5 and FIG. 1-6.
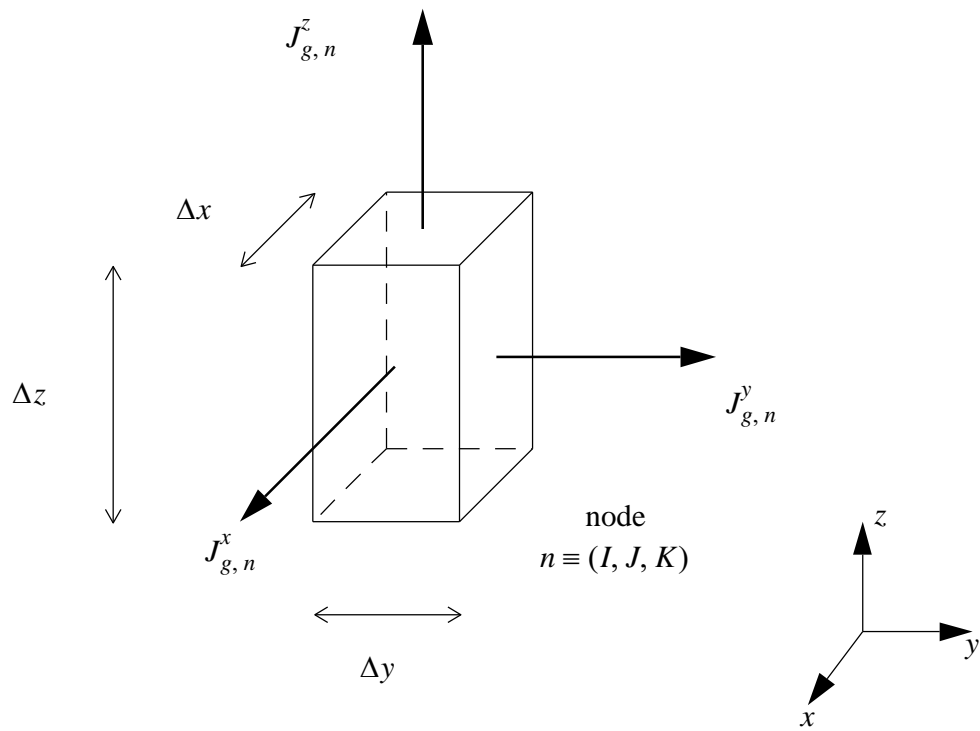
FIG. 1-5. Principles and conventions used for the spatial discretisation of a node n.
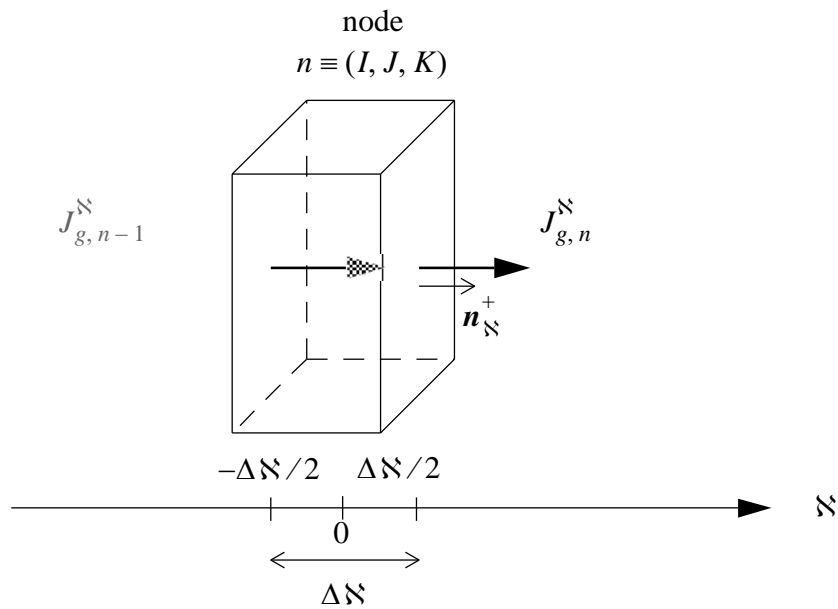
FIG. 1-6. Notations relative to a node n used in the spatial discretisation along a direction $\aleph$.

With Σ_g having the generic meaning of a macroscopic cross-section (either a static cross-section or its fluctuations), φ_g having the generic meaning of the scalar neutron flux (forward/adjoint static flux or eigenmode or neutron noise), and s_g having the generic meaning of a neutron source (forward/adjoint neutron source or its fluctuations), the following node-averaged quantities are defined:

$$\varphi_{g,n} = \frac{1}{V_n} \int_{V_n} \varphi_g(\boldsymbol{r}) d\boldsymbol{r} \tag{34}$$

$$s_{g,n} = \frac{1}{V_n} \int_{V_n} s_g(\boldsymbol{r}) d\boldsymbol{r} \tag{35}$$

$$\Sigma_{g,n} = \frac{\int_{V_n} \Sigma_g(\boldsymbol{r}) \varphi_g(\boldsymbol{r}) d\boldsymbol{r}}{\varphi_{g,n}} \tag{36}$$

where V_n represents the volume of the node n. This way of defining the node-averaged data, which preserves the actual reaction rates per node, is consistent with the group constants provided by any static core calculator.

When integrating each of the terms in the equations presented in Section 1.3.3.2 and Section 1.3.3.3 on a given node n, quantities of the form:

$$\frac{1}{V_n} \int_{V_n} \Sigma_g(\boldsymbol{r}) \varphi_g(\boldsymbol{r}) d\boldsymbol{r} = \Sigma_{g,n} \varphi_{g,n} \text{ and } \frac{1}{V_n} \int_{V_n} s_g(\boldsymbol{r}) d\boldsymbol{r} = s_{g,n}$$

then appear, as well as quantities of the form:

$$\frac{1}{V_n} \int_{V_n} \bar{\nabla} \cdot [D_{g,0}(\boldsymbol{r}) \nabla \varphi_g(\boldsymbol{r})] d\boldsymbol{r}$$

These last quantities cannot be directly expressed with the node-averaged quantities defined in Eqs. (34) and (36) due to the spatial operator $\bar{\nabla}$. Introducing the neutron current density vector $\boldsymbol{J}_g$ using Fick's law as:

$$\boldsymbol{J}_g(\boldsymbol{r}) = -D_{g,0}(\boldsymbol{r}) \bar{\nabla} \varphi_g(\boldsymbol{r}) \tag{37}$$

where, as before, $\boldsymbol{J}_g$ has a generic meaning (neutron current corresponding to the forward/adjoint static flux or eigenmode or neutron noise), one obtains, using Gauss' divergence theorem:

$$\frac{1}{V_n} \int_{V_n} \bar{\nabla} \cdot [D_{g,0}(\boldsymbol{r}) \bar{\nabla} \varphi_g(\boldsymbol{r})] d\boldsymbol{r} = - \sum_{\aleph = x,y,z} \frac{J_{g,n}^{\aleph} - J_{g,n-1}^{\aleph}}{\Delta \aleph} \tag{38}$$

In this equation, $\aleph$ represents the direction x, y, or z, $\Delta \aleph$ is the node width in the $\aleph$-direction. In the following, the subscripts "+1" and "-1" represent the nodes adjacent to the node n along the $\aleph$

-direction for increasing, decreasing, respectively, $\aleph$ values (see FIG. 1-6). Furthermore, the quantities appearing on the right-hand side of Eqs. (34) and (36) are defined as:

$$J_{g,n}^{\aleph} = \frac{1}{\Delta\Im \cdot \Delta\wp} \int_{-\Delta\Im/2}^{\Delta\Im/2} \int_{-\Delta\wp/2}^{\Delta\wp/2} J_g(\boldsymbol{r}_{\aleph}) \cdot \boldsymbol{n}_{\aleph}^{+} d\Im d\wp \tag{39}$$

and correspond to the surface-averaged net neutron current relative to the node n in the $\aleph$-direction, with $\boldsymbol{n}_{\aleph}^{+}$ being the outward normal relative to node n, as represented in FIG. 1-6. In the expression given by Eq. (39), $\boldsymbol{r}_{\aleph}$ thus represents the position of any point belonging to the surface normal to $\boldsymbol{n}_{\aleph}^{+}$ and defined as:

$$\begin{cases} \aleph = \Delta\aleph/2 \\ \Im \in [-\Delta\Im/2, \Delta\Im/2] \\ \wp \in [-\Delta\wp/2, \Delta\wp/2] \end{cases}$$

In order to get a solvable system of equations, a relationship between the surface-averaged neutron net current $J_{g,n}^{\aleph}$ and the node-averaged scalar neutron flux $\varphi_{g,n}$ needs to be derived. Using Fick's law and assuming that the scalar neutron flux in the middle of the nodes is equal to the node-averaged scalar neutron flux (box-scheme), the surface-averaged net neutron currents are approximated by the following formula [12]:

$$J_{g,n}^{\aleph} = -D_{g,0,n}\frac{\varphi_g^b - \varphi_{g,n}}{\Delta\aleph/2} \tag{40}$$

for node n, where φ_g^b represents the scalar neutron flux at the node boundary located in $\Delta\aleph/2$ for node n. Such a net neutron current can also be evaluated from the volume-averaged scalar neutron flux in the adjacent node $n+1$ as:

$$J_{g,n}^{\aleph} = -D_{g,0,n+1}\frac{\varphi_{g,n+1} - \varphi_g^b}{\Delta\aleph/2} \tag{41}$$

where φ_g^b is the scalar neutron flux at the node boundary located in $-\Delta\aleph/2$ for node $n+1$. In the derivation of Eqs. (40) and (41), the continuity of the neutron scalar flux and of the net neutron current at the boundary between the nodes n and $n+1$ is preserved. Combining these two equations allows determining the scalar neutron flux at the interface as:

$$\varphi_g^b = \frac{D_{g,0,n}\varphi_{g,n} + D_{g,0,n+1}\varphi_{g,n+1}}{D_{g,0,n} + D_{g,0,n+1}} \tag{42}$$

Using this expression in Eq. (40) leads to:

$$J_{g,n}^{\aleph} = -\frac{D_{g,0,n}D_{g,0,n+1}}{D_{g,0,n} + D_{g,0,n+1}} \times \frac{\varphi_{g,n+1} - \varphi_{g,n}}{\Delta\aleph/2} \tag{43}$$

Utilizing this result in Eq. (38) finally gives:

$$\frac{1}{V_n}\int_{V_n} \nabla \cdot [D_{g,0}(\boldsymbol{r})\nabla\varphi_g(\boldsymbol{r})]d\boldsymbol{r} = \sum_{\aleph = x,y,z}(a^{\aleph}_{g,n}\varphi_{g,n} + b^{\aleph}_{g,n}\varphi_{g,n+1} + c^{\aleph}_{g,n}\varphi_{g,n-1}) \quad (44)$$

with

$$a^{\aleph}_{g,n} = \frac{2D_{g,0,n-1}D_{g,0,n}}{(\Delta\aleph)^2(D_{g,0,n-1}+D_{g,0,n})} + \frac{2D_{g,0,n}D_{g,0,n+1}}{(\Delta\aleph)^2(D_{g,0,n}+D_{g,0,n+1})} \quad (45)$$

$$b^{\aleph}_{g,n} = -\frac{2D_{g,0,n}D_{g,0,n+1}}{(\Delta\aleph)^2(D_{g,0,n}+D_{g,0,n+1})} \quad (46)$$

$$c^{\aleph}_{g,n} = -\frac{2D_{g,0,n-1}D_{g,0,n}}{(\Delta\aleph)^2(D_{g,0,n-1}+D_{g,0,n})} \quad (47)$$

The expressions of the above coefficients are only valid when the nodes n-1, n, and $n+1$ exist. At the boundaries of the system, boundary conditions need to be defined. In the developed computational tool, Marshak boundary conditions are used. In the case of multi-group diffusion theory, such boundary conditions read as:

$$\boldsymbol{J}_g(\boldsymbol{r}_{\aleph}) \cdot \boldsymbol{n}_{\aleph} = \frac{1}{2}\varphi_g^b \quad (48)$$

where $\boldsymbol{r}_{\aleph}$ represents a spatial point on the boundary with $\boldsymbol{n}_{\aleph}$ being the outward normal to the boundary and φ_g^b represents the scalar neutron flux at the boundary. Assuming again that the scalar neutron flux in the middle of the nodes is equal to the node-averaged scalar neutron flux (box-scheme) and using Fick's law, the neutron current can be approximated and one then obtains:

– When the node n-1 does not exist:

$$\frac{1}{2}\varphi_g^b = D_{g,0,n}\frac{\varphi_{g,n}-\varphi_g^b}{\Delta\aleph/2} \quad (49)$$

– When the node $n+1$ does not exist:

$$\frac{1}{2}\varphi_g^b = -D_{g,0,n}\frac{\varphi_g^b-\varphi_{g,n}}{\Delta\aleph/2} \quad (50)$$

When the node n-1 does not exist, one finds, using Eq. (49), that:

$$\varphi_g^b = \frac{\varphi_{g,n}}{1+\dfrac{\Delta\aleph}{4D_{g,0,n}}} \quad (51)$$

from which one deduces, using Fick's law, that:

$$J_{g, n-1}^{\aleph} = -D_{g, 0, n}\frac{\varphi_{g, n} - \varphi_g^b}{\Delta\aleph/2} = -\frac{1/2}{1 + \dfrac{\Delta\aleph}{4D_{g, 0, n}}}\varphi_{g, n} \tag{52}$$

The coupling coefficients appearing in Eq. (44) are thus expressed as:

$$a_{g, n}^{\aleph} = \frac{2D_{g, 0, n}D_{g, 0, n+1}}{(\Delta\aleph)^2(D_{g, 0, n} + D_{g, 0, n+1})} + \frac{1/2}{\Delta\aleph + \dfrac{(\Delta\aleph)^2}{4D_{g, 0, n}}} \tag{53}$$

$$b_{g, n}^{\aleph} = -\frac{2D_{g, 0, n}D_{g, 0, n+1}}{(\Delta\aleph)^2(D_{g, 0, n} + D_{g, 0, n+1})} \tag{54}$$

$$c_{g, n}^{\aleph} = 0 \tag{55}$$

Likewise, when the node $n+1$ does not exist, one finds, using Eq. (50), that:

$$\varphi_g^b = \frac{\varphi_{g, n}}{1 + \dfrac{\Delta\aleph}{4D_{g, 0, n}}} \tag{56}$$

from which one deduces, using Fick's law, that:

$$J_{g, n}^{\aleph} = -D_{g, 0, n}\frac{\varphi_g^b - \varphi_{g, n}}{\Delta\aleph/2} = \frac{1/2}{1 + \dfrac{\Delta\aleph}{4D_{g, 0, n}}}\varphi_{g, n} \tag{57}$$

The coupling coefficients appearing in Eq. (44) are thus expressed as:

$$a_{g, n}^{\aleph} = \frac{2D_{g, 0, n-1}D_{g, 0, n}}{(\Delta\aleph)^2(D_{g, 0, n-1} + D_{g, 0, n})} + \frac{1/2}{\Delta\aleph + \dfrac{(\Delta\aleph)^2}{4D_{g, 0, n}}} \tag{58}$$

$$b_{g, n}^{\aleph} = 0 \tag{59}$$

$$c_{g, n}^{\aleph} = -\frac{2D_{g, 0, n-1}D_{g, 0, n}}{(\Delta\aleph)^2(D_{g, 0, n-1} + D_{g, 0, n})} \tag{60}$$

1.3.4.2.   *Algorithm used for solving non-homogeneous equations*

After applying the spatial discretization presented in Section 1.3.4.1, the non-homogeneous equations [i.e. Eqs. (5), (12), (20), (26), (28), and (32)] reduce to the following generic form:

$$\overline{\overline{M}} \times \begin{bmatrix} \overline{\varphi}_1 \\ \overline{\varphi}_2 \end{bmatrix} = \begin{bmatrix} \overline{s}_1 \\ \overline{s}_2 \end{bmatrix} \tag{61}$$

where $\overline{\varphi}_1$ and $\overline{\varphi}_2$ are column vectors representing the spatially-discretized generic scalar neutron flux (forward/adjoint static flux or neutron noise) in the fast and thermal groups, respectively, and $\overline{s}_1$ and $\overline{s}_2$ are column vectors representing the spatially-discretized generic neutron source (forward/adjoint neutron source or its fluctuations) or the spatially-discretized fluctuation of the macroscopic cross-sections, in the fast and thermal groups, respectively. If the system was discretized using N nodes, then $\overline{\varphi}_1$, $\overline{\varphi}_2$, $\overline{s}_1$, and $\overline{s}_2$ are N column-vectors, and $\overline{\overline{M}}$ is a $2N$x$2N$-matrix.

The solution to Eq. (61) is readily obtained as:

$$\begin{bmatrix} \overline{\varphi}_1 \\ \overline{\varphi}_2 \end{bmatrix} = \overline{\overline{M}}^{-1} \times \begin{bmatrix} \overline{s}_1 \\ \overline{s}_2 \end{bmatrix} \tag{62}$$

Due to the very large number of nodes used in reactor calculations, the direct determination of the inverse of $\overline{\overline{M}}$ is usually impossible. Instead, the matrix $\overline{\overline{M}}$, which is sparse, is first factorized into a unit lower triangular matrix $\overline{\overline{L}}$ and an upper triangular matrix $\overline{\overline{U}}$ such that:

$$\overline{\overline{L}} \times \overline{\overline{U}} = \overline{\overline{P}} \times \overline{\overline{M}} \times \overline{\overline{Q}} \tag{63}$$

where $\overline{\overline{P}}$ is a row permutation matrix and $\overline{\overline{Q}}$ is a column reordering matrix. The matrices $\overline{\overline{P}}$ and $\overline{\overline{Q}}$ are unitary matrices, i.e. they fulfill the following relationships:

$$\overline{\overline{P}} \times \overline{\overline{P}}^T = \overline{\overline{I}} = \overline{\overline{P}}^T \times \overline{\overline{P}} \text{ and } \overline{\overline{Q}} \times \overline{\overline{Q}}^T = \overline{\overline{I}} = \overline{\overline{Q}}^T \times \overline{\overline{Q}} \tag{64}$$

The row permutation and column reordering matrices are determined so that the lower triangular matrix $\overline{\overline{L}}$ and the upper triangular matrix $\overline{\overline{U}}$ are also sparse, in order to lower the requirements in data storage. Without row permutation and column reordering, the matrices $\overline{\overline{L}}$ and $\overline{\overline{U}}$ would be full. The matrix factorization as given by Eq. (63) is directly performed in *MatLab* via the built-in UMFPACK package [13].

Equation (61), which is rewritten as:

$$\overline{\overline{M}} \times \overline{\varphi} = \overline{s}, \tag{65}$$

can be simply solved by noticing from Eq. (63) that:

$$\overline{\overline{L}} \times \overline{\overline{U}} \times \overline{\overline{Q}}^{-1} = \overline{\overline{P}} \times \overline{\overline{M}} \tag{66}$$

Multiplying Eq. (65) by $\overline{\overline{P}}$ and using Eq. (66), one finds that:

$$\bar{\bar{P}} \times \bar{\bar{M}} \times \bar{\varphi} \ = \ \bar{\bar{L}} \times \bar{\bar{U}} \times \bar{\bar{Q}}^{-1} \times \bar{\varphi} \ = \ \bar{\bar{P}} \times \bar{s} \tag{67}$$

Since $\bar{\bar{L}}$ is a lower triangular matrix, $\bar{\bar{U}} \times \bar{\bar{Q}}^{-1} \times \bar{\varphi}$ can be simply obtained by forward substitution, which can be formally written as:

$$\bar{\bar{U}} \times \bar{\bar{Q}}^{-1} \times \bar{\varphi} \ = \ \bar{\bar{L}} \backslash (\bar{\bar{P}} \times \bar{s}) \tag{68}$$

Likewise, since $\bar{\bar{U}}$ is an upper triangular matrix, $\bar{\bar{Q}}^{-1} \times \bar{\varphi}$ can be simply obtained by backward substitution, which can be formally written as:

$$\bar{\bar{Q}}^{-1} \times \bar{\varphi} \ = \ \bar{\bar{U}} \backslash [\bar{\bar{L}} \backslash (\bar{\bar{P}} \times \bar{s})] \tag{69}$$

from which one finally obtains:

$$\bar{\varphi} \ = \ \bar{\bar{Q}} \times \{ \bar{\bar{U}} \backslash [\bar{\bar{L}} \backslash (\bar{\bar{P}} \times \bar{s})] \} \tag{70}$$

1.3.4.3.   Algorithm used for solving eigenvalue equations

After applying the spatial discretization presented in Section 1.3.4.1, the eigenvalue equations [i.e. Eqs. (14) and (17)] reduce to the following generic form:

$$\bar{\bar{M}} \times \begin{bmatrix} \bar{\phi}_{1,m} \\ \bar{\phi}_{2,m} \end{bmatrix} \ = \ \frac{1}{k_m} \bar{\bar{F}} \times \begin{bmatrix} \bar{\phi}_{1,m} \\ \bar{\phi}_{2,m} \end{bmatrix} \tag{71}$$

where $\bar{\phi}_{1,m}$ and $\bar{\phi}_{2,m}$ are column vectors representing the spatially-discretized eigenfunction corresponding to mode m in the fast and thermal groups, respectively. If the system was discretized using N nodes, then $\bar{\phi}_{1,m}$ and $\bar{\phi}_{2,m}$ are N column-vectors, and $\bar{\bar{M}}$ and $\bar{\bar{F}}$ are $2N$x$2N$-matrices. Extending the inner product introduced in Eq. (9) to spatially-discretized cases as:

$$\left\langle \begin{bmatrix} \bar{\psi}_1 \\ \bar{\psi}_2 \end{bmatrix}, \begin{bmatrix} \bar{\varphi}_1 \\ \bar{\varphi}_2 \end{bmatrix} \right\rangle \ = \ \sum_n V_n \times (\psi_{1,n}\varphi_{1,n} + \psi_{2,n}\varphi_{2,n}) \tag{72}$$

it could be easily demonstrated that the following orthogonality relationship holds:

$$\left\langle \begin{bmatrix} \bar{\phi}_{1,m}^{\dagger} \\ \bar{\phi}_{2,m}^{\dagger} \end{bmatrix}, \bar{\bar{F}} \times \begin{bmatrix} \bar{\phi}_{1,m'} \\ \bar{\phi}_{2,m'} \end{bmatrix} \right\rangle \ = \ \left\langle \bar{\bar{F}}^T \times \begin{bmatrix} \bar{\phi}_{1,m}^{\dagger} \\ \bar{\phi}_{2,m}^{\dagger} \end{bmatrix}, \begin{bmatrix} \bar{\phi}_{1,m'} \\ \bar{\phi}_{2,m'} \end{bmatrix} \right\rangle \ = \ 0, \text{ if } m \neq m' \tag{73}$$

where m and m' represents the mode (i.e. eigenfunction) numbers.

Iterative techniques are required to solve Eq. (71), which can be rewritten as:

$$\overline{\overline{A}} \times \bar{x}_m = k_m \bar{x}_m \qquad (74)$$

with

$$\overline{\overline{A}} = \overline{\overline{M}}^{-1} \times \overline{\overline{F}} \qquad (75)$$

and

$$\bar{x}_m = \begin{bmatrix} \bar{\phi}_{1,m} \\ \bar{\phi}_{2,m} \end{bmatrix} \qquad (76)$$

As earlier explained in Section 1.3.4.2, the calculation of the inverse of $\overline{\overline{M}}$ is avoided by first performing a LU factorization of $\overline{\overline{M}}$ will full pivoting as:

$$\overline{\overline{L}} \times \overline{\overline{U}} = \overline{\overline{P}} \times \overline{\overline{M}} \times \overline{\overline{Q}} \qquad (77)$$

leading for Eq. (74) to:

$$\overline{\overline{Q}} \times \left\{ \overline{\overline{U}} \backslash [\overline{\overline{L}} \backslash (\overline{\overline{P}} \times \overline{\overline{F}} \times \bar{x}_m)] \right\} = k_m \bar{x}_m \qquad (78)$$

Numerous techniques exist for solving the eigenvalue equation given by Eq. (74). They are all based on the power iteration method, which is first recalled hereafter [12].

The power iteration method consists in determining a new and better estimate of the solution $(\bar{x}_m, k_m)$ from a previous estimate. If p represents the iteration number, the power iteration method simply reads as:

$$\bar{x}_m^{(p)} = \frac{1}{k_m^{(p-1)}} \overline{\overline{A}} \times \bar{x}_m^{(p-1)} \qquad (79)$$

The power iteration method can then be seen as an operator $\overline{\overline{A}}$ acting on the vector $\bar{x}_m^{(p-1)}$. When the iterative scheme converges, Eq. (79) becomes:

$$\bar{x}_m^{(\infty)} = \frac{1}{k_m^{(\infty)}} \overline{\overline{A}} \times \bar{x}_m^{(\infty)} \qquad (80)$$

from which one deduces that:

$$k_m^{(\infty)} = \frac{\bar{x}_m^{(\infty),T} \times \overline{\overline{A}} \times \bar{x}_m^{(\infty)}}{\bar{x}_m^{(\infty),T} \times \bar{x}_m^{(\infty)}} \qquad (81)$$

28

Based on this expression for the converged eigenvalue, the new iterate of k_m can be estimated, once the new iterate of the vector $\bar{x}_m$ has been determined, as:

$$k_m^{(p)} = \frac{\bar{x}_m^{-(p-1),T} \times \bar{\bar{A}} \times \bar{x}_m^{-(p-1)}}{\bar{x}_m^{-(p-1),T} \times \bar{x}_m^{-(p-1)}} = k_m^{(p-1)} \times \frac{\bar{x}_m^{-(p-1),T} \times \bar{x}_m^{-(p)}}{\bar{x}_m^{-(p-1),T} \times \bar{x}_m^{-(p-1)}} \tag{82}$$

where the last equality was obtained using Eq. (79). The iterative scheme given by Eqs. (79) and (82) completely defines the power iteration method. In the following, it will be demonstrated that the power iteration method converges to the eigenvector of the iterative matrix $\bar{\bar{A}}$ having the largest eigenvalue. When the power iteration method is applied to any initial start vector $\bar{x}_m^{(0)}$ with a given value for $k_m^{(0)}$, the p iterate can be written, using Eq. (79), as:

$$\bar{x}_m^{-(p)} = \frac{\bar{\bar{A}}^p \times \bar{x}_m^{-(0)}}{k_m^{(p-1)}k_m^{(p-2)}...k_m^{(0)}} \tag{83}$$

The initial vector can be expanded on the eigenvectors $\bar{x}_l$ of the matrix $\bar{\bar{A}}$ as:

$$\bar{x}_m^{-(0)} = \sum_l \alpha_l \bar{x}_l \tag{84}$$

with

$$\alpha_l = \bar{x}_l^{-T} \times \bar{x}_m^{-(0)} \tag{85}$$

Using Eqs. (84) and (74) into Eq. (83) leads to:

$$\bar{x}_m^{-(p)} = \frac{\sum_l \alpha_l k_l^p \bar{x}_l}{k_m^{(p-1)}k_m^{(p-2)}...k_m^{(0)}} = \frac{\alpha_0 k_0^p}{k_m^{(p-1)}k_m^{(p-2)}...k_m^{(0)}} \times \left[\bar{x}_0 + \sum_{l \geq 1} \frac{\alpha_l}{\alpha_0}\left(\frac{k_l}{k_0}\right)^p \bar{x}_l\right] \tag{86}$$

According to Eq. (16), one has:

$$\frac{k_l}{k_0} < 1, \text{ for } l \geq 1 \tag{87}$$

which results, for Eq. (86), in:

$$\lim_{p \to \infty} \bar{x}_m^{-(p)} = \frac{\alpha_0 k_0^p}{k_m^{(p-1)}k_m^{(p-2)}...k_m^{(0)}} \bar{x}_0 \tag{88}$$

Using Eq. (86) into Eq. (82) also leads to:

29

$$k_m^{(p)} = k_m^{(p-1)} \times \frac{\bar{x}_m^{-(p-1),T} \times \dfrac{\alpha_0 k_0^p}{k_m^{(p-1)} k_m^{(p-2)} \dots k_m^{(0)}} \times \left[\bar{x}_0 + \displaystyle\sum_{l \geq 1} \frac{\alpha_l}{\alpha_0} \left(\frac{k_l}{k_0} \right)^p \bar{x}_l \right]}{\bar{x}_m^{-(p-1),T} \times \dfrac{\alpha_0 k_0^{p-1}}{k_m^{(p-2)} \dots k_m^{(0)}} \times \left[\bar{x}_0 + \displaystyle\sum_{l \geq 1} \frac{\alpha_l}{\alpha_0} \left(\frac{k_l}{k_0} \right)^{p-1} \bar{x}_l \right]} \tag{89}$$

or

$$k_m^{(p)} = k_0 \times \frac{\bar{x}_m^{-(p-1),T} \times \left[\bar{x}_0 + \displaystyle\sum_{l \geq 1} \frac{\alpha_l}{\alpha_0} \left(\frac{k_l}{k_0} \right)^p \bar{x}_l \right]}{\bar{x}_m^{-(p-1),T} \times \left[\bar{x}_0 + \displaystyle\sum_{l \geq 1} \frac{\alpha_l}{\alpha_0} \left(\frac{k_l}{k_0} \right)^{p-1} \bar{x}_l \right]} \tag{90}$$

Because of Eq. (87), one thus finds that:

$$\lim_{p \to \infty} k_m^{(p)} = k_0 \tag{91}$$

Equations (88) and (91) therefore mean that the power iteration method, as implemented in Eqs. (79) and (82) leads to the solution corresponding to the fundamental mode, i.e. $(\bar{x}_0, k_0)$. The convergence of the power iteration method is directly related to the ratio between the higher eigenvalues and the first eigenvalue, i.e. k_l / k_0. In the case of nuclear reactor calculations, the eigenvalues are usually clustered eigenvalues, i.e. quite close to each other. This decreases the convergence rate of the power iteration method. In the developed computational tool, other techniques have been implemented in order to be able to determine any eigenmode m (not only the fundamental mode) and to speed up the convergence rate of the iterations. Namely, the explicitly-restarted Arnoldi method and the power iteration method with Wielandt's shift have been used.

Explicitly-restarted Arnoldi method

Some of the most efficient techniques to solve eigenvalue problems are based on Krylov subspace methods. The explicitly-restarted Arnoldi method belongs to this class of techniques [14]. The Arnoldi method is based on the fact that useful information is lost during the application of the classical power iteration method. Namely, only the latest estimates of the eigenvector and eigenvalue are used for subsequently calculating a new estimate of the eigenvector and eigenvalue. In the Arnoldi method instead, a Krylov subspace containing an estimate of the eigenvectors of the matrix $\bar{\bar{A}}$ obtained during the application of the power iteration method during t iterations is first constructed, i.e. the following space is constructed:

$$\Re_t(\bar{\bar{A}}, \bar{v}) = \text{span}\left\{ \bar{v}, \bar{\bar{A}} \times \bar{v}, \bar{\bar{A}}^2 \times \bar{v}, \dots, \bar{\bar{A}}^{t-1} \times \bar{v} \right\} \tag{92}$$

with

$$t \ll \text{dimension of } \bar{\bar{A}} \tag{93}$$

Thereafter, an orthonormal basis of this subspace is determined. Finally, the eigenvectors/eigenvalues of this orthonormal basis are determined. It will be demonstrated thereafter that the eigenvectors of the matrix representing the projection of the original matrix on the Krylov subspace can be used for determining the eigenvectors of the original matrix, and therefore the eigenvectors of $\bar{\bar{A}}$ can be estimated from the eigenvectors of the matrix representing the projection of the original matrix on the Krylov subspace. The main advantage of this procedure is the fact that the projection matrix is an Hessenberg matrix of size t x t, i.e. much smaller than the size of the original matrix. Consequently, the determination of the t eigenvectors and corresponding eigenvalues is relatively easy.

The iterative scheme of the explicitly-restarted Arnoldi method can be sketched as follows [15], [16]:

– First, an orthogonal basis of $\mathfrak{R}_t(\bar{\bar{A}}, \bar{v})$ using the Gram-Schmidt orthogonalization process is constructed as detailed in Algorithm 1. If a breakdown of the algorithm occurs at step j (when the norm of $\bar{w}_{:,j}$ is equal to zero), then the projection on the subspace $\mathfrak{R}_j$ is exact. The matrix $\bar{\bar{V}}_t = (\bar{v}_{:,1}, \bar{v}_{:,2}, ..., \bar{v}_{:,t})$ then represents an orthogonal basis of $\mathfrak{R}_t(\bar{\bar{A}}, \bar{v})$. In addition, this first step also results in the construction of a Hessenberg matrix of dimension t+1 x t:

$$\bar{\bar{H}} = (h_{i,j})_{1 \le i \le t+1, 1 \le j \le t} = \begin{bmatrix} h_{1,1} & h_{1,2} & h_{1,3} & ... & h_{1,t} \\ h_{2,1} & h_{2,2} & h_{1,1} & ... & h_{2,t} \\ 0 & h_{3,2} & h_{3,3} & ... & h_{3,t} \\ ... & 0 & ... & ... & ... \\ 0 & ... & 0 & h_{t,t-1} & h_{t,t} \\ 0 & ... & ... & 0 & h_{t+1,t} \end{bmatrix} \tag{94}$$

Defining the reduced Hessenberg matrix $\bar{\bar{H}}_r$ as the original Hessenberg matrix $\bar{\bar{H}}$ deprived from its last row, i.e.

$$\bar{\bar{H}}_r = (h_{i,j})_{1 \le i \le t, 1 \le j \le t} = \begin{bmatrix} h_{1,1} & h_{1,2} & h_{1,3} & ... & h_{1,t} \\ h_{2,1} & h_{2,2} & h_{1,1} & ... & h_{2,t} \\ 0 & h_{3,2} & h_{3,3} & ... & h_{3,t} \\ ... & 0 & ... & ... & ... \\ 0 & ... & 0 & h_{t,t-1} & h_{t,t} \end{bmatrix} \tag{95}$$

one finds by the application of Algorithm 1 that [15]:

$$\bar{\bar{A}} \times \bar{v}_{:,j} = \sum_{i=1}^{j+1} h_{i,j} \bar{v}_{:,i} \text{ for } j = 1, 2, ..., t \tag{96}$$

resulting in:

$$\bar{\bar{A}} \times \bar{\bar{V}}_t = \bar{\bar{V}}_{t+1} \times \bar{\bar{H}} = \bar{\bar{V}}_t \times \bar{\bar{H}}_r + \bar{w}_{:,t} \bar{e}_t^T \tag{97}$$

where $\bar{e}_t$ represents the t-th column of the t x t identity matrix. Making use of the orthonormality of $\{\bar{v}_{:,1}, \bar{v}_{:,2}, ..., \bar{v}_{:,t}\}$, one finally obtains that:

$$\overline{\overline{V}}_t^T \times \overline{\overline{A}} \times \overline{\overline{V}}_t = \overline{\overline{H}}_r \tag{98}$$

```
choice of an initial vector q̄ and of the subspace dimension t
normalization of the vector q̄, i.e. v̄:,1 = q̄/‖q̄‖₂
for j=1 to t
    w̄:,j = Ā × v̄:,j
    for i=1 to j
        orthogonal projection of w̄:,j on the previous v̄:,i, i.e.
        h_{i,j} = w̄:,j^T × v̄:,i
        deprivation of w̄:,j of its component on v̄:,i, i.e.
        w̄:,j − h_{i,j}v̄:,i → w̄:,j
    end
    h_{j+1,j} = ‖w̄:,j‖₂
    If h_{j+1,j} = 0 then stop
    v̄:,j+1 = w̄:,j/‖w̄:,j‖₂
end
```

Algorithm 1   Gram-Schmidt orthogonalization procedure of the matrix $\overline{\overline{A}}$ in the Arnoldi method.

Thereafter, the pairs of eigenvectors $\bar{x}_{:,j}$ and eigenvalues λ_j of the reduced Hessenberg matrix $\overline{\overline{H}}_r$ (for $1 \le j \le t$) are determined, resulting in:

$$\overline{\overline{H}}_r \times \overline{\overline{X}} = \overline{\overline{X}} \times \overline{\overline{\lambda}} \tag{99}$$

with

$$\overline{\overline{X}} = (\bar{x}_{:,1}, \bar{x}_{:,2}, ..., \bar{x}_{:,t}) \tag{100}$$

and

$$\overline{\overline{\lambda}} = \begin{bmatrix} \lambda_1 & 0 & ... & ... & 0 \\ 0 & \lambda_2 & 0 & ... & ... \\ ... & 0 & ... & 0 & ... \\ ... & ... & 0 & \lambda_{t-1} & 0 \\ 0 & ... & ... & 0 & \lambda_t \end{bmatrix} \tag{101}$$

Since the reduced Hessenberg matrix is chosen to be of small size, the determination of its eigenvectors and eigenvalues is relatively easy. Such a determination is directly carried out in MatLab via the built-in LAPACK package [17].

– Combining Eqs. (98) and (99), one notices that:

$$\overline{\overline{V}}_t^T \times \overline{\overline{A}} \times \overline{\overline{V}}_t \times \overline{\overline{X}} = \overline{\overline{H}}_r \times \overline{\overline{X}} = \overline{\overline{X}} \times \overline{\overline{\lambda}} \tag{102}$$

Making use again of the orthonormality of $\{\bar{v}_{:,1}, \bar{v}_{:,2}, ..., \bar{v}_{:,t}\}$, one finally obtains:

$$\overline{\overline{V}}_t \times \overline{\overline{V}}_t^T \times \overline{\overline{A}} \times \overline{\overline{V}}_t \times \overline{\overline{X}} = \overline{\overline{A}} \times \overline{\overline{V}}_t \times \overline{\overline{X}} = \overline{\overline{V}}_t \times \overline{\overline{X}} \times \overline{\overline{\lambda}} \tag{103}$$

Equation (103) demonstrates that the eigenvectors of $\overline{\overline{A}}$ are given by the columns of $\overline{\overline{V_t}} \times \overline{\overline{X}}$ and the corresponding eigenvalues are then $\overline{\overline{\lambda}}$.

– Since the eigenvalues of the reduced Hessenberg matrix $\overline{\overline{H}}_r$ might be bad approximations of the eigenvalues of the original matrix $\overline{\overline{A}}$, especially if the subspace dimension t is kept small, the algorithm is (explicitly) restarted with a linear combination of the eigenvectors of $\overline{\overline{A}}$ until some convergence criteria on the eigenvectors are fulfilled.

The explicitly-restarted Arnoldi method is an extremely efficient method for calculating the eigenfunctions/eigenvalues in a minimum computational time, since several eigenmodes can be estimated simultaneously. Nevertheless, it cannot be proved that the eigenvalues of $\overline{\overline{H}}_r$ will converge to the extreme eigenvalues of $\overline{\overline{A}}$ when $\overline{\overline{A}}$ is non-symmetric (even if such a convergence is usually observed) [18]. In order to circumvent possible convergence problem, a power iteration method using Wielandt's shift technique was also implemented in the numerical tool, and is explained in the following.

Power iteration method with Wielandt's shift technique

The basic idea in Wielandt's shift technique is to modify the original problem as given by Eq. (71) into the following one [12]:

$$\left(\overline{\overline{M}} - \frac{1}{k_{est}} \overline{\overline{F}} \right) \times \begin{bmatrix} \bar{\phi}_{1,m} \\ \bar{\phi}_{2,m} \end{bmatrix} = \left(\frac{1}{k_m} - \frac{1}{k_{est}} \right) \overline{\overline{F}} \times \begin{bmatrix} \bar{\phi}_{1,m} \\ \bar{\phi}_{2,m} \end{bmatrix} \tag{104}$$

where k_{est} is a known (input) parameter. Eq. (104) can be rewritten as:

$$\overline{\overline{A}}_W \times \bar{x}_m = \alpha_m \bar{x}_m \tag{105}$$

with

$$\overline{\overline{A}}_W = \left(\overline{\overline{M}} - \frac{1}{k_{est}} \overline{\overline{F}} \right)^{-1} \times \overline{\overline{F}} \tag{106}$$

$$\frac{1}{\alpha_m} = \frac{1}{k_m} - \frac{1}{k_{est}} \tag{107}$$

and

$$\bar{x}_m = \begin{bmatrix} \bar{\phi}_{1,m} \\ \bar{\phi}_{2,m} \end{bmatrix} \tag{108}$$

As earlier explained in Section 1.3.4.2, the calculation of the inverse of $\overline{\overline{M}} - \dfrac{1}{k_{est}} \overline{\overline{F}}$ is avoided by first performing a LU factorization of $\overline{\overline{M}} - \dfrac{1}{k_{est}} \overline{\overline{F}}$ will full pivoting as:

$$\overline{\overline{L}} \times \overline{\overline{U}} = \overline{\overline{P}} \times \left(\overline{\overline{M}} - \frac{1}{k_{est}} \overline{\overline{F}} \right) \times \overline{\overline{Q}} \tag{109}$$

leading for Eq. (105) to:

$$\overline{\overline{Q}} \times \left\{ \overline{\overline{U}} \backslash [\overline{\overline{L}} \backslash (\overline{\overline{P}} \times \overline{\overline{F}} \times \bar{x}_m)] \right\} = \alpha_m \bar{x}_m \tag{110}$$

The power iteration method, which was earlier presented, can be applied to the modified equation (105), thus leading to the following iterative scheme:

$$\bar{x}_m^{(p)} = \frac{1}{\alpha_m^{(p-1)}} \overline{\overline{A}}_W \times \bar{x}_m^{(p-1)} \tag{111}$$

and

$$\alpha_m^{(p)} = \frac{\bar{x}_m^{(p-1),T} \times \overline{\overline{A}}_W \times \bar{x}_m^{(p-1)}}{\bar{x}_m^{(p-1),T} \times \bar{x}_m^{(p-1)}} = \alpha_m^{(p-1)} \times \frac{\bar{x}_m^{(p-1),T} \times \bar{x}_m^{(p)}}{\bar{x}_m^{(p-1),T} \times \bar{x}_m^{(p-1)}} \tag{112}$$

Using Eq. (107), one also obtains:

$$k_m^{(p)} = \left[\frac{1}{k_{est}} + \left(\frac{1}{k_m^{(p-1)}} - \frac{1}{k_{est}} \right) \times \frac{\bar{x}_m^{(p-1),T} \times \bar{x}_m^{(p-1)}}{\bar{x}_m^{(p-1),T} \times \bar{x}_m^{(p)}} \right]^{-1} \tag{113}$$

The iterative scheme given by Eqs. (111) and (113) completely defines the power iteration method using Wielandt's shift technique. In the following, it will be demonstrated that this iterative scheme converges to the eigenvector of the matrix $\overline{\overline{A}}$ having the eigenvalue closest to k_{est}. When the iteration method is applied to any initial start vector $\bar{x}_m^{(0)}$ with a given value for $\alpha_m^{(0)}$, the p iterate can be written, using Eq. (111), as:

$$\bar{x}_m^{(p)} = \frac{\overline{\overline{A}}_W^p \times \bar{x}_m^{(0)}}{\alpha_m^{(p-1)} \alpha_m^{(p-2)} ... \alpha_m^{(0)}} \tag{114}$$

The initial vector can be expanded on the eigenvectors $\bar{x}_l$ of the matrix $\overline{\overline{A}}$ as:

$$\bar{x}_m^{(0)} = \sum_l \beta_l \bar{x}_l \tag{115}$$

with

$$\beta_l = \bar{x}_l^T \cdot \bar{x}_m^{(0)} \tag{116}$$

It can also be noticed that the eigenvectors $\bar{x}_l$ of the matrix $\bar{\bar{A}}$ are also eigenvectors of the matrix $\bar{\bar{A}}_W$, i.e. one has both:

$$\bar{\bar{A}} \times \bar{x}_l = k_l \bar{x}_l \tag{117}$$

and

$$\bar{\bar{A}}_W \times \bar{x}_l = \alpha_l \bar{x}_l \tag{118}$$

Using Eqs. (115) and (118) into Eq. (114) leads to:

$$\bar{x}_m^{(p)} = \frac{\sum_l \beta_l \alpha_l^p \bar{x}_l}{\alpha_m^{(p-1)} \alpha_m^{(p-2)} \ldots \alpha_m^{(0)}} = \frac{\beta_q \alpha_q^p}{\alpha_m^{(p-1)} \alpha_m^{(p-2)} \ldots \alpha_m^{(0)}} \times \left[\bar{x}_q + \sum_{l \neq q} \frac{\beta_l}{\beta_q} \left(\frac{\alpha_l}{\alpha_q} \right)^p \bar{x}_l \right] \tag{119}$$

with q being a positive integer. According to Eq. (107), one has:

$$\frac{\alpha_l}{\alpha_q} = \frac{\dfrac{k_{est}}{k_q} - 1}{\dfrac{k_{est}}{k_l} - 1} \tag{120}$$

It can then be noticed from Eqs. (119) and (120) that the iterative algorithm will converge to the mode q fulfilling the following condition:

$$\left| \frac{k_{est}}{k_q} - 1 \right| < \left| \frac{k_{est}}{k_l} - 1 \right| \tag{121}$$

The algorithm will thus converge to the mode q for which k_q is the closest to k_{est} as:

$$\lim_{p \to \infty} \bar{x}_m^{(p)} = \frac{\beta_q \alpha_q^p}{\alpha_m^{(p-1)} \alpha_m^{(p-2)} \ldots \alpha_m^{(0)}} \bar{x}_q \tag{122}$$

Using Eq. (119) into Eq. (112) also leads to:

$$\alpha_m^{(p)} = \alpha_m^{(p-1)} \times \frac{\bar{x}_m^{-(p-1),T} \times \dfrac{\beta_q \alpha_q^p}{\alpha_m^{(p-1)} \alpha_m^{(p-2)} \dots \alpha_m^{(0)}} \times \left[\bar{x}_q + \sum_{l \neq q} \dfrac{\beta_l}{\beta_q}\left(\dfrac{\alpha_l}{\alpha_q}\right)^p \bar{x}_l \right]}{\bar{x}_m^{-(p-1),T} \times \dfrac{\beta_q \alpha_q^{p-1}}{\alpha_m^{(p-2)} \dots \alpha_m^{(0)}} \times \left[\bar{x}_q + \sum_{l \neq q} \dfrac{\beta_l}{\beta_q}\left(\dfrac{\alpha_l}{\alpha_q}\right)^{p-1} \bar{x}_l \right]} \qquad (123)$$

or

$$\alpha_m^{(p)} = \alpha_q \times \frac{\bar{x}_m^{-(p-1),T} \times \left[\bar{x}_q + \sum_{l \neq q} \dfrac{\beta_l}{\beta_q}\left(\dfrac{\alpha_l}{\alpha_q}\right)^p \bar{x}_l \right]}{\bar{x}_m^{-(p-1),T} \times \left[\bar{x}_q + \sum_{l \neq q} \dfrac{\beta_l}{\beta_q}\left(\dfrac{\alpha_l}{\alpha_q}\right)^{p-1} \bar{x}_l \right]} \qquad (124)$$

Because of Eq. (121), one thus finds that:

$$\lim_{p \to \infty} \alpha_m^{(p)} = \alpha_q \qquad (125)$$

which is also equivalent to:

$$\lim_{p \to \infty} k_m^{(p)} = k_q \qquad (126)$$

Equations (122) and (126) therefore mean that the power iteration method with Wielandt's shift, as implemented in Eqs. (111) and (112), leads to the solution corresponding to the mode having its eigenvalue closest to k_{est}. The convergence of this method is directly related to how close to one of the existing eigenvalues k_{est} actually is. In the developed computational tool, a first guess of the different eigenvalues is obtained by applying the Arnoldi method outlined above without performing any restart. Thereafter, each of these estimated eigenvalues is used as the parameter k_{est} in the power iteration method with Wielandt's shift.

1.3.5. Validation of the tool

The computational tool presented in the above sections was successfully benchmarked for a wide range of core configurations ranging from one-dimensional, two-dimensional, and three-dimensional homogeneous, piece-wise homogeneous, heterogeneous systems. Since the tool has the ability to perform several types of calculations (critical/subcritical systems, eigenvalue/non-homogeneous equations), emphasis was put on covering all possible types of situations. The tool was benchmarked against analytical, semi-analytical, and other numerical solutions. A full description of the different benchmark cases is presented in [19], to which the interested reader is referred to. In the following, only a list of the different cases is given:

- One-dimensional calculations:

  - Case of a one-region critical system: static calculations (forward and adjoint), dynamic calculations (forward and adjoint);
  - Case of a one-region subcritical system: static calculations (forward and adjoint);

- Case of a critical two-region system: static calculations (forward and adjoint), dynamic calculations (forward).

  – Two-dimensional calculations:

    - Case of a one-region critical system: static calculations (forward and adjoint), dynamic calculations (forward and adjoint);
    - Case of a one-region subcritical system: static calculations (forward and adjoint).

  – Three-dimensional calculations:

    - Case of a one-region critical system: static calculations (forward and adjoint);
    - Case of a Pressurized Water Reactor (PWR) heterogeneous system: static calculations (forward and adjoint);
    - Case of a Boiling Water Reactor (BWR) heterogeneous system: static calculations (forward and adjoint).

1.3.6. Use and demonstration of the tool

The computational tool presented above is delivered with a complete user's guide [20] explaining:

- – The required software/hardware;
- – What the code package contains;
- – The file architecture and required input;
- – The created output;
- – The format of the input and output variables;
- – The variables necessary in the input files and the available variables in the output file;
- – How to use the code.

Some examples are also available within the package.

The main feature of the computational tool is its flexibility and its simplicity in use, since there is no need of writing any input deck. The minimum input required to run the code is made of two files:

- – A file describing the three-dimensional distributions of the macroscopic cross-sections throughout the system;
- – A file describing the size of an elementary node in the x-, y-, and z-directions.

Some additional optional files can be provided by the user:

- – A file containing some additional kinetic data necessary for calculating the neutron noise in the forward and adjoint problems (required if the neutron noise in the forward or adjoint problem has to be estimated);
- – A file containing the definition of an external neutron source for the forward problem (required if the static neutron flux in the forward problem of a subcritical system with external neutron source has to be determined);
- – A file containing the definition of an external neutron source for the adjoint problem (required for the estimation of the adjoint of the neutron flux for a given source);
- – A file containing the definition of the noise source for the forward problem (required if the neutron noise in the forward problem has to be determined);
- – A file containing the definition of the noise source for the adjoint problem (required if the neutron noise in the adjoint problem has to be determined).

The presence of such files automatically triggers the corresponding optional calculations.

Prior to use the tool, the user might want to change some default settings and/or fine-tune some parameters related to the numerical techniques implemented in the code. For the latter, the parameters are mostly related to the explicitly-restarted Arnoldi method and to the power iteration method with Wielandt's shift technique. These parameters might need to be changed in case of convergence problems. Such settings are defined in a separate file that the user can modify. Default parameters will be used if the user does not modify any of these settings.

After the successful run of the tool, a GUI can be used for visualizing both input and output variables in a rather intuitive manner. A snapshot of this GUI is given in FIG. 1-7. The "Plotting" panel allows choosing the row, column, and level at which cross-sections of the chosen input/output variable will be plotted. Furthermore, since some of the quantities might be complex, the user has to choose whether the magnitude or the phase has to be plotted. The user can then decide to plot the input/output data at the chosen row, column, and level, or can decide to make a "sweep", i.e. a scanning throughout the entire core. Three plots are given: a three-dimensional plot on the left-hand side (with planar cross-sectional cuts at the chosen row, column, and level), a two-dimensional plot on the middle (at the chosen level), and a one-dimensional plot on the right-hand side (at the chosen row and column).
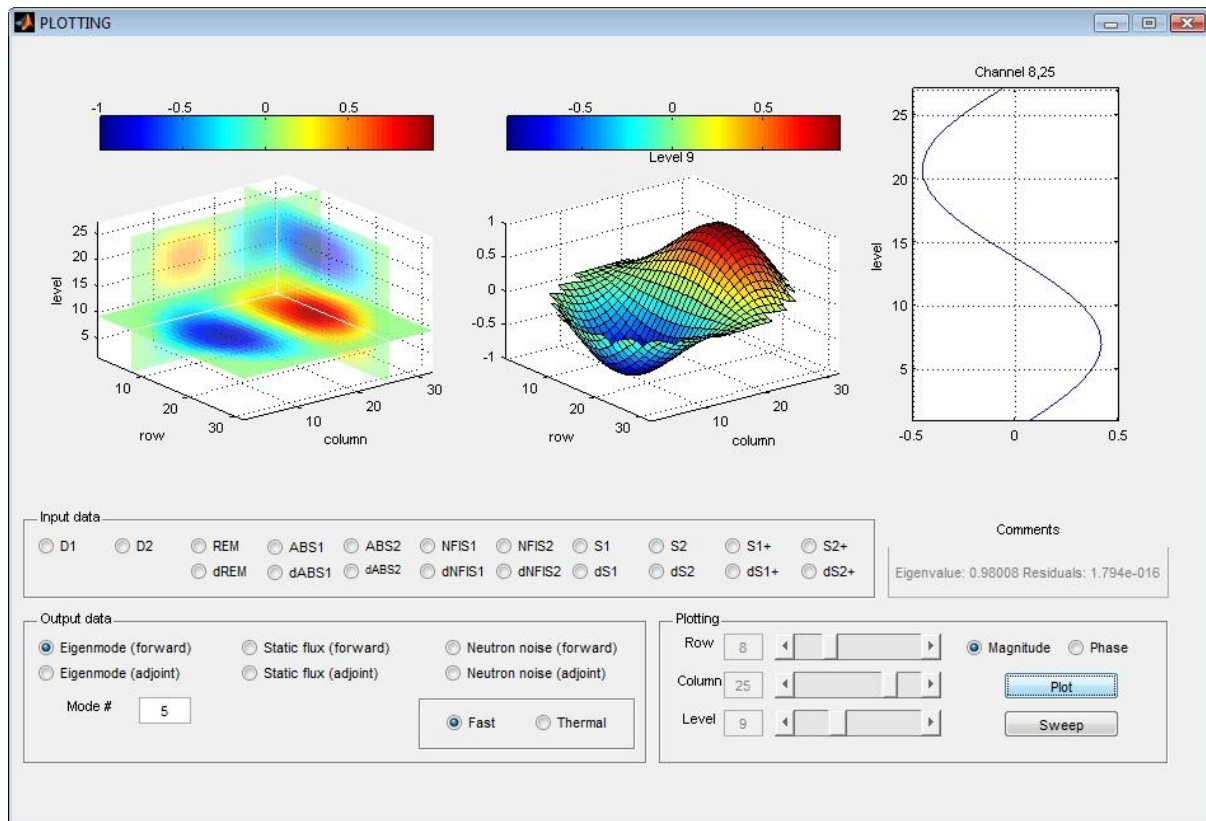
FIG. 1-7. Overview of the Graphical User Interface (GUI) for the visualization of both input and output data in the computational tool.

1.3.7. Conclusions

In this paper, the development and validation of a unique multi-purpose neutronic tool for research and education were reported. The tool can consider both critical systems and subcritical systems with an external neutron source, static cases and dynamic cases in the frequency domain (i.e. for stationary fluctuations). In addition, the tool has the ability to determine the different eigenfunctions of a nuclear core. For each situation, the static neutron flux, the different eigenmodes and eigenvalues, the first-order neutron noise, and their adjoint functions can be determined, as well

as the effective multiplication factor of the system. The tool uses as input two-group macroscopic cross-sections and kinetic parameters as well as geometrical details from other static core simulators.

The coding was implemented in *MatLab*, which makes the pre- and post-processing of data easy, as well as the code highly portable between different operative systems and computer platforms. The code was developed while paying careful attention to data storage requirements and to the robustness of the algorithms. In particular, the numerical algorithms implemented in the tool take advantage of the sparsity of the matrices, and the *MatLab* built-in linear algebra packages LAPACK and UMFPACK are extensively used. In addition, an explicitly-restarted Arnoldi method and a power iteration method using Wielandt's shift were implemented to solve eigenvalue problems. Finally, a GUI was also developed for making the visualization of both input/output data easy and intuitive.

The code was successfully benchmarked against analytical or semi-analytical solutions, as well as against numerical solutions provided by commercial core simulators. A very vast variety of benchmark cases was considered, ranging from one-dimensional, two-dimensional, and three-dimensional cases, homogeneous, piece-wise homogeneous, or heterogeneous cores, critical or subcritical configurations, static or dynamic situations.

This tool is actually the continuation of some earlier work, meant to develop a computational tool allowing the determination of the so-called open-loop reactor transfer function in the frequency-domain [21]. This earlier tool allowed calculating the neutron noise induced by perturbations of the macroscopic cross-sections in the frequency domain in a two-dimensional representation of any nuclear core and in the two-group diffusion approximation, with a spatial discretization based on finite differences. The earlier version of the tool has already been successfully applied to numerous practical problems, such as:

- The unfolding of the noise source from the readings of the neutron detectors (in order to locate unseated fuel assemblies in commercial BWRs) [22];
- The explanation of the space-dependence of the Decay Ratio observed in commercial BWRs [23];
- The development of a new noise estimator for estimating the Moderator Temperature Coefficient (MTC) of reactivity (giving the correct MTC value without calibration) and its experimental verification in a commercial PWR [24];
- The diagnostics and modelling of beam/shell-mode core-barrel vibrations in PWRs [25];
- The investigation of the validity of the point-kinetic approximation in subcritical systems with application to subcriticality monitoring [26];
- The development of a Reduced Order Model for BWR instabilities, including possible unseated fuel assemblies driving self-sustained Density Wave Oscillations [27].

All the applications mentioned above are further described in the corresponding papers, as well as in a review paper [25].

In the version of the computational tool existing today, only the calculation of the neutron density field is performed. The flexibility of the tool in defining the static system directly via the static macroscopic cross-sections and the dynamic system directly via the fluctuations of the macroscopic cross-sections is also one of the main limitations of the tool, since it requires expert knowledge and sometimes arbitrariness in the definition of the static/dynamic cross-sections. While preserving the possibility of defining the three-dimensional distribution of the static/dynamic macroscopic cross-sections, the tool is currently being extended so that actual thermal-hydraulic boundary conditions can also be used. Those are expressed in terms of core-rated thermal power, inlet coolant velocity, and inlet coolant temperature. This requires the development of a thermal-hydraulic module directly coupled to the neutronic module described in this paper. It also means that the coupled neutronic/thermal-hydraulic tool being developed will also have the capability to determine the closed-loop reactor transfer function of any heterogeneous core.

Further improvements on the neutronic side have already been investigated, for instance via the development of a neutronic solver based on the Analytical Nodal Method for both static and dynamic calculations [28]. Extension to fast systems is also being investigated, since rather large fluctuations

have been observed in fast system-prototypes, for which the computational tool has a large area of application.

1.3.8. Acknowledgements

1.4. MODERATOR TEMPERATURE COEFFICIENT THEORY

By: Sándor Kiss, Sándor Lipcsei and János Végh
KFKI Atomic Energy Research Institute

Moderator Temperature Coefficient (MTC) is an of the most important reactivity parameters characterizing the safety of PWRs. Its initial value is determined during the physical start-up measurements after each refuelling in order to verify the safety of a new core. Regular MTC determination during the fuel cycle is required in several countries by the nuclear safety authority, but standard MTC measurements are "intrusive" in that sense that the reactor state must be changed for the sake of the measurement.

Reactor noise diagnostics methods offer "non-intrusive" measurement procedures applicable during normal reactor operation without changing the reactor state. Considerable research and development (R&D) effort was spent to develop and apply robust MTC estimation algorithms, here a new approach is formulated and demonstrated in a VVER-440 reactor with very promising results.

The basic idea behind the new approach is the application of cold leg temperature noise signals and the neutron noise obtained from the background (cable) detectors of SPNDs. In our evaluations a modified MTC-estimator was applied: the traditional estimator was extended to take into account the effects of measurement geometry, coolant velocity and the relatively long time constant of the utilized cold leg thermocouples.

1.4.1. Definition of the moderator temperature coefficient

The definition of MTC by the American National Standard Institute [29] is

$$MTC = \frac{\partial \rho}{\partial T_m^{ave}} \tag{1}$$

Here ρ is the reactivity and T_m^{ave} is the average moderator temperature (the average is taken over the whole reactor core). The reactivity change induced by small temperature fluctuations can be written as

$$\delta \rho(t) = MTC \cdot \delta T_m^{ave}(t) \tag{2}$$

In the frequency domain the connection between the fluctuations of reactivity and neutron flux is given by (see [30], [31], [32]):

$$\delta \rho(\omega) = \frac{1}{G_0(\omega)} \cdot \frac{\delta \phi(r, \omega)}{\phi_0(r)} \tag{3}$$

Here a point kinetic approximation is used; ω denotes the angular frequency, $G_0(\omega)$ stands for the zero transfer function of the reactor, $\delta\phi(r,\omega)$ is the fluctuation of the neutron flux and $\phi_0(r)$ is the average flux. It is well known (see e.g. [32], [33]) that for frequencies between 0.01 Hz and 1.0 Hz the transfer function of a power reactor can be approximated as

$$G(\omega) \cong G_0(\omega) \cong \frac{1}{\beta} \tag{4}$$

Here β is the effective delayed neutron fraction and the closed-loop reactor transfer function was replaced by the open-loop one (see [24]).

1.4.2. Traditional noise MTC estimators

Noise-based MTC estimation methods simply use the fact that moderator temperature fluctuations induce neutron flux fluctuations and these generate fluctuations in the reactivity. The relationship below between neutron flux fluctuations, temperature fluctuations and MTC was first published by Thie [34].

$$rms\left(\frac{\delta\phi}{\phi_0}\right) = G_0(\omega) \cdot rms(\delta T_m) \cdot \alpha_m \tag{5}$$

where rms is the "root mean square", α_m is the MTC, $G_0(\omega)$ is the zero transfer function of the reactor, $\frac{\delta\phi}{\phi_0}$ is the normalized neutron flux fluctuation and δT_m denotes the moderator temperature fluctuation.

In order to increase the accuracy of the estimation, instead of using the full frequency range, the RMS over an appropriate frequency range was applied in the following form:

$$rms(\delta T_m) = \sqrt{\int_{\omega_1}^{\omega_2} APSD_T(\omega)d\omega} \tag{6}$$

The optimal frequency range is the 0.1-1 Hz interval, as it was mentioned earlier.

Neutron flux fluctuations in a reactor core are caused only partly by moderator temperature fluctuations. Further fluctuation sources can be e.g. boric acid concentration changes, stochastic fluctuations in the nuclear chain reaction, fuel assembly, fuel rod or control rod vibrations etc. These components are not separable from neutron fluctuations and they distort the estimation. In order to take into account this effect, Thie's formula (5) was corrected by Pór et al. [35]. In this approximation the MTC is calculated with the so called *H1* estimator (more details on the related equations are given e.g. in [36]):

$$H_1 = \frac{1}{G_0(\omega)} \cdot \frac{CPSD_{\delta\phi/\phi_0,\delta T_m^{ave}}(\omega)}{APSD_{\delta T_m^{ave}}(\omega)} \cdot \tag{7}$$

Here CPSD and APSD are the Cross Power Spectral Density and the Auto Power Spectral Density functions, respectively, and $\delta T_m^{ave}(\omega)$ is the average temperature fluctuation.

Often an alternative estimator called *H2* is used in the following form:

$$H_2 = \frac{1}{G_0(\omega)} \cdot \frac{APSD_{\delta\phi/\phi_0}(\omega)}{CPSD_{\delta T_m^{ave},\delta\phi/\phi_0}(\omega)} \cdot \tag{8}$$

It can be proven that H_1 provides a lower bound of the MTC estimation, while H_2 is an upper bound. The crucial part of the estimations is the calculation of average temperature fluctuation. Demazière et al. [24] obtained a close estimation using estimator H_1 when creating the average fluctuation of the moderator temperature with considering temperature distribution over the whole reactor core.

1.4.3. Estimating temperature fluctuations of the coolant flowing through the core

Average coolant temperature fluctuation over the whole volume of the core is calculated as

$$\delta T_m^{ave}(t) = \frac{\int \delta T_m(\vec{r},t)d\vec{r}}{\int d\vec{r}} \; . \tag{9}$$

However, most of the reactors are not equipped with a sufficient number of temperature sensors to carry out the above calculation correctly over the whole volume of core, thus approximations are needed. A commonly used method to approximate average fluctuations of the coolant temperature over the core is using the average of core inlet / outlet temperatures:

$$\delta T_m^{ave}(t) = \frac{\delta T_m(in,t) + \delta T_m(out,t)}{2} \tag{10}$$

Average core inlet temperature fluctuation is usually estimated with the average cold leg temperature fluctuation. A similar approach is used for the average core outlet temperature fluctuation with average hot leg temperature fluctuation. However, approximation (10) can be problematic for perturbations traveling with the coolant (see FIG. 1-8).
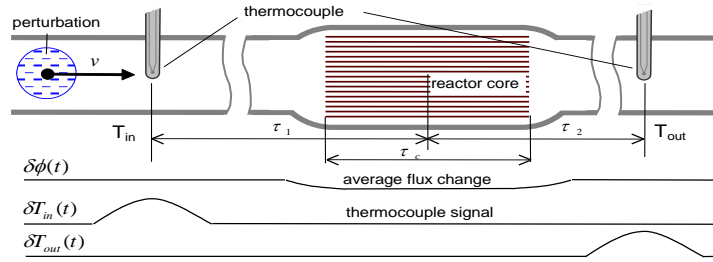
FIG. 1-8. A traveling perturbation and it effect on different signals (cold and hot leg thermocouple arrangement is indicated with transit times).

Temperature measurement positions in hot and cold legs can be quite far from the reactor core. In a VVER-440 reactor cold leg thermocouples are placed about $\tau_1 = 4.45$ sec from the core mid-plane, while hot leg thermocouples are at about $\tau_2 = 2.2$ sec. The transit time of the coolant passing through the core is about $\tau_c = 0.75$ sec. Averaging these signals obviously provides erroneous results for short (in our case shorter than $\tau_1 + \tau_2 = 6.65$ sec) perturbations (e.g. a whole perturbation of this size can be invisible by any of the detectors at a time and it gives zero contribution to the average). Correct averaging method can be obtained by shifting the time series as they were measured at the core mid-plane and then calculating the average over the reactor core:

$$\delta T_m^{ave}(in,t) = \frac{1}{\tau_c} \int\limits_{t-\tau_c/2}^{t+\tau_c/2} \delta T_m(in, t-\tau_1)dt$$

$$\delta T_m^{ave}(out,t) = \frac{1}{\tau_c} \int\limits_{t-\tau_c/2}^{t+\tau_c/2} \delta T_m(out, t+\tau_2)dt \tag{11}$$

$$\delta T_m^{ave}(t) = \frac{\delta T_m^{ave}(in,t) + \delta T_m^{ave}(out,t)}{2}$$

In this way a correct core average of the perturbations can be obtained. Here it is assumed that nothing happens to the temperature fluctuations between the cold leg and the core inlet, and between the core outlet and the hot leg.

Temperature fluctuations traveling with the reactor coolant are handled like propagating perturbations. According to our experience, magnitude of the perturbations is fundamentally not affected by the temperature distribution of the reactor. It is assumed that the perturbations passing through the core are slightly blurred and their specific heat content slightly decreases by dissipation and the expansion of the coolant, but they are not affected by radial or axial temperature distribution in the core.

Temperature fluctuations inducing reactivity fluctuations can be found in their "purest" form in the cold leg temperature signal, if an open-loop reactor transfer function approximation can be applied (it is a good approximation in VVER-440 reactors, due to the strong attenuation effect of the steam generator on the perturbations).

According to our investigations (see [36]) the fluctuation content of the cold leg temperature signal depends only on the measurement system, it is not affected by other components biasing reactivity calculations. It is also free from various feedback effects, therefore it is justified to use cold leg temperature signals in the MTC calculation.

In order to determine the core average of temperature fluctuation from cold leg temperature measurements, a one-dimensional approximation is used in the axial direction x. When measuring a propagating perturbation at different positions the following equation holds

$$\delta T_m(x',\omega) = \delta T_m(x,\omega) \cdot e^{-i\omega\tau} = \delta T_m(x,\omega) \cdot e^{-i\omega\frac{x'-x}{u}}. \tag{12}$$

When a temperature fluctuation is measured at position x then the magnitude of an arbitrary component with frequency ω can be calculated at any x' position. Note that velocity u depends on position; however it is nearly constant in the range investigated (i.e. between the bottom and the top of the reactor core). Average temperature fluctuation $\delta T_m^{ave}(\omega)$ between positions x_1 and x_2 can be expressed as

$$\delta T_m^{ave}(\omega) \cong \frac{1}{x_2 - x_1} \int_{x_1}^{x_2} \delta T_m(x,\omega) \cdot e^{-i\omega\frac{x'-x}{u}} dx' \tag{13}$$

(Here $x_0 \le x \le x_h$). Between the bottom (x_0) and the top (x_h) of the core

$$\delta T_m^{ave}(\omega) \cong \frac{1}{x_h - x_0} \int_{x_0}^{x_h} \delta T_m(x,\omega) \cdot e^{-i\omega\frac{x'-x}{u}} dx'. \tag{14}$$

Calculating the integral:

$$\delta T_m^{ave}(\omega) \cong \frac{i \cdot u}{\omega \cdot (x_h - x_0)} \cdot \left[e^{-i\omega\frac{x'-x}{u}} \right]_{x'=x_0}^{x'=x_h} \cdot \delta T_m(x,\omega) = \frac{i \cdot u}{\omega \cdot (x_h - x_0)} \cdot \left(e^{-i\omega\frac{x_h-x}{u}} - e^{-i\omega\frac{x_0-x}{u}} \right) \cdot \delta T_m(x,\omega) \tag{15}$$

This result can be written as

$$\delta T_m^{ave}(\omega) \cong H_{T_m^{ave}}(x,\omega) \cdot \delta T_m(x,\omega) \tag{16}$$

where

$$H_{T_m^{ave}}(x,\omega)=\frac{i\cdot u}{\omega\cdot(x_h-x_0)}\cdot\left(e^{-i\omega\frac{x_h-x}{u}}-e^{-i\omega\frac{x_0-x}{u}}\right) \tag{17}$$

is a transfer function producing average temperature over the core. Now transform the origin of coordinate system to the mid-plane of the core, let $h=x_h-x_0$ denote the height of the core, and $s=x_0+\dfrac{h}{2}-x$ the distance of the thermocouple from the centre of the core. Because the above form of the transfer function holds only for positions <u>inside</u> the core, signals of the temperature detectors should be transformed to a position inside the core using the appropriate time shift.

$$H_{T_m^{ave}}(s,\omega)=\frac{i\cdot u}{\omega\cdot(x_h-x_0)}\cdot\left(e^{-i\omega\frac{x_h-x_0-\frac{h}{2}+s}{u}}-e^{-i\omega\frac{x_0-x_0-\frac{h}{2}+s}{u}}\right)=\frac{2\cdot u}{\omega\cdot h}\sin\left(\frac{\omega\cdot h}{2\cdot u}\right)\cdot e^{-i\omega\frac{s}{u}} \tag{18}$$

This form of the transfer function has two main parts. The first part describes geometrical properties (size and velocity), while the second part describes the behavior resulting from propagating perturbations. The second part is responsible for the phase and coherence characteristics according to the transit time τ. When temperature signals measured outside the core are shifted to the centre of the core $\tau=0$ should be substituted into the exponent of the second part of the transfer function. More detailed formulas and discussions can be found in [36].

1.4.4. Correction of the H1 and H2 MTC estimators

In the next step, the H_1 and H_2 MTC estimators are corrected with the transfer function (18) of the core average temperature. First the modified form of spectra used in the estimators is:

$$APSD_{\delta T_m^{ave}}(\omega)=\left|H_{T_m^{ave}}(x,\omega)\right|^2\cdot APSD_{\delta T_m}(x,\omega).$$
$$CPSD_{\delta\phi/\phi_0,\delta T_m^{ave}}(\omega)=H_{T_m^{ave}}(x,\omega)^*\cdot CPSD_{\delta\phi/\phi_0,\delta T_m}(\omega). \tag{19}$$
$$CPSD_{\delta T_m^{ave},\delta\phi/\phi_0}(\omega)=H_{T_m^{ave}}(x,\omega)\cdot CPSD_{\delta T_m,\delta\phi/\phi_0}(\omega).$$

Here $\delta T_m=\delta T_m(x,\omega)$ is the <u>real</u> temperature fluctuation at position x.
By substituting the above form of the spectra, estimators will have the following for:

$$H_1(\omega)=\frac{1}{G_0(\omega)}\cdot\frac{CPSD_{\delta\phi/\phi_0,\delta T_m}(\omega)}{APSD_{\delta T_m}(\omega)}\cdot\frac{1}{H_{T_m^{ave}}(x,\omega)}. \tag{20}$$

$$H_2(\omega)=\frac{1}{G_0(\omega)}\cdot\frac{APSD_{\delta\phi/\phi_0}(\omega)}{CPSD_{\delta T_m,\delta\phi/\phi_0}(\omega)}\cdot H_{T_m^{ave}}(x,\omega)^*. \tag{21}$$

Industrial temperature sensors installed in power reactors are usable to measure temperature in the low frequency range; generally they are much slower than the requirements of noise diagnostics. A detector with 0.05 sec time constant will cause nearly 1% error in the results at 0.5 Hz and 5% at 1 Hz, i.e. its transfer function can be neglected. For detectors having longer time constant than 0.05 sec, the actual transfer function must be taken into account during the calculations. Thermocouples installed in the reactor units of Paks NPP have at least 1.6 sec time constant, i.e. they are thirty times slower than the above limit.

The transfer function of a thermocouple with a time constant of τ is

$$H_{TH}(\omega) = \frac{1}{1+i\cdot\omega\cdot\tau} = \frac{1-i\cdot\omega\cdot\tau}{(1+i\cdot\omega\cdot\tau)\cdot(1-i\cdot\omega\cdot\tau)} = \frac{1}{1-\omega^2\cdot\tau^2} - i\cdot\frac{\omega\cdot\tau}{1-\omega^2\cdot\tau^2}, \tag{22}$$

$$\left|H_{TH}(\omega)\right|^2 = \frac{1}{1+\omega^2\cdot\tau^2}. \tag{23}$$

The corrected spectra are as follows:

$$APSD_{\delta T_m}(\omega) = \frac{APSD_{\delta T_m^{measured}}(\omega)}{\left|H_{TH}(\omega)\right|^2}. \tag{24}$$

$$CPSD_{\delta\phi/\phi_0,\delta T_m}(\omega) = \frac{CPSD_{\delta\phi/\phi_0,\delta T_m^{measured}}(\omega)}{H_{TH}(\omega)^*}. \tag{25}$$

$$CPSD_{\delta T_m,\delta\phi/\phi_0}(\omega) = \frac{CPSD_{\delta T_m^{measured},\delta\phi/\phi_0}(\omega)}{H_{TH}(\omega)}, \tag{26}$$

where $\delta T_m^{measured} = \delta T_m^{measured}(x,\omega)$ stands for the temperature fluctuation <u>measured</u> at position x. Taking the effect of the transfer function of the thermocouples into consideration, MTC estimators H_1 and H_2 are modified as

$$H_1(\omega) = \frac{1}{G_0(\omega)}\cdot\frac{CPSD_{\delta\phi/\phi_0,\delta T_m^{measured}}(\omega)}{APSD_{\delta T_m^{measured}}(\omega)}\cdot\frac{H_{TH}(\omega)}{H_{T_m^{ave}}(x,\omega)}. \tag{27}$$

$$H_2(\omega) = \frac{1}{G_0(\omega)}\cdot\frac{APSD_{\delta\phi/\phi_0}(\omega)}{CPSD_{\delta T_m^{measured},\delta\phi/\phi_0}(\omega)}\cdot\frac{H_{T_m^{ave}}(x,\omega)^*}{H_{TH}(\omega)^*} \tag{28}$$

Because estimator $H_2(\omega)$ is based on the APSD of neutron flux fluctuations and it contains considerable components independent of temperature fluctuations, therefore estimator $H_1(\omega)$ is used for the MTC estimation.

1.4.5. Preliminary results of the new MTC estimation method

The MTC calculation was performed with estimator H_1 given by Eq. (27).

1.4.5.1. Preparation of data

Average of 5 cold leg temperature signals of different loops was used for the calculation (one of the six signals was false during the measurements). The average temperature signal was transformed to the centre of the core by time shift of $\tau_1 = 4.45$ sec, i.e.:

$$\delta T_m^{measured}(in,t) = \frac{1}{N_T}\cdot\sum_{i=1}^{N_T}\delta T_{i,m}^{measured}(in,t-\tau_1), \tag{29}$$

where N_T stands for the number of the signals in the average, $\delta T_{i,m}^{measured}(in,t)$ denotes temperature of the moderator measured at the i-th loop. Time constant of the thermocouple at the cold leg was assumed to be 1.6 sec.

Another important factor in the calculation of MTC is the determination of the global neutron flux. Neutron flux measurement in a VVER-440 reactor is performed with 36 SPN detector chains (the radial distribution of SPND chains in the core is close to even). Each chain is inserted into the central tube of a fuel assembly and consists of seven rhodium emitter SPNDs and a compensation cable called "background detector" (the detectors are axially evenly distributed, for further details see [37]).

SPN detectors have a length of 20 cm and their centre is 30.5 cm from each other. The compensation cable has the same length as the length of the cable of the detector with the longest cable (the detector at the lowest position), i.e. it has the length of 202 cm, which is close to the core height, and so it integrates the neutron flux axially (this is the reason why temperature signals are shifted to the centre of the integration range, i.e. to the mid-plane of the core). Global neutron flux was produced as the average of the background detector signals (after an appropriate calibration).

$$\frac{\delta\phi^{ave}(t)}{\phi_0} \cong \frac{1}{N_{bg}}\sum_{j=1}^{N_{bg}} c_j i_j^{bg}(t), \tag{30}$$

where $\delta\phi^{ave}(t)$ stands for the average neutron flux fluctuation, ϕ_0 is the average flux, N_{bg} denotes the number of background detectors, $i_j^{bg}(t)$ is the AC part (i.e. fluctuation) of the current of the j-th background detector and c_j is the calibration factor according to it.

1.4.5.2. Interpretation of the result

For the calculation a four day long measurement with 100 Hz sampling frequency was used with 16384 large block size FFT to increase the resolution of the spectra (with this setting $\Delta f \cong 0.006$ Hz was obtained). The result of the calculation is shown in FIG. 1-9.
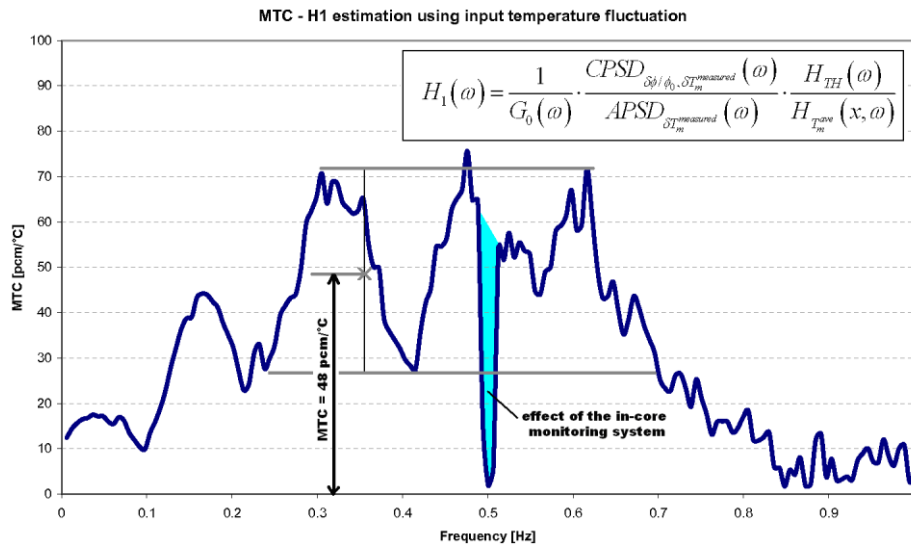
FIG. 1-9. MTC calculated using signals of cold leg thermocouples and background detectors.

The waves in the graph and global decreasing below 0.3 Hz and above 0.7 Hz clearly show that feedbacks cannot be neglected even in the range between 0.1 Hz and 1.0 Hz. The real value of MTC is between local peaks and minima. A correct estimate of the MTC can be determined as the average

of the graph over an appropriate frequency range (see FIG. 1-9). This range was defined from the following considerations:

- Because of the large time constant of the thermocouple, temperature fluctuation decreases below the level of the noise of the measurement electronics above 0.8 Hz;
- Feedback caused by heat transfer between fuel elements and the coolant with a time constant of 3.5-5 sec can be neglected beyond 0.25 Hz (instead of the usual 0.1 Hz);
- The valley around 0.5 Hz is caused by the data acquisition of the core monitoring system and it should be omitted from the averaging;
- Averaging range should be defined with balancing on peaks and sinks.

Using these considerations MTC value was determined by averaging over the frequency range between 0.25 and 0.7 Hz with neglecting the frequency band indicated in the figure around 0.5 Hz. The calculated value is 51.2 pcm/°C which is very close to the "calculated" value of 43.5 pcm/°C (the calculated value was extrapolated from the boron dilution measurement performed at the start of the cycle). Our result was obtained with the time constant of 1.6 sec of a "bare" thermocouple. The real time constant of the thermocouple installed into a guide tube is not known at the moment, it is estimated to be around 2.0-3.0 sec. The calculated value of MTC changes to 41.4 pcm/°C with 2.0 sec time constant and to 33.3 pcm/°C with 2.5 sec.

1.4.6. Systematic investigation of the new MTC evaluation method

A systematic evaluation of measurement settings and evaluation parameters was carried out to determine optimal parameters for the new MTC evaluation method. Optimal evaluation parameters were calculated by considering the frequency dependence of the estimator, and by minimizing the statistical and systematic errors of the results.

1.4.6.1. Data preparation procedure

Measurements used for MTC estimation were performed by the noise data acquisition system of Paks NPP [38]. For the calculations four day long measurements with 100 Hz sampling frequency were used, with 0,015 Hz HP, 40Hz LP and 50Hz notch filter settings. Each measurement contained 344 input signals digitalized quasi-simultaneously. Input signals from the Paks reactors were as follows:

- 252 SPND currents (from the core);
- 36 SPND compensation cable signals (from the core);
- 31 TC signals (selected from 210 in-core TCs);
- 24 loop cold and hot leg TCs;
- 1 reference signal (it can be used for test and measurement validation purposes).

1.4.6.2. Determination of the core inlet temperature fluctuation

In VVER-440 type reactors there are no temperature measurements at fuel assembly inlets, thus appropriate estimations must be used. Average core inlet temperature fluctuation is usually estimated from the average cold leg temperature fluctuation. Five cold leg temperature signals of different loops were averaged for the calculation (one of the six loop signals was false). The average temperature signal was transformed to the center of the core by using a time shift of $\tau_1 = 4.45$ sec, i.e.:

$$\delta T_m^{measured}(centre, t) = \frac{1}{N_T} \cdot \sum_{i=1}^{N_T} \delta T_{i,m}^{measured}(in, t - \tau_1), \tag{31}$$

where N_T is the number of the signals in the average, $\delta T_{i,m}^{measured}(in,t)$ denotes temperature of the moderator measured at the i-th loop. (For more information see FIG. 1-10). Note that with shifting the signals to the centre of the core, and so substituting $s = 0$ into (18), this transfer function will be pure real. In a VVER-440 reactor the core inlet temperature distribution is quite even, in stationary states – even with asymmetric loop temperatures – the deviation between individual assembly inlet temperatures is around $0.1 - 0.2°C$. Therefore, it is justified to assume that the fluctuations measured at the cold legs are radially evenly distributed at the inlet of the core.
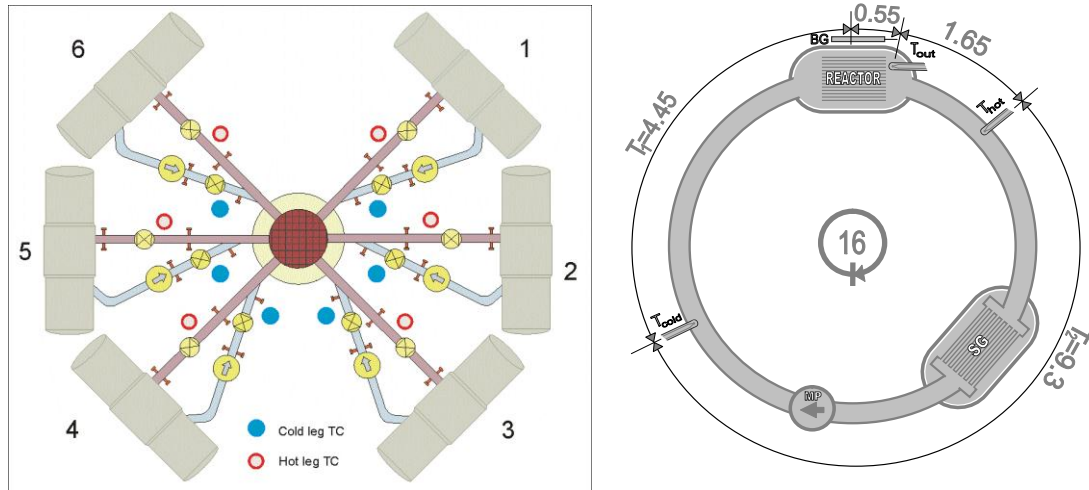
FIG. 1-10. Positions of the thermocouple measurements located in the primary loops and placement of the detectors in the primary loop (transit times are given in second).

1.4.6.3. Determination of the normalized global neutron flux fluctuation

Another important stage of MTC calculation is the determination of the normalized global neutron flux fluctuation.
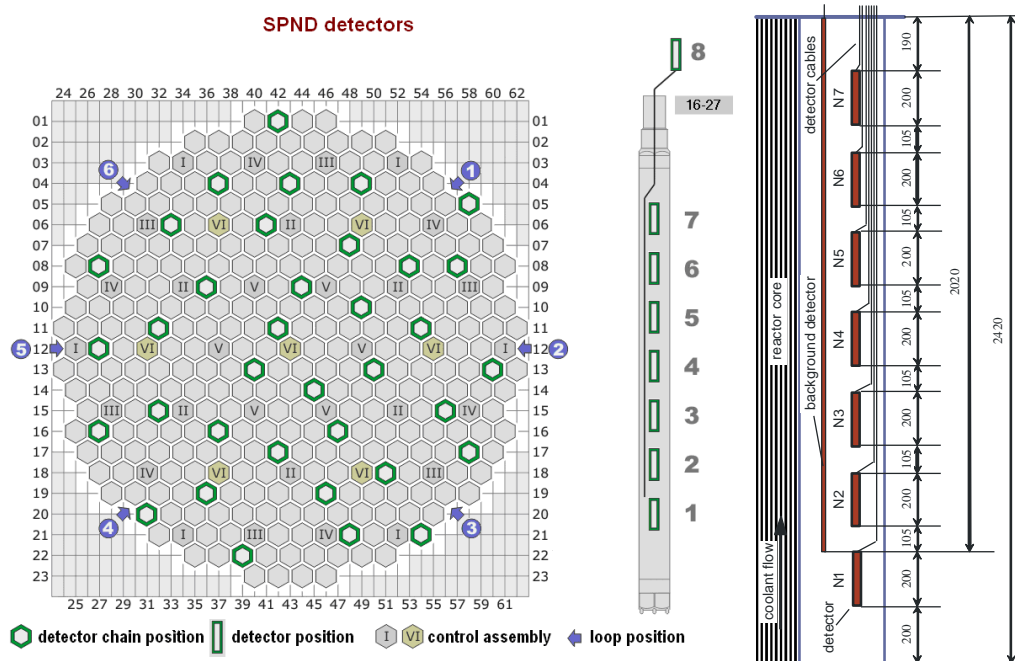
FIG. 1-11. Positions of the measured SPND detector chains in the core and the geometry of an SPND string (lengths are given in mm).

Neutron flux measurement in a VVER-440 type reactor is performed with 36 SPND chains. Each chain is inserted into the central tube of a fuel assembly and consists of seven uncompensated, rhodium emitter SPNDs and a compensation cable called "background detector" (see FIG. 1-11).

Measured SPND currents are biased by parasitic currents produced in the detector cables. In compensated neutron detectors this effect is eliminated by using electronics. In order to be able to restore the undistorted current signal, in VVER-440 reactors an additional detector cable (so called "background detector") is inserted into each detector string.

It has the same length as the length of the cable of the detector with the longest cable, but it is not connected to any detector. The amount of the current measured by the compensation cable is used to calculate the unbiased value of the detector signals measured by SNPDs in the same chain.

A rhodium SPND has a relatively long response time because more than 90% of its current is produced by β-decay with a half-life longer than 42 seconds. However, in addition to nuclear reactions, there are other processes producing prompt electrons in the material of the detector. The ratio of the prompt part of the signal to the total signal is given by the manufacturer of the detector as a percentage of the steady state signal measured by the detector. This ratio is about 6–10 % depending on the production technology, the thickness of the emitter and the burn up of the detector. The delayed part of the signal can be neglected above 0.1 Hz, but the prompt-to-delayed current ratio (0.06-0.08) must be taken into account when performing the normalization of the SPND current fluctuations. The global neutron fluctuation is calculated as the average of the 252 SPND AC signals.

If the longest cable is considered, in the frequency range of 0.1-1.5 Hz the parasitic current can reach or even exceed the value of the current produced by the SPN detector itself [37]. Because the two components cannot be separated, these uncompensated detectors are not suitable to be used in MTC calculations.

Another way of calculating the global neutron flux is to use the background detector signals. This method has two main advantages: a background detector has prompt response only and it integrates the flux in the core axially. However, compensation cables – used as background detectors – have a lower level of quality control than rhodium detectors. Regarding the composition of their material, the quantity and ratio of the components and the presence of trace elements may vary in different detector chains. Moreover, the effect of trace elements changes significantly with neutron fluence, since the speed of depletion depends on the cross-section of each isotope. It can be concluded, that the amount of current produced in the cable depends on its material composition. Therefore cable currents must be calibrated to the SPND currents in the given chain.

At Paks NPP the current measured on a compensation cable has opposite direction compared to the SPND currents; recent measurements have shown that its magnitude is about 6–8 % of the current of the mid-level SPN detectors.

Global normalized neutron flux was calculated as the average of the SPND chain background detector signals

$$\frac{\delta\phi^{ave}(t)}{\phi_0} \cong \frac{\delta i^{ave}(t)}{i_0}, \tag{32}$$

where $\delta\phi^{ave}(t)$ stands for the average neutron flux fluctuation, ϕ_0 is the average flux, $\delta i^{ave}(t)$ is the average fluctuation of the background detector currents, and i_0 is the average background current.

$$\delta i^{ave}(t) = \frac{1}{N_{bg}} \sum_{k=1}^{N_{bg}} C_k i_k^{bg}(t) \tag{33}$$

where N_{bg} denotes the number of background detectors, $i_k^{bg}(t)$ is the AC part (i.e. fluctuation) of the current of the kth background detector, C_k is the calibration factor according to the following definition:

$$C_k = \frac{\frac{1}{7}\sum_{j=1}^{7} i_k^{j,DC} - \frac{i_k^{bg,DC}}{2}}{i_k^{bg,DC}}.$$ (34)

In the above calculation of C_k a half of the current of the background detector is substituted from the average SPND current of the chain, this is an approximate value of the average distortion produced in each SPND by the detector cable.

$i_k^{bg,DC}$ DC of the current in the background detector of index k,

$i_k^{j,DC}$ DC of the current in the SPND of index j of the kth chain,

Finally, the average of the calibrated DC value of cable currents to be used for the calculation of reactivity is given by:

$$i_0 = \frac{1}{N_{bg}}\sum_{k=1}^{N_{bg}} C_k \cdot i_k^{bg,DC}.$$ (35)

1.4.7. Results of the systematic investigation

1.4.7.1. Experimental data

Coupling between moderator temperature fluctuation and neutron flux fluctuation can be investigated in the coherence and phase spectra of average signals as shown in FIG. 1-12 and FIG. 1-13. The coherence reaching 35-50 % in the low frequency range and 30 % even in the investigated range (0.3-0.7 Hz) provides enough connection between the signals to obtain a successful estimation. However, this coherence is still too small to get results close enough to each other from uncorrected H_1 and H_2 estimators.

The wave shape of the coherence functions in FIG. 1-12 and FIG. 1-13 denotes feedback; the connection between the two signals obviously decreases at the "valleys". The MTC calculated with input temperature is expected to have a similar structure.

There is a sharp sink at 0.5 Hz in the coherence of FIG. 1-12 between the average cold leg temperature fluctuation and the average global neutron flux fluctuation which is caused by the 2 sec data acquisition sampling cycle of the core monitoring system affecting temperature signals. The same effect appears in the coherence between the temperature fluctuations of FIG. 1-13 as a narrow band, high coherence peak at 0.5 Hz. This disturbed frequency band around 0.5 Hz must be omitted from the MTC estimation.

The opposite phase at the beginning of the phase diagram of $(T_{cold-ave})$ - (BG_{ave}) indicates negative MTC. The linear phase response visible in the phase functions of FIG. 1-12 and FIG. 1-13 generally indicates propagating perturbations. This is not apparent here, because all signals are time shifted to the centre of the core by using Eq. (31). This effect may be caused by a reactor feedback.

The frequency dependence of H_1 estimation is shown in FIG. 1-14 with a different fast Fourier transform (FFT) window sizes (i.e. with different frequency resolutions). The measurement processed here has 5 days (120 hours) length, thus a larger FFT window size allows smaller number of averaging of spectra (however, it has still more than 1300 averages even for the longest window).

T_{cold-ave}-BG_{ave}
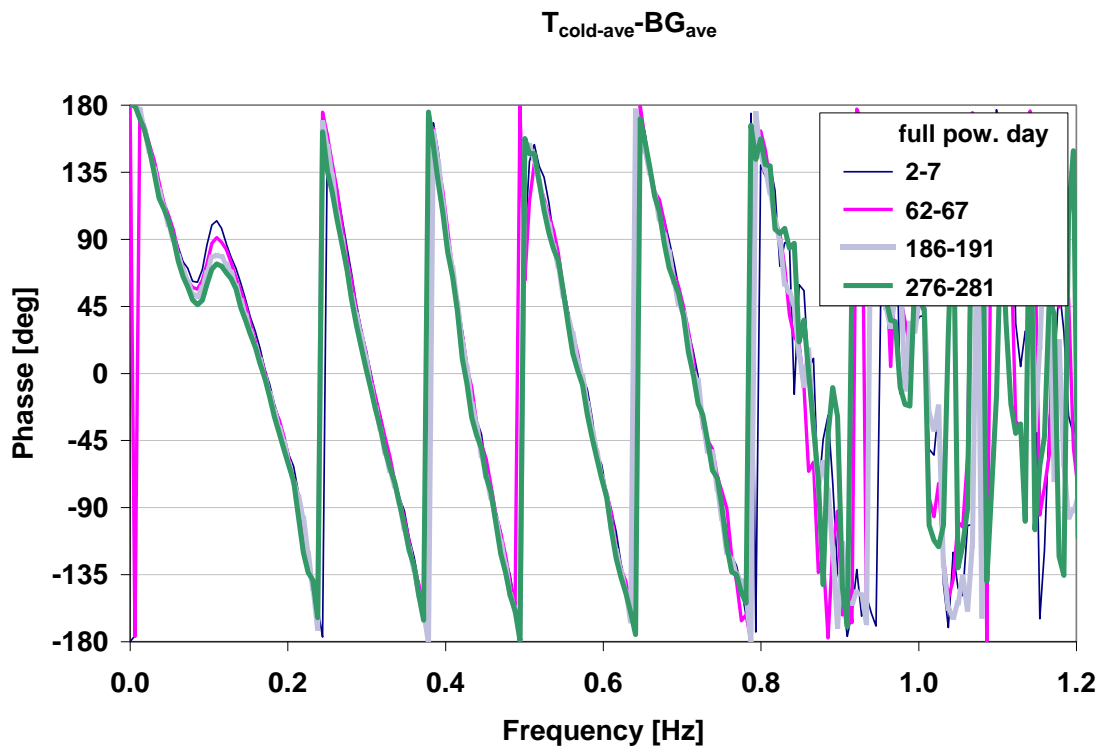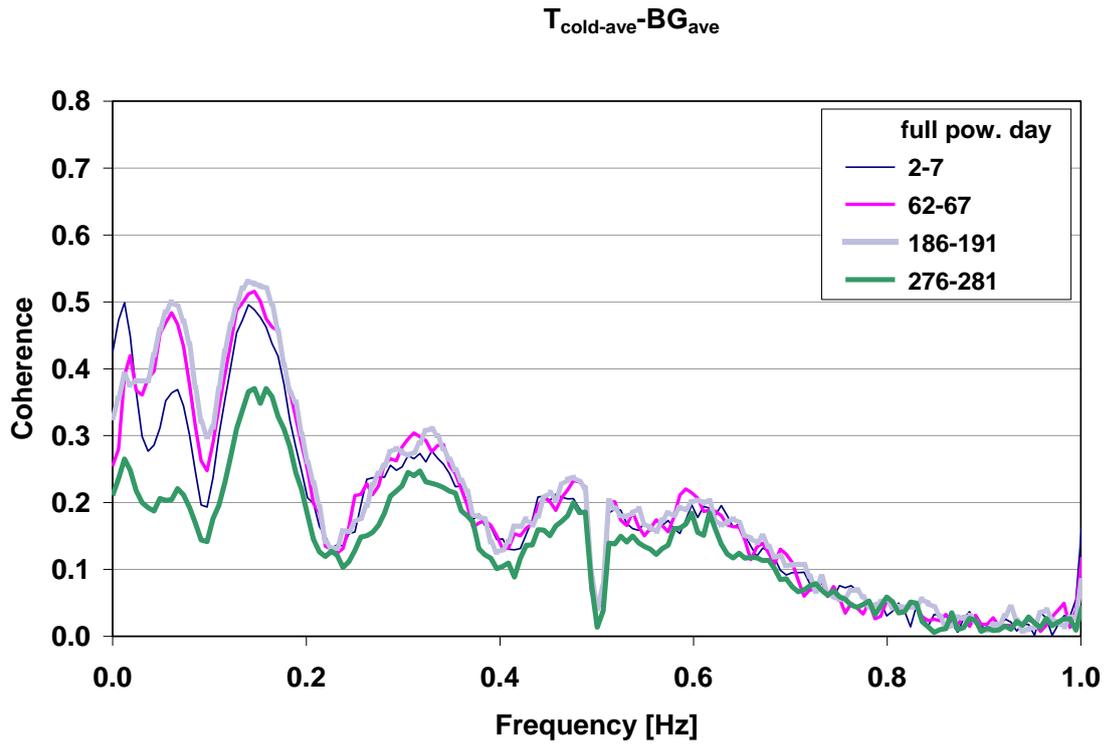
T_{cold-ave}-BG_{ave}

FIG. 1-12. Coherence and phase between average cold leg temperature (Tcold-ave) and average (global) neutron flux (BGave) of the reactor.
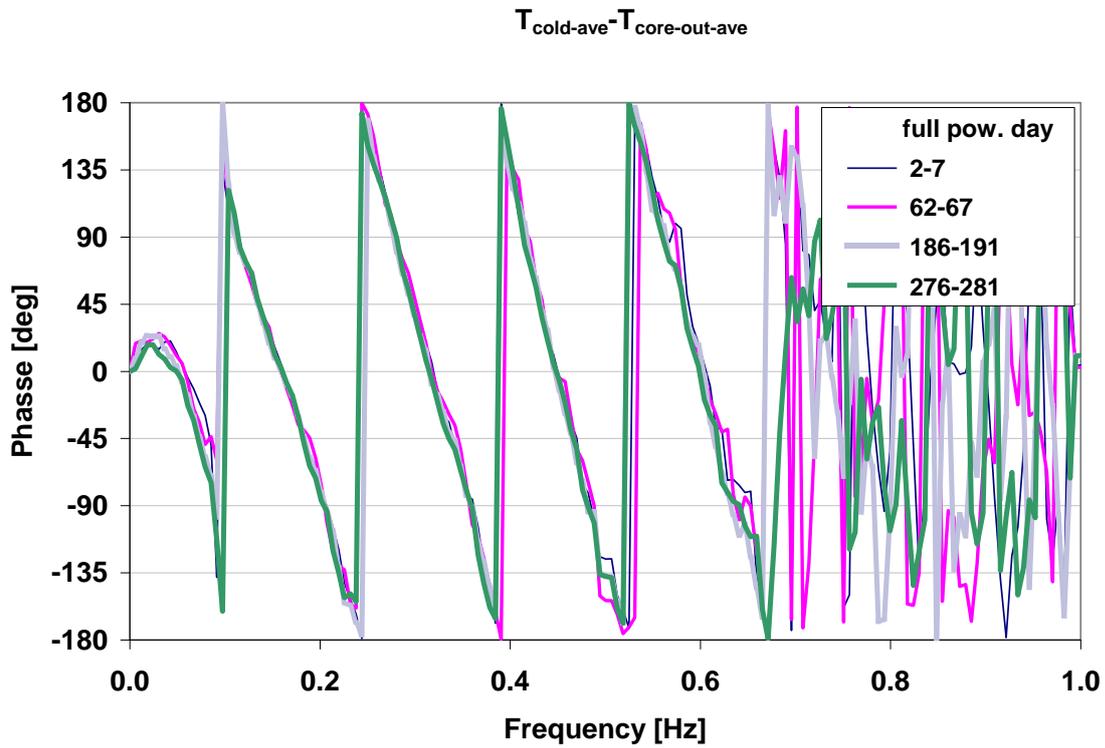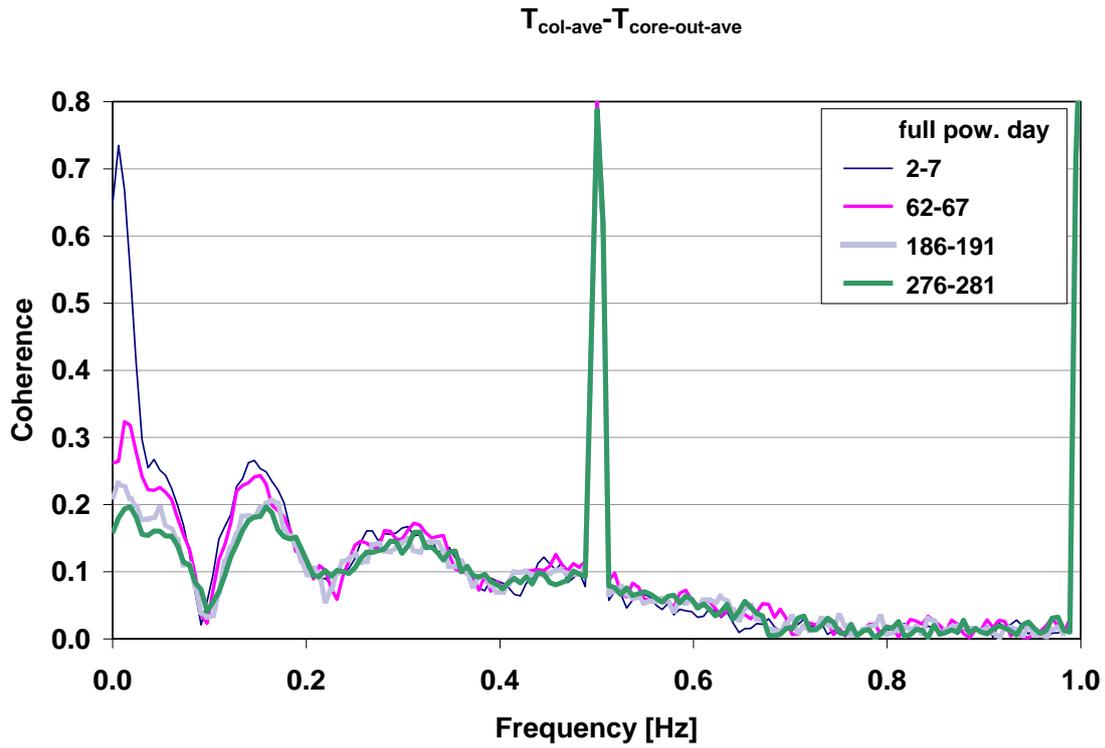
FIG. 1-13. Coherence and phase between the average cold leg temperature (Tcold-ave) and the average core outlet temperature (Tcore-out-ave).
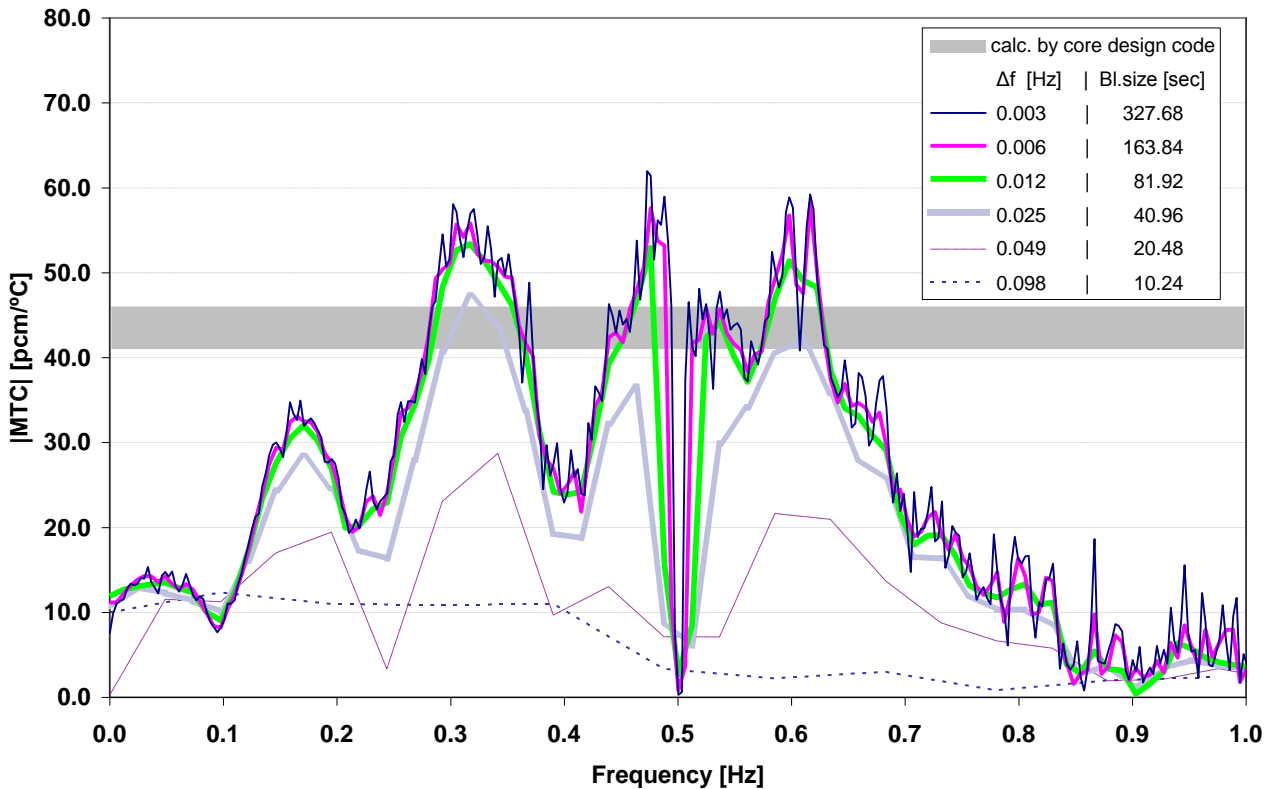
FIG. 1-14. Estimation from a near to end of fuel cycle measurement with different frequency resolutions (different FFT window sizes).

It can be seen in the figure that H_1 decreases below 0.2 Hz due to the power feedback, and it also decreases above 0.7 Hz due to the decreasing coherence (the disappearance of the useful signal is caused by the frequency response of the thermocouple). Also, due to the wave shape of the coherence curve characterizing function H_1, setting the range of integration for creating an average value is critical; it has to keep balance between the "valleys" and "peaks" of the frequency waves. This is the reason of setting the range of integration between 0.25 and 0.65 Hz. The range surrounding the 0.5 Hz sink must be omitted from the integration, as well, because this sink is coming from electronics interference.

Conclusions from these curves are as follows:

− Estimations based on the three longest FFT window sizes are almost identical, for window sizes shorter than 8K results show larger and larger deviations;
− Resolution of the spectra lower than 0.025 Hz is not enough to set the exact range of integration, since the effect at 0,5 Hz becomes too wide;
− At least 80 second long FFT window is needed in order to observe several second long perturbations and their effects.

Consequently acceptable results can be expected from setting the resolution to 0.003-0.012 Hz (8K-32K FFT window size at the used 0.01 Hz sampling frequency). Lower limit of the frequency resolution is connected to the length of the measurement. Treating more than several days' long measurements is problematic, because reactor parameters cannot be considered as constant in this time scale.

54

More H_1 estimations are shown in FIG. 1-15 between the beginning and the end of the same fuel cycle. Frequency characteristics of H_1 calculated from measurements at different time points is very similar to each other with the above settings.
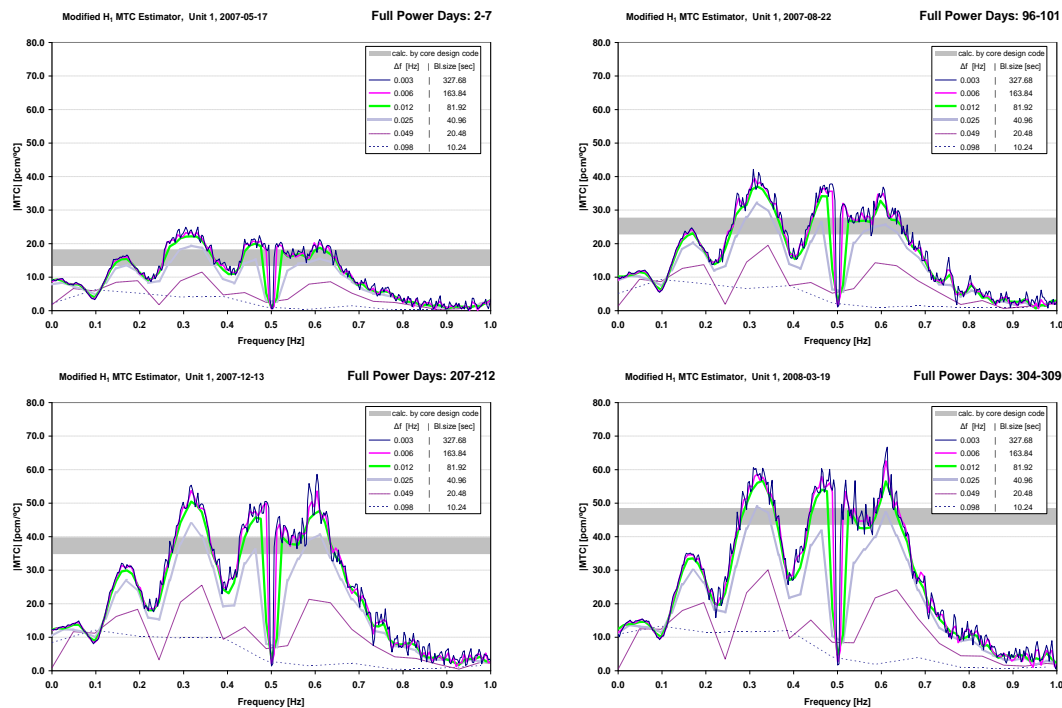
FIG. 1-15. Estimations at different dates of the fuel cycle.

In FIG. 1-16 a series of results of MTC estimation from the measurement at 20/02/2008 is shown with different FFT window sizes.

The aim of this evaluation series was to investigate the stability of the results at different resolutions and averaging. The first evaluation of each series is an averaging over the full length of the 5 day long time series, and then it is repeated on the halves, quarters etc. of the same time series. *L* denotes the length of the range of the time series where the evaluation is made, while *n* stands for the number of averages corresponding to the given length. The calculated values are shown at the middle of the range of the time series they belong to, and they are connected to each other for the same parameters but different ranges.

Fluctuation of the calculated value is decreasing with increasing the number of averages according to statistical laws. Theoretically this statistical error can be decreased to have an arbitrarily small value.

There is also a systematic bias compared to the MTC value calculated by the core design code. The systematic error has three known sources: too small window size of the FFT, setting of the limits of the integral range according to the wave structure of the H_1 estimator, and the not exactly known time constant of the thermocouples.

Results of the first series calculated with 40 second long FFT windows are quite far from the values expected by the core design code, because this window size is too short compared to the length of the perturbations in the coolant. With increasing the length of the window size the results are converging: there is a large change between the 40 sec and 80 sec long windows, the change is definitely smaller between 80 and 160 sec long windows, and it can almost be neglected when moving to the 320 sec window size. It is assumed that these systematic error components disappear when this window size is used.
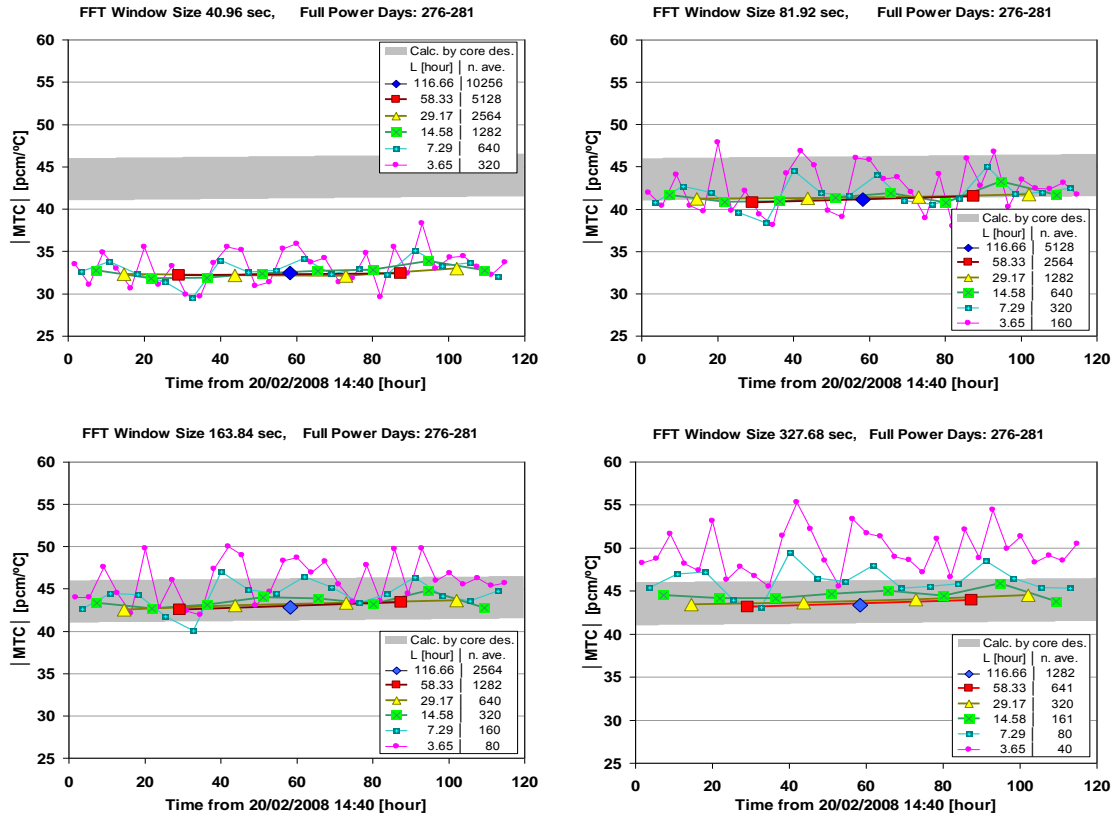
FIG. 1-16. MTC evaluation series of different FFT window sizes and averaging.

The systematic error originating from the improper setting of the integral range can be corrected with a simple calibration, because the locations of the peaks and valleys are stable.

Time constant of the thermocouple guide tube system is not known exactly, but the result of the MTC estimation depends on its value. However, it is constant, and thus this effect can be corrected with calibration, as well.

Calibration is needed to correct two systematic error components and to achieve the most exact results. However, it must be noted that the results presented in this paper are rather satisfactory without using any calibration.

By using the results of the longer window sizes it can be determined that at least 320 averages are needed to decrease the statistical fluctuations, in order to be inside the accuracy range of the calculated MTC value given by the core design code.

It is common in the four graphs that the estimated MTC values obtained from evaluations longer than 24 hours are virtually placed on the same line for all three FFT window sizes. The statistical fluctuation is going to be significant for the other evaluations based on shorter terms.

However, increasing the length of the measurement leads to the following problems:

− During some days the state of the reactor unit changes on a regular base; therefore, the longer the measurement time is, the higher the chance to have a reactor state change;
− For practical reasons longer measurements are more complicated, and it is not easy to reproduce them.

Due to these reasons the length of the measurement for MTC should be kept under one day.

As far as our measurements with 100 Hz sampling rate are concerned, the optimal parameter settings are 163.84 sec FFT window size and 600 averages. This corresponds to about 24 hour's measurement length.

In FIG. 1-17 MTC values are shown: they were calculated by the modified H_1 estimator with evaluation parameters optimized for the practical realization during a whole fuel cycle at 11 nearly equidistant time points. These estimations closely follow the changes of MTC during the fuel cycle if compared to the MTC values calculated by the core design code.
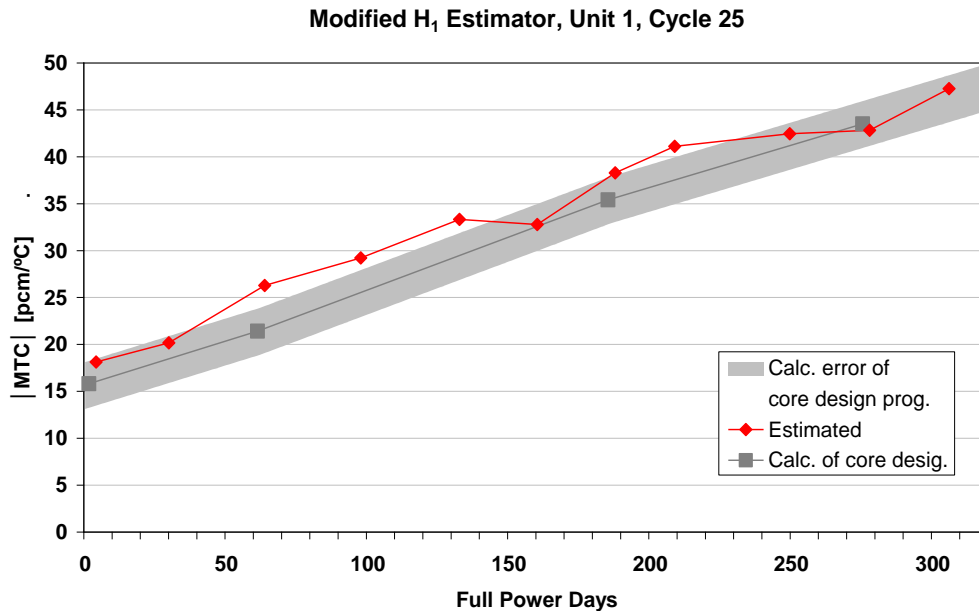
FIG. 1-17. Results of the modified estimator compared to the MTC given by the core design code calculations during a whole fuel cycle.

1.4.8. Conclusions

A new MTC estimation method using noise diagnostics measurements in a VVER-440 reactor was investigated. Several modifications of the traditional noise method were applied:

− Transfer functions were used to take into account the effect of the:

  • geometry (detector positions, core height, coolant velocity), and
  • large time constant of the thermocouples.

− Considering the signal contents:

  • cold leg thermocouple signals were used only,
  • H_1 estimator was used for the evaluation.

− Frequency range of the investigation was narrowed:

  • lower limit was raised, to reduce the biasing effect of the power feedback,
  • upper limit was decreased, since the effect goes below noise due to the relatively large time constant of the thermocouples.

Average neutron flux was obtained from averaging the signals of the 36 SPND compensation cables (also called background detectors), while average input temperature was obtained as an average of the cold leg temperature signals transformed to the centre of the core by time shift.

The traditional H_1 estimator was modified, in order to take into account the effects of the measurement geometry, the coolant velocity and also the effect of the relatively long time constant of the thermocouples. The evaluations were based on five day long measurements performed monthly at a unit of the Paks NPP during a whole fuel cycle.

Optimal processing parameters were determined by considering the frequency dependence of the H_1 estimator, and by minimizing the statistical and systematic errors of the results. From our results it can be concluded that:

- The modified H_1 estimator provides adequate results and its results are close to the MTC given by the core design code calculations;
- Relatively long (≥80 sec) FFT window sizes are needed to obtain correct results, because the cross-power spectral density (CPSD) functions are distorted by the too short correlation length;
- The method needs long but industrially acceptable measurements for robust operation.

As a result of this systematic evaluation series it can be concluded that the modified estimator is applicable to carry out standardized and regular MTC evaluations in VVER-440 NPPs.

1.5. THEORY OF COOLANT VELOCITY DETERMINATION

By: Sándor Kiss, Sándor Lipcsei and János Végh
KFKI Atomic Energy Research Institute

1.5.1. Estimation using correlations and phase portraits

A short theoretical description of the method is given below, with the following notations:

$i(\omega) = \int_{-\infty}^{\infty} i(t)e^{-i\omega t}dt$ is the Fourier transform of a signal $i(t)$

$APSD_1(\omega) = \left\langle i_1(\omega) \cdot \overline{i_1(\omega)} \right\rangle$ is the Auto Power Spectral Density (or auto spectrum)

$CPSD_{1,2}(\omega) = \left\langle i_1(\omega) \cdot \overline{i_2(\omega)} \right\rangle$ is the Cross Power Spectral Density (or cross spectrum)

$\langle \ldots \rangle$ means the expected value of …, ω is the angular frequency and the bar is the complex conjugate.

Equation $i_2(t) \approx i_1(t - \tau_{1,2})$ is valid for the time signals of the detectors in FIG. 1-18, where $\tau_{1,2} = \dfrac{l}{v}$ is the transport time between the detectors, l is the distance between them and v denotes the velocity of the propagating perturbation. The Fourier transform of this equation is $i_2(\omega) = i_1(\omega)e^{-i\omega \tau_{1,2}}$.
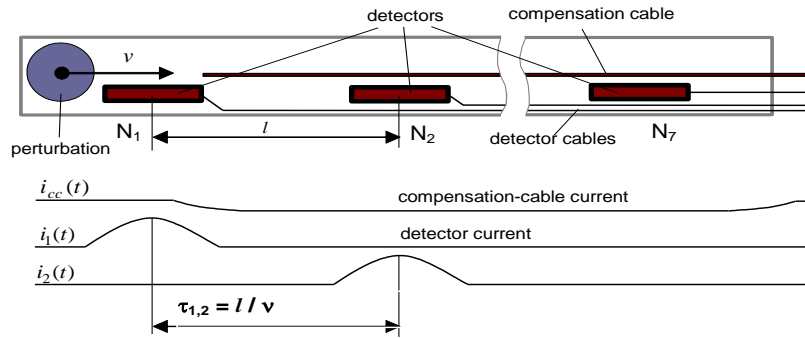
FIG. 1-18. Transit time of a propagating perturbation can be estimated from SPND time signals.

Expressing the cross spectrum between the two signals with the auto spectrum of i_1

$$CPSD_{1,2} = \left\langle i_1(\omega) \cdot \overline{i_2(\omega)} \right\rangle = \left\langle i_1(\omega) \cdot \overline{i_1(\omega)} \right\rangle e^{i\omega \tau_{1,2}} = APSD_1 e^{i\omega \tau_{1,2}} \tag{1}$$

and the linear phase caused by the propagating perturbation is $\varphi = \arg(CPSD_{1,2}) = \omega \tau_{1,2}$. This equals to zero at $\omega = \dfrac{2n\pi}{\tau_{1,2}}$ and equals to π at $\omega = \dfrac{(2n+1)\pi}{\tau_{1,2}}$, where n is an arbitrary integer.

During the investigation of a perturbation propagating through the reactor the so called global noise poses a problem, because this is also sensed by the detectors. It means that the detector "sees" not only the propagating perturbation, but a general (global) noise also (this is present at any point of the reactor). The detector therefore measures a local and a global noise field simultaneously. According to the local-global theorem the signal measured by an in-core neutron detector can be separated into a local and a global component in the following manner:

$$i(t) = i^{lo}(t) + i^{gl}(t) \tag{2}$$

Axially propagating perturbations are e.g. coolant parts of different density caused by the changes of the temperature. Neutron physical parameters of the coolant are changed in the neighbourhood of these perturbations, and as a consequence neutron flux also changes, which change finally appears in the signal of the in-core neutron detectors as fluctuation. When the coolant flows upward in the reactor, the signal $i_2(t)$ of an upper neutron detector can be written as

$$i_2(t) = i_1^{lo}(t - \tau) + i^{gl}(t) + (...) \tag{3}$$

where $i_2^{lo}(t)$, $i_1^{lo}(t)$ are the local neutron noise components at the upper and lower part of the reactor vessel. The first term stands for the process of propagation, while the third term describes uncorrelated background noise (the latter term is neglected in the following treatment). In the frequency domain:

$$i_2(\omega) = i_1^{lo}(\omega)e^{-i\omega\tau_{1,2}} + i^{gl}(\omega) \tag{4}$$

$$CPSD_{1,2} = APSD^{gl} + APSD_1^{lo}e^{i\omega\tau_{1,2}} + CPSD_1^{lo,gl} + CPSD^{gl,lo}_1 e^{i\omega\tau_{1,2}} = APSD^{gl} + APSD_1^{lo}e^{i\omega\tau_{1,2}} \tag{5}$$

(it is assumed that $CPSD_1^{lo,gl} = 0$ and $CPSD^{gl,lo}_1 e^{i\omega\tau_{1,2}} = 0$).
The phase shift between the two points is

$$\varphi = \operatorname{arctg} \frac{G\sin(\omega\tau_{1,2})}{1 + G\cos(\omega\tau_{1,2})}, \text{ where } G = \frac{APSD_1^{lo}}{APSD^{gl}}. \tag{6}$$

The above expression describes quite well the shape of the phase portraits. Unfortunately the measured phase portraits are often much more complex, and therefore the above approximation cannot be used in practical measurements directly. In many cases significant difference was found between the velocities measured in experiments and the velocities determined by noise diagnostics methods based on the linear phase. However, velocity estimation using a correlation technique or impulse response functions can provide useful results, as it is shown in the next section.

1.5.2. Estimation of coolant velocity from the impulse response function

A method of velocity estimation can be based on the fact that the correlation function calculated between two detectors has a local maximum at the position corresponding to the transport time. In the practical analysis of the correlation function difficulties may occur, because the signals of the in-core neutron detectors are highly correlated due to the global fluctuation. This effect can hide the peak corresponding to the transport time; therefore it is a more feasible way to use the so-called impulse response function instead. It is less sensible to the global effect, hence the peak characterizing the transport time can be more accurately identified. There is a peak in the diagrams at 0 sec due to the global noise (reaching all detectors at the same time), and another peak on the right, at about 0,4 sec corresponding to the time delay between the detectors at the 1st and the 5th axial core levels.

The correlation ($CORR_{AB}$) and the impulse response function (IMP_{AB}) between detectors A and B are defined as follows:

$$CORR_{AB} = \int_{-\infty}^{\infty} CPSD_{AB} \cdot e^{i\omega t} d\omega \equiv FFT^{-1}(CPSD_{AB}) \tag{7}$$

$$IMP_{AB} = \int_{-\infty}^{\infty} \frac{CPSD_{AB}}{APSD_A} \cdot e^{i\omega t} d\omega \equiv FFT^{-1} \left(\frac{CPSD_{AB}}{APSD_A} \right) \tag{8}$$

where $CPSD_{AB}$ is the cross spectrum between detectors A and B and $APSD_A$ is the auto spectrum of detector A (here FFT^{-1} indicates inverse Fourier transformation).

$$APSD_A = APSD^{gl} + APSD_A^{lo} \tag{9}$$

$$CPSD_{AB} = APSD^{gl} + APSD_A^{lo} e^{i\omega \tau_{A,B}} \tag{10}$$

After insertion

$$CORR_{AB} = FFT^{-1} \left(APSD^{gl} + APSD_A^{lo} e^{i\omega \tau_{A,B}} \right) \text{ and} \tag{11}$$

$$IMP_{AB} = FFT^{-1} \left(\frac{APSD^{gl} + APSD_A^{lo} e^{i\omega \tau_{A,B}}}{APSD^{gl} + APSD_A^{lo}} \right) = FFT^{-1} \left(\frac{APSD^{gl}}{APSD^{gl} + APSD_A^{lo}} + \frac{APSD_A^{lo} e^{i\omega \tau_{A,B}}}{APSD^{gl} + APSD_A^{lo}} \right) \tag{12}$$

In Eqs. (11) and (12) the first part of the argument is responsible for the peak corresponding to the global part (around zero) and the second is responsible for the peak of propagating perturbations (around the transit time) in the correlation and the impulse response function. In Eq. (12) the distribution produces narrow peaks in the impulse response function and for this reason the evaluation becomes easier. In our regular velocity measurements the impulse response function method is used.

Fluctuations in the SPND signals caused by propagating perturbations are quite small (0.001-0.01% of the DC component), while other noise components can be much larger, making the identification of the transport velocity difficult.

1.6. HIGH SPEED NOISE ANALYSIS DATA LOGGER AT AECL

By: Vinicius Anghel
Atomic Energy of Canada Limited (AECL)

In this section, the main features of the High Speed noise analysis Data Logger (HSDL) being designed at AECL are presented. FIG. 1-19 shows the basic functional structure of such a data logging system. The boxes in FIG. 1-19 are only meant to depict major system functional components. There is no requirement that certain functionality occupy physically distinct 'boxes', however, modularity (and thus flexibility) should be a key factor in choosing an off-the-shelf system. Ideally, a single vendor would supply a 'turnkey' system that meets all requirements, but such an ideal situation may not be possible due to application specific requirements on input impedance, isolation, anti-aliasing, etc. Solutions from multiple vendors or even custom development thus may be required. The following should be high priority goals with respect to the design process:

− Minimize custom development due to its relatively high cost;
− Deal with as few vendors as possible, again to minimize cost and time;
− Select a core system with a wide user base and history of successful application, even if some peripheral 'analogue front end' functionality must be of a more custom nature;
− Select a system that is highly scalable to ensure future needs are met and to reduce one-time costs when initially deploying a system. The initial system may have limited scope, for example, simple data logging where the data is then analyzed to evaluate the systems usefulness to the plant. In this case, it is not feasible to incur the cost of a full system to do this initial evaluation.

FIG. 1-19 depicts how the data logging system could be integrated into a larger permanent noise analysis system at the plant, and in addition be used by other plant systems that require data which it can provide. The design of the data logging system should take these potential future roles into account, and there are several key requirements in this document that seek to enforce this.
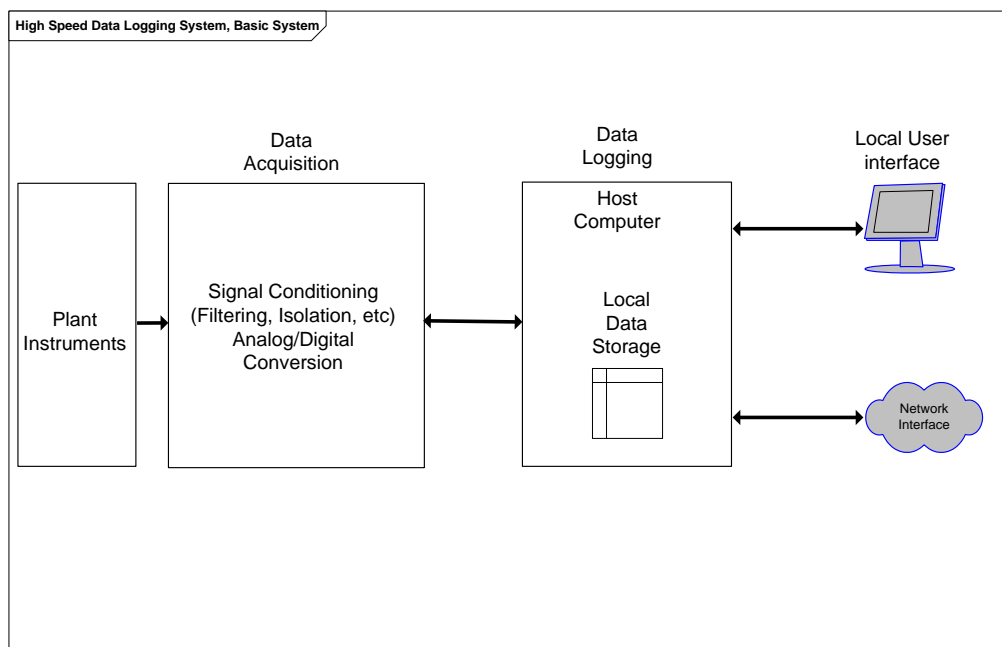
FIG. 1-19. High speed data logging system, basic structure.

1.6.2. Key functional requirements

The High Speed Data Logging System consists of two major functional components (as depicted in FIG. 1-20):

- The data acquisition function, in which the analogue signals are conditioned, digitized, and made available to application software;
- The logging function, which:

  - manages the digitized data: log, analyze, manipulate, serve, etc.,
  - allow user control of the system, both local and remote.

High Speed Data Logging System, Integration

Data Acquisition

Plant Instruments

Signal Conditioning (Filtering, Isolation, etc) Analog/Digital Conversion

Data Logging

Host Computer

Local Data Storage

Local User interface

LAN

Plant Information Systems, Data Historian, Etc

Noise Analysis System
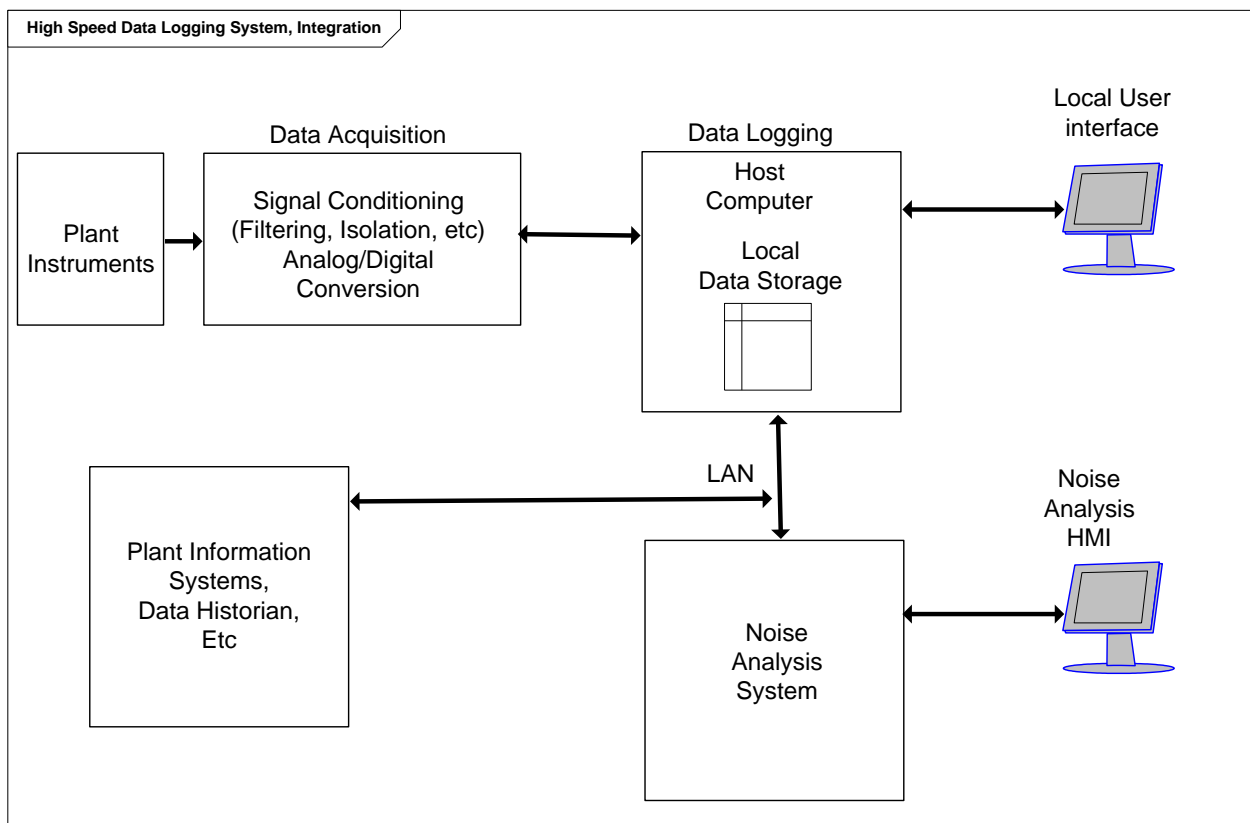
Noise Analysis HMI

FIG. 1-20. Noise analysis HMI and plant LAN integration.

1.6.3. Data acquisition system requirements

The system must be capable of implementing the requirements shown in TABLE 1-1. In addition to this, other criteria must be addressed including:

- The data acquisition system should be modular, so that all costs do not have to be incurred at one time;
- The data acquisition system should have a wide user base, with proven performance;
- The data acquisition system should have complete and comprehensive documentation covering capacities, specifications, setup and configuration, and maintenance.

1.6.4. Requirements for interconnection to plant instruments

The data needed for noise analysis may (and in most cases will) originate from plant instruments that are used in the plant control and safety systems. Therefore, the data logging system must read these signals in parallel with these existing systems (i.e. two inputs in parallel across one voltage source).

TABLE 1-1. DATA ACQUISITION SYSTEM REQUIREMENTS

Parameter	Value	Comments
Number of analogue inputs	Up to 256	
Number of digital inputs	Up to 256	
Resolution	16 bit	Resolutions higher than 16 bit are also acceptable
Input Type	'Standard'	At a minimum, the system shall support input modules for differential voltage and common industrial sensors such as thermocouple, RTD, and bridge based sensors.
Sampling Frequency	Up to 5000 samples per second	
Coupling	AC and DC	Modules that support both shall be available; modules that allow both under software control would be ideal.
Anti-Aliasing	Required	
Input Impedance (ON)	1MΩ or higher	
Input Impedance (OFF)	1MΩ or higher	Input impedance shall not fall when power is not present.
Isolation	Required	Isolation after the converter (digital isolation) is preferable to avoid analogue signal degradation across the isolation barrier.
Input signal Range	'Standard'	Modules shall be available for standard industrial voltage ranges (e.g. +/-10, +/-5, +/-1, etc.).

It is very important that ancillary equipment such as the data logger does not pose a credible threat to the availability of these signals for their original control/safety purpose. There are two credible threats that must be addressed by the data logger system:

- Transient Surge: Protection against this is provided by galvanic isolation between the data logging system and the plant. This is covered by the isolation requirement in TABLE 1-1;
- Signal Loading: The data logging system must not load (or in the worst case, short out) the signals being measured under any possible operation scenario (ON, OFF, input overload). Thus the system input impedance must be on the order of 5-10MΩ under all operating conditions. This requirement will likely necessitate the use of a custom buffer amplifier stage.

1.6.5. Logging function requirements

The Logging function must accomplish the following tasks:

− Log the data to storage (local or remote) for subsequent analysis;
− Allow user control of the system so that data can be collected in a manner that suits the desired analysis;
− Allow the user to retrieve the data, either via local means (flash drive, removable hard drive) or via a LAN;
− Be capable of supporting (supplying necessary data to) a separate noise analysis system (analysis computer and HMI) for analysis tasks that are permanent;
− Arranging logged data into a standard data format that will encapsulate the origin and time (time stamping) of the data;
− Be capable of supporting integration of the data analysis system with other plant systems over the plant LAN (standard business Ethernet based LAN).

These tasks are reflected in the requirements of the following sections.

1.6.6. Application programming interface

The system shall have a software interface such that custom software applications can be created to control and read data from the data acquisition system (i.e. the system must have an API for use by externally created applications).

1.6.7. Logging

It shall be possible for a user (or other software) to specify a location on local or networked storage where the collected data will be stored.

The system shall be capable of using standard, widely available mass storage devices for the recording of data (standard PC hard drive).

The system shall be able to stream data to local storage in real time (i.e. the length of a single acquisition is limited only by local storage space, not buffer overflow issues).

1.6.8. Control and data access

The system shall have at least one network interface through which the user (or other computers) can obtain logged data.

It shall be possible to control the system via a network interface.

The system shall have at least one USB port through which the user can obtain logged data via a removable solid-state memory device (i.e. a flash memory 'stick').

1.6.9. Time stamping

The system shall support time stamping such that any collected data point can be located to within 100 msec of UTC.

1.6.10. Triggering

A data logging system requires flexibility in triggering, both to ensure that desired data around an event is captured and to ensure that large amounts of unnecessary data are not collected. The system triggering requirements are contained in TABLE 1-2.

TABLE 1-2.   REQUIRED LOGGING TRIGGER CAPABILITIES

Trigger	Type (start/stop)	Description
Asynchronous	Start and stop	Logging of data starts or stops under user/software control (through suitable interface such as GUI, etc.).
Digital	Start	Logging of data starts on a falling or rising edge of an external digital trigger input.
Number of samples/duration	Stop	Logging of data stops after a user specified number of samples have been collected OR after a user specified time interval has elapsed.
Low signal threshold	Start	Logging of data starts when the signal on a user specified channel drops below a user specified threshold.
High signal threshold	Start	Logging of data starts when the signal on a user specified channel climbs above a user specified threshold.
Software	N/A	Data from one of the channels is examined continuously by application software that detects the trigger event. When the application detects the trigger event, it causes the data to be logged to storage. This would be a custom application written using the API.

REFERENCES TO CHAPTER 1

[1]   PAKS NUCLEAR POWER PLANT, Requirements Specification for the Reconstruction of the Reactor Diagnostics System, Paks NPP (in Hungarian) (2006).
[2]   PAKS NUCLEAR POWER PLANT, Reconstruction of the PDA-VERONA Core Monitoring System, Requirements Specification, Paks NPP (in Hungarian) (2004).
[3]   HUNGARIAN ATOMIC ENERGY AUTHORITY, Nuclear Safety Regulations Vol. 1-7., Hungarian Atomic Energy Authority, Nuclear Safety Directorate, (in Hungarian) (2005).
[4]   NUCLEAR REGULATORY COMMISSION, Quality Group Classifications and Standards for Water-, Steam-, and Radioactive-Waste-Containing Components of Nuclear Power Plants, Regulatory Guide 1.26 Revision 4, US Govt Printing Office, Washington, DC (2007).
[5]   INTERNATIONAL ATOMIC ENERGY AGENCY, Safety Classification of Structures, Systems and Components in Nuclear Power Plants, IAEA Draft Safety Guide DS367, IAEA, Vienna (to be published shortly).
[6]   KFKI ATOMIC ENERGY RESEARCH INSTITUTE, Quality Control Handbook of KFKI AEKI according to ISO 9001:2001 (in Hungarian) (2008).
[7]   KFKI ATOMIC ENERGY RESEARCH INSTITUTE, System Design Document for the PAZAR Noise Diagnostics Data Collection System, KFKI AEKI (in Hungarian) (2007).
[8]   KFKI ATOMIC ENERGY RESEARCH INSTITUTE, System Design Document for the Signal Evaluation Software of the PAZAR System, KFKI AEKI (in Hungarian) (2008).
[9]   KFKI ATOMIC ENERGY RESEARCH INSTITUTE, Quality Assurance Plan for the VERONA system, PVR-2Q01, V3.3, KFKI AEKI (in Hungarian) (2008).
[10]   LARSSON, V., DEMAZIÈRE C., Comparative study of 2-group P1 and diffusion theories for the calculation of the neutron noise in 1D 2-region systems, Ann. Nucl. Energy 36 10 (2009) 1574.
[11]   LAMARSH, J.R., Introduction to nuclear reactor theory, American Nuclear Society, LaGrange Park, IL (2002).
[12]   NAKAMURA, S., Computational methods in engineering and science with applications to fluid dynamics and nuclear systems, John Wiley & Sons, New York, NY, USA (1977).
[13]   DAVIS, T.A., UMFPACK version 4.6 user guide, Department of Computer and Information Science and Engineering, University of Florida, Gainesville, FL (2002).
[14]   ARNOLDI, W.E., The principle of minimized iterations in the solution of the matrix eigenvalue problem," Q. Appl. Math. 9 1 (1951) 17.
[15]   SAAD, Y., Iterative methods for sparse linear systems, 2nd edn, Society for Industrial and Applied Mathematics, Philadelphia, PA (2003).
[16]   ZINZANI, F., DEMAZIÈRE, C., SUNDE C., Calculation of the eigenfunctions of the two-group neutron diffusion equation and application to modal decomposition of BWR instabilities, Ann. Nucl. Energy 35 11 (2008) 2109.
[17]   ANDERSON, E., BAI, Z., BISCHOF, C., BLACKFORD, S., DEMMEL, J., DONGARRA, J., DU CROZ, J., GREENBAUM, A., HAMMARLING, S., MCKENNEY, A., SORENSEN, D., LAPACK user's guide, 3rd edn, Society for Industrial and Applied Mathematics, Philadelphia, PA (1999).
[18]   ERICSSON, T., Personal communication, Chalmers University of Technology, Gothenburg (2008).
[19]   DEMAZIÈRE, C., CORE SIM: A multi-purpose neutronic tool for research and education, to be submitted to Ann. Nucl. Energy (2011).
[20]   DEMAZIÈRE, C., CORE SIM v1.2 □ User's guide, Chalmers University of Technology, Department of Applied Physics, Division of Nuclear Engineering, Gothenburg (2011).
[21]   DEMAZIÈRE, C., Development of a 2-D 2-group neutron noise simulator, Ann. Nucl. Energy 31 6 (2004) 647.
[22]   DEMAZIÈRE, C., Analysis methods for the determination of possible unseated fuel assemblies in BWRs, Int. Journal of Nucl. Energy Science and Technology 2 3 (2006) 167.
[23]   DEMAZIÈRE, C., PÁZSIT, I., On the possibility of the space-dependence of the stability indicator (Decay Ratio) of a BWR, Ann. Nucl. Energy 32 12 (2005) 1305.

[24]   DEMAZIÈRE, C., PÁZSIT, I., Development of a method for measuring the MTC by noise analysis and its experimental verification in Ringhals-2, Nucl. Sci. Engng. 148 1 (2004) 1-29.

[25]   DEMAZIÈRE, C., PÁZSIT, I., Numerical tools applied to power reactor noise analysis, Prog. Nucl. Energy 51 1 (2009) 67.

[26]   DEMAZIÈRE, C., PÁZSIT, I., WRIGHT, J., Investigation of the validity of the point-kinetic approximation for subcritical heterogeneous systems in 2-group diffusion theory for measurement of the reactivity in ADS, in Proc. Int. Conf. on Nuclear Energy Systems for Future Generation and Global Sustainability (GLOBAL2005), 9-13 October 2005, Atomic Energy Society of Japan, Tsukuba (2005).

[27]   DYKIN, V., DEMAZIÈRE, C., LANGE, C., HENNIG, D., Simulation of local instabilities with the use of Reduced Order Models, submitted to Int. Conf. on Mathematics and Computational Methods Applied to Nuclear Science and Engineering (M&C 2011), 8-12 May 2011, Latin American Section/American Nuclear Society Rio de Janeiro, RJ (2011).

[28]   LARSSON, V., DEMAZIÈRE, C., PÁZSIT, I., TRAN, H.N., Neutron noise calculations using the Analytical Nodal Method and comparisons with analytical solutions, Ann. Nucl. Energy 38 4 (2010) 808.

[29]   AMERICAN NUCLAR SOCIETY, Calculation and Measurement of the Moderator Temperature Coefficient of Reactivity for Water Moderated Power Reactors, an American National Standard, American Nuclear Society, ANSI0ANS-19.11 – 1997 (1997).

[30]   BELL, G.I., GLASSTONE, S., Nuclear Reactor Theory, Van Nostrand Reinhold, New York (1970).

[31]   WILLIAMS, M.M.R., Random Processes In Nuclear Reactors, Pergamon Press, Oxford (1974).

[32]   KOSÁLY, G., Noise investigations in boiling-water and pressurized reactors, Progr. Nucl. Energy 5 (1980) 145.

[33]   THOMAS, J. R. Jr, HERR, J. D. and WOOD, D. S., Noise analysis method for monitoring the moderator temperature coefficient of pressurized water reactors: I. Theory, Nucl. Sci. Engineering 108 (1991) 331.

[34]   THIE, J.A., Neutron noise sources in PWRs, Progr. Nucl. Energy 1 (1977) 283-292.

[35]   PÓR, G., IZSÁK, E., VALKÓ, J., Some Results of Noise Measurements in a PWR NPP, Prog. Nucl. Energy 15 (1985) 387-393.

[36]   KISS, S., LIPCSEI, S., VÉGH, J., MTC estimation based on neutron noise and propagating temperature perturbation in VVER-440 reactors, Ann. Nucl. Energy 37 (2010) 166-174

[37]   KISS, S., LIPCSEI, S., HÁZI, G., Effect of Uncompensated SPND Cables on Noise Signals Measured in VVER-440 Reactors, Nucl. Eng. Des. 220 2 (2003) 179-192.

[38]   LIPCSEI, S., KISS, S., CZIBÓK, T., DEZSŐ, Z., HORVÁTH, CS., Autonomous data acquisition system for Paks NPP process noise signals, Int. J. Nucl. Energy Sci. Techn. 1 (2005) 324-333.

2. ACOUSTIC AND VIBRATION MONITORING (TO CHAPTER 3 OF THE MAIN REPORT)

2.1. TRANSIENT DATA ANALYSIS FOR EQUIPMENT AND STRUCTURAL INTEGRITY MONITORING USING HILBERT-HUANG TRANSFORMATION1

By: Belle R. Upadhyaya
University of Tennessee

In most situations, where information about plant equipment and field devices has to be extracted from measurements, the plant condition is assumed to be at steady-state or stationary. For these cases the analysis of the wide-band component (noise) of measurements from reactors is performed using classical data analysis techniques and/or using stationary discrete-time models derived from the measurements. In some cases we may be interested in monitoring plant equipment and devices using transient signals. The signals may have non-stationary behaviour because of deliberately introduced tests or because of inherent transient behaviour in the system. Such an approach requires a time-frequency analysis, where the system behaviour is tracked as a function of time and frequency.

Several time-frequency techniques have been applied in engineering problems, such as the short-time Fourier transform, wavelet transform, and others. This report addresses the application of a new method, called the Hilbert-Huang Transformation (HHT), to the solution of transient signal analysis. This approach is more general in that the signal is subjected to an empirical-mode decomposition, and then each of the intrinsic components is transformed to the frequency domain using the Hilbert transformation. The latter provides spectral energies as a function of instantaneous frequencies.

The applications of this new technique include structural integrity monitoring of steam generator tubing and diagnosis of induction motor faults. This technique is also shown to be effective under background/process noise. Nuclear power plant equipment and field devices are exposed to high temperature, high pressure, and high radiation environments. Critical components such as steam generators (SG), feed water heaters, and pressure vessels have stringent design requirements regarding their structural integrity. Large motor drives, turbines, and generators are rated for high capacities. In order to increase the safety and reliability of these equipment, it is necessary to develop an on-line monitoring of their structural and dynamic performance integrity.

Information about degradations such as stress corrosion cracking, pitting, fouling, and mechanical fretting, must be available in order to prevent severe damage to heat exchanger and steam generator tubing. Non-destructive testing techniques have been developed and implemented for structural defect inspection during manufacture and routine maintenance. These include eddy current testing, ultrasonic testing, visual inspection, thermography, and others. These methods are fairly effective and accurate in detecting structural flaws in SG tubes, pressure vessels, and steam pipes, but these inspections are usually off-line and must be performed during plant outage. Hence the traditional non-destructive examination (NDE) methods are not suitable for in-situ and on-line monitoring. Currently there are no mature techniques that can be used during plant operation to collect internal information and evaluate the structural integrity of critical components such as the steam generators.

Large and small induction motors are used in power plants, for applications ranging from drives for reactor coolant pumps to various motor-operated valves. Induction motor performance degrades

---

[1] Part of this section was published in a journal article as referenced below:

B. Lu, B.R. Upadhyaya, and R.B. Perez, *Structural Integrity Monitoring of Steam Generator Tubing Using Transient Acoustic Signal Analysis*, IEEE Transactions on Nuclear Science, Vol. 52, No, 1, pp. 484-493, February 2005.

because of either stator faults or rotor faults. These machinery experience large input currents during start-up and the detection of rotor faults may be complicated by the nature of faults. Vibration monitoring and motor current/motor power monitoring during start-up and coast-down, and during steady-state operation provides valuable information about incipient failures.

In order to realize the detection, localization, and classification of flaws in tubular structures, a multi-sensor array is deployed to monitor the wave propagation from multiple perspectives [1], [2]. Although there is a large body of research [3], [4], [5], [6], [7], and [8] performed in (Lamb) wave analysis, many problems still exist. These include the selection of input frequency band, sensor deployment, and feature extraction. Time-frequency analysis methods are being explored to extract representative features and filter out process noise. Pattern classification techniques are being used to categorize defects in either air or in water. A recently developed signal processing method, called the HHT [9], [10], and [11] provides an efficient time-frequency analysis of signals from nonlinear systems. Two other transient signal processing techniques, moving-window and zooming-window, are implemented to deal with acoustic time series such that the localized information could be extracted for defect evaluation of tubular structures. In addition, the concept of mode separation is introduced into this research to simplify the acoustic signal analysis. The development of this new information extraction method, its application to an experimental system, and details of the implementation of the technique are presented. Another application of HHT for induction motor rotor fault detection is also outlined [12].

2.1.1. Elastic waves in metallic tubes

Lamb wave is a special type of surface wave, for which the particle displacements occur in the direction of both propagation and its normal direction with free boundaries. It propagates along different shapes of tubing in a similar way, therefore can be utilized for testing U-tubes, straight, and helical tubes. The stress components on the boundaries must be zero. FIG. 2-1 illustrates the wave propagation along a thin tube. The particle displacement equations are given in Ref. [2], [13], and [14].
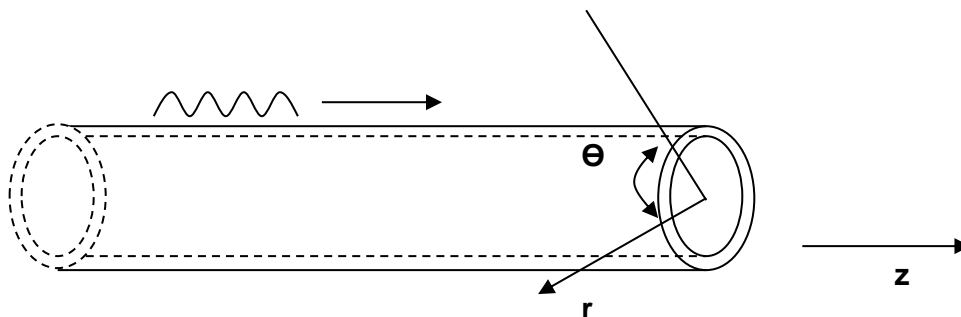
FIG. 2-1. Guided acoustic waves in tubing.

Wave signals in tubing are complicated because they are mixtures of time series with different modes. In addition the impurity of frequency will cause the spread of wave speed even using a pure sine pulse as the input, and further increases the difficulty in analyzing Lamb waves in tubular structures. There are four types of Lamb wave propagation modes in tubular structures. Each of them is discussed briefly.

− Circumferential – non-propagation mode:

  A circumferential mode is a type of wave that transports around the circumferential direction, thus it is non-propagating in the axial direction. This type of mode is not very useful for structural monitoring unless the defect is located at the same axial position and different circumferential location as the active sensor. The wave propagation is illustrated in FIG. 2-2a.

70

− Flexural mode - anti-symmetrical mode:

As shown in FIG. 2-2b, the flexural mode is anti-symmetric with its axial particle displacements being anti-symmetric with respect to the central line of the tube. Therefore if two sensors are deployed at the same axial position on the tube and are at 180-degrees apart in the circumferential direction, the signals collected must have a 180-degree phase difference. This is very important for mode separation. As illustrated later, the flexural mode plays a key role in flaw detection and isolation for tube-like structures.

− Longitudinal-symmetrical mode:

The wave propagation in the longitudinal mode is illustrated in FIG. 2-2c. The particle displacement in the axial direction is symmetric across the structure. The experimental data generated in this research have demonstrated the significance of symmetrical modes in acoustic time series.

− Torsional-symmetrical mode:

Another type of symmetrical mode is the torsional mode, shown in FIG. 2-2d. The characteristics, such as dispersion curves, are described in references [14], [15], and [16]. This type of mode is not very important in this research because the specimen excitation used in this research does not create significant torsional wave propagation mode.
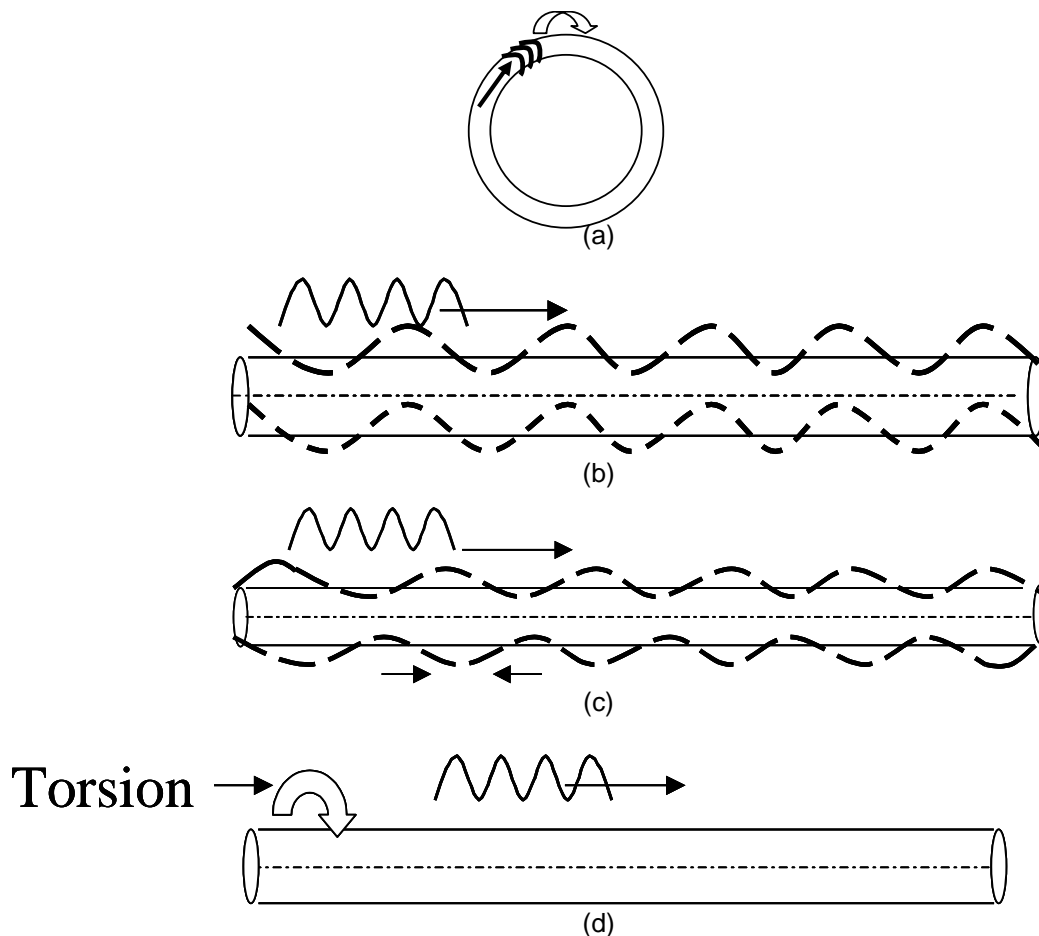
FIG. 2-2. Lamb wave propagation modes in tubular structures.

Because of the complexity of Lamb waves in tubes, advanced nonlinear and non-stationary signal processing methods are necessary for understanding Lamb wave properties, including fault detection, flaw quantification, and classification.

2.1.2. Non-stationary signal processing techniques

Depending on the properties of experimental data and the objectives of this research, several non-stationary signal analysis techniques are proposed for the post signal processing in this study, such that the structural properties would be revealed in the experimental data. Some digital signal processing (DSP) techniques are of recent development and have been used in simple applications [17], [18], [19], and [20]. Since Lamb wave speed changes with the transportation mode and frequency [15], [16], neither time nor frequency analysis alone is able to reveal the phenomenon of Lamb wave dispersion. Therefore, time-frequency analysis is very important in our study. An advanced non-linear non-stationary DSP method, the HHT, is introduced and briefly elaborated below. In addition, localized time information plays an important role in structural flaw detection, localization, and classification. Two new signal analysis techniques, namely, moving windows and zooming windows, are proposed in this research in order to increase the effectiveness of experimental data in revealing material properties.

2.1.2.1. Hilbert-Huang transform

The Hilbert transform (HT) is suitable for processing non-stationary narrow-band signals. The Hilbert transform of a signal $x(t)$ is defined as

$$y(t) = H(x(t)) = \frac{1}{\pi} P \int_{-\infty}^{+\infty} \frac{x(\tau)}{t - \tau} d\tau, \tag{1}$$

where P is the Cauchy principal value. From this we define an analytical signal in the form

$$z(t) = x(t) + iy(t) = A(t) \exp(i\theta(t)), \tag{2}$$

The instantaneous frequency is then derived from the Hilbert transform as

$$\omega(t) = 2\pi f(t) = \frac{d}{dt} \theta(t). \tag{3}$$

However, the integration required to compute the HT is usually not simple, even using numerical calculation methods. Therefore Fourier and its inverse transformation are often adopted to calculate $y(t)$ and is given below.

$$X(f) = FFT(x(t)), \, f = 1 \sim 2N,$$
$$Z(f) = X(f : 1 \sim N), \, padding \; zeroes \; for \; N+1 \sim 2N, \tag{4}$$
$$y(t) = imag(IFFT(Z(f))).$$

This process is trying to find the imaginary part of z(t) through the relationship between Fourier transforms of $x(t)$ and $z(t)$. $X(f)$ should be symmetric with respect to zero, while $Z(f)$ has only positive components. In addition, $X(f)$ and $Z(f)$ have same positive values. The application of the fast Fourier transform and the inverse Fourier transform dramatically reduces the computational complexity of the Hilbert transform. Thus, it is easy to realize its implementation in software.

A time-frequency (T-F) distribution may be developed using the Hilbert transform. Unfortunately, the application of HT is strictly limited by the properties of $x(t)$, that is, the signal should be narrow band around time t. This condition is usually not satisfied by the time series collected from practical applications. Suppose that we have a signal x(t) = cos(ω_1t) + cos(ω_2t), the

Hilbert transform will generate an average instantaneous frequency instead of ω_1 and ω_2 separately. To overcome this problem, Huang [11] proposed an empirical decomposition method to extract intrinsic mode functions (IMF) from time series such that each intrinsic mode function contains a narrow-band component of the signal at a given time instance.

An empirical mode decomposition (EMD) algorithm was developed to create intrinsic modes in an elegant and simple way, called the sifting process. Three assumptions are made to compute the EMD of a time series: 1. The signal must have at least two extrema – one minimum and one maximum; 2. The time interval between the extrema defines the characteristic of the time series; 3. If there are no extrema in the signal, but it contains only inflection points, it can be differentiated to reveal the extrema.

Once the extrema are identified, the maxima are connected using a cubic spline and used as the upper envelope. The minima are interpolated as well to form the lower envelope. The upper and lower envelopes should cover all the data points in the time series. The mean of the upper and lower envelope, $m_1(t)$, is subtracted from the original signal to get the first component $h_1(t)$ of this sifting process,

$$h_1(t) = x(t) - m_1(t). \tag{5}$$

If $h_1(t)$ is an IMF, the sifting process stops. Two conditions are used to check $h_1(t)$ as an IMF: 1. The number zero crossings should equal to the number of extrema or differ at most by one. In other words, $h_1(t)$ should be free of "riding" waves; 2. $h_1(t)$ has the symmetry of upper and lower envelopes with respect to zero. Otherwise, the sifting process should be repeated to approximate the signal $h_1(t)$ to be an IMF. As a result, $h_1(t)$ is sifted to get another first sifted component $h_{11}(t)$.

$$h_{11}(t) = h_1(t) - m_{11}(t), \tag{6}$$

where $m_{11}(t)$ is the mean of upper and lower envelopes of $h_1(t)$. The process continues until $h_{1k}(t)$ is an IMF. The $h_{1k}(t)$ is then designated as the first component $c_1(t) = h_{1k}(t)$.

In order to stop the sifting process a criterion is defined using a standard deviation:

$$SD = \sum_{t=1}^{n} \frac{\left| h_{1,k-1}(t) - h_{1,k}(t) \right|^2}{h_{1,k-1}^2(t)} < threshold. \tag{7}$$

The threshold value is usually set between 0.2 and 0.3. A revised criterion is proposed [21] to accelerate the sifting process.

$$SD = \frac{\sum_{t=1}^{n} \left| h_{1,k-1}(t) - h_{1,k}(t) \right|^2}{\sum_{t=1}^{n} h_{1,k-1}^2(t)} < threshold. \tag{8}$$

The stopping criterion is designed to keep the resulting IMFs to be physically meaningful. The first component c_1 contains the finest scale of the signal, or the highest frequency information at each time point. The residual after the first sifting process is

$$r_1 = x(t) - c_1(t). \tag{9}$$

Then r1(t) is used to replace the raw signal x(t), and the sifting process continues to generate other IMFs. The sifting process should stop according to the requirement of the physical process. However, there are some general requirements, for example, the sum- squared value of the residuals is

less than a predefined threshold value or the residual becomes a monotonic function. The residuals after sifting out n components are:

$$r_n(t) = x(t) - \sum_{i=1}^{n} c_i(t).$$ (10)

The resulting IMFs from the sifting process are then ready for Hilbert transform. These signal components are free from "riding" waves, thus local narrow frequency band is realized. The HHT is adaptive by using the sifting process with the help of cubic interpolations, thus it is a nonlinear transform technique that has great potential applications for complicated non-stationary nonlinear data analysis.

After establishing the IMFs of the signal x(t), the Hilbert transform of each of the IMFs is computed. The analytical function derived from the Hilbert transform is then used to compute the instantaneous frequency and energy in the IMFs at each time instant, and thus a contour plot of time-frequency is generated. As an example, the HHT of a Lamb wave signal from an aluminium plate with a flaw of partial hole, is illustrated FIG. 2-3. These contour plots are then used to establish the features of the acoustic signals for various flaw types.
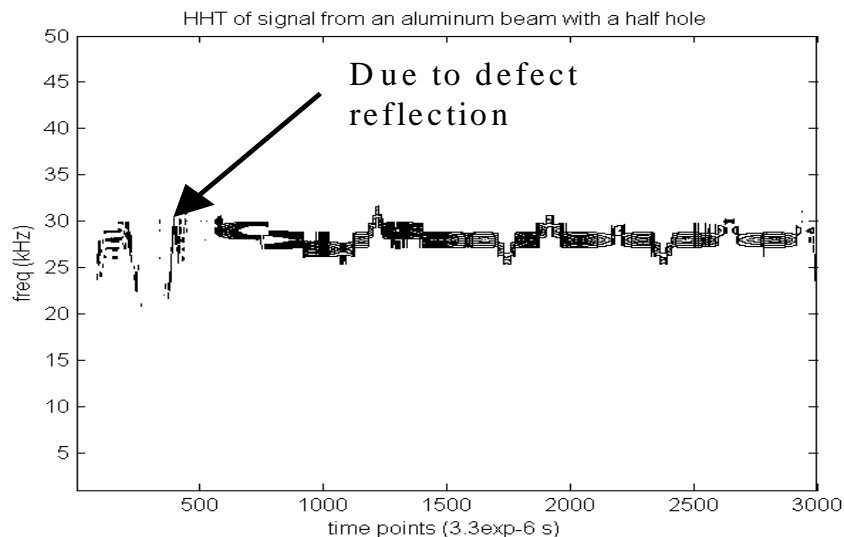
FIG. 2-3. Contour plot of HHT of an acoustic signal for an aluminium plate.

2.1.2.2. *Moving window method for the analysis of Lamb wave signals*

For the finite length tubing, Lamb wave signals collected by the piezo-sensors are the combination of several transport modes that reflect back and forth between the ends or at discontinuities. The reflection from the boundaries forms local peaks in the signals acquired by the piezo-transducers. However, the wave speed changes along with the frequency for a single mode. Therefore, the acoustic time series generally has narrow local peaks at the beginning and wider local peaks later. In addition, the local peaks are not easy to be separated provided enough time is given. The local peaks finally become meaningless because of the dispersion effects. In comparison, the first several peaks have clear physical meaning and thus deserve to be separated from the rest for analysis.

A specific type of structural flaw usually interferes with propagating waves in three forms: refraction of part of the energy into air or water, reflection of part of the energy back in the form of multiple modes, and transmission of the remaining energy forward in complete modes [15]. The reflection and transmission coefficients are a function of modes as studied by Rose [14], the shape of defect, and the flaw dimension. The experimental studies of reflection/refraction coefficients did not generate constructive results that can be directly applied to NDE techniques. However, one definite conclusion is that the reflection rate increases nonlinearly as a function of the defect size.

74

In order to study the effect of structural flaws on the acoustic time series in a tube- like structure, a moving window with flexible size is introduced to localize the properties of the acoustic signals. The principle of this algorithm is demonstrated in FIG. 2-4.
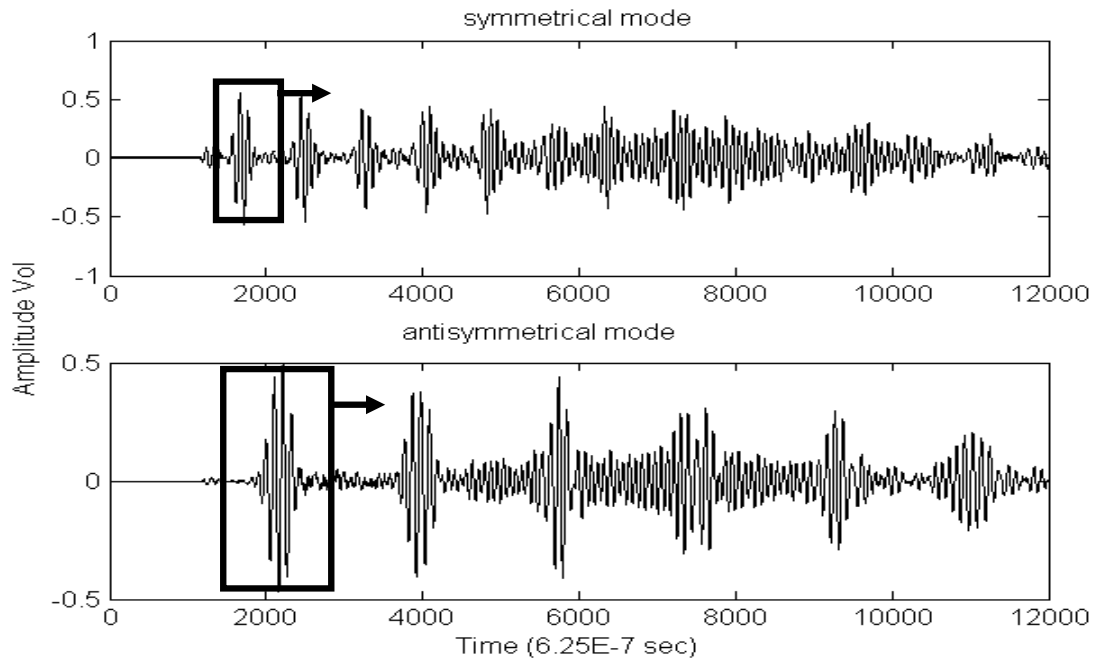
FIG. 2-4. Signal localization using moving windows.

The windowed signals are extracted when the middle of the window coincides with a local maximum point, and it must also be the maximum value of all the points in the window. The width of the moving window is very critical for good feature extraction. For a large window, for example, the window width is larger than two times the distance between two neighbouring peaks, the information extracted may not be useful. Too small a window may also create problems, making the method less sensitive to the existence of structural defects. The selection of optimal window size depends on the characteristics of the signals, and thus it is an empirical process. One option is to define it as slightly smaller than twice the distance between two neighbouring peaks.

Several properties of windowed signals are introduced in this study and defined as follows:

− Amplitude in voltage. The energy of local peaks reflects the energy loss in the Lamb wave propagation property. The energy loss is due to the refraction of acoustic waves into the air or water. A structural discontinuity definitely increases the leakage of acoustic waves into the air or water, and thus decreases the energy of local peaks. Furthermore, a part of the energy is reflected back, while the reflection from the defect has certain time of flight and thus also causes the decrease of local acoustic peaks.

− Variance of the windowed signal is defined as:

$$V(x_w) = \frac{\sum\limits_{i=-n}^{n} \left| i^2 \times x_{wi} \right|}{\sum\limits_{i=-n}^{n} \left| x_{wi} \right|},$$

(11)

Where :

n : *half of the window width*,

x_w : *windowed signals around a local peak*.

The variance of windowed signal increases as a local peak spreads out towards its neighbours.

− Gravity centre is defined as:

$$W_l(x_w) = \frac{\sum_{i=-n}^{0} |i \times x_{wi}|}{\sum_{i=-n}^{0} |x_{wi}|}$$

$$W_r(x_w) = \frac{\sum_{i=0}^{n} |i \times x_{wi}|}{\sum_{i=0}^{n} |x_{wi}|}$$

(12)

$Where: n \ is \ half \ of \ the \ window \ width$

$x_w: windowed \ signals \ around \ a \ local \ peak$

$W_l: gravity \ center \ of \ left \ half \ part \ of \ the \ windowed \ signal$

$W_r: gravity \ center \ of \ right \ half \ part \ of \ the \ windowed \ signal.$

The left gravity centre and the right gravity centre are especially useful in estimating the location of flaw on tubing. Since the first reflection from a structural flaw is located between the first two local peaks selected by the moving window, the right gravity centre of the first peak should shift towards the right, and the left gravity centre of the second peak should shift towards the left, provided that the window is large enough to cover the reflected signals. This is elaborated in the next section on the zooming window algorithm.

2.1.2.3. Zooming window method for the analysis of Lamb wave signals

A zooming window method is proposed to locate the structural defect in a tube-like structure. As will be shown in the next section, the localization of flaw in a tube is much more difficult than that in a plate-like structure. Actually the reflected signal in a tube does not appear as an obvious small peak between the local peaks and it is difficult to locate the position of reflection visually. The reason is that the reflection of Lamb waves in a tube spreads between local peaks with certain distribution without an apparent concentration, while the distribution depends on the properties of input signal, size of defect, and the shape of detect. Zooming window provides a method for the quantification of the flaw location, even estimation of the distribution of the reflection signal as long as a sufficiently small step size is given for the window's expansion. The window expansion is illustrated using dotted lines in FIG. 2-5.
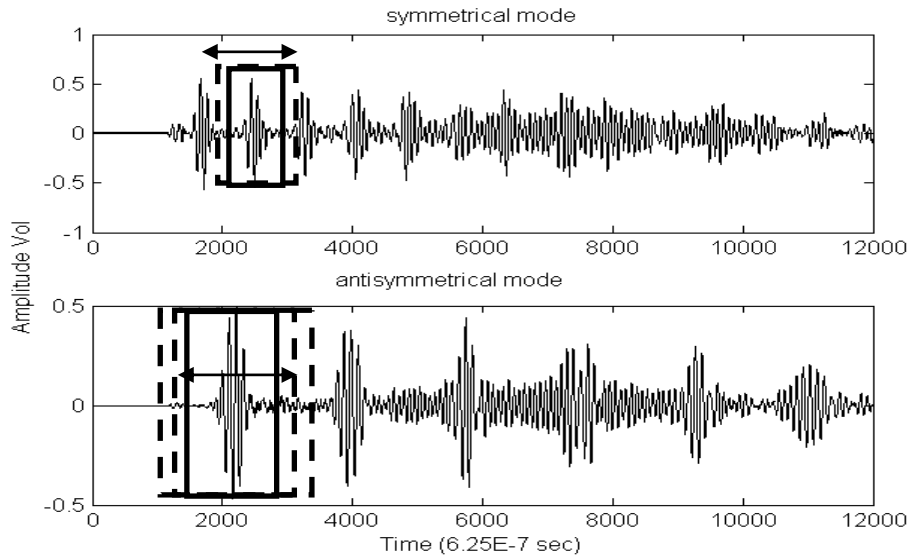
FIG. 2-5. Signal localized properties using zooming windows.

For the use of the zooming window method, only the first few local peaks are of interest because of the dispersion of Lamb waves. In other words, the spread of local peaks distorts the reflection after several local peaks, and thus it is very difficult to distinguish the location about defect from these local peaks with a very large spread.

2.1.2.4.   Features extracted using the moving window for flaw classification of brass tubes

The representative features extracted using the moving window method described above are used for tube flaw classification. A specific structural condition is represented using four vectors: magnitude, spread of local peaks, left gravity centre, and right gravity centre, as defined in the Section 2.1.2.2 on moving window technique. As an example, the matrix in TABLE 2-1 describes a flaw condition of brass tube with a through hole.

TABLE 2-1.   AN EXAMPLE OF FEATURE MATRIX FROM A BRASS TUBE WITH A THROUGH HOLE

Local peak	Magnitude	Spread	Left weight centre	Right weight centre
1st local peak	1.0059	227.2795	119.9736	172.8367
2nd local peak	0.8398	286.4325	169.8980	208.8485
3rd local peak	0.7910	354.7814	235.7749	269.7080
4th local peak	0.5713	389.3638	304.1911	328.0042

In case a brass tube needs to be tested, a feature matrix will be generated using the moving window algorithm. Then normalized distances between the test feature matrix and the training matrices are calculated through the formula defined by

$$d_{xy^j} = \sum_{n=1}^{4} (\sum_{i=1}^{m} \left| x_{n,i} - y_{n,i}^j \right| / \sum_{i=1}^{m} \left| y_{n,i}^j \right|),$$

d_{xy} : *the* distance between matrix x and y^j

(13)

x : the test feature matrix

y^j : j^{th} training feature matrix.

If the distance between x and y^j is the smallest one, x is then classified into class j, which has been trained and stored earlier.

2.1.3. Laboratory testing system

A smart sensor array system has been developed for acoustic signal generation and acquisition. In real applications, each heat exchanger tube should have a sensor suite attached to it for information collection. The sensors are carefully arranged in special circumferential positions such that the signals in the two sensors close to each other have either 180-degree phase difference or no phase difference. The symmetric and anti-symmetric signals are then separated as discussed in the next section.

FIG. 2-6 illustrates the experimental modules. One piezo-sensor is used as an active sensor to generate Lamb waves in laboratory specimens, and the remaining are the passive sensors to collect the transmitted acoustic signals. The active and the passive sensors are interfaced with a PC through a standard National Instruments DAQ card. The testing setup illustrated here is very important for the mode separation presented in next section. FIG. 2-7 shows the experimental setup of a brass tube submerged in water. While the experiments were performed under ambient temperature and pressure conditions, high-temperature high-pressure piezo-sensors are commercially available. A two-phase flow environment is simulated using air bubbles. The bubbles and flowing water in the tube create low frequency and high frequency background noise in Lamb wave signals, which were processed using HHT. The real noisy signals could be processed using the same method, though they may have different frequency properties.
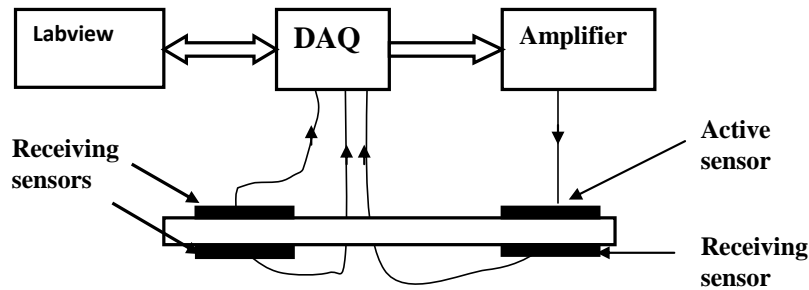
FIG. 2-6. Experimental modules for tubular structure interrogations using lamb wave.
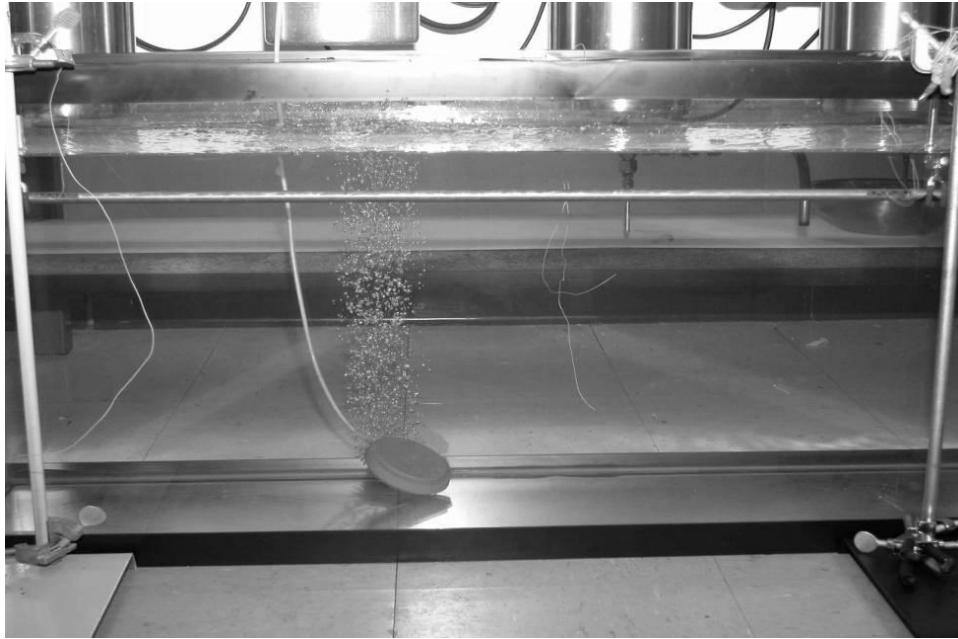
FIG. 2-7. Experimental setup for brass tube examinations.

The active piezo-transducer is interrogated using Hanning-window modulated sine pulses with about five cycles. The data sampling frequencies of 300 kHz and 1.6 MHz are used. The frequency of excitation has been established based on the optimal bandwidth for the specimen of interest. Active frequencies are selected in the range 13 kHz – 16 kHz. This frequency band has been selected for two reasons. The first is the Lamb wave transportation mode in this range is much simpler than high frequency band, so it is easy to perform the mode separation of raw signals. There are only one possible torsional mode, one longitudinal mode, and one flexural mode in this range. The second reason is that it is located in the resonant band of the brass tubes used in the experiments of this research. Hence the energy decay ratio is low.

2.1.4. Acoustic wave mode separation

Mode separation of acoustic signals in tube-like structure is important for defect location and classification. The raw signals and the separated signals are plotted in FIG. 2-4 and FIG. 2-8 respectively. In the raw signals, several modes of acoustic waves interweave together. The local peaks are irregularly distributed along the time axes. However, the separated signals with single mode shown in FIG. 2-8 have regular local peaks and clear patterns that are suitable for analysis using the moving window described in Section 2.1.2.2. The Lamb wave speed under different modes can be calculated through separated signals and have been verified in [2] through numerical solution of tubular Lamb equations.
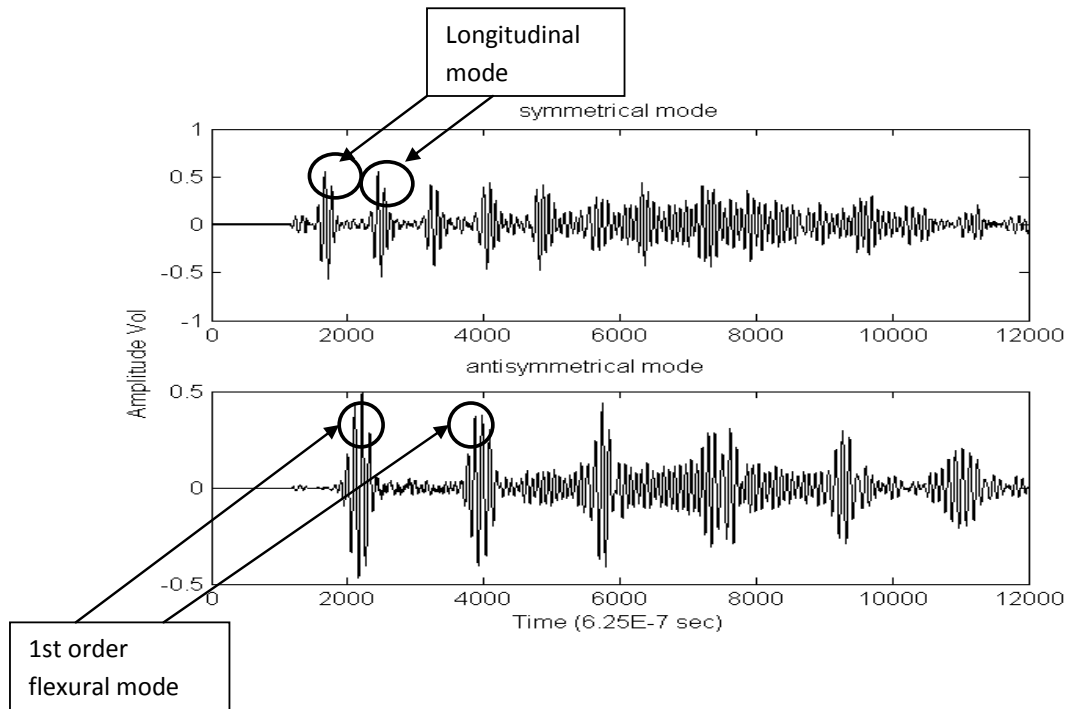
FIG. 2-8. Separated symmetric and anti-symmetric mode signals.

In order to separate symmetric and anti-symmetric modes, a special sensor deployment is required, where two passive sensors are embedded into a tube back to back at the same axial position. The independent pure mode waves are then calculated as follows.

$$S_a = (s_1 - s_2)/2,$$
$$S_s = (s_1 + s_2)/2,$$
$$where:$$
$$s_i : raw \text{ singal } from \text{ } sensor \text{ } i; \text{ } i = 1,2$$
$$s_a : antisymmetric \text{ signals,}$$
$$s_s : symmetric \text{ mode signals.}$$

(14)

2.1.5. Development of tubular structure integrity monitoring algorithm

2.1.5.1. Structural flaw evaluation in air

After mode separation, the acoustic wave signals are processed using the moving window. The properties around local peaks are then calculated as defined in Section 2.1.2.2. Five structural flaw conditions are tested for a 3-foot long brass tube and are listed in TABLE 2-2. These range from partial to through hole defects and a transverse notch. The results of analysis from moving windows are plotted in the following figures. FIG. 2-9 through FIG. 2-11 show the results for a frequency of 14 kHz for the excitation (active) wave. The anti-symmetric mode waves are used for analysis in these figures. It is seen that the structural flaws cause a decrease in the amplitude of local peaks, while the spread of windowed signals increases due to the scattering of structural discontinuity. Other fault mechanisms, such as fouling and corrosion, may also cause changes in statistical features such as local peak amplitude and spread, but they can be distinguished using the pattern classification approach.

TABLE 2-2.   FIVE STRUCTURAL CONDITIONS TESTED FOR A BRASS TUBE

Structural conditions	Activation frequency	Wave propagation direction	Sampling frequency
1. Normal	13 kHz, 14 kHz, 15kHz, 16kHz	Left to right, right to left	1.6 MHz
2. Half hole (d=0.6mm)	13kHz, 14kHz, 15kHz, 16kHz	Left to right, right to left	1.6 MHz
3. Half hole (d=1.8mm)	13kHz, 14kHz, 15kHz, 16kHz	Left to right, right to left	1.6 MHz
4. Through hole (d=1.8 upper, d=0.6mm bottom)	13kHz, 14kHz, 15kHz, 16kHz	Left to right, right to left	1.6 MHz
5. Notch (1.5mm×8mm)	13kHz, 14kHz, 15kHz, 16kHz	Left to right, right to left	1.6 MHz
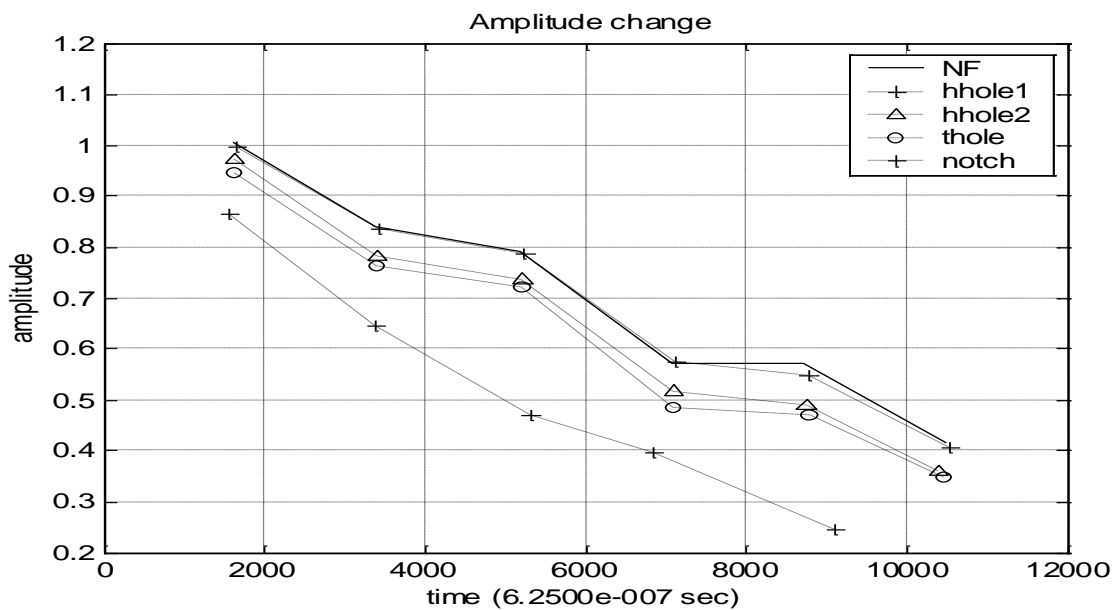
FIG. 2-9. Amplitude change of local peaks of anti-symmetric mode signals, propagating from the right to the left, with 14 kHz input frequency.
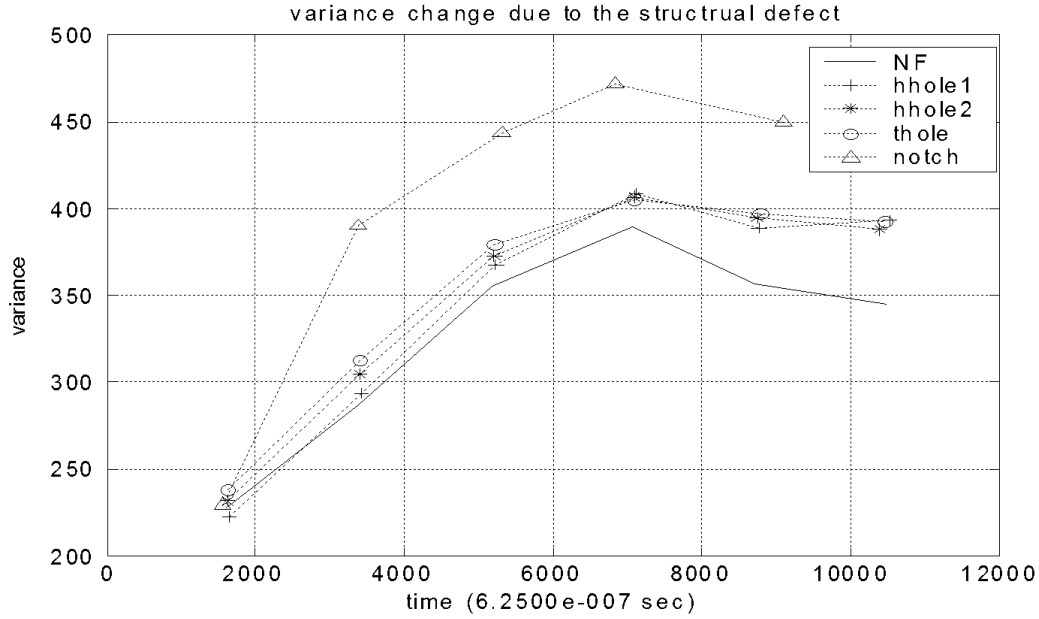
FIG. 2-10. Change of variance of local peaks from anti-symmetric mode signals propagating from the right to the left end, with input frequency 14 kHz.
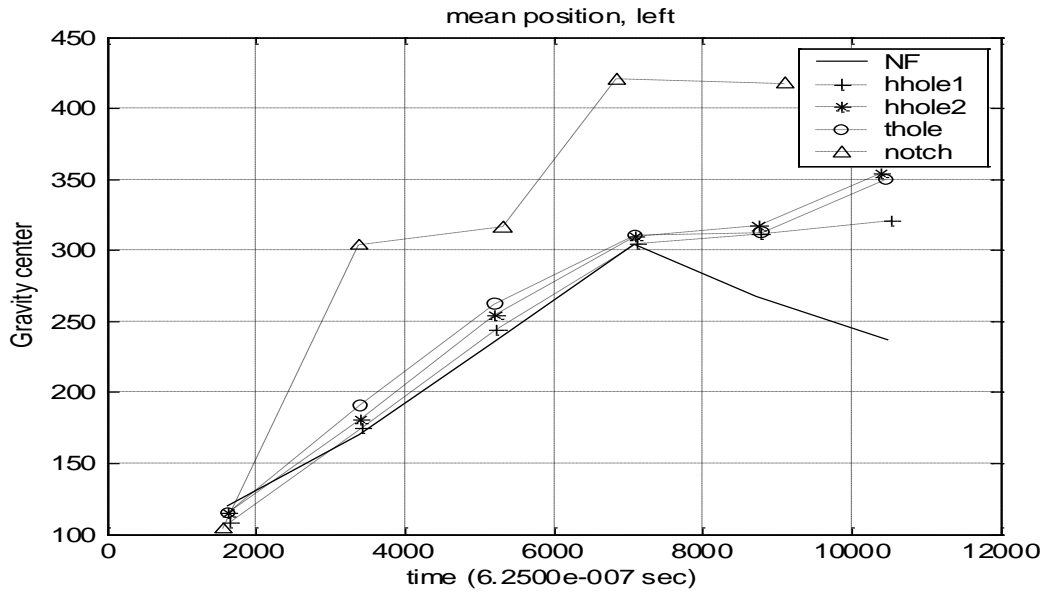
FIG. 2-11. Change of left part weight centre of local peaks from anti-symmetric mode signals propagating from the right to the left end, input frequency 14 kHz.

FIG. 2-11 demonstrates that the gravity centres of windowed signals shift away from the mid-point of the window. Note that the left part weight centre of the first local peak does not change because it is not affected by the scattering of Lamb waves.

The severity of structural defects could be estimated using these figures. The size of a flaw is approximately proportional to the decrease of the amplitude. The spread of the first local peak does not change much under different conditions, but the difference increases with time because of the scattering of internal discontinuities and Lamb wave dispersion. The larger the flaw size is, the bigger the difference between the normal and the flaw-related plots. All of these properties could be used for the evaluation of structural conditions.

Compared with the anti-symmetric mode, the symmetric mode waves are not sensitive to the structural changes. Therefore the symmetric Lamb waves are not used in this paper for monitoring the structural defects in brass tubes.

The severity of structural defects could be estimated using these figures. The size of a flaw is approximately proportional to the decrease of the amplitude. The spread of the first local peak does not change much under different conditions, but the difference increases with time because of the scattering of internal discontinuities and Lamb wave dispersion. The larger the flaw size is, the bigger the difference between the normal and the flaw-related plots. All of these properties could be used for the evaluation of structural conditions.

Compared with the anti-symmetric mode, the symmetric mode waves are not sensitive to the structural changes. Therefore the symmetric Lamb waves are not used in this paper for monitoring the structural defects in brass tubes.

2.1.5.2. *Structural flaw evaluation in water*

Note that all test results presented thus far are for brass tubes in air. However, acoustic propagation along tubes immersed in water is of interest because our final objective is to detect structural flaws in steam generator tubes. To accomplish this goal another tube was tested both in air and in water. The experiments performed are summarized in TABLE 2-3.

TABLE 2-3.   SIX CONDITIONS TESTED FOR A BRASS TUBE (#4)

Structural conditions	Activation frequency	Wave propagation direction	Sampling frequency
1. Normal, in air	16kHz, 17kHz, 18kHz, 19kHz	Left to right, right to left	300 kHz
2. Half hole (d=0.6mm), in air	16kHz, 17kHz, 18kHz, 19kHz	Left to right, right to left	300 kHz
3. Through hole (d=0.6mm), in air	16kHz, 17kHz, 18kHz, 19kHz	Left to right, right to left	300 kHz
4. Normal, in water	16kHz, 17kHz, 18kHz, 19kHz	Left to right, right to left	300 kHz
5. Half hole (d=0.6mm), in water	16kHz, 17kHz, 18kHz, 19kHz	Left to right, right to left	300 kHz
6. Through hole (d=0.6), in water	16kHz, 17kHz, 18kHz, 19kHz	Left to right, right to left	300 kHz

The moving window method is again used for the analysis. However, a different window size is adopted because the sampling frequency is 300 kHz, which is much lower than 1.6 MHz used in the experiments listed in TABLE 2-1. The results of analysis can be found in [2]. The results demonstrate that when the brass tube is immersed in water, it causes more energy leakage from tube to the media around; therefore the amplitude of local peaks of acoustic signals is lower in the water than in the air. On the other hand, the spread of local peaks in the water is larger than in the air. The changes of gravity centres in the water are similar to the changes in the air. In summary, the moving window method is an effective algorithm for the analysis of acoustic waves in tubes submerged in water.

2.1.5.3. *Estimation of defect location*

Defect localization in tubular structures is not as simple as it is in plate-like structures because of the complexity of the scattering phenomenon [4], [5], [6], and [21] in the case of tubular acoustic waves, results in weak and widely spread signals. Therefore, no obvious reflected peaks are found between local peaks in the raw signals. The methods used for defect localization in aluminium plates, using HHT could not generate satisfactory results. Therefore, a new method, named zooming windows, is introduced to estimate the flaw position in tube-like structures. The zooming windows are applied to the first two local peaks in the separated anti-symmetric waves. The right weight centre of

the first local peak is calculated and the left weight centre of the second peak is calculated with the window zooming around its centre.

As illustrated in the FIG. 2-12, the curves of left or right weight centres should diverge due to the effect of structural reflection. The divergent point indicates the approximate position of the defect. Thus, we are able to establish where the flaw is.
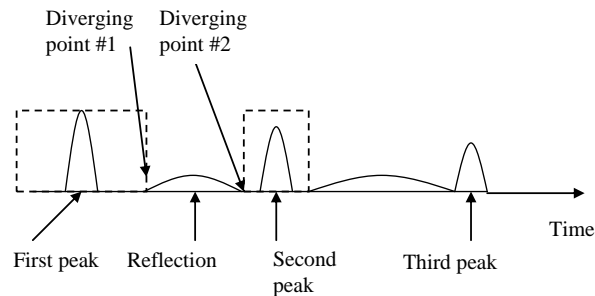
FIG. 2-12. The zooming windows and the diverging points.

FIG. 2-13 through FIG. 2-16 demonstrate the effectiveness of the zooming window. In FIG. 2-13 and FIG. 2-14, we notice that the divergent point for the first peak appears earlier than the second local peak. This indicates that the defect here is near the receiving sensors. In fact the defect here is located at about one-third of the tube length to the receiving sensors. From FIG. 2-15 and FIG. 2-16, the diverging point for the first peak appears later than the second peak. So we can tell the defect is far away from the passive sensors, and we know that the defect is in fact located at about two-thirds of tube length to the passive sensors.
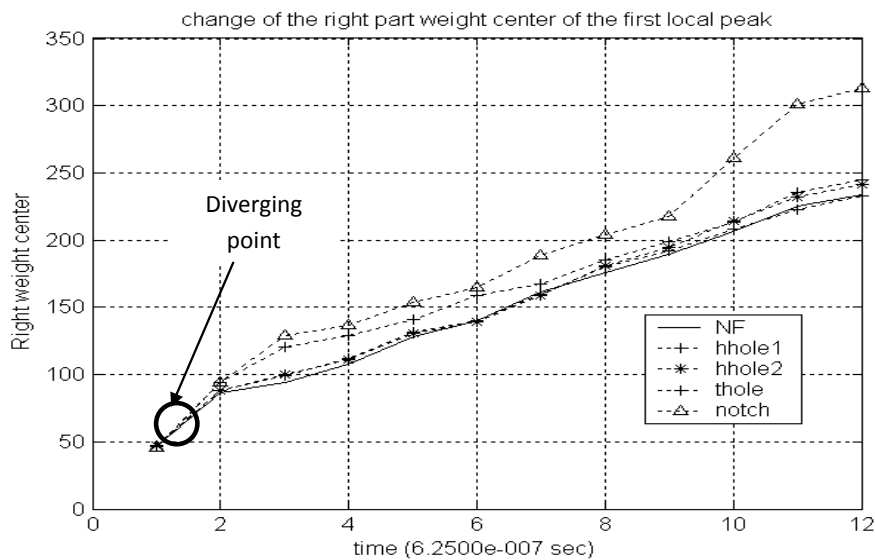
FIG. 2-13. The change of right part weight centre of the first local peak as the zooming window changing size from 100 to 1200, using anti-symmetric mode signals, propagating from the right to the left, input frequency 13 kHz.

84
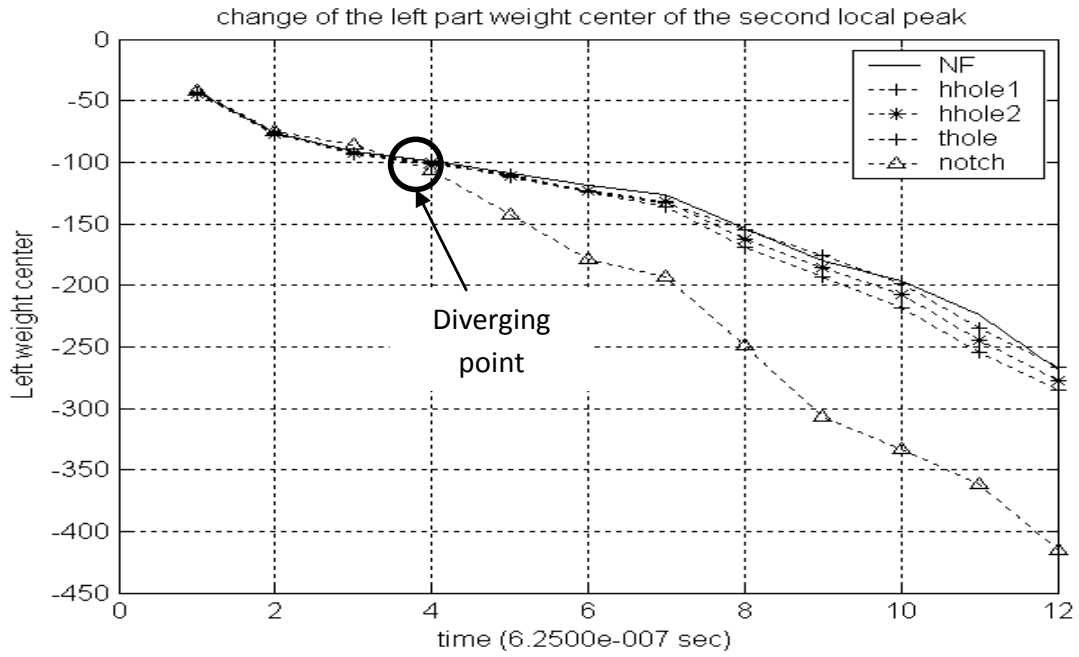
FIG. 2-14. The change of left part weight centre of the second local peak as the zooming window changing size from 100 to 1200, using anti-symmetric mode signals, propagating from the right to the left, input frequency 13 kHz.
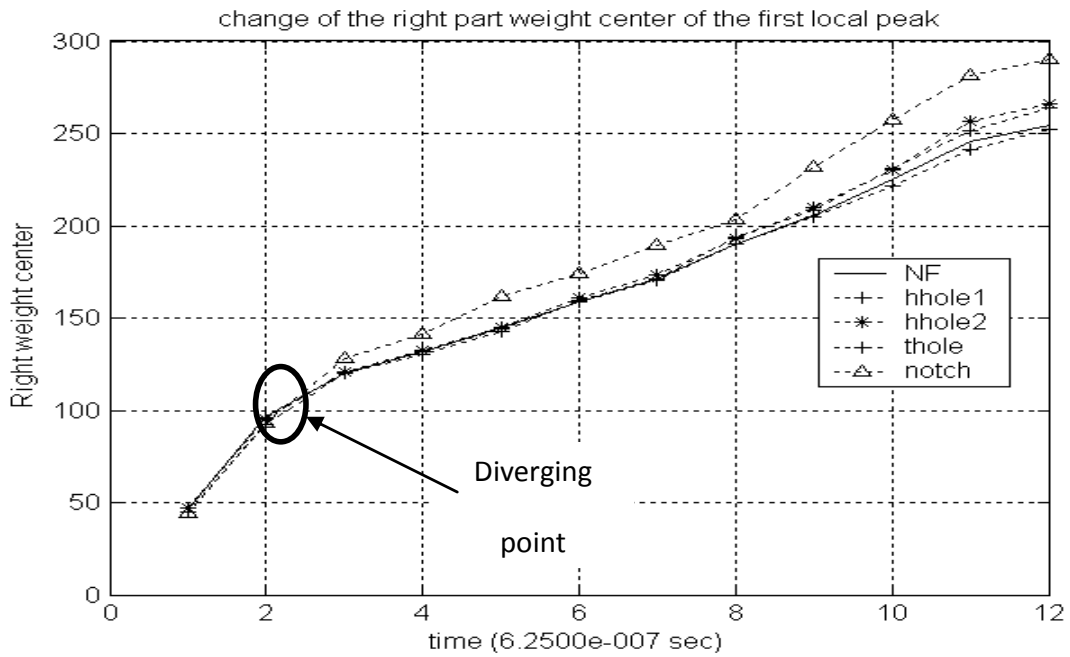
FIG. 2-15. The change of right part weight centre of the first local peak as the zooming window changing size from 100 to 1200, using anti-symmetric mode signals, propagating from the left to the right, input frequency 13 kHz.
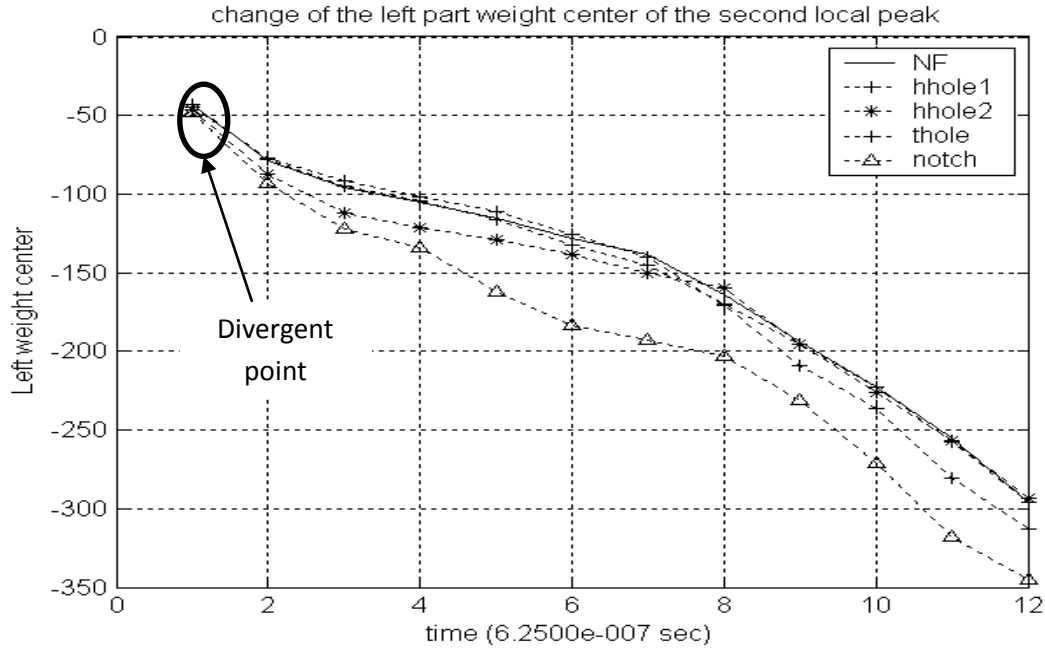
FIG. 2-16. The change of left part weight centre of the second local peak as the zooming window changing size from 100 to 1200, using anti-symmetric mode signals, propagating from the left to the right, input frequency 13 kHz.

2.1.5.4. *Classification of tube defects*

The accuracy of the classification for defects in tubular structures depends primarily on the selection and extraction of representative features. In this research, the features extracted through moving window technique are used for defect classification. Five structural conditions have been trained and the representative feature matrices are collected for classification. Experimental data are collected for each structural condition under different input frequency, and the results generated by moving window method are used for classification. The normalized distance between the tested matrix and the trained matrices are calculated and listed in TABLE 2-4. We can see the matrices for partial-hole and through-hole defects have similar distance to a test matrix, so it is easy to misclassify them. The reason is that these three tube flaws have similar features. Therefore, other classification methods and representative features [1], [2] have also been explored to increase the success rate of the method implemented here; these not be discussed in this paper. FIG. 2-17 illustrates the plots of the measurement residuals between the test and the training conditions. Based on this plot, the test defect is classified into a through-hole in a tube, which is the actual condition in our study.

TABLE 2-4. DISTANCE BETWEEN TEST AND TRAINING MATRICES

Training Test	NF	Half hole (0.6mm)	Half hole (1.8mm)	Through hole(0.6mm)	Notch
NF	0.0272	0.0568	0.0597	0.0650	0.4048
Half hole (0.6mm)	0.0224	0.0074	0.0058	0.0105	0.2745
Half hole (1.8mm)	0.0418	0.0216	0.0087	0.0064	0.2010
Through hole(0.6mm)	0.0573	0.0311	0.0144	0.0082	0.1765
Notch	0.4564	0.3395	0.2760	0.2406	0.0118

86
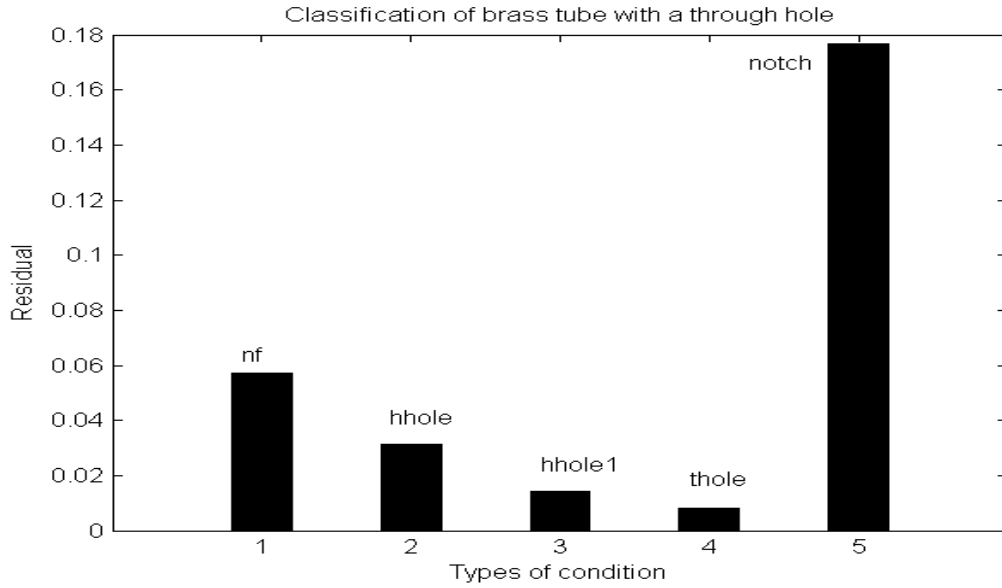
FIG. 2-17. The classification of tube defects.

2.1.5.5.   Noise reduction of measurements in brass tubes

Under a noisy environment, the structural monitoring proposed in this research becomes more complicated because the background/process noise may cause the non-stationary signal processing techniques to be less effective. Hence the de-noising process is very important.

There are two types of noise in a steam generator system, the high frequency noise caused by steam voids and structural vibration, and the low frequency noise caused by the turbulence of water flow. The noisy environment has been simulated in the experiments during this research. The noisy raw signals are shown in FIG. 2-18. We have applied HHT as an advanced de-noising algorithm to extract useful signals in this study. We first decompose the raw signals into multiple IMFs as shown in FIG. 2-18. The number of levels is adjustable based on the complexity of the physical process. Then a purified synthetic time series is reconstructed by selecting important IMFs as shown in FIG. 2-19.
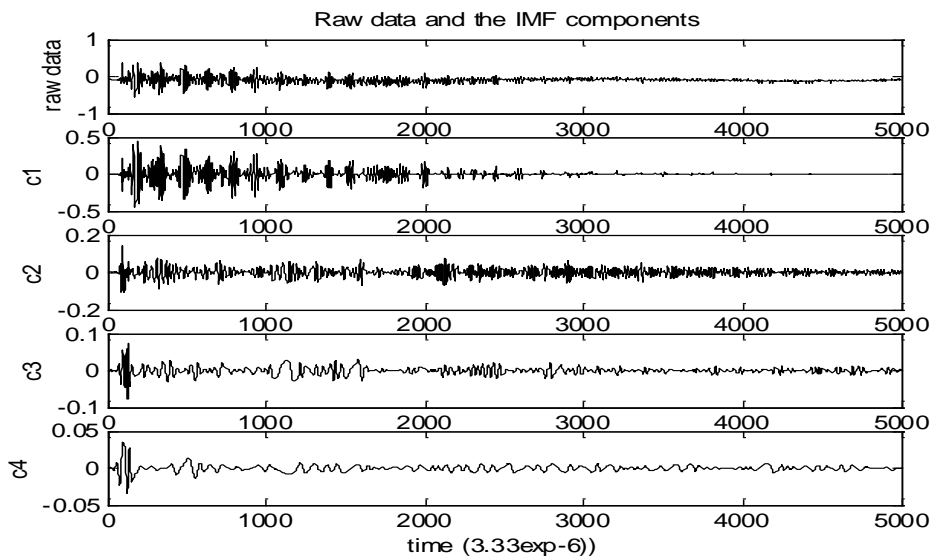
FIG. 2-18. Raw data and the intrinsic mode functions (IMFs) derived from the Hilbert-Huang transform (HHT).
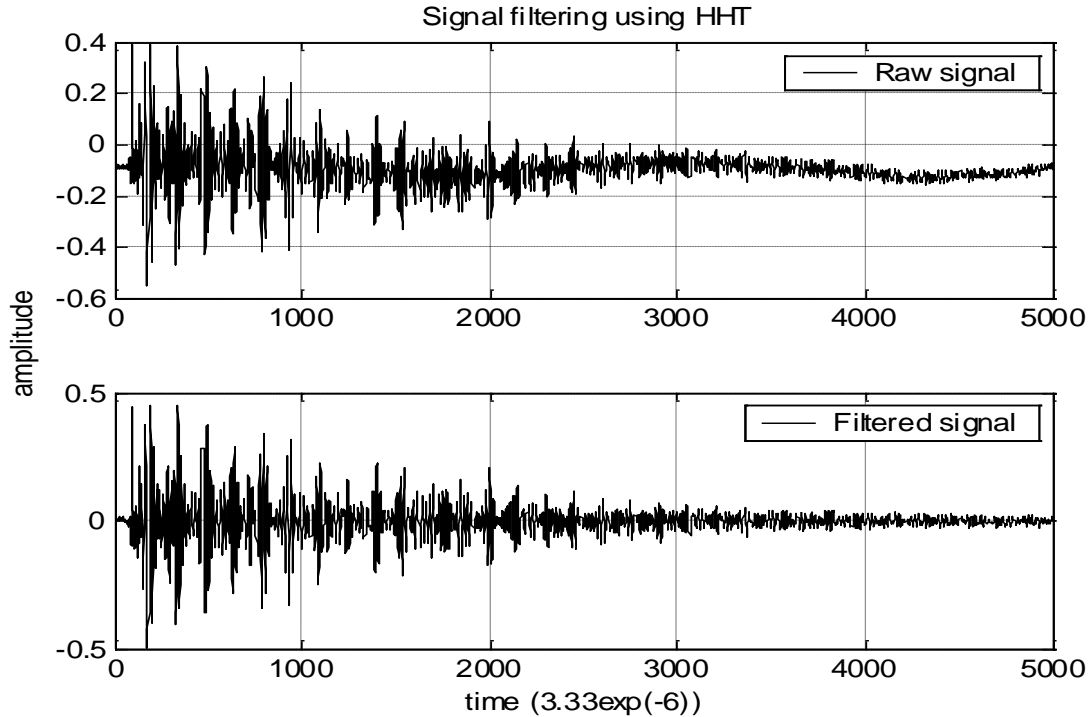
FIG. 2-19. Raw data and the reconstructed data using HHT.

We can see the representative signals can be perfectly extracted from the noisy data, and the pre-processed data are suitable for the implementation of the digital signal processing techniques proposed in this research for structural integrity monitoring.

2.1.6.   Application of Hilbert-Huang transform for detection of faults in induction motors

Induction motors (single-phase and multi-phase) are used extensively in industrial systems and consumer appliances. The size of the motors varies from less than a kilowatt (kW) to a few Mega-Watts (MW). The dynamics of an induction motor is characterized by its slip frequency which is the difference between its synchronous (or no-load) frequency and the actual shaft rotational frequency. The slip frequency increases with the load on the motor. The current drawn by the stator changes with the load, and any load fluctuations on the motor are reflected by the motor current fluctuations. Thus, the motor acts as a transducer. For example when a broken rotor bar is present in a rotor, the current pattern at the broken bar changes, causing additional loads on the motor, and modulates the line current drawn by the motor.

The spectral side-bands created by the modulations in the motor current indicate different forms of faults in the machinery.

In this work the authors applied the HHT technique [12] for detecting the effect of broken rotor bars and the eccentricity between the rotor and the stator in an induction motor. The study was performed for the case of motor start up, during which the speed increases from zero to the steady-state motor speed. This is an example of transient or non-stationary signal analysis, and the HHT was able to decipher the information as a function of instantaneous frequency, with increasing rotor speed.

2.1.7.   Concluding remarks

From the study on transient acoustic signals and analysis of motor variable speed dynamics, it is shown that the HHT has the ability to process non-stationary and nonlinear signals effectively. The Lamb waves used in the analysis of the tubular specimen are very sensitive to structural defects in brass tubes. The defect size, location, shape, and surrounding media are among the factors that affect the Lamb wave propagation along guided structures. The dimension of the smallest flaw illustrated in

this study is about one millimetre. However, smaller defects including micro-structural variations could be monitored because the propagation of elastic wave strictly depends on the microstructure of materials.

The Lamb wave is not as simple as the pure longitudinal and transverse waves that propagate along an infinite medium. The complexity comes from the combination of multi-mode waves in plate or tubular structures. There are four types of Lamb waves in tubular structures. For each mode, the wave speed decreases nonlinearly as frequency-thickness product increases, accompanied by the appearance of new modes. Hence the features of experimental data collected from the piezo-sensor system cannot be easily visualized and analyzed. Non-stationary signal processing is very important for acoustic data analysis, and for successful diagnostics of structural flaws.

The structural flaw may change the characteristics of acoustic signals in time and frequency domains. For this reason Hilbert-Huang transform is introduced for its adaptability and sensitivity in separating wave modes. The HHT is also highly effective in filtering out background noise caused by water flow and void transport. Two transient signal-processing techniques, the moving window and zooming window, are developed for the acoustic signals activated by sine pulses. Sensitive features have been extracted for the detection, localization, size estimation, and classification of structural flaws.

An optimal setup is critical in collecting representative acoustic signals. A multi-sensor suite is deployed in a way that two sensors are diametrically opposite to each other, such that the single mode Lamb wave signals could be separated. The separated Lamb waves have been applied for the flaw diagnosis of brass tubes. Excellent results have been achieved by applying moving and zooming windows to the anti-symmetric mode signals. In addition, the selection of appropriate sampling frequency is necessary for generating distinguishing features.

The methods of transient data analysis are proved to be effective for the brass tubes submerged in the water and under the effect of two-phase flow. The HHT has been successfully implemented for noise reduction. A direct effect of submerging test specimens in water is the increase of energy leakage in Lamb waves.

There are potentially a multitude of applications of this technique in aerospace and civil structure industries. The techniques created here are especially useful for the on-line and in-situ monitoring of critical equipment to improve system reliability and safety.

2.2. A FALSE ALARM FREE, ADVANCED LOOSE PARTS MONITORING SYSTEM, ALPS

By: G. Por
College of Dunaujvaros

2.2.1. Introduction

Basics ideas of Advanced Loose Parts System (ALPS) were developed at the Budapest University of Technology and described in papers [22] through [26]. Monitoring systems for Paks NPP were developed and are maintained by APandSD Ltd, Budapest. This section presents the important parts of the system and some of the results achieved by the system.

2.2.1.1. The main tasks of a loose part system

(1) The first task is to detect the event. The system should be very sensitive to events.
(2) At the same time, it is important to reduce false alarm rate.
(3) An important task is to localize (and if possible to identify) the source of the acoustic event.
(4) What can be the size of the knocking object?
(5) Is it still present? Is the loose part knocking still or is it stuck?
(6) What is the probability of having a loose part?
(7) What can be done to catch them during the initial start of the main pumps after refuelling?
(8) Are there other acoustic noises of interest to the maintenance personnel? Can a loose parts monitoring system be used for detecting those?

2.2.1.2. Sensitivity of the detection

− Earlier systems used either signal intensity, RMS value, or its derivatives;
− Introducing a new solution in ALPS consisting of:

- Auto-regression (AR) modelling,
- Pre-whitening,
- Sequential Probability Ratio Test (SPRT).

This is an effective approach and is sensitive -- how does this work? A typical loose part appears as a burst on relatively large background noise in a NPP (see FIG. 2-20). The background is coloured which means it contains very often harmonic components as well.
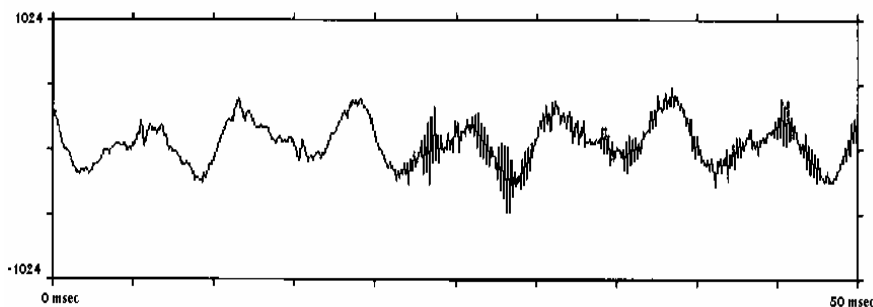
FIG. 2-20. Typical loose part signal on high background noise.

From autoregressive modelling to pre-whitening

If $x(t)$ is the measured signal, the N samples are defined as: $x_1, \ldots x_N$.

- First we fit an AR model to the signal and estimate the coefficients using the recorded background noise (P is the model order):

$$x_k = \sum_{i=1}^{P} a_i x_{k-i} + w_k$$

- Then the background noise is subtracted by calculating the z_N forward linear prediction error, using the y_N measured signal and the autoregressive coefficients of the reference background signal:

$$z_N = y_N - \sum_{i=1}^{P} a_i \cdot y_{N-i}$$

FIG. 2-21 illustrates how dramatic this improvement can be using AR filtering.
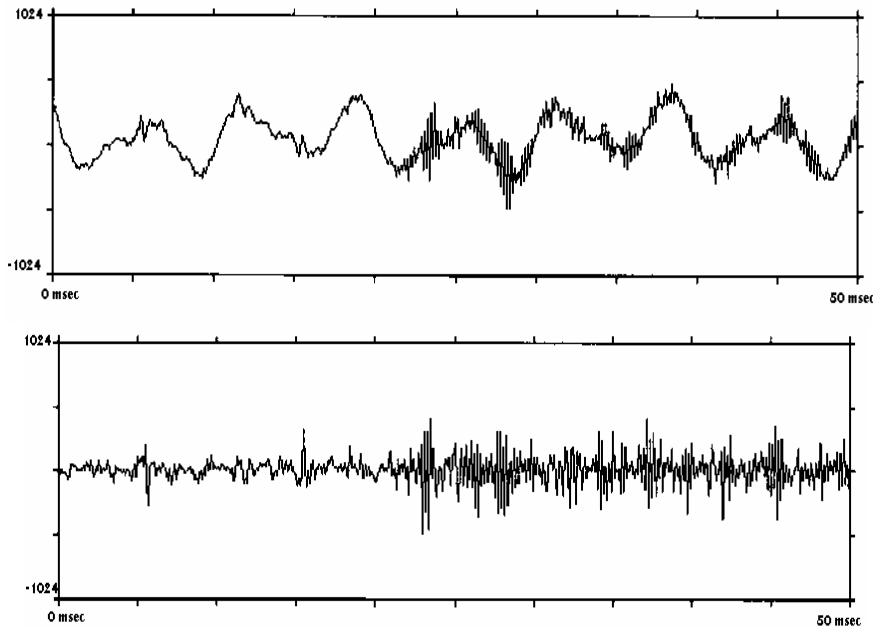
FIG. 2-21. Improvement by using AR filtering.

Sequential probability ratio test (SPRT)

SPRT is a statistical decision function and gives the best estimate with a given uncertainty limits from the shortest record (see details in [23]). The log likelihood function for decision making between the normal hypothesis and the anomaly case is defined by λ_n

$$\lambda_n = \ln \frac{p_n(z_1, z_2, ..., z_n | \sigma)}{p_n(z_1, z_2, ..., z_n | \sigma_0)}$$

where σ and σ_0 are standard deviation for the event and for the background. In case of a Gaussian distribution λ_n can be estimated recursively

$$\lambda_{n+1} = \lambda_n + \frac{\sigma^2 - \sigma_0^2}{2 \cdot \sigma^2 \cdot \sigma_0^2} \cdot z_n^2 + \ln \frac{\sigma_0}{\sigma} \quad , \qquad \lambda_0 = 0$$
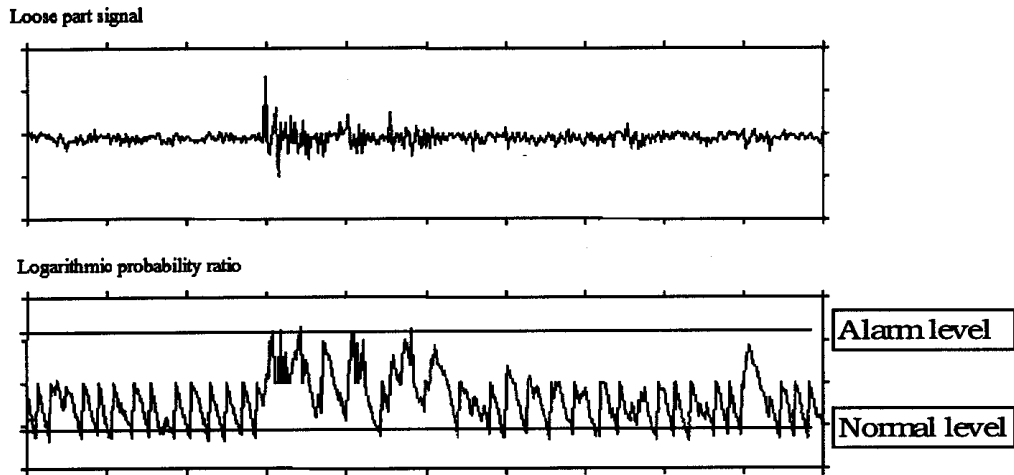
FIG. 2-22. How SPRT works in practice.

The λ_n decreases as the signal moves towards the normal case, and increases as it approaches the anomaly condition.
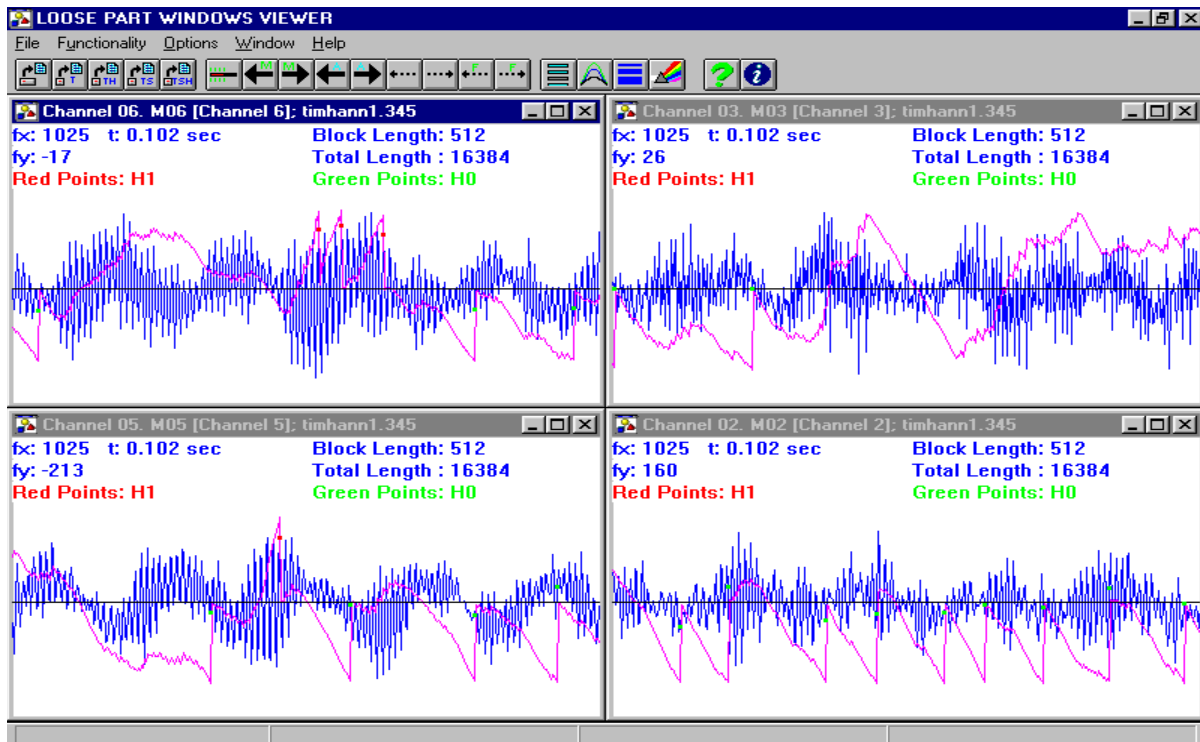
FIG. 2-23. Example of identification of events buried in background noise (Measurement in Paks).

The blue line (in FIG. 2-23.) indicates the noise signal, while the purple line is the result of the SPRT. Red dots mark the events buried in the high background noise, while green dots (when purple line hits the bottom decision level) indicate the normal behaviour of the device.

2.2.2.   ALPS in the Paks NPP

FIG. 2-24 is a schematic of the Paks NPP loops showing the location of sensors.
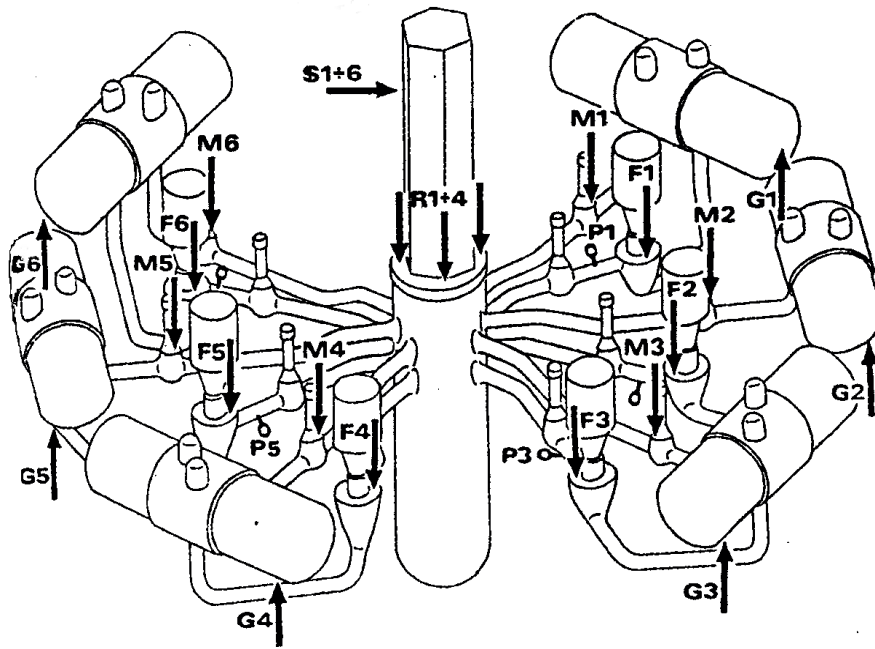
FIG. 2-24. Sensor positions in reality.

Accelerometers are positioned on all main components of a six loop PWR of VVER type (Paks NPP). They are installed on steam generators (G1-G6), on main coolant pumps (F1-F6), on main closing valves of hot legs (M1-M6), on the flange of reactor vessel (R1-R4), and on the control rod drive mechanisms (S1-S6).

2.2.2.2. Calibration procedure by hammering

Calibration is carried out during installation and before each fuel cycle. Its first purpose is to prove its sensitivity. FIG. 2-25 shows a typical hammer test, when hit is made by a hammer close to the sensor.
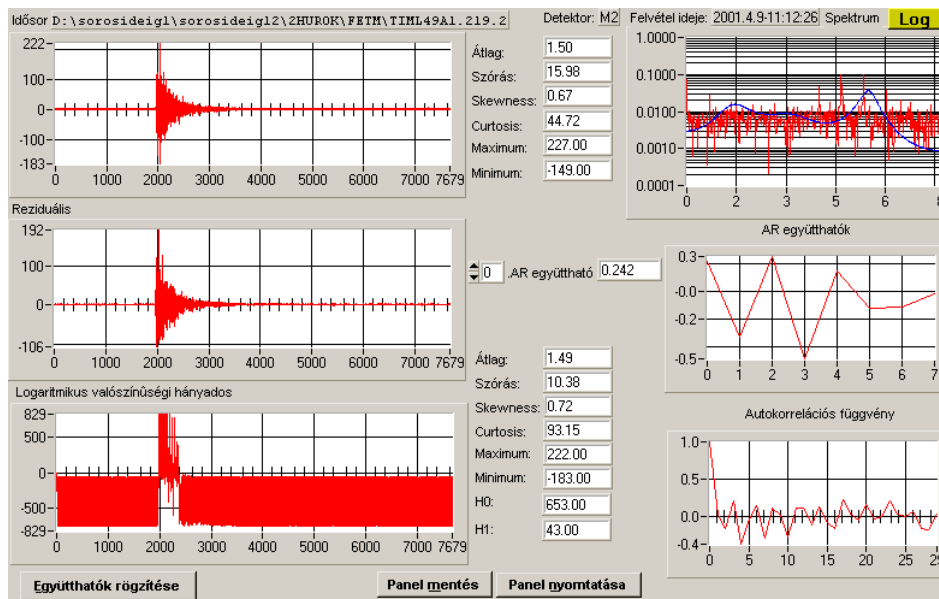
FIG. 2-25. Typical burst from calibration knock near to detector.
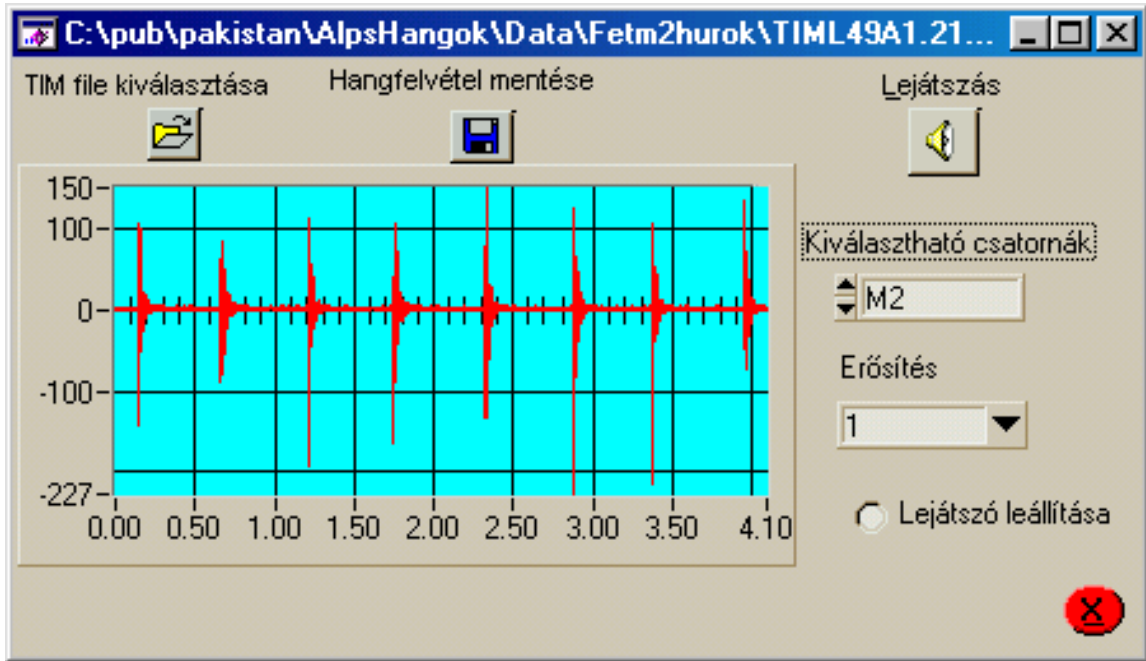
FIG. 2-26. Hammer test record.

During restarting of each Unit hammering test records are fixed and saved for later mass estimation of any events noticed by the ALPS.

If the sensor is at a distance of about half a meter the signal recorded by that sensor (FIG. 2-27) shows some distortions of the signal in comparison with its original form (see FIG. 2-25.)
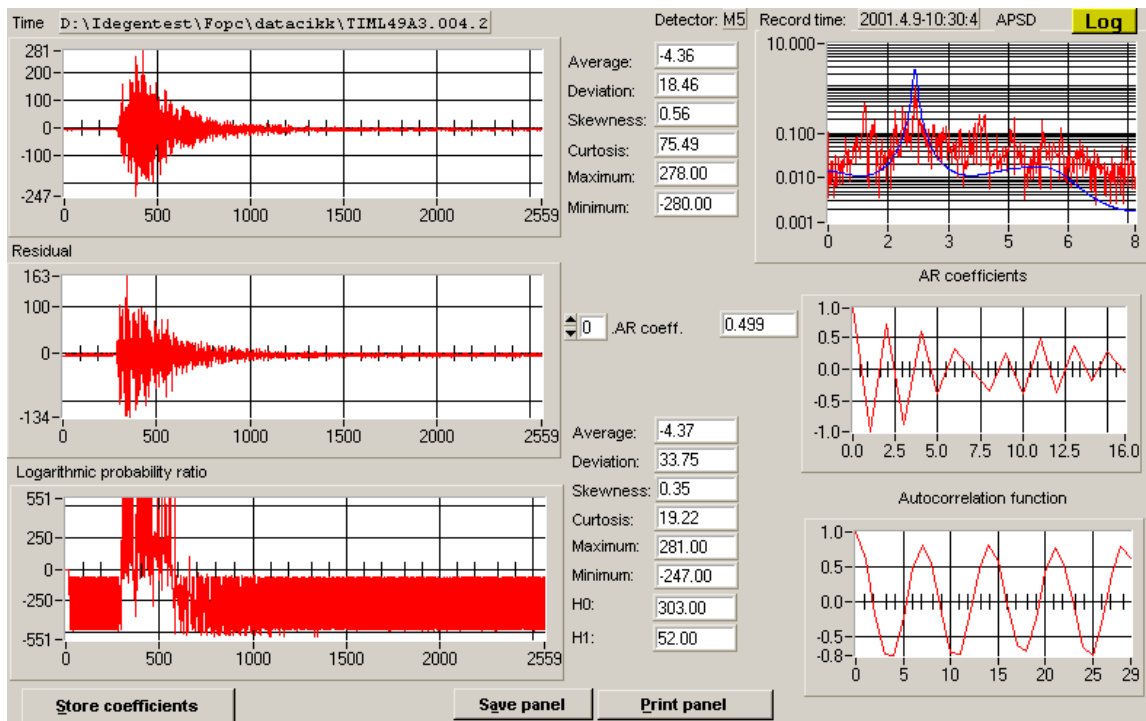
FIG. 2-27. Typical burst from hammering near to sensor (M5-M5).

A sensor that is farther away, about 9 meters (but still in the same loop), records much weaker effect from the same knock (compare FIG. 2-28 with FIG. 2-25).

94
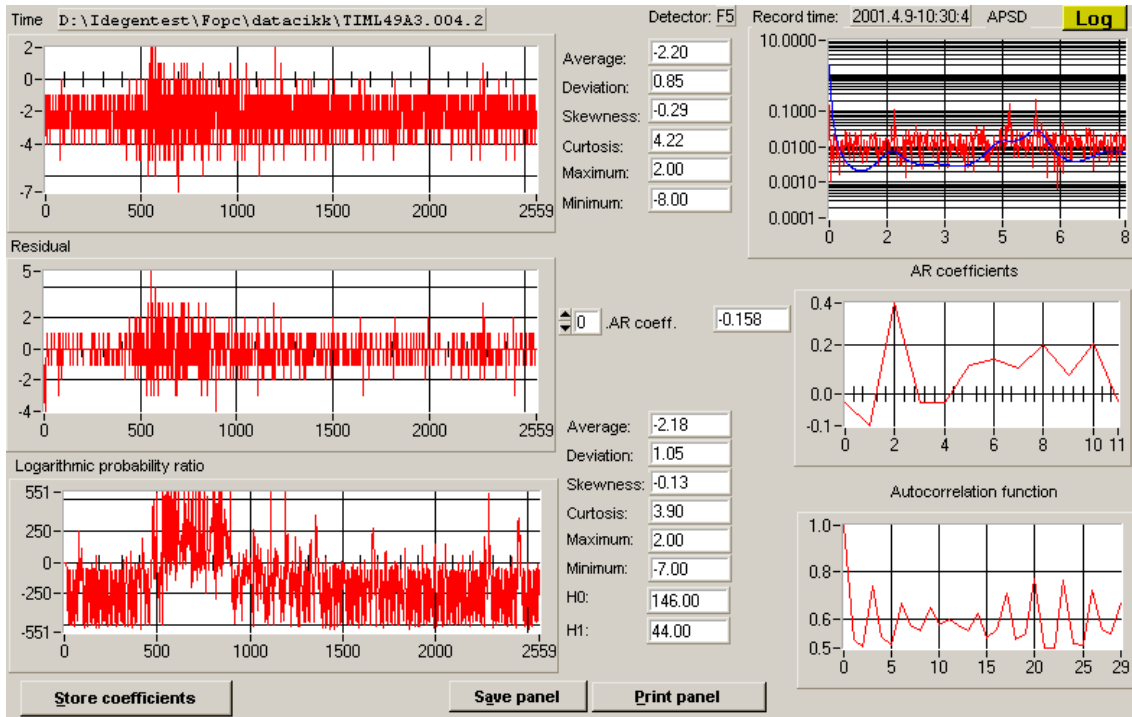
FIG. 2-28. Large distances from the source of the calibration knock (M5-F5).

Finally, the sensor in the next loop can hardly notice this burst. It is almost not seen in the background noise (see FIG. 2-29). ALPS can detect this event using the SPRT. Even though this method is sensitive, the number of alarms is limited because:

− SPRT selects events that have non-Gaussian loose part like distribution;
− We apply an expert system in the next step to reduce the number of false alarms.
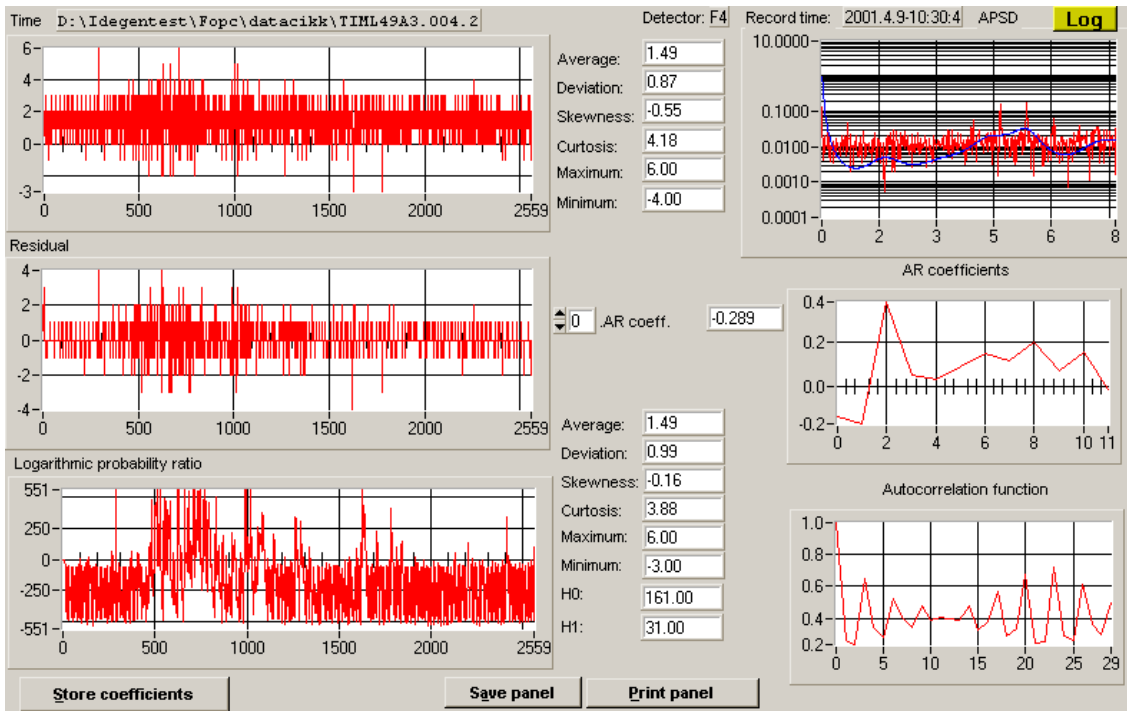
FIG. 2-29. Absolutely poor signal to noise ratio (M5-F4) to the next loop.

2.2.2.3.   How can the expert system improve identification?

The following are the parameters used for the classification:

- Distribution of SPRT events;
- AR coefficients;
- Autocorrelation function;
- Frequency spectra;

  - AR power spectrum,
  - power spectrum from FFT,

- Statistical moments;
- Maxima and minima;
- Distribution of detectors sensitive to events.

2.2.2.4.   Closest neighbour method used in expert system of ALPS

The closest neighbour for the ξ incoming events is one of the $\xi_1, \xi_2, \ldots \xi_n$ events, noted as Ξ, for which:

$$d(\xi) = \left\{ \rho(\xi, \Xi) \leqslant \rho(\xi, \xi_i), i = 1,2,\ldots,n \right\}$$

Where ρ metric function in the event space defined as

$$\rho(\xi, \xi_i) = \left(\sum_{j=1}^{N} \left(\frac{\xi_j - \xi_{i,j}}{\xi_{i,j}} \right)^2 \right)^{-\frac{1}{2}}$$

It was proven that if the incoming event belongs to one of the already defined M classes, then the d(ξ) function fulfils the conditions of the Bayes theorem. The risk of the decision decreases as the number of known events, n, is much larger than the number of existing classes: n >> M.

2.2.2.5.   MOV shaft vibration (M6-case study)

Metal-to-metal impacts were noticed from the main closing valves in many cases. Typical record can be seen in FIG. 2-30. It was shown that it came from the vibration of the shaft of the valve touching the outer wall. So it is not really a loose part. But it can provide an indication of ageing of the given closing valve. Today ALPS is routinely used for monitoring MOV.
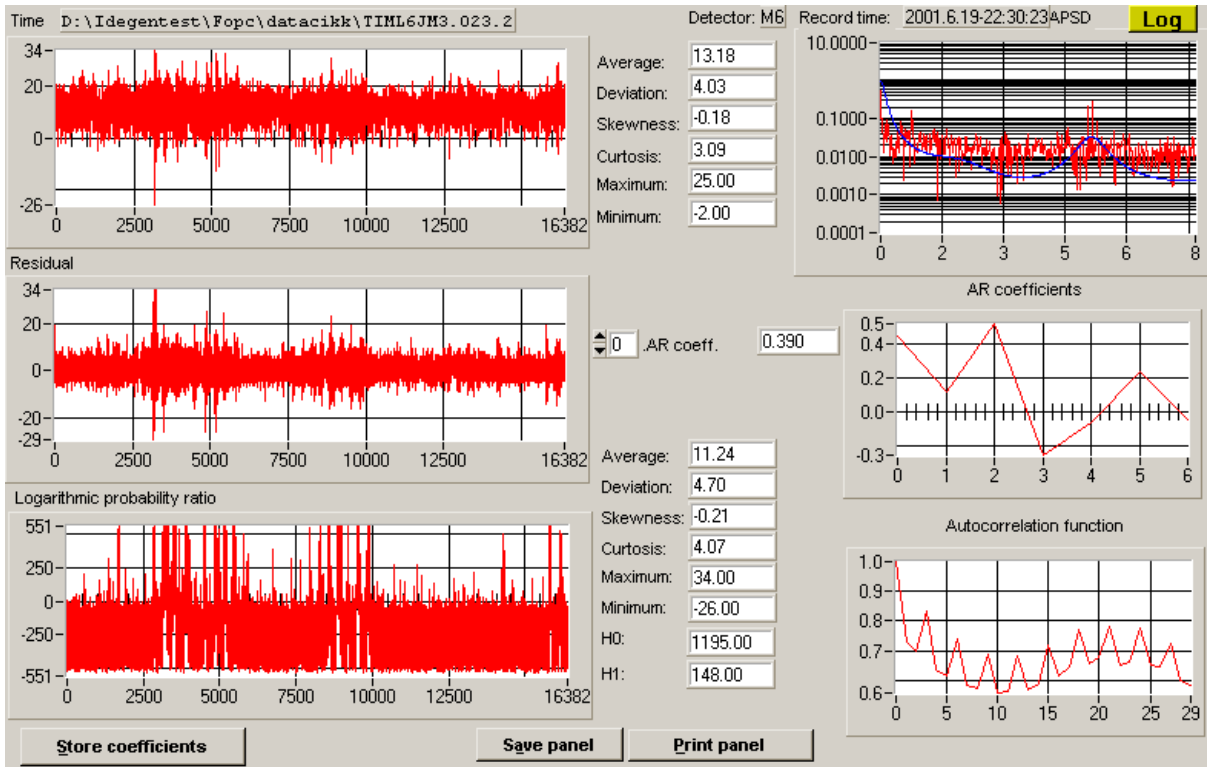
FIG. 2-30. Typical noise from the shaft of main closing valves detected by ALPS system.

2.2.2.6. *When can you find most of the loose parts?*

According to ASME and NRC as well as according to our experience most of the loose parts are noticed during the start-up of the main coolant pumps.

FIG. 2-31 shows the measurements during the start-up of the main coolant pumps (MCP).
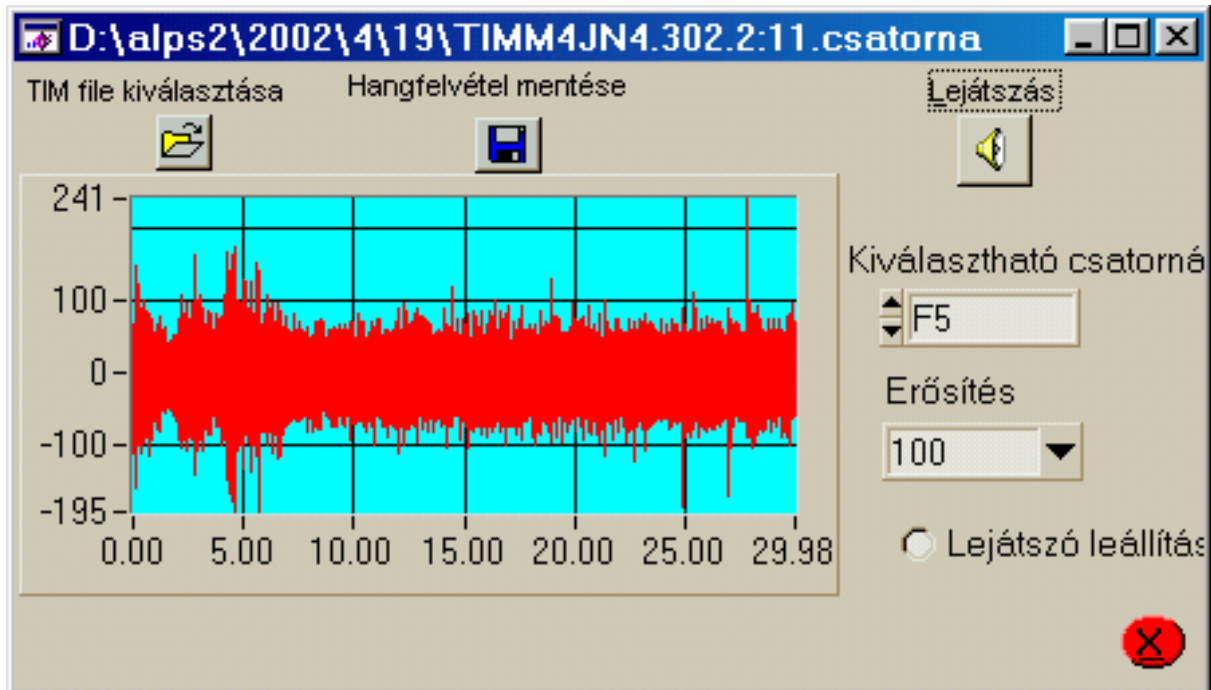
FIG. 2-31. A time record using start up program of ALPS system.

The beginning of the file contains the increasing noise from the electrical motor of the main coolant pump, but from the 5th second there are loose parts, which according to usual classification are called debris. They disappear from the system in one minute.

2.2.2.7. How does the ALPS work at Paks NPP?

- All four units: continuous sampling on each units by the data acquisition PC (16 kHz) on-line event analysis; when an event is found, 3-second records are stored;
- Fixed data transferred to central data processing PC for further analysis and expert system selection;
- When a decision is made, an automatic report is generated.

2.2.3. Summary

- ALPS applies AR+SPRT very effectively for detecting events and reducing false alarm rates;
- ALPS uses the expert system to identify the following:

  - source of the event,
  - reducing further false alarms.

- ALPS has an automatic start-up recording;
- ALPS is routinely used in all the four Units of Paks NPP;
- ALPS can be used for acoustic monitoring of other equipment (MOV, maintenance work, control rods).

2.3. RESULTS OF EVALUATION OF LOOSE PART BENCHMARK DATA MEASURED IN DUNAUJVAROS

By: G. Por, T. Deak, T. Dobjan
College of Dunaujvaros, H-2400. Tancsics M. 1/A, Hungary

2.3.1. Introduction

In the frame of the Coordinated Research Project (CRP) advanced surveillance, diagnostics, and prognostics techniques used for health monitoring of systems, structures, and components in nuclear power plants organized by IAEA, experiments were set up for a benchmark test. In this section, the method and the results of benchmark data evaluation are presented.

2.3.2. A brief description of the measurements

The test loop selected for Benchmark test of CRP was an actual working coolant loop used for a TIRA vibration shaker of the College of Dunaujvaros. A schematic drawing of the loop with sensors is presented on FIG. 2-32. The loop has a relatively large 10 m^3 pool of water. The pump can pick up water from that pool and send it via relatively long tubes. First, there are few bends after the pump (actually not shown in details on FIG. 2-32), and then the water flows into a long straight tube of more than 50 m, where the actual measurement took place in the first elevation of the M building at the College of Dunaujvaros (Hungary).
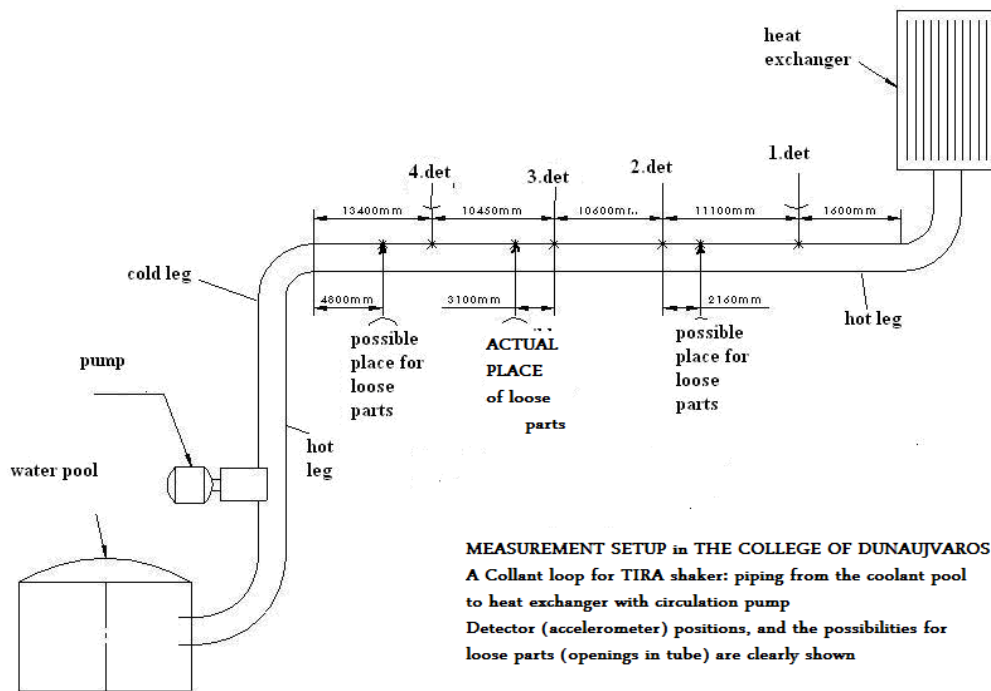
FIG. 2-32. Schematic of the test loop for loose part benchmark showing the place of sensors and possible loose parts.

Four sensors were fixed along this straight part of the loop (see exact positions in FIG. 2-32). The cooling line, after four more bends (not shown on figure) arrives at the heat exchanger (in fact there was a filter just in front of the heat exchanger to catch the loose part if the holding fishing-line were broken). Then the water returns via a parallel hot leg to the water pool (hot leg played no role in actual measurements).

Loose parts in the experiments were: a large and a small metal bolt and also a piece of bakelite. In actual measurement they were put into the tube via a T shaped junction which attaches a short tube to the straight line between detectors number 4 and 3 (see FIG. 2-32). There were other similar T shaped junctions before the water in cold loop arrives to the detector number 4 and between detectors 2 and 1 (see all details for sensor positions on FIG. 2-32) for later experiments, since this experimental place will exist also after terminating CRP. The attached T shaped tubes had a closed end. The loose parts were hanged on a lousy plastic line (fishing-line). Without flow the loose part was just lying on the bottom of the long linear tube from the vertically attached short tube. When flow started the loose part was picked up by the water stream and it was knocking on the inner wall of the tube (one could actually hear that).

Measurements were recorded with different sampling times: 1, 5, 10, 25 and 50 kHz for all three loose parts. To facilitate the localization methods for those who make it via definite sensing tests (for example using neural network method), separate measurements were carried out hitting the tube outside by a metallic rod. Such records were made hitting the tube between each pairs of sensors on half way and on quarter ways.

2.3.3. Measurements data acquisition

The loose parts are shown in FIG. 2-33.

Type:	M10 bolt	M8 bolt	bakelite piece
Mass:	11,16g	5,58g	1,67g
Photo:			

FIG. 2-33. Photos of loose parts selected for benchmark test.

Sensors: Brüel & Kjaer 4513-01, Positions: see FIG. 2-32.
Cable: Type: Belden product 75 Ohm coaxial cable Length: 40 m
ADC: NI cDAQ-9172 frame, NI 9233 sampling card: see FIG. 2-34.
The parameters of NI 9233 DAQ card are:

− 2 mA IEPE signal conditioning for microphones and accelerometers;
− 50 kS/s per-channel maximum sampling rate; AC-coupled (0.5 Hz);
− 24-bit resolution; 102 dB dynamic range; antialiasing filters;
− 4 simultaneously sampled analogue inputs, ±5 V input range;
− Smart TEDS sensor compatibility.

FIG. 2-34. The NI 9233 DAQ card and the NI cDAQ-9172 frame used for data recording.

2.3.4. Description of data acquisition software

(developed by MAID Laboratory, College of Dunaújváros, Hungary)

The necessary program for data acquisition was developed for CRP Benchmark using LabVIEW programming base. The sampling program can handle four channels and it can save these signals by the given parameters. The operator display of the program is shown on FIG. 2-35.
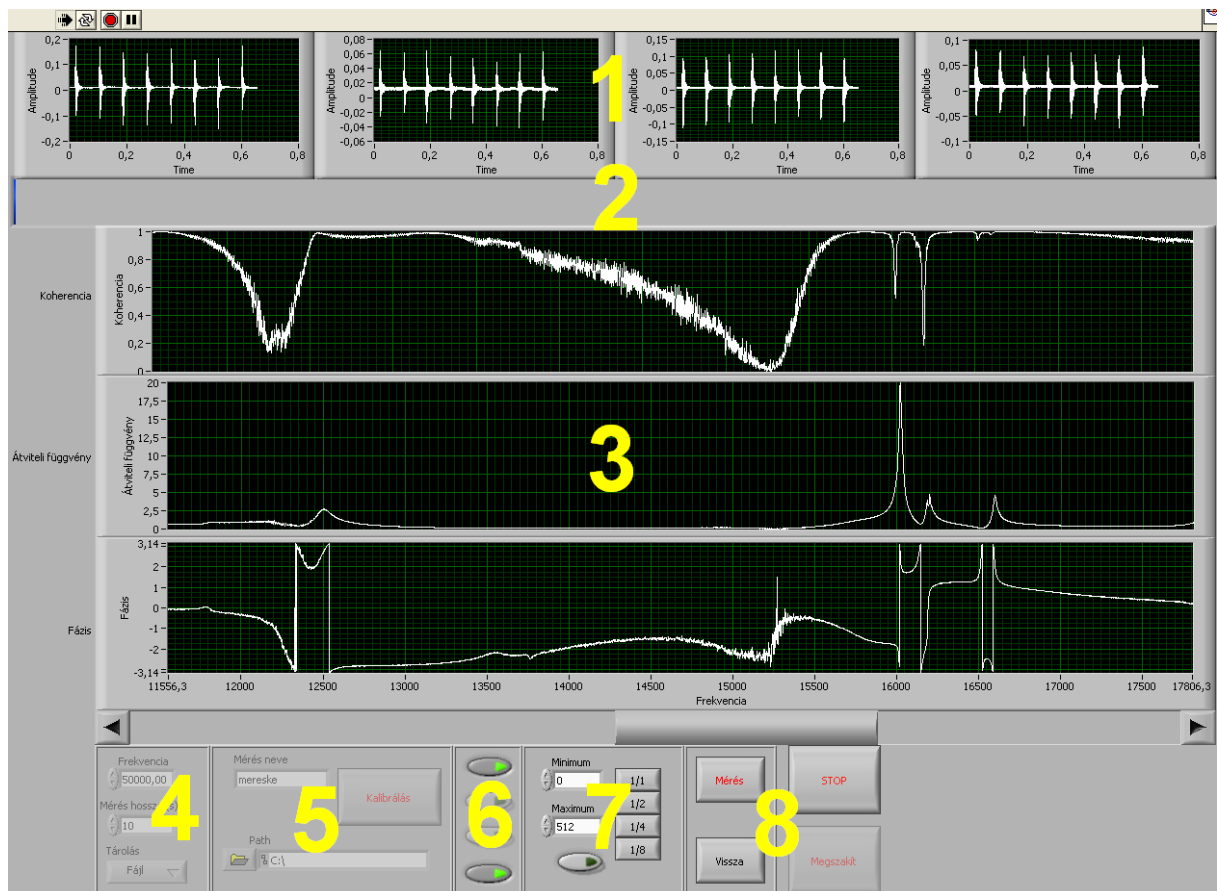
FIG. 2-35. The user interface of the measuring program.

The definition of the numbers shown in FIG. 2-35 is as follows:

1: Indicators of the measured signals
2: Progress bar
3: Coherence, transfer function, and phase of two selected signals
4: Initialization controls
5: Options of data storage
6: Signal selection buttons for functions (3)
7: Zoom
8: Measurement control

The program saves the signals into an ASCII text file. The file has the following format:

Header line:	Date (yyyy.mmm.dd) and time (hh:mm.ss) of the saving and the reciprocal of the sampling frequency (Δt)			
Data:	Time values (in split second)	Values of the 1st channel	Values of the 2nd channel	Values of the nth channel

It is worth to notice (see FIG. 2-35), that during sampling not only time signals were visible, but simultaneously also the coherence, transfer function, and phase function (in window "3" in FIG. 2-35). This ensured that only correctly measured signals were recorded, each set of four signals does contain come kind of correlation.

2.3.5. Basics of the data evaluation procedure

Data were first analyzed using event recognition system based on Sequential Probability Ratio Test (SPRT). That procedure is used in our loose parts monitoring systems ALPS [27] for event detection. To use the well-known algorithm [23], beforehand one has to filter the signal using an adequate filter. For this purposes we used autoregressive adaptive filter (AR filter) developed also in LabVIEW. Then SPRT was applied to the signal. The SPRT routine was also programmed in LabVIEW. Finally we estimated the power spectra for background parts (we shall call them event A from now on) and for those parts of the signal, which had been selected by SPRT (from now they are referred as events B. Spectrum estimation was carried out using MATLAB. In the following, the details of the method and the programs are given.

2.3.5.1. Filtering the signal using AR modelling

The theory of SPRT derived mainly for stochastic processes. Therefore it is advisable to remove at least partly most of deterministic components. Also SPRT work better for stochastic processes with zero mean. Therefore it is practical to filter out the deterministic and DC components of the time series. For this purposes we use the AR filter. The formula for AR filter reads as:

$$y_i^{filtered} = y_i^{measured} - \sum_{j=1}^{P} \Phi_j y_{i-j}^{measured} \qquad . \qquad (1)$$

In this equation i=1,2,…,N where N is the size of the array, Φ_j is the autoregressive coefficients and P is the order of the autoregressive model.
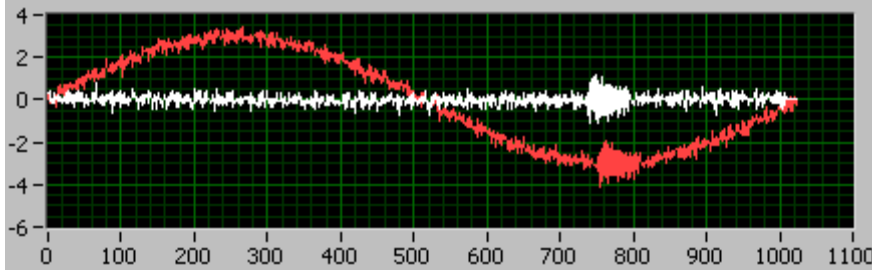
FIG. 2-36. An example for an AR filter (red – measured data, white – filtered data).

The autoregressive coefficients of the model are estimated using the Levinson–Durbin recursion [28].

$$\Phi_{p+1,j} = \Phi_{pj} - \Phi_{p+1,p+1}\Phi_{p,p-j+1} \qquad \text{j=1, 2, ..., p} \qquad (2)$$

$$\Phi_{p+1,p+1} = \frac{r_{p+1} - \sum_{j=1}^{p}\Phi_{pj}r_{p+1-j}}{1 - \sum_{j=1}^{p}\Phi_{pj}r_{j}} \qquad (3)$$

In (2) and (3) "r" is the normalized autocorrelation function. To understand the procedure of the recursion, here is an example where r0=0 r1=0.806, r2=0.428 and r3=0.07.

At first we have to initialize the recursion:

$$\Phi_{21} = \frac{r_1(1-r_2)}{1-r_1^2} = 1{,}316 \qquad (4)$$

$$\Phi_{22} = \frac{r_2 - r_1^2}{1-r_1^2} = -0{,}632 \qquad (5)$$

After the initialization we calculate the new value at the 3rd order of the model:

$$\Phi_{33} = \frac{0{,}07 - (1{,}316)(0{,}428) + (-0{,}632)(0{,}806)}{1 - (1{,}316)(0{,}806) + (-0{,}632)(0{,}428)} = 0{,}079 \,. \qquad (6)$$

And when we get the new value we have to "recalculate" the previous values:

$$\Phi_{31} = 1{,}316 + (0{,}079)(0{,}632) = 1{,}366 \qquad (7)$$

$$\Phi_{32} = -0{,}632 - (0{,}079)(1{,}316) = -0{,}737 \qquad (8)$$

This recursion stops when the procedure reaches a "p" order when the value of $\Delta\Phi$ in Equation (9) is less than a predefined ε limit.

$$\Delta\Phi_{p+1,j} = \Phi_{p+1,j} - \Phi_{p,j} \qquad (9)$$

The absolute value of $\Delta\Phi$ typically decreases, but not necessarily monotonically. It is possible to stop the recursion preselecting an ε limit. Generally we need model order of $p=2n+1$ to have an effective filter for a process with n degree of freedom. For example, if we have a signal which has a 7 degree of freedom then 15 elements of the autoregressive model can effectively filter our signal.

2.3.5.2.   A short description of SPRT

To find all events different from the average background, we used the λ decision-maker function from Wald method [23]:

$$\lambda_i = \ln \frac{f_i(x_1,...,x_i|H_1)}{f_i(x_1,...,x_i|H_0)} , \tag{10}$$

where "f" is a probability density function. "$x_1,...,x_i$" are the measured (and filtered) data. H_0 is the condition for characterizing the background and H_1 is the condition (hypothesis) which describes the event. In our analysis of benchmark data we used the standard deviation of "$x_1,...,x_i$" for the hypothesis H_0 and twice its value for H_1.

If the elements are statistically independent "enough", that means practically, if the filtering was sufficient enough to filter out deterministic part of the background, then the joint probability function can be replaced by the multiplication of individual probability functions in (10) and in one step the increment of the lambda function $\Delta\lambda$ can be expressed as:

$$\Delta\lambda = \lambda_i - \lambda_{i-1} = \ln \frac{f_1(x_i|H_1)}{f_1(x_i|H_0)} . \tag{11}$$

Supposing that individual probability density function follows the standard distribution formula i.e.:

$$f_1(x_i \mid H_1) = \frac{1}{\sqrt{2\pi\sigma_1^2}} e^{-\frac{x_i^2}{2\sigma_1^2}} . \tag{12}$$

We get the expression for $\Delta\lambda$:

$$\Delta\lambda_i = \frac{\sigma_1^2 - \sigma_0^2}{2\sigma_1^2\sigma_0^2} x_i - \ln \frac{\sigma_1}{\sigma_0} , \tag{13}$$

where "xi" is an element of the measured data, $\sigma0$ is the standard deviation of the measured data and $\sigma1$ is another standard deviation which we are able to set.

We decided to set

$$\sigma_1 = c\sigma_0 \tag{14}$$

where "c" is a constant which is an input value determined in the program by us (in our analyses c=2).

Starting the value of lambda function from zero and increasing or decreasing according to (11) in each step, "λ_i" will reach an upper or a lower limit. These two limits mean decision making on two events. One of these events means the measured data similar to the background noise and we call this background decision or event A. We state "λ_i" reached this limit, when its value is less than the limit of A [28].

$$\lambda_i \leq A \tag{15}$$

The other event is when the measured data differs from the background noise and we call it as event B. It happens when "λ_i" exceeds the limit of B [28].

$$\lambda_i \geq B \tag{16}$$

After "λi" is reached one of these limits, we register (save) the decision and set lambda value back to zero. Mathematically we should set this value randomly between A and B but the practice showed that this solution leads to a conservative and also a robust estimation. So we set "λi" to zero, then its evaluation starts again.
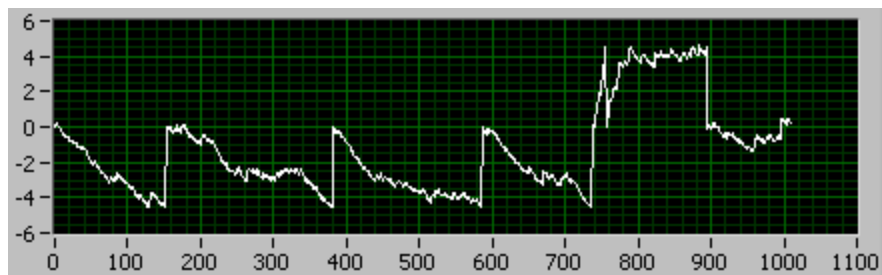
FIG. 2-37. A graph of the decision-making function.

At the setting of the two limits we have to keep two factors in mind. One of these factors is the False Alarm Probability (FAP). This means when we find an event which differs from the background noise but it is a false alarm because actually there is no event B in the time series.

The other factor is the Alarm Failure Probability (AFP) when there is an event B in the measured data but we did not find this event. From these level A and B can be calculated mathematically and they are shown in TABLE 2-5.

TABLE 2-5. DECISION-MAKING LIMITS FOR FIRST AND SECOND ORDER ERRORS

AFP	FAP	A	B
10%	10%	-2,2	2,2
1%	1%	-4,6	4,6
0,1%	0,1%	-6,91	6,91
1%	10%	-4,5	2,29
0,1%	10%	-6,8	2,3

2.3.5.3.   The applied programs for the evaluation

We created MATLAB functions for evaluation. The main function which runs the evaluation called "esmspekt". This function needs five parameters and returns back four values and the spectral figures of the A and B events.

(eventA,eventB,lambda,numberOfClearEvents]=esmspekt(order,blocksize,A,B,sigma1)

The five parameters are:

− Order of autoregressive model for the filtering;
− Size of a block – this is the block size of the measured points when the lambda function returns only A or B verdict;
− A limit of SPRT;
− B limit of SPRT;
− The value of σ_1.

After the function was started a dialog box appears and asks for the source of the measured data. Then this function starts the processing like this:

(1)   Reading the values…
(2)   Evaluation of the 1st channel…
(3)   Evaluation of the 2nd channel…
(4)   Evaluation of the 3rd channel…
(5)   Evaluation of the 4th channel…
(6)   Done…

So the algorithm runs one-by-one on the channels and selects the clear events. When it successfully finds all clear events then it computes the Auto Power Spectral Density (APSD) and calculates the averages of the A and B events separately.

The program automatically saves these averaged APSD functions into "*.fig" files in a directory next to the measurement file. This file can be opened by MATLAB and this is an easy way of graphing and saving the results of APSD. The "fig" file saves the values as a graph, and later we can edit it.

If the function terminates normally, it will return four values:

− eventA – the line number of A events;
− eventB – the line number of B events;
− lambda – the decision-maker function;
− numberOfClearEvents – the number of clear events in a matrix which first column is the number of A events and second column is the number of B events. The rows are the channels and the first one means the first channel.

The "esmspekt" function uses the next sub functions:

− beolvas.m – for reading the measured values;
− acfAndApsd.m – for calculating the autocorrelation function;
− normacf.m – for normalizing ACF;
− durbin.m – for computing the autoregressive model;
− aruszres.m – to filter out the ambient noise;
− sprt.m – for using the SPRT algorithm and finding the clear A and B events;
− apsd_esm – to graph the APSD of A and B events.

2.3.6. Results of spectrum estimation

Once decisions were made, that means sections of background noises and events different from the background have been selected using SPRT we typically estimate (and average) the spectra of the time slices of events A and B as it was described in details in the previous section.

In the followings we present the results of spectrum estimation of the background and the events. To understand the results one has to realize that SPRT presented in the previous section was used to select data arrays for background and for events as well. Time segments with definite length were selected for FFT transform producing spectrum. Then these spectra were averaged. The number of averages and the length of time data blocks and since that the frequency resolution of the spectra depends on measured data. In reality if the event is weak, then it takes too much time until SPRT can take decision on the event. (Please remember, that mathematically it is proven, that SPRT is an algorithm which can produce that decision in the shortest time at the given uncertainty level!). Therefore the acceptance level should be chosen correspondingly. However, if we set the acceptance level low, then we shall have more frequent decision, thus the length of the block used for spectrum estimation depends on the acceptance level. Since the spectrum resolution is reciprocal to the length of the block sometime we get sometime better sometimes worse frequency resolution. This leads to differences in the width of the resonances and consequently in the magnitude of the peak as well.

Here we present a selection from the results of data evaluation. The main aim is to show, what kind of results can be achieve for comparison. The full set of results can be found on open site http://diag.duf.hu

2.3.6.1. Loose part: big bolt, record sampled by 25 kHz

Remark for all the following tables: SPRT algorithm makes decision in the record as follows:

- Event background;
- Event loose part.

TABLE 2-6. NUMBER OF DETECTED EVENTS IN RECORD 25N-ZIP

	A event	B event
1. channel	4654	253
2. channel	4661	196
3. channel	4844	33
4. channel	4747	124

The numbers in the table serve as number of averages of the corresponding spectra
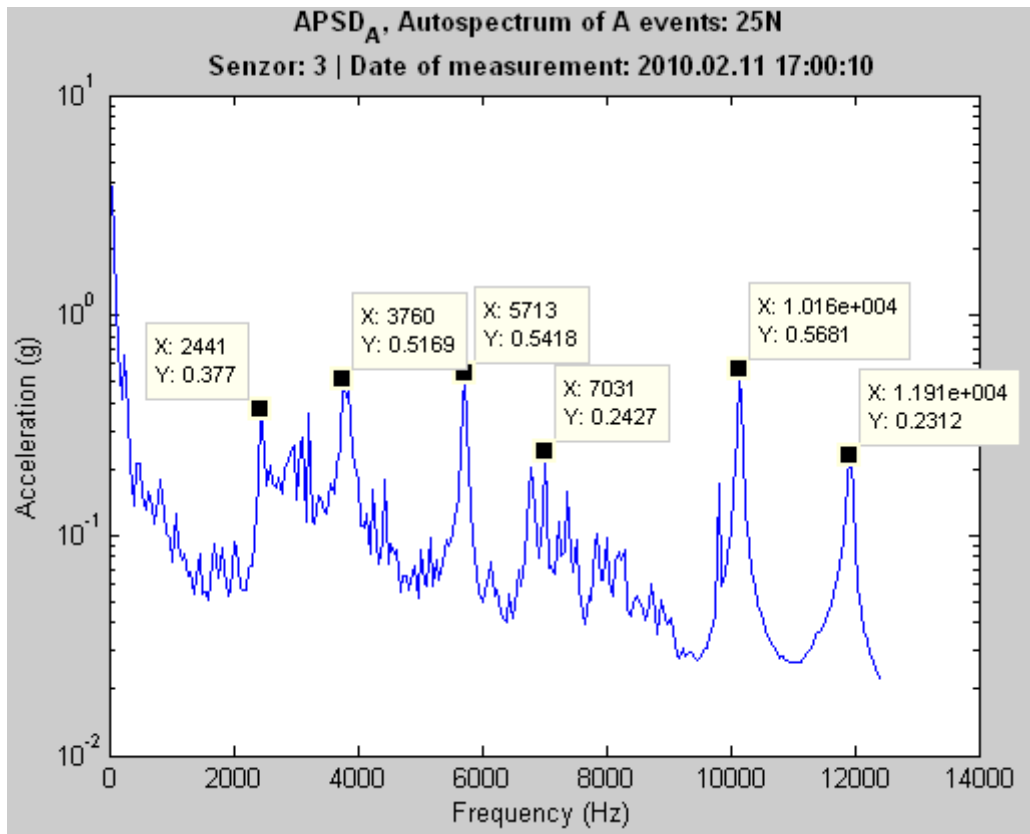
FIG. 2-38. APSD of the background of channel 3. (events A)It exhibits peaks due to standing wave of the tube. Driving source is the flow.
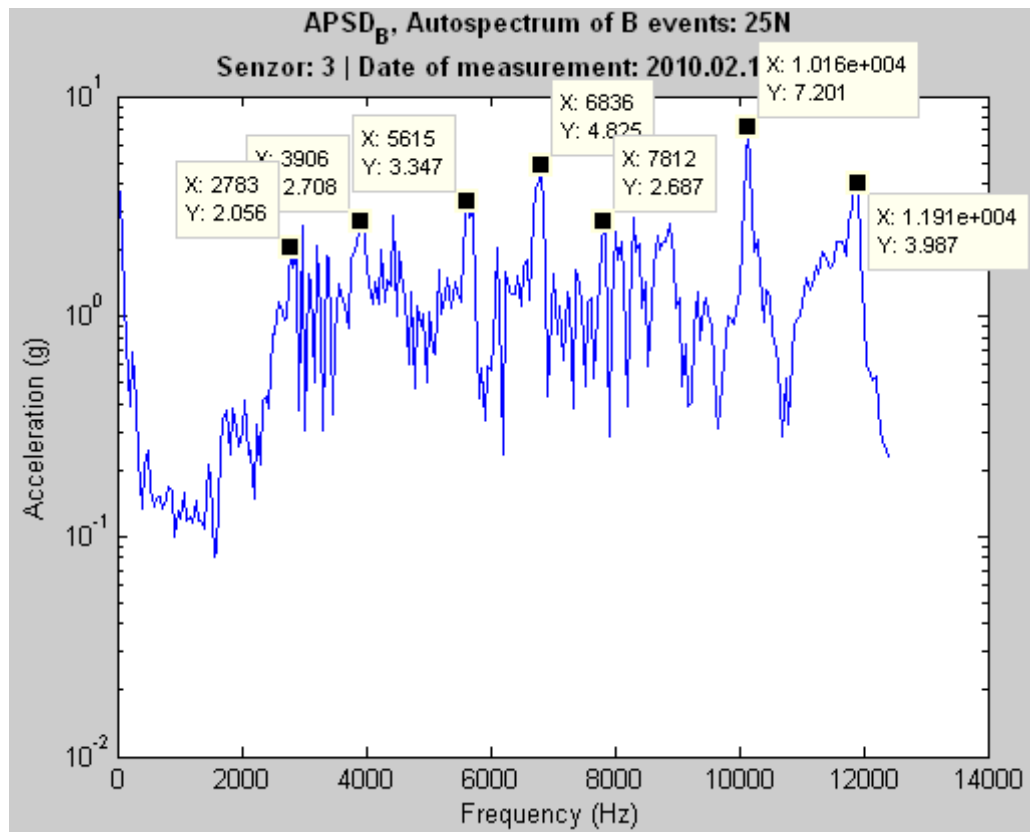
FIG. 2-39. APSD of the channel 3. during registered events (events B by SPRT).

108
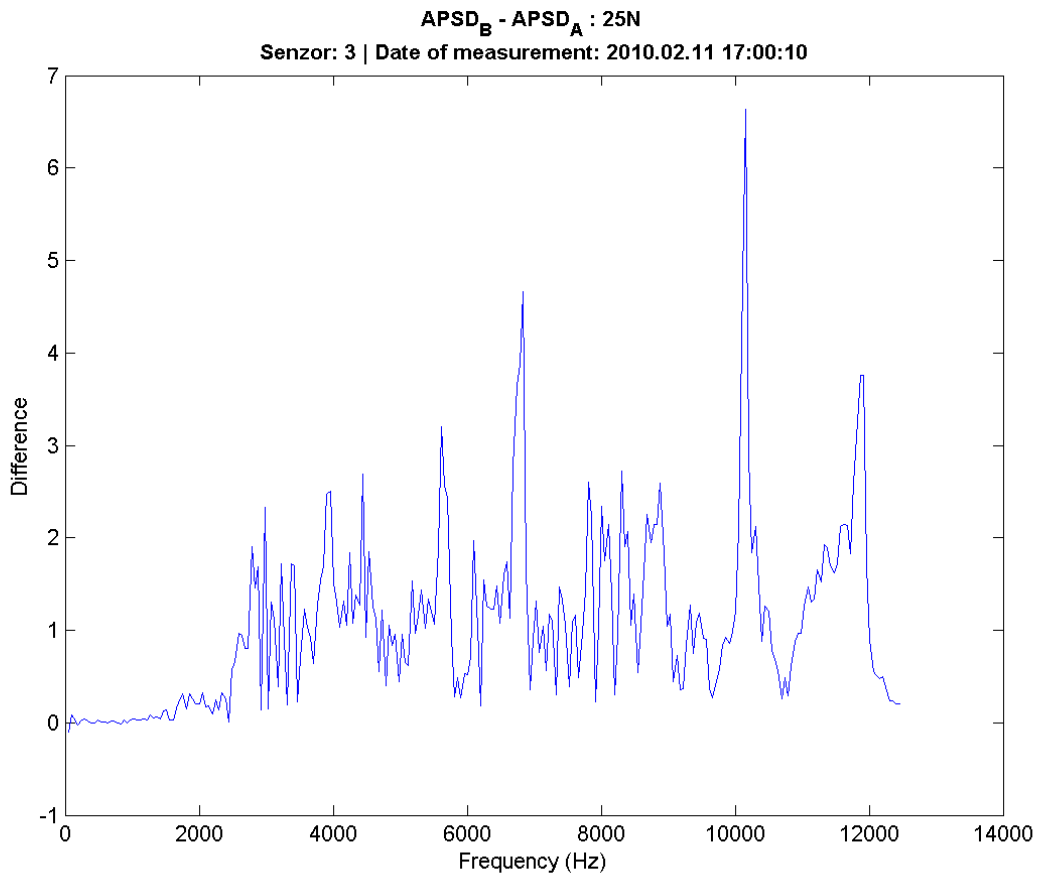
FIG. 2-40. Differences between averaged spectrum of events B and event A (background) (channel 3), i.e. this is the additional spectrum caused by the hits.

It is interesting to notice here, but it will be true in the followings as well, that we have typically well expressed peaks in the background spectra. They are due to standing wave of the tube. The generating force is the flow of the water pressed by the pump. Notice that in the spectra of loose part events(B) the same peaks exist, just popping out sometimes from the added white noise, which is due to knocks of the loose part. That almost white spectrum overlaps the background spectrum.
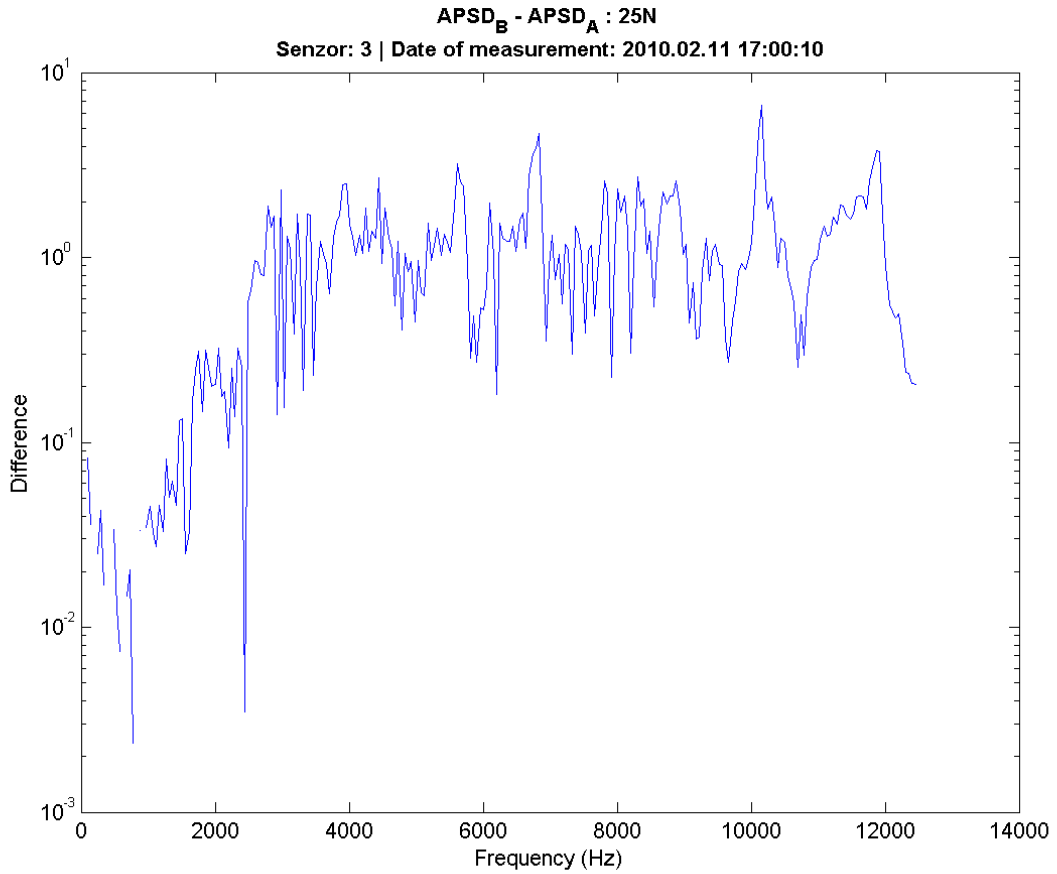
FIG. 2-41. Differences between averaged spectrum of events B and events A (background) (channel 3), i.e. this is the additional spectrum caused by the hits in log scale.

Conclusion:
Impact of big bolt produced white additional noise in the frequency range 3000-12500 Hz.

2.3.6.2. *Loose part: big bolt, sampled by 50 kHz*

TABLE 2-7.   NUMBER OF DETECTED EVENTS IN RECORD 50N-ZIP

	A events	B events
1. channel	6415	283
2. channel	6403	301
3. channel	6750	266
4. channel	6606	335

The numbers in the table are the number of averages of the corresponding spectra.

110
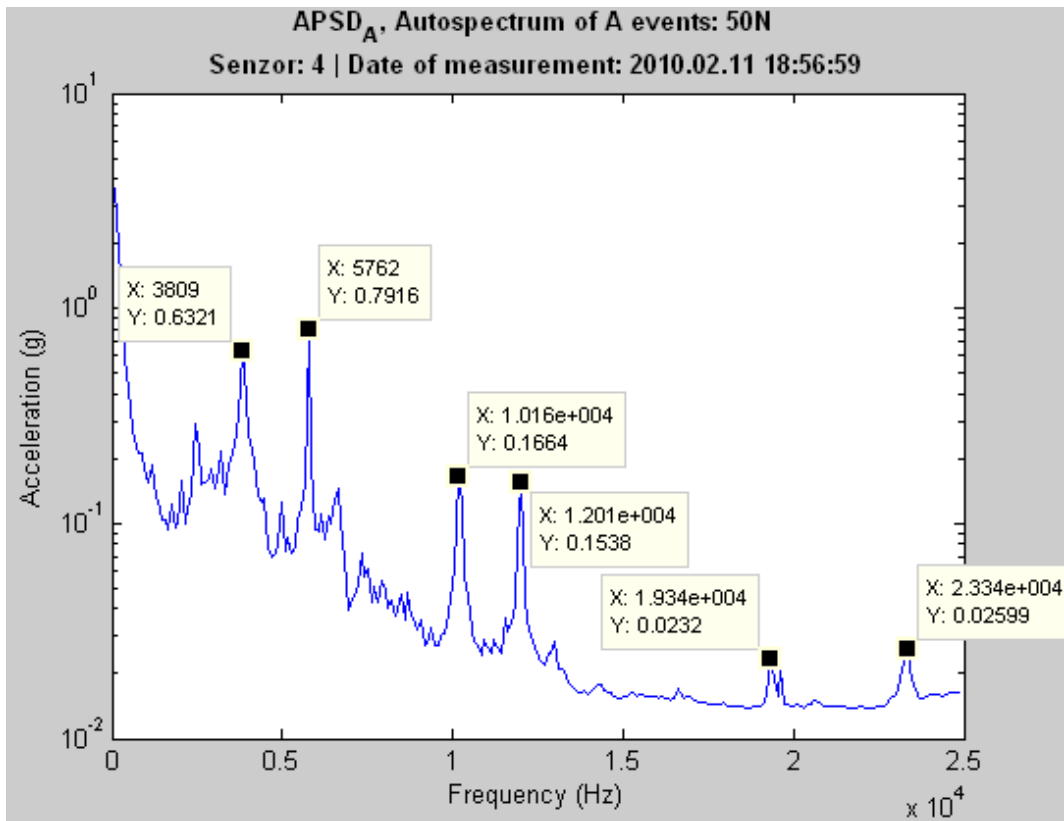
FIG. 2-42. Background spectrum measured by channel 4 (spectrum of time segments selected by events A).
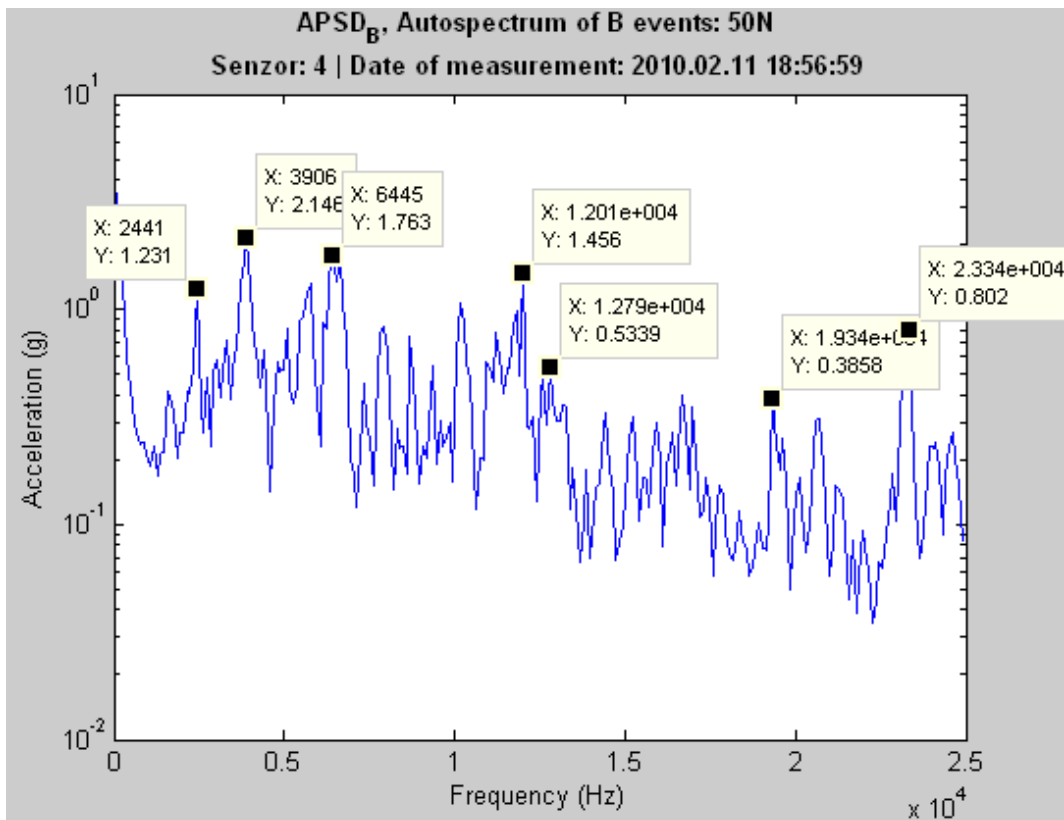
FIG. 2-43. Spectrum of events B for channel number 4.
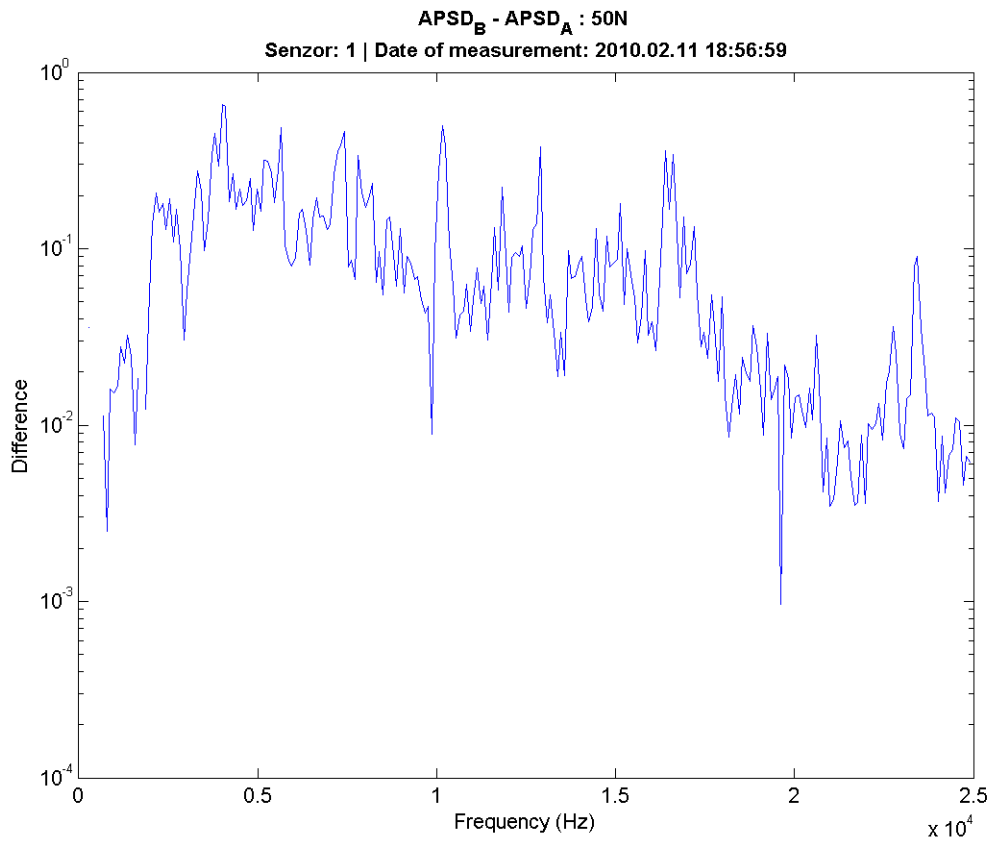
FIG. 2-44. *Difference of the spectra for events B from background (events A) (channel 4).*
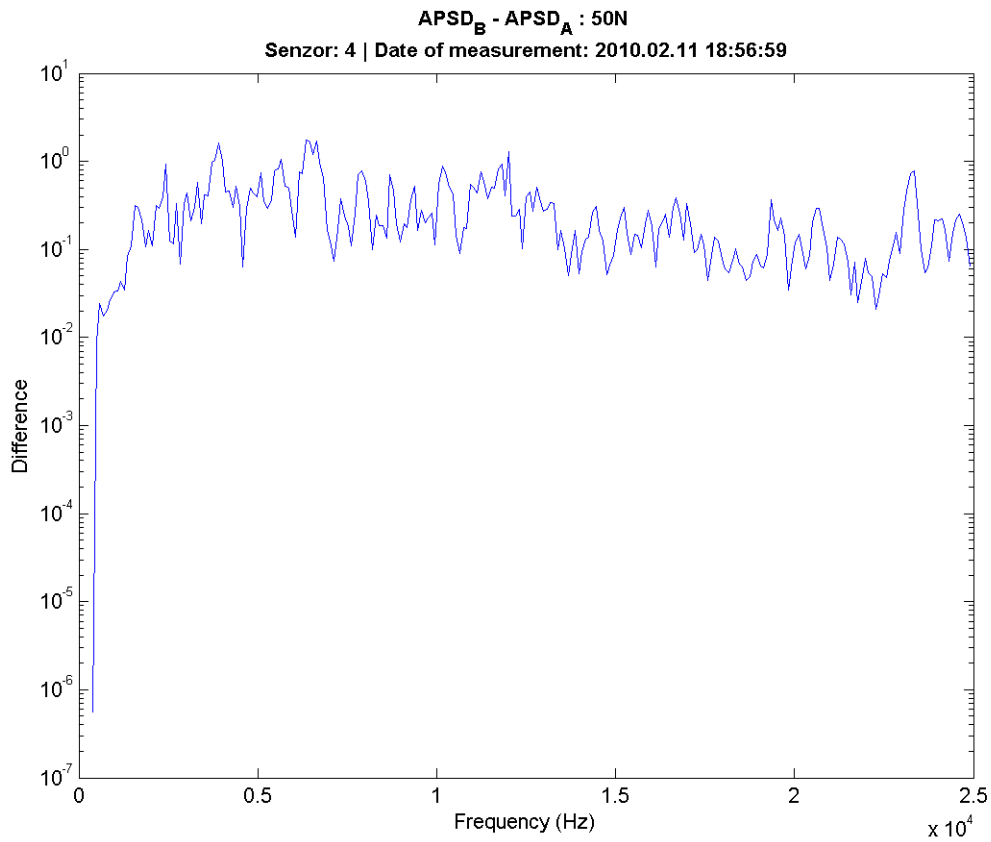
FIG. 2-45. *Difference of spectra of events B and A in log scale measured by sensor number 4).*

TABLE 2-8.   NUMBER OF EVENTS REGISTERED BY SPRT IN 10N.ZIP MEASUREMENT

	A event (background)	B event
1. channel	3768	145
2. channel	3737	136
3. channel	3708	86
4. channel	3659	132

The numbers in the table are the number of averages of the corresponding spectra.
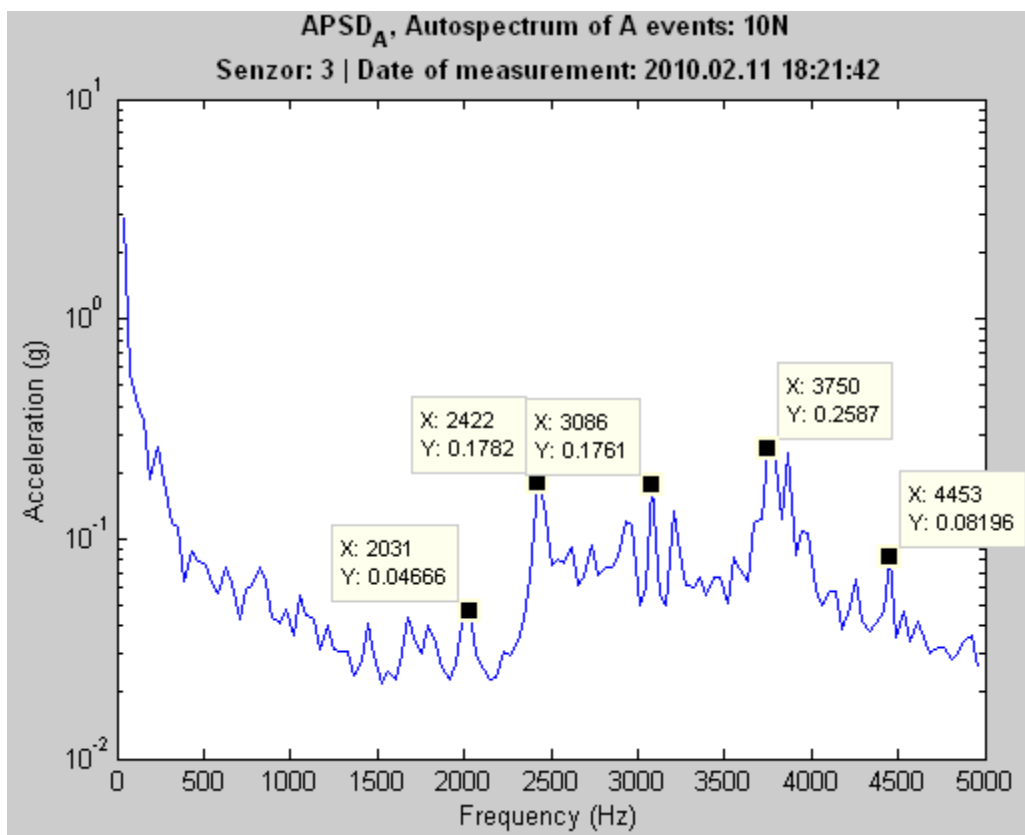
FIG. 2-46. Spectrum of background measured by channel 3(due to event A).
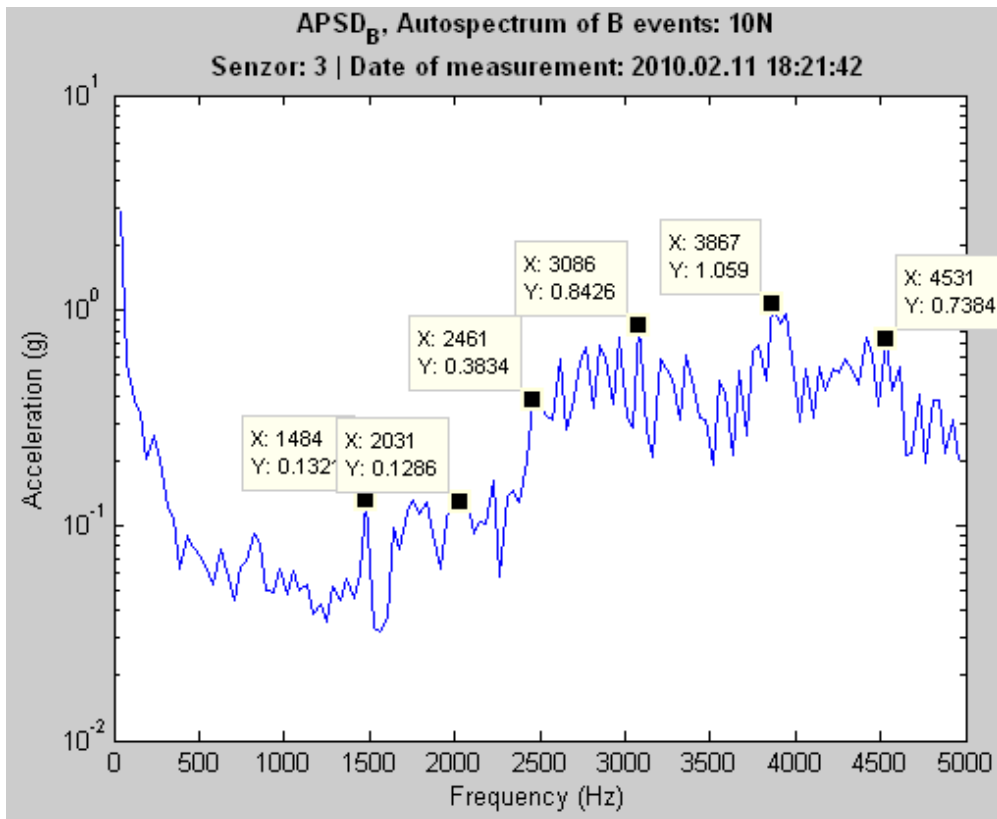
FIG. 2-47. Spectrum when event B took place (channel number 3).
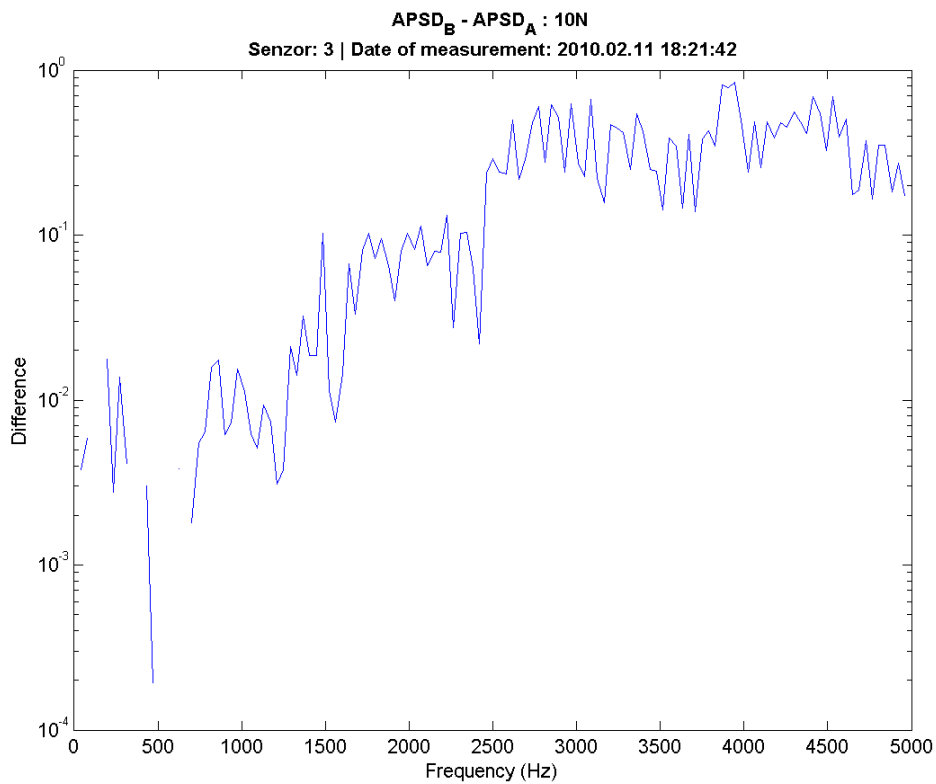
FIG. 2-48. Difference of spectra of event B and A measured by sensor number 3.

Conclusion: from this frequency range we can just say that the effect of loose part starts not lower than 2500 Hz

2.3.6.4. Loose part: big bolt, sampled by 5 kHz

TABLE 2-9. NUMBER OF EVENT FOUND IN RECORD 5N.ZIP

	A event	B event
1. channel	4372	36
2. channel	4396	42
3. channel	4045	80
4. channel	4029	72

The numbers in the table are the number of averages of the corresponding spectra.
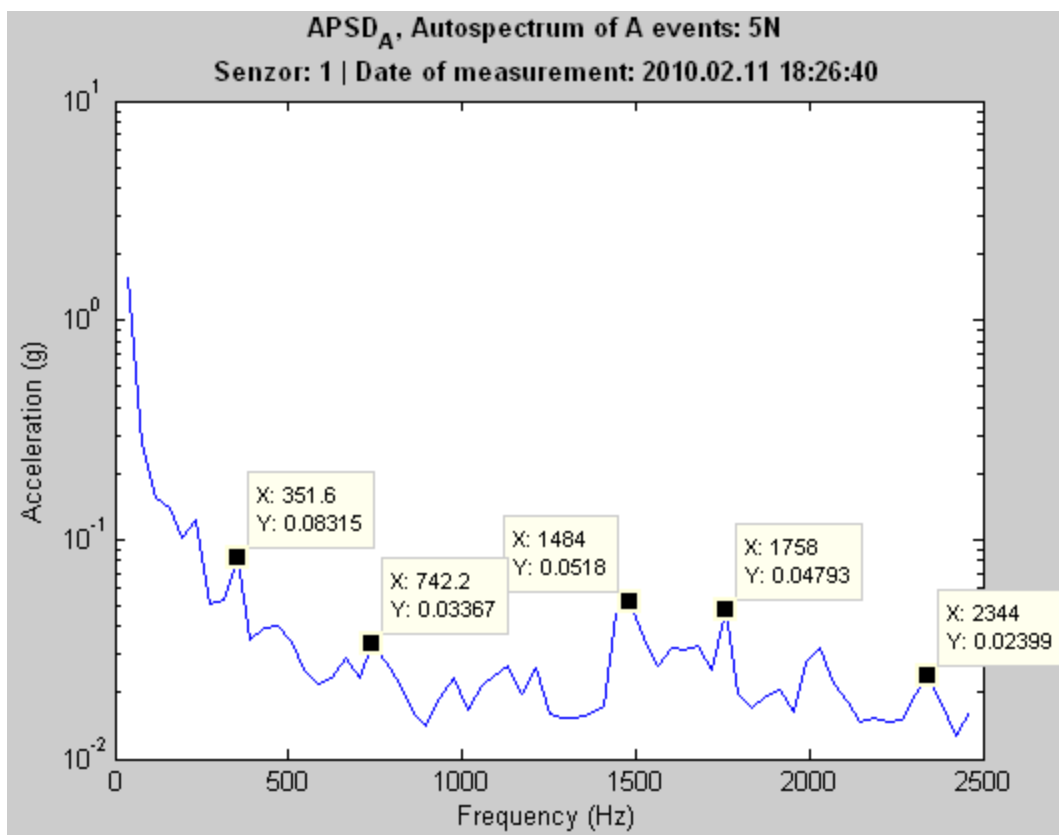
FIG. 2-49. Background spectrum measured by channel No1 (events A).
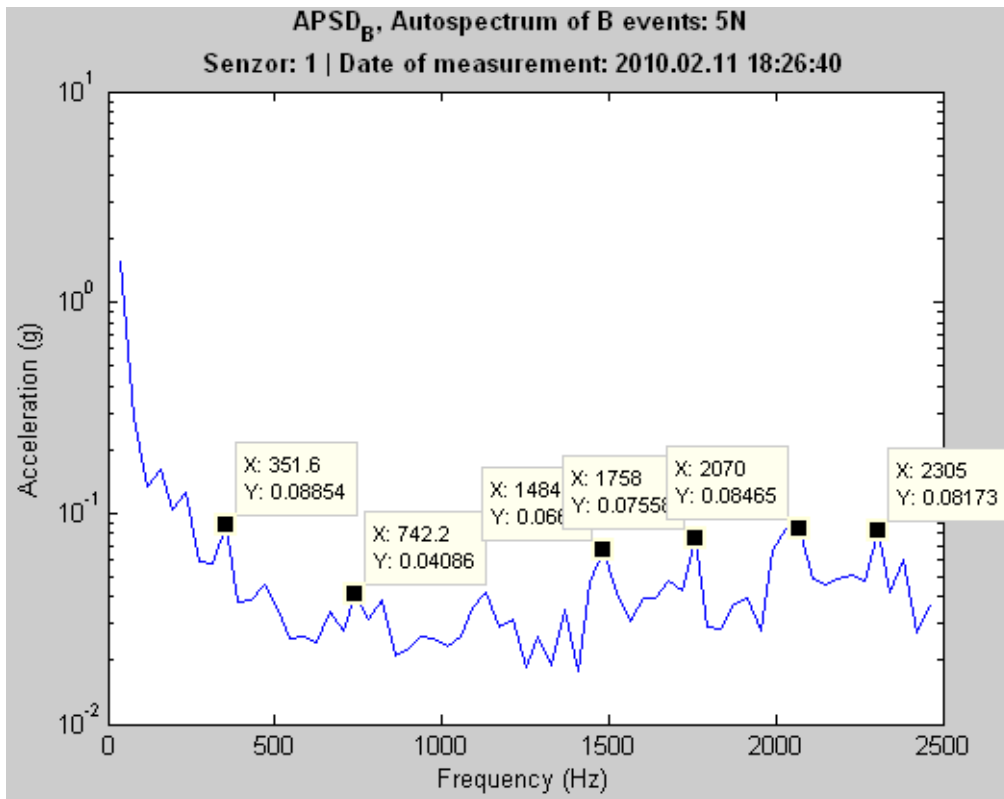
FIG. 2-50. Spectrum of B events measured by channel number 1.
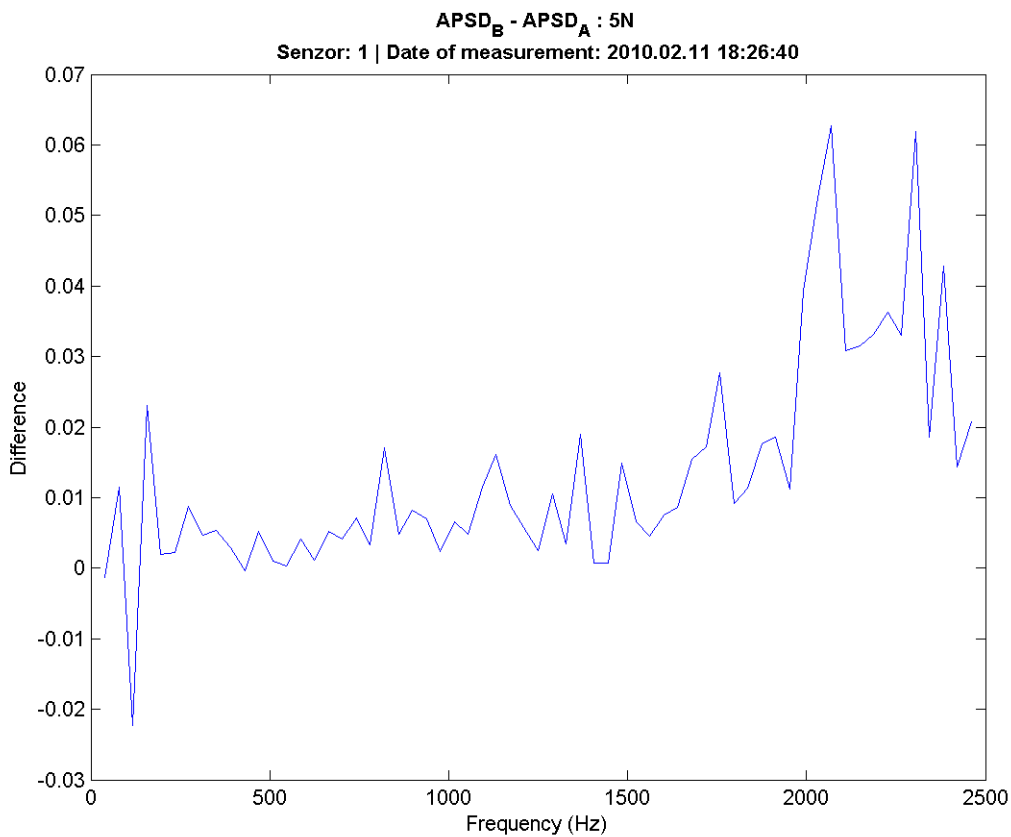
FIG. 2-51. Difference of spectra of B event and the background (A events) measured by channel No 1.

Conclusion: We can really state, there is no effect below 2 kHz.

116

2.3.6.5. Loose part: small bolt, sampled by 50 kHz

TABLE 2-10. NUMBER OF EVENTS FOUND BY OUR METHOD IN FILE 50K.ZIP

	A event	B event
1. channel	7352	144
2. channel	7406	116
3. channel	7409	73
4. channel	7395	79

The numbers in the table are the number of averages of the corresponding spectra.
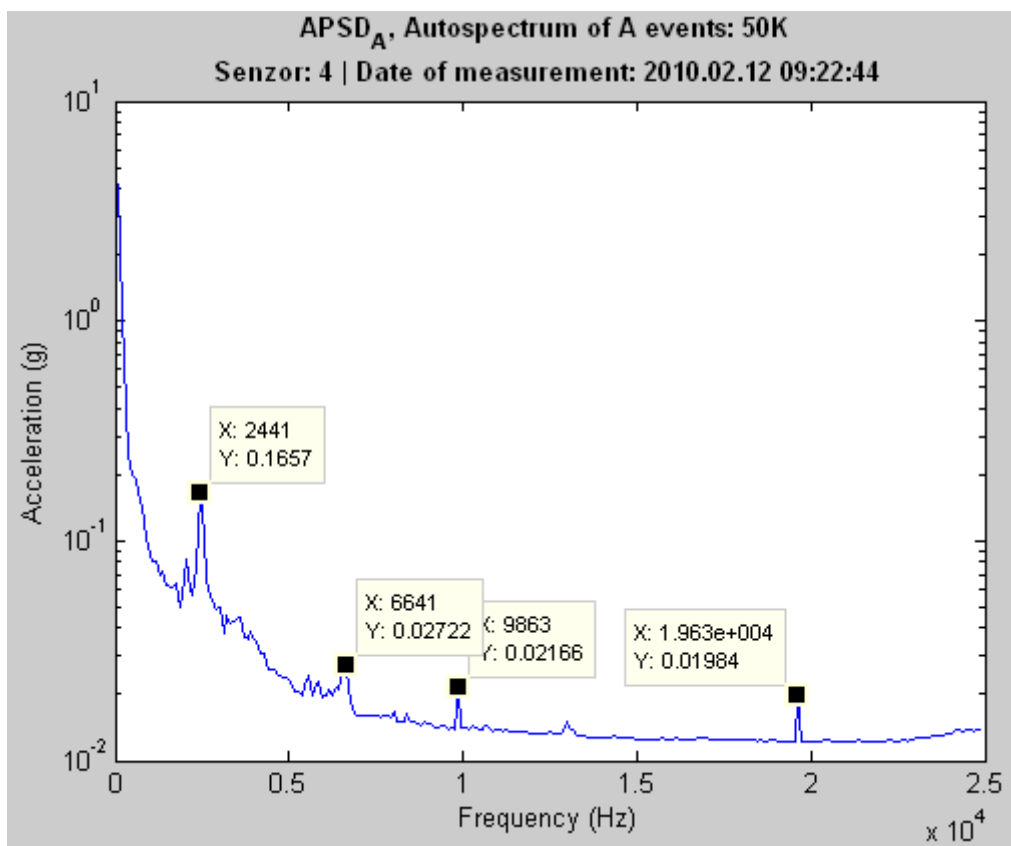
FIG. 2-52. This is the background spectrum measured by channel 4 (i.e. Events A).
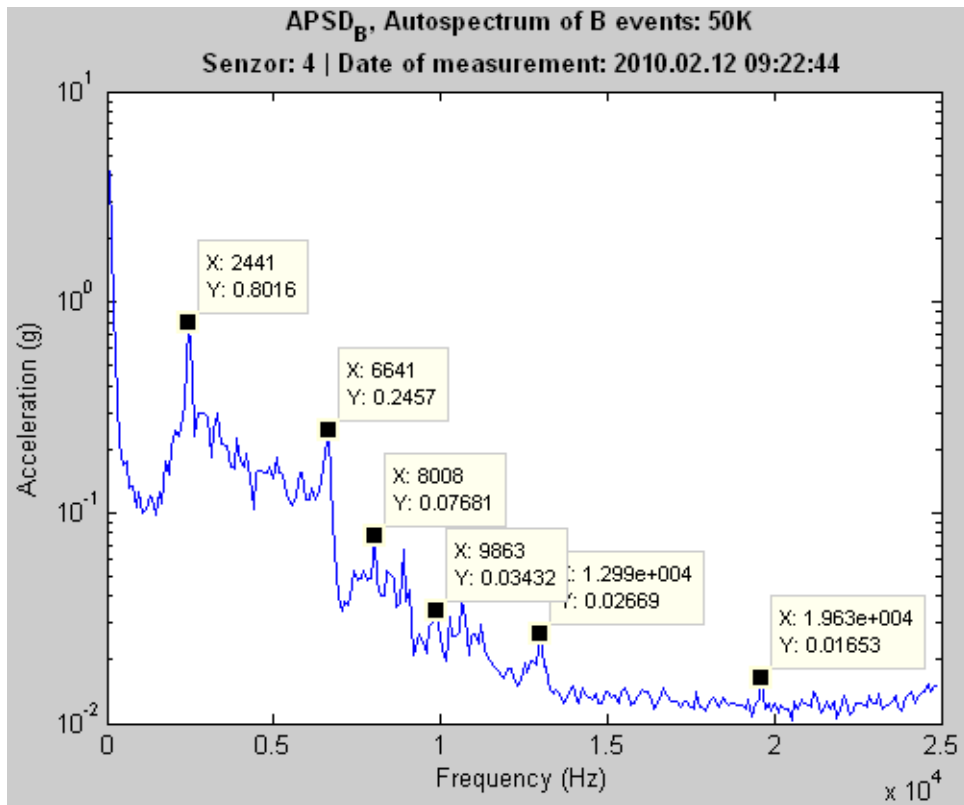
FIG. 2-53. Spectrum measured by sensor number 4 when event B had been registered.
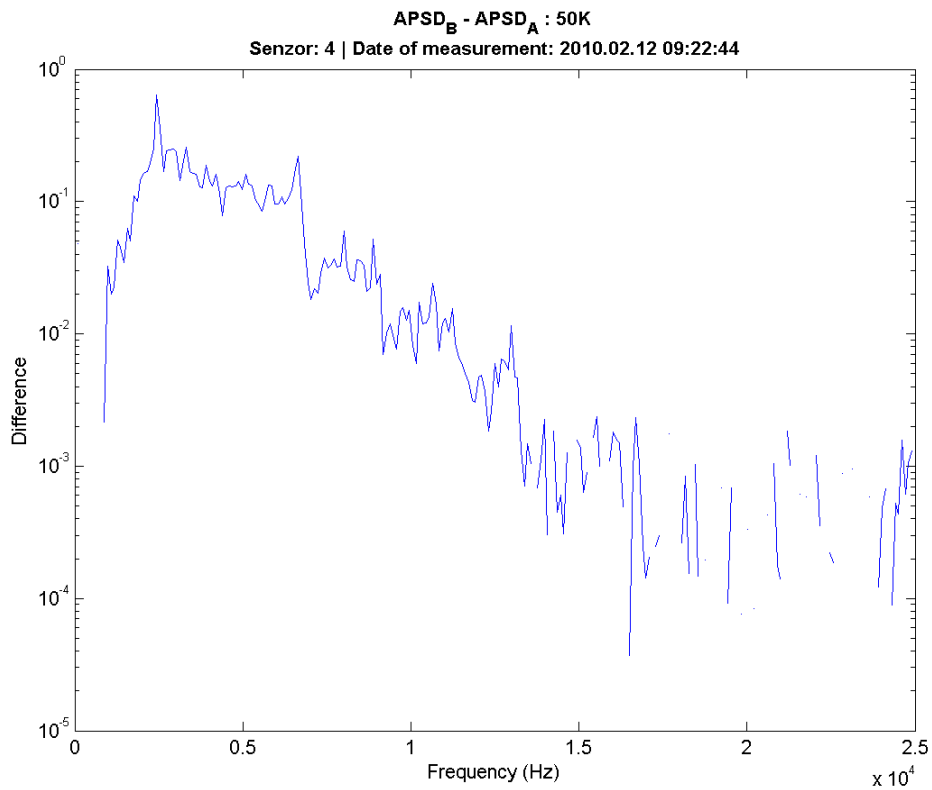
FIG. 2-54. Difference of spectrum of event B and the background (event A) for small bolt measured by sensor number 4 in log scale.

Conclusion: Small bolt caused additional noise in frequency range 2000-7500Hz

2.3.6.6. *Loose part: small bolt, sampling by 25 kHz*

TABLE 2-11. NUMBER OF EVENTS FOUND IN MEASUREMENT 25K.ZIP

	A event	B event
1. channel	5213	13
2. channel	5419	5
3. channel	5394	13
4. channel	5460	9

The numbers in the table are the number of averages of the corresponding spectra.
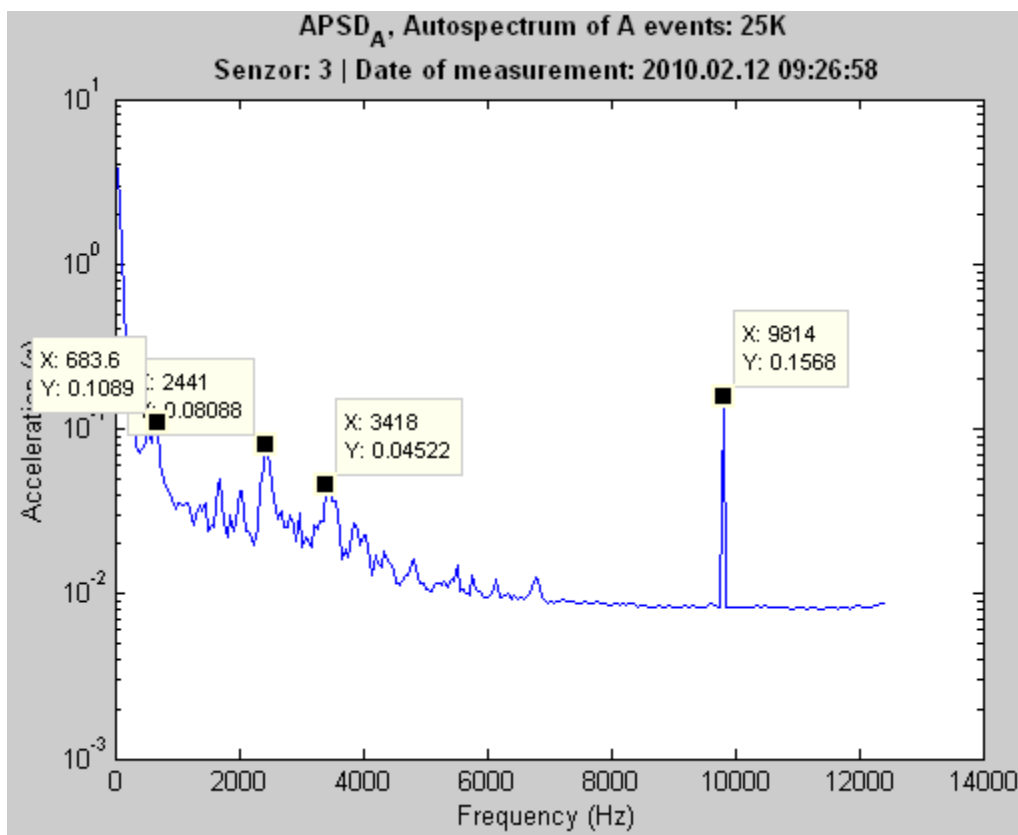
FIG. 2-55. Spectrum of background measured by sensor 3. during small bolts experiment (events A).
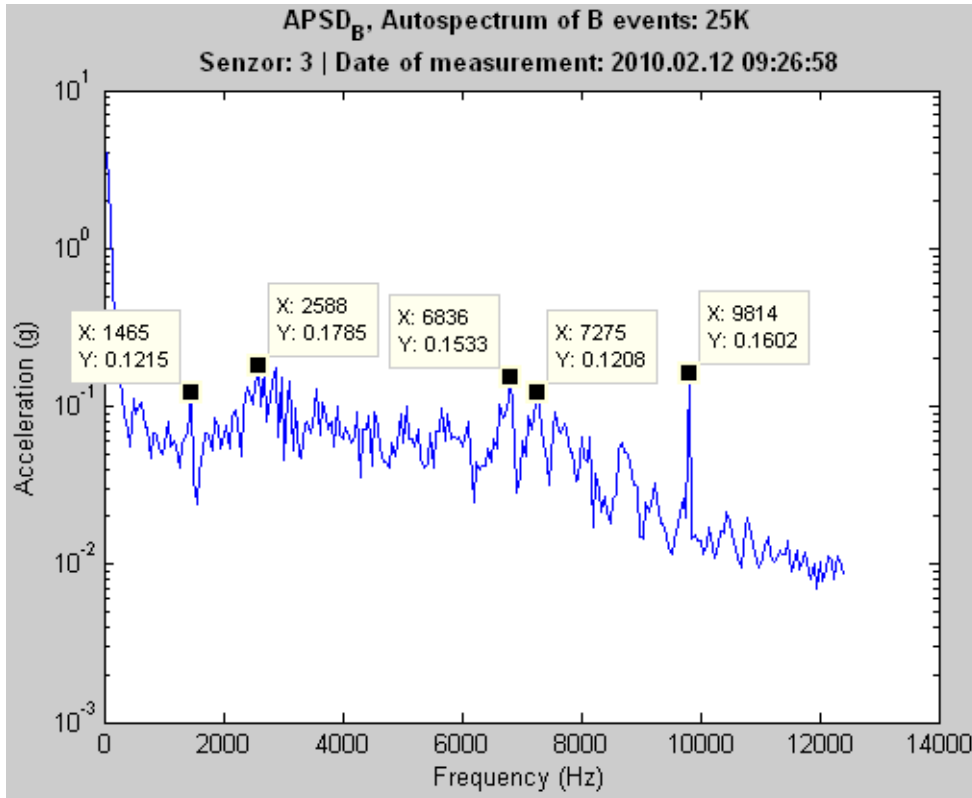
FIG. 2-56. Spectrum measured by sensor 3 during impacting small bolt (events B).
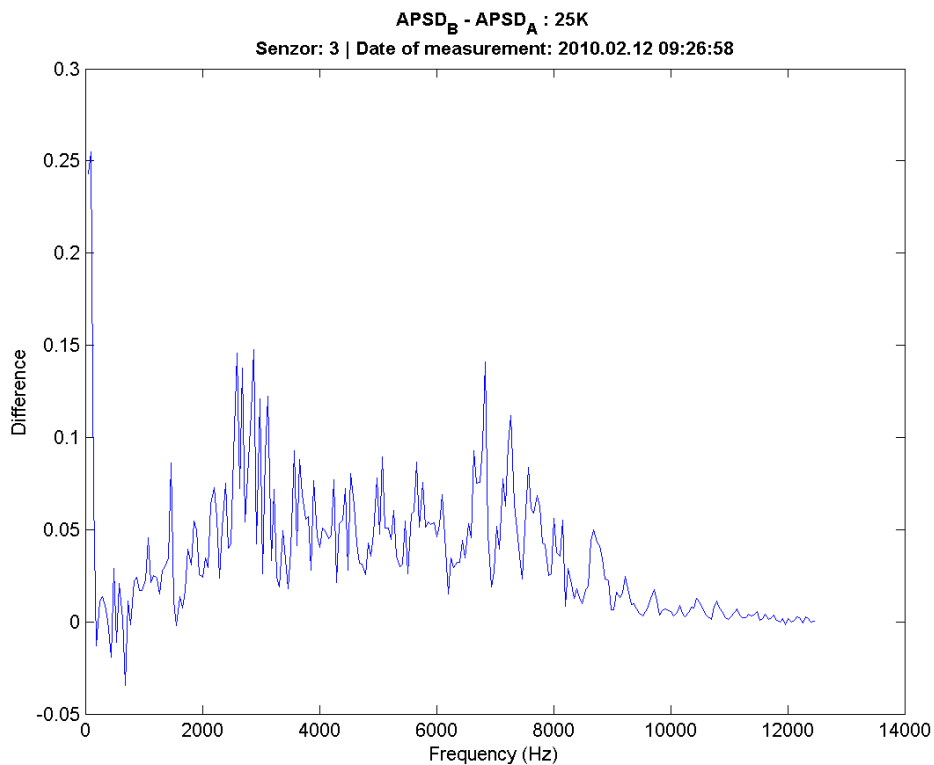
FIG. 2-57. Difference of spectra of event B and A i.e. the effect of small bolt in linear scale (sensor number 3).

Conclusion: From the linear scaled difference spectrum it is clear that the effect of small bolt is weak, but clearly located in frequency range of 2500-7800Hz.

TABLE 2-12. NUMBER OF EVENT FOUND BY OUR METHOD IN FILE 10K.ZIP

	A event	B event
1. channel	9150	36
2. channel	9129	53
3. channel	8972	102
4. channel	9060	116

The numbers in the table are the number of averages of the corresponding spectra.
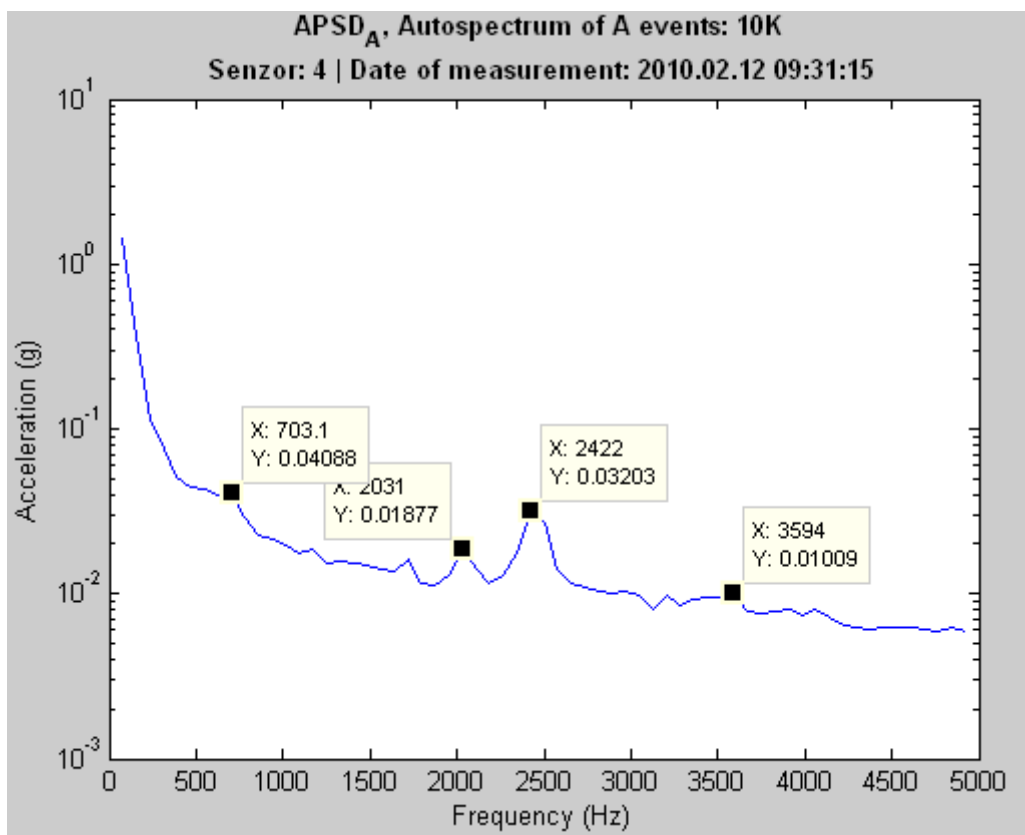
FIG. 2-58. Background spectrum measured by sensor No4. channel (events A).
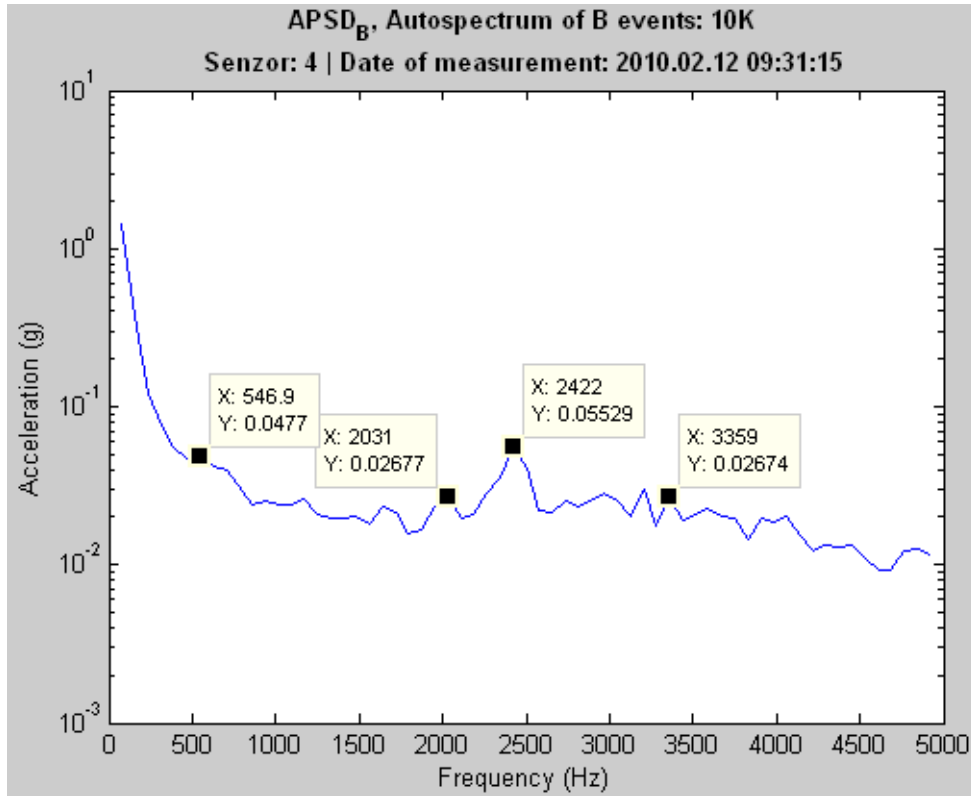
FIG. 2-59. Spectrum of B events measured by sensor 4. when small bolt was hitting.
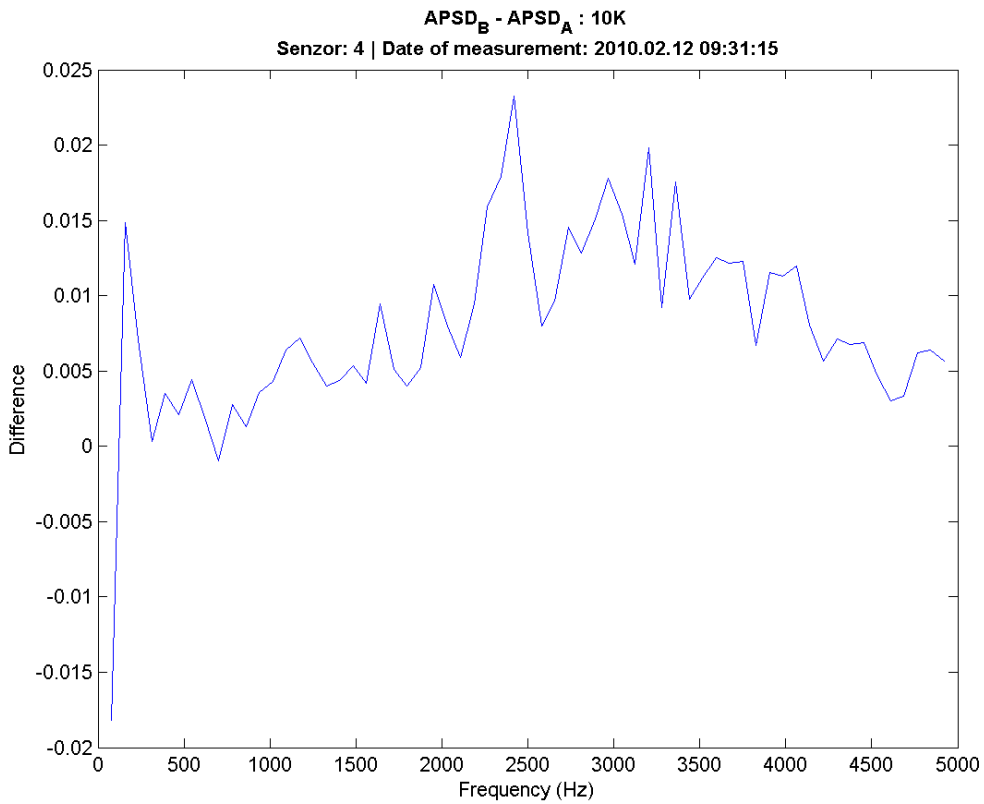
FIG. 2-60. Difference of spectra of event B and event A in linear scale measured by sensor No. 4.

Conclusion: In this frequency range it would be impossible to detect the small bolt

TABLE 2-13. NUMBER OF EVENTS FOUND BY OUR METHOD IN MEASUREMENT 50B.ZIP

	A event	B event
1. channel	28247	785
2. channel	29126	210
3. channel	29589	4
4. channel	29688	12

The numbers in the table are the number of averages of the corresponding spectra.
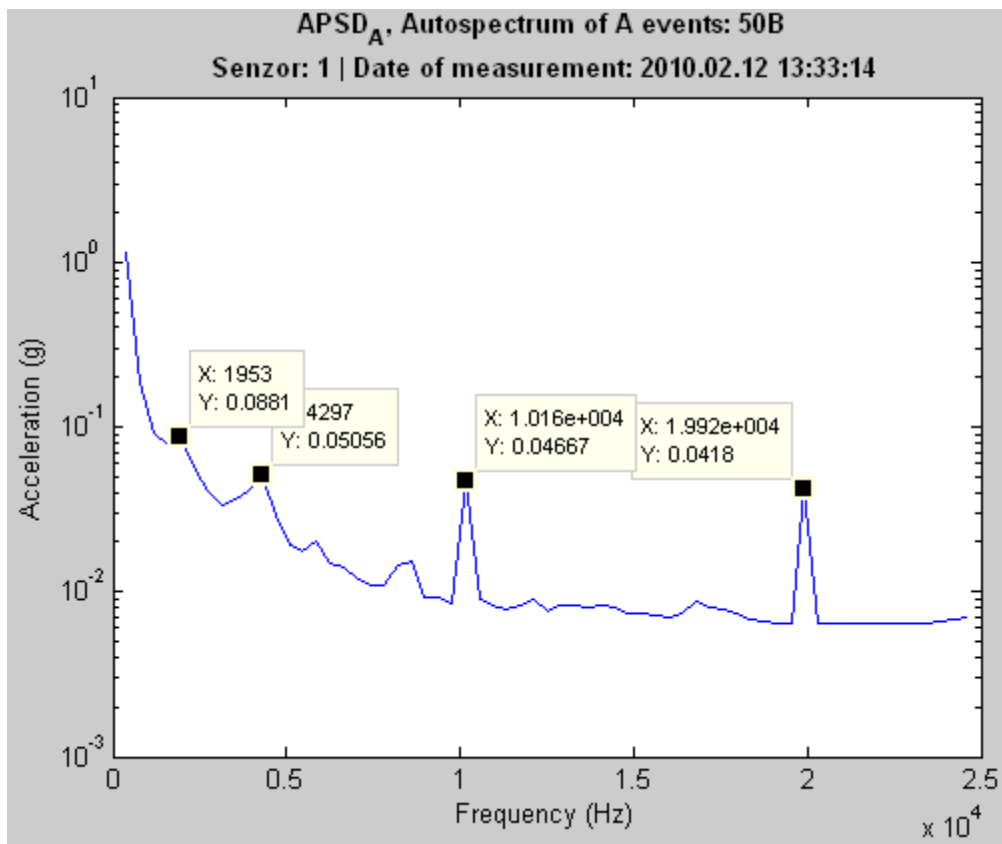
FIG. 2-61. Spectrum of background measured by sensor No1 (events A).
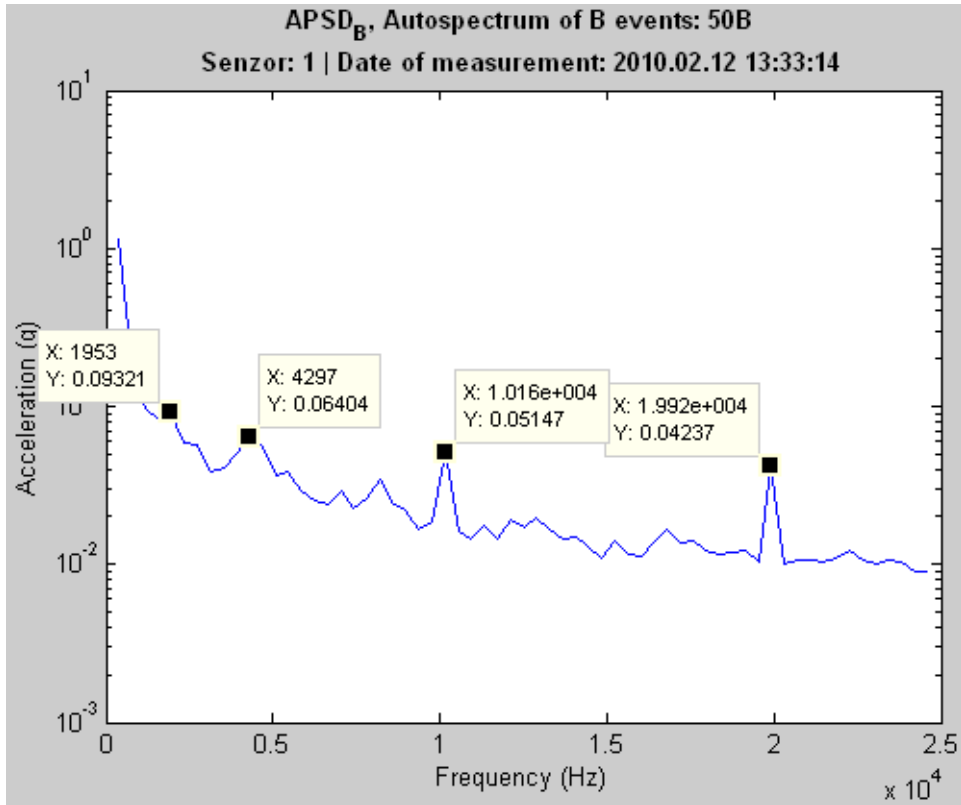
FIG. 2-62. Spectrum measured by sensor No1 during bakelite impact (events B).
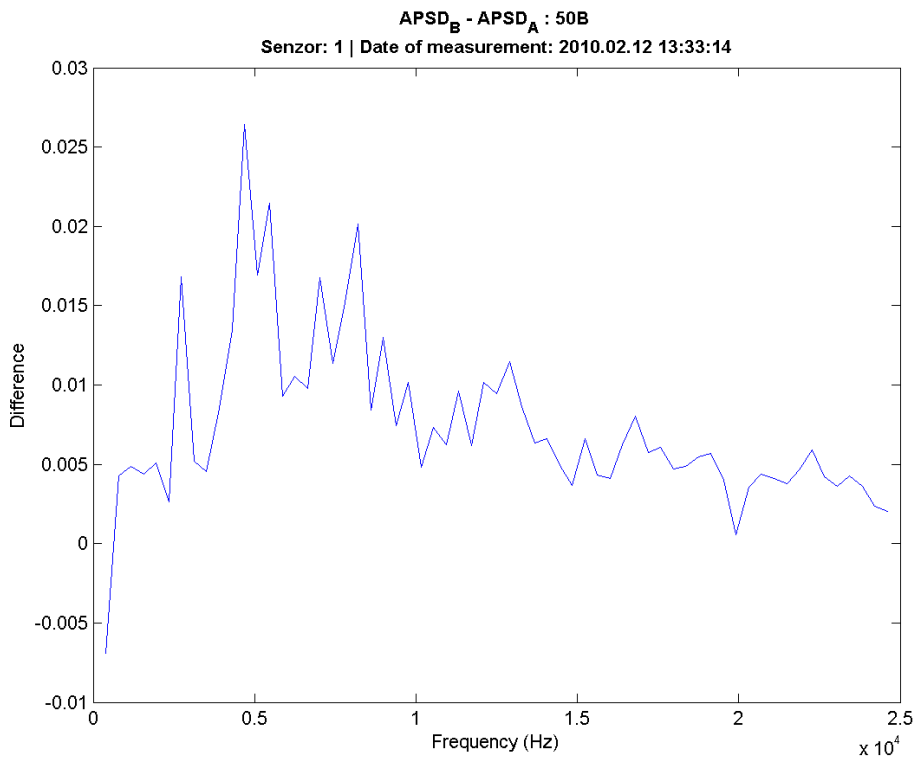
FIG. 2-63. Difference of spectra of events B and events A i.e. effect of bakelite measured by sensor number 1.

Conclusion: Bakelite impact adds to spectrum only relatively low frequency components between 2500-10000 Hz. But mainly at about 2500 and 5000 Hz

TABLE 2-14. NUMBER OF EVENTS FOUND IN MEASUREMENT 25B.ZIP

	A event	B event
1. channel	22966	74
2. channel	23359	7
3. channel	23393	10
4. channel	23406	34

The numbers in the table are the number of averages of the corresponding spectra.
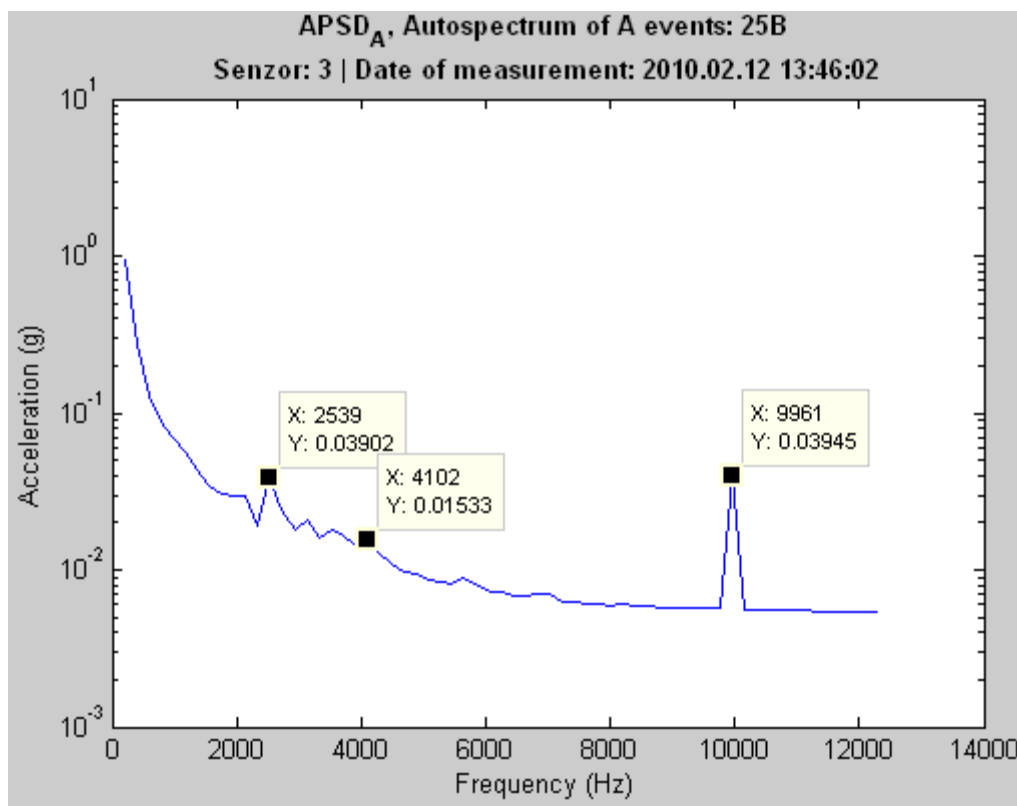
FIG. 2-64. Background spectrum of channel 3, when bakelite loose parts were in the tube (A events).

The background spectrum was estimated from the signal between knocks of loose parts found by SPRT. It selects background segments of time signal (SPRT A selection). There are two eigenvalues, which are the main frequencies of the tube vibration
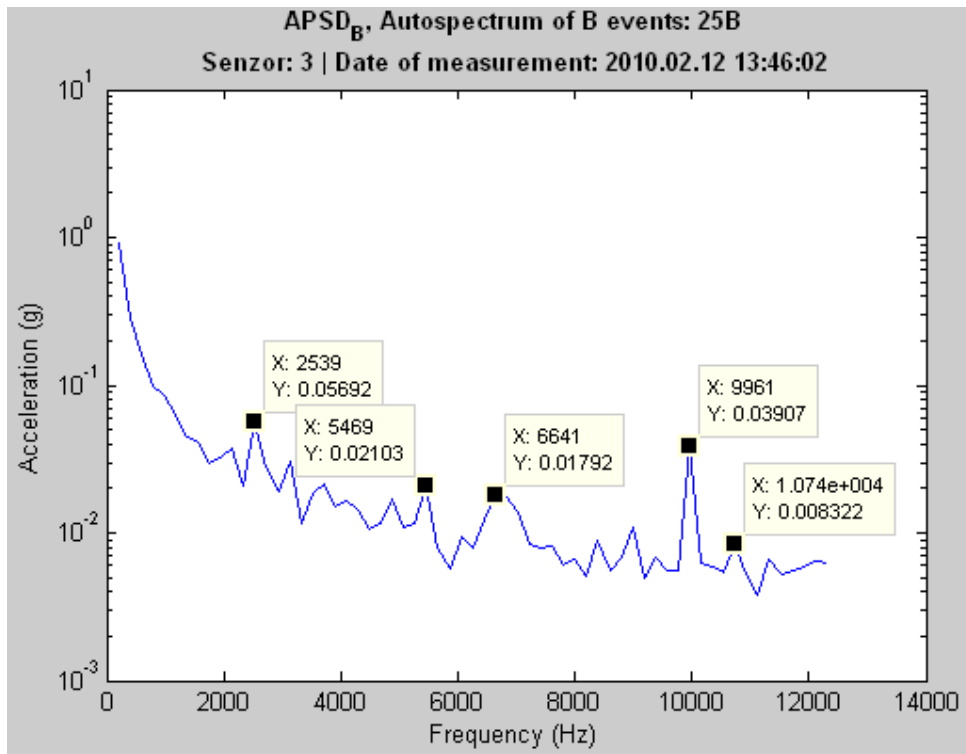
FIG. 2-65. Event B Spectrum of the 3. channel during bakelite loose part knockings.

The standing wave peak at 9961Hz remained at the same level like in the background spectrum, but the widened and noise due to loose part clearly seen between at 2500Hz and 10000Hz.
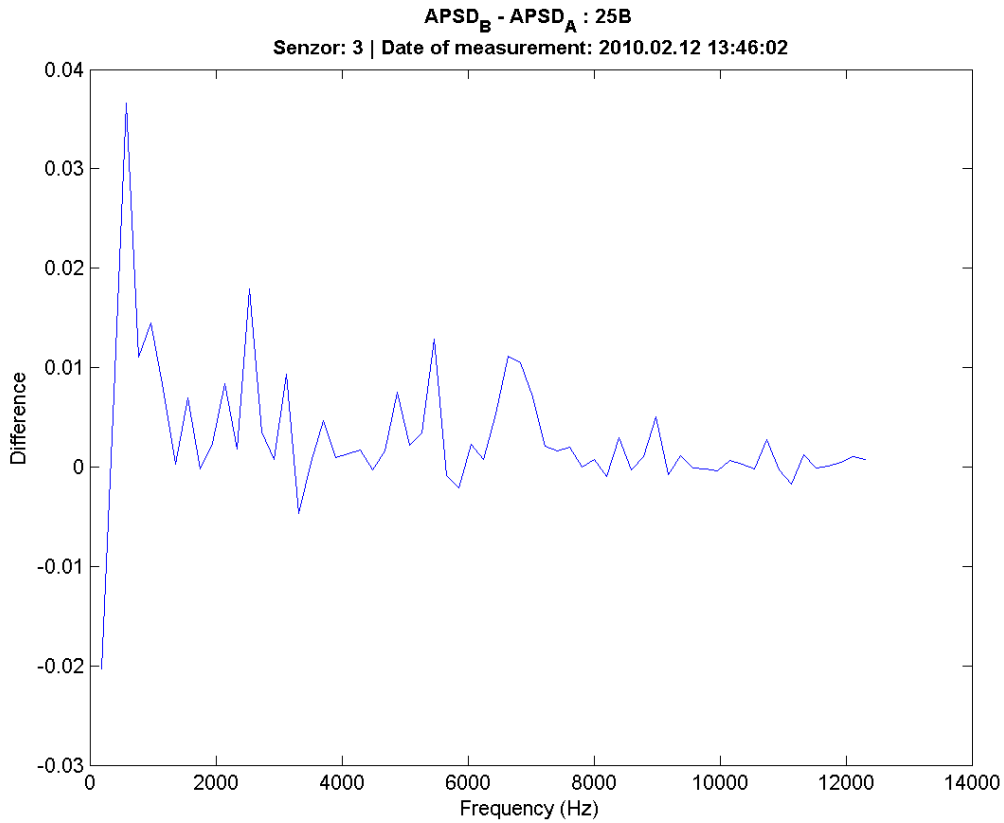
FIG. 2-66. Difference of the effect and background for bakelite case sampled 25 kHz (3. sensor).

TABLE 2-15. NUMBER OF EVENTS REGISTERED BY OUR METHOD IN FILE 10B.ZIP

		A background	B event
1	Channel	9284	4
2	Channel	9273	9
3	Channel	9244	11
4	Channel	9276	19

The numbers in the table are the number of averages of the corresponding spectra.
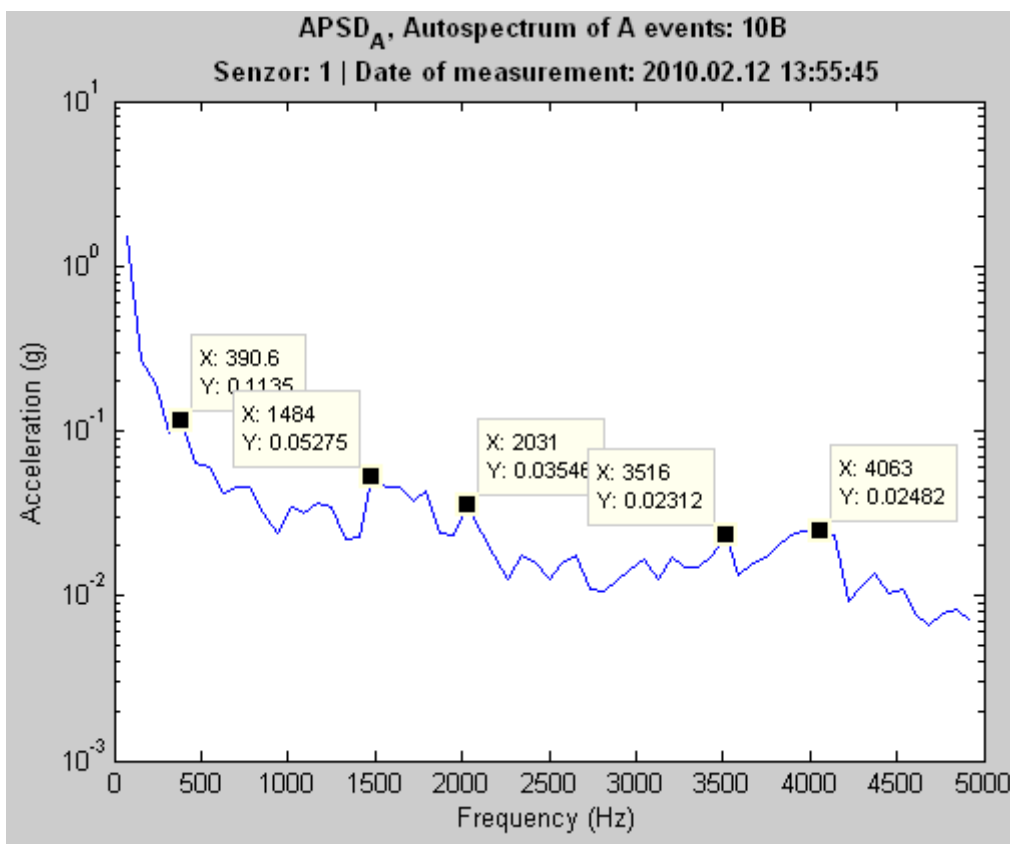
FIG. 2-67. Background mastered by channel No1 (A events).
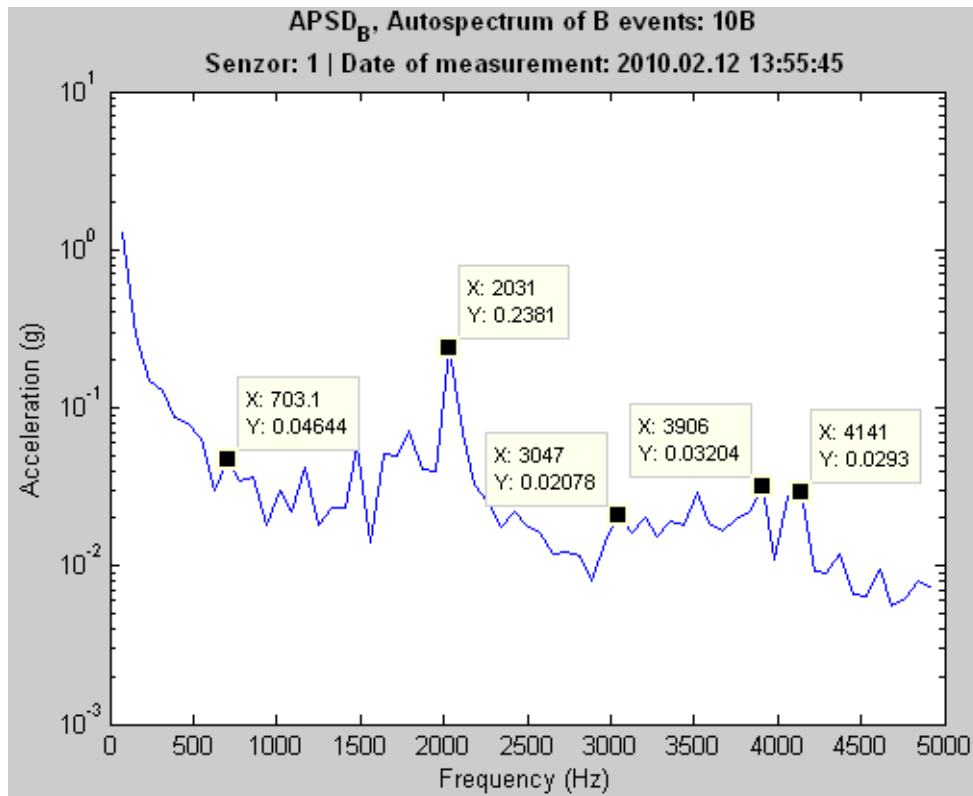
FIG. 2-68. Spectrum estimated from bakelite hits (events B) measured by channel No1.
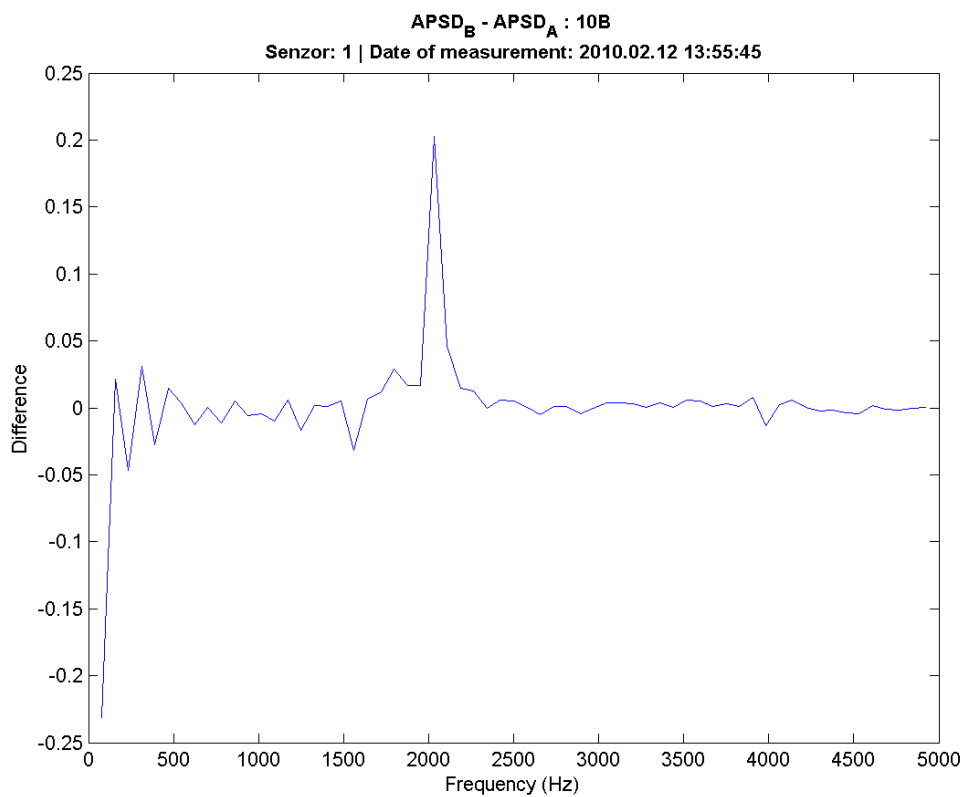
FIG. 2-69. Difference of spectra of event B and A in case of bakelite measured by channel No1 in linear scale.

Conclusion: There is only one single peak due to Bakelite impact at 2 kHz

128

2.3.7. Summary

We have analyzed the Benchmark data proposed by the Coordinated Research Project (CRP) advanced surveillance, diagnostics, and prognostics techniques used for health monitoring of systems, structures, and components in nuclear power plants. In our contribution we gave a detailed description of the method proposed by us. It consists of an autoregressive pre-filtering and an event selection based on sequential probability ratio test. We demonstrated that this method is very good in finding the events in high background nose and it is very effective. Collecting most of the events based on that method and also selecting the most prominent parts of background using the same methods, auto-spectra were estimated using traditional FFT technique to collect spectral parameters for identification of the object. We found that the so called big bolt produced additional white noise components in frequency range 2500-12500Hz. The small metallic bolt produced additional spectral component in much smaller frequency range 2000-5000 Hz. While Bakelite added component at around 1-2 kHz in a very narrow frequency peaks. This result is not in line with previous finding and therefore it needs some verification. However, this is the results of our estimation. In our further identification system we have comparison using the closest neighbours and neural network. Also we are developing skeleton method. However until the spectral data have not been verified it is premature to feed those data to other sophisticated pattern recognition systems.

TABLE 2-16. DESCRIPTION OF BENCHMARK DATA FILES

Date	Time [hour]	Measurement condition	File name	Sampling rate [kHz]	Place of knocks
2010.02.11	8	Normal water flow, the big metal screw in the tube	1N.zip	1	behind sensor 4 (see drawing)
	9	Normal water flow, the big metal screw in the tube	5N.zip	5	behind sensor 4 (see drawing)
	10	Normal water flow, the big metal screw in the tube	10N.zip	10	behind sensor 4 (see drawing)
	11	Normal water flow, the big metal screw in the tube	25N.zip	25	behind sensor 4 (see drawing)
	12	Normal water flow, the big metal screw in the tube	50N.zip	51	behind sensor 4 (see drawing)
2010.02.11	13	Normal water flow, a small metal screw in the tube	1K.zip	1	behind sensor 4 (see drawing)
	14	Normal water flow, a small metal screw in the tube	5K.zip	5	behind sensor 4 (see drawing)
	15	Normal water flow, a small metal screw in the tube	10K.zip	10	behind sensor 4 (see drawing)
	16	Normal water flow, a small metal screw in the tube	25K.zip	25	behind sensor 4 (see drawing)
	17	Normal water flow, a small metal screw in the tube	50K.zip	50	behind sensor 4 (see drawing)
2010.02.12	8	Normal water flow, a bakelite piece in the tube	1B.zip	1	behind sensor 4 (see drawing)
	9	Normal water flow, a bakelite piece in the tube	5B.zip	5	behind sensor 4 (see drawing)
	10	Normal water flow, a bakelite piece in the tube	10B.zip	10	behind sensor 4 (see drawing)
	11	Normal water flow, a bakelite piece in the tube	25B.zip	25	behind sensor 4 (see drawing)
	12	Normal water flow, a bakelite piece in the tube	50B.zip	50	behind sensor 4 (see drawing)
2010.02.18	10	No water flow! Metal knocks (by hand) on the outer surface of the tube	01A50.rar, 01B50.rar, 01C50.rar	50	between sensors 0 and 1; A-first quarter, B- halfway; C- third quarter
	13	No water flow! Metal knocks (by hand) on the outer surface of the tube	12A50.rar, 12B50.rar,1 2C50.rar	50	between sensors 1 and 2; A-first quarter, B- halfway; C- third quarter
	14	No water flow! Metal knocks (by hand) on the outer surface of the tube	23A50.rar, 23B50.rar, 23C50.rar	50	between sensors 2 and 3; A-first quarter, B- halfway; C- third quarter

2.4. THE RUSSIAN EXPERIENCE ON DESIGNING AND APPLICATION OF VIBRONOISE DIAGNOSTIC SYSTEMS OF WWER-440 REACTORS

By: A. Usanov
VNIIAES

2.4.1. Purpose of the system

The VibroNoise Diagnostic System (VNDS) of WWER-440 reactors is intended for identification of operating conditions of reactor internals (RI) and fuel assemblies (FA) on basis of vibration parameters with early detection of undesired conditions which are caused by the increase of loads from the flow or by wearing of supporting structures. The schematic image of reactor internals supporting structures, fuel assemblies and emergency regulating assemblies are presented on FIG. 2-70 together with RI & FA main oscillation directions.
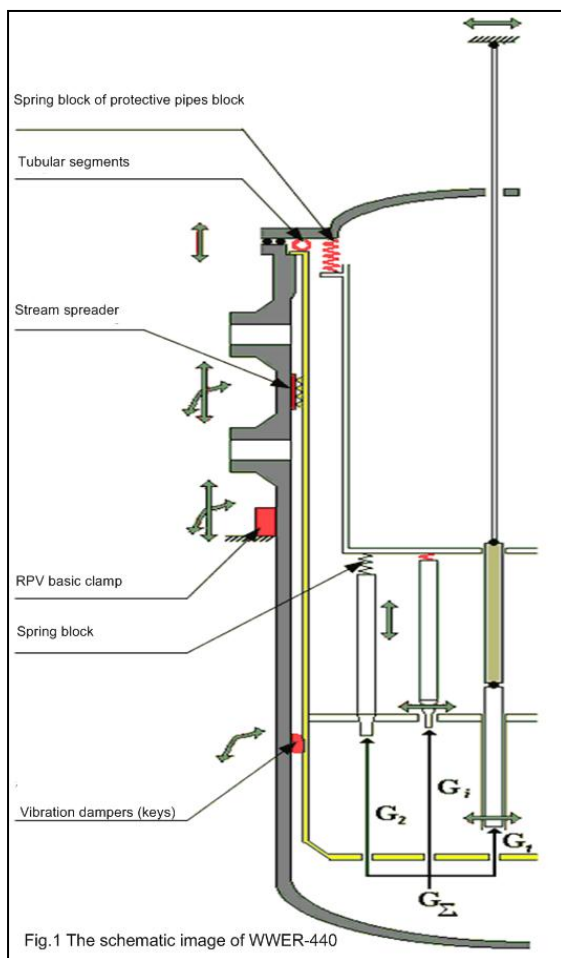
FIG. 2-70. Interferences of the elements of in vessel components.
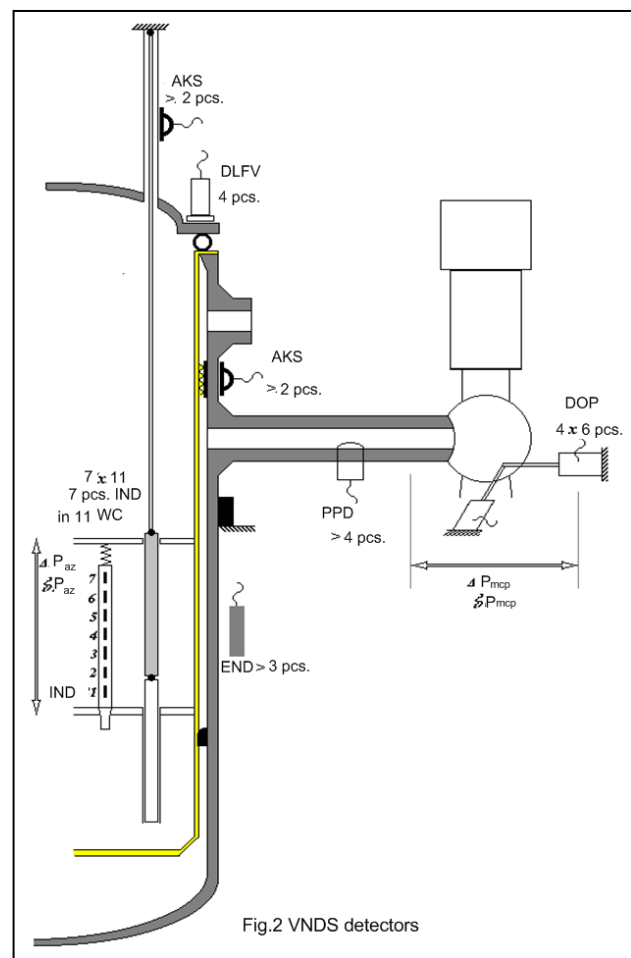
FIG. 2-71. Sensors used in vibronoise detection system.

Recently programs are accepted and realized in Russia directed on increase of economics of operating nuclear power plants (NPPs) with the aims of:

- Extending the NPP project lifetime with conversion to the long term operation which is now considered within the framework of lifetime management;
- Increasing operating reactors power.

To realize this in operating reactors the following detailed knowledge is required:

- Characteristics of hydro-elastic transfer between in vessel instrumentation and flow;
- Actual operating conditions of the equipment;
- Understanding of possible degradation caused by continued NPP operation.

These are the circumstances supporting the importance of the application of VNDS.

2.4.2.   A system configuration

Full-scale configuration of VNDS of WWER-440 (in fact is repeating the earlier version elaborated for WWER-1000 reactors) includes following detectors (FIG. 2-71):

Pressure pulsation detectors (PPD) which are positioned on the main circulating pipelines and produce information about the flow instability as the root cause of RI&FA oscillations. Monitoring the pressure pulsations is the most valuable in case of increasing of reactor power. In this case frequencies of acoustic standing waves (ASW) of pressure change because of their dependence on coolant temperature (FIG. 2-72). This can lead to the resonant phenomena and increases the vibrations of the equipment.

Detectors of low-frequency vibrations (DLFV) are fixed on the top of the reactor vessel. These detectors provide the information about joint oscillations of a reactor pressure vessel (RPV) and reactor internals. The frequency spectrum of DLFV signals essentially changes when supporting structures of reactor core barrel (CB) diminish (see FIG. 2-73 with the results of vibration measurements before and after repair of supporting structures that were made at one of the WWER-440 reactor type V-230).

Moreover, the DLFV detectors allow to carry out the monitoring of reactor internals (and to make the decision on an acceptability of vibrating conditions) during a reactor start-up when the neutron flux is absent.

In-core neutron detectors (SPND) are part of the RI control system.

According to the world experience, noise components of SPND signals are used in three major tasks:

- Estimation of neutron-physical and thermo-hydraulic characteristics of the reactor core;
- Measurements of flow rates through fuel assemblies;
- Monitoring the vibration conditions of fuel assemblies.

The last task is accomplished by the fact, that SPND noise signals are sensitive both to vibrating and thermo-hydraulic sources of neutron noise, which can compete among themselves, being in one frequency range.

In particular, the low-frequency area up to 6.0 Hz, that contributes the greatest value for the vibrating analysis, has the form of "pink noise" due to effects of the global neutron noise. As an example, auto power spectral density of SPND signal in reactor WWER-440/230 (Units №1 and 2 of Kola NPP) and reactor WWER-440/213 (units №3,4 of Kola NPP) are presented at FIG. 2-74.

Fig.3 Changing of ASV frequencies during of a reactor start-up
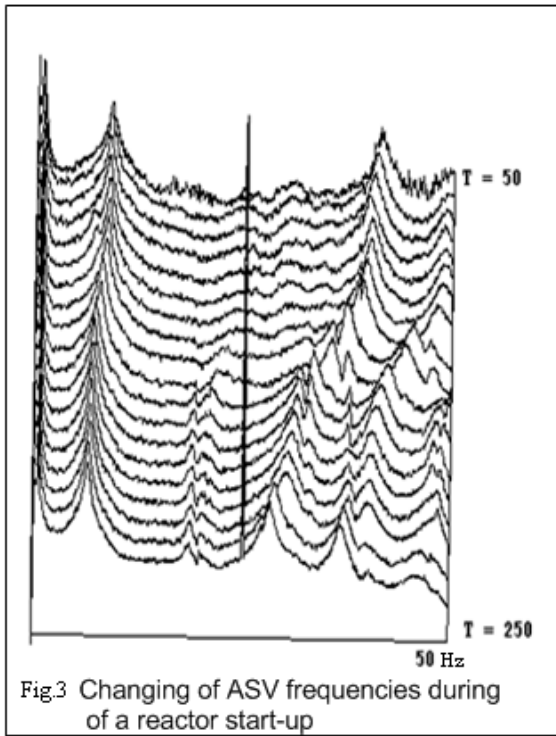
FIG. 2-72. Changing of acoustic standing waves (ASV) frequencies.

Fig. 4 DLFV spectrums at different conditions of CB supporting structures
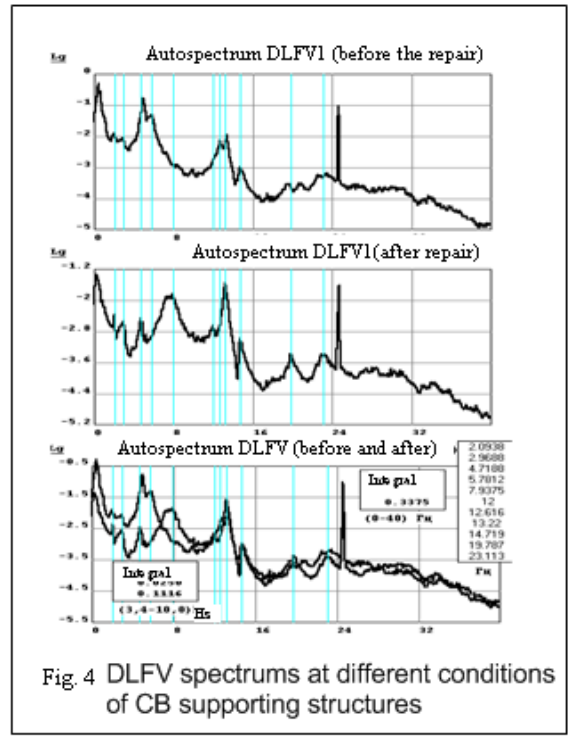
FIG. 2-73. Differences in neutron spectrum with and without core barrel support.

Fig 5a IND autospectrum of working cassettes of Kola unit 2 (V-230)

Fig 5b IND autospectrum of working cassettes of Kola unit 3 (V-213)
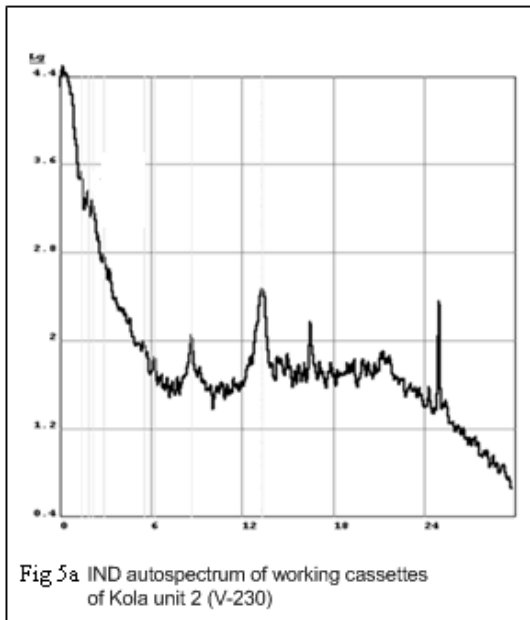
FIG. 2-74. Auto-spectra of in-core neutron detectors (SPND or IND) in WWER-440 type Russian reactors.

It is also important to note that the detector sensitivity decreases monotonically during one fuel cycle (for one campaign) and this will affect measurements results and is characteristic of neutron noise.

An additional problem which can limit application of neutron noise signals is that it is affected not only by vibration, but also other sources of neutron noise, in particular, concentration of boric acid

133

changes during the campaign. Regular vibronoise measurements that are performed at reactors WWER-440 have shown that neutron APSD can grow up to two and a half times during the campaign due to reduction of boric acid concentration.

In Russian practice, the application of SPND noise signals assumes their cross analysis with other vibronoise diagnostic system. Such analysis is carried out in two ways:

A) Identification of coherence function of signals couples "PPD-SPND", "PPD- EXND ", " EXND -SPND", "IND-SPND" (where SPDN stands for in-core neutron detectors, which are really SPND type detector, while EXND stand for ex-core neutron detector which are typically ionisation chambers).

So, coherence function between SPND and EXND signals shows all essential phenomena connected with acoustic standing waves calculated in reactor vessel internals, and it is in a contrast state at practical absence of a global background. The Eigenfrequencies of core barrel and fuel assemblies appear also in all measurements. Consequently, making use of cross spectral characteristics between EXND and SPND signals can provide information on the basic features of in vessel reactor equipment vibrating conditions and thus can be used for vibroloads management of RI. The results and short comments of the cross-spectral analysis of signals pairs " EXND -SPND" in reactor WWER-440 of type V-230 are presented on FIG. 2-75.

B) Carrying out of multidimensional autoregressive analysis of signals couples "PPD-SPND", "PPD- EXND ", " EXND -SPND", "SPIND-SPND". Such analysis allows finding the primary source of one or another resonance in a spectrum of oscillations under mutual contributions of one signal to another. A detailed explanation of the multidimensional autoregressive analysis method is given in [29].

Ex-core neutron detectors (EXND) are part of the reactor safety system. Application of noise components of EXND signals is necessary in VNDS for several reasons:

− These detectors are part of the original design that essentially reduces the installation cost of VNDS;
− Noise components of EXND signals have considerable magnitude (to 0.5% from level of neutron flux signals) that alleviates the problem of their registration and interpretation;
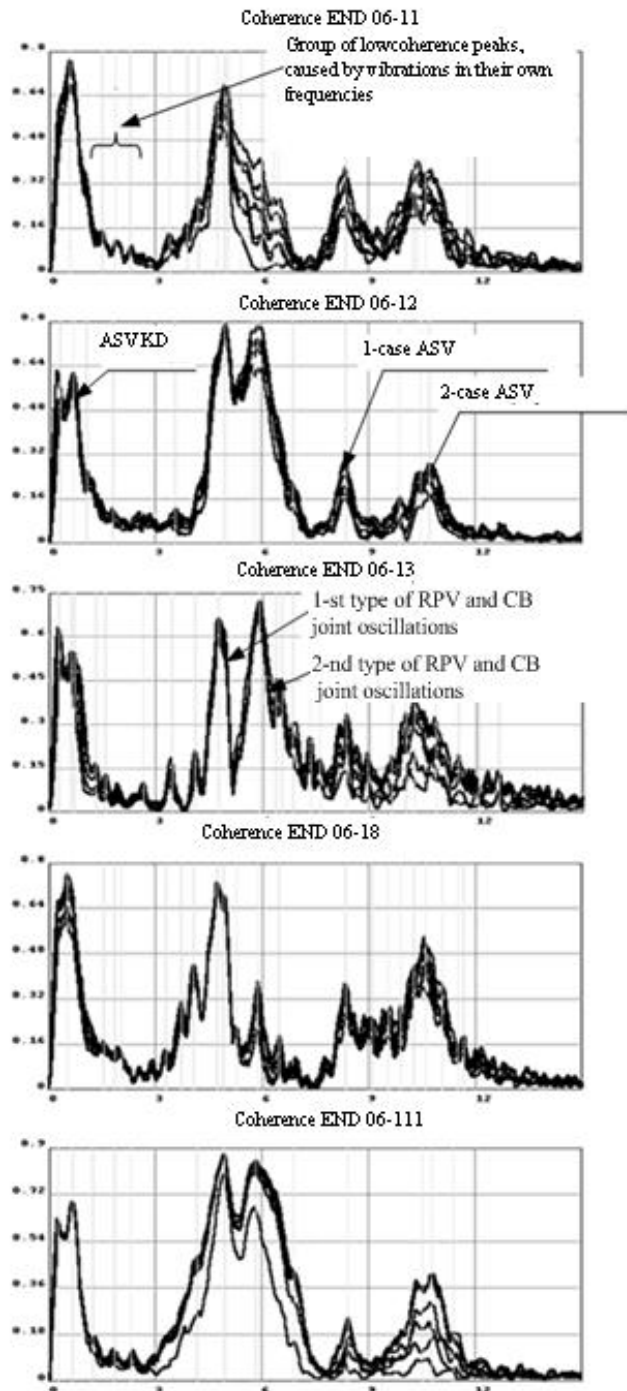
FIG. 2-75. EXND-SPND coherence function (seven pieces) of the Kola NPP (Unit 2).

− Despite dependence of EXND signals intensity on concentration of boric acid (that is characteristic for all noise signals), their spectral images are steady enough during operational campaign (see FIG. 2-76 with APSD of EXND signals in the beginning and the end of operational campaign);

− In-core detectors are sensitive to changes in rigidity of the reactor's core barrel supporting structures, making them a basic instrument of early detection of non-designed vibrating conditions, which are connected with deterioration of supporting structures.
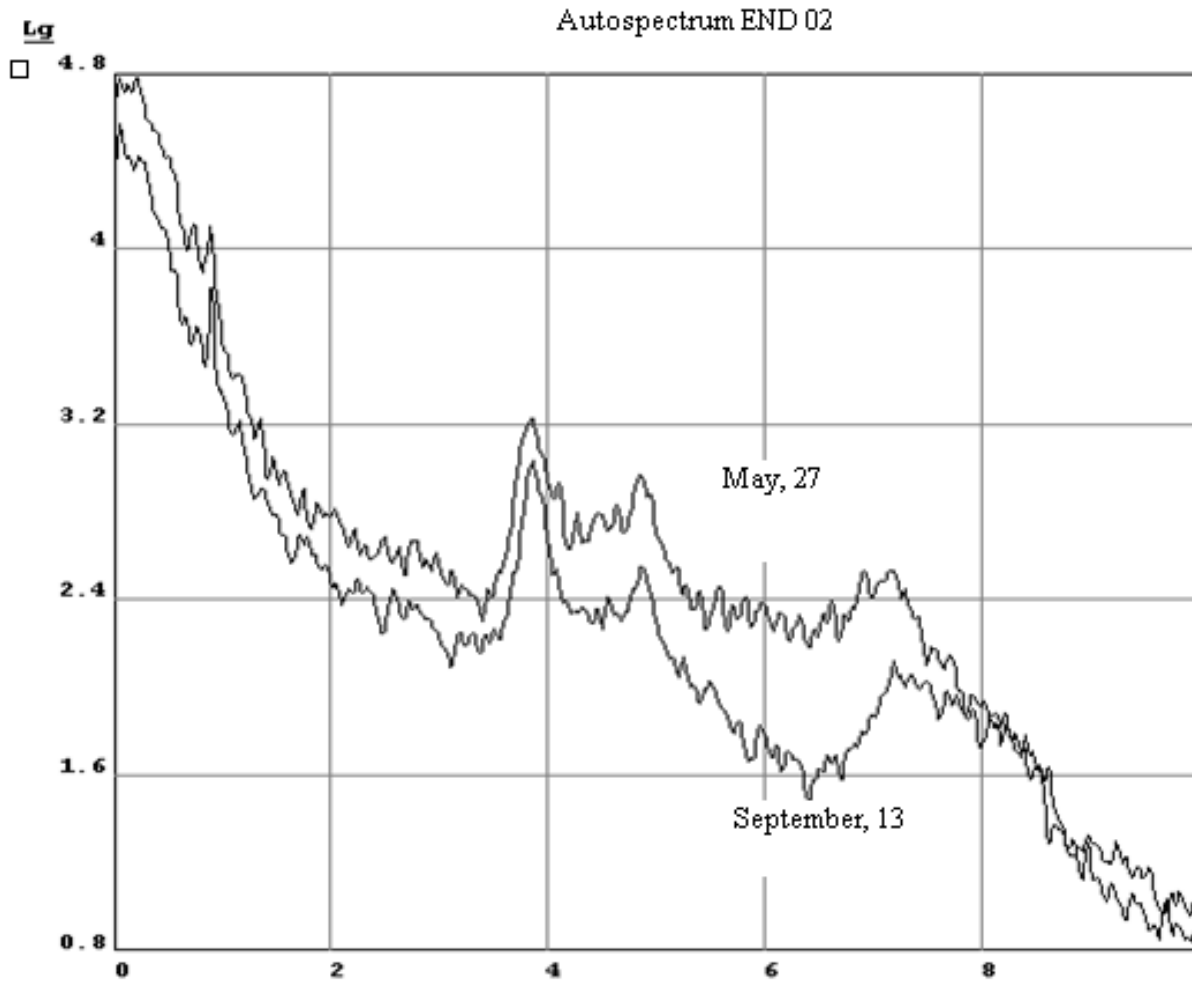
FIG. 2-76. Auto power spectral density (APSD) of EXND №2 signal at the beginning (September, 2003) and the end (on May, 27th, 2004) of operational campaign.

Direction to core barrel vibrating conditions monitoring is connected with fact that it is the basing element of the reactor core which therewith in many respects defines fuel assemblies vibrating conditions.

In the Russian practice together with traditional parameters of vibro-diagnostics, such as the amplitude and frequency of a resonance, a trajectory of the movement of core barrel at its vibration is used as a diagnostic tool. Trajectories of core barrel oscillations essentially vary at partial abatement of one or several keys rigidity in the bottom of core barrel (FIG. 2-77).
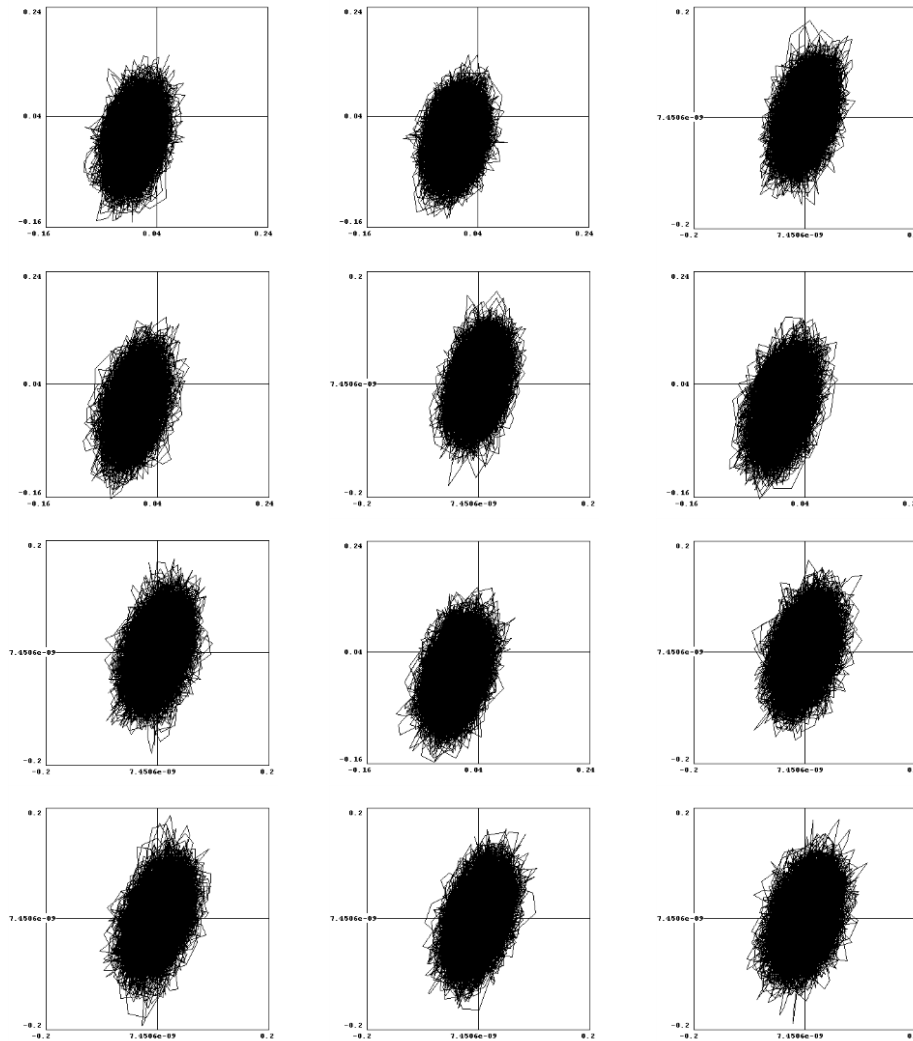
FIG. 2-77. Oscillations trajectories of reactor WWER- 440 core barrel at frequency 3.85 Hz at partial deterioration of its fastening keys.

The estimation method of core barrel trajectories using ex-core neutron noise has been presented in [29].

Along with the above described full-scale stationary system, which focused on the use only of regular signals EXND and SPND, its mobile option is also applied in the Russian practice. Such option claimed by those nuclear power plants with WWER which are not equipped with the systems of operative diagnostics.

The most optimal variant of mobile system application is its joint work with modern systems RICS (Reactor Internal Control System) and NFCE (Neutron Flux Control Equipment), in which:

- RICS equipment has function of separation of main and noise components of SPND signal;
- NFCE has function of a noise component separation from frequency-modulated EXND signal by means of specialized equipment.

The given equipment is developed by the specialized Russian organizations and introduced at a number of WWER-440 and WWER-1000 power generating units. For example, periodic vibronoise measurements with its application are performed at power generating units 3 and 4 of Kola nuclear power plant with reactors WWER-440 type V-213.

2.4.3. A technique of reactor internals and fuel assemblies' diagnostics on vibroloads parameters

The technique applied in the Russian practice takes into account distinctions of design and operating conditions of reactors WWER-440 on various projects. Accordingly, the technique is developed for specific types of monitored reactors. The detailed exposition of a reactor internals and fuel assemblies` diagnostics technique on vibroloads parameters is given in [30].

To summarize, the technique includes the following basic stages:

− Periodic collection of noise and vibrating signals;
− Identification of the current vibrating condition using a database of known vibrating conditions developed by using the results of bench and commissioning vibrating activities of prototype reactors.

Two alternative sets of actions are performed depending on results of identification:

A) In case of current condition conformity to design, the further actions are performed using the methods of signature diagnostics:

− Current spectrograms are announced as reference ones;
− Statistical processing of vibration parameters is performed for operational campaign, at least, with definition of confidence intervals of amplitudes and frequencies changes of each monitored parameters. The set of the "generalized" spectrograms is derived in which the top limit of a confidence interval is accepted as supposed intensity of a frequency component.

The current condition is marked as "normal" if all current characteristics do not exceed corresponding characteristics of the generalised spectrograms.

Similarly (by using statistical processing of vibronoise measurements for campaign) thresholds of frequencies characteristic of reactor internals and fuel assemblies' oscillations changes are identified. In the first order such actions should be performed on vibrating conditions of reactor core barrel, which is the basic bearing element of a reactor core. In second plan it is very important, in many respects to define vibrating conditions of fuel assemblies. Accordingly, signals of ex-core detectors are analyzed first. "Normal" values for parameters of reactor core barrel vibration are presented in TABLE 2-17 as an example. Such data are intended for the personnel of the nuclear power plant using VNDS.

TABLE 2-17. NORMAL VALUES OF CORE BARREL VIBRATION

Monitored frequencies, Hz	3,8	7,0	8,0
The first threshold on admissible shift of frequencies, Hz	0,2	0,5	0,3
The second threshold on admissible shift of frequencies, Hz	0,5	1,0	0,8
Admissible amplitude, micron	110 ± 2	110 ± 2	110 ± 2

B) In case of accessing current parameters values, the following set of actions is performed.
At excess of the first admissible threshold on frequency, the specialized branch organizations with the arsenal of research (a modal analysis, a monitoring of trajectories) are involved to the

analysis, and calculations on mathematical model are also carried out at consecutive modelling of reactor internals and fuel assemblies supporting structures wearing (see FIG. 2-70). Such analysis allows pointing to the probable reason of the equipment abnormal (increased) vibrations.

Further inspections and measurements of the most probable defective units are performed by the NPP personnel during the next scheduled outage. The decision on repair of defected unit is made in collaboration by utility experts and the main designer organization. To check the efficiency of the repair a repeated vibronoise measurements is performed during the next operational campaign. This technique of WWER-440 vibronoise diagnostics is approved for Russian reactors WWER-440 in their preparation for long term operation.

The above-stated basic procedures can be commented as follows:

A) The full-scale mathematical model of the given type of a reactor together with modelling of mass-stiffness characteristics of basic equipment, and including the control rod driving mechanism on the top of the reactor should be applied to calculations. The finite element model is shown on FIG. 2-78.

B) The interpretation of numerous vibrating effects carried out for a present time allows reducing the analysis of flow-induced vibration of core barrel to monitoring of its most interesting (beam and pendulum) oscillations.
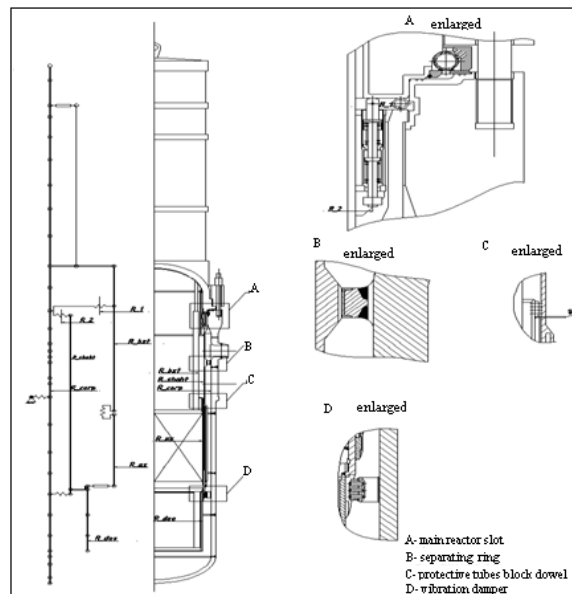
FIG. 2-78. Finite-element vibration model of reactor WWER-440 under project V-230.

2.5. THE DESCRIPTION OF VALVES TIGHTNESS MONITORING TECHNIQUE

By: A. Usanov
VNIIAES

The ultrasonic monitoring allows detecting valves malfunctions for the purpose of planning corresponding repairs at early stage of their occurrence.

The ultrasonic monitoring represents a quite fast and rigorous method of localizing leakages. Since the ultrasound represents short-wave signals, they will be the most accurate in all spectra. They will be perceived in the best way at the place of leakage.

When the coolant or gas passes the pipeline which does not have obstacle or bend, minimum turbulence in the stream or its full absence is observed. When the working medium leaks through a crack, damages occur (on tightening surfaces of valves lacking parts, in a cover connection, in a stuffing box connection) and whirlwinds are formed. The regular Carmen vortex is formed at high Reynolds numbers Re > (102 - 105). An impulse of force, which leads noise formation, appears. It allows detecting a leakage by using ultrasonic devices.

The consecutive listening in the pipeline section upstream from the valve, in the valve case around a saddle and in the pipeline section downstream from the valve is carried out for detecting leakages through the shut valves. The noise monitoring before and after the valve is carried out for the purpose of avoiding false detection of a leakage from another possible source of noise.

Monitoring of valve tightness is carried out by gauging of signal level on a flow stream using a method of four points ("ABCD method ") by means of an ultrasonic locator – FIG. 2-79.

FIG. 2-79. Carrying out of measurements by ultrasonic locator Ultraprobe 10000.
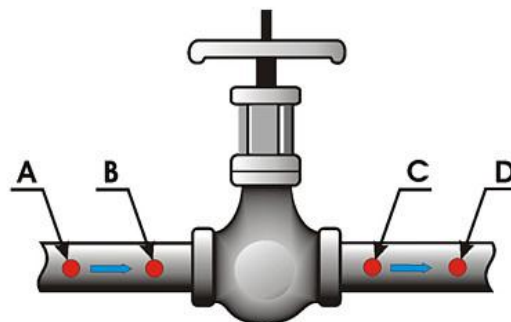
FIG. 2-80. Sequence of the monitoring points relative to a medium stream.

The measurements of noise level in points A, B, C and D are carried out for leaking definition (FIG. 2-80). Then comparison of the ultrasonic signal intensity in points A, B, C and D is carried out. If the level of an ultrasonic signal in point C is bigger, than in points B and A, the valve is considered not tight. In the case of increased level of a signal in point D, it is possible to assert, that noise from off-site sources (throttling, pumps) is registered.

Work related to leakage detection and characterization (volume of leakage through valves) has been started at the Volgodonsk nuclear power plant since 2005. For this purpose, registration and analysis of signals for various media (water, steam) at various degree of working body opening has been executed in real conditions of process technology. An ultrasonic locator with stethoscope module Ultraprobe 10000 has been used for registration of signals.

Registration and record of signals for ultrasonic locator flash-memory have been carried out during the investigations. Signals were registered around the valve working body. The sampling frequency of the signal acquisition was 50 kHz. The assessment of leakage size was performed by volume measurement at equal time intervals. The leakage was simulated by changing the opening of the valve.

The authors of this experiment noticed that both the amplitude of the direct signal and the nature of the spectrum change with increasing flow rate [31].

The authors carried out spectral analysis for an assessing the dependence between the volume of leakage through a shutter, the parameters of ultrasonic signals, and the estimated parameters. The analysis of the graphical representation of spectral power allows revealing dependence between the parameters of a signal and the leakage volumes. As the most informative parameters, the following ones were identified (see FIG. 2-81):

− Value of the integral signal level;
− The ordinate to abscissa ratio corresponding to the centroid of points of the figure limited to a spectral curve.
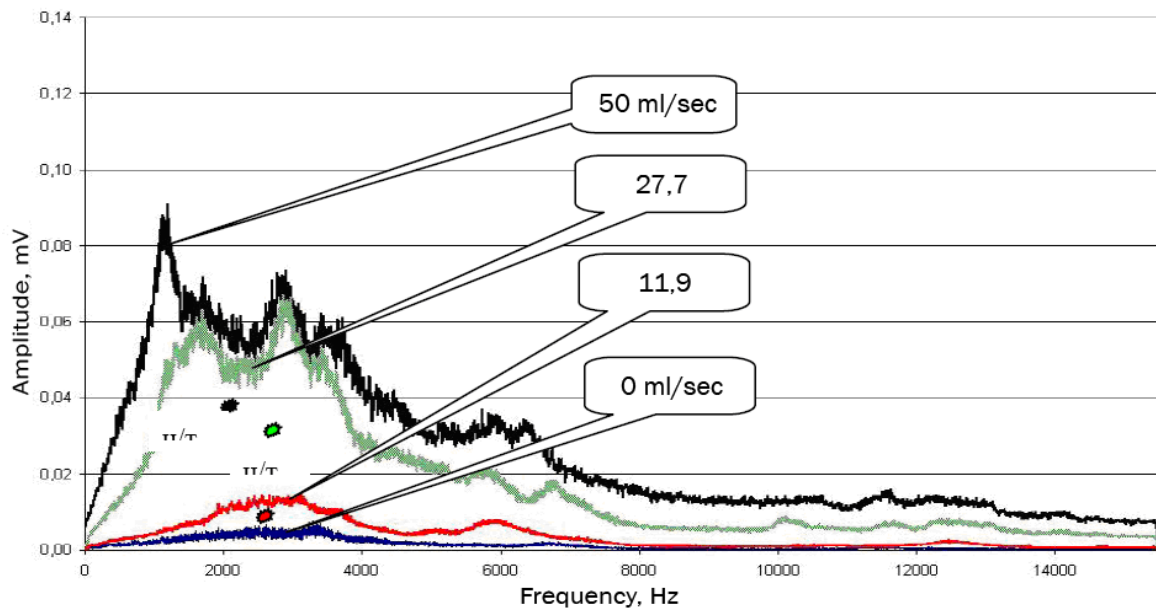
FIG. 2-81. Graphs of US signals spectra for various leakage volumes.

The observed graphical dependences between signal parameters and leakage volume are of a difficult nature, which can be explained by the presence of two modes of liquid outflow (turbulent and cavitational). Moreover, these dependences cannot be easily converted into empirical expressions.

Thereafter, operations have been executed for searching the characteristic dependence of leakage volume from ultrasonic signal parameters:

− Values of each parameter have been normalized: the signal levels, and the ordinate to abscissa ratios corresponding to the figure's centroid of points;
− Ratios of normalized quantities are calculated;
− The calculated values are accepted as the generalized parameters;
− The graph representing the dependence of the generalized dimensionless parameters on leakage volume (FIG. 2-82) is constructed.
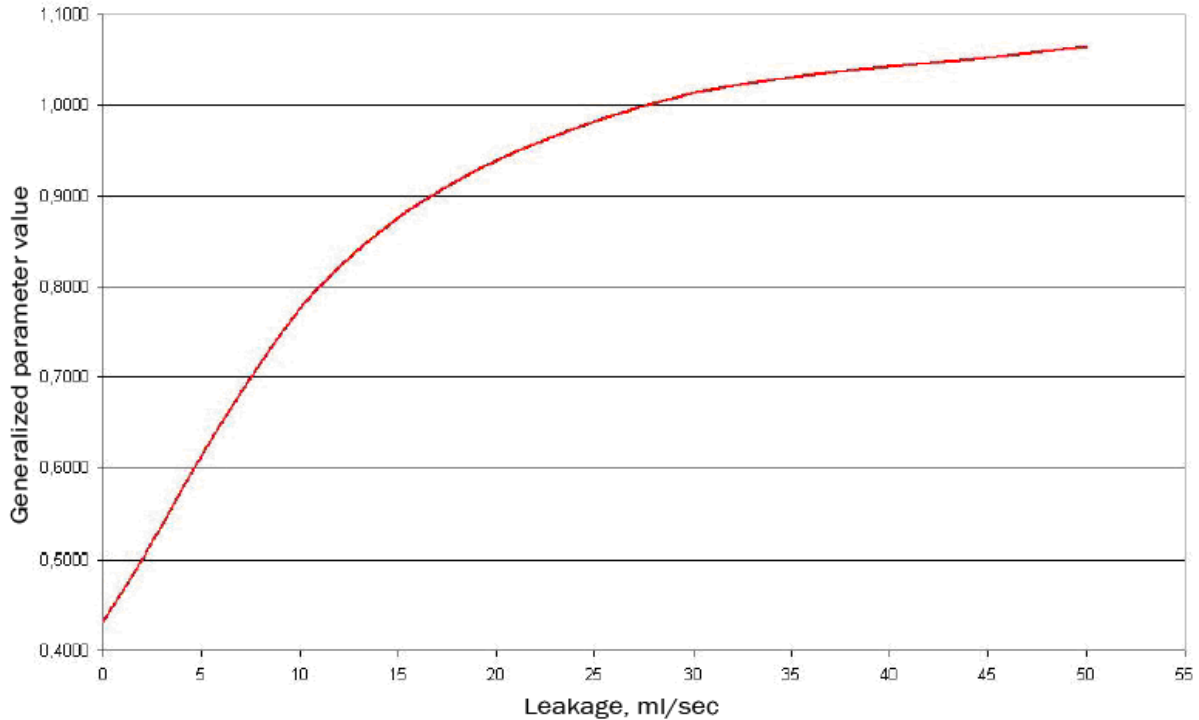
FIG. 2-82. Dependence "leakage volume - value of the generalized parameter".

The received curve has a strongly pronounced exponential nature and allows easily revealing the empirical dependence "leakage volume - value of the generalized parameter".

The search of the empirical dependence was carried out in a package called Statistica. The dependence between leakage volume and the generalized ultrasonic signal parameter, constructed on a basis of regression models (using a nonlinear fit method) for the investigated valve that is working at concrete parameters of a working medium (water), looks as follows:

$$P = 0,43 + 0,646 \cdot (1 - e^{-0,077L})$$,

where P is the parameter which is equal to the ratio of the normalized quantity of an ultrasonic signal level to coordinate of the centroid of points, and L is the leakage volume (in ml/sec).

The further development of a method requires additional bench tests for assessing the dependences between the registered ultrasonic signals and parameters, such as valve dimension type, working medium and its parameters. It will allow carrying out an authentic estimation, based on the following algorithm:

− Preliminary imitation of a leakage by changing the opening magnitude of a concrete valve, direct measurement of leakage volume, signal registration in an ultrasonic range, calculation of an average level of a signal spectrum and definition of the centroid of points coordinate, which is applied to the figure formed by a curve of spectral density and an abscissa axis;
− Identification of leakage volume dependence on ultrasonic signal level value and on coordinate of signal centroid of points, rate setting of last quantities and calculation of their ratio in the form of a dimensionless parameter;
− Identification of exponential dependence of leakage volume on the calculated dimensionless parameter by a regression analysis method, in a following form:

$$P = A + B \cdot (1 - e^{-C \cdot L})$$,

142

where A, B and C are the factors defined by the technological parameters of the medium and a dimension type of tested valve.

- Formation of the database containing the identification number of the valve and its characteristics, the analytical data concerning the dependence of leakage through a valve shutter on parameters of an ultrasonic signal;
- Registration by the operator of the ultrasonic signal on a flash-memory for the device during the valve inspection in a place of a technological position and comparison with the values contained in the database;
- Conclusion about the tightness of a shutter by automatic program calculation on the above specified dependence, identification of the medium passing through a working body in the case of leakage.

2.6. KIR (LOOSE PARTS AND VIBRATION MONITORING SYSTEM) FROM CHINA

By Shi Ji
I&C Engineering Dept.
China Nuclear Power Design Co.

2.6.1. Operating function

The KIR system has two main functions

− Loose part monitoring system (LPMS) and;
− Vessel vibration monitoring system (VMS).

The view of the KIR system cabinets can be seen in FIG. 2-83.

FIG. 2-83. View of the cabinets of the KIR system.

2.6.1.2. *The loose part monitoring system (LPMS)*

The function of the loose part monitoring system is to detect and locate loose parts in the reactor primary coolant system during reactor operation. The system allows monitoring simultaneously the three steam generators and the reactor vessel. Three accelerometers are used for each monitoring area. The LPMS will generate two alarms (loose part detected and system failed) in the control room.

2.6.1.3. The vessel vibration monitoring system (VMS)

The function of the vessel vibration system is to monitor in-service vibration response of the reactor vessel and internals. The surveillance of vibration response in the reactor vessel and internals is used to detect mechanical deterioration.

The system monitors ex-core signals of the RPN nuclear instrumentation system as well as vessel accelerometers. Neutron fluctuations or neutron noise reflect variations in the thickness of the water gap between the reactor internals and the reactor vessel and are consequently indicative of the motion of the internals.

Periodically, the operator starts up automatic sequences, which perform:

− Scan and measurements of all the channels that have been defined in the VMS;
− Configuration;
− Storage of the measurements on the hard disk.

On request, the results of the measurements can be printed out.

2.6.2. Safety function

The KIR is not a safety system.

2.6.3. Design basis and safety criteria

2.6.3.1. Design basis

Design principles

The KIR uses accelerometers as sensors for both functions: loose part detection and reactor vibration monitoring. Those functions are performed on two computers, each for one function.

Loose part detection

The sensitivity of the system is such as to detect a loose part that weights between 0.1 kg and 15 kg and impacts with a kinetic energy over 0.7 joule on the wall within 1 m of a sensor when one pump is on duty.

Loose part detection uses accelerometers within the 1 to 10 kHz bandwidth.

A selector switch directs the signals related to a component (vessel or steam generator) to an audio amplifier which shall help the operator to detect a loose part in one of the three steam generators or in the vessel bottom head.

The KIR system computer screen shows:

− Alarms and evolution of the detection criteria;
− Detected defaults;
− Location of the alarms presented;
− Sensor signal visualization.

Reactor vessel vibration behaviour monitoring

The accelerometers mounted on the reactor vessel deliver signals proportional to the vibration of the vessel. Neutron noise measurements provide signals which are indicative of the vibration behaviour of the vessel internals. These signals are processed by a calculator.

Monitoring of vessel vibration shall be performed once a month. However, this frequency shall be greater when the system is being brought into service.

2.6.3.2.   Safety criteria

− Safety class: The safety class is NC;
− Quality category: The quality category is Q3;
− Seismic class: The equipment is not seismic classified.

2.6.3.3.   General equipment architecture

The KIR system has two cabinets: LPMS, VMS.
The equipment in the LPMS cabinet includes:

− 1 LPD signal conditioning rack;
− 1 LP monitoring rack;
− 1 alarm processing rack;
− 1 19" LCD display;
− 1 slide-out keyboard and a keypad;
− 1 power distributing panel;
− 1 UPS.

The equipment in the VMS cabinet includes:

− 1 data acquisition rack;
− 1 vibration analysis rack;
− 1 19" LCD display;
− 1 slide-out keyboard and a keypad;
− 1 printer (shared with the LPMS cabinet);
− 1 toolbox.

2.6.3.4.   Choice of material construction

All materials used inside the reactor building (RX) on the vessel and the steam generators comply with environmental conditions.
Temperatures:

− Vessel head closure head: 340℃;
− End of guide tubes at vessel bottom head: 293℃;
− Steam generator heads: 327℃.

Radiation behaviour during operation:

− In contact with the equipment: up to 2 Gy/h.

2.6.4.   Description

2.6.4.1.   Introduction to KIR system

The KIR system is designed to work with accelerometers mounted on the reactor vessel (LPMS+VMS) and the steam generators (LPMS only).

2.6.4.2.   General KIR functions description

Accelerometers through charge converter provide current signals to the LPMS cabinet.
Voltage signals from the RPN system are available in the VMS cabinet.

The signal conditioning rack is used for conditioning and filtering the accelerometer signals and the LP monitoring rack is used for LP detection.

The vibration analysis rack in the VMS cabinet is used for conditioning and normalizing the neutronic noise signals.

The cabinets include a printer for all reports, a selector/audio amplifier to listen to the LPD signals and a data acquisition rack for manual or automatic signals recordings.

Functions of the LPMS

The main functions of the LPMS are:

− To perform a continuous acoustic monitoring of the plant primary system;
− To give plant operators means to directly listen to the noise made by the primary system in operation;
− To automatically generate an alarm in case of repetitive acoustic impulses, occurring with a specific pattern, which may indicate the existence of a loose part inside the primary circuit;
− In case of an LPMS alarm, to automatically store acoustic signals and information for diagnosis purpose;
− In case of an LPMS alarm, to automatically display and print basic information which are useful for diagnosis purpose.

In case of noise in the primary system, the diagnosis (i.e. the identification of the cause of the noise) is made in the end by the plant operators, with the help of the information stored, displayed and printed by the LPMS. Operators have to be trained to be able to perform identification of known primary system noise.

There are 13 accelerometers for each plant unit:

− Three accelerometers will be installed on each steam generator;

  • One will be fitted to the bottom of the hot side of the steam generator, fixed on the thermal insulation support;
  • Two, diametrically opposite, will be fitted to the tube sheet leve1 in the plane of the separation plate between hot and cold side of the steam generator head channel, fixed on the jacketing support. This layout allows detecting loose parts which are located in the hot leg side of the channel head of the steam generator and also in the secondary cooling system of the steam generator above the tube sheet, if they generate energetic impacts.

− Four accelerometers will be installed on the reactor vessel;

  • Three of them will be installed under the reactor vessel on in-core instrumentation tubes in horizontal measurement axis;
  • Two of them will be installed in the plane of neutron noise chambers, the third one will be fitted in the opposite part of the vessel bottom head, at equal distances;
  • One will be fitted at the top of the reactor vessel closure head in vertical axis. This accelerometer is not used in the automatic loose part detection processing. The charge converters convert the electrical charges transmitted by the accelerometers into a voltage signal that can be run through long cables to the cabinet. These signals are directed to the signal conditioning rack.

These signals are amplified and band-pass filtered in the signal conditioning rack, and then delivered to the LP monitoring rack, the data acquisition rack, and the audio amplifier.

The LP monitoring device realizes treatments of accelerometer measurement channels.

Functions of the VMS

The main function of the VMS is to give plant operators means to detect and monitor an abnormal vibration behaviour of the reactor internals (e.g. hold down spring, thermal shield, fuel rod assemblies, core barrel, etc.). The VMS is used by a plant operator when the reactor is in operation, at steady power (power equal or above to 30%). It uses ex-core neutron-sensor signals and accelerometer signals. A vibration reference state is performed at 100% power just after the first criticality.

In case of an evolution of the vibration signatures, the final diagnosis is to be made by the plant operators. The diagnosis is made upon the knowledge of the natural frequencies of the structures and the incidence of structure degradations at these natural frequencies.

REFERENCES TO CHAPTER 2

[1]   LU, B., UPADHYAYA, B.R.,. HINES, J.W, Time-frequency Analysis of Acoustic Signals for Flaw Monitoring in Steam Generator Structures, Proceedings of MARCON 2003 (May 2003).

[2]   LU, B., On-line Structural Integrity Monitoring and Defect Diagnosis Steam Generators Using Analysis of Guided Acoustic Waves, Ph.D. Dissertation, University of Tennessee (2004).

[3]   CLEZIO, E., CASTAINGS, M., HOSTEN, B., The Interaction of the S_0 Lamb Mode With Vertical Cracks in an Aluminum Plate, Ultrasonics, Vol. 40 (2002) 187-192.

[4]   MCKEON, J.C.P., HINDERS, M.K., Lamb Wave Scattering From A Through Hole, J. of Sound and Vibration, Vol. 224, No. 5 (1999) 843-862.

[5]   BARSHINGER,J., ROSE, J.L., AVIOLI, M.J., Guided Wave Resonance Tuning for Pipe Inspection, J. of Pressure Vessel Technology, Vol. 124 (2002) 303-310.

[6]   ROSE, J. L., A Baseline and Vision of Ultrasonic Guided Wave Inspection Potential, J. of Pressure Vessel Technology, Vol. 124 (2002) 273-282.

[7]   ROSE, J., RAJANA, K., CARR, F., Ultrasonic Guided Wave Inspection Concept for Steam Generator Tubing, Material Evaluation, Vol. 53 (1994) 307-311.

[8]   GILBERT, V.P., Surface Acoustic Wave Device Designed to Monitor Frequency Shifts due to Adsorption of Mass on to a Piezoelectric Crystal, M.S. Thesis, University of Tennessee (May 1992).

[9]   YANG, J. N., LIN, S., PAN, S., Damage Identification of Structures Using Hilbert-Huang Spectral Analysis, 15th ASCE Engineering Mechanics Conference, 2-5 June 2002 (2002).

[10]   MONTESINOS, M.E., MUNOZ-COBO, J.L., PEREZ ,C., Hilbert-Huang Analysis of BWR Neutron Detector Signals: Application to DR Calculation and to Corrupted Signal Analysis, Annals of Nuclear Energy 30 (2003) 715-727.

[11]   HUANG, N.E. et al., The Empirical Mode Decomposition and the Hilbert Transformation for Nonlinear and Non-stationary time series analysis, Proc. R. Soc. Lond. A 454 (1998) 903-995.

[12]   ANTONINO-DAVIU, J.A. et al, Fault Diagnosis in Induction Motors Using the Hilbert-Huang Transform, Proceedings of the 6th ANS International Topical Meeting on Nuclear Plant Instrumentation, Control, and Human-Machine Interaction Technologies (NPIC & HMIT 2009), Knoxville, TN (April 2009).

[13]   GAZIS D. C., Exact Analysis of the Plane-Strain Vibrations of Thick-Walled Hollow Cylinders, J. Acoust. Soc. Am., Vol. 30, No. 8 (1958) 786-794.

[14]   ROSE J.L., Ultrasonic Waves in Solid Media, Cambridge University Press (1999).

[15]   AULD B.A., Acoustic Fields and Waves in Solids, 2nd Edition, Robert E. Krieger Publishing (1990).

[16]   VIKTOROV I.A., Raleigh and Lamb Waves, Plenum Press, New York (1967).

[17]   VALLE, C., LITTLE, J., Jr, Flaw Localization Using the Reassigned Spectrogram on Laser-generated and Detected Lamb Modes, Ultrasonics, Vol. 39 (2002) 535-542.

[18]   KINO, G., "The Application of Reciprocity Theory to Scattering of Acoustic Waves by Flaws," J. Applied Physics, Vol. 49, No. 6, pp. 3190-3199, June 1978.

[19]   WANG, L., ZHANG, J., WANG, C., HU, S., Identification of Nonlinear Systems Through Time-frequency Filtering Technique, Journal of Vibration and Acoustics, Vol. 125 (2003) 199-204.

[20]   KETTIG, R. L., LANDGREBE, D.A., Classification of Multi-spectral Image Data By Extraction and Classification of Homogeneous Objects, IEEE Transactions on Geoscience Electronics, Vol.GE-14, No.1 (1976) 19-26.

[21]   ALLEYNE, D., LOWE, M., CAWLEY, P., The Reflection of Guided Waves From Circumferential Notches in Pipes, J. of Applied Mechanics, Vol. 65 (1998) 635-641.

[22]   SZAPPANOS, G., FEHER, A., LORINCZ, J., NEMES, L., POR, G., CSIKOS, T., GLODI, O., LIPCSEI, S., TRI T.D, A New Digital Expert Loose Part Detection System, Annals in Nuclear Energy, vol.24, No14 (1997) 1097-1103.

[23]   SZAPPANOS, G., POR, G., Improvements in the Theory of Identification of Burst-Shaped Events for Fault Diagnosis, Nuclear Science and Engineering, Vol. 13 (1999) 261-267.

[24] SZAPPANOS, G., POR, G., Basic Ideas and Realization of Completely Digitised Loose Part Detection System HELPS, Progress in Nuclear Energy, vol. 34, No. 3 (1999) 195-201.

[25] POR, G., SZAPPANOS, G., Advanced Loose Part Monitoring System for Nuclear Power Plants, Proc. of International Conference Nuclear Energy in Central Europe 2000, 11-14 September 2000, Bled (2000).

[26] POR, G., SZAPPANOS, G., ALPS, Advanced Loose Parts System for Paks NPP, Proc. of International Conference Nuclear Energy in Central Europe 2001, Portoroz (2001).

[27] POR, G., SZAPPANOS, G., Advanced Loose Part Monitoring System for Nuclear Power Plants, Proc. of International Conference Nuclear Energy in Central Europe 2000, 11-14 September 2000, Bled (2000).

[28] BOX, G.E.P., JENKINS, G.M., Time series analysis: Forecasting & Control, Revised Edition (1976).

[29] ARKADOV, G.V, PAVELKO, V.I, USANOV, A.I., Vibronoise diagnostics of WWER, M: Energoatomizdat (2004) 344.

[30] ARKADOV, G.V, et al., Design of vibration standards for WWER-440 reactor internals, 4th International scientific and technical conference, Podolsk, May, 20-23 (2005) 211-225.

[31] ADAMENKOV, A., et al., A method of an estimation of NPP pipeline valves tightness, Mechanical engineering 10 (2008) 8.

3. PROGNOSTICS AND STRUCTURAL MATERIAL INTEGRITY (TO CHAPTER 4 OF THE MAIN REPORT)

3.1. BACKGROUND - PROGNOSTICS AND STRUCTURAL HEALTH ASSESSMENT

Establishing the technical and economic basis for longer-term operations (LTO) for nuclear power plants presents significant challenges. It is essential that safe operation practices are maintained, while at the same time capacity factors are kept high. However, it is recognized that ageing of components (particularly materials ageing due to the harsh environmental conditions) can potentially limit the operating lifetime of critical systems. It is therefore important to develop technology and a more holistic philosophy to manage existing power plants more effectively.

The approaches being developed in different parts of the world do have many commonalities, however the term LTO has different meanings in terms of the time periods being considered. For some countries LTO starts at the end of initial license period (30 or 40 years), whereas for others, such as in the USA a second license period from 40-60 years is accepted and LTO is being used to refer to the second period of license extension (60-80 years). In looking at LTO there is, in general, a move to look beyond current periodic in-service inspections (ISI), as defined in aging management plans (AMP's) and to adopt new methodologies that transition from the reactive "find-and-fix" approach with NDT/NDE to more proactive strategies [1].

There is a growing consensus that activities which enable LTO, especially beyond 60 years, will be focused more on passive systems and structures (e.g. pressure vessel, civil structure, core internals, cables, etc.) [2]. Active systems (pumps, valves etc.) are, and can continue to be, well managed and routinely monitored, diagnosed, analyzed and upgraded as needed using condition based maintenance and the methods adopted for on-line monitoring of these systems are considered to be within the scope of TAG #4 activities. Passive systems and structures, in contrast, are not easily or economically upgraded when degradation is detected at an in-service inspection (ISI) [3]. If not monitored and managed, degradation has the potential to become a problem for all nuclear components, and their safety margin can potentially be reduced.

Long-term operation of nuclear power plant (NPP) will therefore require that the technical challenges related to detecting, characterizing, monitoring, managing and mitigating materials degradation and remaining life prediction (prognostics) be identified and addressed. The technologies developed will also be required to enhance the ability to contain operation and maintenance costs, and enable operators to avoid extended or unplanned outages [4].

In order to ensure safe long-term NPP operation, it is necessary to consider adoption of a new paradigm for operation and maintenance practices, which moves beyond current periodic in-service inspection (ISI) as defined in aging management plans. At the heart of this new paradigm, called proactive management of material degradation (PMMD), is the assessment of materials degradation starting with understanding the phenomena from early in the degradation development life-cycle, establishing monitoring, and then managing the aging processes. In integrating data it is also required to understand the effects of stressors, as measured through the plant operational parameters on degradation . [5].This approach can provide early notice of potential component failure, and provided for the detection and assessment of degradation which can then be used to estimate the remaining useful life (RUL). The ability to estimate the RUL, using a prognostic methodology, for passive components with degradation, is recognized as being important [6]. Such a prognostic has the potential to provide a basis for determining whether continued safe operation (over some pre-defined interval) is possible, and whether operating conditions need to be changed to limit or mitigate the rate of further degradation and/or to establish the basis for other mitigation or repair actions that need to be employed. However, accurate prediction of the remaining useful life (RUL) of passive nuclear components is challenging, largely due to the dependence of the methodology on providing accurate knowledge of current material state and future stressor levels: both of which are in general either unknown or at best known only within some limited bounds. Analyses of rates of degradation are in

some cases also dependent on the past history of stressor levels, which will also only be known within limited bounds. There is further complexity in the assessment of degradation, in the way it relates to physical size and scale. This involves the scale of material microstructure and part geometry. Conventional NDT/NDE performed as part of an ISI program under an aging management plan is currently focused on detection of macroscopic defects, commonly in the form of cracks, corrosion or erosion. To better manage part life early degradation must be characterized. The focus for detection of early degradation is the characterization of features that are typically more diffuse, less severe or easily recognized, when compared with a feature such as a crack and many features of interest will be on a smaller scale. The significance of early degradation may also be less easily assessed, again when compared with a crack and facture mechanics which is now well established in codes and standards. Macro-defects, such as cracks have the potential to give a defined condition, such as when a crack penetrates a pipe wall to give a leak. Such an event provides an easily defined failure condition.

Monitoring and diagnostics, including advanced on-line monitoring, is aimed at detection of anomalies and degradation characterization, i.e. determining the current state of the material. However, assessing material state, including the significant of a defect, from NDE measurements, requires analysis and integration of data which can be an inherently an ill-posed inverse problem. The problem can be further complicated due to the availability of only limited or sparse data that is sensitive to measurement noise, and in many cases assessment of material state does not have a unique solution. A model is needed to translate NDT measurements into a defect, with some specific characteristics, the significance of which can then be assessed by an NDE process, such as fracture mechanics. The uncertainty in the current material state, including inherent inhomogeneity in materials and variability introduced in processing, coupled with the uncertainty in future stressor levels on a component or system scale add to the complexity in remaining life which is most likely best managed through the use of probabilistic methods for RUL estimation.

3.1.1. Degradation and aging

Degradation and aging issues for metal components were most recently reviewed by an expert panel and the insights gained are summarized in NUREG/CR-6923 [7]. This material complements that given in the NRC Generic Aging Lessons Learned (GALL) Reports [8] ,[9], and the recently issued GALL, Revision 2 [6]. There is also an extensive literature that discusses light water reactors aging issues, including material that supported the development of the case for the first US reactor license extensions from 40-60 years and these documents go back over many years [10], [11].

Component degradation and failure progress though phases that evolve over time. The life cycle for a material with degradation is shown in schematic form as FIG. 3-1. The phases in degradation for the example of stress corrosion cracking (SCC) evolve from: (1) an initial condition, before the operational environment is applied: (2) precursor: defines conditions necessary for initiation of (microscopic) crack nucleation sites through: to (3) Incubation: formation of crack precursors, but generally not visible penetration; (4) slow growth: linkage of small cracks, visible under a microscope and finally; (5) rapid growth: large cracks which develop prior to component failure.

Current NDT techniques used for ISI are typically applied to detection and characterization of large defects that occur near the end of component life. The PMMD or prognostic philosophy seeks to detect defects well before crack aggregation (Phase 5) occurs. This can be achieved only by monitoring both the stressor time history and the macroscopic materials properties which are precursors to macro-crack formation (e.g. changes in bulk electrical, magnetic, or acousto-mechanical properties). Stressor time history is commonly derived from a long-term data record of component temperature, internal pressure, strain, and vibration levels, which are typically held in some form in the plant historian. This data record is ideally obtained from sensors installed in or on components at the beginning of their service life. A library of component stressor histories coupled with traditional NDT data (i.e. defect characteristics) allows development of a prognostic model that can then be utilized in a component service life prediction, for those defects which are in Phase 4 and/or 5 of life (as defined in FIG. 3-1)
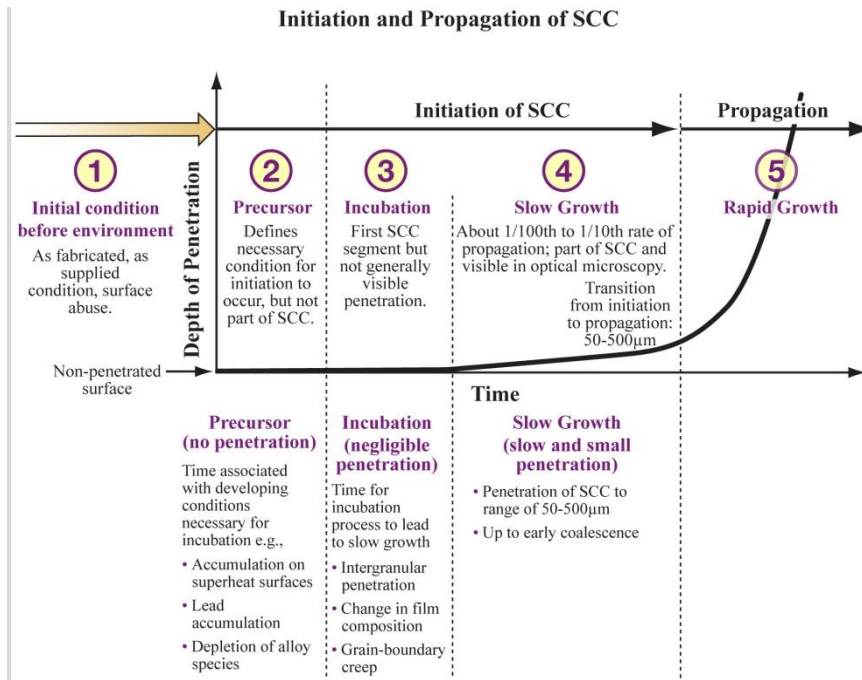
FIG. 3-1. Phases in degradation.

Examples of materials aging mechanisms for the case of BWRs, considered in terms of the four stages of aging degradation development corresponding to those shown in FIG. 3-2 [4], are shown in FIG. 3-3. The available inspection tools are identified in yellow, and it is seen that for early degradation new tools are required.
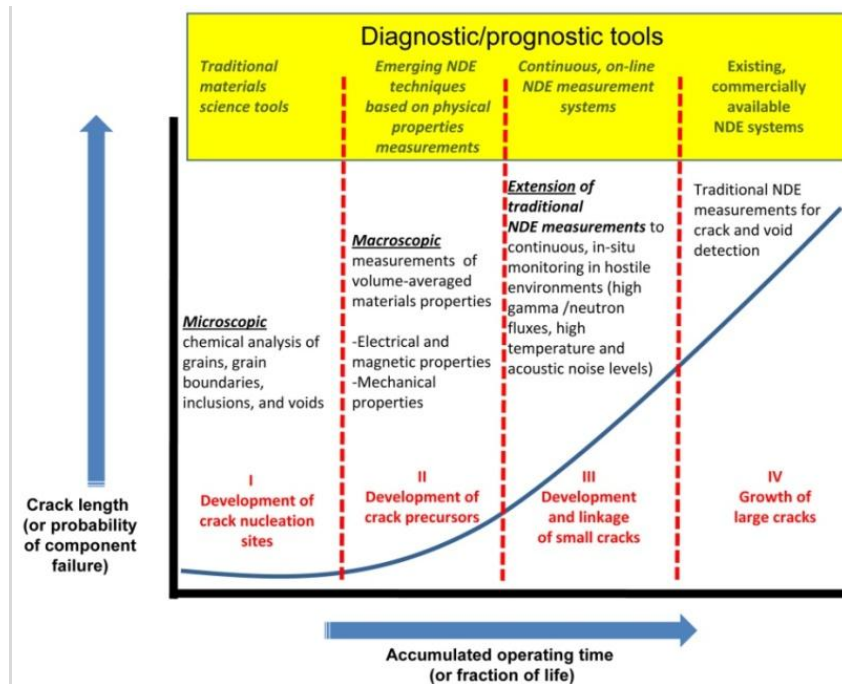
FIG. 3-2. Relationships between degradation development and measurement tools for development of a PMMD system.

Material	Degradation Mechanism	Phase			
		I	II	III	IV*
Low Alloy Steel	Irradiation Enbrittlement				x
	Environmental Fatigue	x	x	x	x
Carbon Steel	Erosion Corrosion	x	x	x	x
	Thermal Fatigue	x	x	x	
	Environmental Fatigue	x	x	x	x
Stainless Steel	Stress Corrosion Cracking	x	x	x	x
	Irradiation assisted Stress Corrosion Cracking	x	x	x	x
	Thermal Fatigue	x	x	x	
	Environmental Fatigue	x	x	x	x
	Irradiation Enbrittlement				x
	Thermal Ageing				x
Ni-based Alloy	Stress Corrosion Cracking	x	x	x	x
	Environmental Fatigue	x	x	x	x

* Including fracture (Deterioration of fracture toughness)

Inspection tool available

Inspection tool available (Topic)

FIG. 3-3. Examples of material aging mechanisms in boiling water reactors.

3.1.2. Advanced diagnostics for materials degradation assessment

Recent years have seen the development of a better understanding of the in-service inspection (ISI) using NDT/NDE measurement processes. There is now commonly quantification of inspection performance in terms of a probability of detection (POD) rather than a minimum detectable flaw size identified as an ultimate detection limit. In manual inspections the operator or inspector is also recognized as a key element in the inspection system, and not all operators perform to the same level [12]. In part to address performance reliability for ISI, there has been a move to automation. The best automated systems ensure higher levels of repeatability, although they usually do not attain the ultimate sensitivity/detection limits achieved by the best inspectors. The move to automation potentially benefits legacy and new NPPs, particularly when using advanced on-line monitoring and diagnostics for condition-based maintenance, for research into the characterization of materials in aging systems [12].

The challenges associated with characterization of aging in NPP materials, especially irradiated reactor components, are significant [13]. However, recent years have seen a gradual move towards assessing the state-of-the-art in NDE for early damage detection in NPP materials [14]. The various technologies that have been considered for assessment of early degradation were recently reviewed and reported [15].

A diverse set of NDT/NDE tools are being considered for characterizing aging phenomena [13]. Techniques such as ultrasonic backscatter and acoustic birefringence are being investigated, to complement acoustic emission and guided waves as possible tools for in-service monitoring. Several studies are investigating acoustic emission for legacy plants [16]. The development of concepts for advanced on-line structural health monitoring for next-generation reactor designs such as the International Reactor Innovative & Secure (IRIS) has also been initiated [17]. However, there are still no accepted in-service measurement technologies for the detection and assessment of some degradation mechanisms unique to NPPs, such as void swelling. To address these challenges, a convergence is developing that is bringing together capabilities in the materials science and NDT/NDE communities.

154

3.1.3. Prognostics

Prognostics for nuclear applications is starting to receive some attention [18], [19] and it has received significant attention in other fields of engineering. The data streams derived from an operational PMMD system consist of stressor as well as material property data. Fusion of these long-term, high-quality data has the potential to enable the development of diagnostic and prognostic models of NPP components and subsystems.

Prognostics is the prediction of a remaining useful, safe or service life, based on an analysis of system or material condition, stressors, and the understanding of the degradation phenomena. The range of approaches used for prognostics based on observed data is illustrated in FIG. 3-4. The simplest are the general statistical data based assessments, based on populations, such as the performance of all pumps of a particular type or class, where the cost of implementation is low but uncertainty for a specific item potentially large. The most reliable are those methods which utilize physics-based degradation models, and are applied using specific data taken on a particular part or component. These give much lower uncertainty, but at a significantly higher cost. As the prognostic approach becomes more closely based on physics-based models, the range of applicability narrows and the measurement and implementation cost increases.

The various empirical methods for process and equipment prognostics have been reviewed by Hines [20]. An extensive review of machinery diagnostics and prognostics for condition-based maintenance is provided by Jardine et al. [21] but this study does not consider nuclear power systems. An assessment of the state of diagnostics and prognostics technology maturity was recently provided [22].
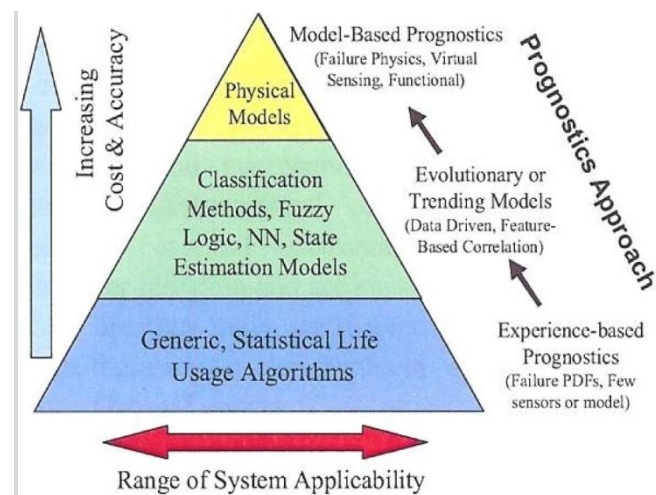
FIG. 3-4. Range of prognostic approaches [4].

Technologies are being developed for non-nuclear applications, including instrumentation and system health monitoring for electronics ([23]), and structural and system health monitoring (SHM) for advanced fighter aircraft and unmanned aerial vehicles [24]. For existing NPPs, life extension affords opportunities to deploy on-line monitoring/prognostics, assuming it can be demonstrated that there is still remaining useful life (RUL) in the plant.

Key to developing advanced prognostic schemes in *active systems* such as pumps and valves is monitoring the stressor rather than solely the subsequent effects of aging and degradation. Monitoring the stressor (e.g. a temperature, fluid cavitation, mechanical vibration, or a pressure) combined with active system control parameter management provides "warning time" to adjust operational parameters and limit or at least control rates of degradation for a path to failure [18].

A similar philosophy may be developed for passive components such as welds in pressure vessels. For instance, Wallin et al [25] discuss a quantitative assessment methodology for accumulation of flaws due to stochastic causes or environment-related flaws in steam generators. This

method combines deterministic information regarding flaw initiation and growth with stochastic elements, connected to environmental effects. It only requires knowledge of the experimental flaw accumulation history. In general, such models require a baseline material state (for instance, the level of service-induced degradation in the material, which must be estimated from measurements), and stressor time histories prior to application of a prognostic. Stressor time history is derived from a long-term data record of component temperature, internal pressure, strain, vibration levels, etc. - data commonly held in the plant historian. This record is ideally obtained from sensors installed in or on components at the beginning of their service life. However, the stochastic variations in macro- and microstructure and stressor history will result in variations in the degradation growth process. These factors, combined with measurement noise, will result in uncertainty in the material state estimate from NDE measurements. A further challenge is due to "sparse data" – data providing a comprehensive characterization of major system components is hard to obtain, and may be impossible due to local environment conditions (e.g. radiation) and/or a failure to consider design for inspectability at the time of fabrication. Additionally, future stressor levels are usually unknown, and at best, their statistical properties may be assumed based on the stressor history. The use of probabilistic prognostic algorithms is therefore considered essential to manage, and constrain/bound, these uncertainties in the RUL estimation problem.

Several approaches to prognostics have been proposed in the literature, although most of these have been used for active components[21],[24],[26],[27].

Prognostic methods for passive components (specifically, residual life estimation from cracking) typically use a damage index [25] that is a progressive index quantifying the amount or degree of damage in a material. In the CRP study a similar approach was adopted to provide prognostics derived from estimates of the effects of damage precursors and early damage on remaining useful life (RUL). The underlying assumption is that the relationship between the material state and damage index computed from NDT measurements is "reasonably" well understood, and that a damage index may be computed that correlates well with the progress of degradation from precursor to macro-crack initiation, and then on to growth and component failure, under some well constrained set of stressors.

A key requirement for the use of a damage index for prognostics is the availability of a physical or physics-based model of the change in damage index over time, given the stressor values. If such a model is available or may be postulated, it can be used in conjunction with a prognostic algorithm for RUL estimation. In general, a staged prognostics approach is preferable:

(1) Early in the component's service life, the best prognostic mode is a failure-history-based reliability model (e.g. Weibull). At this point there is no information related to stressors or degradation and it is reasonable to predict how long the average component will last under average usage conditions.
(2) Next, as the component accrues service hours, the stressor data can be used to bound or constrain the estimate and give better predictions of remaining useful life. This can require use of a proportional hazards model that predicts the average life of a component under actual usage conditions.
(3) Finally, as stressor data accrue, "degradation parameters" can be developed. These parameters enable prediction of the remaining useful life of an individual component under actual extended usage conditions.

This section of the CRP report presents a project undertaken by the TAG that sought to test the feasibility of providing a prediction of a remaining useful life for a structure material, with potential for application to a nuclear power plant. The project investigated methods for early degradation detection: testing them with fatigued samples as the model system and investigated techniques to integrate data for a prognostic, or prediction of remaining life.

3.2. BENCHMARK / DEMONSTRATION DATA

3.2.1. Sample preparation

3.2.1.1. Target phenomenon

With the growing importance of dealing with aging atomic power generation plants and standards for implementing countermeasures are being studied. Such studies have suggested items to be considered in the evaluation of plant aging. For example, the items for evaluation of degradation with age identified by the Atomic Energy Society of Japan in a 2008 overview of aging criteria for atomic power generation plants include low-cycle fatigue, brittleness caused by neutron radiation, radiation-induced stress and corrosion cracking, and high-cycle thermal fatigue [28]. As we show here, fatigue is a particularly important item. We therefore, take up fatigue as a factor in age degradation in TAG3.

3.2.1.2. Modelling degradation phenomena

Materials of kinds that are commonly used in atomic power plants are subjected to repeated loading in the laboratory to produce fatigue damage. Test specimens for which the degree of fatigue damage differs are made, such as multiple specimens that vary in degree of degradation equivalent to different numbers of years used.

3.2.1.3. Selection of materials

The main structural members in which there fatigue damage may occur are pipes [29]. In a BWR plant, stainless steel and carbon steel are the main materials used for pipes. Stainless steel, which is an austenite, and carbon steel, which is a ferrite, have different properties. We assume that the damage to the different materials from cyclic loading will take different forms. We therefore select both stainless steel and carbon steel as materials for evaluation.

3.2.1.4. Specimen materials

We used Type 304 stainless steel, a typical austenitic stainless steel that is sometimes used in BWR plant pipes. Using Type 304 allows a basic evaluation of austenitic stainless steels.

For some of the test conditions, we also used Type 316NG stainless steel, an austenitic stainless steel for atomic power use that is used in the recirculation system pipes of BWR. The chemical compositions of austenitic stainless steel are given in TABLE 3-1 and the mechanical properties are listed in TABLE 3-2.

For the carbon steel, we chose JIS STS410, which is used in water feed pipes, etc. The chemical compositions of carbon steel are given in TABLE 3-3 and the mechanical properties are listed in TABLE 3-4.

TABLE 3-1.   CHEMICAL COMPOSITIONS OF AUSTENITIC STAINLESS STEELS (%)

	C	Si	Mn	P	S	Ni	Cr	Mo	Reference
SUS304	0.08	1.00	2.00	0.45	0.30	10.50	20.00	-	
316NG	0.08 以下	1.00 以下	2.00 以下	0.045 以下	0.030 以下	10.00~14.00	16.00~18.00	2.00~3.00	JIS G4304

TABLE 3-2.   MECHANICAL PROPERTIES OF AUSTENITIC STAINLESS STEELS

	0.2% proof stress MPa	UTS MPa	Elongation %	Reference
SUS304	205	520	40	
316NG	≧205	≧520	≧40	JIS G4304

TABLE 3-3.   CHEMICAL COMPOSITIONS OF CARBON STEELS (%)

	C	Si	Mn	P	S	Fe	Reference
STS410	0.30 以下	0.10~0.35	0.30~1.40	0.035 以下	0.035 以下	Bal.	JIS G3455

TABLE 3-4.   MECHANICAL PROPERTIES OF CARBON STEEL

	Yield Stress MPa	UTS MPa	Elongation %	Reference
STS410	≧245	≧410	≧24	JIS G3455

3.2.1.5.   Test specimens

We began by making the Type 316NG test specimens for the fatigue test. The two types of specimens used are shown in FIG. 3-5. For smooth plates, it is assumed that fracture will originate from a corner of the gage length, so a minute dimple (non-penetrating cylindrical notch) is made at the centre of the gage length.

For Type 304, so as to be able to obtain a large area for non-destructive test, test specimens larger than those shown in FIG. 3-5 were prepared. The shape and dimensions of the Type 304 test specimens are also presented in FIG. 3-5. For Type 304, both unaltered smooth specimens and specimens dimpled at the centre of the gage length to prevent fracture from the corner of the gage length were used

For the carbon steel STS410, too, we chose the same specimen shape and dimensions as used for Type 304 to obtain a large area at the site for non-destructive test. Currently, unaltered smooth test specimens are used.

158
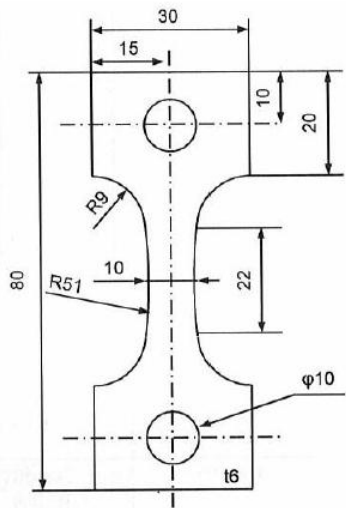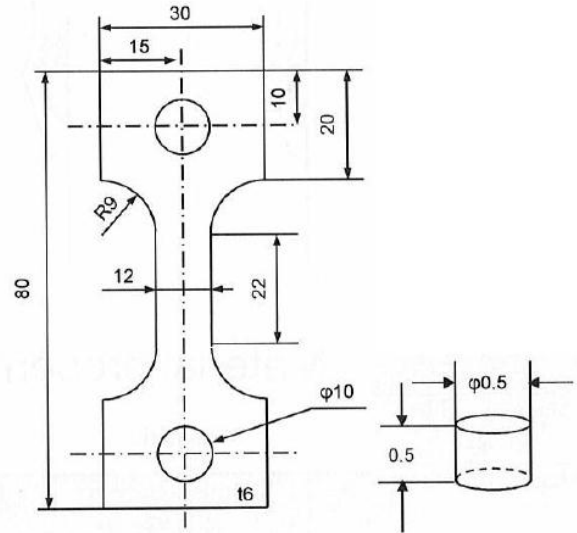
(a) Type 316NG(A).   *(b) Type 316NG(B).*
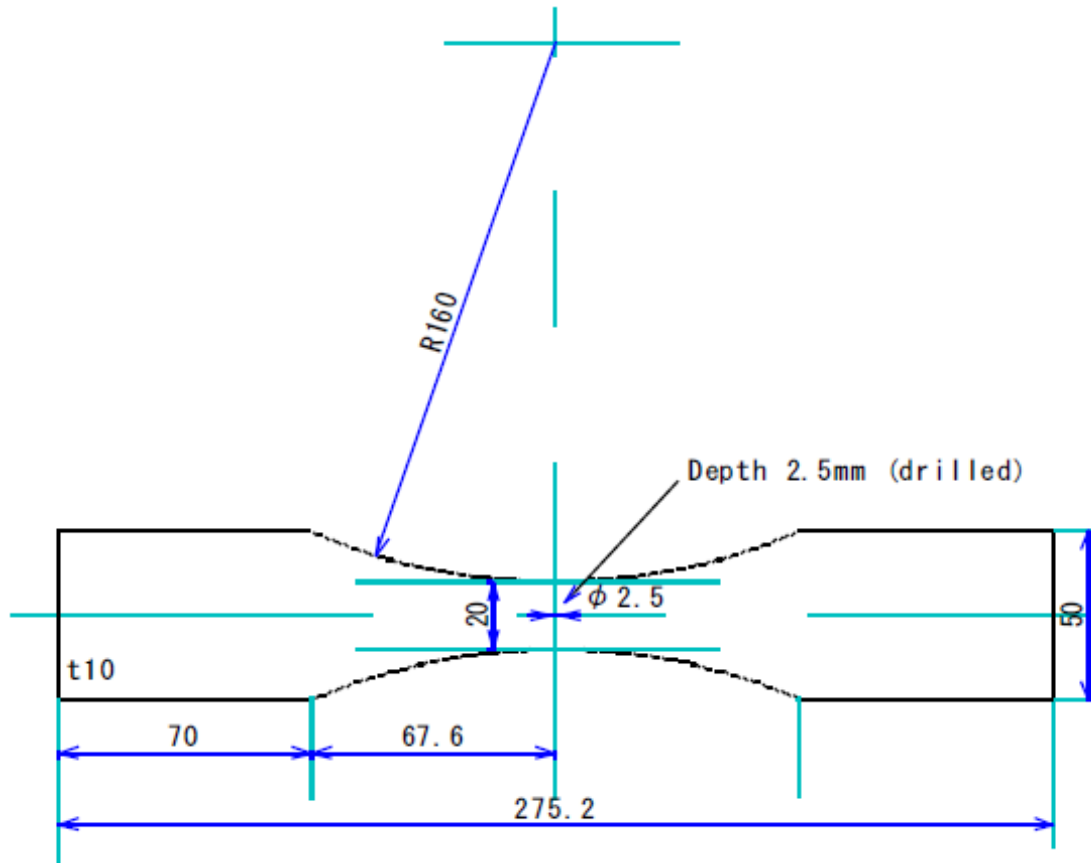
(c)Type 304©

FIG. 3-5. Fatigue test specimen (Type 316NG stainless steel, Type 304 stainless steel and carbon steel JIS STS410).

3.2.2. Fatigue test method and results

The fatigue tests were all done at Kyoto University. The circumstances of the fatigue test are shown in FIG. 3-6(a) and the setting of the test specimens and the gripping unit is shown in FIG. 3-6(b).

| *(a) Fatigue test.* | *(b) Setting of the test specimen and gripping unit.* |

FIG. 3-6. Situations of fatigue test.

3.2.2.2. Type 316NG stainless steel

The fatigue test of Type 316NG stainless steel used a 50-kN hydraulic servo fatigue tester under the conditions listed below.

- Control: load control;
- Stress ratio: R = − 1;
- Frequency: 20 Hz;
- Environment: room temperature, in air.

The Type 316NG fatigue test results are presented in TABLE 3-5 and FIG. 3-7. Type A and B test specimens were used; for Type A, cracking originated from outside the gage length and proceeded to failure, so Type B was used for non-destructive test. For specimen number F1-S3NG-1, the load was varied until the specimen failed to obtain the fatigue life. The obtained value was 189,925 cycles under a nominal stress amplitude of 220 MPa. From this fatigue life value, under the same nominal stress amplitude, the cumulative fatigue coefficients are 0.2 (20%), 0.4 (40%), 0.6 (60%), 0.8 (80%) and their respective numbers of cycles are 38,000, 76,000, 114,000, and 152,000. We made test specimens for which test was stopped at the number of cycles for which the cumulative

fatigue coefficients were about 0.2 and 0.4 and used them in the non-destructive test. For test specimen number F1-S3NG-9, we temporarily stopped the cyclic loading at the number of cycles for which the cumulative fatigue coefficients are 0.2, 0.4, 0.6, and 0.8 to perform the non-destructive test. We then continued to increase the load, thus using the same specimens with different degrees of fatigue damage for the non-destructive test.

TABLE 3-5.   FATIGUE TEST CONDITIONS AND RESULTS (TYPE 316NG STAINLESS STEEL)

TP No.	TP Type	Nominal stress amplitude (MPa)	Stress Ratio	Number of cycles	Fatigue usage	NDE test	Remarks
F1-S3NG-1	B (W=10mm)	220	-1	189,925	Failure	-	
F1-S3NG-2	A (W=12mm)	250	-1	Not counted	-	-	Failure around pin hole
F1-S3NG-3	B (W=10mm)	220	-1	38,100	0.2	PNNL	
F1-S3NG-4	A (W=12mm)	200	-1	49,551	-	-	Failure at R position
F1-S3NG-5	B (W=10mm)	220	-1	76,100	0.4	Kyoto Univ.	
F1-S3NG-6	A (W=12mm)	200	-1	120,925	-	-	Failure at R position
F1-S3NG-7	B (W=10mm)						Referential specimen (0% fatigue)
F1-S3NG-8	B (W=10mm)	140	-1	1,470,751	not evaluated	Kyoto Univ.	Interupted
F1-S3NG-9	B (W=10mm)	220	-1	38,100	0.2	Kyoto Univ.	Incremental tests
				↓			
				76,100	0.4		
				↓			
				114,100	0.6		
				↓			
				152,100	0.8		

W: Specimen width in gage length
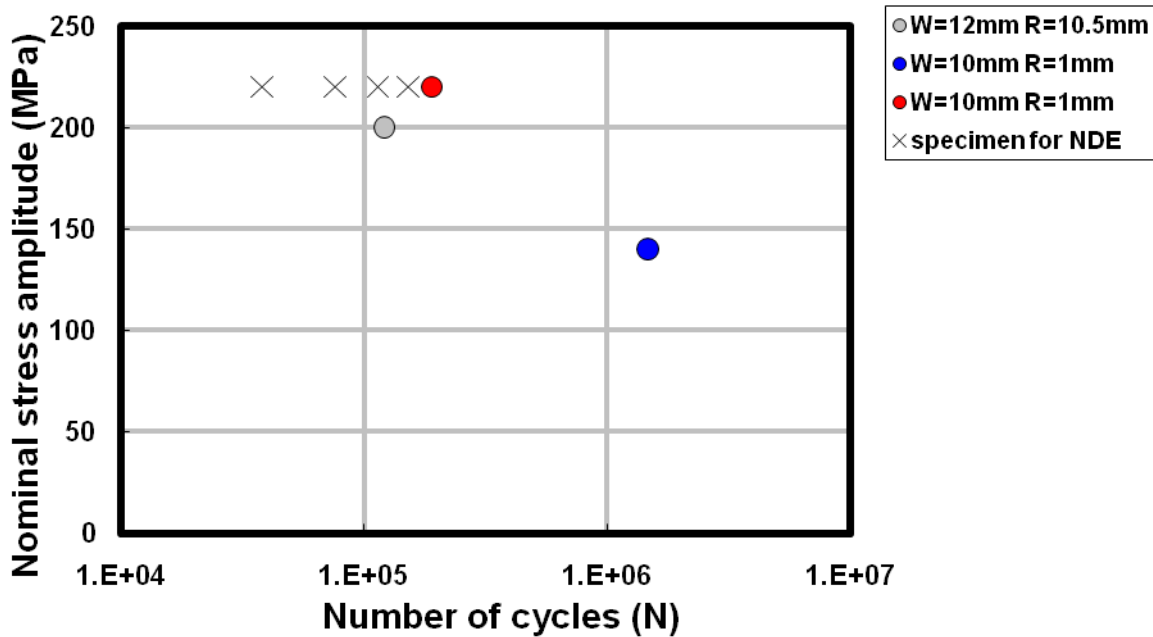
FIG. 3-7. Results of fatigue tests (Type 316NG stainless steel).

3.2.2.3. Type 304 stainless steel

For the Type 304 stainless steel fatigue test, a 100-kN servo fatigue tester was used under the conditions listed below

- − Control: load control;
- − Stress ratio: R = -1;
- − Frequency: 10 Hz (20 Hz in parts);
- − Environment: room temperature, in air.

The results of the Type 304 fatigue test are shown in TABLE 3-6 and FIG. 3-8.

TABLE 3-6.   FATIGUE TEST CONDITIONS AND RESULTS (TYPE 304 STAINLESS STEEL)

TP No.	Notch	Nominal stress amplitude (MPa)	Stress Ratio	Number of cycles	Fatigue usage	NDE test	Remarks
F2-S304-1	none (smooth)	300	-1	600	Failure		Temperature increased
F2-S304-2	none (smooth)	200	-1	166,284	Failure		Temperature increased
F2-S304-3	none (smooth)	170	-1	3,000,000	-		Temperature increased test abort
F2-S304-4	Hole notch	180	-1	292,606	Failure		Temperature increased
F2-S304-5	Hole notch	185	-1	0	0	PNNL	Referential specimen
F2-S304-6	Hole notch	185	-1	0	0	Kyoto univ.	Referential specimen
F2-S304-7	Hole notch	185	-1	31,250	0.2	PNNL	Interupted
F2-S304-8	Hole notch	185	-1	31,250	0.2	Kyoto univ.	Interupted
F2-S304-9	Hole notch	185	-1	62,450	0.4	PNNL	Interupted
F2-S304-10	Hole notch	185	-1	62,450	0.4	Kyoto univ.	Interupted
F2-S304-11	Hole notch	185	-1	93,650	0.6	PNNL	Interupted
F2-S304-12	Hole notch	185	-1	93,650	0.6	Kyoto univ.	Interupted
F2-S304-13	Hole notch	185	-1	124,850	0.8	PNNL	Interupted
F2-S304-14	Hole notch	185	-1	156,178	Failure		
F2-S304-15	Hole notch	190	-1	51,071	Failure		
F2-S304-16	Hole notch	180	-1	4,289,169	-		Test abort
F2-S304-17	Hole notch	170	-1	2,936,366	-		Test abort
F2-S304-18	Hole notch	180	-1	82,911	<0.6 (failure)[1]		Temperature increased test failed
F2-S304-19	Hole notch	180	-1	81,395	<0.8 (failure)[1]		Temperature increased test failed
F2-S304-20	Hole notch	180	-1	232,000	0.8		Temperature increased

[1] Specimen was failed at cycles less than programmed fatigue usage.

For some of the test specimens shown in TABLE 3-6, the test was done at 20 Hz, but there was large variance in the obtained fatigue life values. In fact, FIG. 3-8 shows that failed plots at 20Hz do not seem to lie on the smooth S-N curve. Generation of heat in the specimen was seen during the cyclic loading. A factor of the variance in the fatigue life of the stainless steel is considered that the internal heat due to the large hysteresis in the load and displacement relationship is accumulated at high frequency test.

FIG. 3-8. Results of fatigue tests (Type 304 stainless steel).

In the test of specimens from F2-S304-5 to F2-S304-14, the frequency was decreased to 10 Hz and the specimens were ventilated with fan to promote heat release at room temperature. For specimen F1-S3NG-14, the cyclic load was continued until failure to obtain the fatigue life. The obtained value was 156,178 cycles under the nominal stress amplitude 185 MPa. Based on this fatigue life value, we prepared the specimens with the cumulative fatigue coefficients 0.2 (20%), 0.4 (40%), 0.6 (60%), 0.8 (80%) of the fatigue life under the same nominal stress amplitude. Then the numbers of load cycles become 31,200, 62,400, 93,600, and 124,800, respectively. Thus prepared specimens at all fatigue degrees were used for the non-destructive test. It should be noted, however, that specimens F2-S304-18 and 19 were failed at less cycles than the above fatigue life. This fact indicates that the above fatigue life of Type 304 is not absolute and may have a variation for individual specimens in our test condition including specimen shape. Instead of performing fatigue test more times, we interrupted fatigue test of F2-S304-50 at each 10% of the above fatigue life and performed non-destructive test until 90%. Because the specimen did not fail at 100% of the original fatigue life, i.e. 156,178 cycles, we further continued the fatigue test until failure, i.e. 380,921 cycles. During the fatigue test, we interrupted the fatigue test and performed non-destructive test at 100%, 150% and 200% of the original fatigue life. Based on this number of cycles to failure, the fatigue degrees to be examined were recalculated as 4.09%, 8.19%, 12.3%, 16.4%, 20.5%, 24.6%, 28.7%, 32.8%, 36.9%, 40.9%, 61.4% and 81.9%. In what follows the result of each NDE test will be shown only for either of the above two kinds of specimens, so that used 'fatigue degree' does not necessarily indicate the absolute extent of the fatigue.

3.2.2.4. Carbon steel STS410

For fatigue test of carbon steel STS410, a 100-kN servo fatigue tester was used under the conditions listed below

- Control: load control;
- Stress ratio: R = -1;
- Frequency: 10 Hz (20 Hz in parts);
- Environment: room temperature, in air.

The results of fatigue tests on STS410 carbon steel are shown in TABLE 3-7 and FIG. 3-9.

TABLE 3-7. FATIGUE TEST CONDITIONS AND RESULTS (STS410 CARBON STEEL)

No.	surface	stress	frequency	heat affected	fatigue degree(%)	number of cycle	remarks
F3-STS410-1		240MPa	10~20Hz	−	fracture	427,895	pilot test
F3-STS410-2	smooth	240MPa	20Hz	−	fracture	777,913	
F3-STS410-3		240MPa	20Hz	−	fracture	222,718	
F3-STS410-4		235MPa	20Hz	−	fracture	791,091	
F3-STS410-5		230MPa	10Hz	△	fracture	39,368	HAZ around hole notch?
F3-STS410-6		210MPa	10Hz	△	fracture	94,755	HAZ around hole notch?
F3-STS410-7		190MPa	10Hz	△	fracture	297,544	HAZ around hole notch?
F3-STS410-8					0	0	even No. specimen > Japan
F3-STS410-9					0	0	odd No. specimen > U.S.
F3-STS410-10					80	238,050	fatigue crack visually confirmed
F3-STS410-11					80	238,050	fatigue crack visually confirmed
F3-STS410-12					60	178,550	fatigue crack visually confirmed
F3-STS410-13					60	178,550	fatigue crack visually confirmed
F3-STS410-14					40	119,050	fatigue crack visually confirmed
F3-STS410-15					40	119,050	fatigue crack visually confirmed
F3-STS410-16					20	59,550	
F3-STS410-17	hole				20	59,550	
F3-STS410-18	notch	190MPa	10Hz		70	208,300	fatigue crack visually confirmed
F3-STS410-19					70	208,300	fatigue crack visually confirmed
F3-STS410-20					50	148,800	fatigue crack visually confirmed
F3-STS410-21					50	148,800	
F3-STS410-22					30	89,300	
F3-STS410-23					30	89,300	
F3-STS410-24					10	29,800	
F3-STS410-25					10	29,800	
F3-STS410-26					0	0	incremental fatigue & testing
F3-STS410-27					−	−	reserve
F3-STS410-28					−	−	reserve
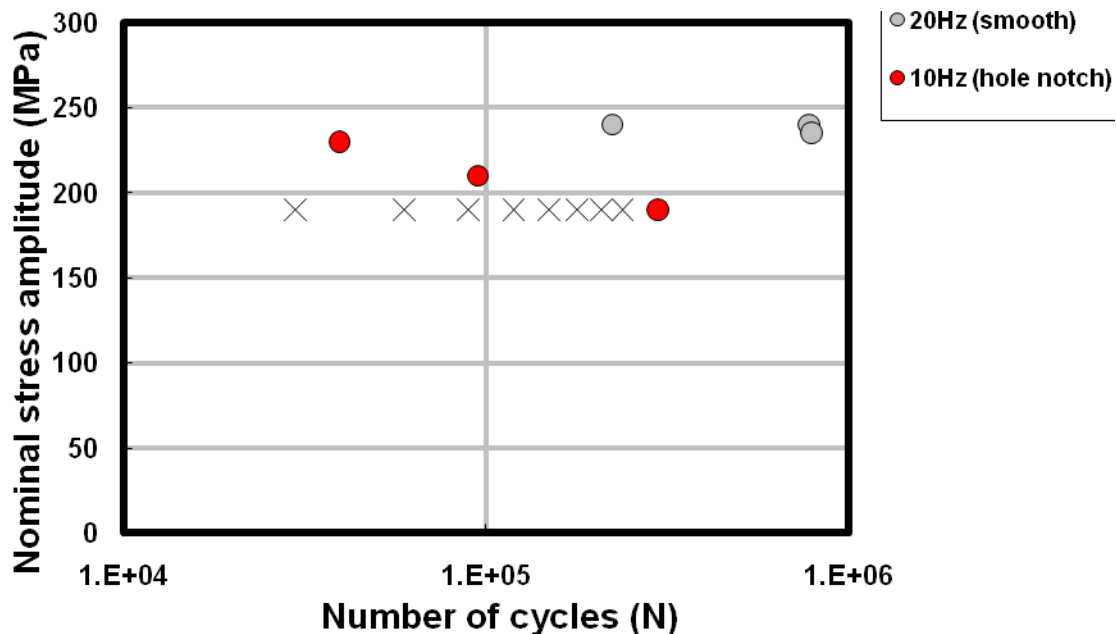
FIG. 3-9. Results of fatigue tests (STS410 carbon steel).

Some fatigue tests were done at 20 Hz, but similarly to the case of Type 304, there was large variance in the obtained fatigue lives. Such specimens changed the colour around the fracture surfaces, which can be considered heat affected regions. The internal heat due to the mechanical hysteresis of carbon steel may be accumulated in the fatigued or the stress-concentrated regions for cyclic loading with higher frequency. Since this effect is considered to be one of the factors of the variation in the fatigue life, we decreased the frequency to 10Hz for F3-STS410-5 and subsequent specimens, and ventilated specimens with fan at room temperature. Specimen F3-STS410-7 was

failed at 297,544 cycles under the nominal stress amplitude of 190MPa, and we employed the condition as the standard for specimens used for NDE tests. That is, we prepared notched specimens with several fatigue degrees, i.e. the cumulative fatigue coefficients (the per cents of the fatigue life, load cycles) 0.1 (10%, 29800), 0.2(20%, 59600), 0.3(30%, 89400), 0.4(40%, 119200), 0.5(50%, 149000), 0.6(60%, 178800), 0.7(70%, 208600), 0.8(80%, 238400). Similarly to the case of Type 304, we interrupted fatigue test of specimen F3-STS410-26 at each 20% of the fatigue life and performed non-destructive test until 80%. In this case, we employed the above number of cycles to failure at 10MPa as the fatigue life, because each plot for failure seems to lie on the smooth S-N curve in FIG. 3-9.

3.2.3. Examination of specimens after non-destructive test

Some of the specimens subjected to fatigue test or incurred fatigue damage were used in non-destructive test and then examined for the circumstances of cracking. It was assumed that cracking would first occur at the stress concentration points near the dimple in all of the dimpled specimens, so the area near the dimple was examined. The examination results are described below.

3.2.3.1. Test specimen examination methods

The test specimens were examined as described below.

(1) Examination of the surface:

First, the entire test specimen was photographed, and then the centre area that includes the dimple was examined at magnification with a digital microscope. Next, the ends of the specimen in the two directions perpendicular to the load direction at the dimple were examined with a scanning electron microscope (SEM) as shown in FIG. 3-10.
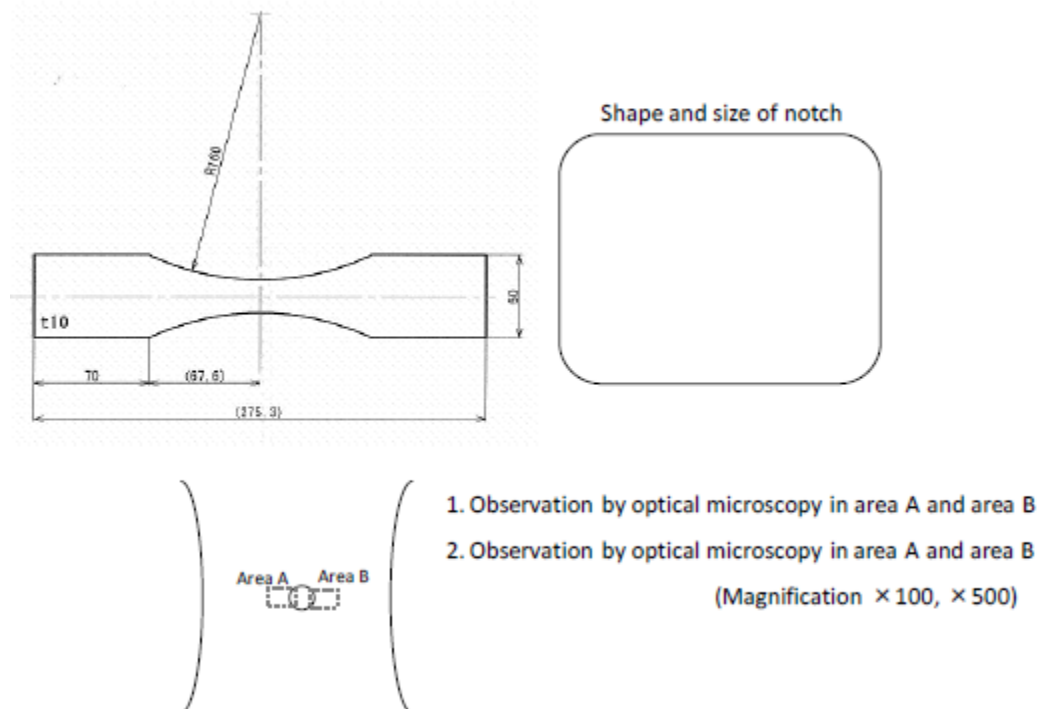
FIG. 3-10. Observation area on the specimen surface.

(2) Surface replicas:

After examination of the surface, the test specimens were to be cut for examination of their cross-section. To allow the state before cutting to be confirmed even after cutting, surface replicas were prepared. Acetyl cellulose film was used for the replication.

(3) Cross-section examination:

One of the two sides of the dimple area in the direction perpendicular to the load direction is selected and the specimen is cut along the load direction near the dimple. The specimen is cut again in the direction perpendicular to the load direction at a position sufficiently far from the dimple in the load direction. The guidelines for the cutting are illustrated in FIG. 3-11. The cut specimen that includes the dimple is embedded in resin, and the cross-section near the dimple is polished for examination.
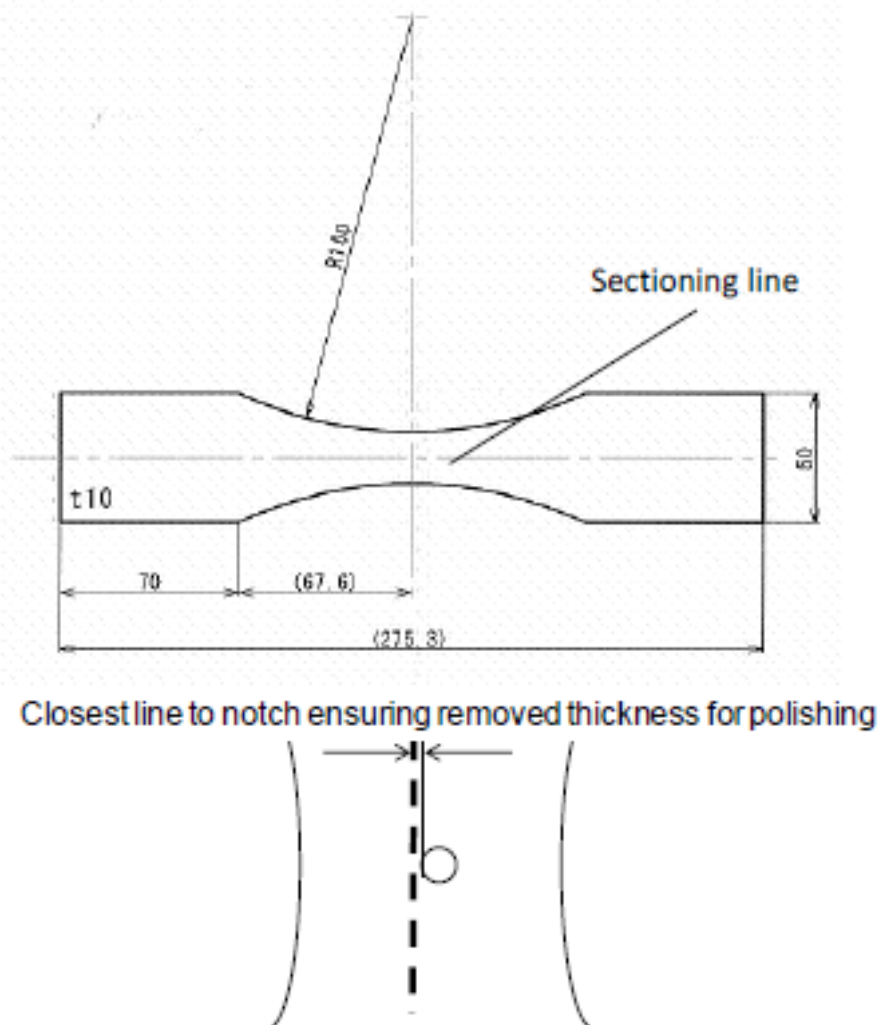
FIG. 3-11. Sectioning line for sectioning face observation.

After polishing, the cut surface was examined by optical microscope. The same face was then examined by SEM. The cross-section examination method is illustrated in FIG. 3-12.
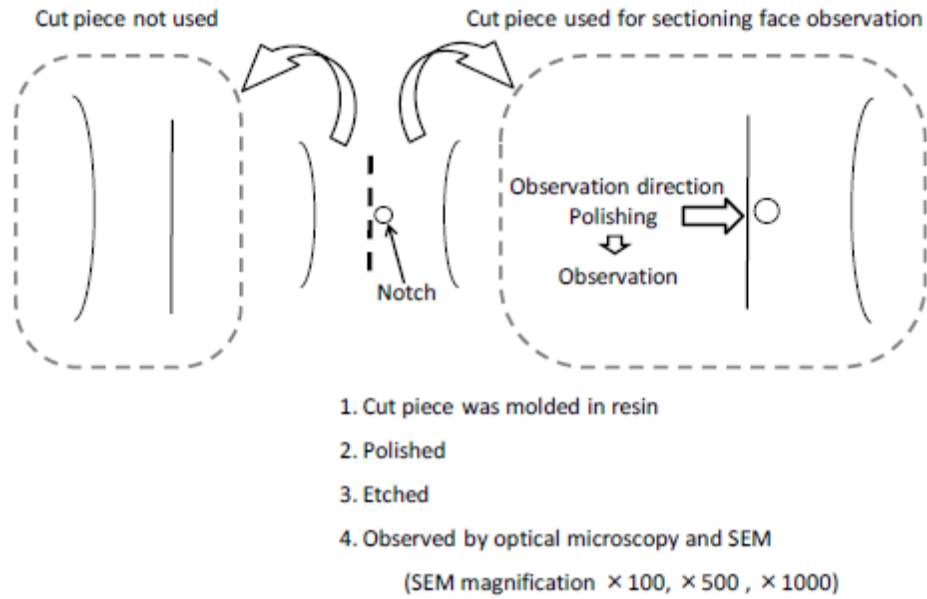
FIG. 3-12. Observation processes for sectioning face observation.

3.2.4. Examination results of sectioning face observations

3.2.4.1. Type 316NG stainless steel

Non-destructive test was performed on the samples for which fatigue test was halted at the cumulative fatigue coefficients of 0.2, 0.4, 0.6, and 0.8, and finally the F1-S3NG-9 specimen with the cumulative fatigue coefficient of 0.8 was examined.

The results of examination of the surface by digital microscope are presented in FIG. 3-13.
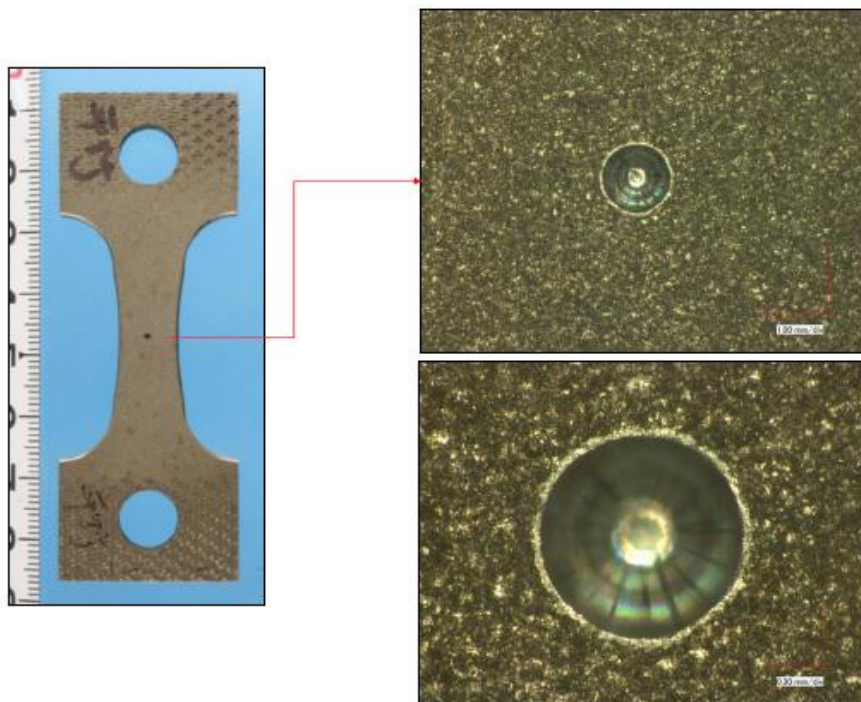
FIG. 3-13. Specimen surface observation (Type 316NG) (TP No.:F1-S3NG-9, Fatigue usage 0.8).

Although the damage is considered to be concentrated in the vicinity of the dimple, the surface examination by digital microscope revealed no shapes relevant to damage. The results of SEM examination of the surface are presented in FIG. 3-14. At the side of the dimple, shapes perpendicular to the load direction that are considered to be cracks were seen. The cross-section of the part where crack shapes were seen in FIG. 3-14 was examined. FIG. 3-15 presents the results of the optical microscope examination. Cracking from the surface extending in the plate depth direction is clearly observed. The depth of the crack is 450 μm. We can also see that the crack propagates within the crystal grains. The results of SEM examination of the same B cross-section are shown in FIG. 3-16. In the same way as seen in FIG. 3-15, the SEM clearly reveals cracking. Therefore, cracking near the dimple is confirmed under a nominal stress amplitude of 220 MPa and at the cumulative fatigue coefficient of 0.8.

3.2.4.2. *Type 304 stainless steel*

We examined the F2-S304-8 test specimen, for which non-destructive test was performed after stopping at the cumulative fatigue coefficient of 0.2. The results of digital microscope examination of the surface are shown in FIG. 3-17. Although the damage is considered to be concentrated in the vicinity of the dimple, the surface examination by digital microscope revealed no shapes relevant to damage. The results of SEM examination of the surface, shown in FIG. 3-18, also revealed no crack shapes. Examination of the cross-section near the dimple by optical microscope (FIG. 3-19) showed no cracking. The results of SEM examination of the same cross-section are shown in FIG. 3-20. In the same way as the optical microscope examination (FIG. 3-19), the SEM examination revealed no cracking. Therefore, under the nominal stress amplitude of 185 MPa and at the cumulative fatigue coefficient of 0.2, no cracking near the dimple was confirmed.

We examined the F2-S304-10 test specimen, for which non-destructive test was performed after stopping at the cumulative fatigue coefficient of 0.4. The results of digital microscope examination of the surface are shown in FIG. 3-21. Although the damage is considered to be concentrated in the vicinity of the dimple, the surface examination by digital microscope revealed no shapes relevant to damage. The results of SEM examination of the surface, presented in FIG. 3-22, also revealed no cracking shapes. FIG. 3-23 presents the results of optical microscope examination of the cross-section near the dimple; no cracking shapes are seen. The results of SEM examination of the same cross-section, shown in FIG. 3-24, also reveal no cracking. Therefore, under the nominal stress amplitude of 185 MPa and at the cumulative fatigue coefficient of 0.4, no cracking near the dimple was confirmed.

We examined the F2-S304-12 test specimen, for which non-destructive test was performed after stopping at the cumulative fatigue coefficient of 0.6. The results of digital microscope examination of the surface are shown in FIG. 3-25. Although the damage is considered to be concentrated in the vicinity of the dimple, the surface examination by digital microscope revealed no shapes relevant to damage. The results of SEM examination of the surface, presented in FIG. 3-26, also revealed no cracking shapes. FIG. 3-27 presents the results of optical microscope examination of the cross-section near the dimple; no cracking shapes are seen. The results of SEM examination of the same cross-section, shown in FIG. 3-28, also reveal no cracking. Therefore, under the nominal stress amplitude of 185 MPa and at the cumulative fatigue coefficient of 0.6, no cracking near the dimple was confirmed.

Fatigue test results and the test in which crack was observed for Type 316NG stainless steel were shown in FIG. 3-29. And fatigue test results and the tests in which crack was not observed for Type 304 stainless steel were shown in FIG. 3-30.
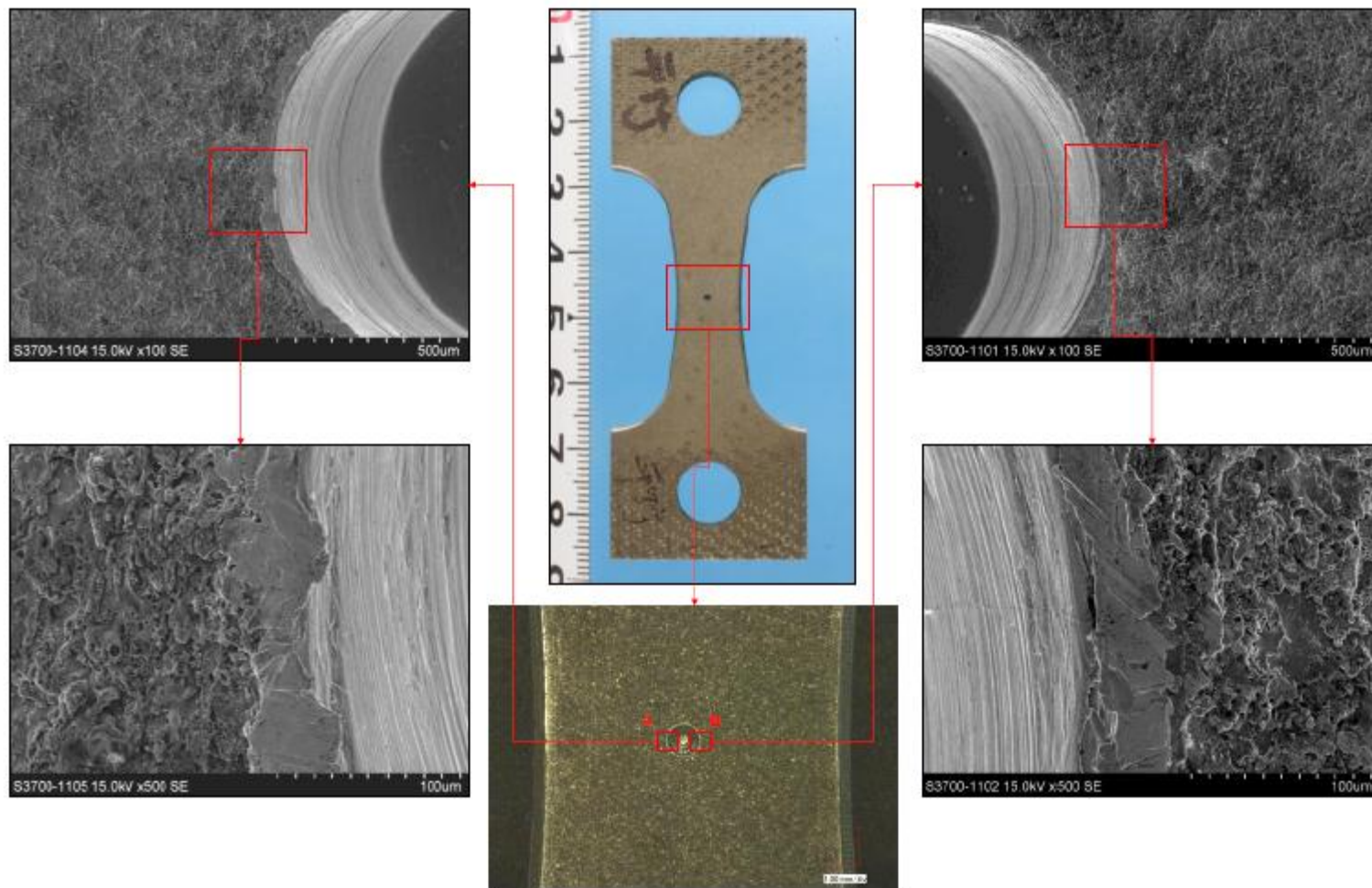
FIG. 3-14. Notch part observation (Type 316NG) (TP No.:F1-S3NG-9, Fatigue usage 0.8).
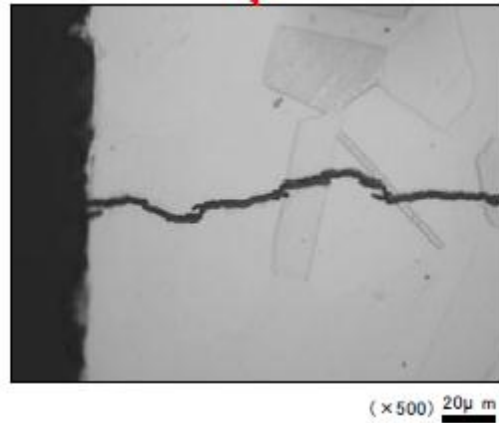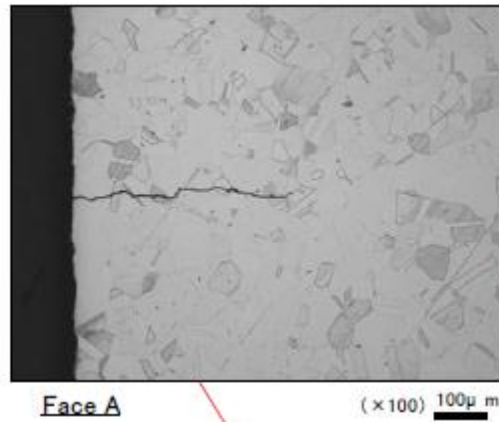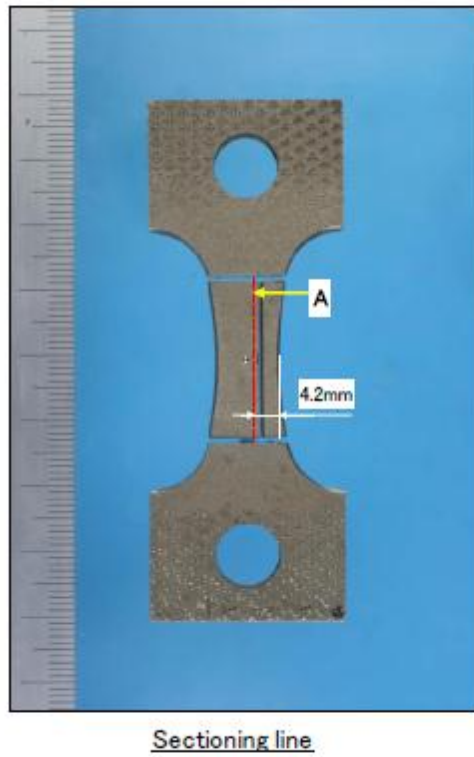
FIG. 3-15. Sectioning face observation by optical microscopy (Type 316NG) (TP No.:F1-S3NG-9, Fatigue usage 0.8).

170
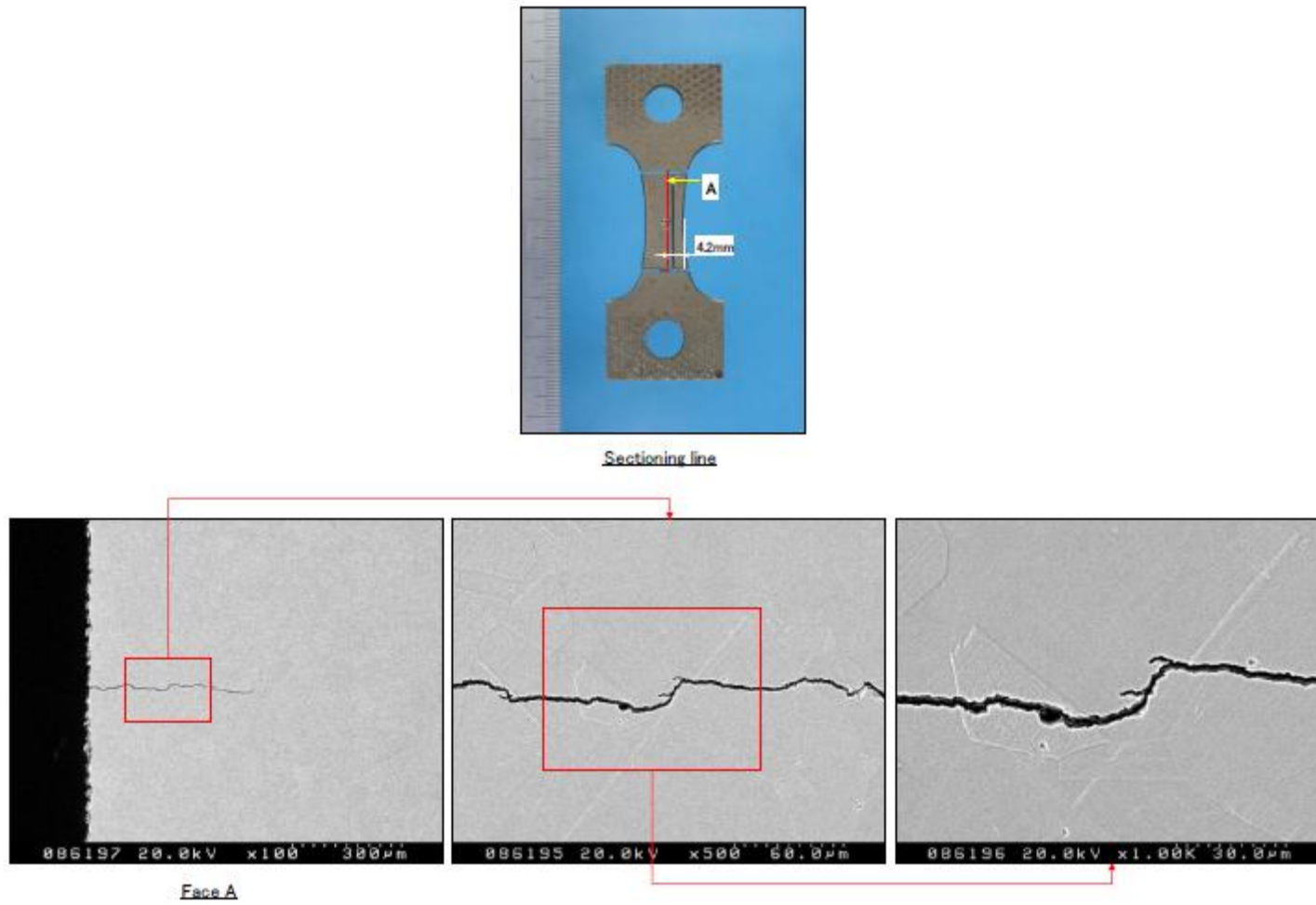
FIG. 3-16. Sectioning face observation by SEM (Type 316NG) (TP No.:F1-S3NG-9, Fatigue usage 0.8).
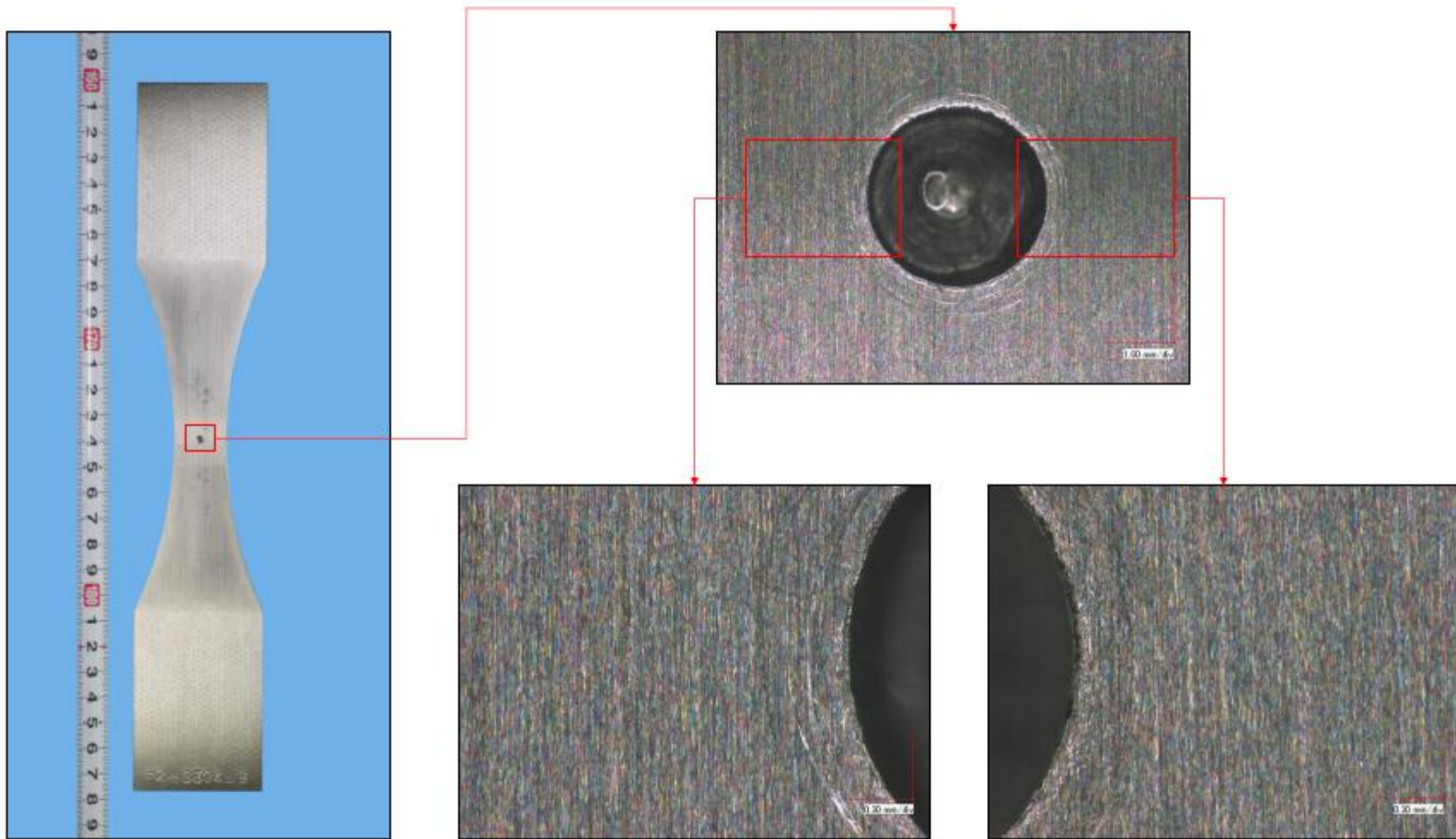
FIG. 3-17. Notch part observation (Type 304) (TP No.:F2-S304-8, Fatigue usage 0.2).
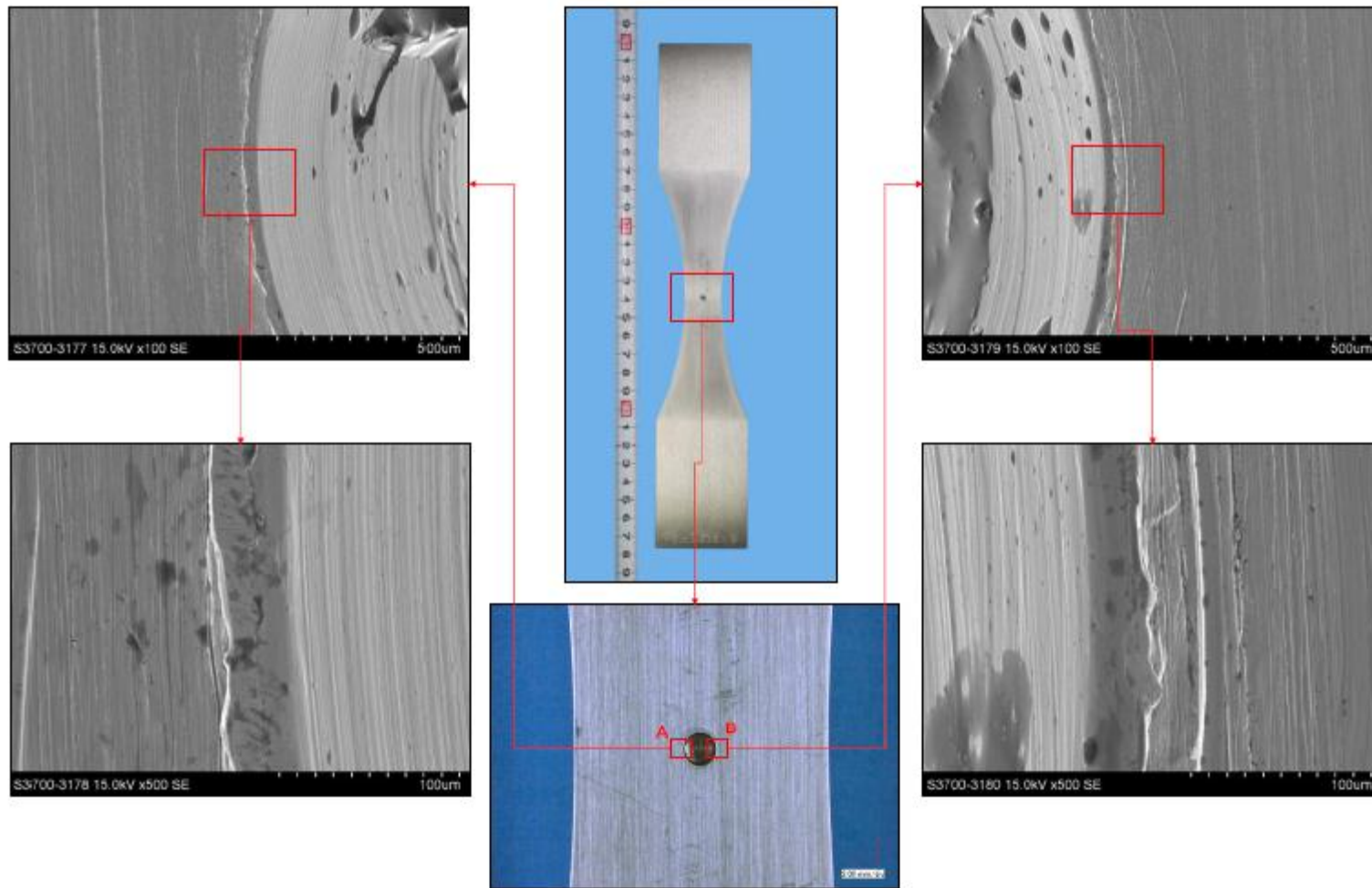
FIG. 3-18. Notch part observation by SEM (Type 304) (TP No.:F2-S304-8, Fatigue usage 0.2).
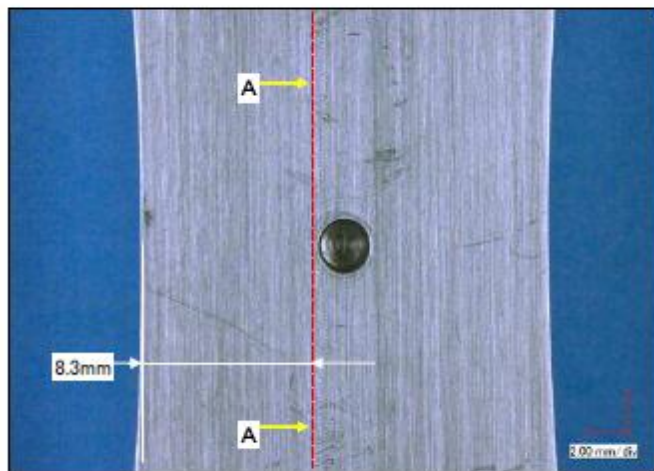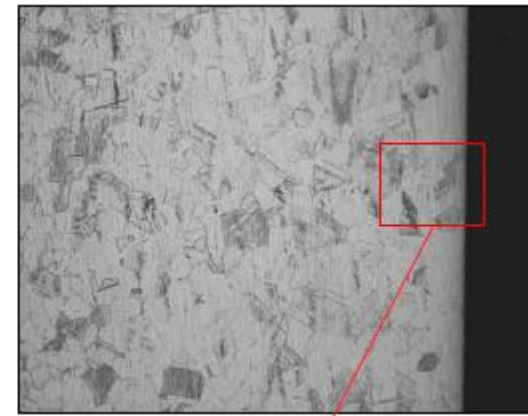
FIG. 3-19. Sectioning face observation by optical microscopy (Type 304) (TP No.:F2-S304-8, Fatigue usage 0.2).
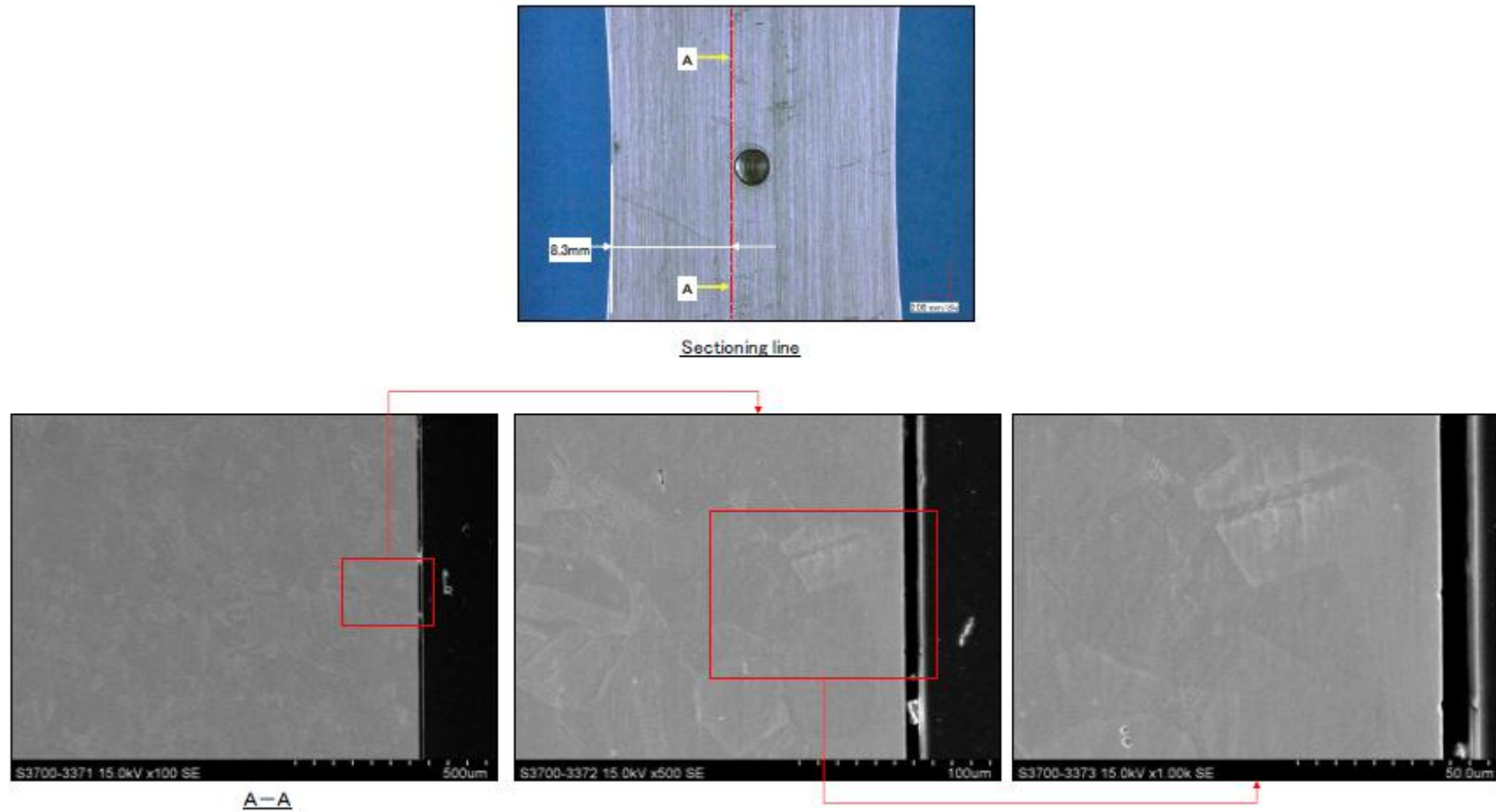
FIG. 3-20. Sectioning face observation by SEM (Type 304) (TP No.:F2-S304-8, Fatigue usage 0.2).
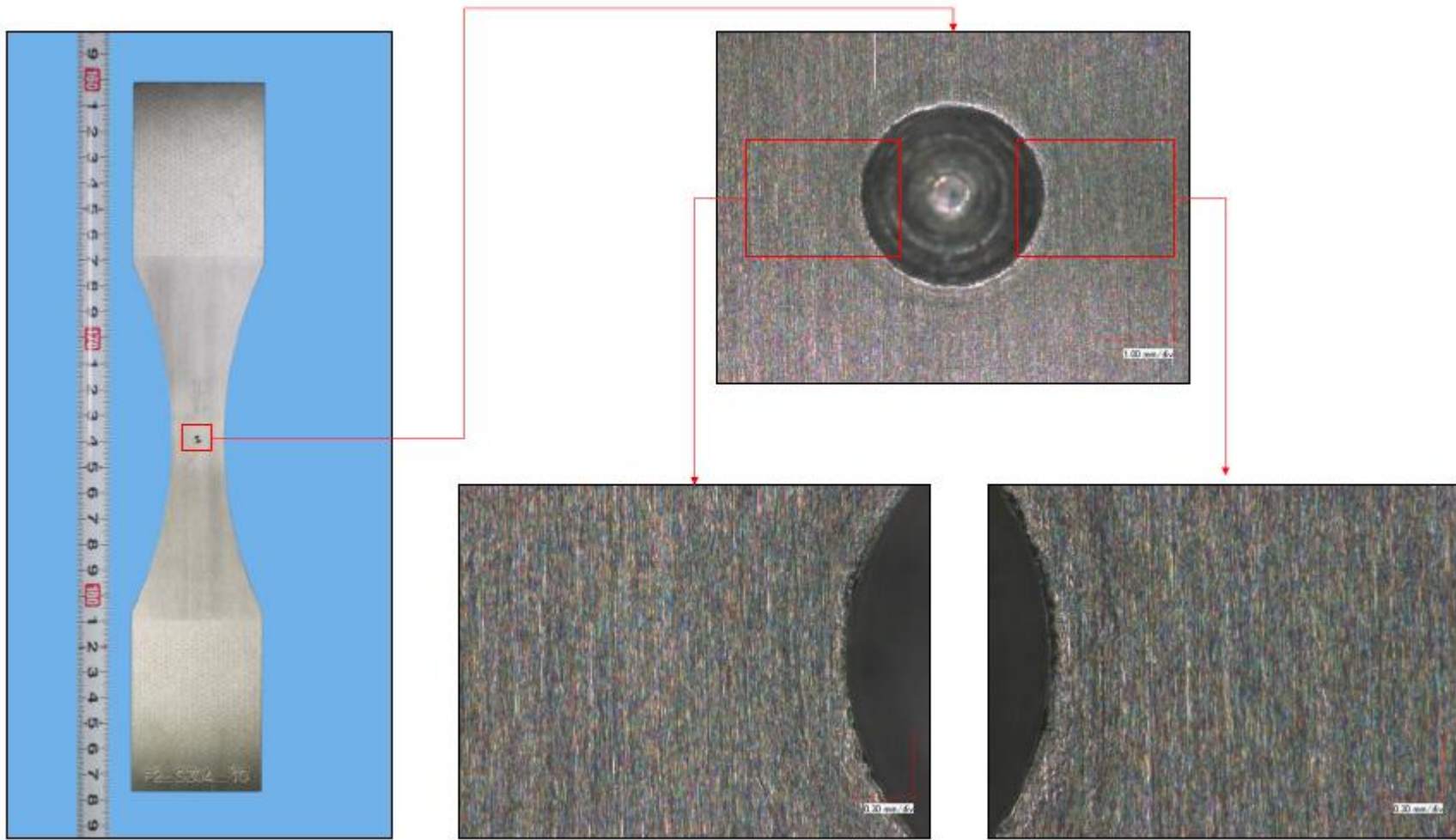
FIG. 3-21. Notch part observation (Type 304) (TP No.:F2-S304-10, Fatigue usage 0.4).
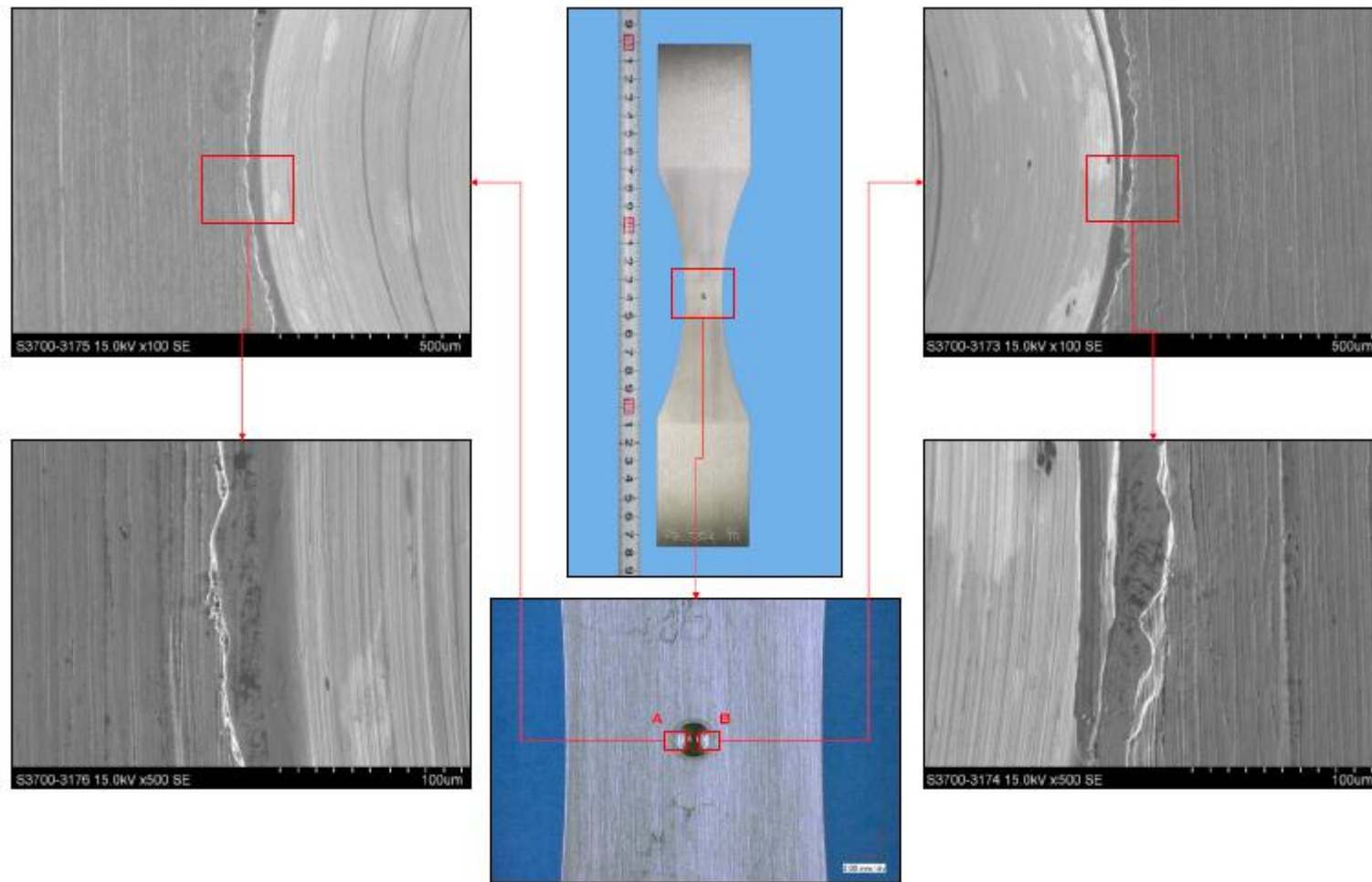
FIG. 3-22. Notch part observation by SEM (Type 304) (TP No.:F2-S304-10, Fatigue usage 0.4).
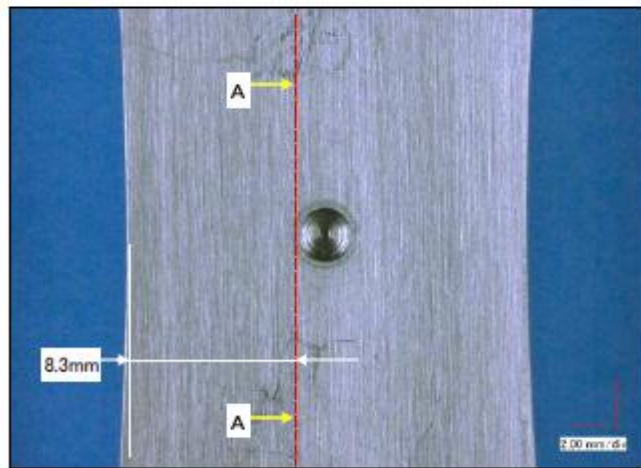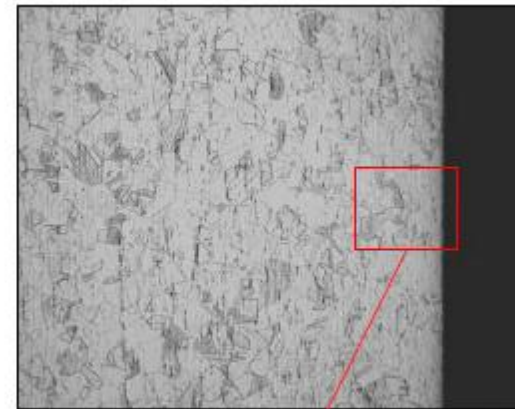
FIG. 3-23. Sectioning face observation by optical microscopy (Type 304) (TP No.:F2-S304-10, Fatigue usage 0.4).
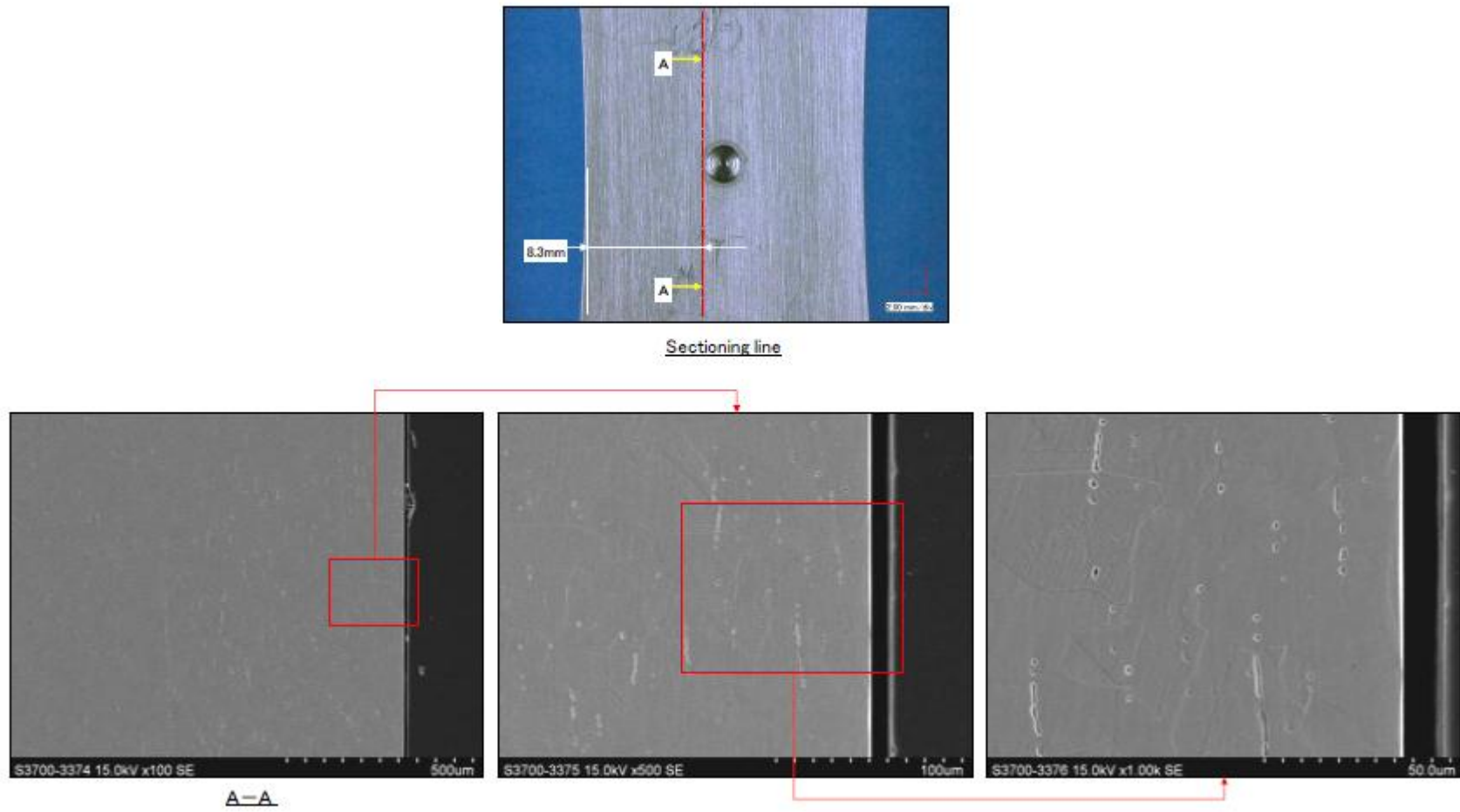
FIG. 3-24. Sectioning face observation by SEM (Type 304) (TP No.:F2-S304-10, Fatigue usage 0.4).
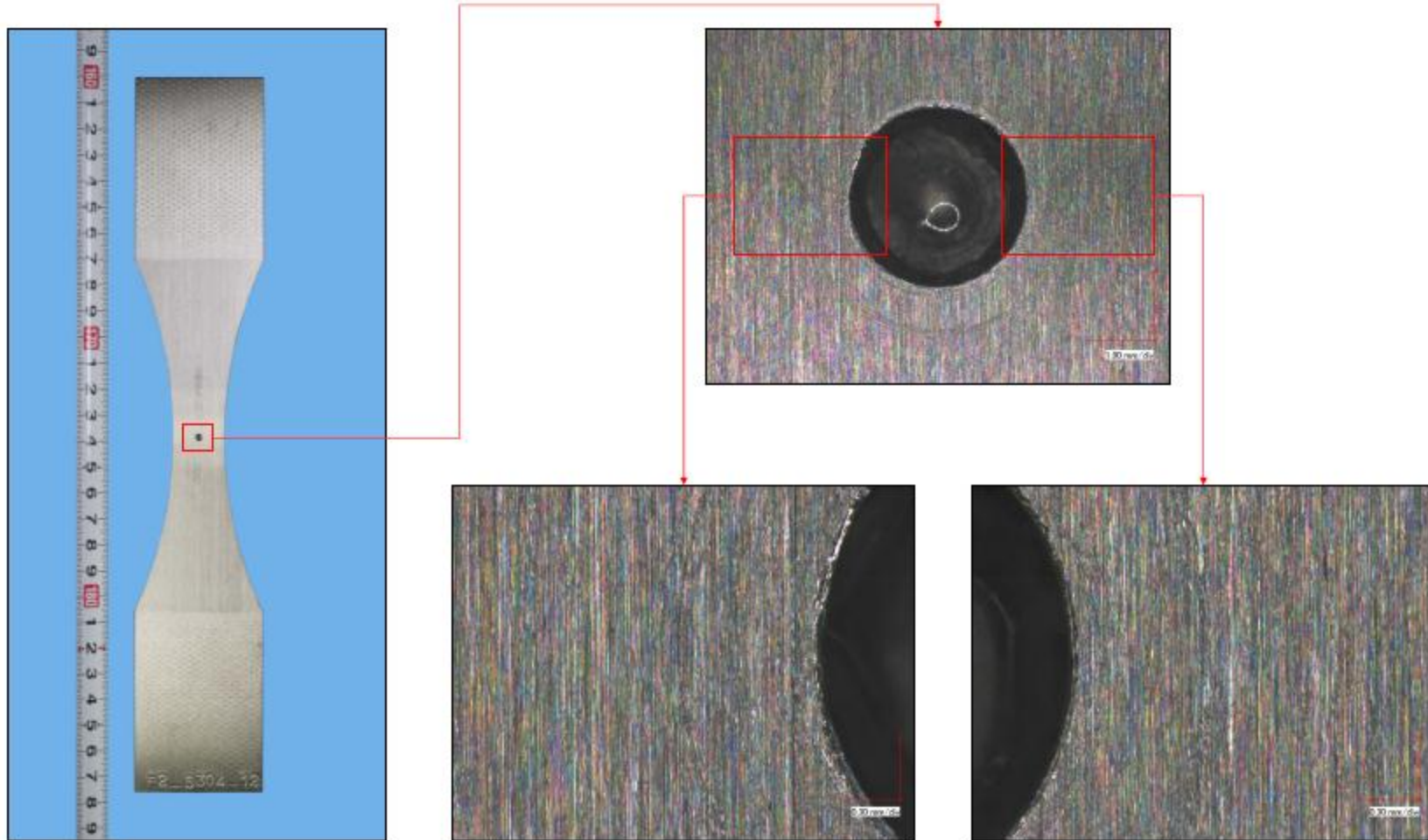
FIG. 3-25. Notch part observation (Type 304) (TP No.:F2-S304-12, Fatigue usage 0.6).

180
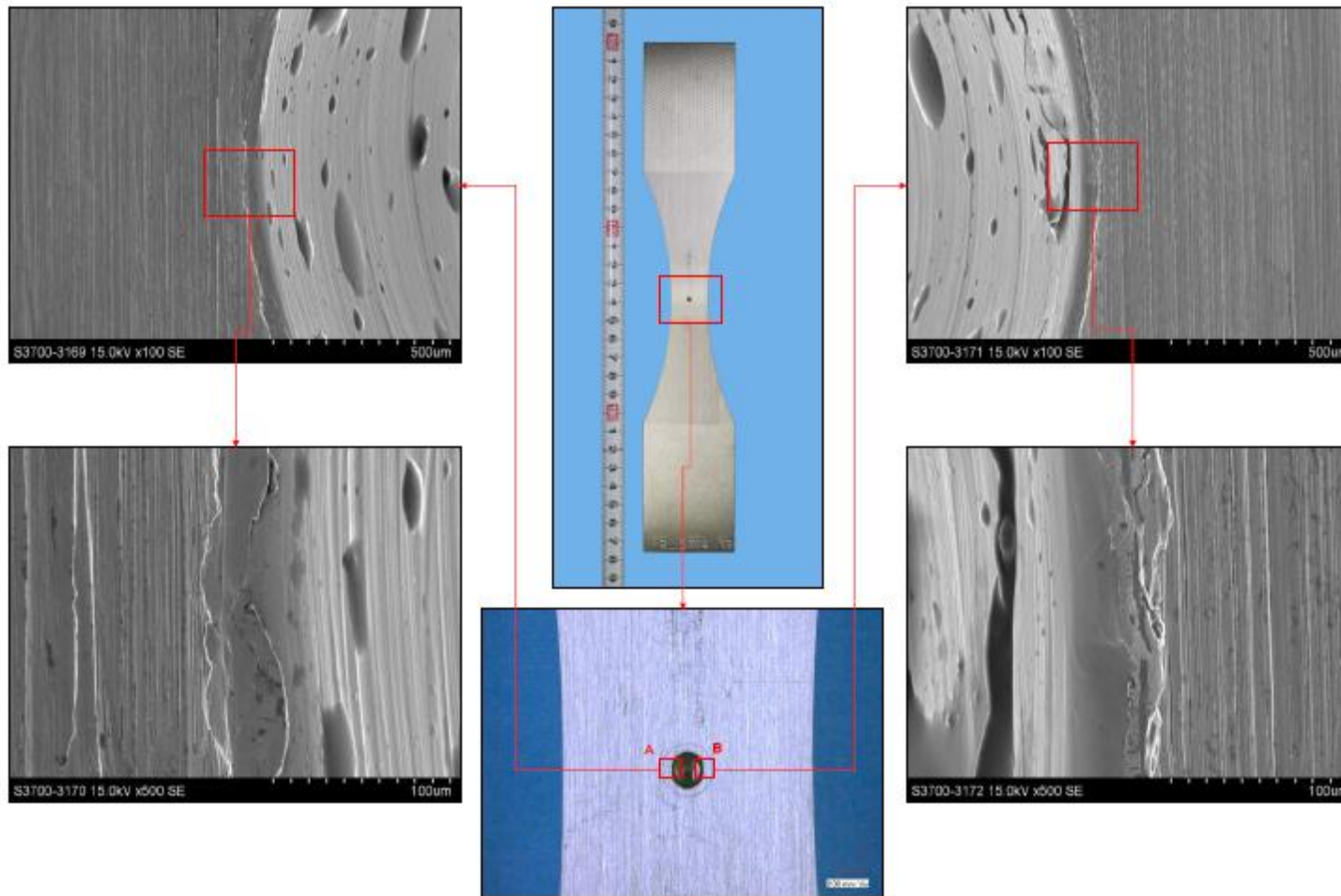
FIG. 3-26. Notch part observation by SEM (Type 304) (TP No.:F2-S304-12, Fatigue usage 0.6).
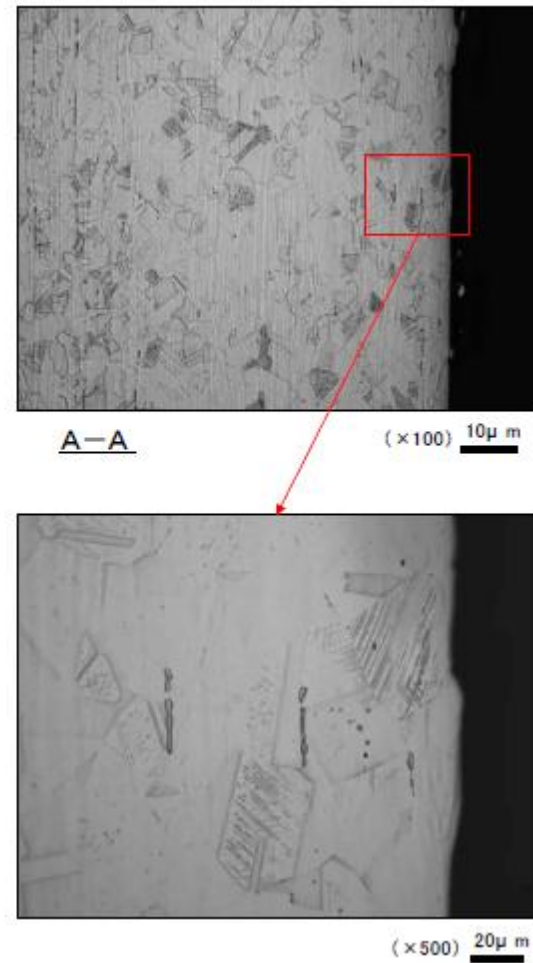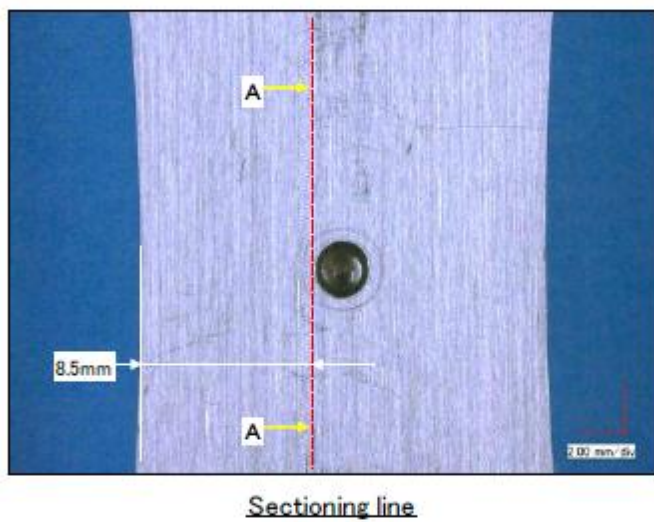
FIG. 3-27. Sectioning face observation by optical microscopy (Type 304) (TP No.:F2-S304-12, Fatigue usage 0.6).
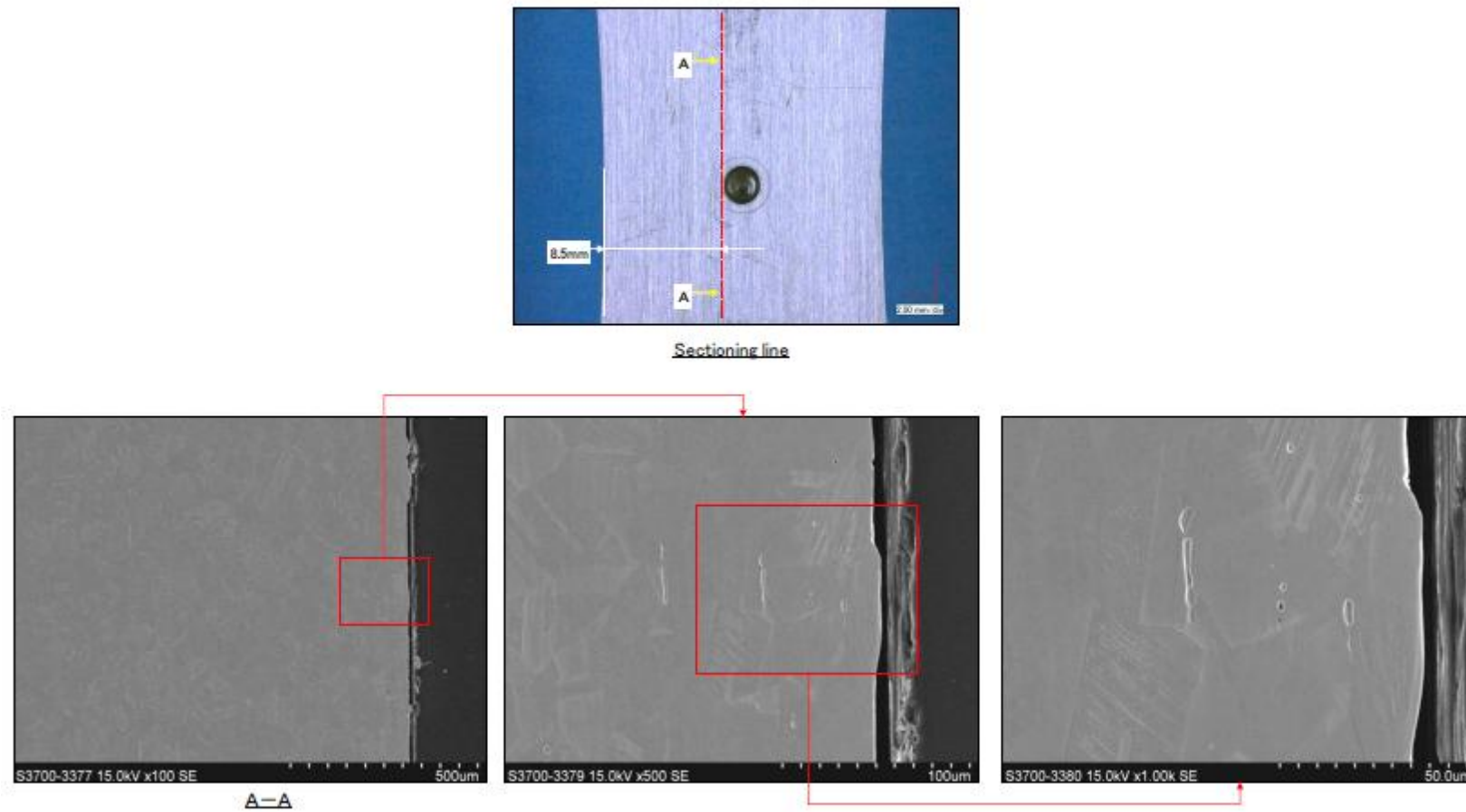
FIG. 3-28. Sectioning face observation by SEM (Type 304) (TP No.:F2-S304-12, Fatigue usage 0.6).
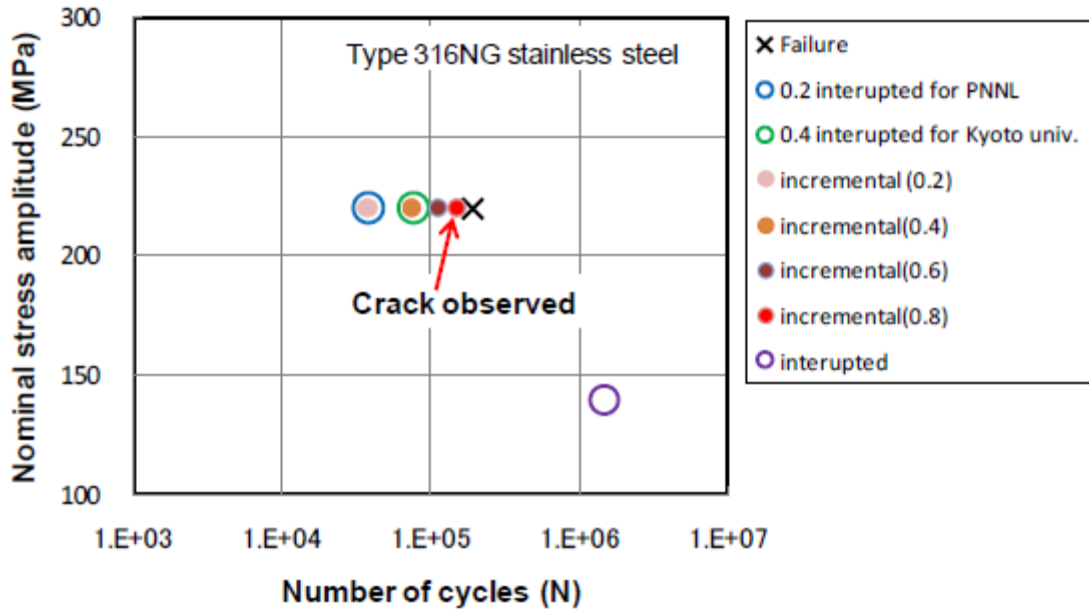
FIG. 3-29. Fatigue test results and observation result (Type 316NG).
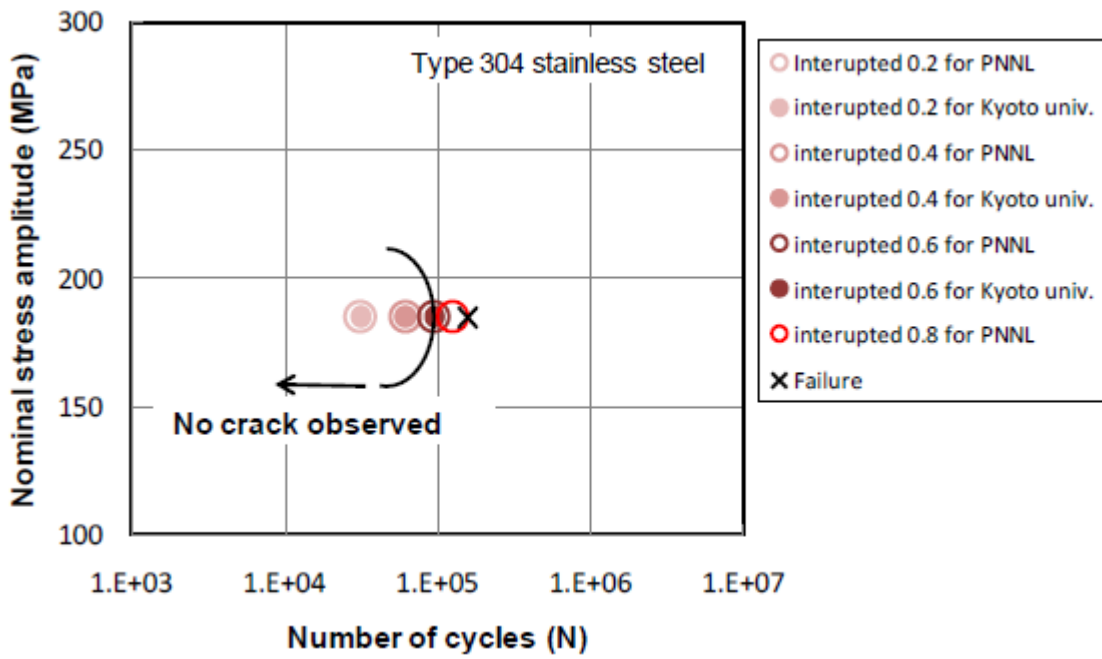
FIG. 3-30. Fatigue test results and observation result (Type 304).

3.2.5. Non-destructive test method

In this section we shall discuss the basic principles of employed non-destructive tests, their measuring instruments and the examples of their application to material degradation.

3.2.5.1. Acoustic impedance method

Basic principle of acoustic impedance method [30]

a) Propagation, reflection and transmission of mechanical waves in elastic solid

The method to determine the acoustic impedance distribution by waveform analysis is referred to as the acoustic impedance method in the main text of the report. The principle is described below. Consider first a discontinuous plane surface of the elastic properties located at $x=0$, parallel to y-z lane. When an elastic wave propagating along x axis collides with the discontinuous surface, the continuity conditions of the displacement and the stress should be satisfied. If the incident wave is a harmonic wave with frequency ω, wave number k_1 and amplitude a_1, the displacements u in both sides of the discontinuous surface can be expressed in the complex form:

$$u_1 = a_1 \exp\{i(\omega t - k_1 x)\} + b_1 \exp\{i(\omega t + k_1 x)\} \tag{1}$$

$$u_2 = a_2 \exp\{i(\omega t - k_2 x)\} \tag{2}$$

The speeds of the elastic waves in two media are given by $c_1 = \omega/k_1$ and $c_2 = \omega/k_2$, respectively. Here the quantities in each side of discontinuous surface are distinguished by subscripts 1 or 2 as in FIG. 3-31.
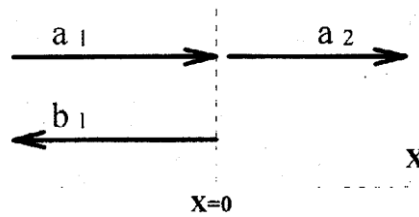
FIG. 3-31. Reflection and transmission of elastic wave [30].

Substituting the above displacements into the two boundary conditions at $x=0$, we can express the amplitudes of the reflected and the transmitted waves, b_1 and a_2 in terms of the one of the incident wave a_1. Then the reflection coefficient is defined by the ratio of the amplitudes of the reflected and the incident waves, which becomes

$$R = \frac{b_1}{a_1} = \frac{\rho_1 c_1 - \rho_2 c_2}{\rho_1 c_1 + \rho_2 c_2} \tag{3}$$

Here $\rho_1 c_1$ and $\rho_2 c_2$ are the acoustic impedances. Thus, the reflection coefficient at the discontinuous surface is determined only by the acoustic impedances on both sides of the surface. When the incident wave is more general, i.e. $h(x - c_1 t)$ and the discontinuous surface is located at $x = x_0$, it is not difficult to show that the reflected waves is given by $Rh(-x + 2x_0 - c_1 t) = Rh(-x - c_1(t - 2x_0/c_1))$, where $2x_0/c_1$ is the flying time of the elastic wave

coming back to $x=0$ from $x=x_0$. If the waveform of the incident wave observed at $x=0$ is $f(t)$, the received waveform at $x=0$ becomes $Rf(t-2x_0/c_1)$ from the above discussion. Hence the reflected wave from the discontinuous surface includes the information of the discontinuous surface, i.e. its reflection coefficient and the location. If the acoustic impedance of the media in the incident side is known, the acoustic impedance in the other side can be calculated from Eq. (3).

b) Reflection coefficient in material with continuously changing structures

We next consider that the material has a layered inhomogeneity and the acoustic impedance is continuously changing such that it can be expressed as a smooth function $\rho c(x)$ of the coordinate x. We regard the smooth change of the acoustic impedance as the limit of the distribution of discontinuity surfaces with infinitesimal jumps and widths. That is, the acoustic impedance $\rho c(x)$ at x jumps to $\rho c(x)+d\{\rho c(x)\}$ at $x+dx$ as shown in FIG. 3-32. Then from Eq. (3), the reflection coefficient $R(x)$ at x can be calculated as

$$R(x)=\frac{\rho c(x)-[\rho c(x)+d\{\rho c(x)\}]}{\rho c(x)+[\rho c(x)+d\{\rho c(x)\}]}\cong -\frac{1}{2}\frac{d\{\rho c(x)\}}{\rho c(x)} \tag{4}$$

That is, if the distribution of the reflection coefficient $R(x)$ is determined by waveform analysis, the acoustic impedance $\rho c(x)$ can be obtained as a function of x by integrating Eq. (4).
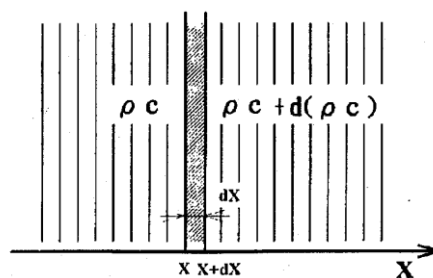
FIG. 3-32. Continuous changes in acoustic impedance [30].

c) Waveform analysis of incident and reflected waves

We next show how the reflection coefficient $R(x)$ of the material can be determined by waveform analysis of a plane elastic wave.
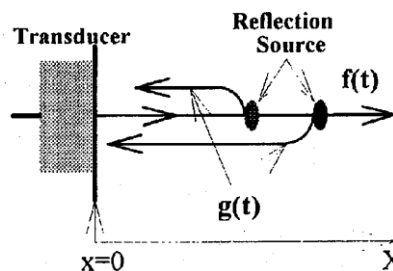
FIG. 3-33. Incident wave $f(t)$ and reflected wave $g(t)$ [30].

186

Suppose that the plane elastic wave with waveform $f(t)$ at $x = 0$ propagates in the increasing direction of x, reflects at each point up to the position $x = l$, and comes back to the incident position $x=0$ as shown in FIG. 3-33. From the above result the waveform of the reflected wave observed at $x=0$, $g(t)$ is given by the convolution

$$g(t) = \int_0^l R(x) \cdot f\{t - 2\tau(0,x)\}dx \tag{5}$$

Here $\tau(0,x) = \int_0^x c(\xi)^{-1}d\xi$ represents the flying time of the wave from $x = 0$ to x and $c(x)$ the wave speed at x. We note that Eq. (5) takes into account only single reflected waves at each reflection source, not multiple reflections more than once. This assumption will be valid in the case of the continuous inhomogeneity because except single reflected waves, triple or more reflected waves come back to the incident point whose amplitudes are expected very small.

The Fourier transforms the incident waveform $f(t)$ and the reflected waveform $g(t)$ are expressed as $F(\omega)$ and $G(\omega)$, respectively. Then the reverse Fourier transform of the ratio of $F(\omega)$ to $G(\omega)$, $h(t)$ can be calculated as

$$h(t) = \frac{1}{2\pi} \int_{-\infty}^{\infty} \frac{G(\omega)}{F(\omega)} \exp(i\omega t)d\omega = = \int_0^l R(x) \cdot \delta\{t - 2\tau(0,x)\}dx \tag{6}$$

Here $\delta(t)$ is the delta function. Procedure to obtain function $h(t)$ is called the de-convolution of the received wave $g(t)$ with respect to the incident wave $f(t)$. Taking the upper bound of the integral l sufficiently large, and using the formula $x(t) = \int_0^t c(t)dt$, we can obtain

$$\int_0^t h(2t)dt = \frac{1}{2} \int_0^{x(t)} R\{x(t)\}dx(t) \tag{7}$$

Here $x(t)$ represents the propagation distance from the incidence plane of the wave for time interval t. The above formula means that the integration of the continuous reflection coefficient $R(x)$ up to the location $x(t)$ equals to the integration of the de-convoluted function $h(2t)$ obtained by the spectral analysis of the received and the incident waves.

d) Acoustic impedance distribution

From the above discussions, we can derive a formula to calculate the distribution of the acoustic impedance ρc as a function of flying time t of the considered wave. That is, integrating Eq. (4) with respect to x and substituting $x(t)$ into x in the result, the integral of the left hand side is found to equal to the one of the right hand side of Eq. (7). That is, we obtain

$$\frac{\rho c\{x(t)\}}{\rho c\{x(0)\}} = \exp\left[-4\int_0^t h(2t)dt\right] \tag{8}$$

In conclusion, by integrating the de-convoluted waveform $h(t)$ of the received wave with respect to the incident wave, we can obtain the acoustic impedance $\rho c\{x(t)\}$ as the function of the

flying time of the considered wave, where we note that the acoustic impedance at the incidence plane, $\rho c\{x(0)\}$, can be measured from Eq. (3).

e) Two-dimensional extension of acoustic impedance method [31]

The procedure of calculating the acoustic impedance of a layered inhomogeneity described in the previous subsection can be extended to two-dimensional inhomogeneity. Instead of scanning two ultrasonic transducers, we developed a phased-array ultrasonic transducer. The system consists of array-type 32 small transmitting and receiving elements and can record 1024 waveforms transmitted and received by each of 32 elements. We consider one of 1024 received waveform which is obtained for a fixed pair of the transmitting and the receiving elements. In FIG. 3-34, the transmitting and the receiving elements are located at different points on a straight line on the material surface. Let us consider the flying path of the wave transmitting by an element, reflected from a material point P and received by another element. The reflection coefficient $R(x)$ of the point P is assumed not to depend on the incidence and reflection angles. If the waveform of the transmitted wave is $f(t)$, the received waveform $g(t)$ can be expressed as follows.

$$g(t) = R(x) \cdot f\{t - \tau(a,b)\} \tag{9}$$

Here $\tau(a,b)$ represents the flying time of the wave along the path $a+b$. It is assumed that the received wave is reflected only once at any material point. In other words, we neglect multiple reflected waves which may be considered very small in the case of the reflection by the smooth inhomogeneity.
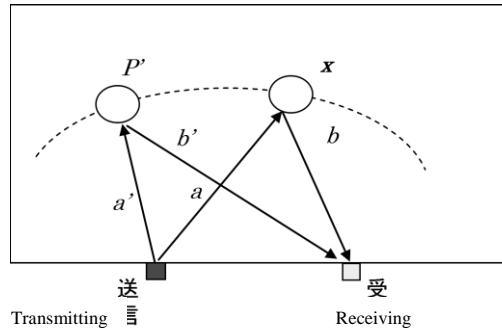
FIG. 3-34. Ultrasonic wave transmitting and receiving path [31].

On the other hand, the received waveform given by the same pair of transmitting and receiving elements should include reflected waves from different positions. In a result, the waveform with the same phase delay, Eq. (9), has a possibility to be reflected waves from all the points x' such that the flying time along the path $a'+b'$ is the same:

$$\tau(a,b) = \tau(a',b') \tag{10}$$

In other words, the reflection coefficient $R(x)$ included in (9) needs to be distributed to all the point x' satisfying (10). If the wave speed is uniform in the material, such points are on the circumference of an ellipse with the focal points at the transmitting and receiving elements. Although all the points do not necessary have the reflection coefficient $R(x')$, the actual reflection points will be emphasized if averaged are the reflection coefficients obtained for all pairs of different transmitting and receiving elements. Furthermore, the received wave given by each pair of transmitting and receiving elements will be superposition of all reflected waves whose flying path is larger than the distance between the two elements. That is,

188

$$g(t) = \int_0^l R(\boldsymbol{x'}) \cdot f\{t - \tau(a',b')\}dl \tag{11}$$

Here the integration is performed with respect to the distance along the flying path $a'+b'$ from the transmitting element to the receiving one passing through the position $\boldsymbol{x'}$, where l is the maximum flying distance to be examined. The lower limit of the integral has been extended from the distance of two elements l_0 to 0 because $R(\boldsymbol{x'})$ should vanish for such non-existent paths. We apply the above procedure for the layered acoustic impedance to the obtained waveform. The de-convolution of the received waveform with respect to the transmitted waveform becomes then

$$h(t) = \frac{1}{2\pi} \int_{-\infty}^{\infty} \frac{G(\omega)}{F(\omega)} \exp(i\omega t)d\omega = \int_0^l R(\boldsymbol{x'}) \cdot \delta\{t - \tau(a',b')\}dl = R(\boldsymbol{x''}) \cdot c(t) \tag{12}$$

Here $F(\omega)$ and $G(\omega)$ are, respectively, the Fourier spectra of the transmitted and the received waves and $c(t)$ the wave speed at a point located at time t away from the transmitting element and $\boldsymbol{x''}$ any point at which the transmitted wave is reflected at time t. Eq. (4) follows also along the flying path in the two dimensional inhomogeneity. Thus, integrating Eq. (4) and Eq. (12) with respect to t, and combining the results, we obtain the following expression which enables us to obtain the acoustic impedance at position $\boldsymbol{x}(t)$ on the flying path:

$$\frac{\rho c\{\boldsymbol{x}(t)\}}{\rho c\{\boldsymbol{x}(0)\}} = \exp\left[-2\int_0^t h(t)dt\right] \tag{13}$$

Acoustic impedance measuring device

A measurement system for acoustic impedance is shown in FIG. 3-35. The figure shows an example of a single ultrasonic transducer system using longitudinal waves. The longitudinal ultrasonic wave is transmitted and received by the transducer driven by the pulser-receiver and the reflected waveform is imported into the computer via the high-speed AD conversion board. A delay shoe is attached to the transducer to catch the complete waveform including the reflected echo from the specimen surface. In general a high frequency pulse with small pulse width and the wide spectral range is desirable for high spatial resolution and accurate Fourier analysis. Since the incident pulse in the received waveform caught by the pulser-receiver is a mixture of the driving voltage and the induced voltage by the transducer, it cannot be employed as an incident waveform. We first measure the reflected pulse from the free surface of the delay shoe without contact to the specimen, and next measure the received waveform after attaching the delay shoe to the specimen surface. From the large difference in the acoustic impedances between the air and the specimen, it is easy to show that the received pulse from the free surface of the delay shoe can be regarded as the incident pulse from the contacting surface of the delay shoe and the specimen.
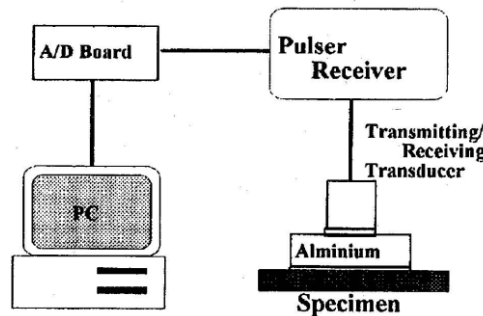
FIG. 3-35. Measuring device.

As in the case of ultrasonic inspection, Glycerin and the like coupling is used to smooth contact among the transducer, the delay shoe and the specimen surface.

In order to obtain the distribution of the acoustic impedance, we developed a phased array ultrasonic transducer consisting of 32 small elements, see FIG. 3-36. A multiplexer (channel switcher) switches the connection with the pulser-receiver and all the combinations of the transmitting and receiving elements, and 32 x 32 waveforms are imported to the computer.
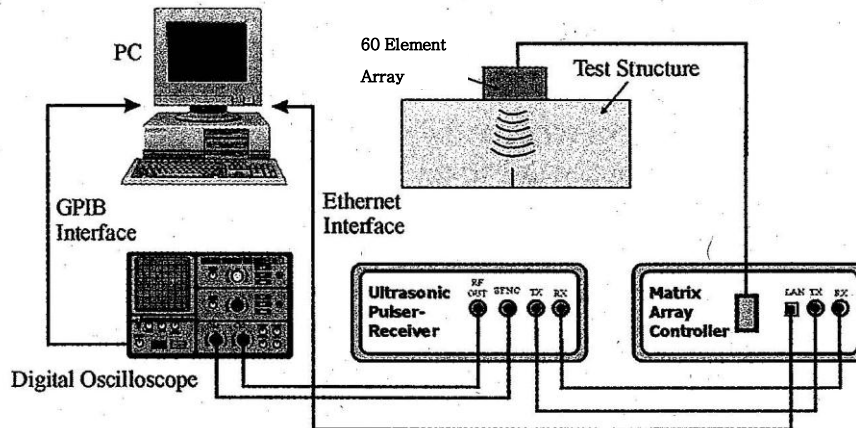
FIG. 3-36. Measuring device.

Application to materials degradation diagnosis

The acoustic impedance method can measure the distribution of the acoustic impedance on a material surface or inside of the material [32], [33], and the applicability to the measurement of inhomogeneity was examined for functionally gradient materials [30]. If the material degradation gives rise to the change of the acoustic impedance, it can be measured by this method in a logical sense. Furthermore, for geometrical changes associated with material degradation such as cracks and wastage, the scanning image of the obtained acoustic impedance will be much clearer than the conventional ultrasonic images from the following reason. That is, the spatial resolution from the de-convoluted waveform depends not on the pulse width but on the sampling period of the waveform and the opening boundary such as crack surface is empathized from large difference in the acoustic impedance between the material and the air. This study is the first attempt in application of the acoustic impedance method to material degradation, so that the techniques of experiment and data manipulation have not been fully specialized for that purpose. The following result will only show the possibility of the applicability of this method to estimation of material degradation.

3.2.5.2.   Magnetic leakage flux method

Principle of magnetic leakage flux method [34]

Two surfaces of a surface flaw of a ferromagnetic material will form a dipole in the magnetic field and the magnetic flux leaks into the air along an arch between the poles as shown in FIG. 3-37.
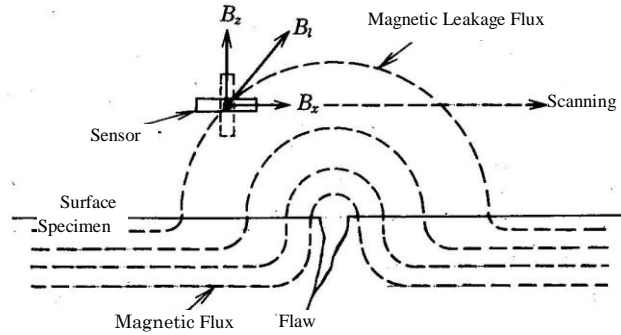
FIG. 3-37. Magnetic leakage flux occurring in vicinity of flaw [34].

In addition, when the local magnetic properties changes due to the material degradation like fatigue, the magnetic flux also leaks. That is, the region with higher magnetic permeability forms dipoles in the magnetic field. If the external magnetic field is removed, the remanent magnetization will be distributed in the ferromagnetic region. The spatial size, the distribution and the strength of the magnetic leakage flux depend on the shape of the surface flaw or the fatigued region. When the flaw or the material degradation, and the magnetic field can be regarded as two-dimensional, we divide the magnetic leakage flux B_l into the tangential component B_x and the normal component B_z. Scanning a small magnetic sensor along the material surface with a small lift-off, the distribution of the normal component B_z or the tangential component B_x can be obtained by using a biaxial sensor or by changing the sensing direction of a uniaxial sensor. Typical distributions of the normal and the tangential components of the magnetic leakage flux are sketched in FIG. 3-38. For a quantitative estimation of flaws or fatigue by this method, we should compare the obtained flux leakage distribution with the reference data under the same condition of the external magnetic field. Otherwise, we should normalize the reference data so as to be available for other conditions of the magnetic field. In this sense, it should be noted that the following results will not be employed as the reference for qualitative estimation because they are obtained under definite conditions for magnetic fields and specimens in laboratory.
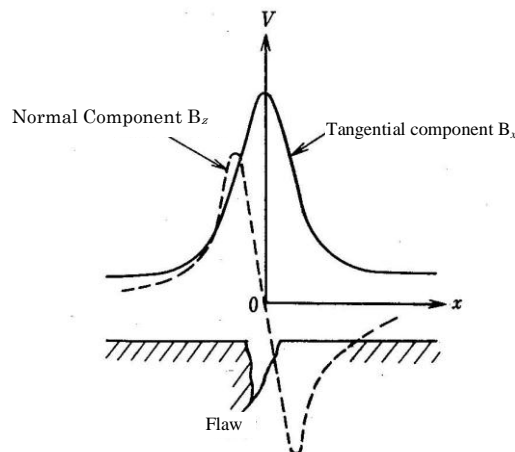
FIG. 3-38. Waveforms of tangential component B_x and normal component B_z of magnetic leakage flux occurring in vicinity of flaw [34].

Magnetic leakage flux measuring device

a) Magnetic leakage flux sensor

The functions and characteristics required for the sensor to detect the magnetic flux leakage from the flaw or the fatigue include [34]: (i) shape and size suitable to detect the magnetic flux leaking from the flaw with fidelity; (ii) high magnetic sensitivity; (iii) mechanical robustness—not easily affected by the operating environment, e.g. temperature; and (iv) being operable for prolonged periods and inexpensive as an industrial measuring sensor.

Currently available sensors are search coils, Hall elements (FIG. 3-39(a)), magnetic diodes (FIG. 3-39(b)), magneto-resistance (MR) and magnetic impedance (MI) elements. The latter element utilizes the magnetic impedance effects of amorphous magnetic wires.

(a) Hall element.   *(b) Magnetic diode.*
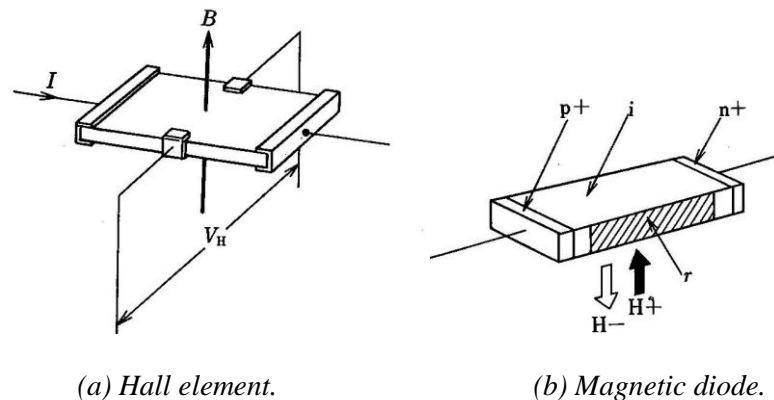
FIG. 3-39. Examples of magnetic leakage flux sensors [34].

b) Magnetizing Device

Magnetization methods normally used for magnetic flux leakage testing of flaws include the Yoke Method and the Coil Method shown in FIG. 3-40. The Yoke Method is applied to bar, pipe and plate to detect axial flaws by circumferential magnetization. The Coil Method is used to detect circumferential flaws of pipes by axial magnetization. In the following tests, Yoke Method was employed because of convenience for many specimens.

(a) Magnetization by Yoke method.   *(b) Magnetization by coil method.*
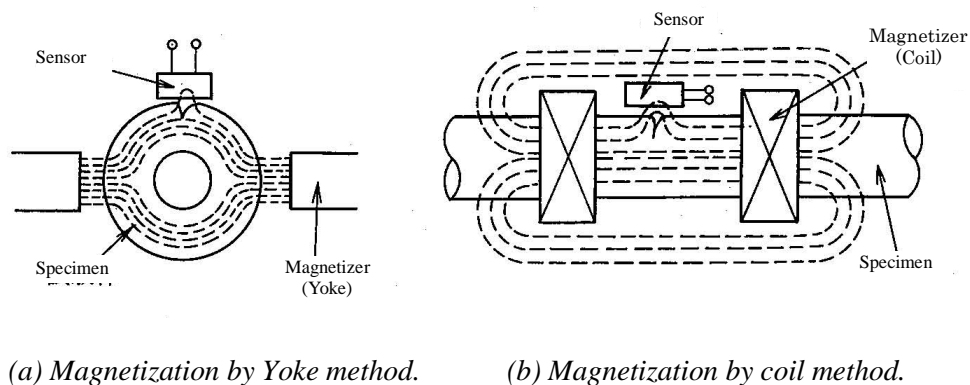
FIG. 3-40. Yoke magnetization method and coil magnetization method [34].

Application to materials degradation diagnosis

Applicability of the magnetic leakage flux method to material degradation has been verified for Type 304 and Type 316 steels subjected to out-of-plane bending fatigue [35]. Focusing on the martensitic phases induced by fatigue, the relationship with fatigue degree was examined in the magnetic leakage flux after demagnetizing or magnetizing the specimen. The Hall sensor was used for Type 304 series steel and relatively high-sensitive TFG sensor (thin film flux gate magnetic sensor) for Type 316. The measurement result shows that the magnetic flux density increases as the cycle fatigue frequency increases.

The novelty of this measurement presented in the report is that it targets magnetic leakage flux from high-cycle fatigue of three typical metals and it attempts to identify the fatigued region, by use of advantage of a new Hall element with high sensitivity, $1 \times 10^{-8} \sim 1 \times 10^{-10}$ (T) [3] and high spatial resolution.

3.2.5.3. Magnetoacoustoelasticity

Principle of magnetoacoustoelasticity

a) Elastic coefficients of ferromagnetic material under stress and magnetic field

Magnetoelastic coupling is an interaction between the mechanical and the magnetic fields in ferromagnetic materials such as the magnetostriction and the stress-magnetization effect. Magnetoelastic coupling is also seen as the change of the magnetic or the mechanical properties of the material, respectively, by the applied stress or the magnetic field. Theoretical study of magnetomechanical behaviours with magnetoelastic coupling has been done by Brown [36] in the frame of continuum theory for deformable magnetic materials, which was extended to include finite deformations by Pao et al. [37]. Matsumoto [38] derived rate-type constitutive equations which can represent many magnetomechanical behaviours including magnetic and mechanical nonlinearity and hysteresis.

Neglecting the effect of the exchange energy, we can assume that the mechanical and the magnetic states of a deformable magnetic material are prescribed by the current values and the past histories of the strain E and the magnetization M. In order to take into account the magnetic or the mechanical hysteresis, Matsumoto [38] and Suzuki et al. [39] proposed the rate type constitutive equations expressed as

$$
\begin{aligned}
\dot{H}_i &= P(\boldsymbol{T}, \boldsymbol{E}, \boldsymbol{H}, \boldsymbol{M})^{\pm}_{ij} \dot{M}_j + Q(\boldsymbol{T}, \boldsymbol{E}, \boldsymbol{H}, \boldsymbol{M})^{\pm}_{ijk} \dot{E}_{jk}, \\
\dot{T}_{ij} &= R(\boldsymbol{T}, \boldsymbol{E}, \boldsymbol{H}, \boldsymbol{M})^{\pm}_{ijk} \dot{M}_k + S(\boldsymbol{T}, \boldsymbol{E}, \boldsymbol{H}, \boldsymbol{M})^{\pm}_{ijkl} \dot{E}_{kl},
\end{aligned}
\tag{14}
$$

Here dot denotes time derivative, double indices are summed from 1 to 3, and $\boldsymbol{T}$ and $\boldsymbol{H}$ are the stress and the magnetic field, respectively. Superscripts $\pm$ of the coefficients distinguish the different functional forms corresponding to the increasing and the decreasing curves of the hysteresis. Since the constitutive equations are homogeneous with respect to the time derivatives, they exhibit rate-independent magnetoelastic behaviours. The inverse form of Eq. (14) becomes

$$
\begin{aligned}
\dot{M}_i &= A(\boldsymbol{T}, \boldsymbol{E}, \boldsymbol{H}, \boldsymbol{M})^{\pm}_{ij} \dot{H}_j + B(\boldsymbol{T}, \boldsymbol{E}, \boldsymbol{H}, \boldsymbol{M})^{\pm}_{ijk} \dot{T}_{jk}, \\
\dot{E}_{ij} &= C(\boldsymbol{T}, \boldsymbol{E}, \boldsymbol{H}, \boldsymbol{M})^{\pm}_{ijk} \dot{H}_k + D(\boldsymbol{T}, \boldsymbol{E}, \boldsymbol{H}, \boldsymbol{M})^{\pm}_{ijkl} \dot{T}_{kl},
\end{aligned}
\tag{15}
$$

Then coefficient A is the differential susceptibility tensor under fixed stress and B the slopes of the stress-magnetization curves under fixed magnetic field. Coefficient C is the slopes of the magnetostriction curves under fixed stress and D the tangential elastic compliances (the inverse of the tangential elastic coefficients) under fixed magnetic field. When the magnetomechanical process is

reversed, M and E are governed by the constitutive equations with the other set of coefficients with the opposite sign. In this case, we implicitly assume that the initial values of M and E for the new process are given by the final values for the previous process such that M and E change continuously. If we pay attention to the mechanical and magnetic process on one side of hysteresis, M (or H) and E will be determined by the given change of the H (or M) and T. Thus in what follows, we shall omit M (or H) and E as the arguments of the coefficients of the constitutive equations.

Let us consider a small dynamic motion superposed on the bios stress and magnetic fields. It is easy to see that the mechanical (elastic) property for the superposed motion becomes anisotropic due to the bias fields, e.g. the uniaxial anisotropy is induced along the applied magnetic field through the magnetoelastic coupling, or along the uniaxial stress through the mechanical nonlinearity. In general, a mechanical deformation follows the magnetic change from the magnetoelastic coupling through the terms with Q or B in the above constitutive equations. In the case of ultrasonic waves, however, the variation of the mechanical field is very small and fast, so that movement of the magnetic domain walls does not occur, which implies that for the ultrasonic wave we can neglect the magnetoelastic terms and the change of the magnetic arguments of the coefficients in the constitutive equations. Thus the stress-stain relation for ultrasonic waves is given by the tangential elastic coefficients S or D depending on the bias magnetic field and stress. Let σ and ε denote small variations of the stress and the strain tensors associated with the ultrasonic waves. Then from the above discussion σ and ε are governed by the generalized Hooke's law with anisotropy:

$$\sigma_{ij} = S(\boldsymbol{H},\boldsymbol{T})^{\pm}_{ijkl}\varepsilon_{kl} \quad \text{or} \quad \sigma_{ij} = S(\boldsymbol{M},\boldsymbol{T})^{\pm}_{ijkl}\varepsilon_{kl} \tag{16}$$

When the induced anisotropy by the bias stress or the magnetic fields is uniaxial, the independent elastic coefficients are five as expressed in the form

$$\begin{pmatrix} \sigma_{11} \\ \sigma_{22} \\ \sigma_{33} \\ \sigma_{23} \\ \sigma_{31} \\ \sigma_{12} \end{pmatrix} = \begin{bmatrix} S_{1111} & S_{1122} & S_{1122} & 0 & 0 & 0 \\ S_{1122} & S_{2222} & S_{2233} & 0 & 0 & 0 \\ S_{1122} & S_{2233} & S_{2222} & 0 & 0 & 0 \\ 0 & 0 & 0 & S_{2323} & 0 & 0 \\ 0 & 0 & 0 & 0 & S_{1212} & 0 \\ 0 & 0 & 0 & 0 & 0 & S_{1212} \end{bmatrix} \begin{pmatrix} \varepsilon_{11} \\ \varepsilon_{22} \\ \varepsilon_{33} \\ 2\varepsilon_{23} \\ 2\varepsilon_{31} \\ 2\varepsilon_{12} \end{pmatrix} \tag{17}$$

Here the arguments of the coefficients are omitted and the following relation should be satisfied from the symmetry

$$S_{2323} = \frac{1}{2}\left(S_{2222} - S_{2233}\right) \tag{18}$$

b) Ultrasonic Wave Propagating under Bias Stress and Magnetic Field
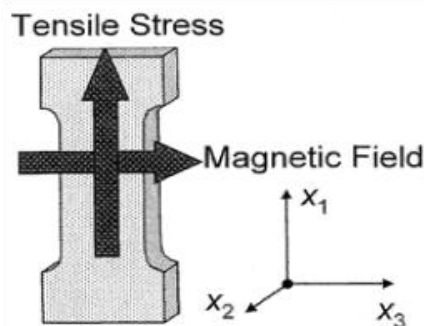
FIG. 3-41. Specimen under stress and magnetic field environment.

Let us consider ultrasonic waves propagating along X_2 direction in the material with uniaxial symmetric along X_1 axis induced by the uniaxial stress and the magnetic field as in FIG. 3-41. The governing equations consist of the equation of motion, the stress-strain relation and the strain-displacement relation:

$$\rho \frac{\partial^2 u_i}{\partial t^2} = \frac{\partial \sigma_{ij}}{\partial X_j} \ , \ \sigma_{ij} = S_{ijkl}\varepsilon_{kl} \ , \ \varepsilon_{ij} = \frac{1}{2}\left(\frac{\partial u_i}{\partial X_j} + \frac{\partial u_j}{\partial X_i} \right) \tag{19}$$

Here u is the displacement and ρ the material density. The elastic coefficients take the form in Eq. (17) with condition Eq. (18). A plane harmonic wave propagating in X_2 direction is expressed in the form

$$u = \bar{u}\, e^{i(kX_2 - \omega t)} \tag{20}$$

where k is the wave number, ω the frequency and $\bar{u}$ is the amplitude indicating the polarized direction.

In the case of the longitudinal wave, the displacement and the related stress-strain relation are given by

$$\bar{u} = (0, \bar{u}_2, 0) \ , \ \sigma_{22} = S_{2222}\varepsilon_{22} \tag{21}$$

Substituting Eq. (21) into the governing Eq. (19), we obtain the speed of the longitudinal wave

$$V_L = \frac{\omega}{k} = \sqrt{\frac{S_{2222}}{\rho}} \tag{22}$$

The uniaxial anisotropy is a special case of orthotropic anisotropy. Then it is known that only two polarized directions are allowed for the transverse wave propagating along one of the anisotropy axes. That is, the polarized directions coincide with X_1 and X_3 axes in our case. For the transverse wave polarized in X_1 direction, the displacement and the related stress-strain relation are given by

$$\bar{u} = (\bar{u}_1, 0, 0) \ , \ \sigma_{12} = 2S_{1212}\varepsilon_{12} \tag{23}$$

Similarly to the above from Eqs. (19) and (23) we obtain speed of transverse wave polarized in in X_1 direction

$$V_{T1} = \frac{\omega}{k} = \sqrt{\frac{S_{1212}}{\rho}} \tag{24}$$

In the case of the transverse wave polarized in X_3 direction, the displacement and the related stress-strain relation are given by replacing the suffix 1 with 3 in Eq. (23), and the wave speed becomes

$$V_{T3} = \frac{\omega}{k} = \sqrt{\frac{S_{2323}}{\rho}} = \sqrt{\frac{S_{2222} - S_{2233}}{2\rho}} \tag{25}$$

If we remember that the uniaxial anisotropy has been induced by the bias magnetic field and the uniaxial stress along X_1 axis, the elastic coefficients depend on amplitude M of the magnetization and

uniaxial stress T, and so do the wave speeds in Eqs. (22), (24), (25). That is, the speeds of the longitudinal and two transverse waves can be expressed as functions of M and T, or equivalently, of H and T:

$$V_{L,T1,T3} = V_{L,T1,T3}^{\pm}(M,T) \quad \text{or} \quad V_{L,T1,T3} = V_{L,T1,T3}^{\pm}(H,T) \tag{26}$$

Here, similarly to the elastic coefficients, the above wave speeds may have hysteresis for increasing and decreasing magnetization as indicated by superscript ±. Dependence of the wave speeds on the stress T is called the acoustoelastic effect which is caused by the mechanical nonlinearity, and dependence on the magnetization M the magnetoacoustic effect by the magnetoelastic coupling. The coupled effects are called magnetoacoustoelasticity, which has been applied to the precise residual stress evaluation.

Magnetoacoustoelasticity measuring device

A magnetoacoustoelasticity measuring device is composed of an electromagnet to apply the magnetic field to the object and an ultrasonic wave speed measurement unit. An example of a measuring system is shown in FIG. 3-42. Since it is necessary to measure the flying time of an ultrasonic wave with a high degree of accuracy, often used are the sing-around system in which the flying time is integrated by repeating transmission and reception, and the pulse-echo overlap system based on signal processing of overlapped receiving waveforms.

Application to materials degradation diagnosis

This method including conventional acoustoelasticity has been studied for non-destructive measurement of stresses (residual stresses, in particular) and few cases are known for estimation of materials degradation. If the elastic or the magnetoelastic properties are influenced by the material degradation, the stress strain relation for small deformation, the coefficients in Eq. (16) will also depend on some parameters of the material degradation, and so do the wave speeds. Thus we shall verify whether there exist the dependences of the wave speeds on the fatigue degree.
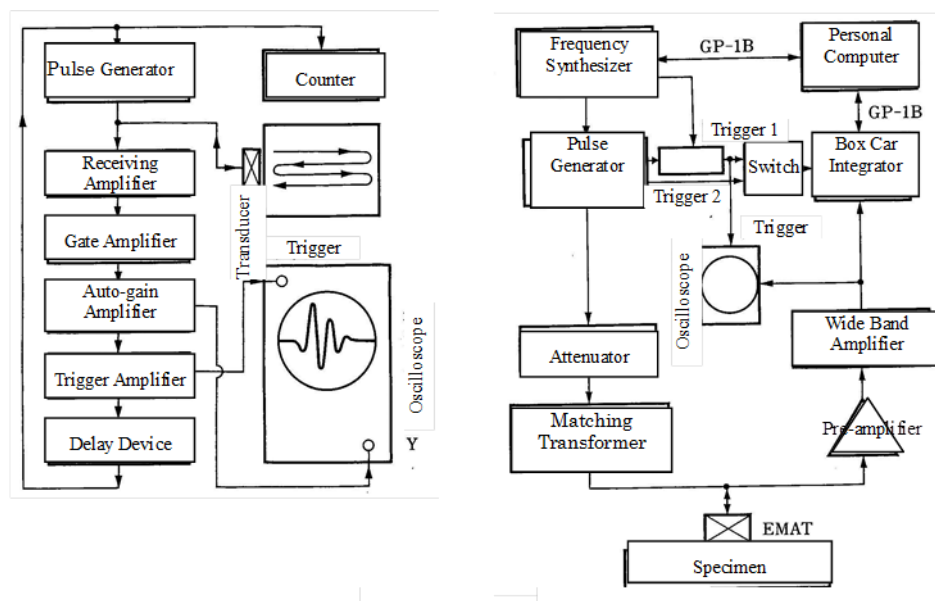
FIG. 3-42. Example of magnetoacoustoelasticity measuring device (Ultrasonic wave propagation time measuring system) [40],[41].

196

3.2.5.4. *Magnetic acoustic emission [42],[43]*

Principle of magnetic acoustic emission

Ferromagnetic materials, such as nickel, iron, and cobalt, are composed of numerous magnetic domains divided by magnetic walls. In a single magnetic domain, magnetic moments are aligned in the same direction, causing spontaneous magnetization. Magnetic walls have a thickness in which the direction of magnetic moments changes gradually. In a demagnetized state, the directions of magnetic moments of individual magnetic domains are random, causing no magnetization macroscopically. If an external magnetic field is applied, however, the macroscopic magnetization will increase due mainly to the movement of magnetic walls in a weak magnetic field and the revolution of magnetic moments in a strong magnetic field. If a periodic magnetic field is applied, a hysteresis will appear due to the resistance (pinning site) of the magnetic domain wall movement. Such domain wall movement will be affected by the direction of magnetization, impurities, stresses, grain boundaries, dislocations, and so on. Each magnetic domain has also spontaneous strain along the magnetic moment with positive (elongation) or negative (compression) signs, so that the macroscopic positive or negative magnetostriction appears during the magnetization. FIG. 3-43 shows changes in the magnetic domain structure due to a stress for a material with negative magnetostriction like nickel. Applying a tensile stress to the initial state (a) will result in a magnetic domain structure like (b) and by a compressive stress, the magnetic domain structure will change into (c), because such domain structures will be more stable under the stresses. If we apply the magnetic field to the material along the tensile stress, the magnetic domain wall movement will be suppressed for tensile stress and enhanced by the compressive stress, which gives rise to stress dependence of the magnetization curve.
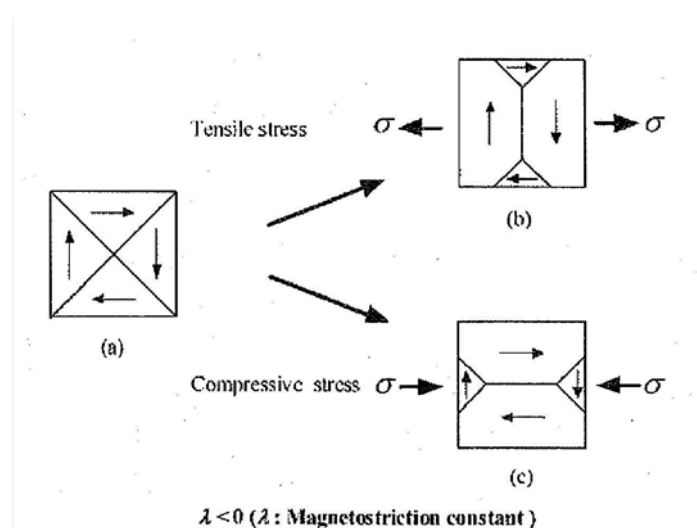
FIG. 3-43. Changes in magnetic domain structure due to stress.

In general, in case of a polycrystalline ferromagnetic material, magnetic wall movements during magnetization process will be discontinuous due to lattice defects, impurities, grain boundaries, and other pinning sites. In other words, there occur intermissive rotations of magnetic moment and intermissive variations of local strains during magnetization process, which induce Barkhausen noises and magnetic acoustic emissions, respectively. Thus the magnetic acoustic emissions will depend on some factors which affect the magnetic domain wall movement. For example, mechanical fatigue induces or accumulates dislocations, slip lines, fatigue cracks, stress concentration etc., so that the pinning sites for magnetic domain wall movement and hence the frequency of the magnetic acoustic emissions will increase. Stress concentration, plastic deformation and phase transformation associated with mechanical fatigue may also influence the emissions through change of the magnetic properties of the material.

Magnetic AE measuring device

An example of a measuring device is shown in FIG. 3-44. A periodic magnetic field is applied by supplying an electric current with a triangular waveform to the coil of the electromagnet (e.g. 0.1 Hz, maximum current of 3A in the following tests). The specimen is cyclically magnetized in the direction of its axis by the electromagnet. The AE search probe (e.g. mean frequency 150 kHz) catches elastic waves (acoustic pulses) with amplitudes larger than a threshold and records the number of pulses caught in each 0.1sec in several cycles of the magnetic field. The measurement method of the magnetic acoustic emission is the same as the conventional AE measurement with ring-down counting method.
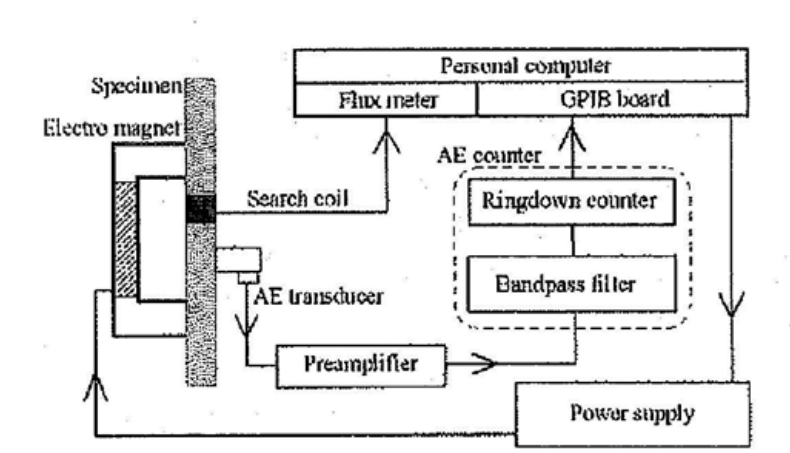
FIG. 3-44. Example of measuring device.

Application to materials degradation diagnosis

It has been reported that magnetic AE was used for creep damage analysis of low-alloy steel [44]. The measurement results on artificially damaged specimens show a trend in which the enumerated value of magnetic AE increases with the degree of damage. For both magnetic materials like carbon steel and non-magnetic materials like austenite stainless steel, there is a possibility that magnetic AE is influenced by the mechanical fatigue through the factors discussed above.

3.2.5.5. *Piezoelectric thin film [45],[46]*

Principle of piezoelectric thin film method

Piezoelectric effects are the interaction between the mechanical and the electric fields in a special class of dielectric materials. In particular, piezoelectric high-polymer film has low stiffness and high sensitivity, so that it is suitable for the strain or the train-rate sensors, cf. Lee [47] and Tzou [48]. Direct measurement of the polarized voltage at a point of a piezoelectric film gives us the information on the local strain. Egashira et al [49] measured the local strains in notched plates in tension from the voltages of mounted piezoelectric films. Biwa et. al [50] presented the method to obtain the surface strain distribution by measuring the electric potentials of two piezoelectric films mounted in different directions. Komagome et. al [46] visualized back-surface defects of a plate in compression by absorption of charged powder to a mounted piezoelectric film.

According to [45], the electric potential on the upper surface of a piezoelectric film can be given by the following formula using the normal strains S_1 and S_2 of the film surface, where the first axis in the film is set in the stretching direction, the third axis in the polarization direction, and the second axis perpendicular to the both axes as in FIG. 3-45.
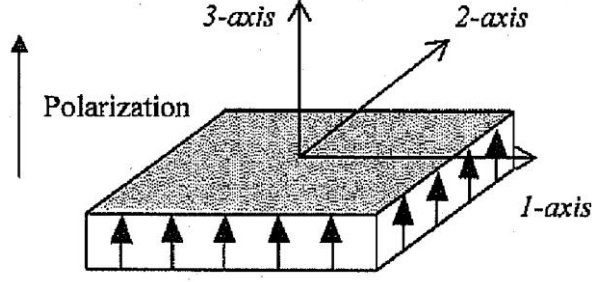
FIG. 3-45. PVDF film coordinate system.

$$V = p_1 S_1 + p_2 S_2 \tag{27}$$

Here the electrode layer on the upper surface of the film is removed and p_k is the electromechanical coupling coefficients defined as for $k = 1,2$,

$$p_k = \frac{d(c_{33}e_{3k} - c_{3k}e_{33})}{(c_{33}\varepsilon_3 + e_{33}^2)} \tag{28}$$

In the above formula, the independent components of the stress and the strain tensors are denoted by Voigt notation, i.e. subscripts are transformed as 11→1, 22→2, 33→3, 23→4, 31→5 and 12→6. Here ε_{ij} is the piezoelectric constants, d the thickness of the film, $\square_3$ the dielectric constant in x_3-direction, and c_{31}, c_{32}, c_{33} are the elastic coefficients between the normal stress in x_3-direction and the strain components S_1, S_2, S_3, respectively..

We attach a PVDF film, a typical piezoelectric film, to the surface of a structure such that its electrode layer is in contact with the structure. The strain components of the PVDF film is denoted by S_1 and S_2 in coordinate axes defined in the above. Since the PVDF film is thin enough with low stiffness, the strain components can be considered to coincide with the surface strain components of the structure. As shown in FIG. 3-46, x-y coordinates are set on the structure surface and denote S_x, S_y and $S_{xy,}$ being the normal strains and the shear strain of the surface.
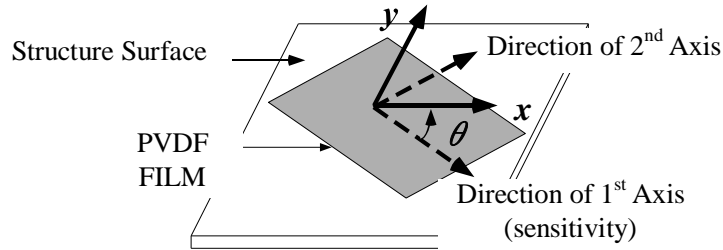
FIG. 3-46. Local coordinate system [45].

If x axis on the structure surface and the first axis (stretching direction) of the film make the angle θ, from Eq. (27) the electric potential $V(\theta)$ of the upper surface of the PVDF film can be expressed in the form:

$$V(\theta) = \left(p_1 \cos^2\theta + p_2 \sin^2\theta\right)S_x + \left(p_1 \sin^2\theta + p_2 \cos^2\theta\right)S_y + \left[(p_1 - p_2)\sin 2\theta\right]S_{xy} \tag{29}$$

If the surface strain of the structure is not uniform due to defects, material inhomogeneity, stress concentration etc., the electric potential on the film surface also becomes non-uniform. In other words, from the distribution of the electric potential on the PVDF film, we can obtain the information on the above factors.

Since the PVDF film has the sensitive direction, i.e. the stretching direction, the obtained distribution of the electric potential depends on the angle to be attached on the structure. This is inconvenient to identify the inhomogeneity from the distribution of the electric potential on the film. In order to eliminate the sensing directivity of the film, we laminate two PVDF films such that the polarization directions are parallel and the stretching directions are perpendicular to each other. We remove the electrode layers on both surfaces of the upper film and that of the upper surface of the lower film. The electric potential distribution appearing on the uppermost surface of the laminated films is equal to the sum of the surface potential distributions on each of the two films. Summation of $V(\theta)$ and $V(\theta+90°)$ in Eq. (29) yields the relationship between the electric potential of the laminated films and the normal strains in the form:

$$V^{'}(\theta)=V(\theta)+V(\theta+90°)=(p_1+p_2)(S_x+S_y)$$ (30)

The right hand side of the above formula does not depend on the angle θ, so that the laminating film has an isotropic sensitivity. We see also that the sensitivity of the film, the electromechanical coupling coefficients becomes larger for the laminated films.

Piezoelectric thin film measuring device

A piezoelectric thin film measuring device is shown in FIG. 3-47. The surface potential of the PVDF film can be measured by the surface electrometer without contact. To measure the two-dimensional surface potential distribution, the probe needs to be scanned in the prescribed region. Furthermore, the stress should be applied to the structure in some way, e.g. application of pre-pressure in case of pipes or containers.

- **Present strategy**
  Electrostatic Voltmeter
  Conductive layer   V(x)
  Piezo
  Structure
  $V(x) \propto S(x)$: local strain
  "Local" strain can be probed.
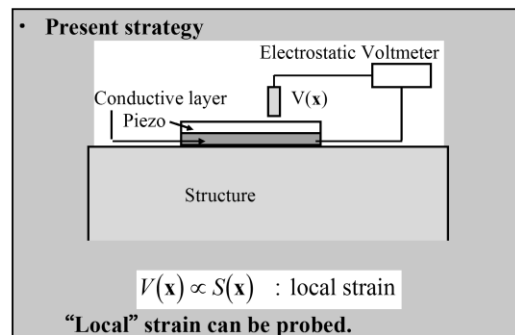
FIG. 3-47. Example of configuration of piezoelectric thin film measuring device.

Application to materials degradation diagnosis

This method has been applied to measurement of the surface strains and to identification of back surface defects, while no case has been reported for estimation of materials degradation. To apply this method to non-destructive evaluation, we should attach the film to the structure surface and measure the change of the electric potential distribution under the stress, and hence the applicable cases will be limited. Instead, this method will be effective to obtain the exact strain distribution and the exact mechanical inhomogeneity of specimens in laboratory as if the structure surface is covered with an

infinite number of infinitesimal strain gages. We shall apply this method only to Type 316NG to demonstrate the existence of inhomogeneity caused by the material degradation.

3.2.5.6. Hysteresis heating method

Principle of hysteresis heating method [51]

When a ferromagnetic material is magnetized from a demagnetized state by a cyclic magnetic field with a low frequency and constant amplitude H_0, the magnetic flux density B will change along the curve OA and then draws the steady loop ABCDEFA with amplitude B_0 as shown in FIG. 3-48.
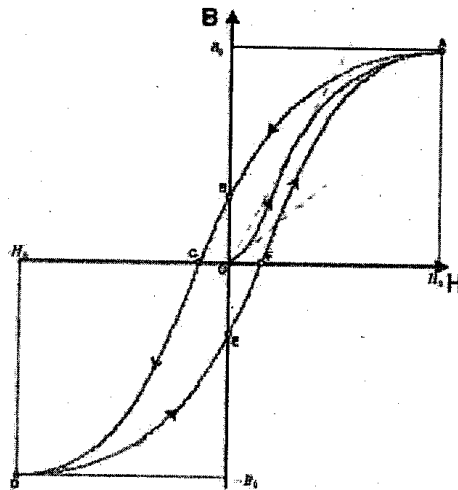
FIG. 3-48. B-H curve [51].

The B-H curve of a ferromagnetic material has hysteresis consisting of different curves for increasing and decreasing H. Then the magnetic field does work on the material given by the area of the hysteresis loop, which will be dissipated in the material (called iron losses in some cases). The loss of the magnetic energy for unit volume for once cycle of magnetic field is given by the following formula:

$$w_h = -\oint HdB \tag{31}$$

This dissipated energy induces a heat source and the temperature of the material increases. In general, when a ferromagnetic structure with a constant cross-section is magnetized, it constitutes a magnetic circuit and the magnetic field and the magnetic flux density will be almost uniform over a wide area. If a heated material has surface defects, the heat transfer to the circumstances changes around the defects, which gives rise to the temperature distribution. Thermography method is one of NDE techniques to inspect the surface defects by means of such a mechanism. In order to apply this method, the material should be heated in some way, e.g. lamp heating, induction heating by high frequency magnetic field, Joule heating and mechanical heating. The above magnetic hysteresis heating can uniformly heat the magnetic material over a wide region by a low frequency magnetic field, which will be expected as a high-precision and wide range inspection technique when coupled with a thermography.

If the cyclic magnetic field is f Hz, heat $P = fw_h$ (J/m^3) will be generated per the unit volume and time over the magnetized area of the material.

On the other hand, when the amplitude of the magnetic field or the magnetic flux density is not uniform in the material, the dissipated energy given by Eq. (31) will be also inhomogeneous which

brings the temperature distribution. For example, when the ferromagnetic material has a defect like a crack, it is known that the magnetic flux density near the defect increases and a larger temperature distribution is induced than the cooling process. Thus the magnetic hysteresis heating coupled with a thermography will make it possible to visualize the location and the opening shape of the defect.

Hysteresis heating measuring device

A hysteresis heating measuring device is shown in FIG. 3-49. A magnetizer (yoke) used for magnetic particle inspection can be used. A thermography is used to visualize the temperature distribution and record the temperature change at each point in the inspection area. The thermography uses a radiation thermometer to detect infrared radiation from the surface of an object and visualize the target object depending on the energy intensity. In order to measure the exact temperature, calibration is required by employing the appropriate radiation coefficient of the material.

Magnetized yoke manufactured   Thermography manufactured
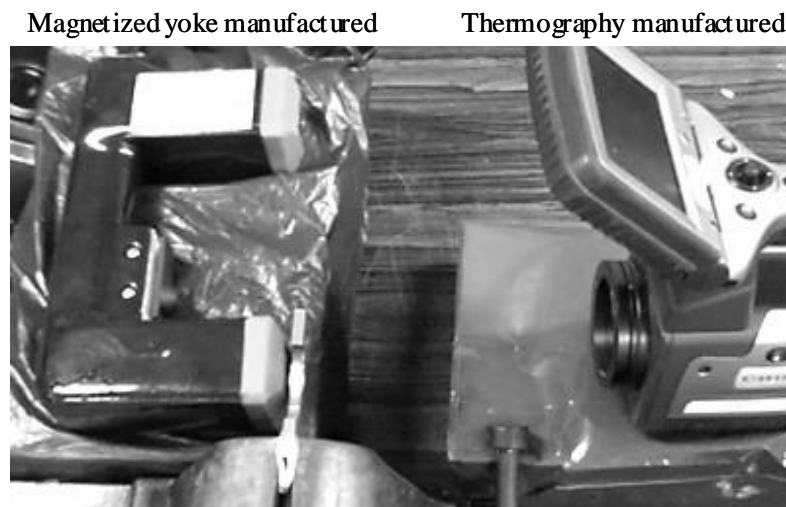
FIG. 3-49. Hysteresis heating measuring device.

Application to materials degradation diagnosis

As the evaluation of materials integrity using the thermography method, several mechanisms have been used to bring the temperature distribution. That is, for crack detection, different heat transfer performance around a crack from that at healthy sections [52], heat generation in fatigue processes [53], selectively vibrating closed cracks by transmitting ultrasonic waves (thermo-sonic method) [54], etc. On the other hand, few cases are known in which the thermography method is used to estimate materials integrity in early degradation processes before cracking.

The measuring method presented in the CRP main report uses selectively heating of the fatigued region, in which the martensitic phase is induced for austenite stainless steel and ferromagnetic properties are changed for carbon steed.

3.2.5.7. *Electrical conductivity*

Principle of electromagnetic impedance method

The measurement mechanism of the electromagnetic AC impedance method shown in FIG. 3-50 is as follows. When a cyclic current is applied to the coil, the magnetic field is generated in and around the coil. The induced dynamic magnetic field generates a current flow and a magnetic field in the material. The magnetic permeability of the material changes due to the application of a static external magnetic field using an electromagnet or a permanent magnet.
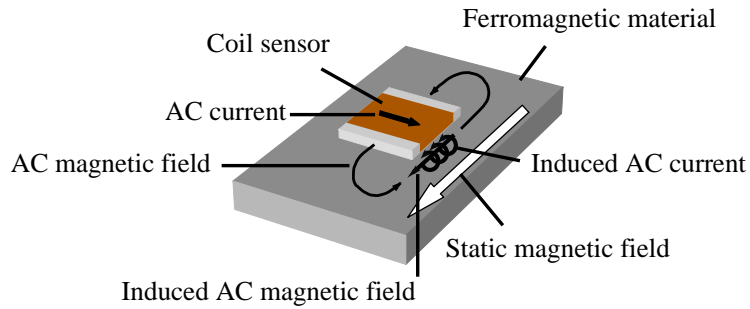
FIG. 3-50. Mechanism for measuring electromagnetic impedance method.

The magnetic field in the conductive material exited by the coil changes with the bias magnetic field, which can be measured as the impedance change of the coil. This method can evaluate the change of the electric conductivity or the magnetic permeability, and hence some factors giving rise to these changes.

This method has two salient aspects. That is, it can measure the magnetic properties of ferromagnetic thin film or the ferromagnetic surface layer. Such measurement has been difficult because their magnetic volume is small. However, if high frequency AC current (greater than a few MHz) is applied to the coil, magnetic properties up to a few micrometres or less in depth can be evaluated by skin effect. [55]

This method can also measure vector magnetic properties. That is, we may arbitrary set the directions of the exited and the bias magnetic fields by arranging the coil and the magnet. For example, stress vectors can be evaluated by exciting the rotational magnetic field in the specimen [56]

Electromagnetic impedance method measuring device

As an example of a measuring device, FIG. 3-51 shows a self-prepared system. Coil sensor is placed at the centre position on the surface where there is no defect (0mm lift-off). The quasi-static DC magnetic field is applied to the specimen by an electromagnet supplied with 2A triangular current. The AC impedance of the coil sensor is measured every 0.02A in excitation current with 5MHz frequency.
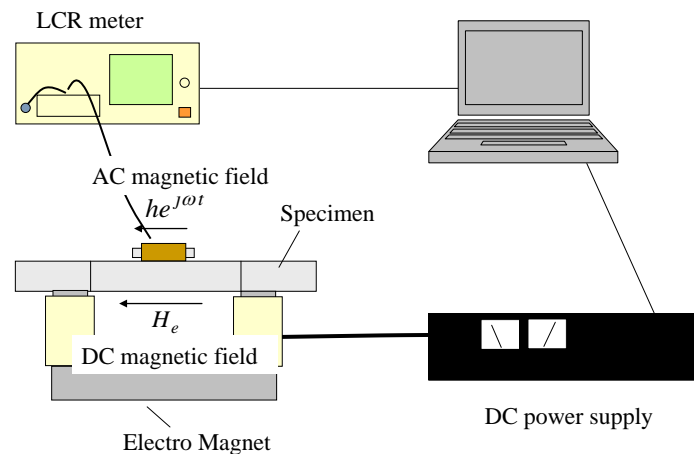
FIG. 3-51. Schematic representation of the electromagnetic impedance method measurement system.

Application to materials degradation diagnosis

High-cycle fatigue properties of aluminium alloy coated with an electroless Ni-Co-P deposit were estimated using electromagnetic AC impedance (EMI) method [55]. Fatigue tests were carried

out under completely reversed plane bending conditions. Results of measurements by the method shows that it is possible to predict the fatigue life of the aluminium alloy coated with the above deposit. In addition, we could identify the breaking point by changing the measurement position.

3.2.5.8. Eddy current testing

In an eddy current measurement system, a coil is excited with an AC at a specific frequency (FIG. 3-52). In accordance with Lenz's law [57], eddy currents are induced in the specimen under test. The corresponding induced magnetic flux density changes the net flux linked with the coil, resulting in a change in its inductance. At the same time, losses due to the induced currents in the specimen manifest themselves as an increase in the resistance of the coil. Thus, an eddy current coil will present a change in electric impedance (relative to its impedance in air) when placed near a conducting specimen.
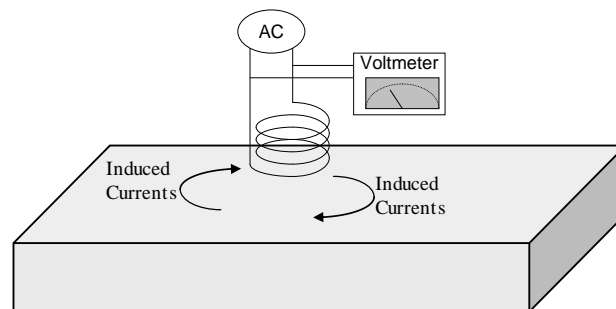
FIG. 3-52. Principle of eddy current inspection.

Differences arise between the eddy current measurements over ferromagnetic and non-ferromagnetic specimens. In the case of non-ferromagnetic specimens, the presence of the specimen (and therefore the induced currents) results in a decrease in the inductance with an increase in the resistance. However, for ferromagnetic specimens, the inductance typically increases as well [57] with an increase in magnetic permeability. This forms the basis for most permeability measurement systems as well as for instruments that measure ferrite levels using the magnetic permeability variations.

Three other factors (besides the permeability) also play a role in determining the response of eddy current measurements in ferromagnetic specimens. These are the conductivity, probe lift-off, and frequency. FIG. 3-53 shows the direction of change in the impedance due to increasing lift-off, conductivity and frequency. For ferromagnetic specimens, the change is in the direction opposite that of increasing permeability. For a constant permeability, lift-off, and conductivity, the effect of changing frequency is to rotate the signal.
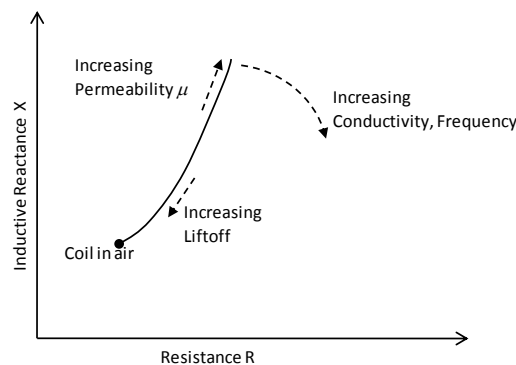
FIG. 3-53. Impedance trajectories as a function of permeability, lift-off, conductivity, and frequency.

Like all electromagnetic methods, the eddy current method is predominantly a surface (or near-surface) measurement, with the standard depth of penetration of the eddy currents (defined as the distance into the material where the eddy current density decreases to 37% of its value at the surface) decreasing as the frequency increases [57]. The standard depth of penetration is defined as:

$$\delta = \sqrt{\frac{1}{\pi f \mu \sigma}}$$

(32)

where f is the excitation frequency, μ is the permeability of the material and σ is the conductivity. For non-ferritic steel (such as Type 316NG), the skin depth at 1 kHz is about 13.1 mm (0.52 in.).

In two-phase stainless steels, the effect of increasing damage (through mechanisms such as fatigue loading) results in an increase in dislocation density, potentially increasing the resistance to the flow of current. At the same time, damage can result in an increase in the ferritic phase (martensite). The impact of these changes is two-fold, resulting in changes in conductivity and permeability. However, these changes are likely to occur locally rather than globally in the material, and scanning the material using an eddy current probe (while also varying the frequency) is likely to result in differences due to these effects. Eddy current NDE has previously been used successfully for detecting cracking in nuclear and non-nuclear components, including steam generator tubing and surface inspection in primary pressure boundary components. The method is designated by the ASME Boiler and Pressure Vessel Code as an acceptable surface inspection method (and for limited volumetric inspection, such as for SG tubing) in operating nuclear power plants. Thus, variations on this technique for detecting early degradation in nuclear power plants would likely be of interest.

3.2.5.9. *Magnetic Barkhausen noise*

The primary physical phenomenon behind magnetic Barkhausen noise is the same as that giving rise to magnetic acoustic emission (described earlier in this chapter). The magnetic Barkhausen effect is a result of the magnetic hysteresis of ferromagnetic materials. The magnetic flux density in ferromagnetic materials placed in an external applied magnetic field is a function of the applied magnetic field, with larger numbers of magnetic domains within the material aligning with the applied field direction with increasing applied field strengths. This realignment is, however, not a continuous process, with the presence of dislocations or other damage precursors resulting in domain wall pinning. Increasing the applied field strength will result in an abrupt realignment of some of the domains accompanied by a release of energy. The energy release may be detected magnetically or acoustically, with the corresponding measurement methods referred to as magnetic Barkhausen emission and magnetic acoustic emission, respectively.

The Barkhausen noise measurement methods has been applied to determine residual stresses in ferritic steels, and to determine the amount of hardening or cold work. Studies have also shown that this technique is sensitive to damage precursors in ferromagnetic materials, and quantities such as the energy and peak value in the Barkhausen signal have been shown to correlate well with level of damage in materials.

3.2.6. Results of non-destructive test method

All techniques done by Kyoto University had not been applied to evaluation of material degradation, and the following results as well as those in the CRP main report were obtained after try and error. Thus the experimental and the data processing techniques will not be enough refined suitable for estimation of material degradation. In these circumstances, we shall only describe the rough outline of the employed measurement methods and the experimental data which were used to obtain the correlations between the measured data and the fatigue degree shown in the CRP main report, and some other data which seem useful for other researches who are interested in these techniques.

3.2.6.1. Acoustic impedance method

Ultrasonic phased array transducer used to obtain the acoustic impedance distribution has a larger width compared with Type 316NG specimen, so that the material is not estimated by this method. We first obtain the waveforms transmitted and received by the same elements of the transducer from the free surface of the delay shoe with and without contact to the specimen. Then a_1 and b_1 in Eq. (3) are given by the amplitudes of the received pulses from the free and the contacting-with-specimen surfaces of the delay shoe. Then the acoustic impedance of the specimen surface $\rho_2 c_2$ can be calculated from the formula if $\rho_1 c_1$ for the delay shoe is known. Thus we can measure the acoustic impedances at 32 points of the probe elements. FIG. 3-54 shows the location of the probe for measurement of surface acoustic impedance at the notched surface, and FIG. 3-55 the distribution of calculated acoustic impedance at position D for ten times measurements. Then averaging the acoustic impedances at each position of the probe for each fatigue phase, we have FIG. 3-56, where the curve E denoted the averaged value of all measured regions for each fatigue phase. Here the result is obtained for individual specimens with each fatigue phase unlike the result in the CRP main report.
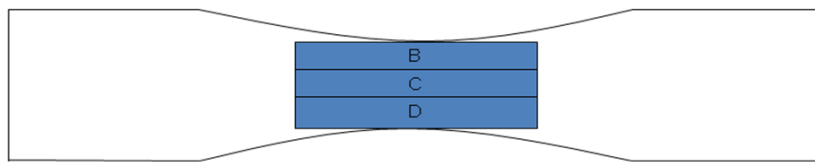
FIG. 3-54. Locations of ultrasonic phased array transducer (Type 304).
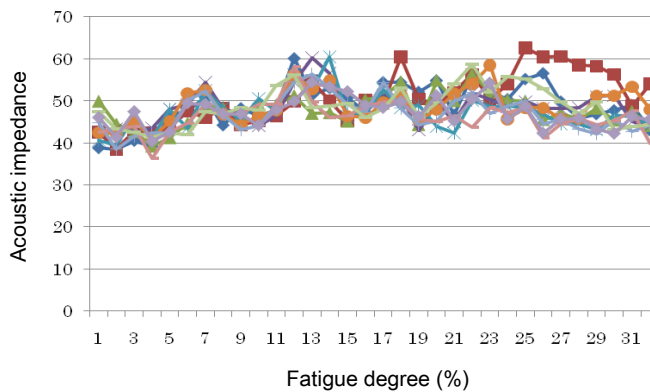
(a) 10% fatigue.
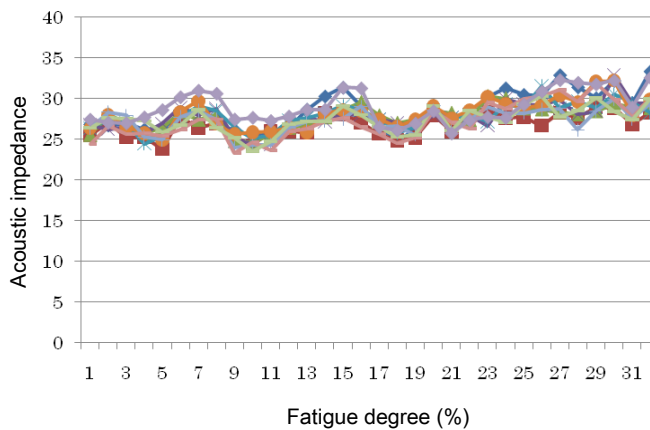
(b) 80% fatigue.

FIG. 3-55. Distribution of surface acoustic impedance of fatigued specimen (Type 304).
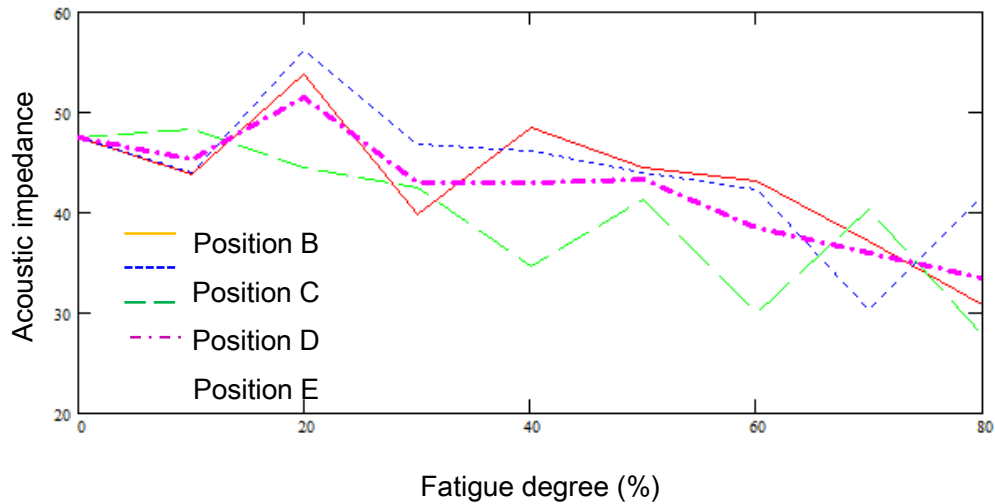
FIG. 3-56. Surface acoustic impedance at each fatigue phase (Type 304).

We next obtain 32 x 32 waveforms transmitted and received by each element for each fatigue phase of Type 304 specimen where the probe is placed at the centre of the smooth surface of the specimen. According to the procedure discussed in Section 3.2.5.1, we obtain the two-dimensional distribution, the vertical cross-section of the specimen, of the acoustic impedance. FIG. 3-57 shows the obtained vertical distribution of the acoustic impedance, where the bottom and upper edges mean the notched and the smooth surfaces of the specimen.

(a) 0% fatigue.
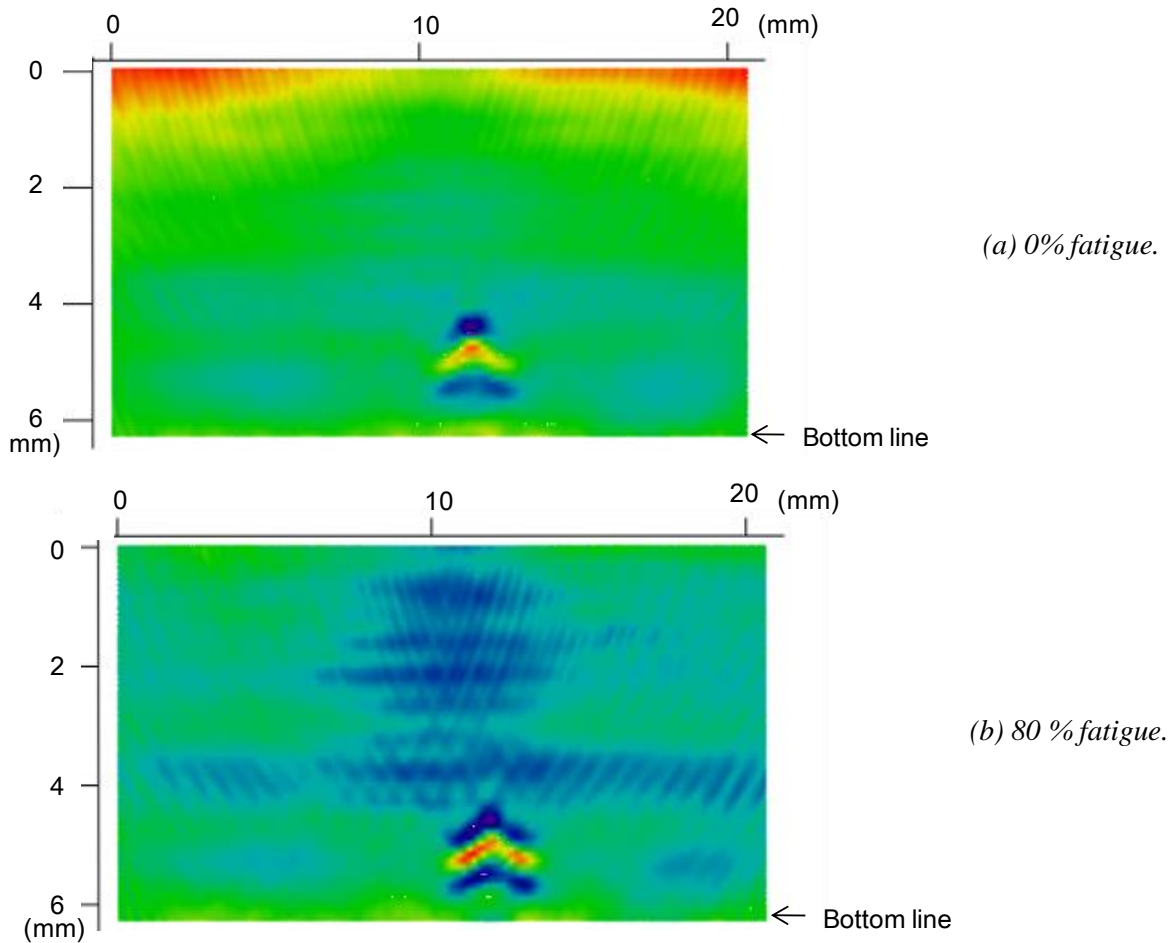
(b) 80 % fatigue.

FIG. 3-57. Vertical distribution of acoustic impedance (Type 304).

We can see the bottom shape of the notch in the lower centre of both images and the low acoustic impedance region above the notch for 80% fatigued specimen. In a logical sense, we can transform the acoustic impedance at each point to the fatigue degree by referring to the correlation in FIG. 3-56, but we have not succeeded in the two dimensional case. To do it, we should take into account the exact directivities of the transmitting and receiving characteristics of each element in the aperture synthesis procedure for the acoustic impedance. Thus the colours of the image are automatically mapped to emphasize the contrast and only the relative variation has a meaning. The oblique striped pattern comes from moiré interference between the waveform sampling period and the spatial discretization.

By a similar procedure, for STS410 specimens we obtained the distribution of surface acoustic impedance in FIG. 3-58, the averaged surface acoustic impedance for each fatigue phase in FIG. 3-59, and the vertical distribution of the acoustic impedance in FIG. 3-60. Here the surface acoustic impedance in FIG. 3-59 is given by the average of central 4 elements unlike the case of Fig. 56(c) in the CRP main report, which implies that by the fatigue the acoustic impedance decreases larger in the central region near the notch.
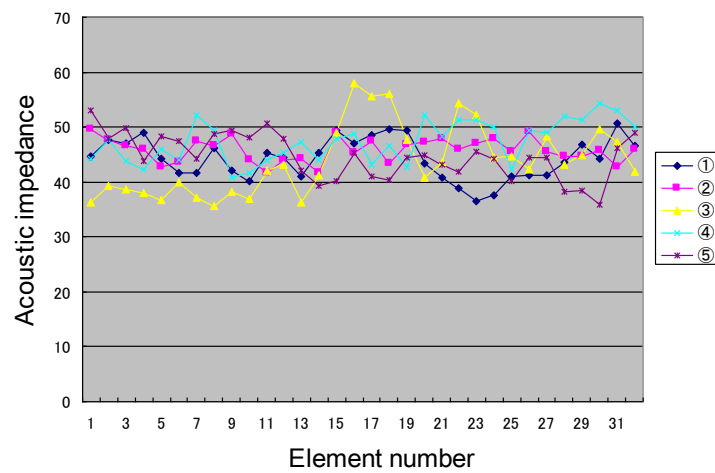
(a) 10% fatigue.
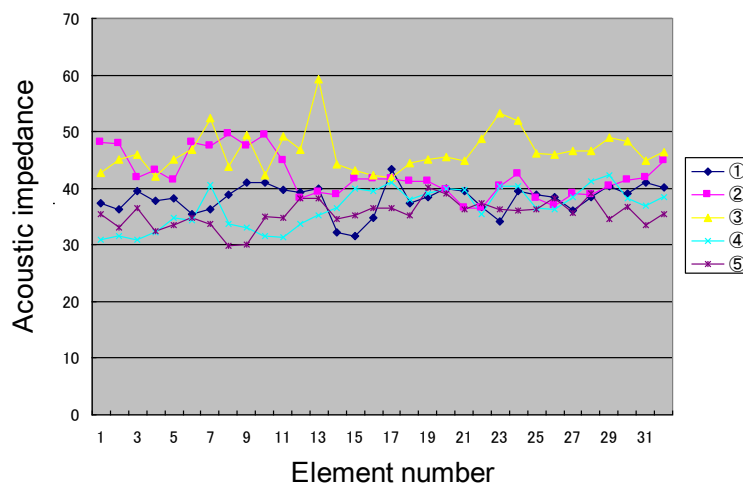
(b) 80% fatigue.

FIG. 3-58. Distribution of surface acoustic impedance of fatigued specimen (STS410).
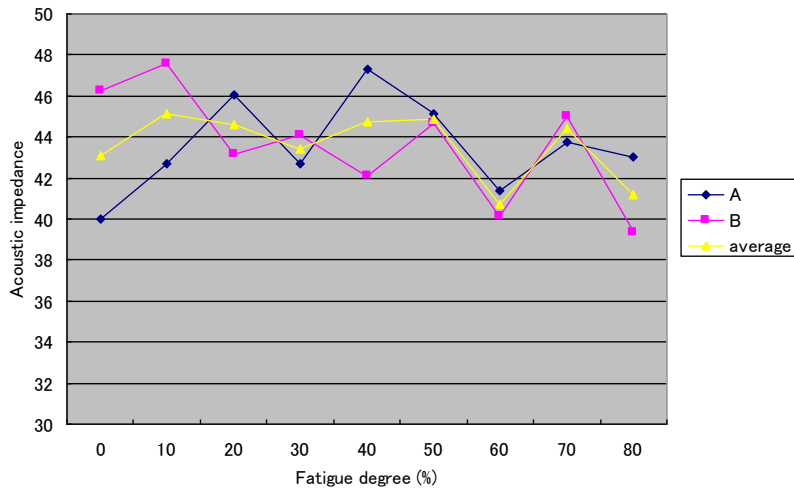
FIG. 3-59. Surface acoustic impedance near notch at each fatigue phase (STS410).

(a) 0% fatigue.

(b) 80% fatigue.
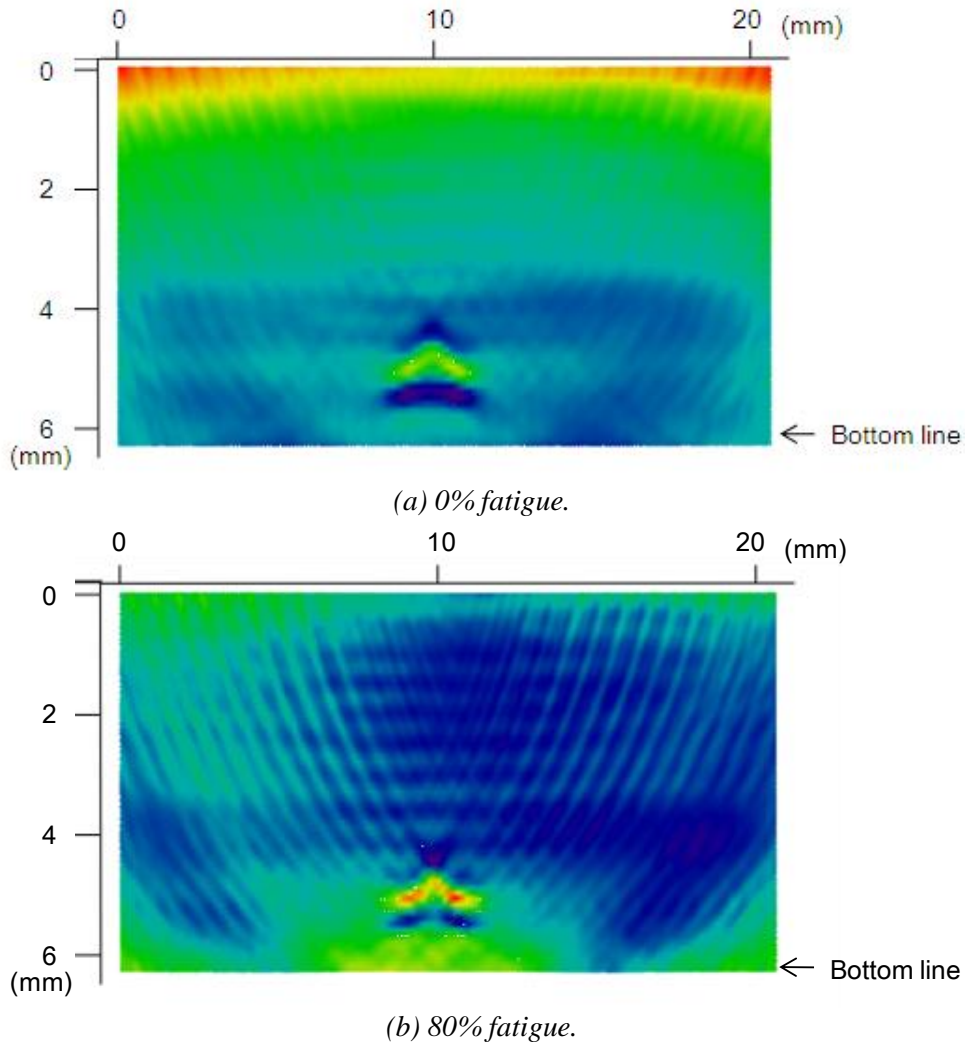
FIG. 3-60. Vertical distribution of acoustic impedance (STS410).

At the end of this section, for comparison FIG. 3-61 shows the close up of the vertical distribution of the acoustic impedance and the ultrasonic vertical image near the notch by the commercial phased array ultrasonic transducer with 32 elements. Here the images are obtained for 20% and 0% fatigued STS410 specimen, respectively. In view the figure, it is found that the image of

the notch is largely improved in the acoustic impedance distribution calculated by the present technique.
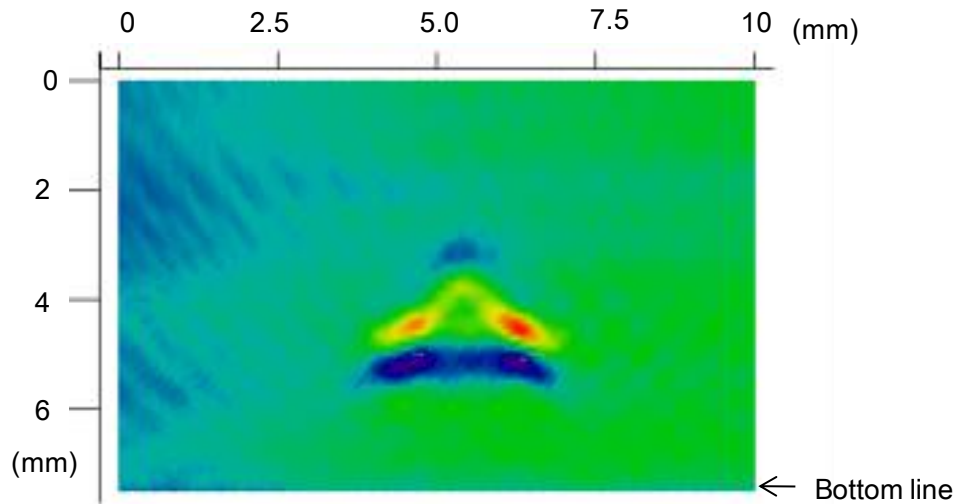
(a) Close up of vertical distribution of acoustic impedance (STS410 20%).
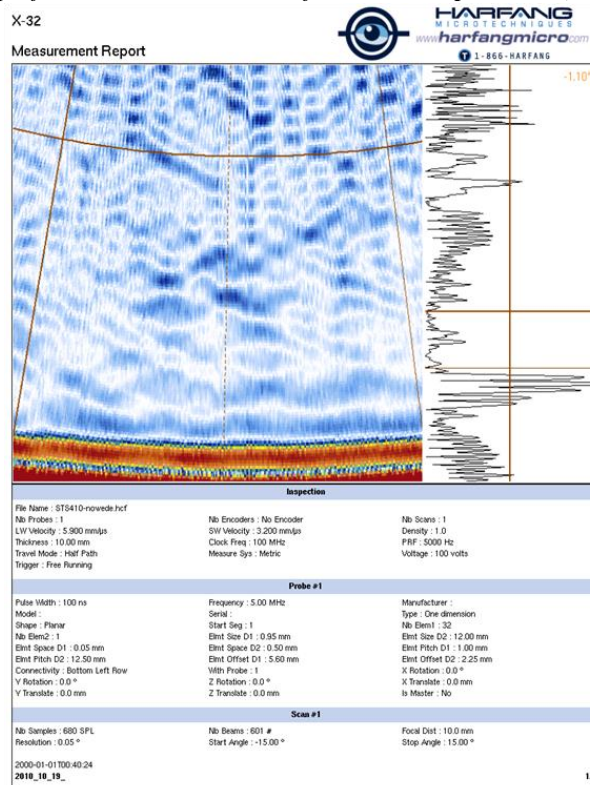
(b) Close up of ultrasonic vertical image by X-32 (STS410 0%).

FIG. 3-61. Comparison of close up images near notch by present and conventional techniques.

3.2.6.2. Magnetic leakage flux method

For Type 316NG specimens, we first apply the magnetic field with 40kA/m by an electromagnet along the axis of the specimen with each fatigue phase and remove the magnetic field. We next scan the AMI (amorphous magnetic impedance) sensor with 1mm lift-off by 0.25mm pitch over 8mm x

20mm central region of the notched surface of the specimen. Distributions of the normal and the tangential components of the magnetic leakage flux are shown in FIG. 3-62. The normal distribution of the magnetic leakage flux shows a pattern around the notch, but so does not the tangential component. Taking the maximum value of the leakage flux components for each specimen, we have FIG. 3-63. We see that the maximum tangential component of the magnetic leakage flux increases with the fatigue degree, while the normal component does not show the explicit trend with the figure degree.
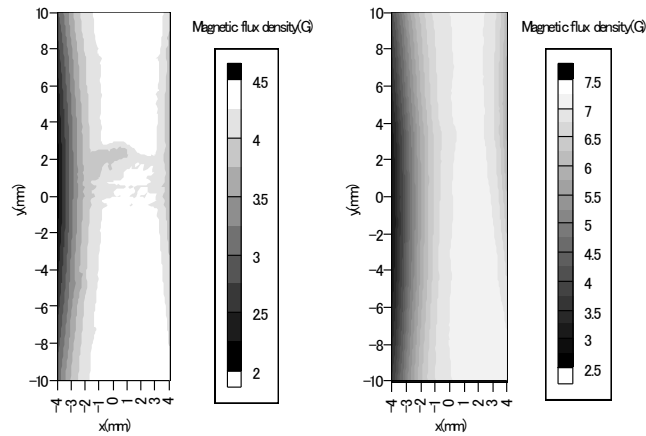
(a) Normal and tangential components (0% fatigue).
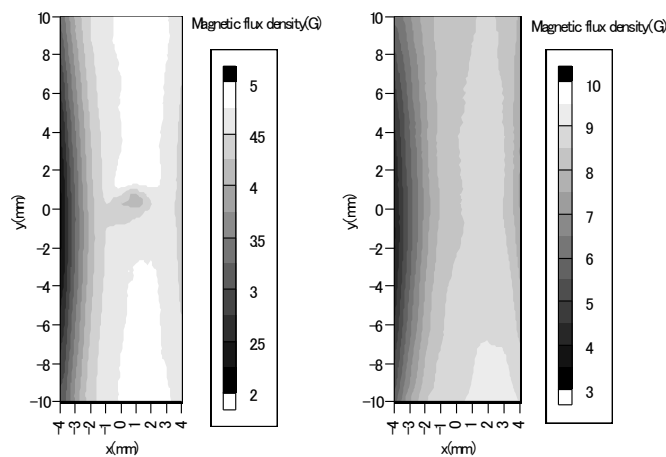
(b) Normal and tangential components (80% fatigue).

FIG. 3-62. Distribution of magnetic leakage flux from residual magnetization (Type 316NG).
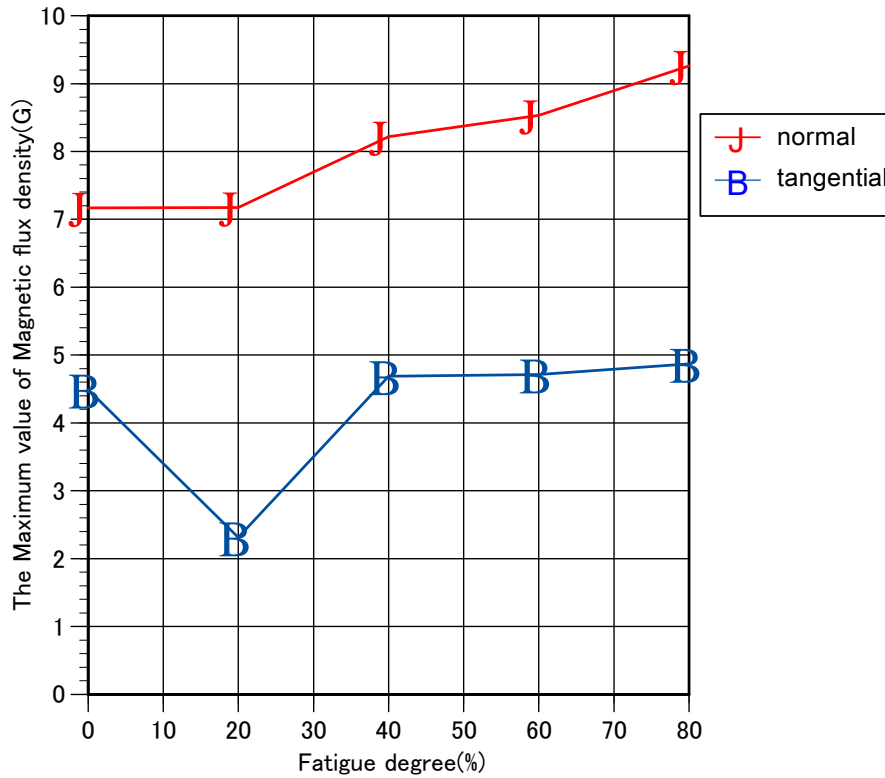
FIG. 3-63. Maximum magnetic leakage flux from residual magnetization at each fatigue phase (Type 316NG).

For Type 304 and STS410 we used a Hall sensor with larger flexibility of lift-off. For these materials, we scanned the sensor over 10mm x 10mm region around the notch with 1mm lift-off and by 0.25mm pitch. We applied the magnetic field along the axis of the specimen by an electromagnet with 3.0A current. The leakage flux from the active magnetization under the magnetic field as well as the residual magnetization was measured. FIG. 3-64 shows such distributions of the normal and tangential components of leakage flux from the active and the residual magnetizations. A local pattern around the notch can be seen in the distribution of the leakage flux in several distributions of the leakage flux components. In particular, the absolute value of the leakage flux from the residual magnetization for 80% fatigue becomes larger in the side region of the notch. The stress is concentrated in that region, and the local volume ratio of the ferromagnetic phase may be increased by the cyclic loads. The variation of the leakage flux from the active magnetization will be caused by the increase of the magnetic permeability by the fatigue.

(a) Normal and tangential components from active magnetization (0% fatigue).
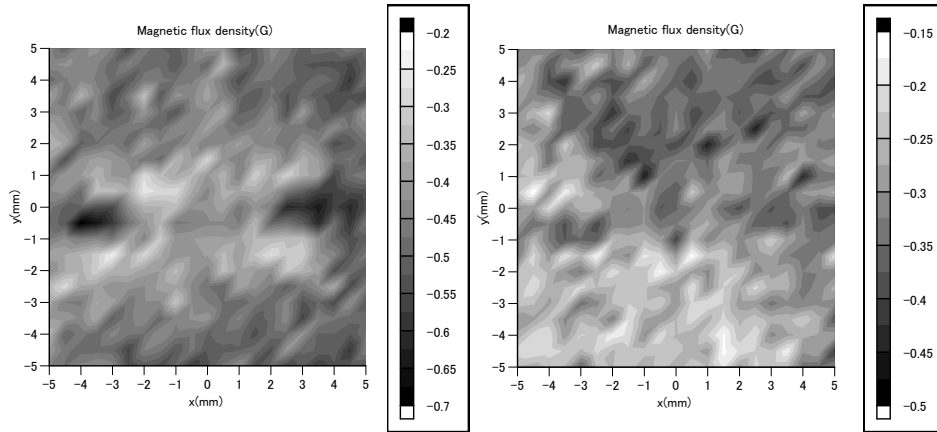
212

(b) Normal and tangential components from residual magnetization (0% fatigue).

(c) Normal and tangential components of leakage flux from active magnetization.
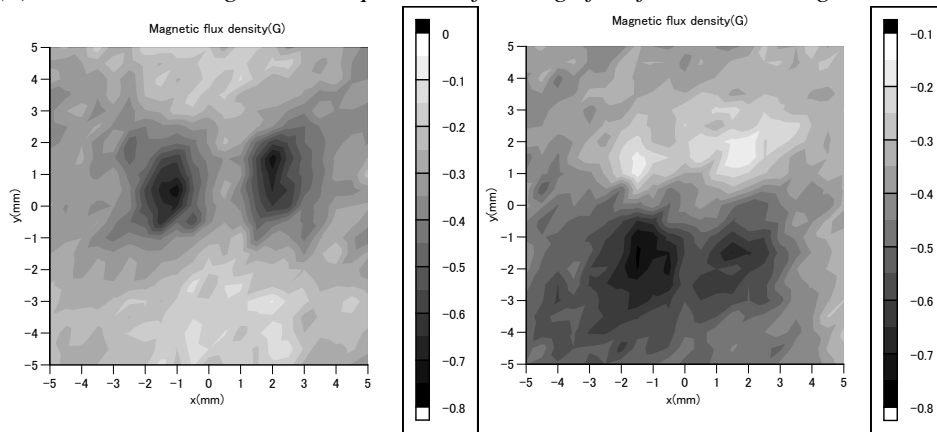
(d) Normal and tangential components from residual magnetization (80% fatigue).

FIG. 3-64. Distribution of magnetic leakage flux from active and residual magnetizations (Type 304).

In FIG. 3-65 we show the maximum leakage fluxes from the active and the residual magnetizations, where we took the differences from the bias leakage flux components averaged in the measured region. Each maximum component of the magnetic leakage flux seems to increase with fatigue.
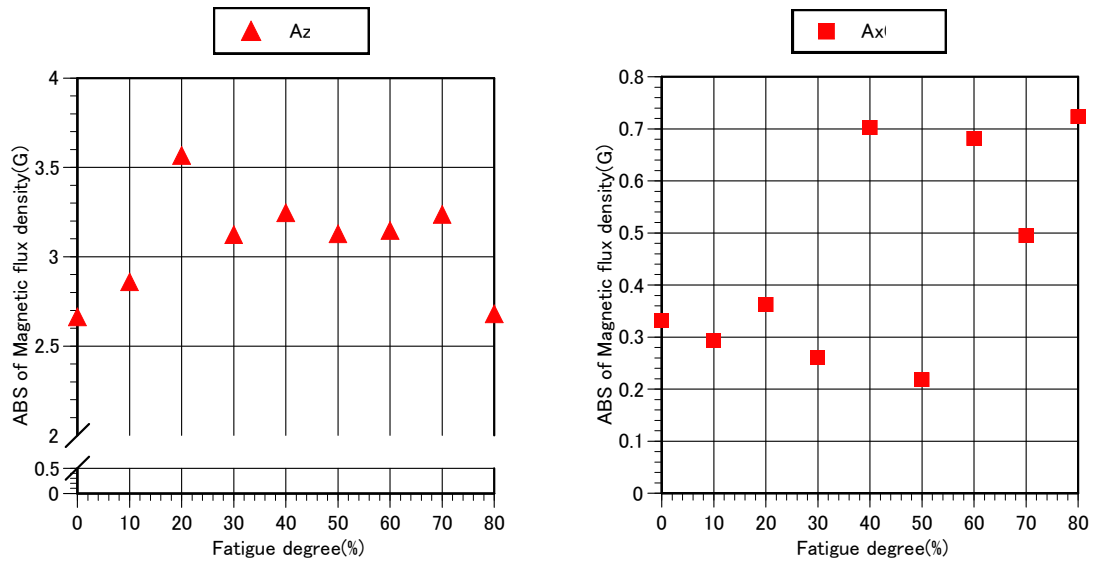
(a) Normal and tangential components from active magnetization.
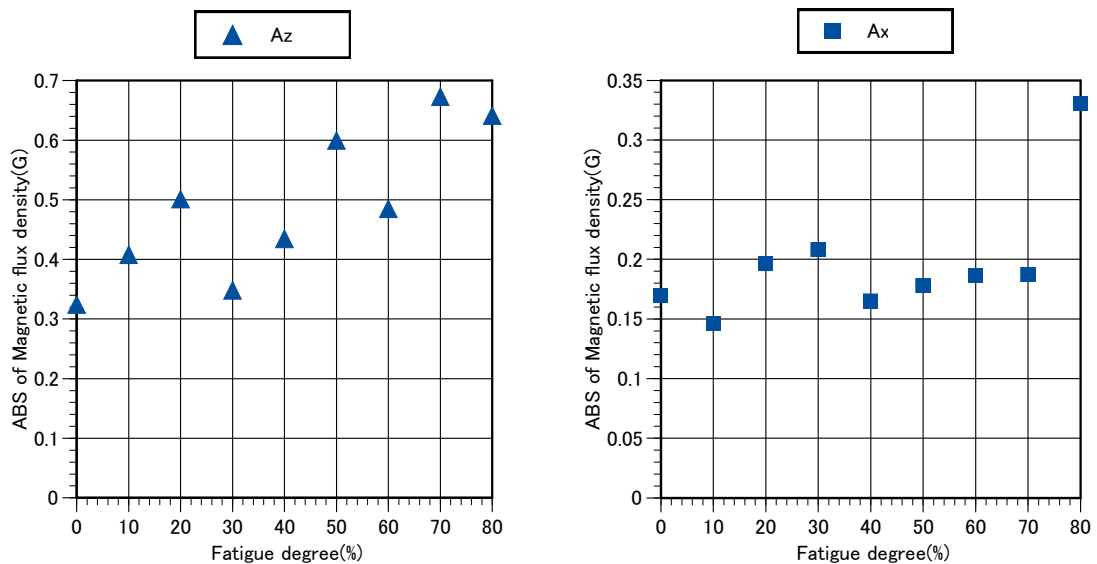
(b) Normal and tangential components from residual magnetization.

FIG. 3-65. Maximum magnetic leakage flux from active and residual magnetizations at each fatigue Phase (Type 304).

Similarly to the case of Type 304, for STS410 we obtain the distribution of the leakage flux components from the active and residual magnetization in FIG. 3-66 and the maximum components of the leakage flux at each fatigue phase in FIG. 3-67. Since STS410 is ferromagnetic, all the distributions of the leakage flux show typical patterns around the notch, which become complicated shape for larger fatigue degree. The normal component of the leakage flux from the active magnetization and the tangential component from the residual magnetization seem to increase for larger fatigue degree.
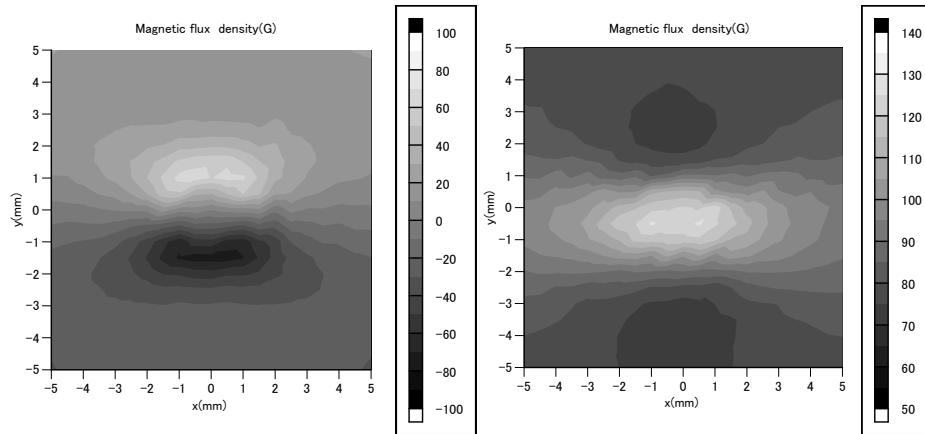
(a) Normal and tangential components from active magnetization (0% fatigue).
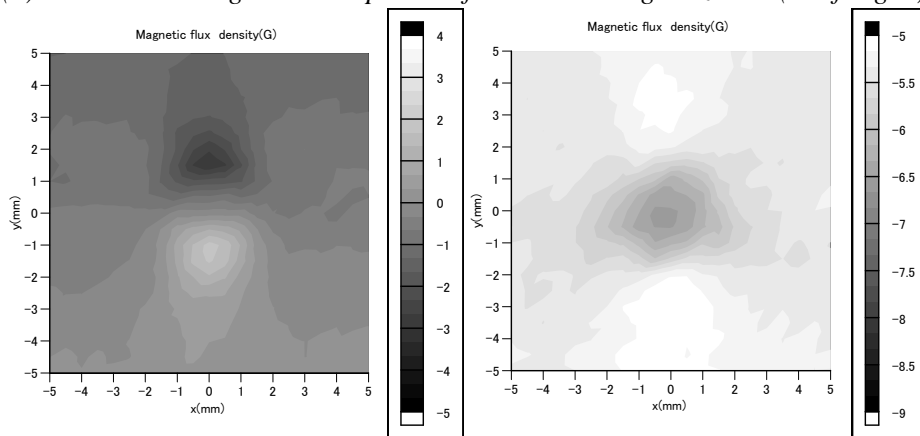
(b) Normal and tangential components from residual magnetization (0% fatigue).
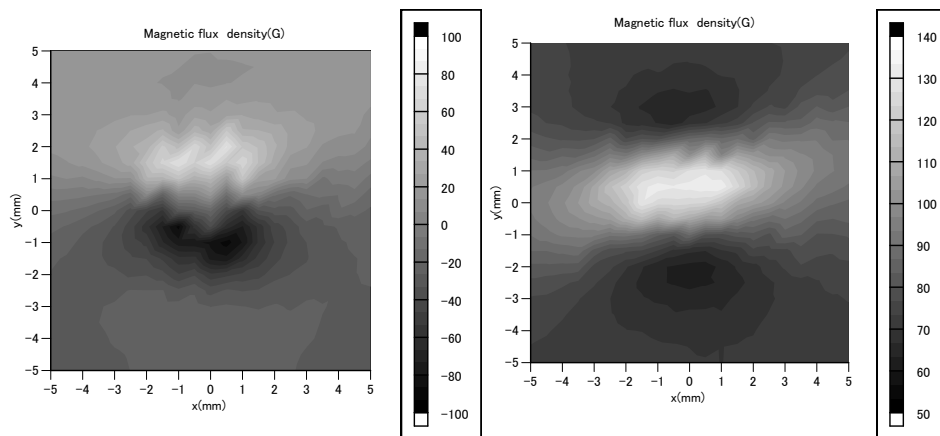
(c) Normal and tangential components from active magnetization (80% fatigue).
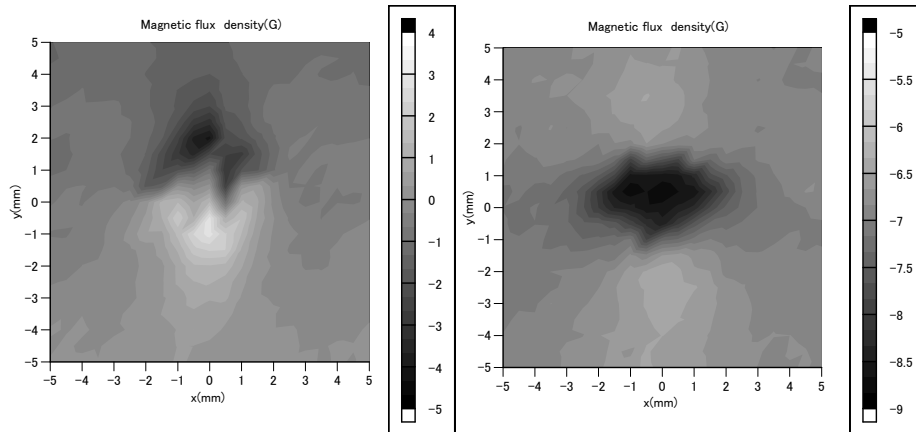
(d) Normal and tangential components from residual magnetization (80% fatigue).

FIG. 3-66. Distribution of magnetic leakage flux from active and residual magnetizations (STS410).
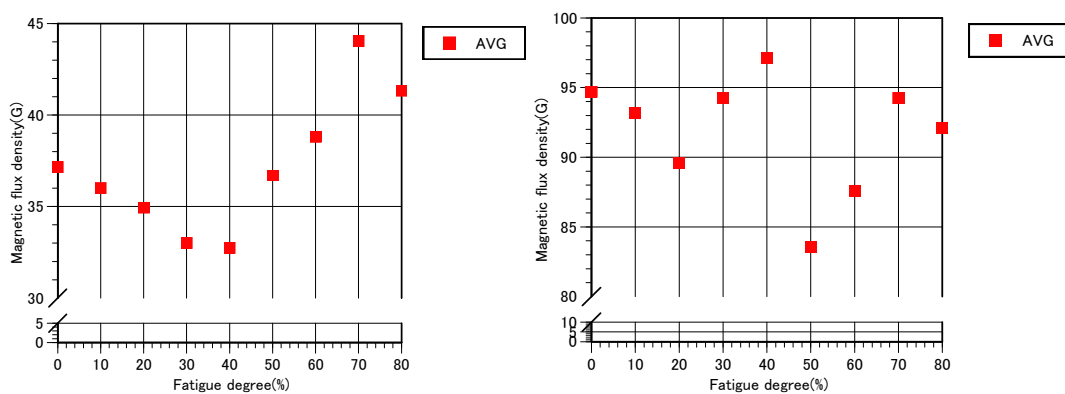
(a) Normal and tangential components from active magnetization.
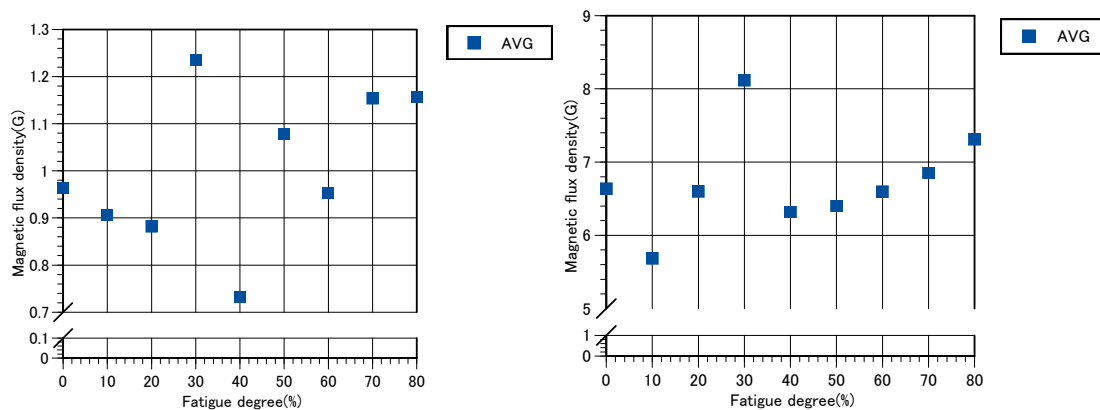
(b) Normal and tangential components from residual magnetization.

FIG. 3-67. Maximum magnetic leakage flux from active and residual magnetizations at each fatigue phase (STS410).

216

3.2.6.3.   Magnetoacoustoelasticity

Since the speed measurement of ultrasonic waves for acoustoelasticity or magnetoacoustoelasticity needs a certain level of specimen depth enough to distinguish the reflected echoes. Thus we have not applied the method to Type 316NG specimens. We apply the magnetic field to Type 304 and STS410 specimens along their axis by the electromagnet with 3.0A current. We measure the wave speed at each current 0.01A from 0A to +0.2A or -0.2A and each 0.1A for the other region. FIG. 3-68 shows the variation of the longitudinal wave speed under the magnetic field in the specimen at each fatigue degree. We see that the speed does not change by the magnetic field at each fatigue degree, which implies that the magnetoelastic effect is not large in Type 304 even when the ferromagnetic phase may be induced in some extent at fatigued specimen. Similar trends are found in the wave speeds of the transverse ultrasonic waves polarized to the anisotropy axes, i.e. the longitudinal and the width axes of the specimen. Thus we pay attention to the wave speed at 0A, at the demagnetized state. FIG. 3-69 shows the speeds of the longitudinal and the two transverse waves at each fatigue degree. Only the speed of the transverse wave oscillating in the width direction of the specimen seems to increase with fatigue degree.
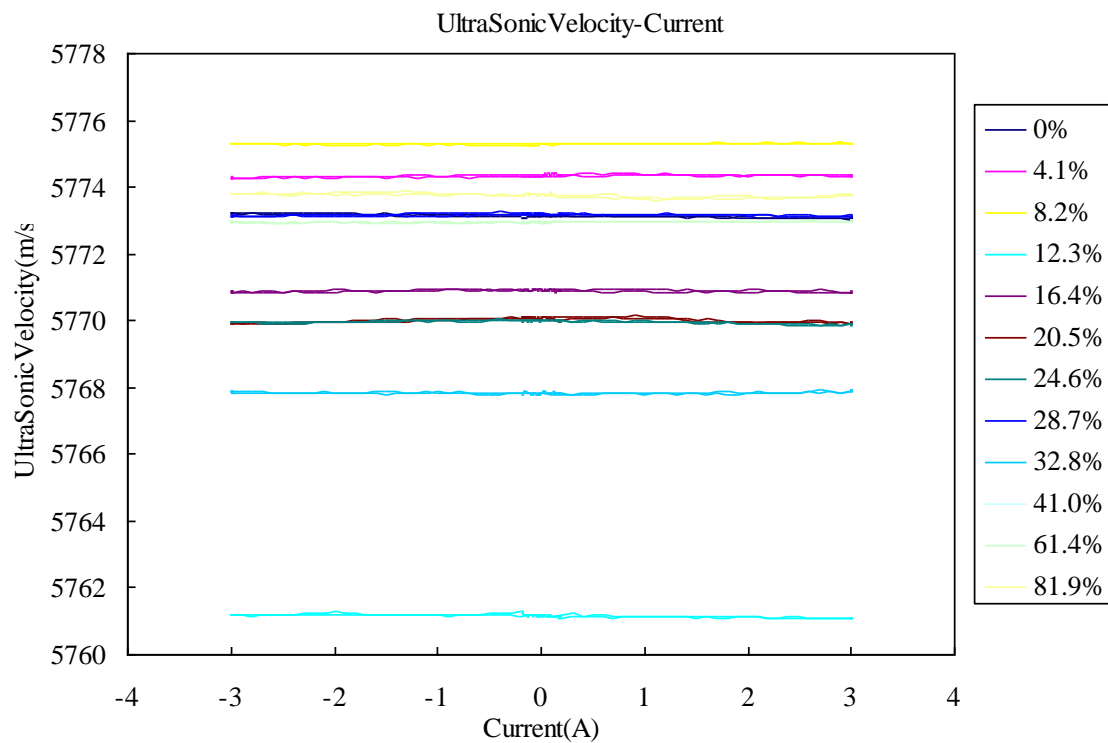
FIG. 3-68. Speed change of longitudinal ultrasonic wave under magnetic field at each fatigue phase (Type 304).
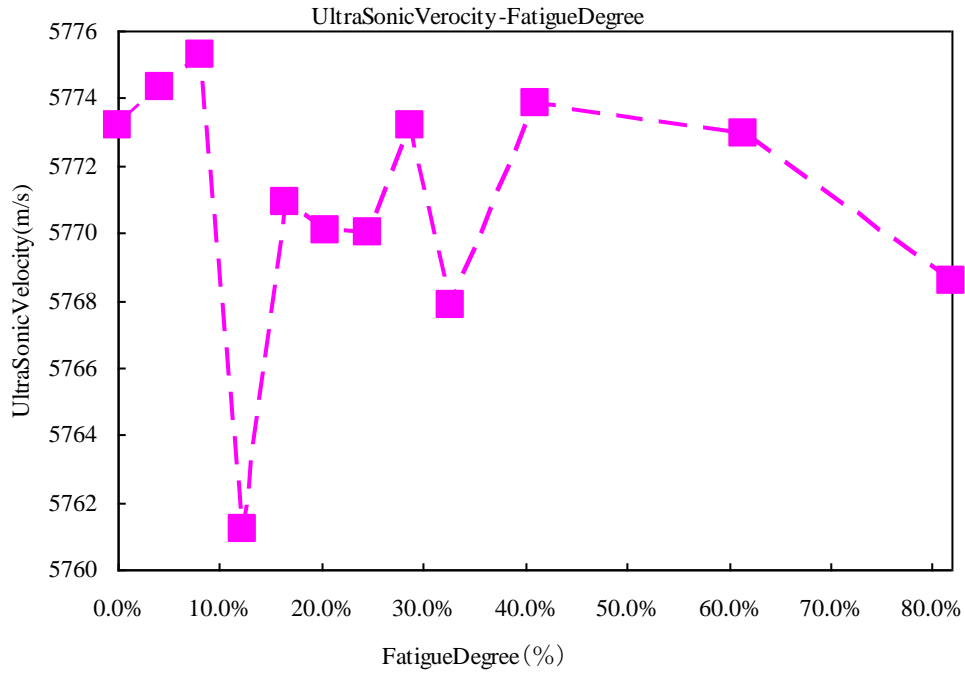
(a) Longitudinal wave.
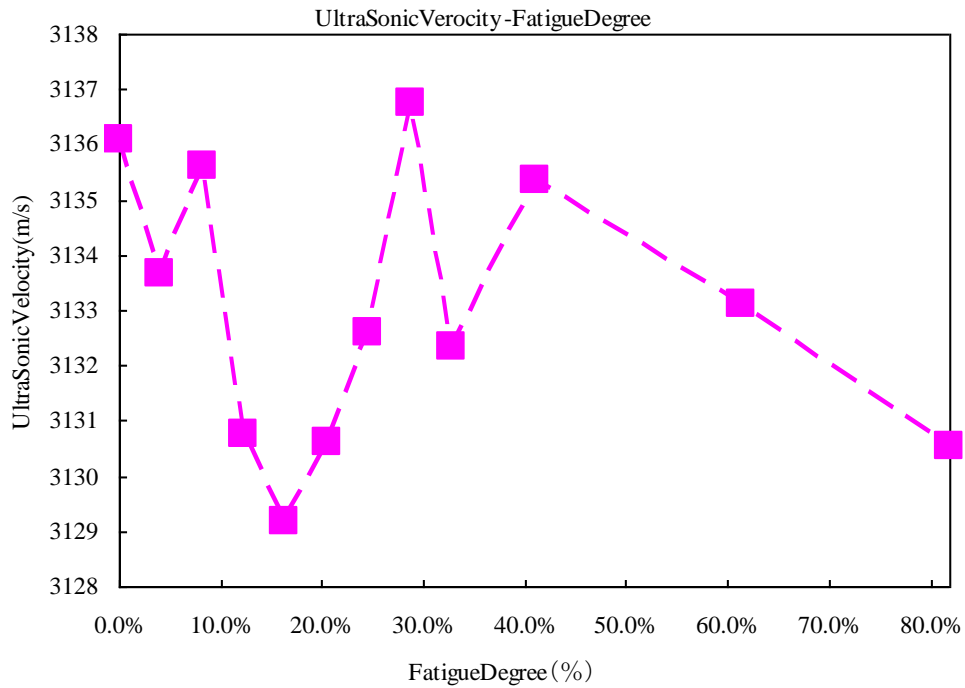
(b) Transverse wave oscillating in parallel direction to specimen axis.
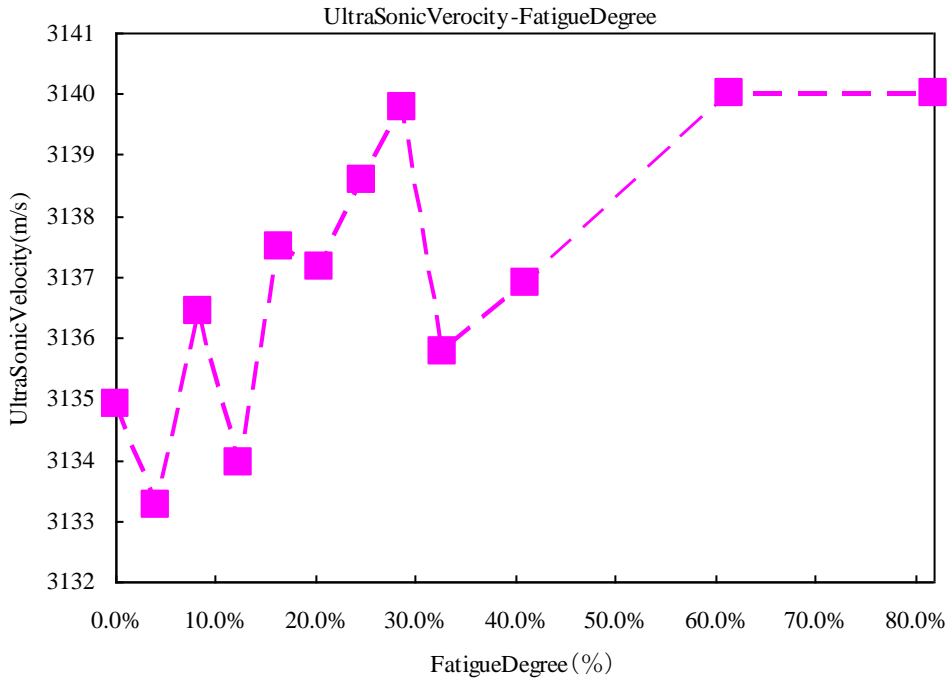
(c) Transverse wave oscillating in normal direction to specimen axis.

FIG. 3-69. Speed change of ultrasonic waves at each fatigue phase (Type 304).

Similarly to the case of Type 304, for STS410 we measure the wave speeds of the longitudinal and two transverse waves at demagnetized and magnetized states at each fatigue degree. FIG. 3-70 shows the change of the speeds of the three waves under the magnetic field at each fatigue degree.
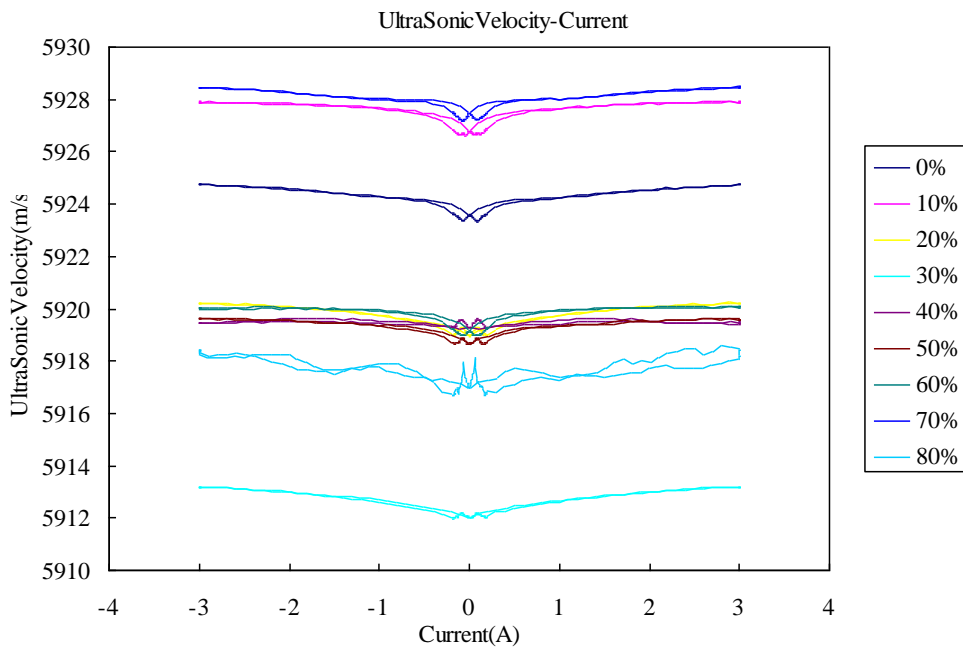
(a) Longitudinal wave.
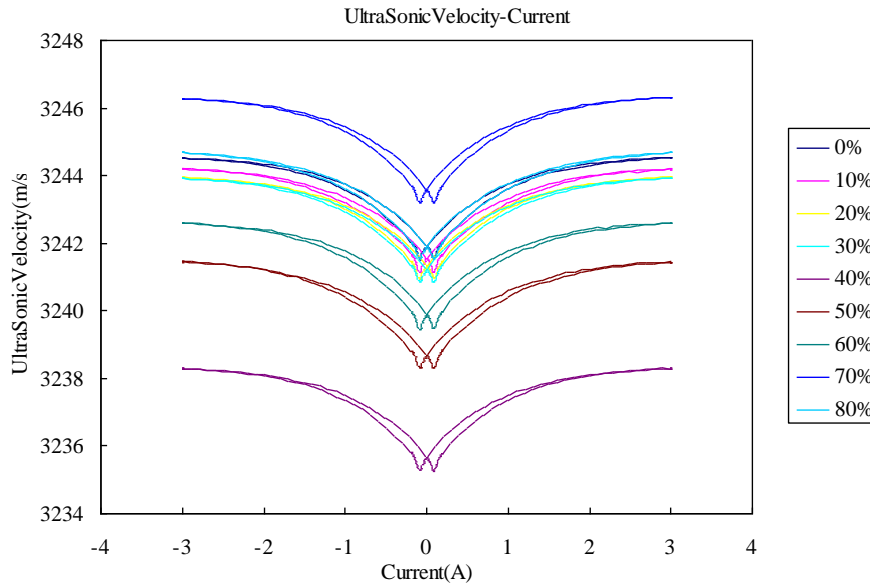
(b) Transverse wave oscillating in parallel direction to specimen axis.
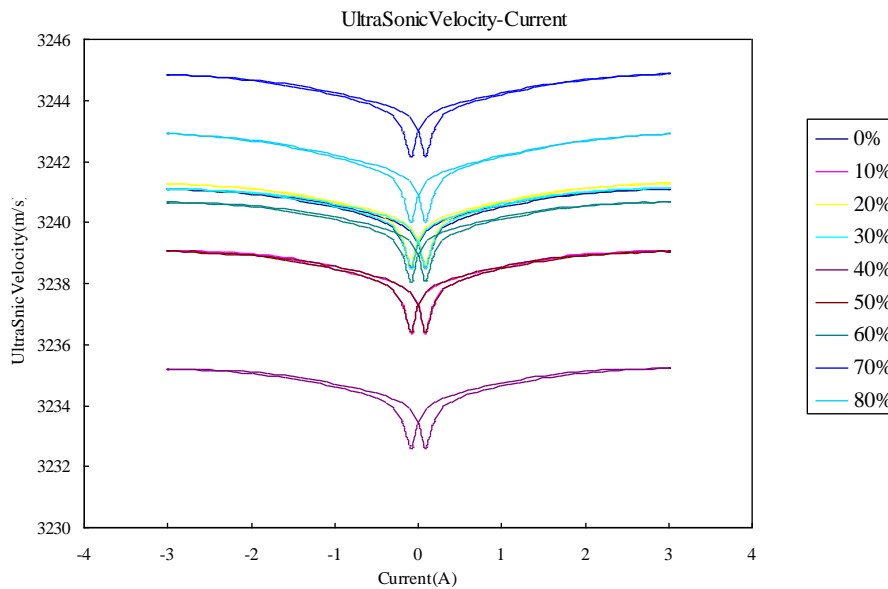
(c) Transverse wave oscillating in normal direction to specimen axis.

FIG. 3-70. Speed change of ultrasonic waves under magnetic field at each fatigue phase (STS410).

It is found that the speed of each wave at each fatigue degree changes by the applied magnetic field with a small hysteresis. The speed of the transverse wave oscillating in parallel direction to the specimen axis changes most largely by the magnetic field. From the value of each curve at 0A, we have the speed of each wave at the demagnetized state as in FIG. 3-71. The speed of the transverse wave oscillating in the normal direction to the specimen axis seems to increase with the fatigue degree. Taking the difference of the speeds of each wave at 3.0A and 0A, we have the speed change of the wave by magnetization caused by the magnetoelastic or magnetoacoustic effect as shown in FIG. 3-72. Form the figure, we see that the speed change of the transverse wave oscillating in the parallel direction to the specimen axis by magnetization seems to increase with fatigue degree.

UltraSonicVerocity-FatigueDegree
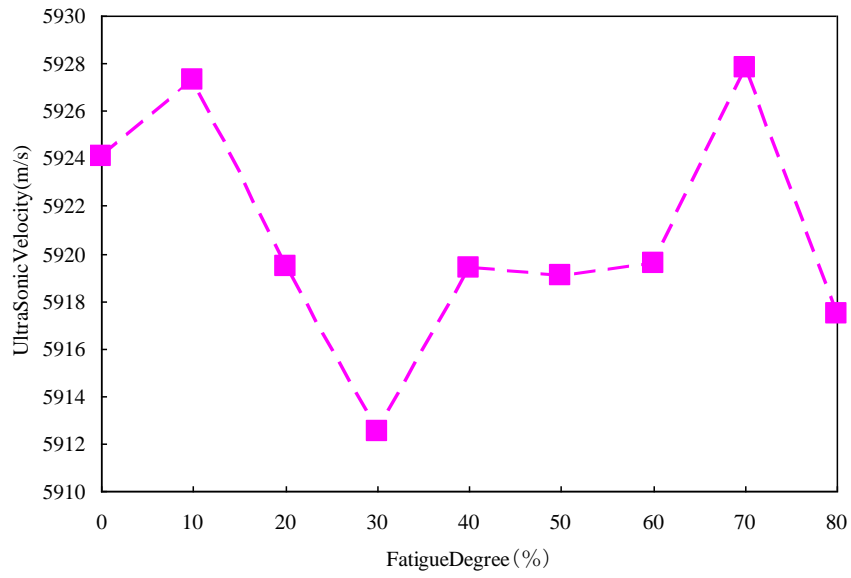
(a) Longitudinal wave.

UltraSonicVerocity-FatigueDegree
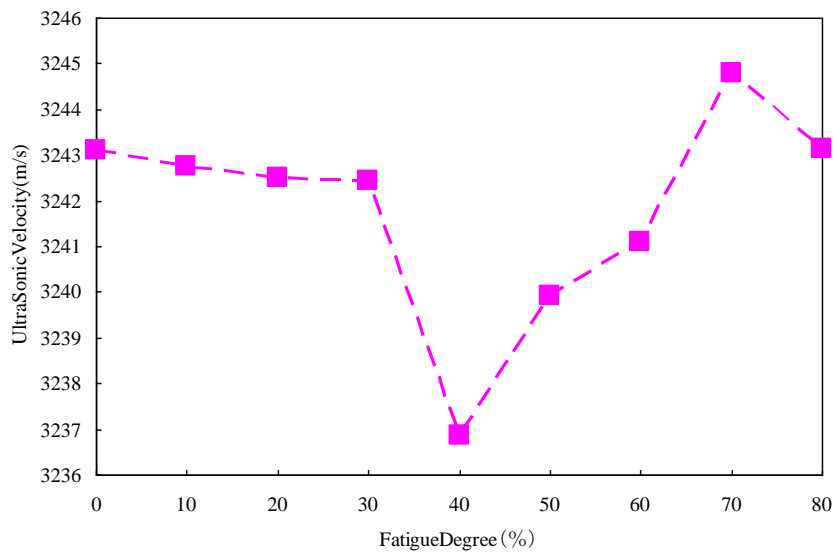
(b) Transverse wave oscillating in parallel direction to specimen axis.

UltraSonicVerocity-FatigueDegree
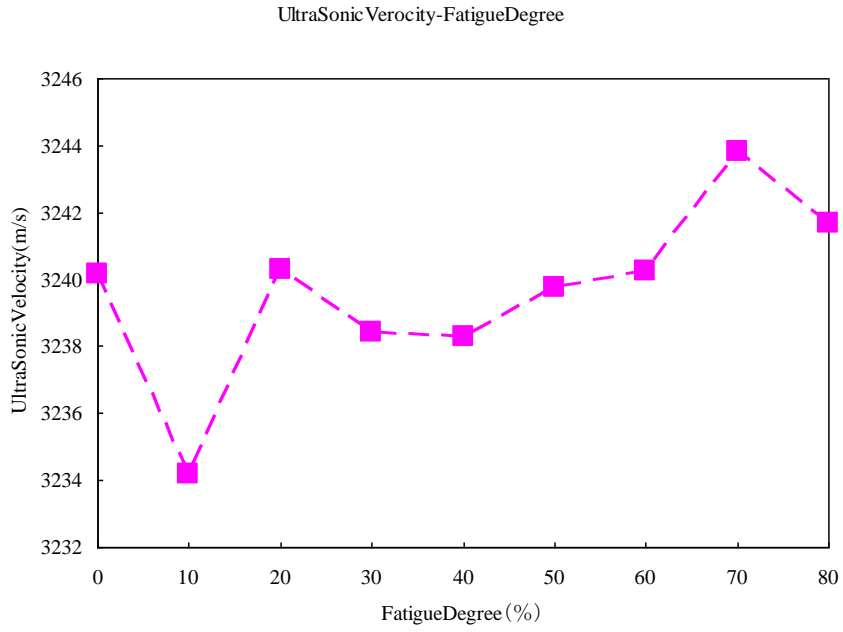
(c) Transverse wave oscillating in normal direction to specimen axis.

FIG. 3-71. Speed change of ultrasonic waves at each fatigue phase (STS410).
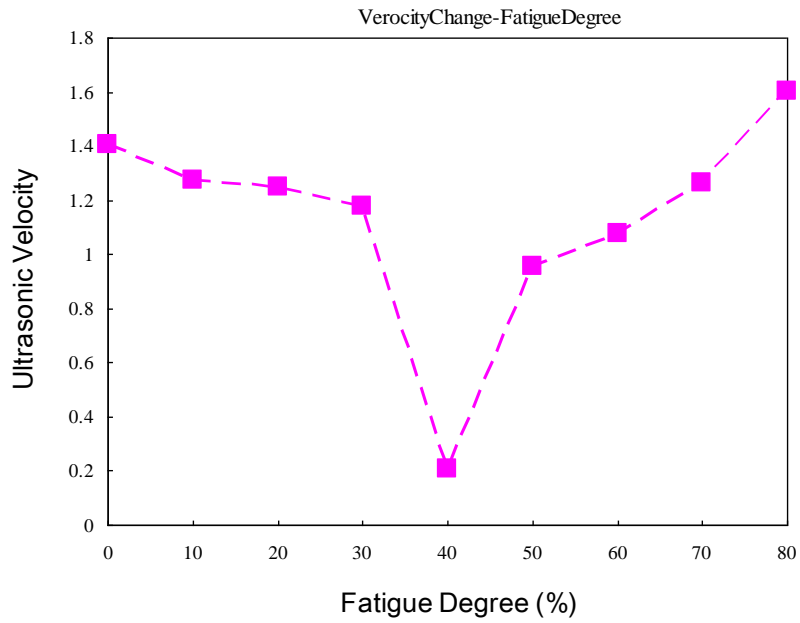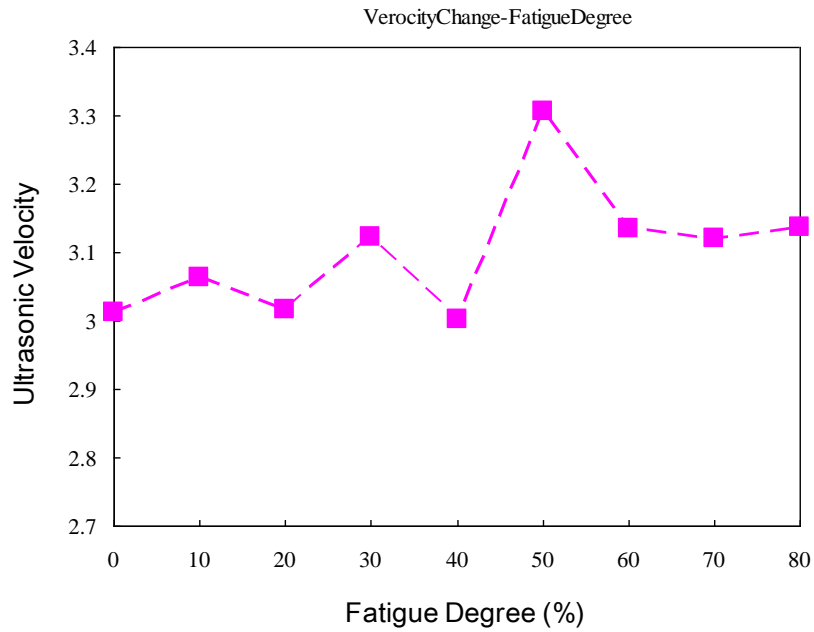
VerocityChange-FatigueDegree

(a) Longitudinal wave.

(b) Transverse wave oscillating in parallel direction to specimen axis.
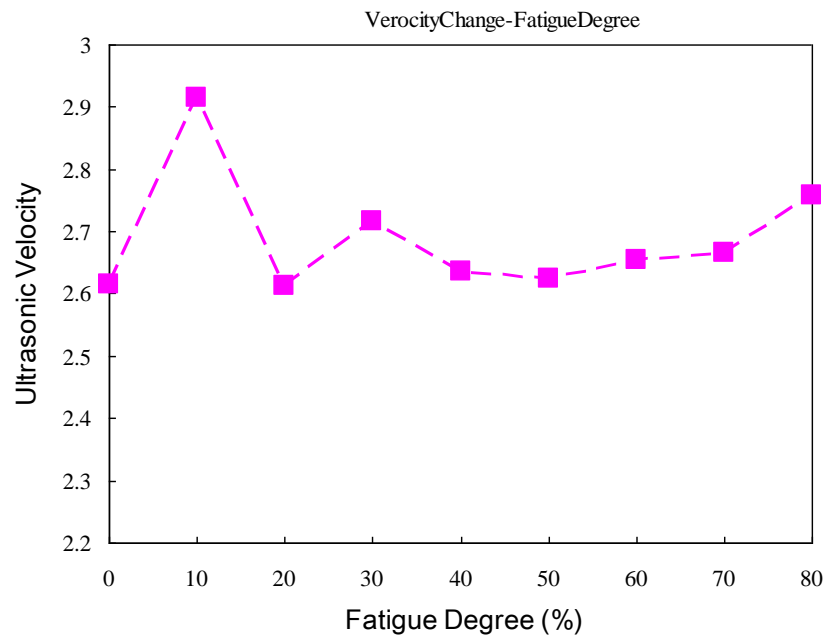
(c) Transverse wave oscillating in normal direction to specimen axis.

FIG. 3-72. Speed change of ultrasonic waves by magnetization at each fatigue phase (STS410).

3.2.6.4. Magnetic acoustic emission

Measurement of magnetic acoustic emission needs a certain level of the magnetized volume because it is a stochastic process and little number of emissions occurs in austenite stainless steels. Thus we have not measured MAE for Type 316NG specimen. We apply the cyclic magnetic field with 0.1Hz and amplitude 40kA/m along the specimen axis and measure the number of emissions at each 0.1 sec. FIG. 3-73 shows the distribution of the frequencies of the magnetic acoustic emissions at each 0.1sec in one-cycle of the magnetic field for Type 304 specimen. There is no apparent variation

in one-cycle, while the frequency level seems to slightly increase by fatigue. In fact, FIG. 3-74(a) shows that the total of MAEs in one-cycle of the magnetic field seems to increase with fatigue degree. FIG. 3-74(b) shows that the maximum count at 0.1sec, i.e. the peak value of the frequency distribution has no apparent trend with fatigue degree.
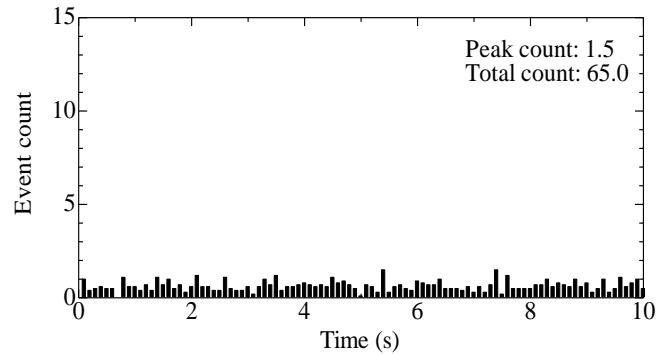
(a) 0% fatigue.
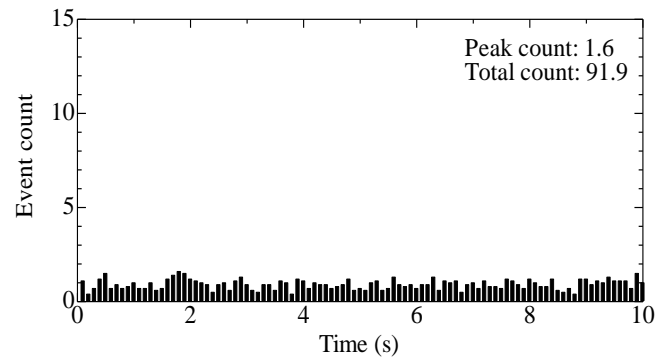
(b) 80% fatigue.

FIG. 3-73. Distribution of MAE frequencies at 0.1sec (Type 304).
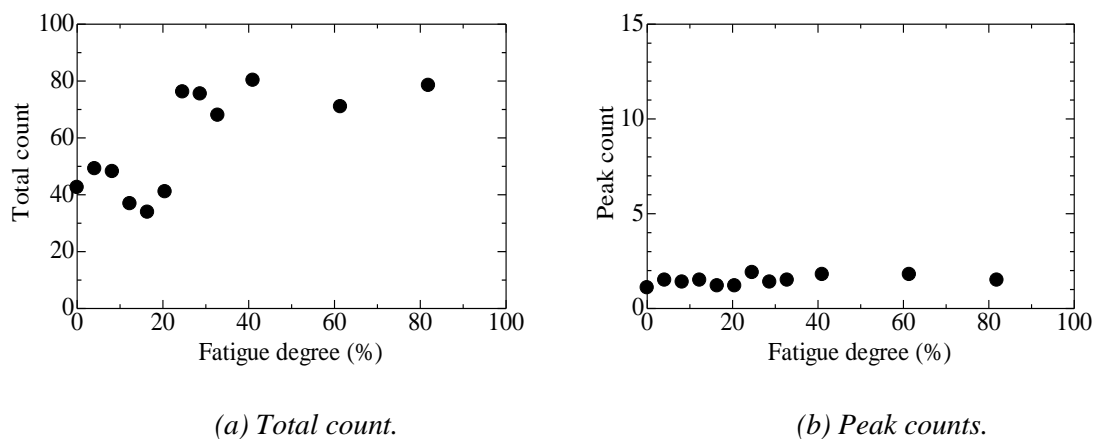
| *(a) Total count.* | *(b) Peak counts.* |

FIG. 3-74. MAE counts at each fatigue phase (Type 304).

In a similar way we measure MAE of STS410 specimen. From FIG. 3-75 we see that the frequencies distribution has two peaks at which the slope of M-H curve becomes the maximum. This fact implies that increase of the magnetization of the ferromagnetic material by the magnetic field

follows the domain wall movement and hence MAEs. According to fatigue, the bias counts of the emissions seem to increase. In fact, FIG. 3-76 shows that the total count of MAEs increases when the fatigue degree exceeds 30%. In this case the peak count does not show the apparent trend with fatigue degree. It is known that both the total and the peak counts of MAEs depend on the applied stress, so that we can distinguish the effects by the stress and the fatigue by observing the peak count.

| (a) 0% fatigue. | (b) 80% fatigue. |
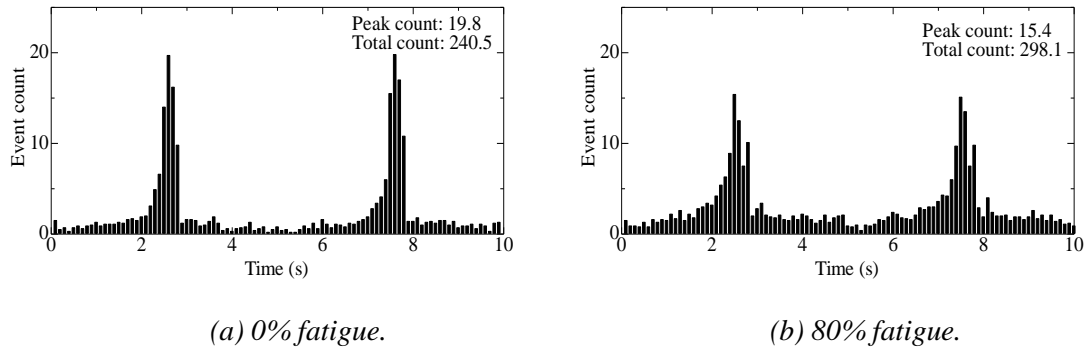
FIG. 3-75. Distribution of MAE frequencies at 0.1sec (STS410).

| (a) Total count. | (b) Peak counts. |
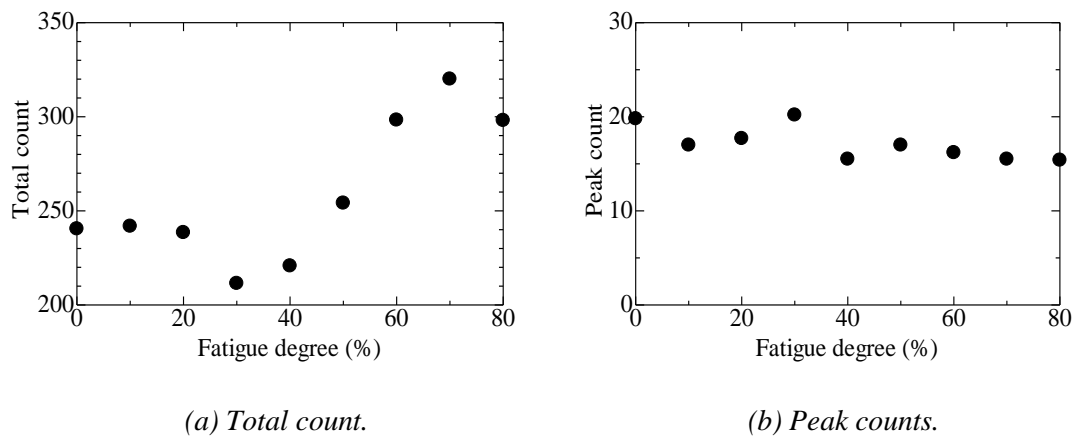
FIG. 3-76. MAE counts at each fatigue phase (STS410).

3.2.6.5. Piezoelectric thin film

As stated in Section 3.2.5.5, we only applied this method to demonstrate the mechanical inhomogeneity induced by fatigue. That is, we measured the electric potential distribution on PVDF film attached on the Type 316NG specimen with 80% fatigue. In order to avoid the discontinuous electric conditions at the specimen edge, we attach the film with 40mm x 15 mm area whose width is larger than the specimen. We apply 0.15% strain along the specimen axis and measure the electric potential at each 1mm lattice point. FIG. 3-77 and TABLE 3-8 show the measurement results to determine the electromechanical coefficients p_1 and p_2 of PVDF films with 30μm and 40μm thickness in Eq. (27). That is, we attach a single layer PVDF film on a specimen with the sensitive (stretching) direction (a) parallel and (b) normal to the uniaxial tension. From the relation between the measured voltage and the longitudinal and transverse strains, we can obtain two coefficients for the films with different thicknesses. We laminate two PVDF films of 40μm thickness with sensitive direction perpendicular to each other and measure the electric potential distribution on the most upper surface of the films. The result is given in Fig. 60 in the CRP main report. Since the specimen width is the minimum at the centre and the stress and the strain becomes the maximum there. The obtained potential distribution, however, shows the strain becomes much larger around the notch than expected

from the stress concentration due to the specimen shape. This fact may be caused by the local decrease of the elastic coefficients by fatigue.

(a) Parallel to uniaxial stress.   *(b) Normal to uniaxial stress.*
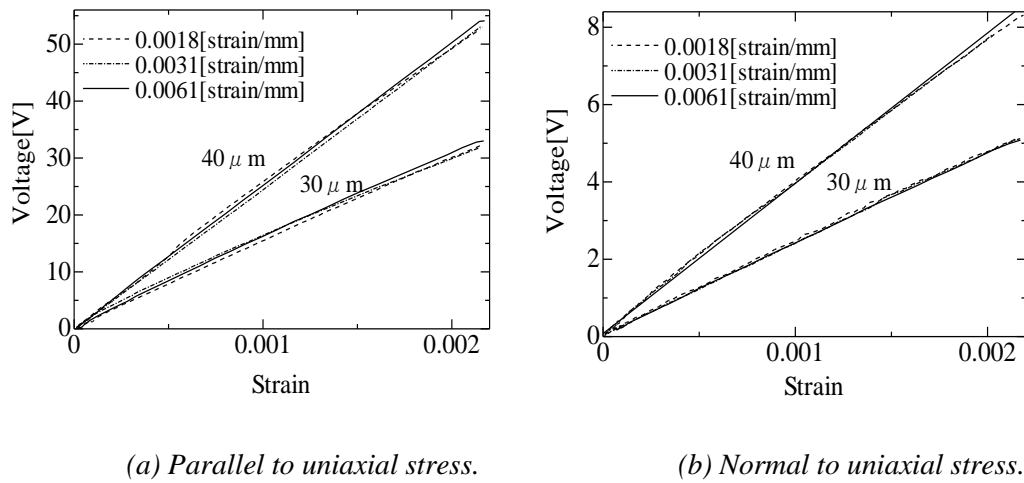
FIG. 3-77. Determination of electromechanical coefficients of single layer PVDF film.

TABLE 3-8.   ELECTROMECHANICAL COUPLING COEFFICIENTS OF TWO KINDS OF PVDF FILMS

PVDF thickness	p_1[V]	p_2[V]
30μm	1.90×10^4	9.81×10^3
40μm	3.19×10^4	1.63×10^4

3.2.6.6.   Hysteresis heating method

We apply the cyclic magnetic field to Type 316NG specimen by the magnetizer with 60Hz along the axis during 70sec, and measure the temperature distribution by the thermograph as the infrared image with several frames per second. In FIG. 3-78 we average the temperature in central 30mm x 45mm area including notch on the specimen surface for each second. We see that the temperature rise becomes larger with fatigue degree, whose result is shown in Fig. 61(a) in the CRP main report.
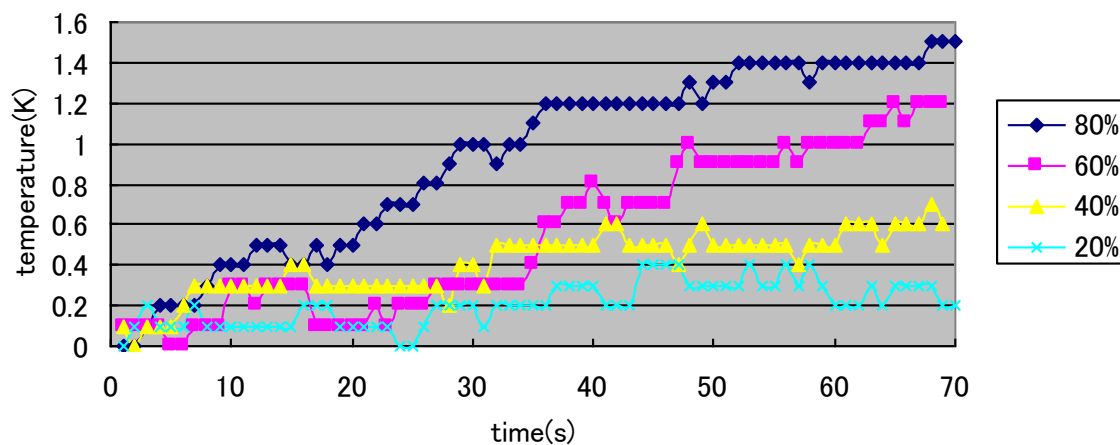
FIG. 3-78. Temperature rise around notch by magnetic hysteresis heating at each fatigue phase (Type 316NG).

We next apply the cyclic magnetic field to Type 304 specimen with each fatigue phase during 40sec and measure the temperature distribution. The averaged temperature change during hysteresis heating is shown in FIG. 3-79. Here the averaged temperature at 80% fatigue has a periodic variation, which may come from the characteristics of the magnetizer to avoid its excess temperature rise.
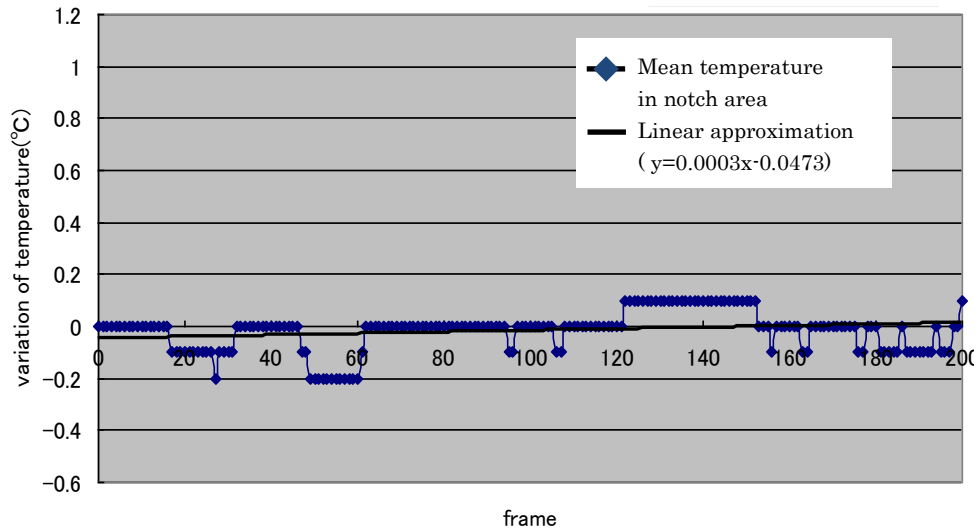
(a) 0% fatigue.
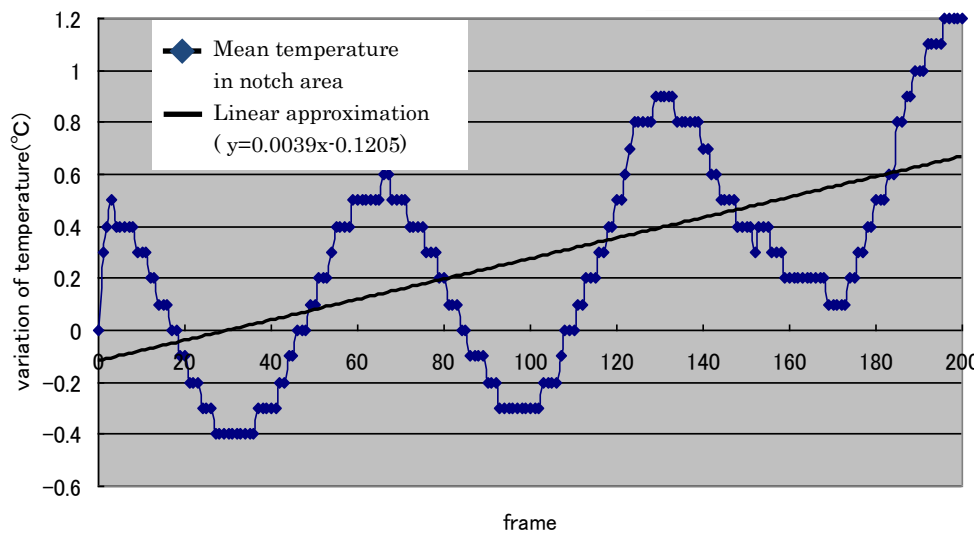
(b) 80% fatigue.

FIG. 3-79. Temperature variation around notch during magnetic hysteresis heating (Type 304).

To obtain some effective temperature rise by hysteresis heating, we approximate the curve by a straight line and define the rate of the temperature rise by the slope of the approximated line. Such rate of the temperature rise inside the notch at each fatigue phase is given by FIG. 3-80. A similar tendency can be seen for the side region of the notch in Fig. 61(b) of the CRP main report.
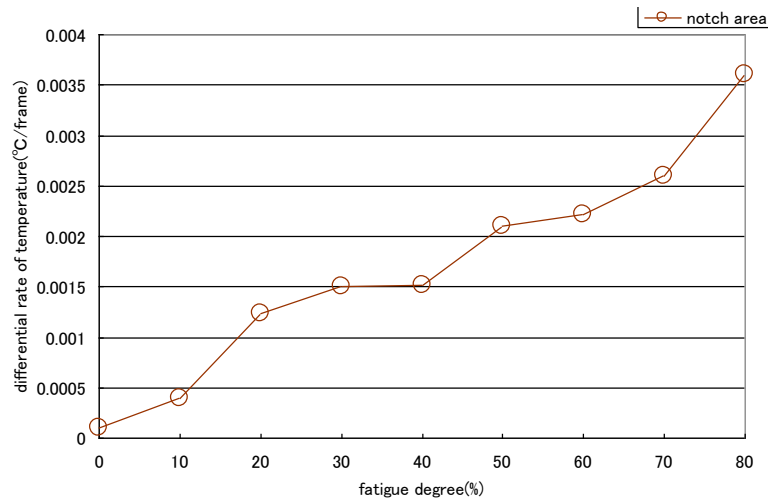
FIG. 3-80. Temperature rise inside notch by magnetic hysteresis heating at each fatigue phase (Type 304).

In case of STS410, the temperature rise by hysteresis heating is much larger even for 0% fatigue because it is a ferromagnetic material. Furthermore the temperature of the specimen is higher than the circumstances after other measurements and it takes a long time for the specimen to be cooled to the stable temperature. To save the time and to obtain the small difference in the temperature change due to fatigue degree, we employed the following procedure in this case. We first measured the temperature variation in the 240sec of the cooling process before heating as FIG. 3-81(a), from which it is expected that the specimen temperature will linearly decreases with time for the same time interval as the heating period. As shown in FIG. 3-81(b), the observed temperature variation during 240sec of heating is large and tends to a stable temperature at which the heat supply and the heat transfer to the circumstances are balanced. Thus we approximate the measured temperature rise by least square method as the heat retardation form;

$$T(t) - T(0) = A\left(1 - e^{-Bt}\right) \tag{33}$$

We regard approximated value A as the temperature rise from the temperature at $t=0$ for a long heating period. Then we employed the sum of the estimated temperature decrease given by the above linear extrapolation and the estimated temperature rise A as the temperature rise by hysteresis heating.

(a) Temperature variation before heating (example).

(b) Temperature variation during magnetic hysteresis heating (example).
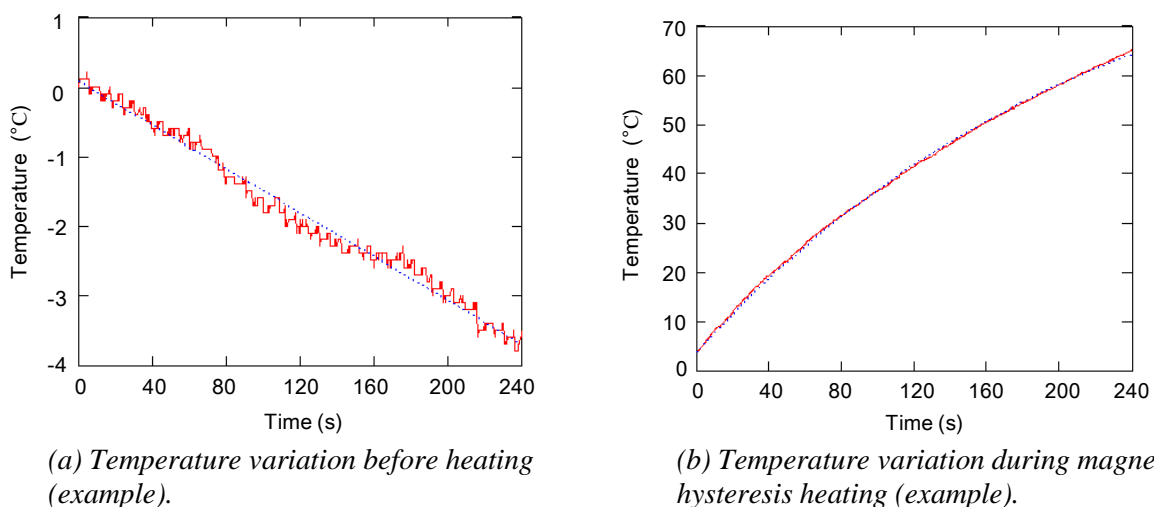
FIG. 3-81. Temperature variation (cooling and heating process) and approximated curves (STS410).

228

The estimated temperature rise in the anteroposterio region of and inside the notch by hysteresis heating is plotted for each fatigue degree in FIG. 3-82. Similarly, estimated temperature rise in the side region of the notch is shown in Fig. 61(c) in the CRP main report.
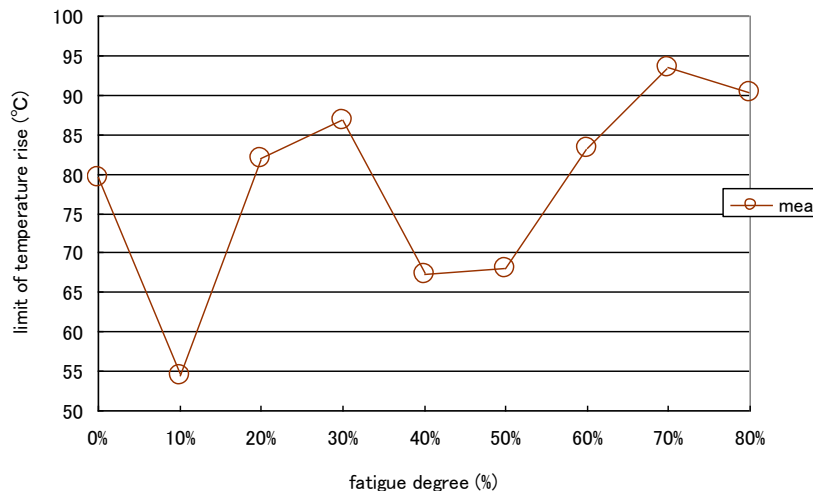
(a) Estimated temperature rise in inside notch.
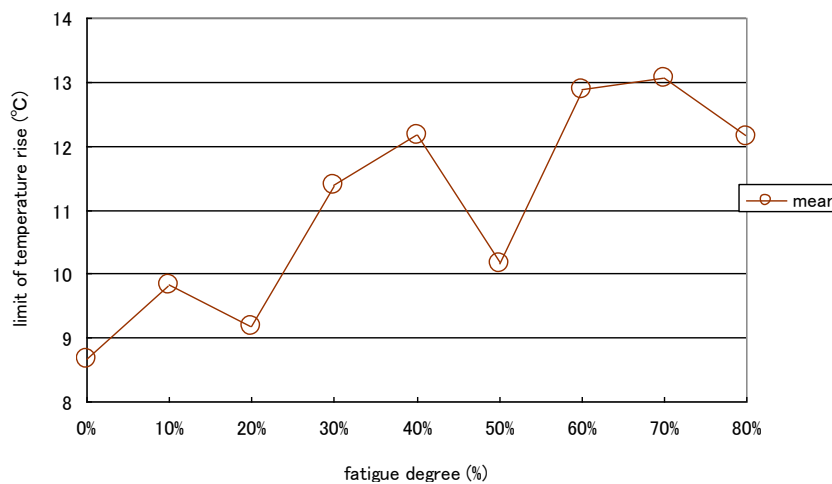
(b) Estimated temperature rise in anteroposterio region of notch.

FIG. 3-82. Estimated temperature rise by magnetic hysteresis heating at each fatigue phase (STS410).

3.2.6.7. Electrical conductivity

The measured results of the electromagnetic impedance on the Type 304 are shown in FIG. 3-83. Here ΔZ is the impedance variations at each excite current from the impedance at 0A. According as the fatigue degree increases from 20% to 60%, the maximum values of ΔZ (ΔZ_{max}) also increase. FIG. 3-84 shows ΔZ_{max} for each fatigue degree. ΔZ_{max} rises up slightly up to 30% fatigue degree, and then increases substantially up to 60%. When the fatigue degree exceeds 60%, ΔZ_{max} decreases rapidly. The cause of such a variation of ΔZ_{max} with the fatigue degree is being studied.
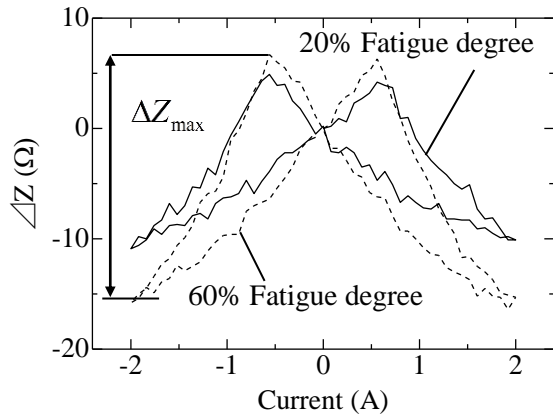
FIG. 3-83. Electromagnetic impedance waves for each fatigue phase (SUS304).
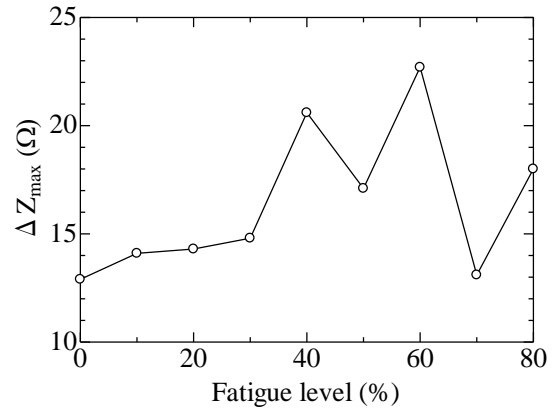
FIG. 3-84. Maximum values of ΔZ for each fatigue phase.

The measured results of the electromagnetic impedance on the STS410 are shown in FIG. 3-85. By comparison of the results for STS410 and Type 304, the variation of ΔZ_{max} with the fatigue degree is found to be lower for STS410. However, the shape of the ΔZ-current curve changes with the fatigue degree. FIG. 3-86 shows the ninth coefficients in the polynomial approximation by the least square method for the ΔZ-current curve, which is indicated by the red line in FIG. 3-85 for 60% fatigue degree. The ninth coefficient seems to increase with fatigue degree.
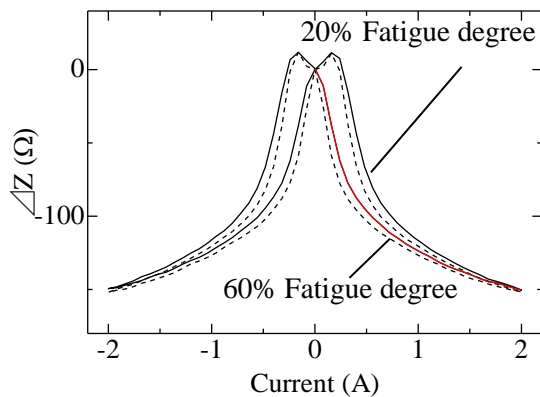
FIG. 3-85. Electromagnetic impedance waves of for each fatigue phase (STS410).
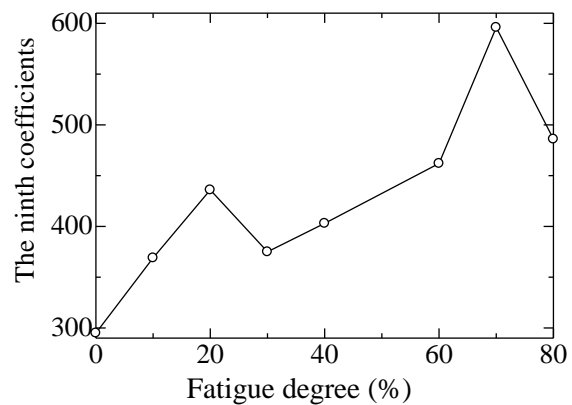
FIG. 3-86. The ninth coefficients for each fatigue phase.

3.2.7.   Results of eddy current testing

The eddy current measurements were made using an absolute shielded probe (mm in diameter) and a Nortec 500d instrument, at 12 kHz, 100 kHz, 250 kHz and 500 kHz. An x-y scanner with computer controlled software was used to scan the specimens and record the complex probe impedance measurements as a function of frequency and spatial location (FIG. 3-87). FIG. 3-88 shows two examples of the real (FIG. 3-88(a) and (c)) and imaginary components (FIG. 3-88(b) and (d)) of the complex probe impedance from Type 304 specimen with nominally 0% (FIG. 3-88(a) and (b)) and 80% (FIG. 3-88(c) and (d)) fatigue damage. FIG. 3-89 summarizes the eddy current measurements for the Type 304 and Type 316NG mechanical fatigue specimens. Measurements on STS410 specimens were not conducted due to the need for a saturation probe that drives the ferritic material to saturation and eliminates the effect of variable permeability on the eddy current measurements.

FIG. 3-87. Eddy current measurement instrumentation with scanning stage.

(a)

(b)

(c)

(d)
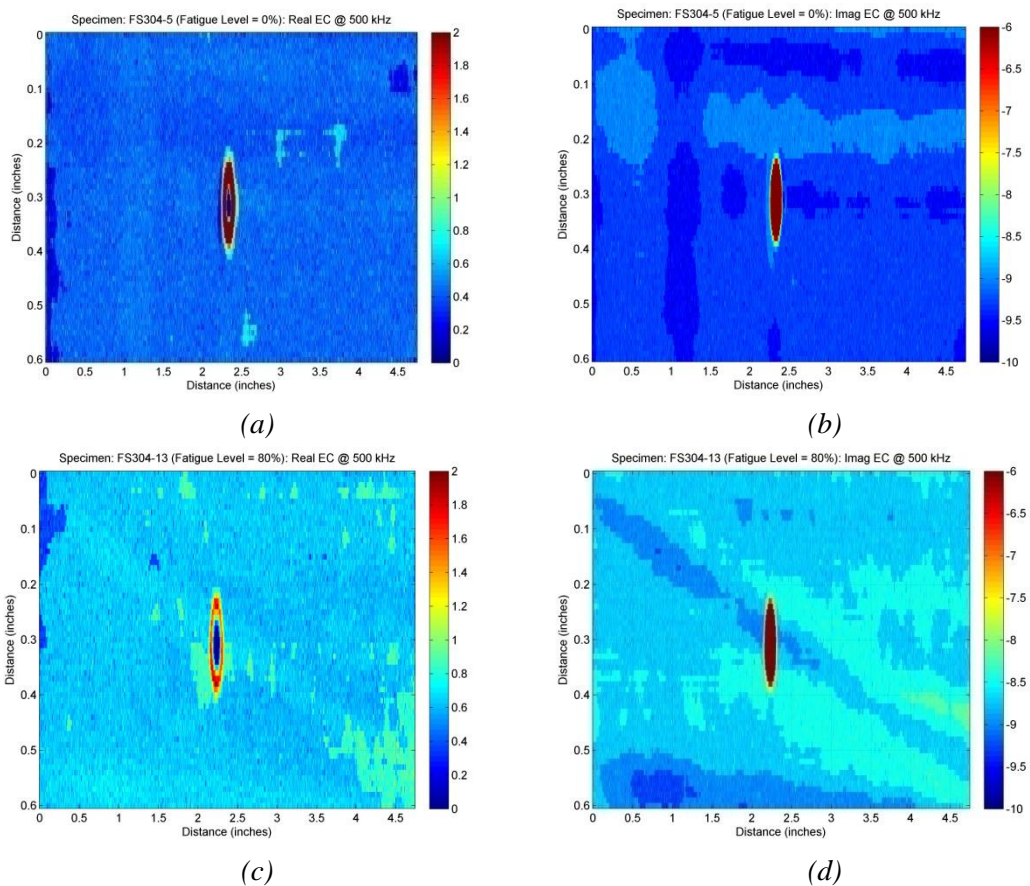
FIG. 3-88. Complex eddy current probe impedance at 500 kHz for Type 304 specimen: (a) Real component, 0% fatigue damage; (b) imaginary component 0% fatigue damage; (c) Real component, 80% fatigue damage; (d) imaginary component 80% fatigue damage.

The data presented are the difference in the phase between measured at two different frequencies, averaged over the scan region. As seen from the data, the change in the measured probe impedance as a function of fatigue is small, though a measurable correlation appears to exist between the measurement and the amount of accumulated fatigue damage.
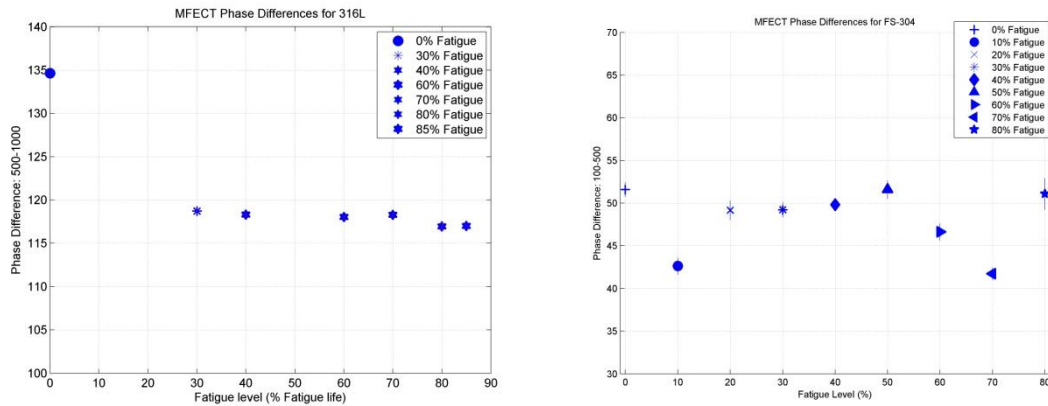
(a) Type 316NG.   (b) Type 304.

FIG. 3-89. Difference in eddy current phase at two frequencies.

3.2.8. Results of magnetic Barkhausen noise testing

The MBN measurements were made using an electromagnet with input current control capability to generate the external field. A coil wrapped around the specimens was used to record the MBN data (FIG. 3-90). The applied field strength was sinusoidally varied by controlling the magnet current using a sinusoidal voltage source, with data recorded as a function of applied voltage. FIG. 3-91 and FIG. 3-92 shows an example of the recorded signals from 0% and 80% fatigued STS410 steel and 316L specimens. The MBN energy was computed from the measurements and is plotted as a function of nominal accumulated fatigue level (in per cent) in FIG. 3-93. FIG. 3-93(a) shows the MBN energy for the 316L specimens as a function of fatigue level, while FIG. 3-93(b) shows the same quantity for the STS410 specimens. Each plot shows the results of three independent measurements on the same specimen, to quantify the effect of uncontrollable experimental factors. Again, a likely correlation is observed between the measurements and the accumulated fatigue damage in the specimen. The recorded MBN energy is seen to be higher in the STS410 specimens, due to their higher ferritic content.
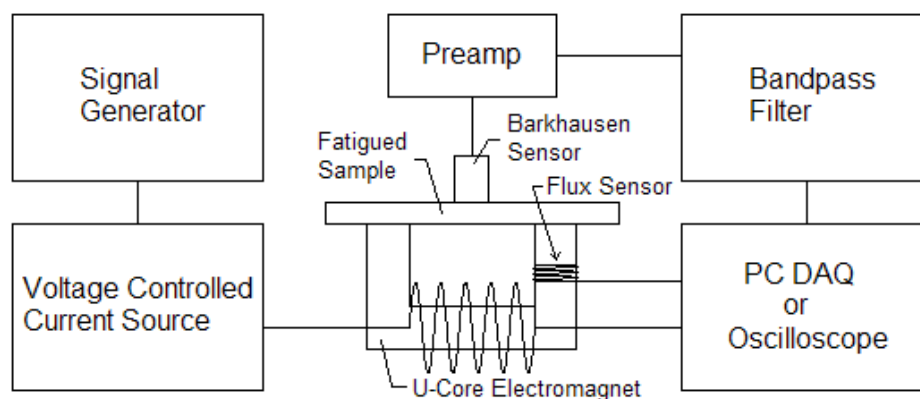
FIG. 3-90. Magnetic Barkhausen noise (MBN) measurement schematic.
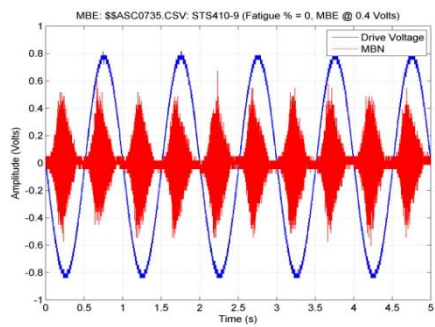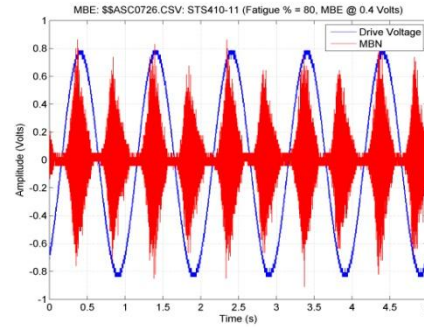
(a)   *(b)*

FIG. 3-91. Magnetic Barkhausen noise (MBN) signal from STS410 with (a) 0% and (b) 80% fatigue level.
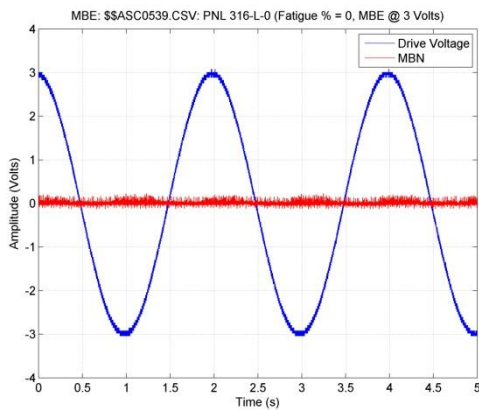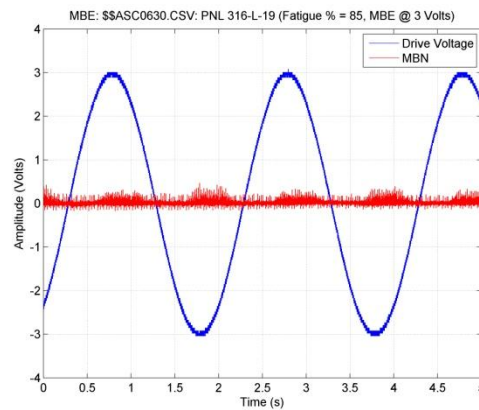
(a)   *(b)*

FIG. 3-92. Magnetic Barkhausen noise (MBN) energy from 316L with (a) 0% and (b) 80% fatigue level.
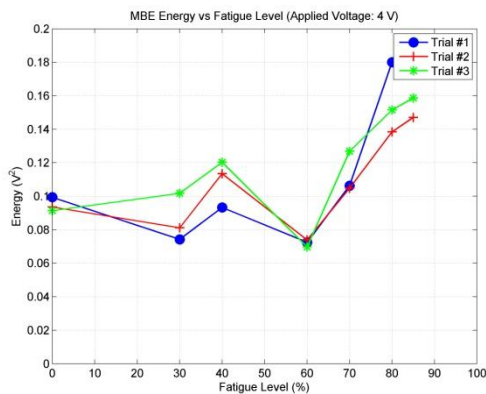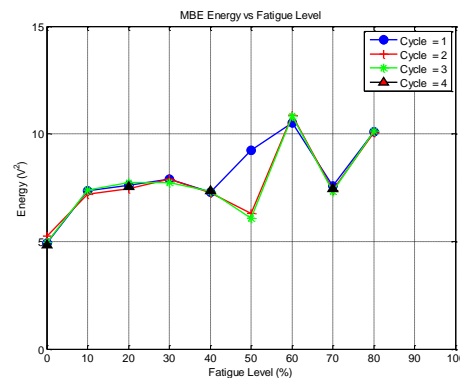
(a) 316L   *(b) STS410*

FIG. 3-93. Magnetic Barkhausen noise (MBN) energy as a function of accumulated fatigue level.

3.3. PROGNOSTICS AND REMAINING USEFUL LIFE PREDICTION

Intuitively it would seem that the RUL in passive components can potentially be estimated by using the following process. Damage accumulates in the material over time due to one or more stressors. The stressor information, as well as the resulting material state, is monitored at periodic intervals using non-destructive testing (NDT) methods. The assessment of material state from NDE measurements requires a model defining the relationship between the material state and the measurement. Given an assessment of the current material state, the RUL can be estimated by using a model of degradation accumulation and growth or development (which is also a function of stressor history). Note that, as additional measurements become available, the current material state estimate and RUL can be updated using the same process and the estimate for RUL refined

Formally, the intuitive approach described above can be described mathematically as follows. Define x_k as the "material state" at time k. The material state is a numeric quantity that describes the condition of the material in the early (or later) stages of damage. In practice, a "damage index", which is generally a scalar quantity between 0 and 1 (corresponding to virgin and cracked material respectively), is computed from the NDE measurements and may be used as a proxy for the underlying material state. Also define z_k as the measurement at time k. The problem of RUL estimation may be decomposed into two related problems as discussed above – the first is the estimation of the material state x_k from the measurements z_k, and the second is the estimation of the corresponding time-to-failure (TTF) and the RUL.

In this section, one potential formulation for estimating the RUL from NDE measurements is described. The formulation enables the application of a statistical algorithm for RUL estimation. Details of the algorithm are provided here, with references for additional information for the interested reader. Other approaches to prognostics are also possible and are not explored further here. The reader is referred to the published literature [58], [59], [60] for details of alternative approaches to prognostics.

3.3.1. Prognostics problem formulation

Several approaches to estimating x_k from z_k exist. In this study, however, the problem is formulated in terms of a state transition (or process) model, that defines the relationship between x_k and x_j ($k > j$). The process model is therefore a model of the accumulation of damage in the material with time. This model may also include information on stressor history, i.e.

$$x_k = f\left(x_j, \sigma_k, \sigma_{k-1}, ...\sigma_j, \eta_k\right) \tag{34}$$

where $\sigma_k, \sigma_{k-1}, ..., \sigma_j$ are the stressor values at times $k, k-1, ..., j$, with $j < k$. An additional term, η_k , is used to represent the uncertainty in the state transition model. Typically, this is represented by a probability density function (PDF). A second model relates the material state (or damage index) to the NDE or online monitoring measurements:

$$z_k = h\left(x_k, \nu_k\right) \tag{35}$$

Again, the stochastic quantity ν_k is used to represent noise in the measurement process.

3.3.2. Material state estimation from measurements

The problem of estimating x_k from z_k using these two models is mathematically identical to the formulation of a tracking problem [61], [62], [63], and therefore, solutions to the tracking problem can also be applied to the material state estimation and prediction problem. Assuming that the functions $f(\bullet)$ and $h(\bullet)$ are linear [64], and that the noise terms are Gaussian distributed, then the optimal solution to the tracking problem can be shown to be the Kalman filter [61]. However, when the

functions are nonlinear and/or the noise terms are non-Gaussian (as is likely in the early degradation estimation problem), then more general solutions to the tracking problem are necessary. One of the generalized solutions to the tracking problem is based on the application of the Monte Carlo method, and is referred to as a sequential Monte Carlo (SMC) algorithm or a particle filter. Basically, the SMC algorithm represents the posterior PDF at time step k by a weighted set of samples:

$$p(x_k \mid z_k) \approx \sum_{i=1}^{N_s} w_k^i \delta(x_k - x_k^i) \tag{36}$$

Here, x_k^i are the samples (or particles) used to represent the posterior density, $i = 1:N_s$, where N_s is the total number of samples used and w_k^i is the weight associated with sample x_k^i. The samples are drawn from the prior distribution $p(x_k^i \mid x_{k-1}^i)$. Normalized weights are generally chosen using the principle of importance sampling [65], and are updated as additional information (i.e. measurements) becomes available. This approach is used in this study. Details of the SMC algorithm are summarized in the literature [66], [67].

3.3.2.1. Implementation

The sequence of steps for estimating the material state is as follows. The posterior PDF of the material state is represented by samples and associated weights. At each time step, N_S samples are sampled from the prior PDF, which relates the state at time step k to the state at time step k-1 using the state transition model. The next step is the assignment of weights to each sample. Weights are assigned using the likelihood PDF (represented by the measurement noise density) which relates material state to NDE measurements.

In general, measurements may not be available at all instants. For instance, in ISI, measurements are only available during an outage (which may occur, on average, once every couple of years). Even with online monitoring, data will be available only at discrete instants in time (for instance, once every few minutes or hours). The traditional particle filter approach can be modified to handle missing measurements at intermediate time steps as discussed in [59].

The result of the particle filter is a PDF that describes the (conditional) probability of occurrence of all possible material states (conditioned on the sequence of measurements) at a given time step. A different PDF is obtained for each time step. A single estimate of the material state can be computed from these densities as either the maximum a posteriori (MAP) or posterior mean estimate (PME) [63]. However, the probability density itself is used to compute the remaining useful life as described next.

3.3.2.2. Remaining useful life (RUL) estimation

The result of the particle filter is a set of PDFs, giving the probability of the material state damage index given the measurement. Estimating the RUL from this information is a two-step process [67]. First, a failure probability density $p(\text{failure at time } k \mid x_k)$ is defined giving the probability of failure for a given damage index or material state. Typically, such a failure density would be defined using either simulation studies or experiments. Using the law of total probability [68], the probability of failure at time k is:

$$p(\text{failure at time } k \mid z_k) = \sum_m p(\text{failure at time } k \mid x_k, z_k) p(x_k \mid z_k) \tag{37}$$

where $p(x_k \mid z_k)$ is the result of the particle filtering algorithm described above. The time-to-failure (TTF) probability density $p(TTF)$ can then be computed using

$$p\left(TTF = r \mid z_k\right) = p\left(\text{failure at time } r \mid z_k\right)\prod_{j=1}^{r-1}\left[1 - p\left(\text{failure at time } j \mid z_k\right)\right] \tag{38}$$

The TTF density gives the probability of failure at all time instants, and the mean TTF is computed as the expected value of this PDF:

$$TTF_e = E\left[p\left(TTF\right)\right] \tag{39}$$

The TTF density can also be used to compute the confidence limits (for instance, the 95% confidence limits) for bounding the mean TTF estimate. The remaining useful life is then the difference between the measurement time instant and the mean TTF estimate.

3.3.3. Prognostics case study

A case study for prognostics was performed using non-linear acoustics measurements [69] on cyclic fatigue-damaged carbon steel. The material state was assumed to be represented by a normalized damage index parameter (computed from the acoustic nonlinearity parameter defined as in [70]) that tracks the accumulation of damage in the material. Nominally, a damage index (DI) of 0 corresponds to a virgin sample, while a DI equal to 1 corresponds to failure, defined as visible macrocrack initiation. However, variations across specimens will result in some specimens failing prior to a DI equal to 1. This variability is captured using a Weibull failure density in this study. The damage process model [69]

$$x_k = 1 - \left[\left(1 - x_j\right)^{n+1} - \frac{k-j}{t_c}\left(1 - \frac{2r_c\left(\bar{\sigma}\right)}{\Delta\sigma}\right)^m\left(n+1\right)\right]^{\frac{1}{n+1}} + \eta_k \tag{40}$$

was used to relate the damage index x_k at time k to the damage index x_j at time j ($k > j$). t_c is a normalizing constant on the order of the number of cycles to failure, $r_c\left(\sigma_0\right)$ is the yield strength, while $\Delta\sigma/2$ is the average stress in a single fatigue cycle. The noise term quantity η_k accounts for any uncertainties in the model. The measurement model assumed that the damage index was measured, with some error due to measurement noise ν_k :

$$z_k = x_k + \nu_k \tag{41}$$

The noise terms were assumed to have a Gaussian or normal distribution with known parameters. The data used in this study is adapted from Kulkarni et al [69] and is shown in TABLE 3-9, with the normalized DI assumed to be measured at intermittent times.

TABLE 3-9. SUMMARY OF DATA USED FOR PROGNOSTICS (adapted from [69])

Number of Cycles	Normalized Damage Index
0	0.28
24640	0.46
27440	0.52
30800	0.62
33040	0.77
33880	0.91
34440	1.00

3.3.3.2.   RUL estimation

FIG. 3-94(a) shows an example of the predicted DI (and the confidence limits) from the SMC filter. The plot shows the true DI (blue, solid line), and the predicted DI (green, stars). The upper and lower 95% confidence intervals are shown in red and black. A single measurement (at k=0) is assumed to be available. The plot also shows the failure density as a color-coded image, and the failure density is assumed to be the same regardless of the time instant. This information is used to compute the TTF density (FIG. 3-94(b)), the mean TTF and the 95% TTF confidence bounds. The RUL is defined as the time difference between the TTF and the measurement instant. Note that, assuming a measurement at, k=0, the RUL is simply an estimate of the time for a visible crack to appear in a virgin (non-fatigued) specimen. Since the approach is Bayesian (and allows for an update step as new measurements become available), the expectation is that the RUL and RUL confidence bound estimates will get better with additional data. The process of updating the RUL estimates as additional data becomes available was repeated using all of the data in TABLE 3-9, and the resulting RUL and RUL confidence bounds are shown in TABLE 3-10. The true RUL is also indicated.

3.3.3.3.   Discussion

The results from this case study indicate that the proposed approach is capable of estimating the RUL and RUL confidence bounds reasonably accurately. However, the estimates are dependent on three factors – a good process model (i.e. model of how degradation evolves and accumulates in the specimen), measurements that are sensitive to the early stages of degradation, and a reasonable failure PDF. In this study, the failure PDF parameters were varied, and the result was not observed to be particularly sensitive to the failure PDF. However, estimates of the error (or noise) in the process and measurement models need to be reasonably good in order to obtain good RUL estimates. This is important since other studies have shown some variability in the measurements obtained (and in degradation evolution) from sample to sample. The process noise terms are necessary to capture this variability and additional studies are needed to define these noise terms for fatigue and other degradation mechanisms.

(a)   (b)
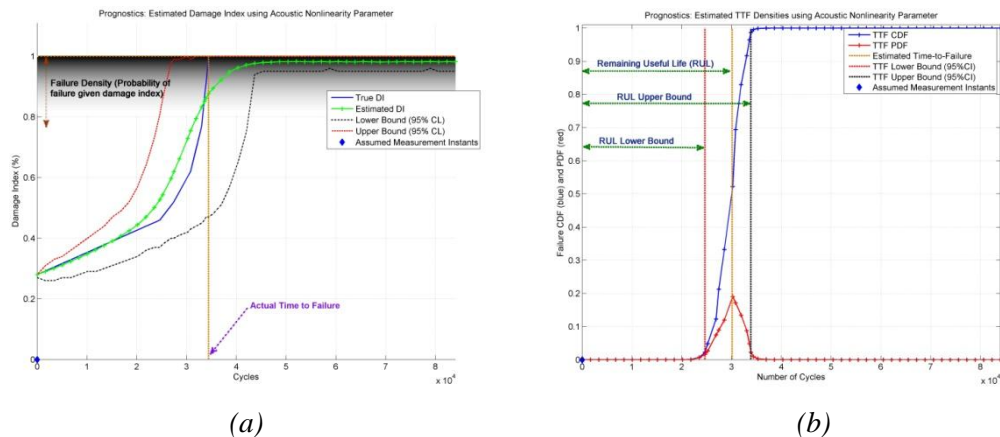
FIG. 3-94. (a) Predicted damage index from a single measurement and (b) the computed TTF density, RUL and RUL confidence bounds.

TABLE 3-10. SUMMARY OF RUL ESTIMATES.

Measurement at (Cycles)	True RUL (Cycles)	Estimated RUL (Cycles)	95% Lower Confidence Bound for RUL Estimate (Cycles)	95% Upper Confidence Bound for RUL Estimate (Cycles)
0	34440	30367	24640	33880
24640	9800	11217	7280	14000
27440	7000	6699	3360	7840
30800	3640	4381	1120	6160
33040	1400	1736	0	2240
33880	560	605	0	1400

3.4. SUMMARY AND OPEN PROBLEMS

TAG #3 in this Coordinated Research Program investigated non-destructive approaches to assessing materials degradation in passive components in operating power reactors, and estimating RUL from such measurements. Mechanical fatigue was chosen as a representative degradation mechanism for this study, and several NDE methods for assessing the material state were investigated. The results indicate that both electromagnetic and acoustic NDE approaches are capable of determining material state when degradation is the precursor (or early degradation) stage. However, the sensitivity of the different techniques may differ, depending on the degradation mechanism and the material under test (for instance, stainless steel vs. carbon steel). One conclusion from this study is that online NDE monitoring is necessary to account for stressor history as well as variability across materials.

Several approaches to prognostics, i.e. estimating the RUL from NDE measurements, were investigated, and a probabilistic approach was selected for additional study. Results from a case study indicate the feasibility of prognostics from degradation precursor material states, provided that information about environmental stressors (such as fatigue loads) is also available.

While the focus of CRP study was on fatigue, the approaches outlined are general and can be applied to any degradation mechanism. Sensitivity studies are necessary to match NDE techniques to degradation mechanisms. Further, techniques for rendering sensors robust to typical LWR operating environments are necessary if online monitoring for material degradation and stressor information is necessary. However, evaluating sensors for robustness to environmental factors was not within the scope of this CRP.

The prognostics approach outlined in this report is also general, and applicable to any degradation mechanism/measurement as long as three factors outlined above (a good model of how degradation evolves and accumulates in the specimen, measurements sensitive to the early stages of degradation, and a reasonable failure PDF) are available. Additional studies may need to be conducted to determine these factors for other degradation mechanisms. Further, while the case study in this paper used a simple mathematical model to describe fatigue progression, the framework is general enough to be able to use more complex models (such as simulation models). Further studies will be necessary to fully study such an integrated Bayesian framework for prognostics.

REFERENCES TO CHAPTER 3

[1]   BOND, L. J., Moving beyond NDE to proactive management of materials degradation, Proc. ASME 2010 K-PVP Conference (PVP2010) (2010).

[2]   ASME, Long-term operations: the feasibility of extending the life of US nuclear facilities to 60 years and beyond, ASME, Sloan Foundation Grant B2009-23,Workshop report, 17-18 February 2010, Arlington, VA (2010).

[3]   BOND, L.J., DOCTOR, S R., JARRELL, D.B., BOND, J.W.D., Improved Economics of Nuclear Plant Life Management, 2nd International Symposium on Nuclear Power Plant Life Management, Paper # IAEA-CN-155-008KS, Shanghai, China (2007).

[4]   BOND, L.J., DOCTOR, S.R., GRIFFIN, J.W., HULL, A.B., MALIK, S.N., Damage Assessment Technologies for Prognostics and Proactive Management of Materials Degradation (PMMD), Nuclear Technology (2011).

[5]   BOND, L.J., DOCTOR, S.R., TAYLOR, T.T., Proactive Management of Materials Degradation - A Review of Principles and Programs, PNNL-17779, Pacific Northwest National Laboratory, Richland, WA (2008).

[6]   UNITED STATES NUCLEAR REGULATORY COMMISSION, Generic Aging Lessons Learned (GALL) Report - Summary, NUREG-1801, Rev. 2, Office of Nuclear Reactor Regulations, USNRC, Washington, D.C. (2010).

[7]   ANDRESEN, P.L., FORD, F.P., GOTT, K., JONES, R.L., SCOTT, P.M., SHOJI, T., STAEHLE, R.W., TAPPING, R.L., Expert Panel Report on Proactive Materials Degradation Assessment, USNRC, NUREG/CR-6923, BNL-NUREG-77111-2006, Washington, DC (2007).

[8]   UNITED STATES NUCLEAR REGULATORY COMMISSION, Generic Aging Lessons Learned (GALL) Report - Summary, USNRC, NUREG-1801, Vol. 1, Rev. 1, Washington, DC (2005).

[9]   UNITED STATES NUCLEAR REGULATORY COMMISSION, Generic Aging Lessons Learned (GALL) Report - Tabulation of Results, USNRC, NUREG-1801, Vol. 2, Rev. 1, Washington, DC (2005).

[10]   LIVINGSTON, J.V., CHATTOPADHYAY, S., HOOPINGARNER, K.R., PUGH, E.A., MORGAN, W.C., SPRINGER, G.D., PAWLOWSKI, R.A., A Review of Information for Managing Aging in Nuclear Power Plants, PNL-10717, Part 2 of 2, Pacific Northwest Laboratory, Richland, Washington, DC (1995).

[11]   MORGAN, W.C., LIVINGSTON, J.V., A Review of Information for Managing Aging in Nuclear Power Plants, PNL-10717, Part 1 of 2, Pacific Northwest Laboratory, Richland, Washington, DC (1995).

[12]   BOND, L.J., Review of Existing NDT Technologies and Their Capabilities, Proc. of AGARD/SMP Review of Damage Tolerance for Engine Structures; 1. Non-Destructive Evaluation, Review of existing NDT technologies and their capabilities, AGARD, Luxembourg (1988) 16.

[13]   DOBMANN, G., DEBARBERIS, L., COSTE, J.-F., Aging Material Evaluation and Studies by Non-Destructive Techniques (AMES-NDT) – A European Network Project, Nucl. Eng. Des., Vol. 206 (2001) 363-374.

[14]   RAJ, B., MOORTHY, V., JAYAKUMAR, T., RAO, K.B.S., Assessment of microstructures and mechanical behaviour of metallic materials through non-destructive characterisation, International Materials Reviews, Vol. 48, No. 5 (2003) 273-325.

[15]   BOND, L.J., DOCTOR, S.R., GRIFFIN. J.W., HULL, A.B., MALIK, S.N., Damage Assessment Technologies for Prognostics and Proactive Management of Materials Degradation (PMMD), ANS NPIC HMIT 2009 Topical Meeting - Nuclear Plant Instrumentation, Controls, and Human Machine Interface Technology, American Nuclear Society, Knoxville, Tennessee (2009).

[16]   CUMBLIDGE, S.E., DOCTOR, S.R., BOND, L.J., TAYLOR, T.T., LUPOLD, T.R., HULL, A.B., MALIK, S.N., Analysis of Emerging NDE Techniques- Methods For Evaluating And Implementing Continuous Online Monitoring, Proceedings of the 17th International Conference on Nuclear Engineering I CONE17, Paper # ICONE17-75340, 12-16 July 2009, Brussels (2009).

[17] NAKAGAWA, N., INANC, F., FRISHMAN, A., THOMPSON, R.B., JUNKER, W.R., RUDDY, F.H., DULLOO, A.R., BEATTY, J.M., ARLIA, N.G., On-line NDE and Structural Health Monitoring for Advanced Reactors, Advanced Nondestructive Evaluation I, Parts 1 and 2, Proc. Key Engineering Materials, On-line NDE and Structural Health Monitoring for Advanced Reactors (2006) 321-323 and 234-239.

[18] JARRELL, D.B., SISK, D.R., BOND, L.J., Prognostics and conditioned-based maintenance: a new approach to precursive metrics, Nucl. Tech. 145:275-286 (2004).

[19] BOND, L.J., TAYLOR, T.T., DOCTOR, S.R., HULL, A.B., MALIK, S.N., Proactive Management of Materials Degradation for Nuclear Power Plant Systems, 2008 International Conference on Prognostics and Health Management, IEEE 9778-1-4244-1936-4 (2008).

[20] HINES, J.W., GARVEY, J., PRESTON, J., USYNIN, A., Empirical Methods for Process and Equipment Diagnostics, Tutorial Notes, IEEE Reliability and Maintainability Symposium (RAMS-08), 23-26 January 2008, Las Vegas, NV (2008).

[21] JARDINE A., LIN, D., BANJEVIC, D., A Review on Machinery Diagnostic and Prognostics Implementing Condition Based Maintenance, Mech. Syst. Signal Process., Vol. 20 (2006) 1483-1510.

[22] HOWARD, P., Prognostic Technology – New Challenges, in Proc. 59th MFPT Soc., Soc. Machinery Failure Prevention Technology, Virginia Beach, VA (2005) 3-8.

[23] URMANOV, A., Electronic Prognostics for Computer Servers, in 2007 53rd Annual Reliability and Maintainability Symp., RAMS, Orlando, FL, 22-25 January 2006, IEEE, Piscataway, NJ (2006) 65-70.

[24] ORCHARD, M.E., VACHTSEVANOS, G.J., A particle filtering-based framework for real-time fault diagnosis and failure prognosis in a turbine engine, Proc. Mediterranean Conf. Control and Automation, Athens (2007).

[25] WALLIN, K., VOSKAMP, R., SCHMIDBAUER, J., OSTERMEYER, H., NAGEL, G., Statistical Assessment Method for the Optimization of the Inspection Need for Nuclear Steam Generators Based on Existing Inspection Data, 20th International Conference on Structural Mechanics in Reactor Technology, 9-14 August 2009, SMiRT 20, Book of Abstracts, Vol. 2, Espoo (2009) 359-360.

[26] KOTHAMASU, R., HUANG, S.H., VERDUIN, W.H., System Health Monitoring and Prognostics – A Review of Current Paradigms and Practices, International Journal of Advanced Manufacturing Technology 28 (2006) 1012-1024.

[27] HINES, J.W., BAILEY, K., COBLE, J., HUMBERSTONE, M., SHARP, M., Recent Advances in Empirical Methods for Equipment Condition Monitoring and Prognostics, Proceedings of the 2010 Maintenance and Reliability Conference, Knoxville, TN (March 2010).

[28] ATOMIC ENERGY SOCIETY OF JAPAN STANDARDS (AESJ-SC-P005), 2008 Overview of Atomic Power Standards for Generation Plant Aging Countermeasures, Atomic Energy Society of Japan Standards Committee, Subcommittee on System Safety PLM Subcommittee Meeting (2009).

[29] JAPAN WELDING ENGINEERING SOCIETY, Proceedings of the Symposium on Fatigue Design for Atomic Power Plants, Atomic Power Research Committee (2009).

[30] IZUMIYA, T., MATSUMOTO, E., SHIBATA, T., Nondestructive Measurement of In homogeneity of Functional Gradient Materials by Using Elastic Wave Analysis (in Japanese), The Japan Society of Mechanical Engineers, Vol. 61, No. 59 (1995) 2421-2428.

[31] MATSUO, K., MATSUMOTO, E., BIWA, S., Evaluation of Inhomogeneity by Phased Array Ultrasonic Transducer (in Japanese), Proceedings of the 20th Symposium on Electromagnetics and Dynamics (SEAD20) (2008) 51-54.

[32] TATEMATSU, N., MATSUMOTO, E., Non-Destructive Evaluation of Welding Part of Stainless Steels by Phased Srray System (in Japanese), Proceedings of 6th Annual Conference of Japan society of Maintenology (2009) 405-408.

[33] DAISUKE, E., TATEMATSU, N., MATSUMOTO, E., Non-Destructive Evaluation of Fatigue Degree of Metal by Ultrasonic Phased Array System (in Japanese), Proceedings of the 19th Conference on Electromagnetic Phenomena and Dynamics (2010) 261-164.

[34] JAPANESE SOCIETY FOR NONDESTRUCTIVE INSPECTION, New Enchiridion of Nondestructive Inspection (in Japanese), JSNDI, Nikkan Kogyo Shinbun Ltd. (2009) 516-534.

[35] TSUCHIDA, Y., et al., Evaluation of Strain and Bending Fatigue for Type 304 and Type 316NG Series Steel by Magnetic Sensors (in Japanese), Journal of the Japanese Society for Nondestructive Inspection, Vol. 57, No. 9 (2008) 433-436.

[36] BROWN, W.F., JR., Magnetoelastic Interactions, Springer-Verlag (1966).

[37] PAO, Y.-H., YEH, C.-S., A Linear Theory for Soft Ferromagnetic Elastic Solids, International Journal of Engineering Science, Vol. 11 (1073) 415-436.

[38] MATSUMOTO, E., Stress-Magnetization Effects based on Rate-Type Constitutive Equations of Deformable Ferromagnetic Materials, Romanian Journal of Technical Sciences-Series E&E, Vol. 43, No. 3 (1998) 391-396.

[39] SUZUKI, T., MATSUMOTO, E., Stress Magnetization Effect derived from Magnetization and Magnetostriction Curve under Tensile Stress, JSAEM Studies in Applied Electromagnetic and Mechanics, Vol. 14 (2002) 47-54.

[40] FUKUOKA, H., et al., Basic and Application of Acoustoelasticity (in Japanese), Ohmsha, Ltd., (1993) 36.

[41] TODA, H., et al., Analysis of Residual Stress using Electromagnetic Acoustic Method (in Japanese), Proceeding of 60th Kansai-Branch Conference of Japan Society of Mechanical Engineers, No. 854-1 (1985) 65-67.

[42] HANE, N., MATSUMOTO E., SHIBATA T., Stress Effect on Magnetoacoustic Emission of Nickel, Journal of the Japan Society of Mechanical Engineers (A), Vol. 65, No. 635 (1999) 193-198.

[43] ABE, M., MATSUMOTO, E., Degradation Detection of Metallic Material by Magneto-Acoustic Emission (in Japanese), Proceedings of the 19th Conference on Electromagnetic Phenomena and Dynamics (2009) 254-257.

[44] SHINKE, N., et al., Nondestructive Evaluation of Creep Damage by Magnetomechanical Acoustic Emission (in Japanese), Journal of the Japanese Society for Nondestructive Inspection, Vol. 41, No. 11 (1992) 650-656.

[45] MATSUMOTO, E., OMOTO, Y., IGUCHI, K., SHIBATA, T., Visualization of Strain Distribution by Piezoelectric Thin Film, Studies in Applied Electromagnetics and Mechanics, Vol. 18 (2000) 305-308.

[46] KOMAGOME, Y., MATSUMOTO, E., Visualization of Back-Surface Defects by Piezoelectric Film, International Journal of Applied Electromagnetics and Mechanics, Vo. 14, Nos. 1-4, (2001) 425-428.

[47] LEE, C.-K., Piezoelectric Laminates: Theory and Experiments for Distributed Sensors and Actuators, Tzou, H.S., Anderson, G.L., (ed.), Intelligent Structural Systems, Kluwer Acadmic Publishers, New York (1992) 75-167.

[48] TZOU, H.S., Piezoelectric Shells, Kluwer Acadmic Publishers, New York (1993).

[49] EGASHIRA, M., SHINYA, N., Local Strain Sensing using Piezoelectric Polymer, Journal of Intelligent Material Systems and Structures, Vol. 4, (1993) 558-560.

[50] BIWA, S., et al., Strain Distribution with Piezoelectric Film, Journal of Electrical Engineering, Vol. 48, No. 8/S, (1997) 50-53.

[51] YAMADA. S, MATSUMOTO, E., BIWA, S., Visualization of Surface Defects of Steel Using Iron Loss and Infrared Thermography, 5th Annual Conference of the Japan Society of Maintenology (2008) 231-236.

[52] YAOITA, T., Application of Thermography to Measurement of Stress and Determination of Fatigue-Limit using Dissipated Energy (in Japanese), Journal of the Japanese Society for Nondestructive Inspection, Vol. 51, No. 6 (2002) 333-337.

[53] SHIRATORI, M., et al., Detection of Cracks and its Image Processing by Infrared Thermography (in Japanese), Journal of the Japan Society of Mechanical Engineers (A), Vol. 58, No. 556 (1992) 42-47.

[54] SUKIGARA, N., et al., Detection of closed fatigue crack with thermosonic technique (in Japanese), Proceeding of 16th Spring Conference of Japanese Society for Nondestructive Inspection (2004) 99-100.

[55] OTSUJI, K., KINOSHITA, K., KAMINISHI, K., Estimation of Breaking-Point of Aluminum Alloy to High-Cycle Fatigue Tests using Ferromagnetic Deposit and Electromagnetic AC Impedance Method (in Japanese), Proceedings of the 19th Conference on Electromagnetic Phenomena and Dynamics (2010) 555-558.

[56] KINOSHITA, K., Evaluation of Magnetic Anisotropy by Electromagnetic AC Impedance Method using Rotating Magnetic Field, Proceedings of the 15th Conference on Electromagnetic Phenomena and Dynamics (2006) 250-253.

[57] AMERICAN SOCIETY FOR NONDESTRUCTIVE TESTING, Nondestructive Testing Handbook, Third Edition: Volume 5, Electromagnetic Testing, ed. Udpa, S.S., Moore, P.O., ASNT, Columbus, Ohio (2004)

[58] KULKARNI, S.S., ACHENBACH, J.D., Structural Health Monitoring and Damage Prognosis in Fatigue, Structural Health Monitoring 7(1) (2008) 37-49.

[59] KOTHAMASU, R., HUANG, S.H., VERDUIN, W.H., System Health Monitoring and Prognostics – A Review of Current Paradigms and Practices, Int. J. Adv. Manuf. Tech. 28 (2006) 1012-1024.

[60] HINES, J.W., BAILEY, K., COBLE, J., HUMBERSTONE, M., SHARP, M., Recent Advances in Empirical Methods for Equipment Condition Monitoring and Prognostics, in Proc. 2010 Maintenance and Reliability Conference, Knoxville, Tennessee (2010).

[61] RISTIC, B., ARULAMPALAM, S., GORDON, N., Beyond the Kalman Filter, Artech House, London (2004).

[62] ARULAMPALAM, S., MASKELL, S., GORDON, N., CLAPP, T., A tutorial on particle filters for on-line non-linear/non-Gaussian Bayesian tracking, IEEE Trans. Signal Process, vol. 50 (2002) 174–189.

[63] KHAN, T., RAMUHALLI, P., A Recursive Bayesian Estimation Method for Solving Electromagnetic NDE Inverse Problems, IEEE Transactions on Magnetics, 44(7) (2008)1845-1855.

[64] HORN, R.A., JOHNSON, C.R., Matrix Analysis, Cambridge University Press (1985).

[65] DOUCET, A., GODSILL, S., ANDRIEU, C., On sequential Monte Carlo sampling methods for Bayesian filtering," Stat. Comput., Vol. 10 (2000) 197–208.

[66] RAMUHALLI, P., BOND, L.J., GRIFFIN, J.W., DIXIT, M., HENAGER, C.H., JR., A Bayesian prognostic algorithm for assessing remaining useful life of nuclear power components, Proc. 7th International ANS Topical Meeting on Nuclear Power Instrumentation, Control and Human-Machine Interaction Technologies, (NPIC-HMIT), 7-11 November 2010, Las Vegas, NV (2010) 875-886.

[67] ORCHARD, M.E., VACHTSEVANOS, G.J., A particle filtering-based framework for real-time fault diagnosis and failure prognosis in a turbine engine, in Proc. Mediterranean Conf. Control and Automation, Athens (2007).

[68] CARLSON, A.B., CRILLY, P.B., Communication Systems – An Introduction to Signals and Noise in Electrical Communication (5th Edition), McGraw-Hill (2010).

[69] KULKARNI, S.S., ACHENBACH, J.D., Structural Health Monitoring and Damage Prognosis in Fatigue, Structural Health Monitoring 7(1) (2008) 37-49.

[70] OGI, H., HIRAO, M., AOKI, S., Noncontact monitoring of surface-wave nonlinearity for predicting the remaining life of fatigued steels, Journal of Applied Physics 1 (2001) 438–442.

4. INSTRUMENT AND EQUIPMENT CONDITION MONITORING AND ENABLING TECHNOLOGIES (TO CHAPTER 5 OF THE MAIN REPORT)

4.1. OVERVIEW

Presented here is supplementary material to Chapter 5 of the main report. A description is provided of each technique used in the instrumentation failure benchmark. Following this, material covering the cable ageing demonstration is provided, with further supplementary material describing other cable degradation work.

4.2. SUPPORTING MATERIAL FOR INSTRUMENT FAILURE DETECTION TECHNIQUES

4.2.1. Introduction

This benchmark activity focused on the problem of drift in a set of 29 PWR transmitters, grouped into two component areas.

− Steam generator (17 sensors):

- steam pressure (BarG) - 4 devices,
- SG level wide range (%) - 2 devices,
- SG level narrow range (%) - 4 devices,
- feedwater flow (kg/s) - 4 devices,
- steam flow (kg/s) - 3 devices.

− Pressuriser (12 sensors):

- pressuriser pressure (BarG) - 4 devices,
- pressuriser level (%) - 4 devices,
- RCS pressure wide range (BarG) - 4 devices.

6 sets of data were recorded for each of these transmitters, sampling from the conditioning monitoring system. It should be reiterated that all transmitters are subject to some kind of redundancy, ranging from 2 to 4 transmitters per measurand. This provides the basis for the statistical analysis in much of this field of study, and the relationship between coupled devices allows for drift to be characterised much more tangibly.

Measurements were taken in instalments at November 2006, December 2006, March 2007, July 2007, September 2007 and December 2007. Measurement records are taken every 10 seconds, each period lasting for 12 hours. The first set represents the 'Training Data', where the transmitters were recently calibrated and operating correctly. This set represents the initial data that is used to set benchmarks or be used in the training of intelligent software systems.

The aims are to examine the data sets and determine the steady state drift analysis of each sensor over the 6 periods of measurement, and determine which devices requite re-calibration. This benchmarking process was undertaken by 6 separate groups using a variety of techniques. It should be noted there is no associated physical model of the underlying process, so the analyses that were undertaken were restricted to statistical approaches.

4.2.2. Technique 1: Average deviation from mean

The use of redundant transmitter averaging as a method for denoting drift status (taking the average of all other transmitters in the group vs. the transmitter in question) is a basic approach to analyzing the data. The philosophy behind this is that total transmitter averaging process could include exceptional deviations in the average if the transmitter in question is included. In effect, this could mask a much bigger drift if the average were to appear closer due to this.

Deviation from the holistic average among groups of transmitters can be monitored online, and upper/lower limits can be set to trigger alarms if deviation matches or exceeds that expected for drift candidacy. This provides an illustration of the signals and their deviation from the mean of the transmitter group, as shown in FIG. 4-1. The signals are subject to pre-set limits of operation, in this arbitrary example, ±0.4% (historically, the tolerance tends to be around the ±1% mark). If a value were to exceed these limits, an alarm would be raised, thus informing of the drift.

This technique is useful as a starting point in identifying drift candidates, but arguably has some notable weaknesses. In the case of systematic drift (where multiple sensors exhibit drift of the same orientation), the deviation from the holistic mean will not provide indication of a problem. Presently, counter-action of this problem involves scale testing of a single sensor to note its input response. A non-linear result would suggest re-calibration is required in this case.

Using this approach, the following sensors were identified as abnormal, and thus would require calibration.
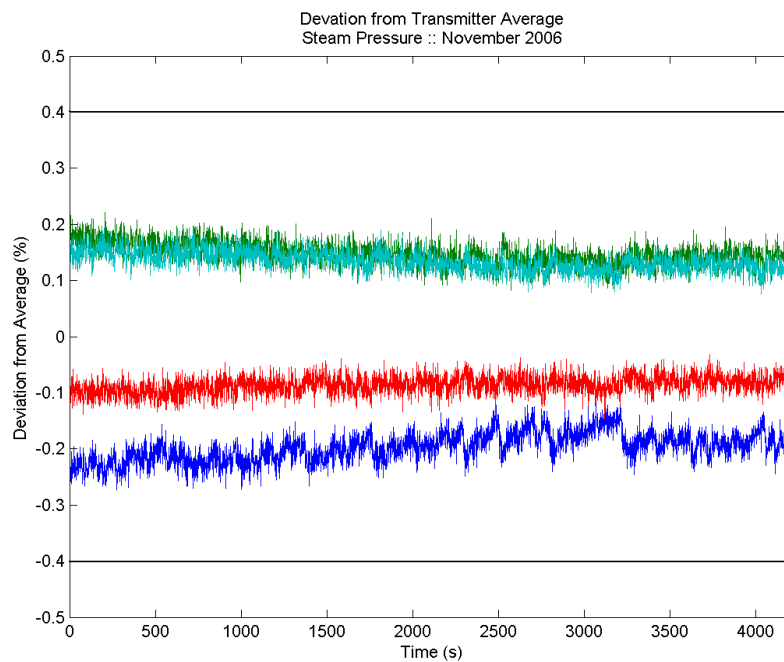
FIG. 4-1. Deviation of signal from total transmitter average.

Note: set limits at ±0.4%, defining the normal envelope of behaviour. In this example, this dataset exhibits normal behaviour over a short time period (12 hours)

4.2.3. Technique 2: Skewness and kurtosis

In addition to examining the mean of the data set, examining other statistical techniques such as skewness and kurtosis can be used to detect anomalies. The probability density function provides a good means of visualizing these properties.

4.2.3.1. Kurtosis

The kurtosis of a sample set is a measure of how 'peaked' the probability distribution function is. Higher kurtosis is characteristic of a 'more peaked' or sharper distribution, while small kurtosis values are indicative of wider, flatter distributions. Kurtosis can be formally defined as:

$$k = \frac{(E(x - \mu))^4}{\sigma^4} \tag{1}$$

where k is the kurtosis; x is the sample value, μ is the mean of the sample set, σ is the standard deviation and E(...) is the expectation (or average) value. The kurtosis of an ideal normal distribution is therefore equal to 3; values above this can be referred to as leptokurtic, and below platykurtic [1]. The change in kurtosis can be seen in FIG. 4-2.
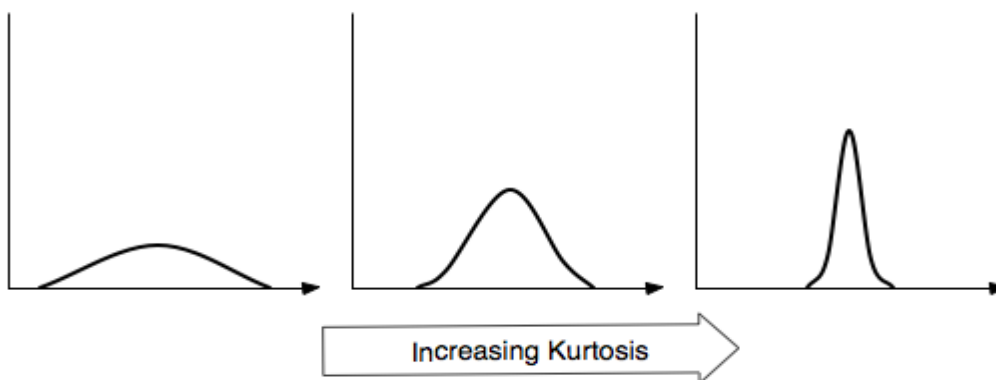
FIG. 4-2. Illustration of change of kurtosis value on a PDF.

4.2.3.2. Skewness

The skewness of a sample set is a measure of how asymmetrical the probability distribution function is. That is, if a distribution has a longer 'tail' to the right of the central peak; it is considered to be positively skewed, and vice versa. Skewness can provide a good measure of the 'preferential' spread of a transmitter's 'noise span' - as it could be argued that it is more likely for the trace to show greater impetus to measure below the true value of the parameter, rather than above. Skewness can be formally defined as:

$$s = \frac{(E(x - \mu))^3}{\sigma^3} \tag{2}$$

where s is the skewness; x is the sample value, μ is the mean of the sample set, σ is the standard deviation and E is the expectation (or average) value. The skewness of an ideal normal distribution is therefore zero. The sign of the skewness value therefore is indicative of which direction, or preference, the sample set is skewed in as shown in FIG. 4-3.
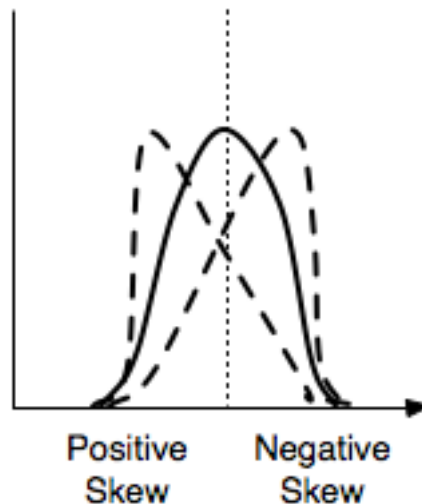
FIG. 4-3. Illustration of orientation of skewness value on a PDF.

4.2.3.3. Approach

The concepts of kurtosis and skewness are suggested here to be useful parameter values to monitor over the time evolution of the transmitter. Changes in these values could indicate a whole manner of different scenarios: step changes in signal, degradation of transmitter accuracy and, importantly, the presence of subtly drifting signals.

Taking the PDFs of entire periods of data (i.e. the full 12 hour period taken for each transmitter each month) allows for the kurtosis and skewness of these to be compared month to month. A notable change in one of these between sets can be thought of as a change in sample behaviour, useful knowledge to acquire when diagnosing the steady-state drift status from month to month.

The concept behind the statistical evolution method studied here is to compare the parameters in each month set; and determine if a transmitter is drifting in any of the groups. The origins of a change in behaviour will stem from a change in the parameter, and it is the goal of monitoring these parameters that a measurement of such change is acquired. Once these measurements are gained, it is then possible to correlate the larger, notable changes in statistical parameter magnitude or orientation with an anomaly of behaviour.

The method used to examine the drift status of the transmitters was as follows:

− Generate PDF for each transmitter at each month grouping;
− Determine the skewness and kurtosis of each;
− Compare the changes in these over the months.

At each month, the following is calculated:

− The kurtosis/skewness of all transmitters;
− The 'span' of these values (MAX-MIN).

The kurtosis/skewness span is indicative of how similar each transmitter is to each other at that particular moment in the progression of the dataset. When values for all months have been determined for a group of transmitters, various calculations or 'behaviour ratings' can be acquired.

− The magnitude of change in parameter span from Nov06 to Dec07 (CKS, CSS);
− The maximum magnitude of change in parameter span in the dataset (MAX(KS, SS)-MIN(KS, SS));

- The average 'total' parameter value for the group of transmitters over the months (Total μ);
- The corresponding 'redundant' value of Total μ, excluding the transmitter in question (Redundant μ);
- The deviation between the parameter value & the total average of the group (X - Total μ);
- The deviation between the parameter value & the redundant average of the group (X - Redundant μ).

Candidates exhibiting drifting behaviour will have large deviation values from their corresponding redundant average. The total average values are also included as means of reference for future discussion in the 'total average vs. redundant average' argument.

Also worth note is the 'span' of the parameters in each grouping; both at the start/end of the dataset and the maximum span value among this. Changes in span values could possibly denote a group of transmitters changing their orientation relative to each other.

4.2.3.4. Results

The devices RCS Pressure Wide Range 4 and Feedwater Flow 4 are identified to be the drifting transmitters.

4.2.4. Technique 3: Kernel principle components analysis (KPCA)

Information on the KPCA benchmarking is presented in Ref. [1].

4.2.5. Technique 4: Auto-associative kernel regression

4.2.5.1. Methodology

The core technique that Kyung Hee University adopted to detect sensor drift is based on the auto-associative kernel regression (AAKR). The various nature of AAKR such as data-driven, non-parametric, and similarity-based was, therefore, inherited to this methodology. In order to easily and systematically apply AAKR, we developed the framework of applying the AAKR based empirical model and a series of modules as shown in FIG. 4-4. The execution mode, usually referred to 'test mode' is almost same as the other empirical approaches. In case of the training mode, we designed several routines to construct a better AAKR model: Grouping, Shrinking, and Selecting of kernel parameters.
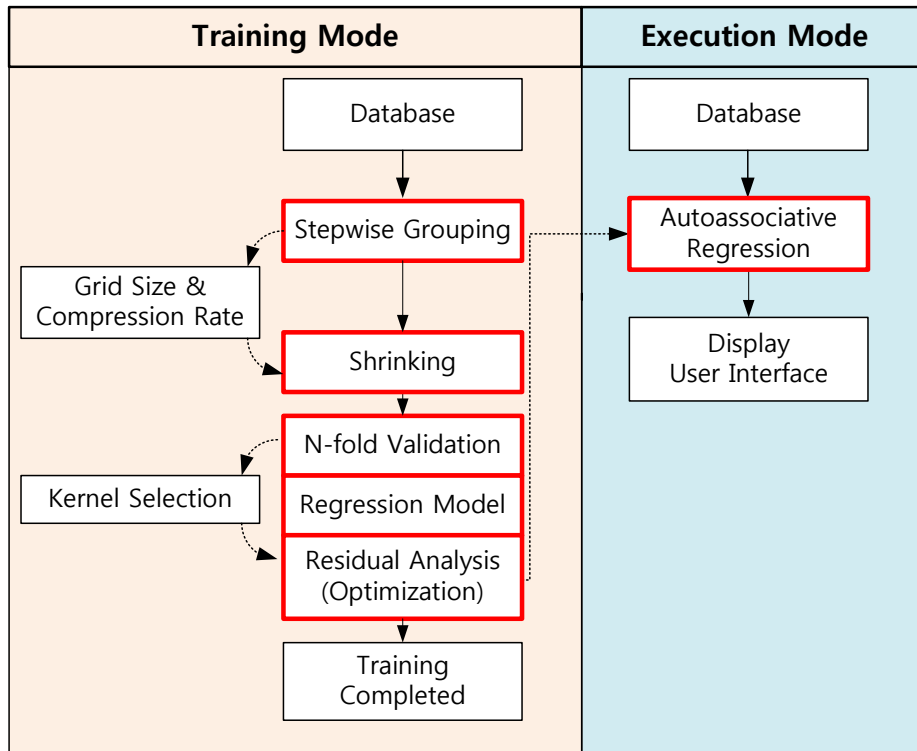
FIG. 4-4. Schematic flowchart for detecting sensor drifts.

We used the stepwise grouping, which is one of methods to select optimal combination of independent variables. From our experiences, using the only correlation coefficients was not enough to make a reasonable set of variables, particularly for the case of power plants which are operating steadily over the whole year. In the grouping module, the preliminary groups are made up using the correlation coefficients between variables. For the remaining variables, each one is evaluated in terms of the 'Sum of Square Error (SSE)' metric to decide optimal bandwidth of the kernel selected. The stepwise grouping helps to take variables with even low correlation coefficients depending on operational characteristics.

The shrinking technique which can be referred as dimension reduction was designed to resolve the curse of dimension, which is most of empirical models' trouble. One method of reducing dimension is to control the sample frequency which is time-based. The other method was to reduce the number of redundant samples on the basis of the deviation-based grid size. In FIG. 4-5, the left shows the distribution of initial training data sets and the right corresponds to the reduced one after shrinking algorithm.
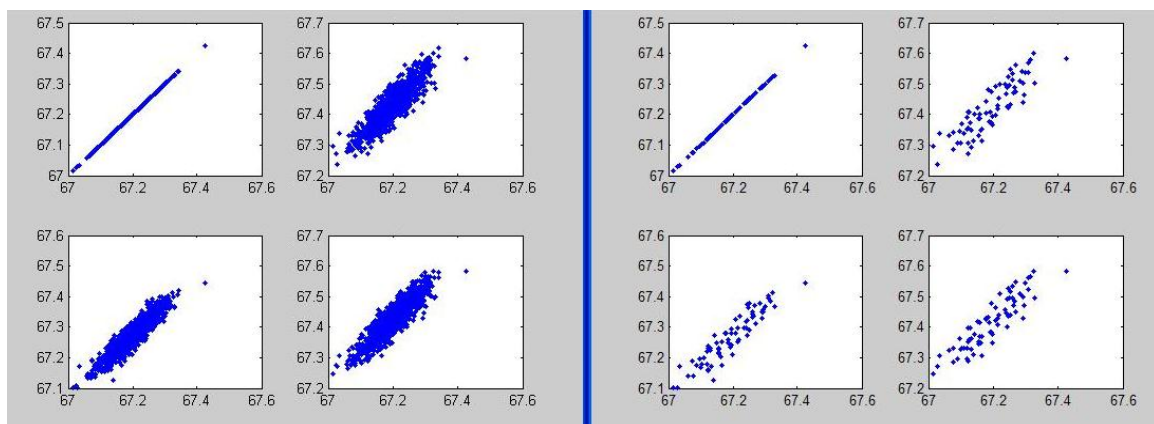
FIG. 4-5. Results of dimension reduction for training data.

This method has a characteristic to leave small number of outliers considered as reasonable information no matter how shrink rate is strong.

In this method, the kernel was chosen as a normal distribution, with a kernel bandwidth h and Euclidean distance d.

In order to determine the kernel bandwidth, we used the nested grid search method based on 4-fold validation. In K-fold cross-validation, the original sample is randomly partitioned into K subsamples. Of the K subsamples, a single subsample is retained as the validation data for testing the model, and the remaining K−1 subsamples are used as training data. The nested grid search finds optimized h by iterating from possible minimum value (hmin) to possible maximum value (hmax) divided by a certain number. For each h, SSR is examined by 4-fold cross validation and the h which showed minimum SSR is regarded as optimized h.

4.2.5.2. Results

We classified 29 variables into 5 groups. The results are as follows:

- 1, 2, 3, 4, 19, 20, 21, 22 into Group 1;
- 11, 12, 13, 14 into Group 2;
- 15, 16, 17, 18, 23, 24, 25, 26 into Group 3;
- 27, 28, 29 into Group 4;
- 5, 6, 7, 8, 9, 10 into Group 5.

After applying the algorithms to all of five groups, we could recognize the first variable in Group 5 should have drift as shown in FIG. 4-6. However, it should be noted that all of eight variables in Group 3 shows abnormal deviation which seems drifts in FIG. 4-7. From more investigation on the training data, we concluded that the given data did not cover the whole operating range so that the empirical model could not extrapolate the expected values. In the CRP main report, the variables in Group 3 was marked as 'suspicious.' Other groups did not provide any deviation so there was no symptom to consider sensor drifts. Since the benchmarking data in this case can be also intuitively grouped into several categories in terms of their redundancy, it may be more effective to use other models for each category to distinguish the deviation between redundant sensors to detect drifts.
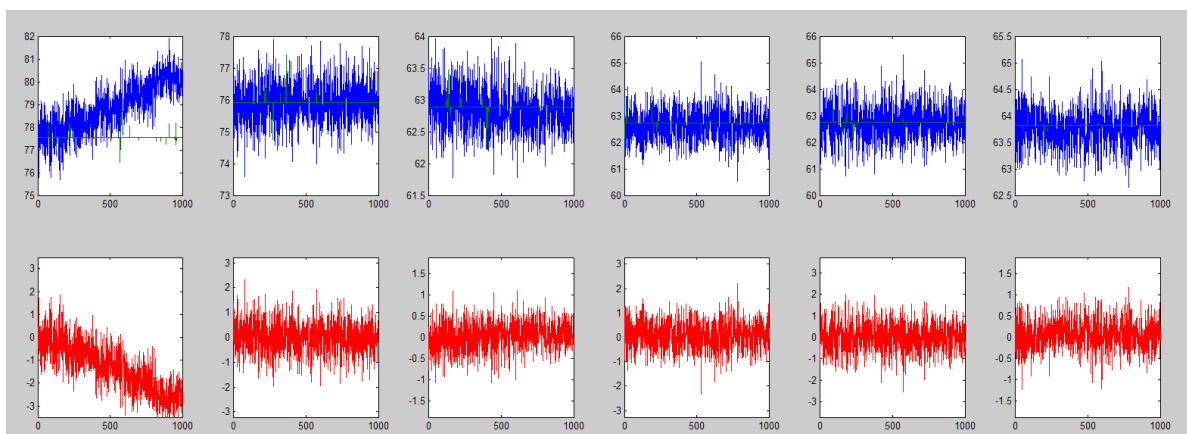
FIG. 4-6. Testing results for Group 5 (Upper charts: Blue is actual value, Green is expected value, Lower charts: Red is residual).
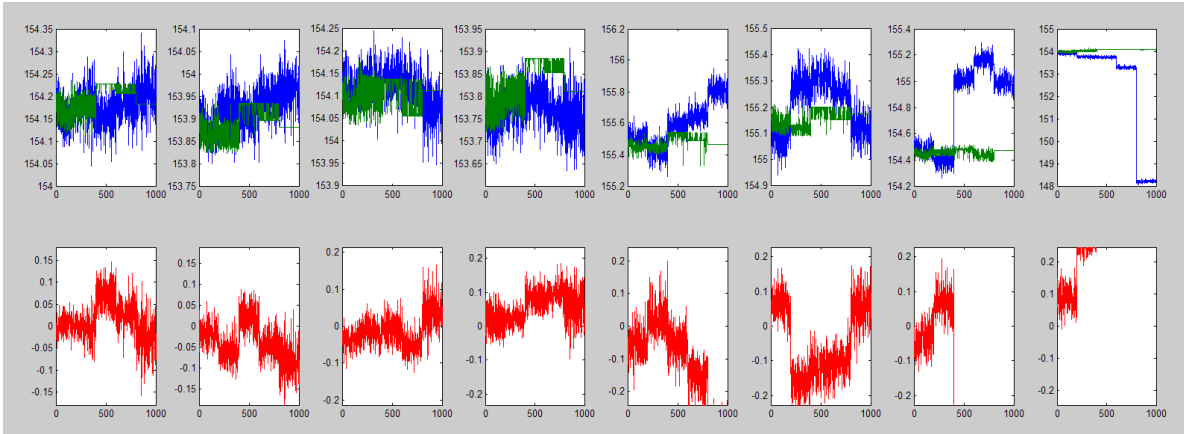
FIG. 4-7. Testing results for Group 3 (Upper charts: Blue is actual value, Green is expected value, Lower charts: Red is residual).

4.2.6. Technique 5: PEANO approach

Two approaches have been used to develop PEANO models for this set of benchmark data:

- A model was developed, which contained all the 29 signals;
- Since the signals represented different loops in the process the training data was split into four sets. Each set contained to measurements relevant for one loop and a model was developed for each of the loops. The data was split according to the following TABLE 4-1.

TABLE 4-1. FOUR LOOPS USED TO DEVELOP PEANO MODELS

Loop 1	Loop 2	Loop 3	Loop 4
STM PSR 1	STM PSR 2	STM PSR 3	STM PSR 4
SG LVL WR 1	SG LVL WR 2		
SG LVL NR 1	SG LVL NR 2	SG LVL NR 3	SG LVL NR 4
FEED FLOW 1	FEED FLOW 2	FEED FLOW 3	FEED FLOW 4
PZR PSR 1	PZR PSR 2	PZR PSR 3	PZR PSR 4
PZR LVL 1	PZR LVL 2	PZR LVL 3	PZR LVL 4
RCS PSR WR 1	RCS PSR WR 2	RCS PSR WR 3	RCS PSR WR 4
STM FLOW 1	STM FLOW 1	STM FLOW 1	STM FLOW 1
STM FLOW 2	STM FLOW 2	STM FLOW 2	STM FLOW 2
STM FLOW 3	STM FLOW 3	STM FLOW 3	STM FLOW 3

The "Steam Generator Level Wide Range" was only available for the first two loops. Furthermore, the three steam flow measurements are common for the whole process and not unique for the loops and where therefore included in each of the models.

4.2.6.2. PEANO results on tests

The five consecutive test sets (4230 measurements in each set) where processed with both the models to assess the presence of faults (drifts or offsets) in one or more sensors.

In general the findings with the two different modelling approaches are similar. In the approach where the loops were modelled individually it can be seen that the reconstructions calculated are less

250

noisy. We can also see that some spill-over effects seem to be reduced, e.g. Steam Pressure reconstruction (see the attached figure with reconstruction results).

Results show that 8 sensors might be affected by small faults (drifts or offsets), 1 is clearly affected by a drift and 1 is clearly affected by an offset. In details:

− Steam pressure 1: small offset (up to 0.2 BARG) in test sets 2 and slightly smaller drift (±0.1 BARG) in test sets 3, 4 and 5 (FIG. 4-8).
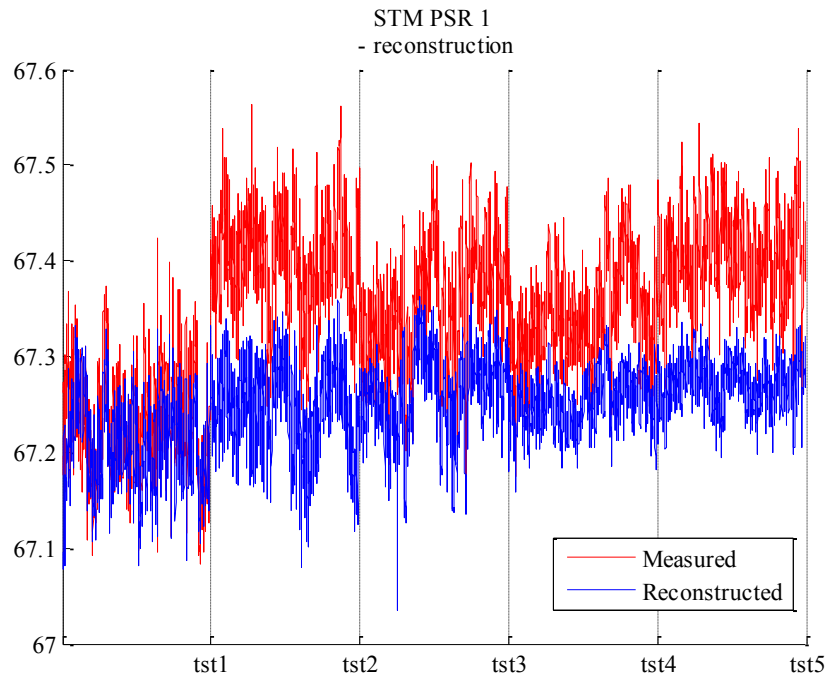
FIG. 4-8. Steam pressure 1.

− Steam pressure 2: small offsets (up to ±0.1 BARG) in test sets 2, 3, 4 and 5 (FIG. 4-9).
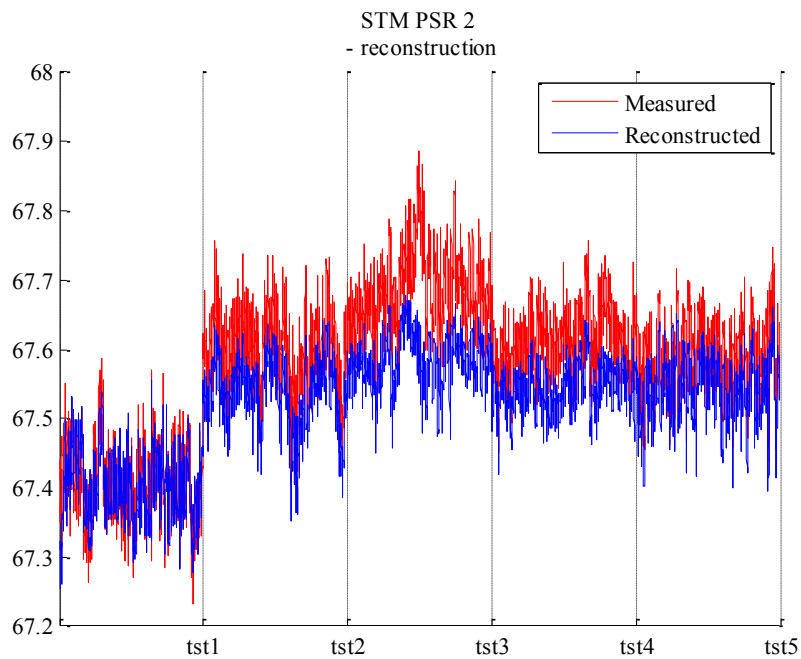
FIG. 4-9. Steam pressure 2.

251

− Steam pressure 3: small drift (up to 0.3 BARG) slowly growing from test set 2 to 5 (FIG. 4-10).
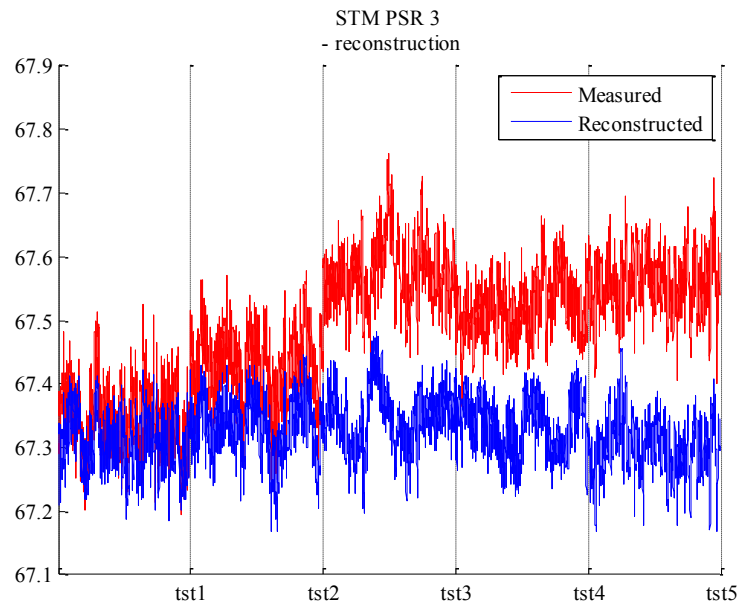
FIG. 4-10. Steam pressure 3.

− Steam pressure 4: small offset (up to ±0.2 BARG) in test sets 2, 3, 4 and 5 (FIG. 4-11).
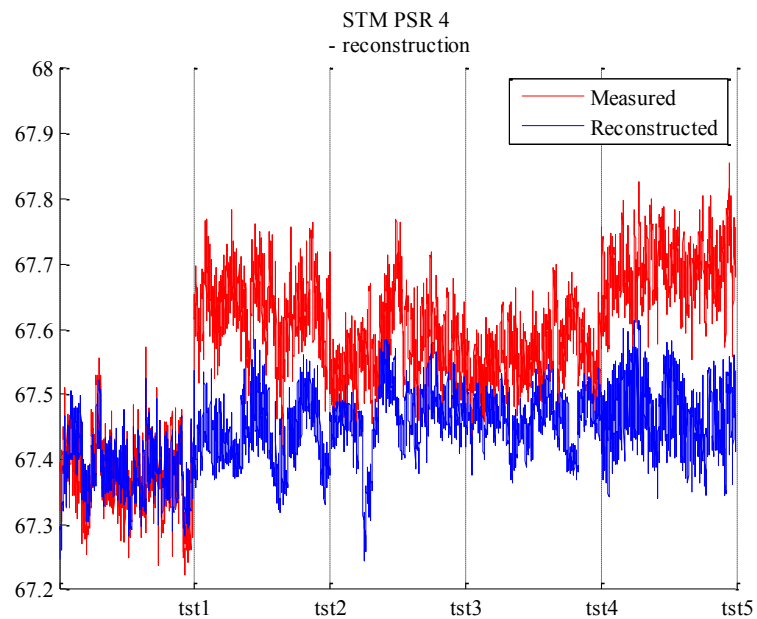
FIG. 4-11. Steam pressure 4.

− Steam generator level wide range 1: clear drift growing from test set 2 to 5 up to 3% (FIG. 4-12).
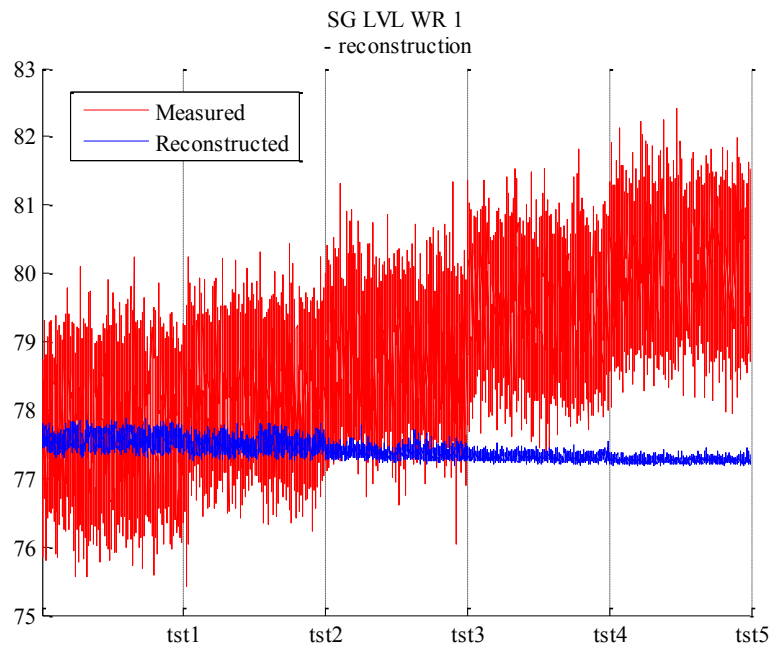
FIG. 4-12. Steam generator level wide range 1.

− Pressurizer pressure 2: small drift (up to ±0.1 BARG) in test set 5 (FIG. 4-13).
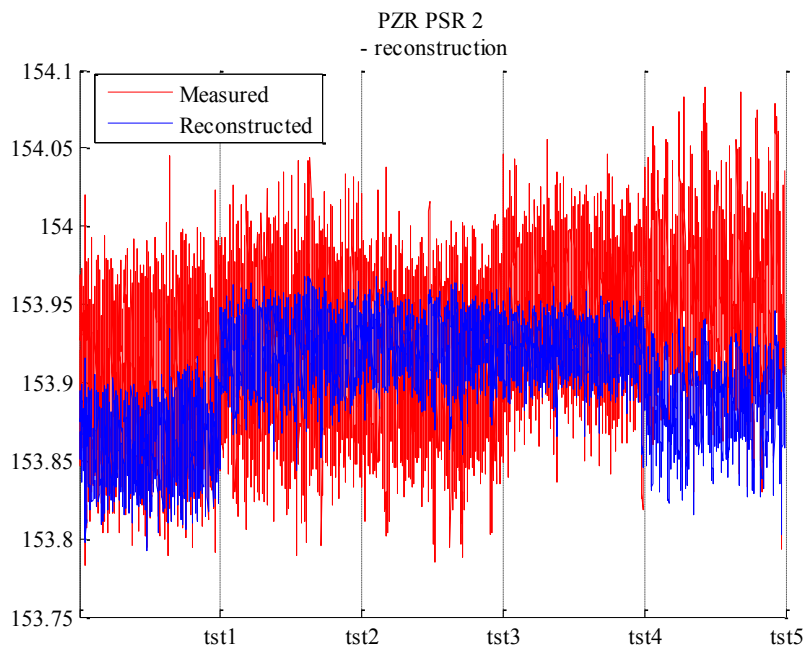
FIG. 4-13. Pressurizer pressure 2.

— RCS pressure wide range 1: small offsets in test sets 3, 4 and 5 up to ±0.3 BARG (FIG. 4-14).
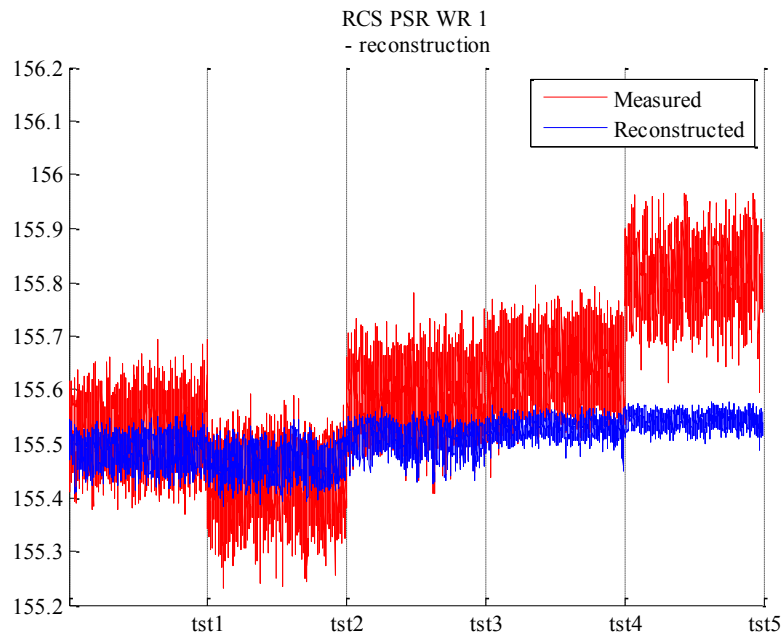
FIG. 4-14. RCS pressure wide range 1.

— RCS pressure wide range 2: small offsets in test sets 2, 3 and 4 up to ±0.1 BARG (FIG. 4-15).
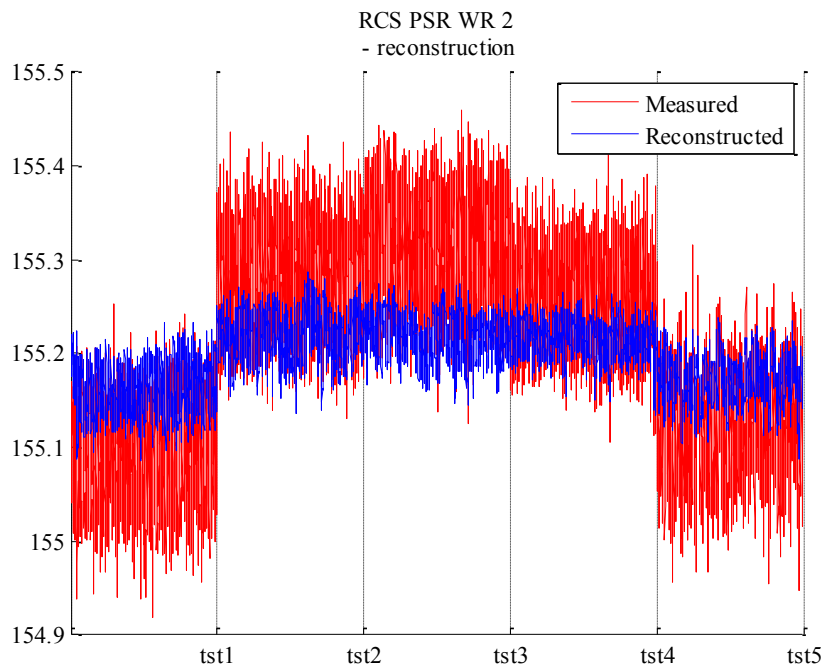
FIG. 4-15. RCS pressure wide range 2.

— RCS pressure wide range 3: small offsets in test sets 3, 4 and 5 up to ±0.6 BARG (FIG. 4-16).
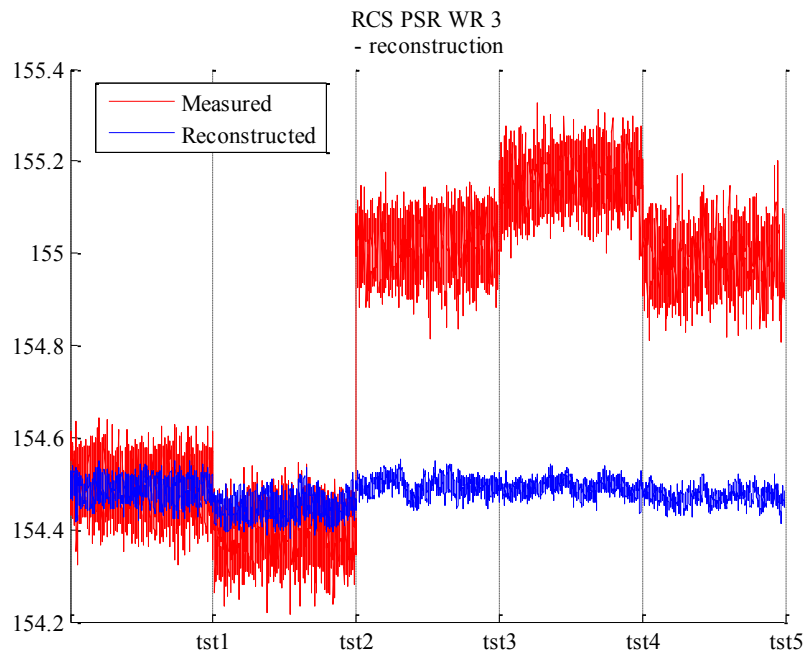
FIG. 4-16. RCS pressure wide range 3.

— RCS pressure wide range 4: small offsets in test sets 2 and 3 up to 0.3 BARG and clear offsets in test sets 4 and 5 up to ±6 BARG (FIG. 4-17).
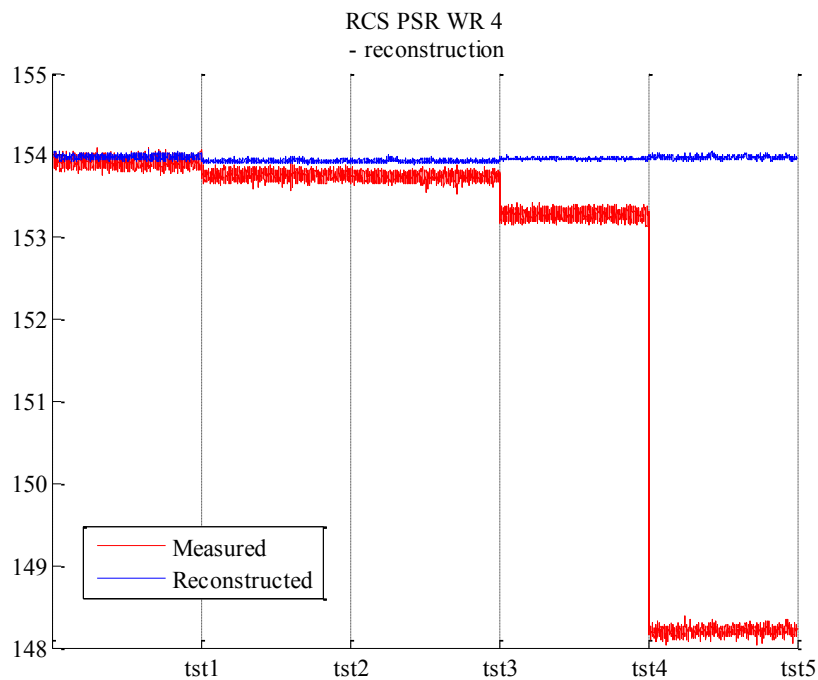
FIG. 4-17. RCS pressure wide range 4.

4.2.7. Technique 6: Evolving cluster method (ECM)

4.2.7.1. *Basic concept of ECM models*

The ECM is a fast, one-pass algorithm for dynamic clustering of an input stream of data. It is a distance-based clustering method where the cluster centres are represented by evolved nodes in an on-line mode. The clustering process starts with an empty set of clusters. The data stream, i.e. the training samples, is used to generate a number of multi-dimensional clusters identified by their position in the sample space and their width. Given a maximum allowed cluster width, during the training process, the position and width of the clusters are continuously updated and a near-optimal cluster distribution is eventually obtained. Based on these clusters, the model is expected to generalize by associating to an unseen sample the (multi-dimensional) value of the centre of the closest cluster.

4.2.7.2. *ECM for sensor fault detection*

A robust ECM model must be capable of detecting sensor failures, such as drifts or offsets. In this view, a faulty sensor sends a faulty signal as input to the reconstruction model which should still be capable of providing a good estimate of the true value of the signal by exploiting the information coming from the other non-faulty signals. The comparison between the measured signals values sent as inputs and the model signal reconstruction provides indications of the presence of sensor faults.

4.2.7.3. *ECM training and test results*

Training of the ECM has been performed using the IAEA benchmark dataset collected in November 2006 (4229 measurements for each of the 29 signals). Signals have been normalized in the range [0, 1] and the maximum allowed cluster width has been set by trial and error equal to 1/100 of the data normalized range. The total number of clusters generated in the training has been 1601. Then the ECM has been fed with the five consecutive test sets (4230 measurements in each set) to assess the presence of faults (drifts or offsets) in one or more sensors.

Results show that 8 sensors might be affected by small faults (drifts or offsets), 1 is clearly affected by a drift and 1 is clearly affected by an offset. In details:

− Steam pressure 1: small offset (up to 0.2 BARG) in test sets 2 and 3 and small drift (up to 0.25 BARG) in test sets 4 and 5 (FIG. 4-18).
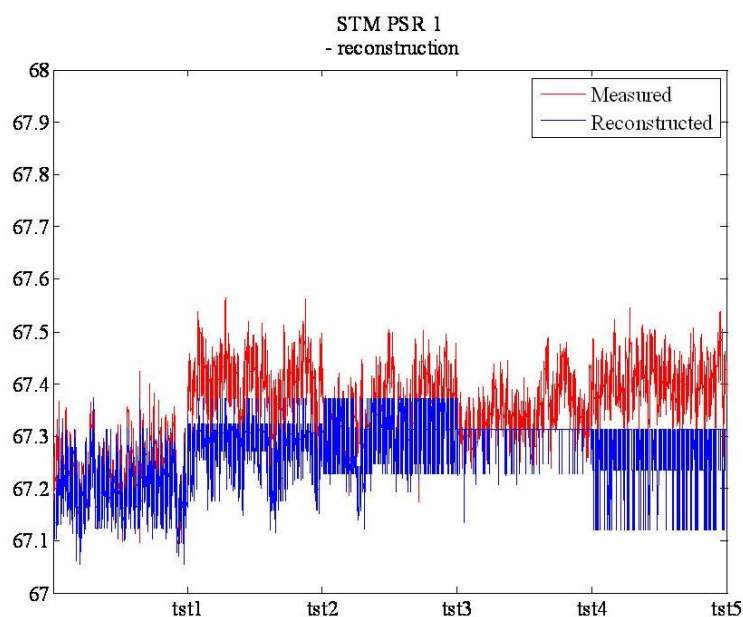
FIG. 4-18. Steam pressure 1.

− Steam pressure 2: small offsets (up to 0.3 BARG) in test sets 3, 4 and 5 (FIG. 4-19).
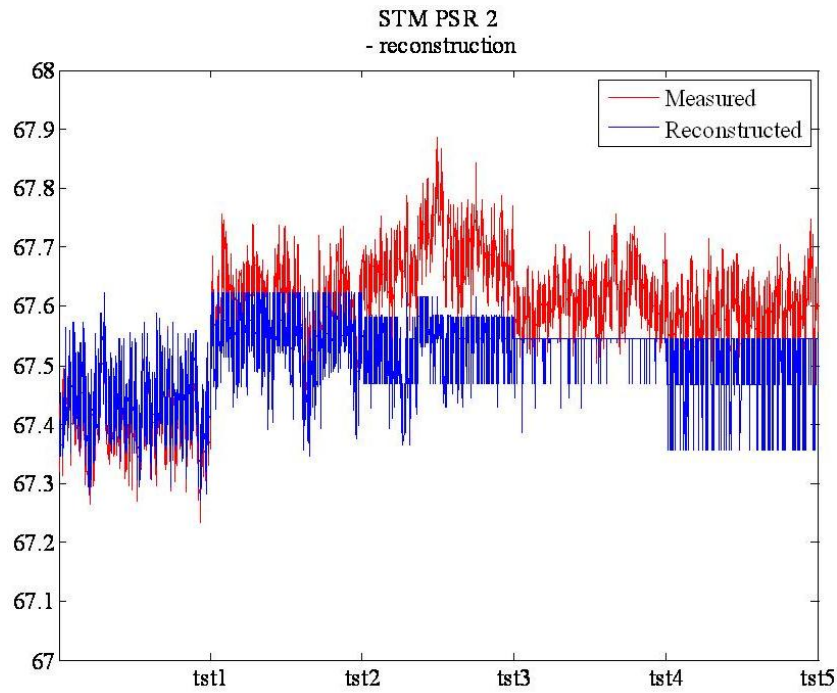
FIG. 4-19. Steam pressure 2.

− Steam pressure 3: small drift (up to 0.35 BARG) slowly growing from test set 2 to 5 (FIG. 4-20).
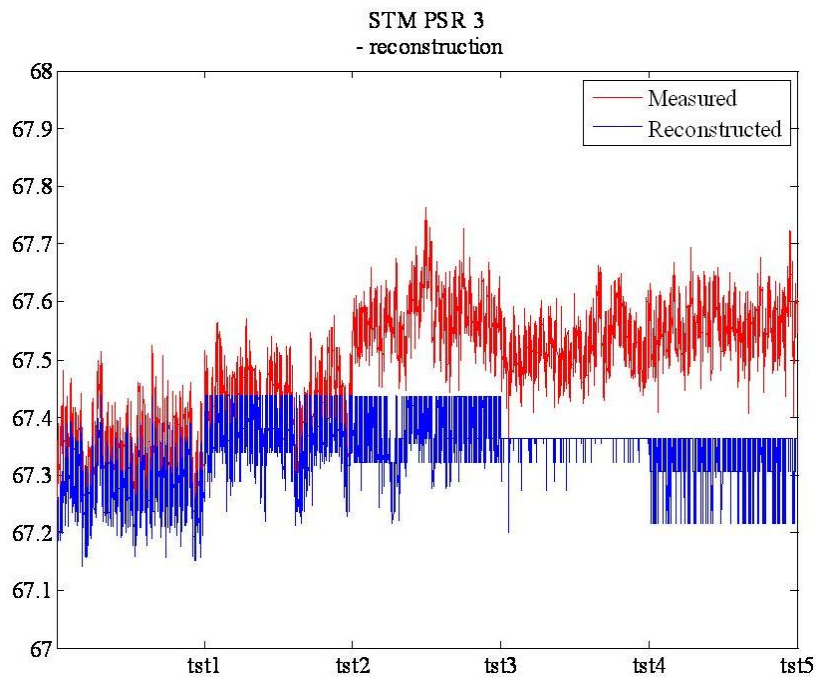
FIG. 4-20. Steam pressure 3.

− Steam pressure 4: small offset (up to 0.3 BARG) in test sets 2, 3, 4 and 5 (FIG. 4-21).
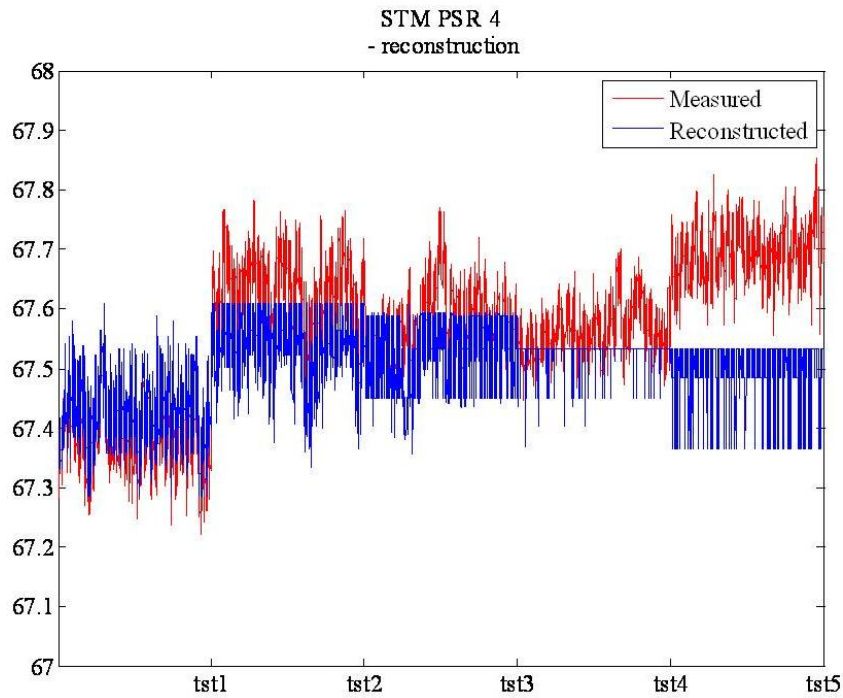
FIG. 4-21. Steam pressure 4.

− Steam generator level wide range 1: clear drift growing from test set 2 to 5 up to 3% (FIG. 4-22).
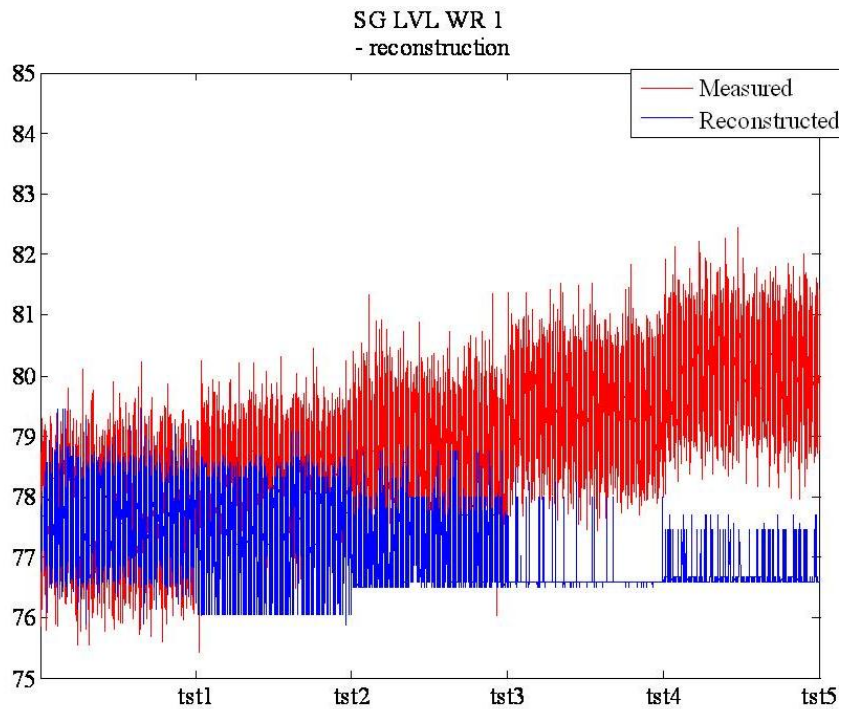
FIG. 4-22. Steam generator level wide range 1.

− Pressurizer pressure 2: small drift slowly growing from test set 2 to 5 up to 0.15 BARG (FIG. 4-23).
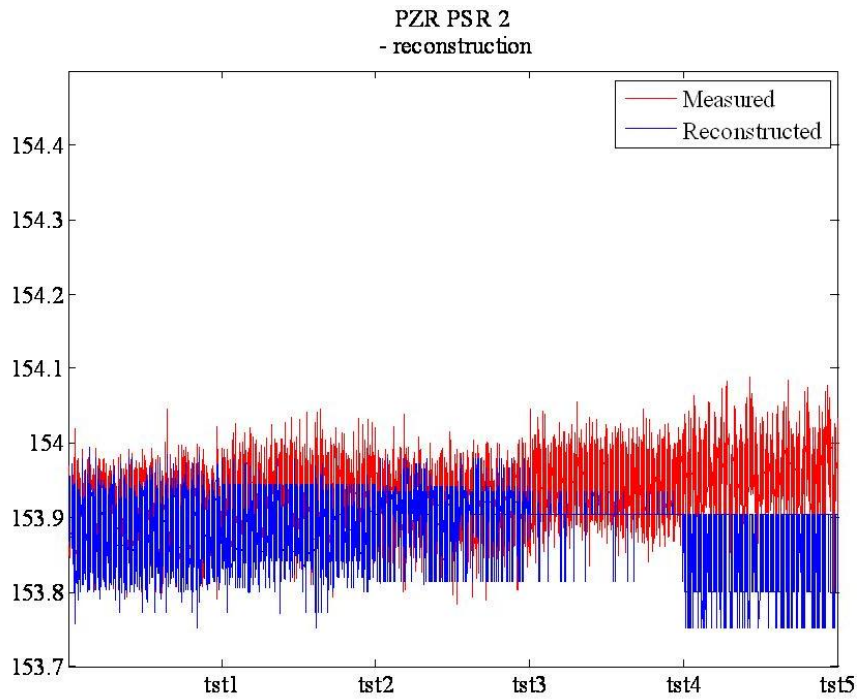
FIG. 4-23. Pressurizer pressure 2.

− RCS pressure wide range 1: small offsets in test sets 3, 4 and 5 up to 0.4 BARG (FIG. 4-24).
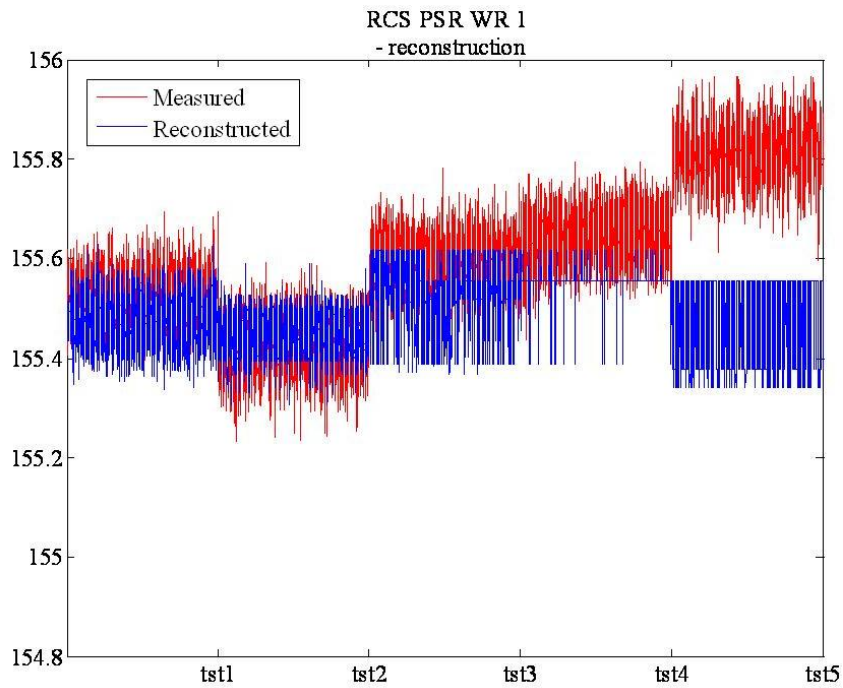
FIG. 4-24. RCS pressure wide range 1.

− RCS pressure wide range 2: small offsets in test sets 2, 3 and 4 up to 0.15 BARG (FIG. 4-25).
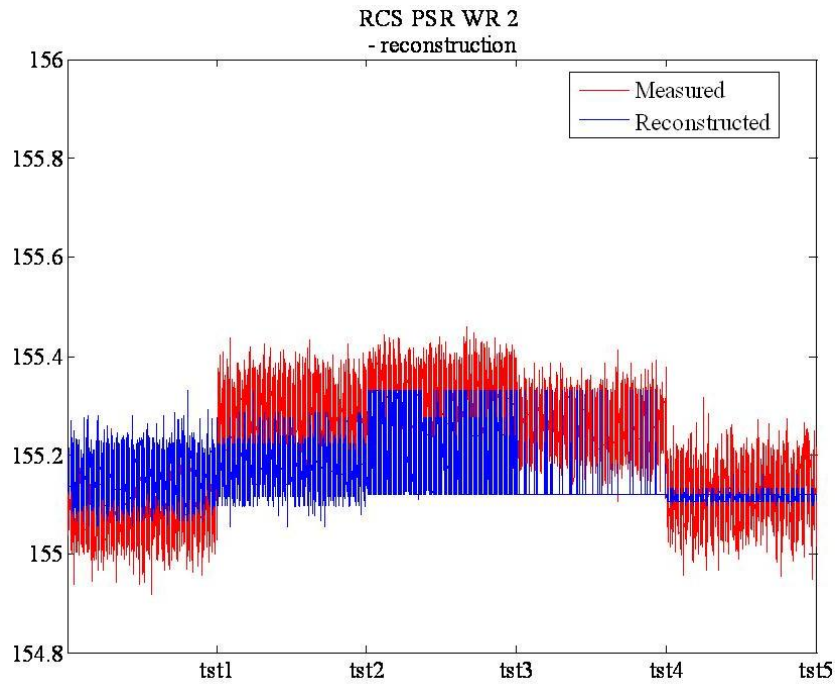
FIG. 4-25. RCS pressure wide range 2.

− RCS pressure wide range 3: small offsets in test sets 3, 4 and 5 up to 0.6 BARG (FIG. 4-26).
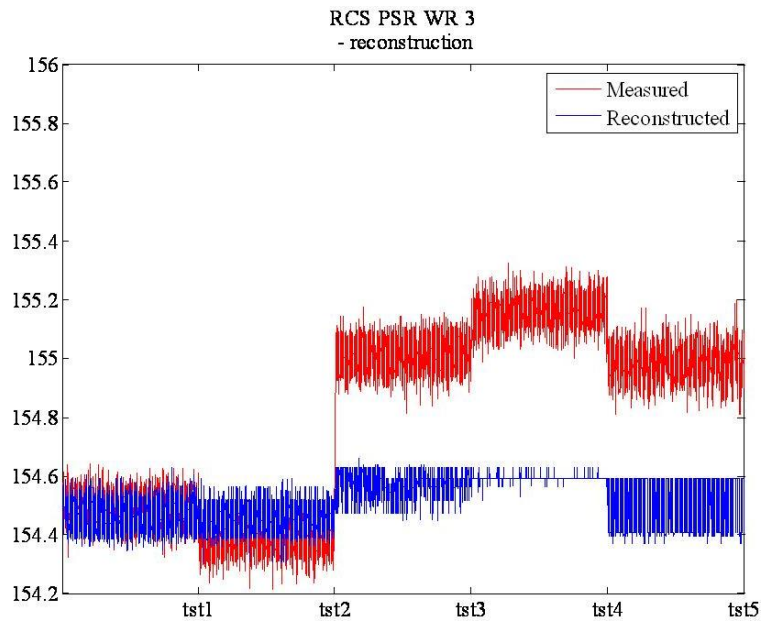
FIG. 4-26. RCS pressure wide range 3.

− RCS pressure wide range 4: small offsets in test sets 2 and 3 up to 0.3 BARG and clear offsets in test sets 4 and 5 up to 6 BARG (FIG. 4-27).
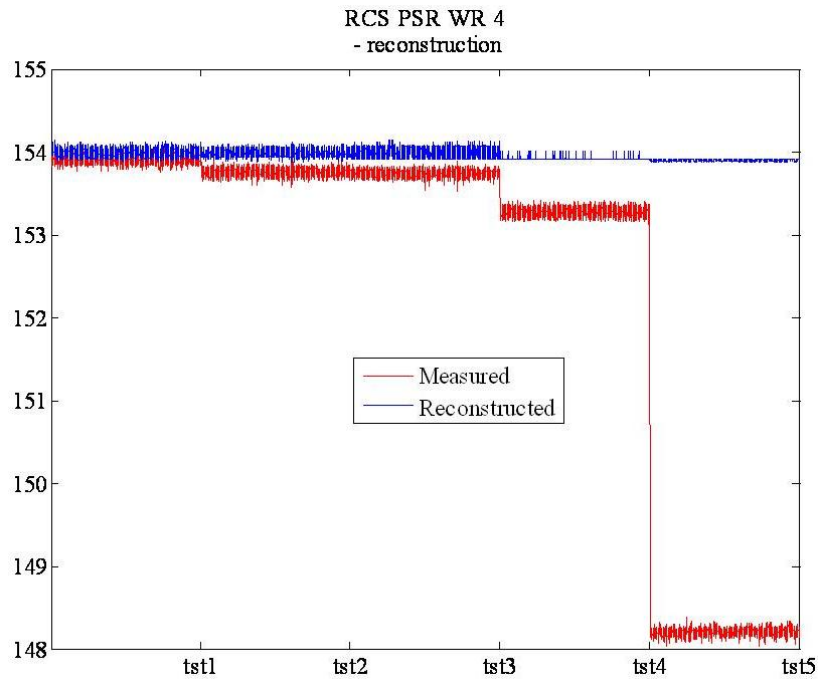
FIG. 4-27. RCS pressure wide range 4.

4.2.8. Technique 7: JDL/RSA data analysis

This method is exhaustively described in Chapter 5 of the CRP main report and in Refs [2] to [4]. The following identifies results of the benchmark data processing shown in TABLE 11 of the CRP main report.

It is important to notice here that the benchmark data, used for TABLE 11 results in the CRP main report, do not contain enough information to fully utilize data fusion technique capabilities. Only 2 out of 5 levels of fusion was used for processing via the JDL/RSA technique (see Chapter 5 in the CRP main report):

− Data pre-processing;
− Data processing.

The illustrations of the MATLAB processing of the SG levels in FIG. 4-28 to FIG. 4-31 show obvious faults in the WR SG level sensors. SG level 4 sensor has a long term decrease in the weighting factor and can be clearly identified as a faulty one. The WR SG 3 level sensor has a long-term decrease in its weight; but after some time returns to the pre-defined range. The existing data does not allow making a conclusive decision on the data quality of this sensor.
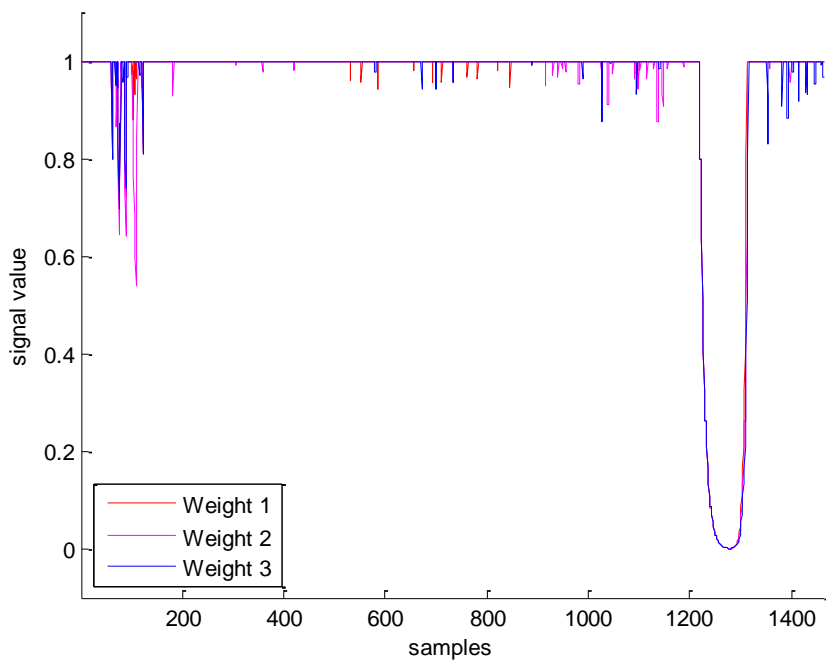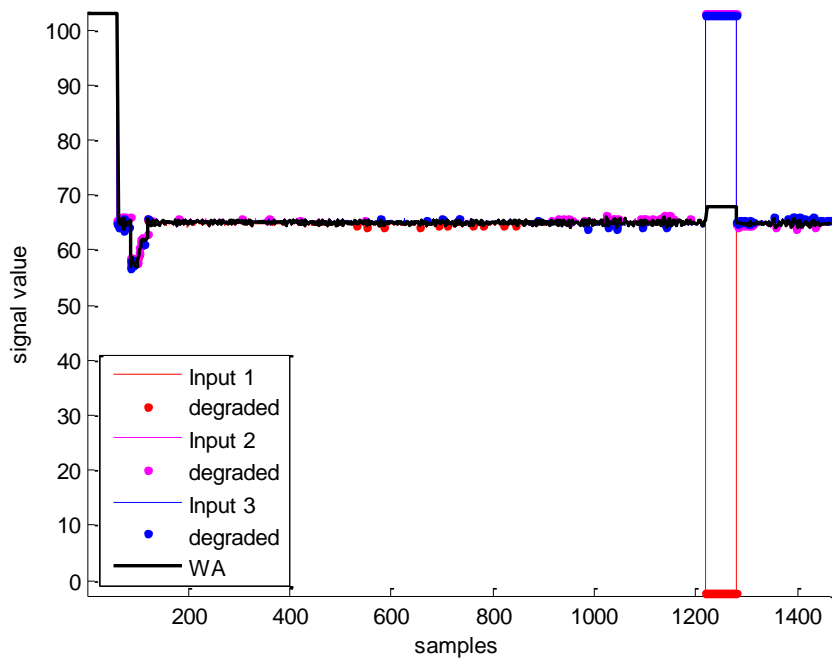
FIG. 4-28. Steam generator NR 1 – weight decreases for all examples at 0.5%.
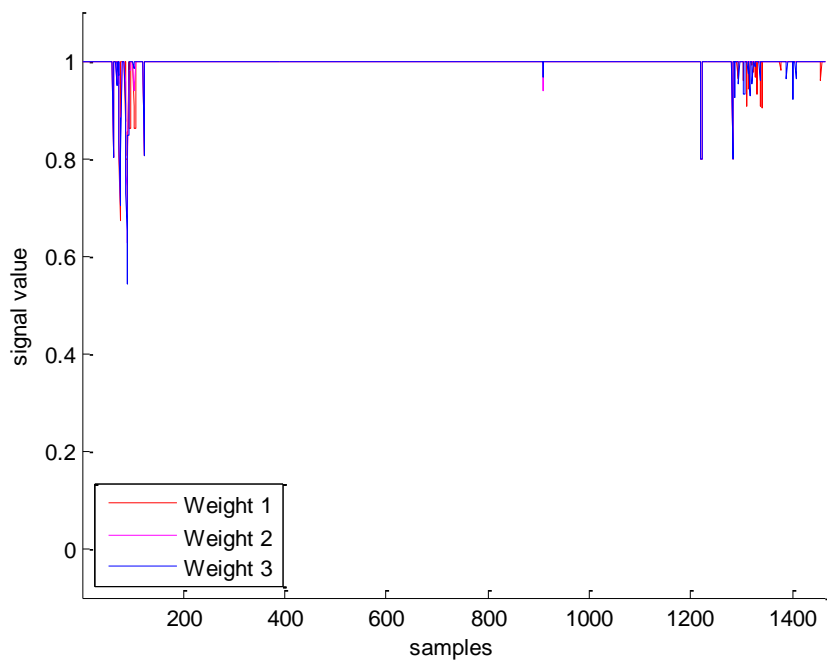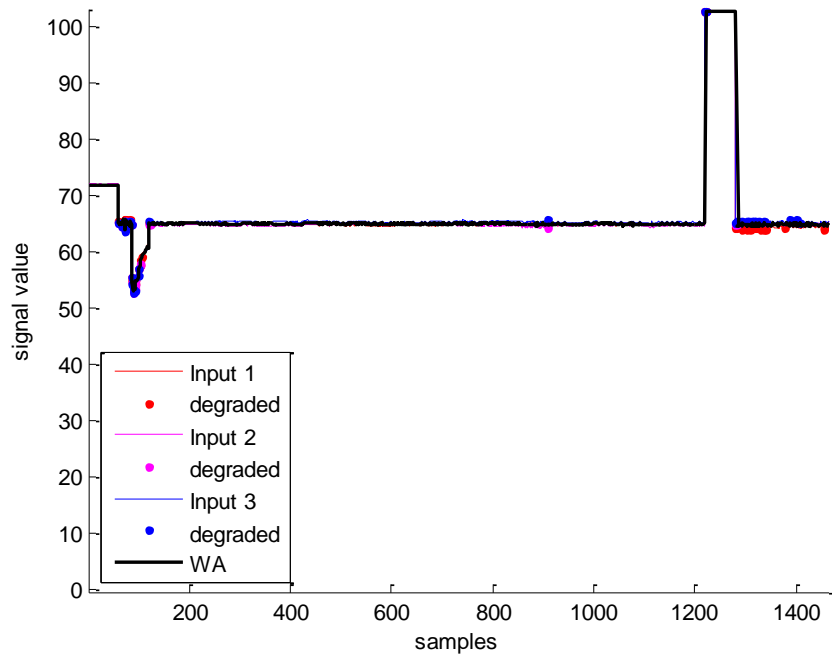
FIG. 4-29. Steam generator NR 2 – weight decreases for all examples at 0.5%.
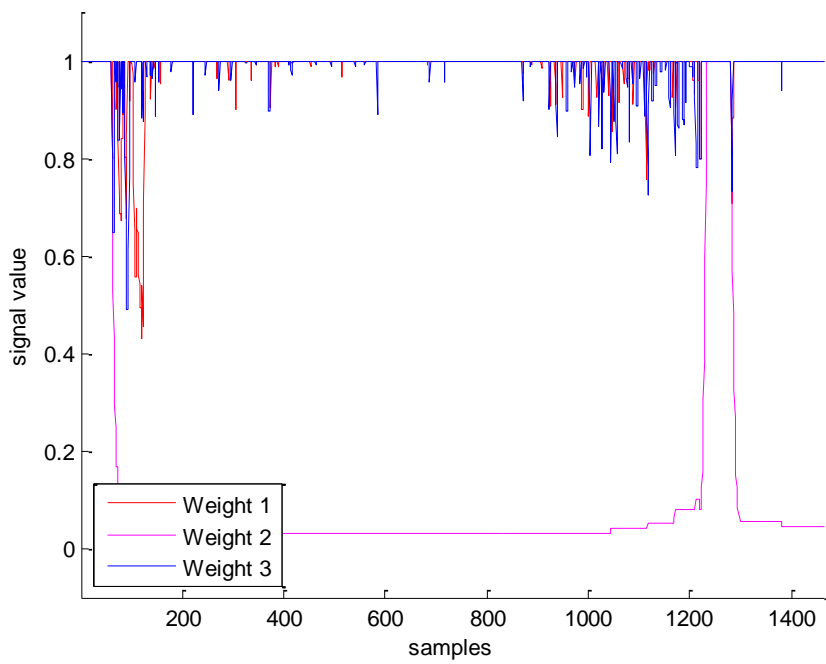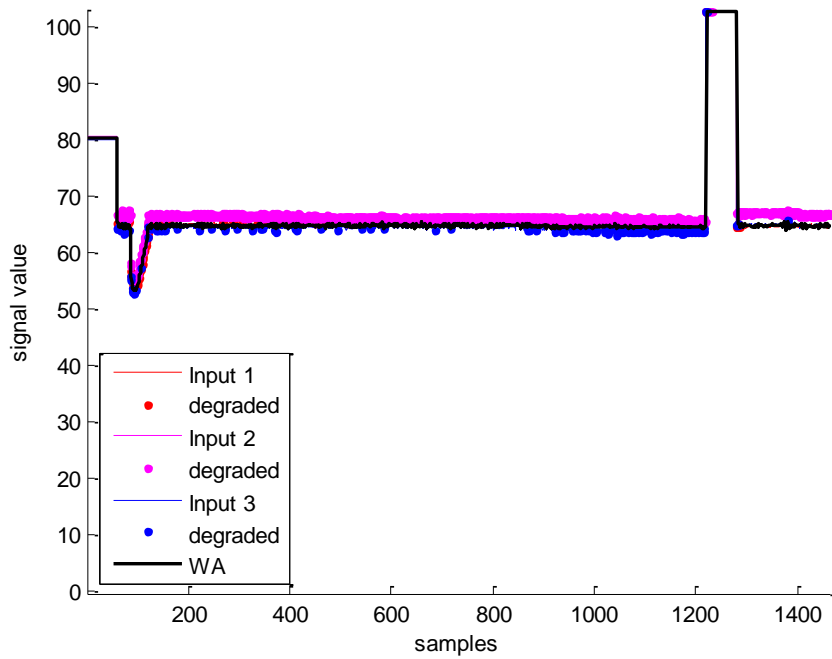
FIG. 4-30. Steam generator NR 3 – weight decreases for all examples at 0.5%.
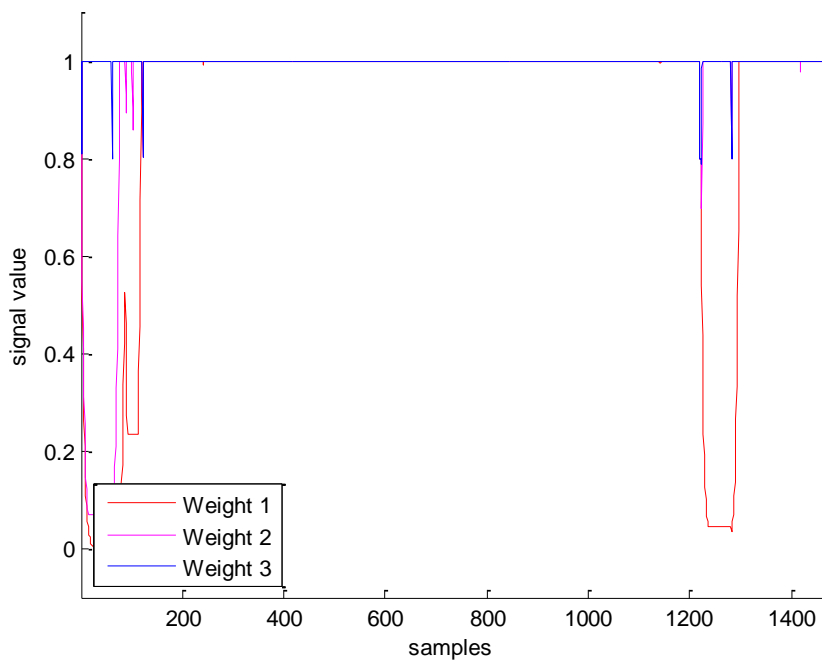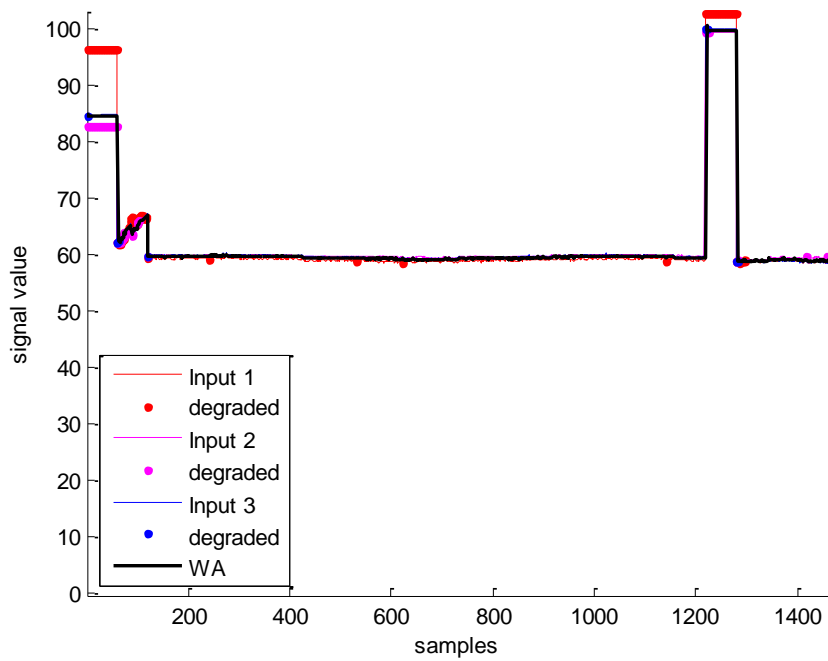
FIG. 4-31. Steam generator WR – weight decreases for all examples at 0.5%.

The same conclusion is valid for the WR RCS pressure (see FIG. 4-32 below). Stable deviation of the RCS pressure from expected value might be due to RCS average temperature change.
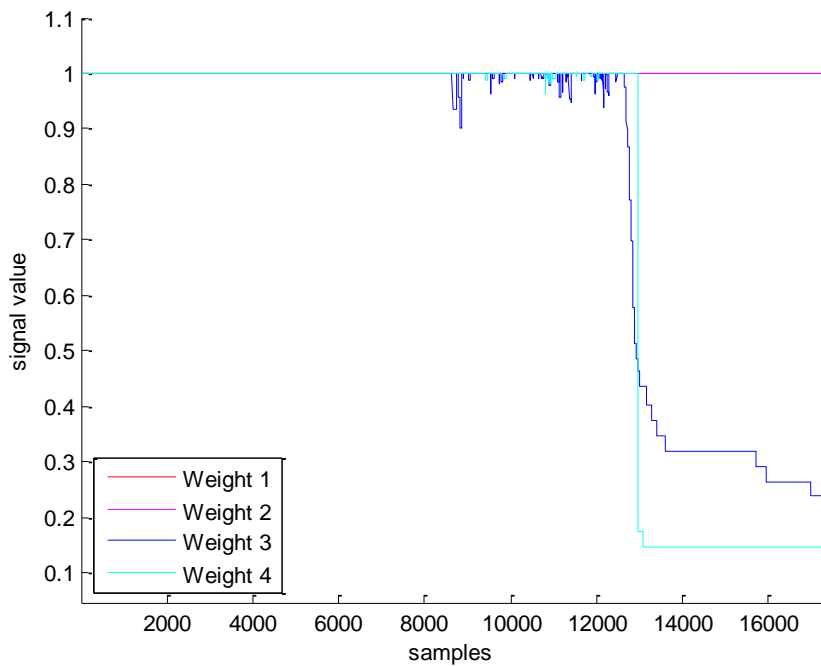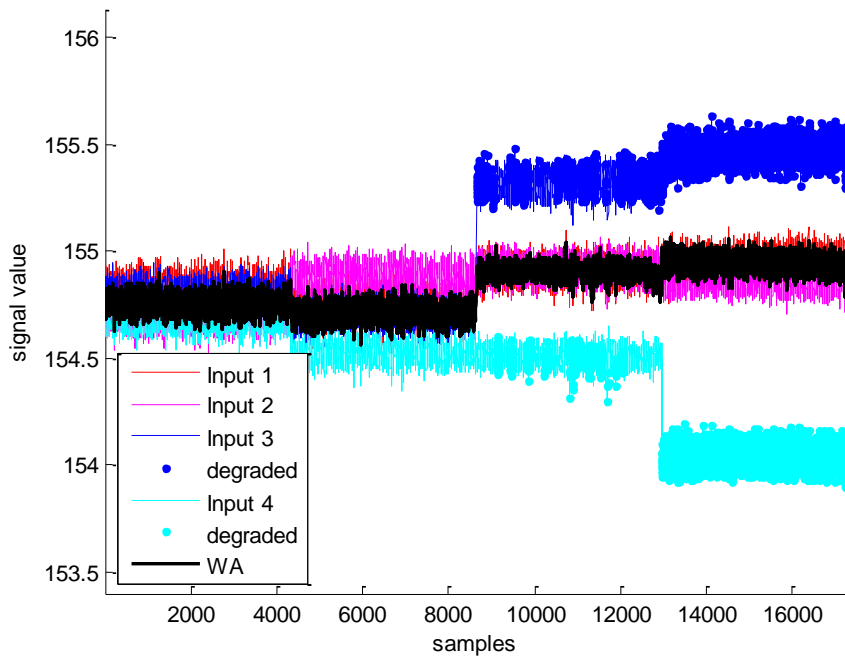
FIG. 4-32. RCS WR pressure.

4.2.8.2.   *Demonstration of the JDL/RSA technique for SUNPP primary side pressure and delta P data.*

Since the previous data set could not allow demonstrating full capacity of the JDL/RSA technique, another set of data has been used to apply all levels of the data fusion architecture. The plant data used in this demonstration is available from the accompanying CD.

4.2.8.3.   Brief description of the data set

The following parameters are available from Sheet 1 of the SUNPP 2005.xls file

Id	Description	EU
dP RCP-1	Delta pressure at RCP-1	kg/cm2
dP RCP-2	Delta pressure at RCP-2	kg/cm2
dP RCP-3	Delta pressure at RCP-3	kg/cm2
dP RCP-4	Delta pressure at RCP-4	kg/cm2
N RCP-1	Active power consumed by RCP-1	MW
N RCP-2	Active power consumed by RCP-1	MW
N RCP-3	Active power consumed by RCP-1	MW
N RCP-4	Active power consumed by RCP-1	MW
N POWER	Ex-Core neutron power (NIKE-1)	MW
dP Core	Coolant delta pressure at core	kg/cm2
dP SG-1	Coolant delta pressure at SG-1	kg/cm2
dP SG-2	Coolant delta pressure at SG-1	kg/cm2
dP SG-3	Coolant delta pressure at SG-1	kg/cm2
dP SG-4	Coolant delta pressure at SG-1	kg/cm2
P prim-1	Coolant Pressure	kg/cm2
P prim-2	Coolant Pressure	kg/cm2
P prim-3	Coolant Pressure	kg/cm2

Comments
P Prim-1 - P Prim-3 are redundant sensors.
dP RCP-1 = dP Core + dP SG-1 + dp-pipes
dp-pipes is assumed to be small.

This data is used to identify status of the RCS Main Circulation Pumps (MCP), which then transmitted to the BEACON^{TM} program.

When the raw data of MCP delta pressure was used, the quality of the data was so poor that the BEACON^{TM} program indicated presence of the Xenon-135 oscillation in the reactor core, which was obviously wrong.

Use of the raw data and the 1st principle model on Level 4 of the data fusion technique allowed avoiding this situation. An example of delta P raw and processed data by the JDL/RSA algorithm is presented below in FIG. 4-33 and FIG. 4-34.
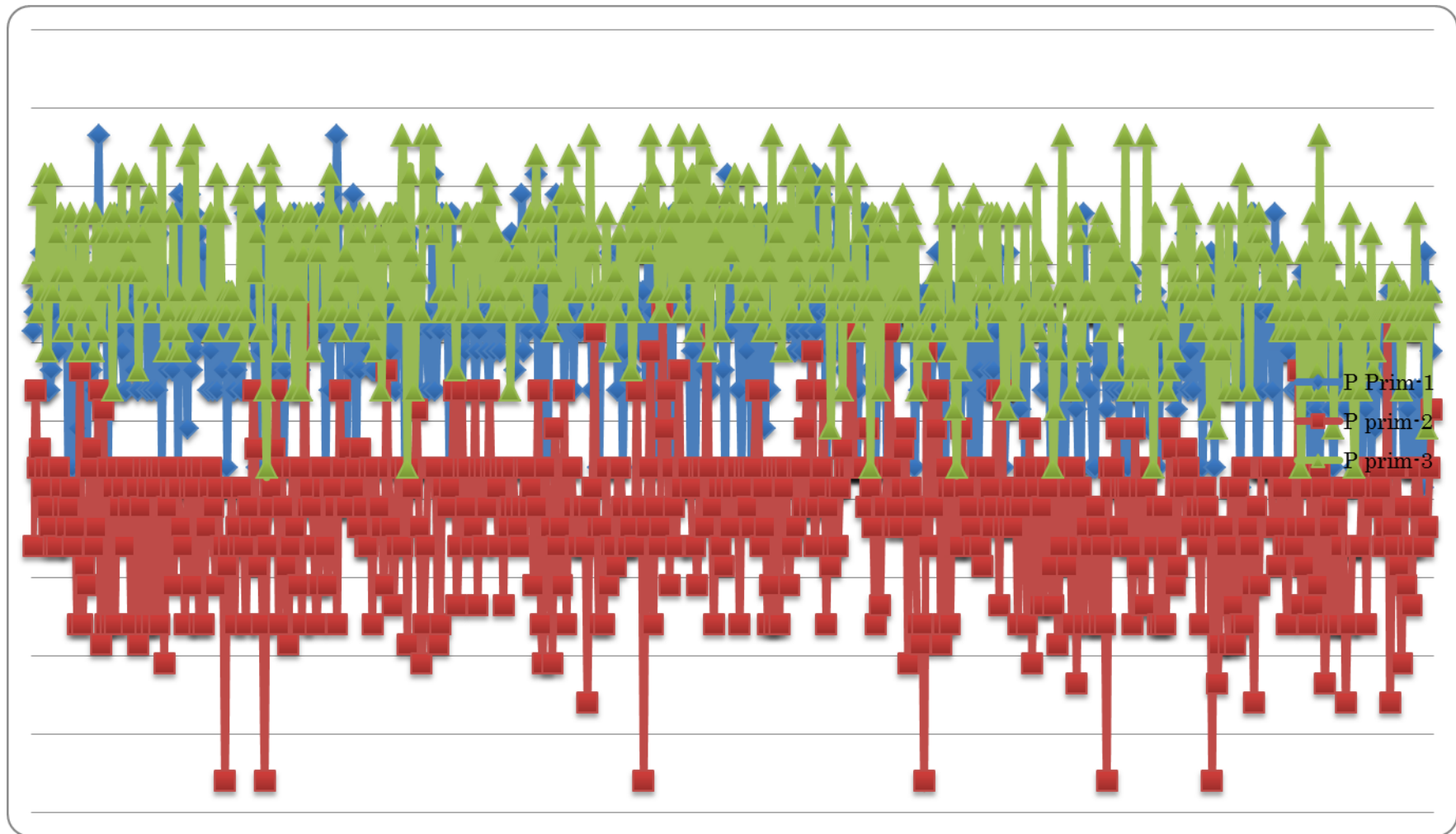
FIG. 4-33. Raw data for the RCS WR pressure.
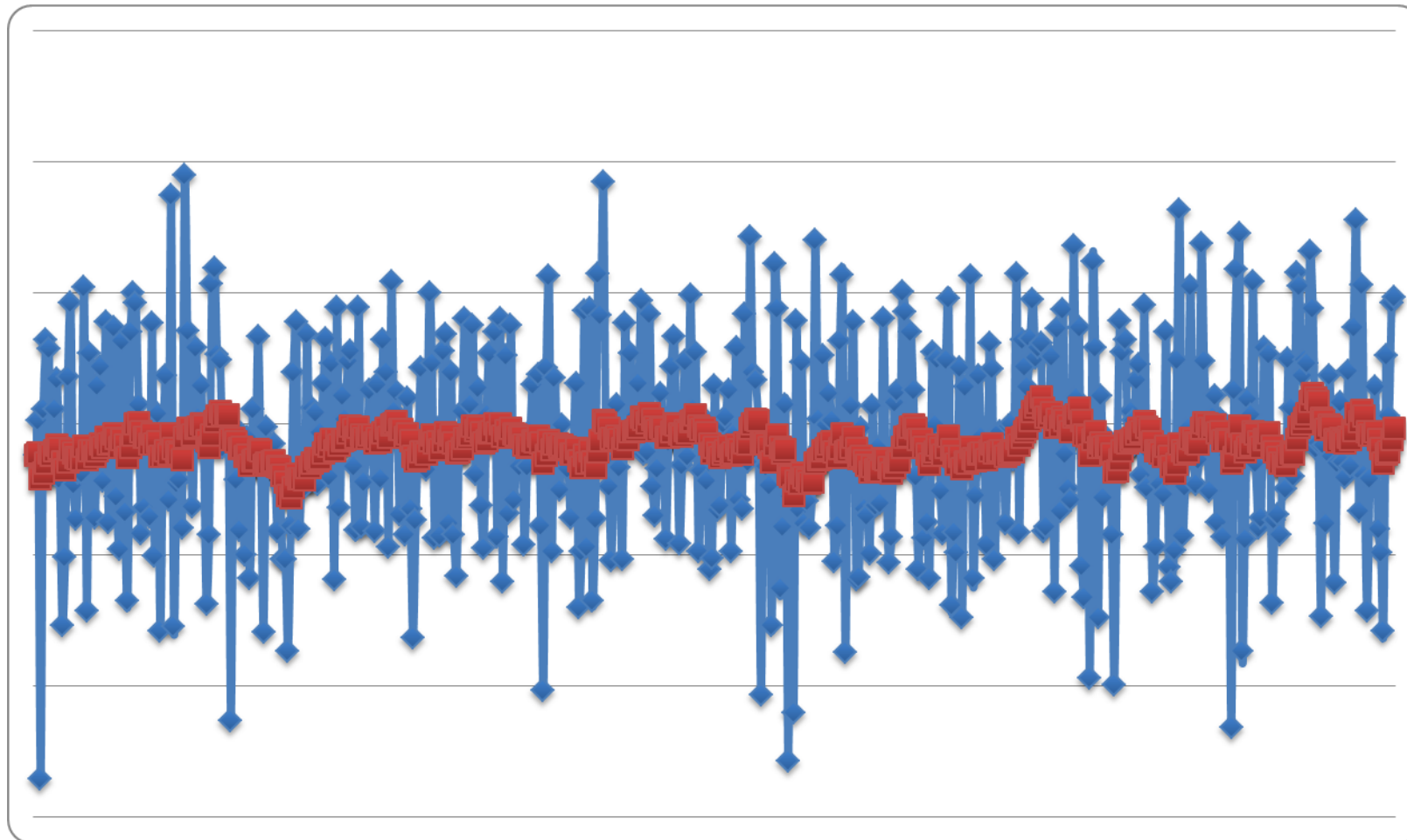
FIG. 4-34. Raw and reconciled data for the faulty delta P sensors.

4.3. SUPPORTING MATERIAL FOR CABLE DEGRADATION DETECTION
DEMONSTRATION

This section describes results of Thermal and Mechanical Degradation Detection on Low Voltage Cables Using Modern Techniques

4.3.1. Introduction

The interest of safety aspects of wire systems aging (especially those wire systems used for control and instrumentation) is increasing worldwide because of their impact on several industrial fields, like power generation, transportation and defence. Although the environment conditions and degradation mechanisms of installed cables can be different from target to target, the negative consequences of wire failures, both from a safety and performance standpoint, are so important that almost all the countries in the industrialized world have some research project in progress in this area.

In the nuclear field, where cables are normally qualified before installation for an expected life of 40 years, there are a number of issues that are not completely solved today. These issues include:

- The effect of the particular adverse environment conditions (high radiation, humidity and temperature), especially during and after a Design Basis Accident (DBA);
- Extending the plant life after 40 years involves the requirement to assess and qualify the cable conditions for a longer time;
- Many cables condition monitoring techniques do exist today, but none of them is considered accurate and reliable enough for all the cable materials in use and conditions. In addition to that, only few of them are non-destructive techniques and are applicable in situ;
- Accelerated aging techniques, for qualification purposes under DBA conditions, are often not conservative and should be complemented with reliable condition monitoring methods.

An important issue is the assessment of the condition of installed cables that have been exposed for a long time (more than 30 years) to relative high temperature and gamma radiation (the condition of cables inside the reactor containment). Several techniques have been proposed to monitor and identify cables that are close to the end of their qualified life. The purpose of this work was to evaluate two well-known techniques in detecting localized damage due to thermal and mechanical stresses. These techniques are the Time Domain Reflectometry (TDR) and the Line Resonance Analysis (LIRA). TDR is well known technique based on the measurement of a reflection, together with the elapsed time, caused by a damage along the line. LIRA (© Wirescan AS) is an emerging technique based on the evaluation of electrical properties and their trends with the aging conditions. The TDR measurements have been performed by AMS Corp. on 3 samples of low voltage cables, while the LIRA measurements have been performed by IFE using the LIRA equipment provided by Wirescan AS. (See also Refs. [5] to [8].)

4.3.2. Test description

TABLE 4-2. describes the test cables with the different type and position of the spot damages.
FIG. 4-35 to FIG. 4-38 show how the described damages have been produced on each of the three cables. The cables have been prepared for the tests by AMS Corp. in their laboratory in Knoxville, TN.

TABLE 4-2. CABLES TESTED IN THE TDR/LIRA EXPERIMENT

Cable #7	m	
Length	29.43 (96.5ft)	

Known Faults #8	From (T) m	ft
Smash with hammer	9.14	30
Butt splice	14,8	48.5
Extreme bending	23.3	76.4
Vice grip squeeze	26.4	86.6

Cable #8	m	
Length	29,66 (97.3ft)	

Known Faults #8	From (T) m	ft
Butt Splice	14.33	47
Shield burn	23.47	77
Jacket burn	26.52	87

Cable #9	m	
Length	29,90 (98ft)	

Known Faults #9	From (T) m	ft
Jacket cut	10.67	35
Butt splice	14.63	48

FIG. 4-35. Vice grip squeeze.

FIG. 4-36. Extreme bend.

FIG. 4-37. Jacket burn.

FIG. 4-38. Shield burn.

4.3.3. TDR tests

The following tables and figures show the TDR results using a CHAR system from AMS Corp.. Eleven measurements for each cable sample were conducted, one between each conductor, each conductor and the shield, and the shield to ground.

4.3.3.1. Cable 7

TABLE 4-3. CHAR SUMMARY REPORT OF CABLE 7

Parameter	Baseline	Mechanical Damage Tests	% Change
DC Resistance	16.11 MOhms	14.82 Mohms	0.087045
1 KHz Resistance	341.00 Ohms	342.30 Ohms	0.000964
1 KHz Capacitance	2.31 nF	2.29 nF	0.008734
1 KHz Dissipation	4.95 m	4.93 m	0.004057
Insulation DCR	1.71 Tohms	2.97 TOhms	0.424242
Polarization Ratio	1.79	2.81	0.362989
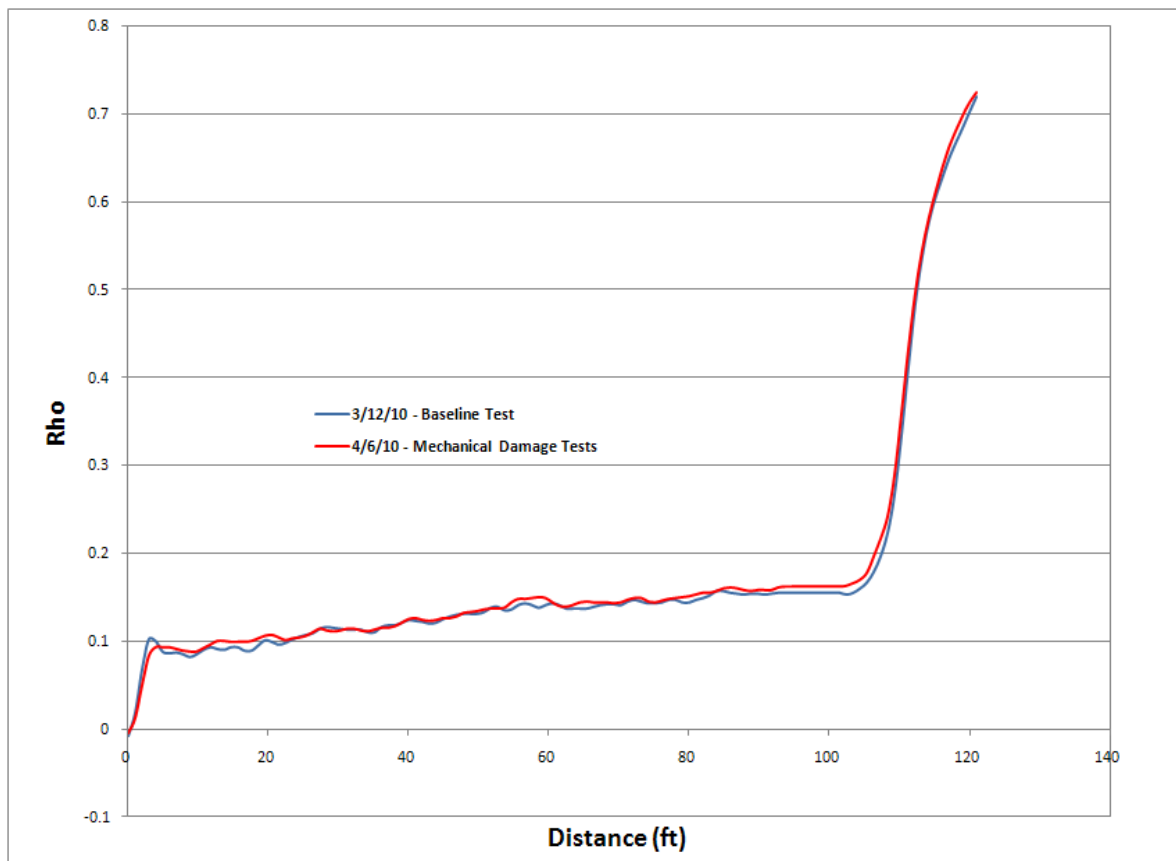
FIG. 4-39. TDR traces comparing baseline and mechanical damages.
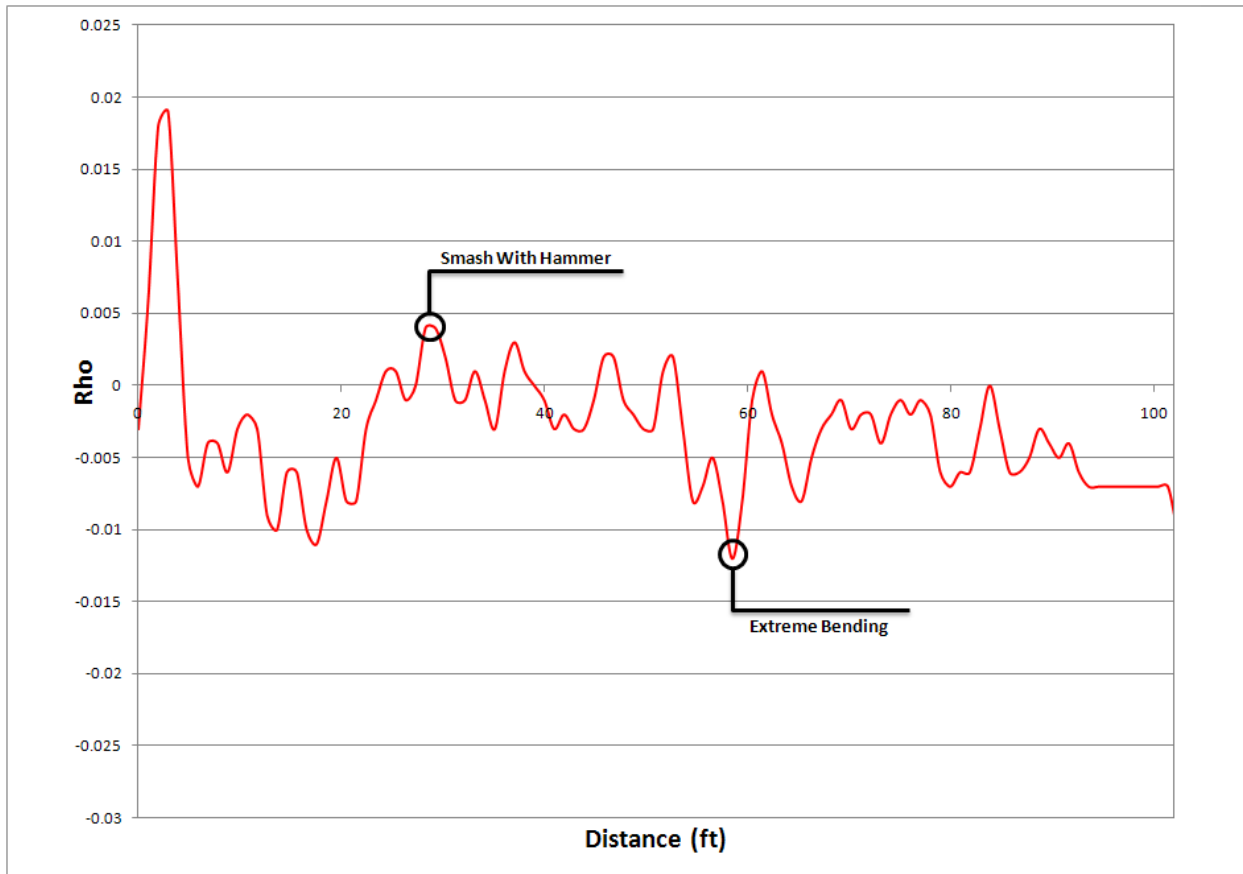
FIG. 4-40. Cable 7 difference plot.

4.3.3.2.   Cable 8

TABLE 4-4.   CHAR SUMMARY REPORT OF CABLE 8

Parameter	Baseline	Burn Tests	% Change
DC Resistance	15.97 MOhms	15.56 Mohms	0.02635
1 KHz Resistance	345.81 Ohms	345.98 Ohms	0.000491
1 KHz Capacitance	2.27 nF	2.26 nF	0.004425
1 KHz Dissipation	4.92 m	4.92 m	0
Insulation DCR	1.82 TOhms	1.7 TOhms	0.070588
Polarization Ratio	2.16	1.68	0.285714
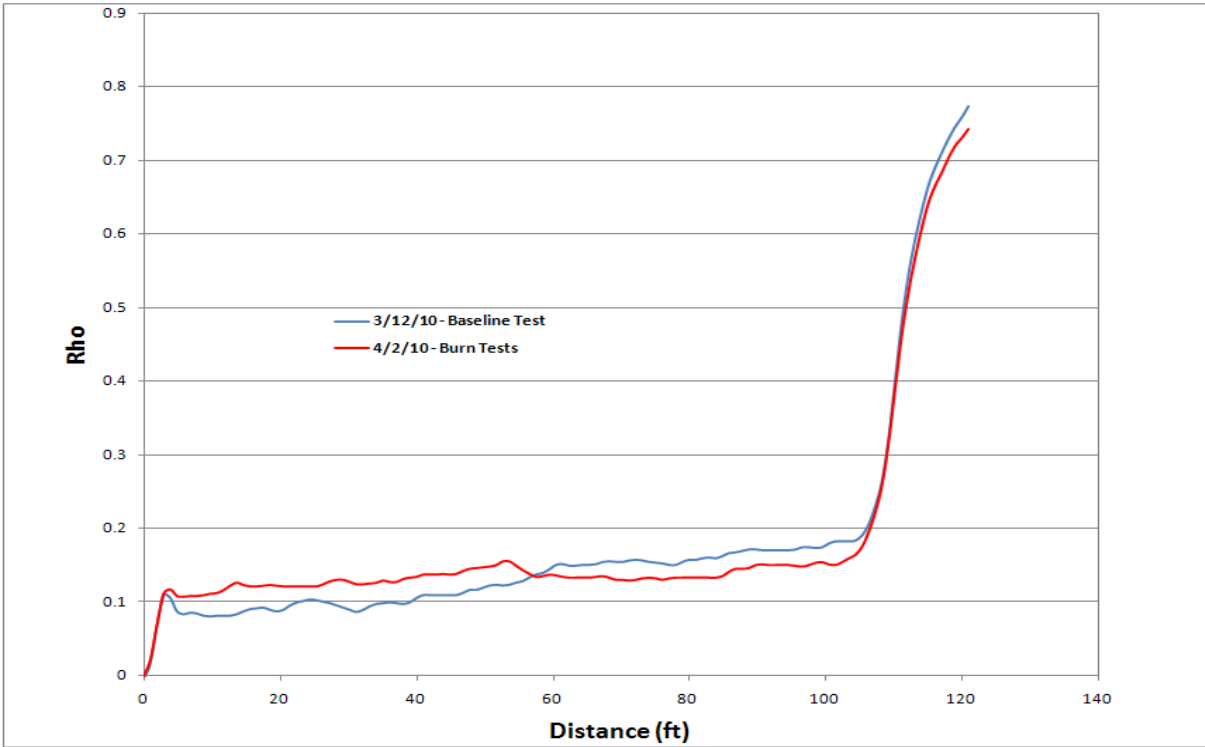
FIG. 4-41. TDR traces comparing baseline and burns.
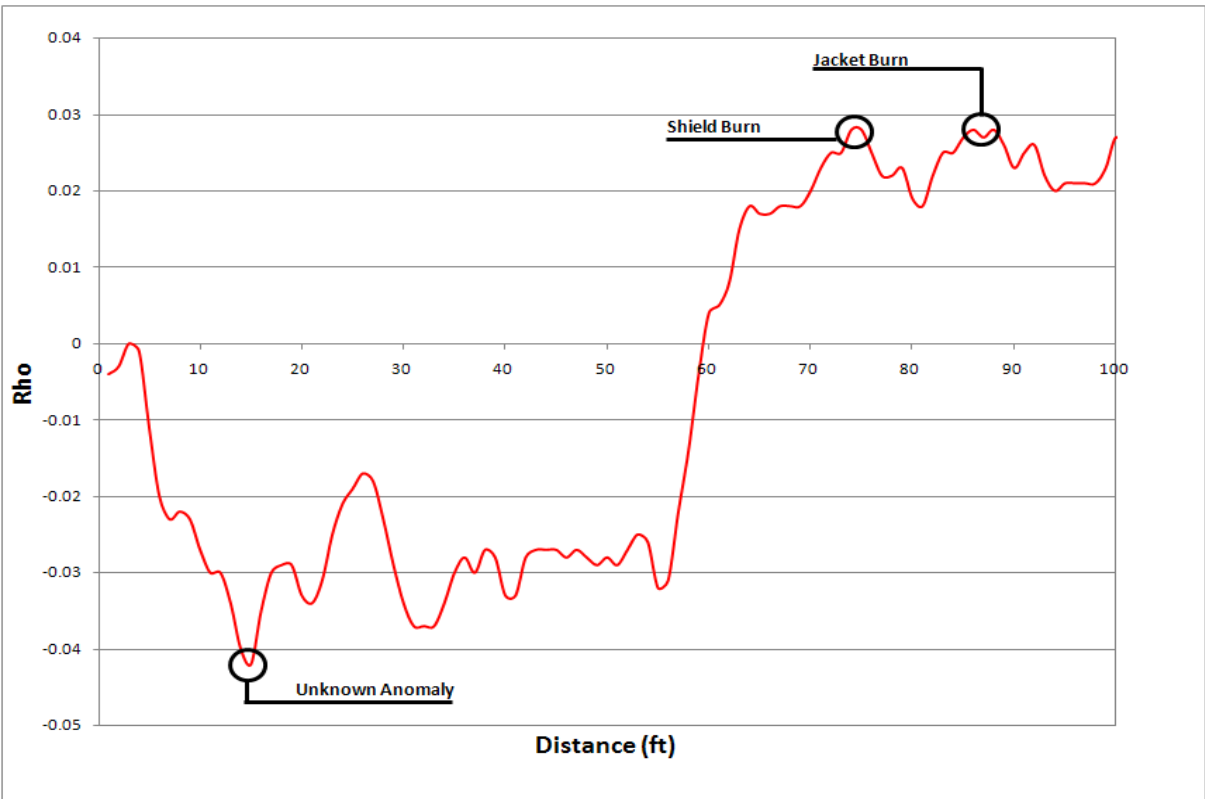
FIG. 4-42. Cable 8 difference plot.

4.3.3.3.   Cable 9

TABLE 4-5.   CHAR SUMMARY REPORT OF CABLE 9

Parameter	Baseline	Jacket Cut Test	% Change
DC Resistance	16.37 MOhms	15.29 Mohms	0.070634
1 KHz Resistance	341.97 Ohms	341.69 Ohms	0.000819
1 KHz Capacitance	2.3 nF	2.3 nF	0
1 KHz Dissipation	4.94 m	4.94 m	0
Insulation DCR	1.75 Tohms	4.06 TOhms	0.568966
Polarization Ratio	2.04	3.66	0.442623
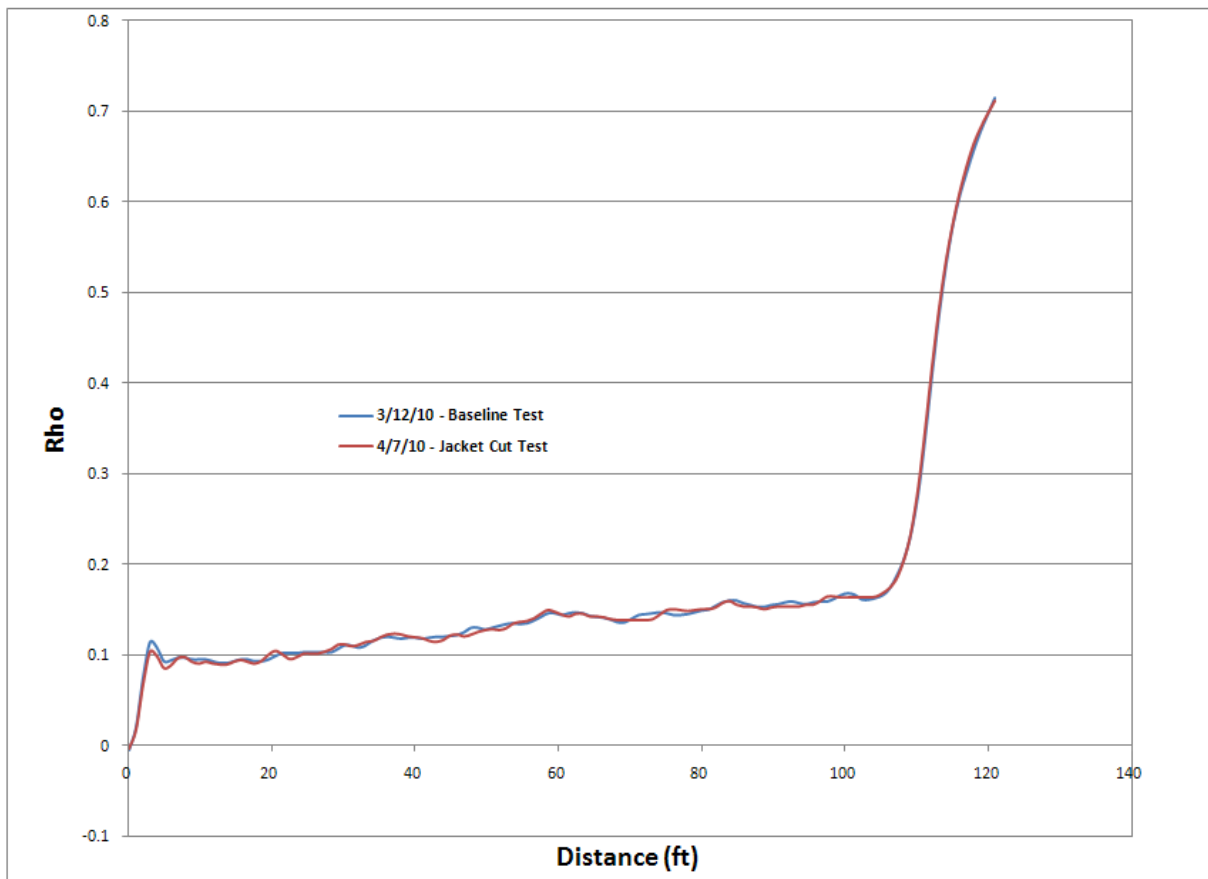
FIG. 4-43. TDR traces comparing baseline and jacket cut test.
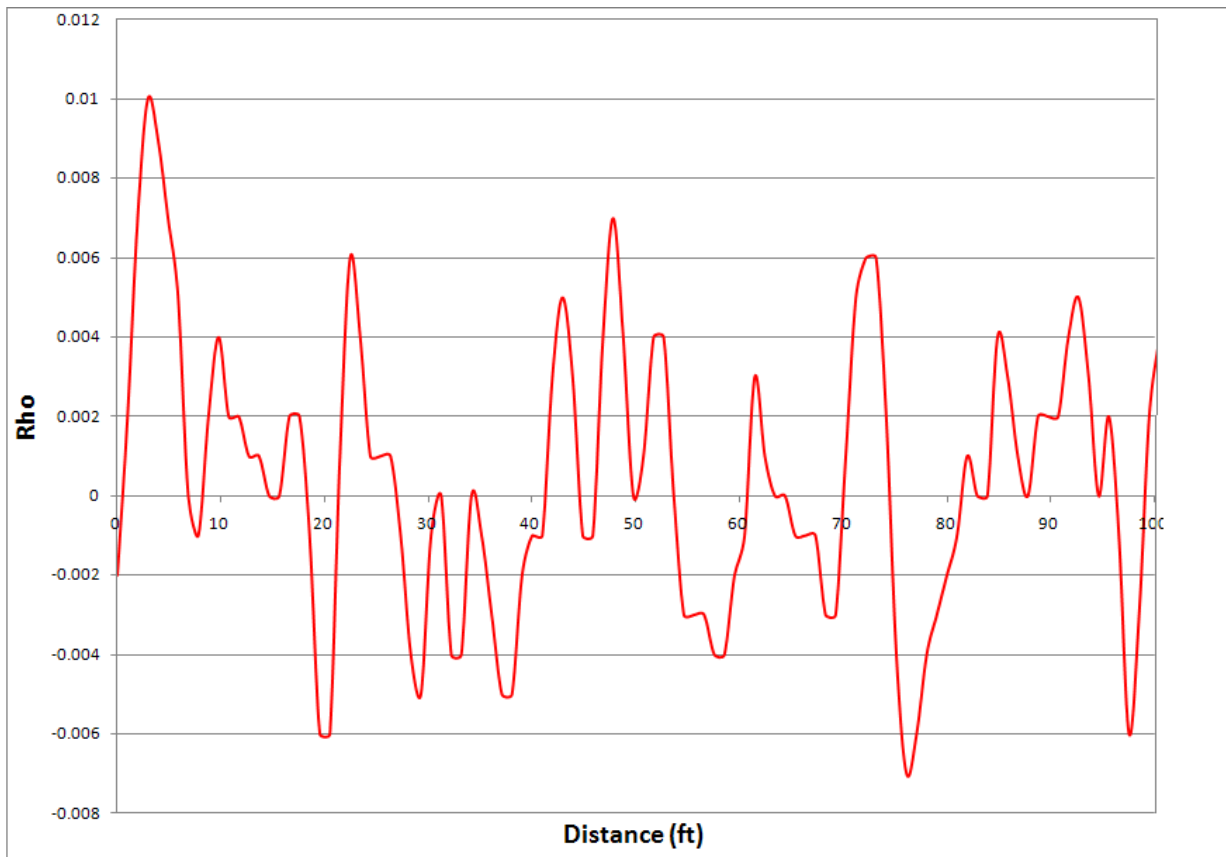
FIG. 4-44. Cable 9 difference plot.

4.3.4. LIRA tests

The following tables and figures show the LIRA results performed by Wirescan AS, Norway. All the measurements were performed using one conductor and the shield. Four measurements for cable sample were conducted, one for each conductor.

The cables before damage were not available for LIRA baseline measurements, so the LIRA analysis and results are based on one shot measurements on the damaged cables and no difference plot was possible to draw.

TABLE 4-6.   MAIN ELECTRICAL PARAMETERS ESTIMATED BY LIRA

Overall Results				
Cable Id	7	8	9	AVG
Length (m)	29.43	29.66	29.9	
Velocity Ratio	0.714	0.721	0.726	**0.72**
Char. Impedance (Ω)	64.5	62.7	63.9	**63.7**
Inductance (µH/m)	0.3	0.3	0.29	**0.3**
Capacitance (pF/m)	73	76	73	**74**

4.3.4.2. Cable 7

Abs. Spot Signature
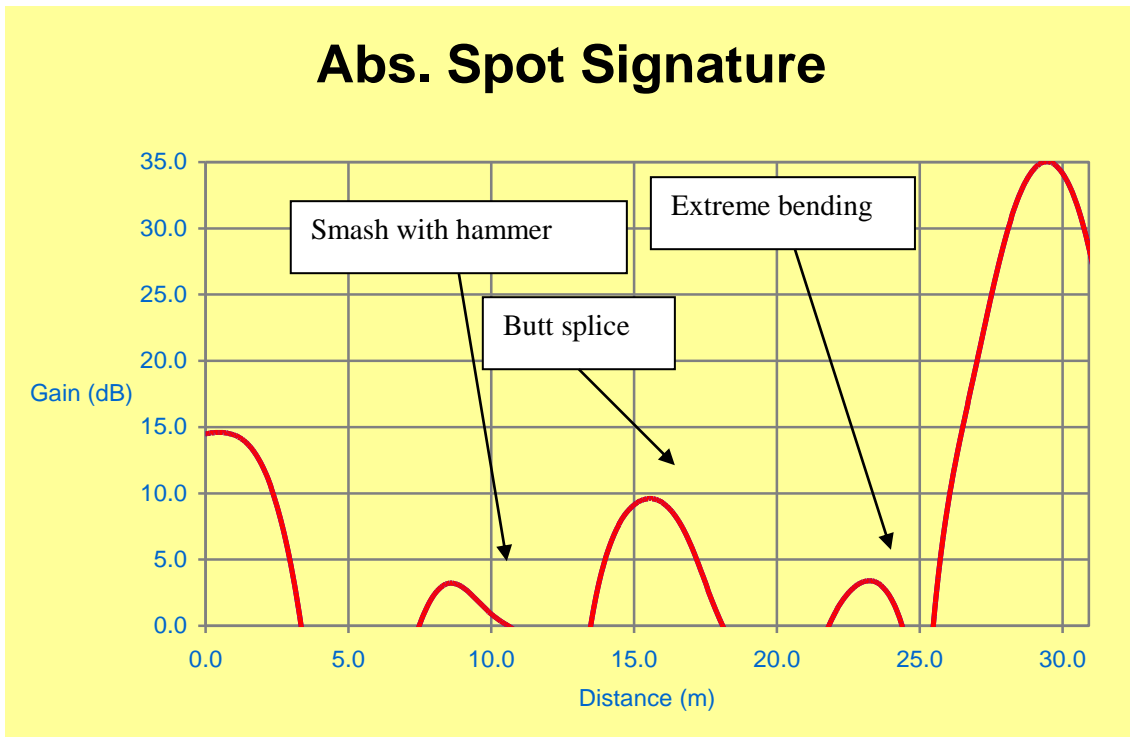
FIG. 4-45. Cable 7 LIRA signature.

TABLE 4-7.   LOCATION OF DETECTED FEATURES ON CABLE 7

HotSpot			
Loc (m)	Peak (dB)	Delta	DNORM
8.6	1.6	23.3	31.3
15.55	5.2	19.8	39
23.23	-4.2	29.1	31.6
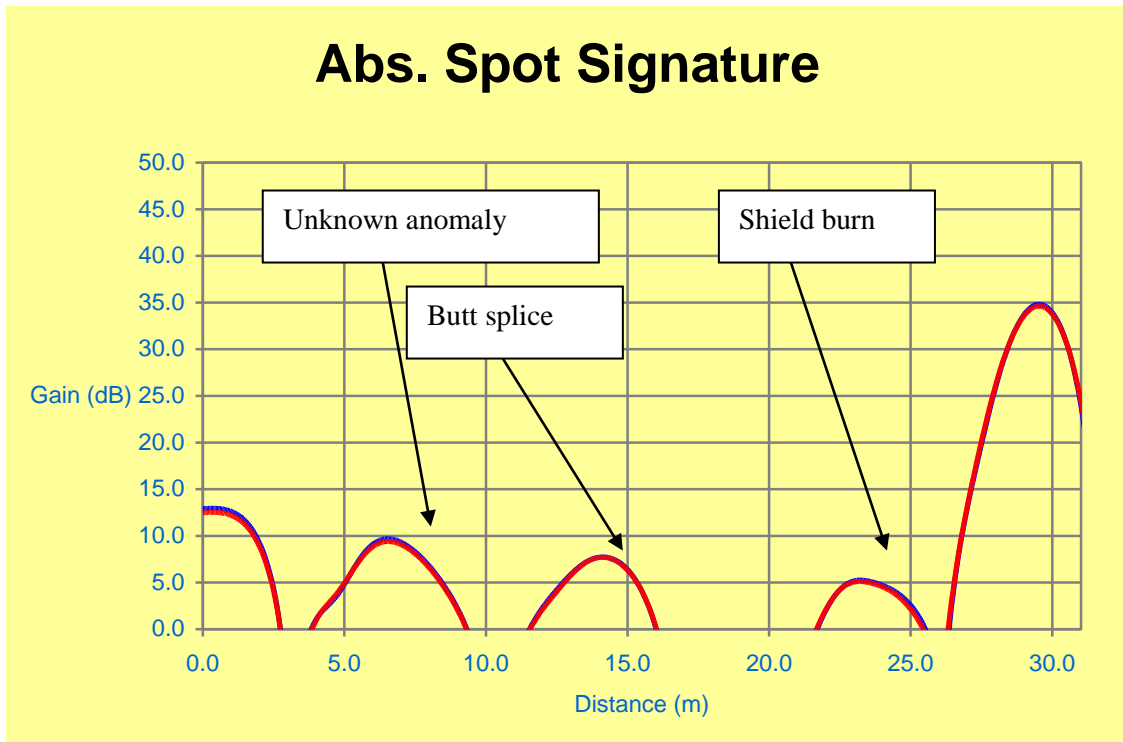
FIG. 4-46. Cable 8 LIRA signature.

TABLE 4-8.   LOCATION OF DETECTED FEATURES ON CABLE 8T

HotSpot			
Loc (m)	Peak (dB)	Delta	DNORM
6.53	9.1	16.2	39.3
14.13	4.2	21.1	36.7
23.23	-1.8	27.1	33.8
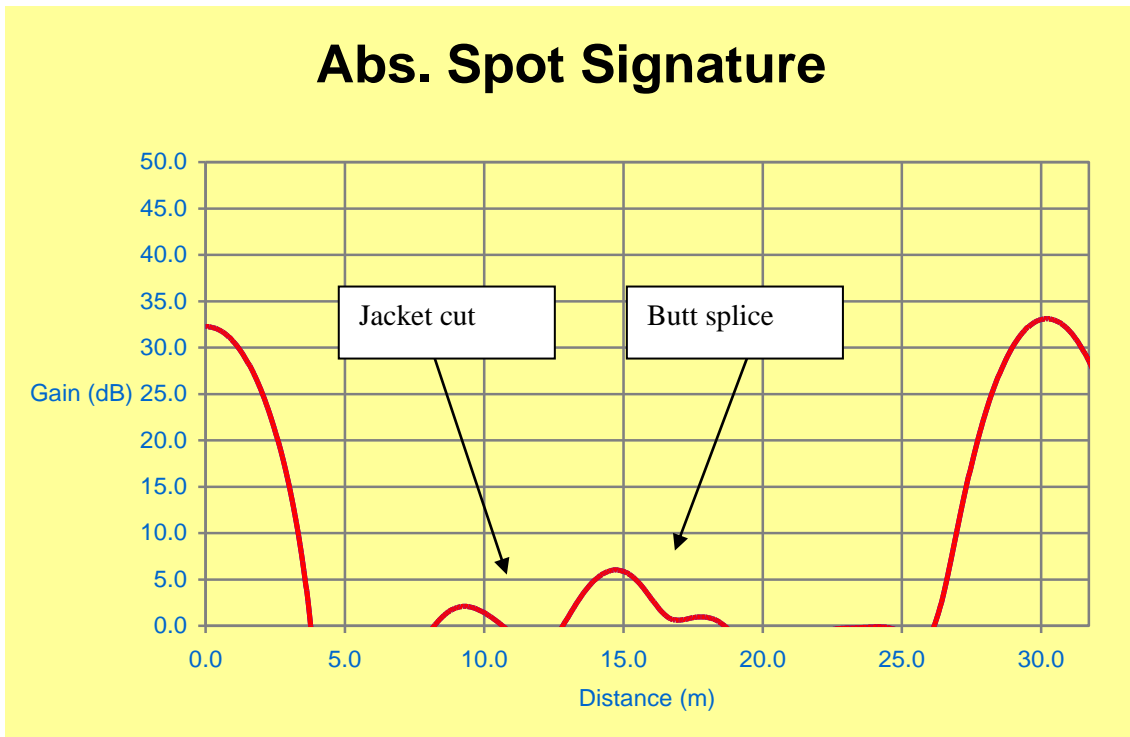
FIG. 4-47. Cable 9 LIRA signature.

TABLE 4-9.   LOCATION OF DETECTED FEATURES ON CABLE 9

HotSpot			
Loc (m)	Peak (dB)	Delta	DNORM
9.3	0	25.5	32.2
14.73	2.5	23	36.8

4.3.5.   Discussion of the results

The LCR and insulation resistance, IR, measurements made using the CHAR equipment were unable to detect the faults that were created on any of the three cables. However, the TDR traces and TDR difference plots were able to pinpoint the location of several of the faults created on the cables. The portion of Cable 7 that was hit with a hammer was detected along with the section that experienced an extreme bend. These results can be seen in FIG. 4-40. The shield and jacket burn were both detected on Cable 8 and can be seen in FIG. 4-42. Also, an unknown anomaly was discovered in the TDR difference plot. TDR was unable to detect jacket cut that was made in Cable 9.

LIRA was able to detect the point that experienced the smash with a hammer, the butt splice and the extreme bend. These results can be seen in FIG. 4-45 and TABLE 4-7. Neither cable testing techniques were able to detect the vice grip squeeze. LIRA is unable to detect the vice grip squeeze due to the termination shadow it produces. Detection of features close to the termination would require higher bandwidth using LIRA. The LIRA system discovered both of the burns created on Cable 8 along with the unknown anomaly just as the CHAR equipment. However, LIRA was able to

detect the butt splice that is in Cable 8, whereas the CHAR equipment did not. These results can be seen in FIG. 4-46 and TABLE 4-8. The jacket cut and the butt splice were detected in Cable 9 by the LIRA equipment and can be seen in FIG. 4-47 and TABLE 4-9.

4.4. ADDITIONAL SUPPLEMENTARY MATERIAL

4.4.1. Thermal ageing of EPR/EPDM insulated cables in nuclear power plants

(A comparative assessment of existing techniques)

An important issue is the assessment of the condition of installed cables that have been exposed for a long time (more than 30 years) to relative high temperature and gamma radiation (the condition of cables inside the reactor containment). Several techniques have been proposed to monitor and identify cables that are close to the end of their qualified life. The purpose of this work was to evaluate 3 well known techniques and finding the correlation among them. These techniques are the Elongation-At-Break (EAB), the Indenter [9], and the Line Resonance Analysis (LIRA) [10] to [16]. The first one is the reference technique, for which a limit of 50% absolute was set by several international standards [17]. The Indenter is a local technique that has got good results, mainly with EPR2 insulated cables. LIRA is an emerging technique based on the evaluation of electrical properties and their trends with the aging conditions.

The cable tested are low-voltage, EPDM3 insulated cables produced by the Swedish Lipalon. The reason for this choice is that this type of cables is widely in use in all the Swedish nuclear power plants. Samples 5m long of 3 Lipalon cable types were globally aged artificially for different times in 2 different environments: air (simulating the containment environment in PWR plants) and nitrogen (simulating the inert environment in BWR plants). After exposure to thermal degradation, the cable samples were analyzed using the 3 methods mentioned above. This paper describes the findings and results if this analysis.

4.4.2. Experimental setup

4.4.2.1. Cable specification

The materials used in this study are unexposed Lipalon cables that have been stored in a cold and dark environment at Ringhals. Three different types of unexposed cables have been aged and studied by mechanical and electrical testing. The jacketing of Lipalon cables is based on chlorosulfonated polyethylene (Hypalon) and the core insulation has a thin outer layer of Hypalon and a thicker inner layer of EPDM rubber [18]. The diameters of the cables were between 11 to 16 mm. In TABLE 4-10 the cables are presented with their codes.

TABLE 4-10. CABLE TYPES USED IN THE EXPERIMENT

Code	Start condition	Denoted
FSAR-TG 3x1+S	Unexposed	Medium
FSFR 7x1	Unexposed	Large
FSSR 3x1	Unexposed	Small

---

[2] EPR: Ethylene Propylene Rubber
[3] EPDM: Ethylene Propylene Diene Monomer

4.4.2.2. Oven characteristics

The unexposed cables were cut into 5.4 m long samples and winded onto aluminium cylinders. The diameter of the cylinders were calculated from the least bending radius (> 8 times the cable diameter) allowed for the cables. These cylinders with the winded cables were aged in ULE-600 ventilated ovens (Memmert, Germany) at a temperature of 140 °C in two different environments: air and nitrogen. To be able to verify that the LIRA method works even for long cables, which is the case in real life, two long samples of 20 and 30 meter of the small cable were aged at two different ageing times in air at 140 °C.

4.4.2.3. Ageing in air environment

Cable objects from the three different types, small, medium and large, were aged in air directly in the ovens. The samples of each cable type were aged at 10 different ageing times at 140 °C.

4.4.2.4. Ageing in nitrogen environment

Cable objects from the small cable were aged in glass chambers specially made to fit the small aluminium cylinders. Chambers that were large enough to fit the aluminium cylinders with the larger cables, type medium and large, were constructed from ventilation cylinders. The samples were flushed with nitrogen for 24 hours at room temperature before oven ageing. The nitrogen flow was 20 ml/min during both the pre-flush and the ageing. The samples were aged at 10 different ageing times in 140 °C.

4.4.3. Ageing indicators

4.4.3.1. Indenter

The indenter ageing indicator [9], called the indenter modulus, is the ratio between the force of a needle penetrating the insulation and the consequent displacement. Normally measured in N/mm, it ranges between 4 (new insulation) and 15 (degraded insulation). The indenter indicator is a local measure and it is normally averaged among several measurements (10 in this work) to produce a statistically significant value.

4.4.3.2. Elongation-at-break (EAB)

EAB [9] is another mechanical test that measures the maximum elongation of an insulation strip sample before it breaks. The ratio between the sample length before and after the stretch is called the absolute EAB indicator. This is the only indicator for which a consensus exists about an acceptable and conservative threshold value: 50% absolute. For this reason, other indicators as the indenter of the LIRA indicator must correlate with EAB to produce a threshold value.

4.4.3.3. LIRA

Several tests [9], [10], [11], [13], [14], and [15] have shown that global degradation in a cable insulation results in changes in the dielectric capacitance and cable inductance, at some degree. These changes affect the cable attenuation, which can be expressed as:

$$\alpha(dB/km) = Kf^{\,a}\sqrt{\frac{C}{L}} \tag{3}$$

where K is constant for a particular cable type and geometry, and depends on the DC resistance; f is the signal frequency, and the exponent "a" takes into account the skin effect and ranges between 0.5 and 1.

Equation (3) shows that frequency acts as a gain factor in the relation between α and C/L and for this reason LIRA uses high frequency attenuation values as the basis for a global condition indicator. High frequency attenuation is estimated by LIRA through a proprietary method called 3rd-harmonic analysis [15].

However, the use of an attenuation figure as it is would not be enough for condition assessment, because of its dependence on the ratio C/L. Degradation affects C and L in a complex way and the shape of its ratio might be non-monotonic through the entire cable life. For this reason, LIRA implements a method where the contributions from C and L are isolated, resulting in an indicator sensitive only to C (CBAC2) and another indicator sensitive only to L (CBAL). Since it has been demonstrated that degradation affects C at a higher degree than L [14] to [16], CBAC2 is used as a global condition indicator. Note that no attempt is done to estimate directly C or L: CBAC2 is calculated through the estimation (using frequency analysis) of:

− The high frequency attenuation (3rd harmonic analysis);
− The cable characteristic impedance Z0;
− The signal phase velocity VR.

4.4.4. Results

The following graphs show the traces of the 3 condition indicators on the same plot, to visually evaluate the correlation existing among the different methods. In all these plots, the y-axis scale has been adjusted so that the 3 indicators trend toward the same side (downtrend) and the total deviation in the ageing period is similar.

The first 3 plots, FIG. 4-48 to FIG. 4-50, refer to the air environment. In the small type, the 3 methods correlate well, although EAB and CBAC2 at a better degree. Note the reverse trend of CBAC2 and Indenter in the first 20 hours. EAB and CBAC2 seem to give a better indication then IND, up to 95 hours (accelerated). After that, EAB and CBAC2 tend to flatten out, while IND is still trending well.
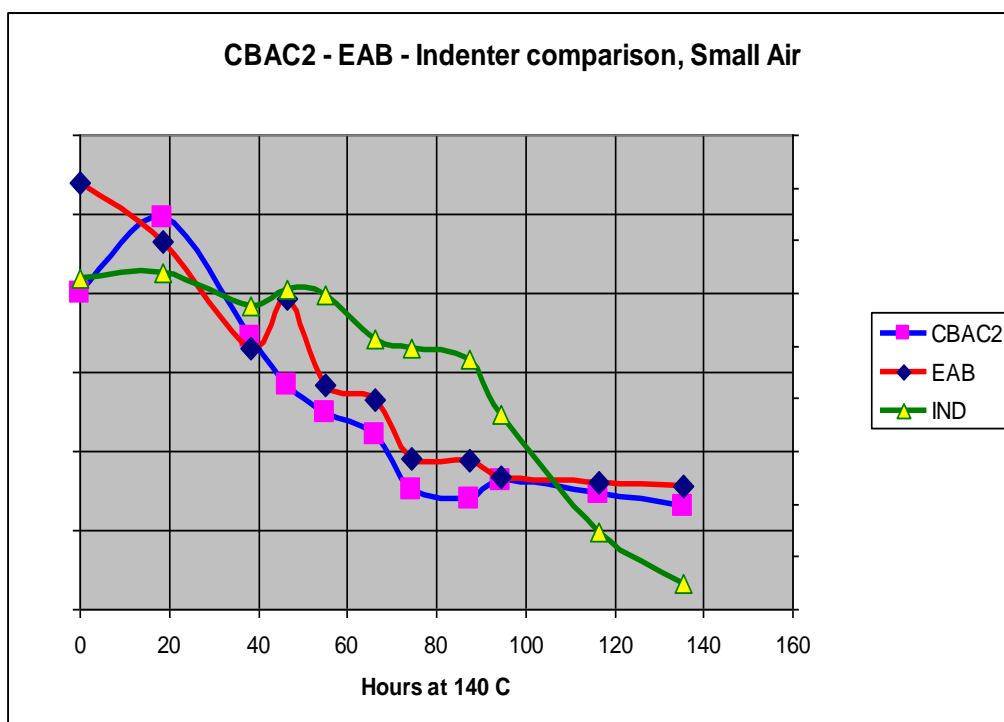
FIG. 4-48. Small type, air environment.

In the Medium Air case, CBAC2 has an initial sharp change during the first 20 hours, but all methods have a flat behaviour between 20 and 95 hours, and then drop consistently. Note the reverse peak at 96 hours, visible in all the 3 indicators.

Except for the first 20 hours, the 3 indicators are well correlated but, unfortunately, very little information can be achieved in the 20-96 hours period.
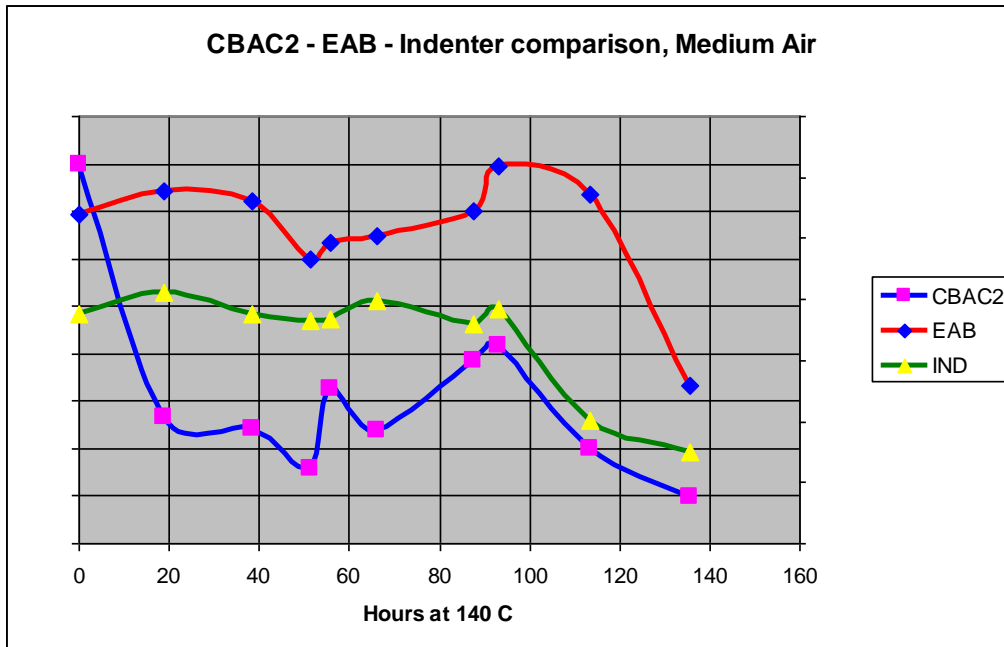
FIG. 4-49. Medium type, air environment.
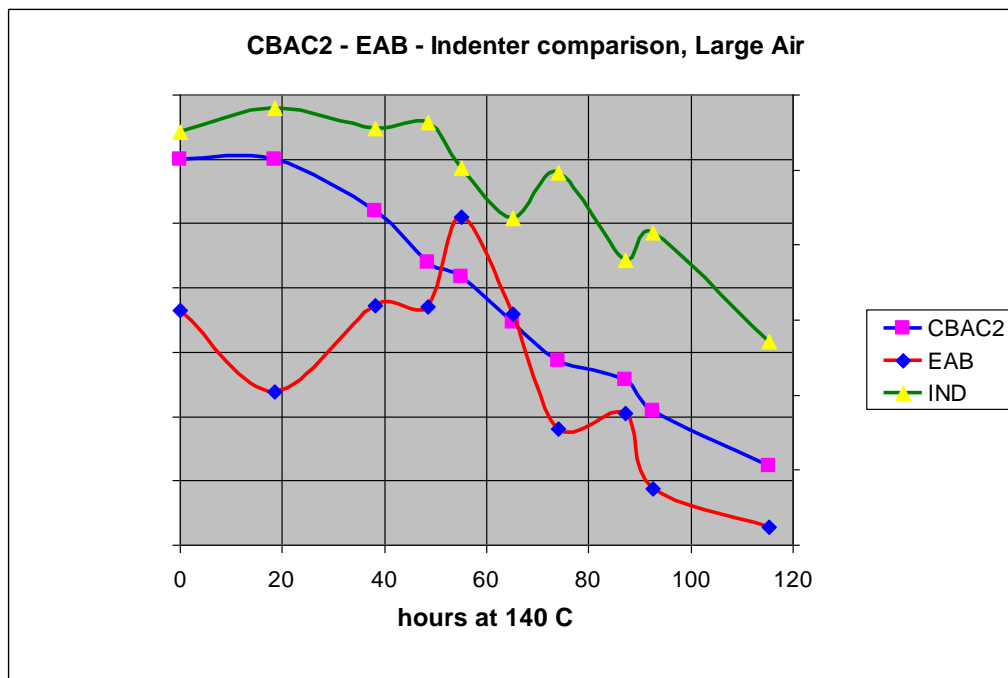
FIG. 4-50. Large type, air environment.

In the Large Air case, IND and CBAC2 correlate quite well. EAB has a significant reverse trend in the 20-55 hours period. CBAC2 is the only indicator not suffering any reverse trend in the entire time window.

About the nitrogen cases, FIG. 4-51 to FIG. 4-53, EAB and CBAC2 correlate very well in all the three types, with consistent small reverse trends at the same time.

IND has a consistent, significant reverse trend up at 350 hours, in all the three cases. A remarkable behaviour that appears in these N2 plots, is that, while the three indicators trend to the same side with time, the reverse peaks in IND appear to be in counter phase respect to EAB and CBAC2. This is a strange phenomenon that would be worth to investigate further.
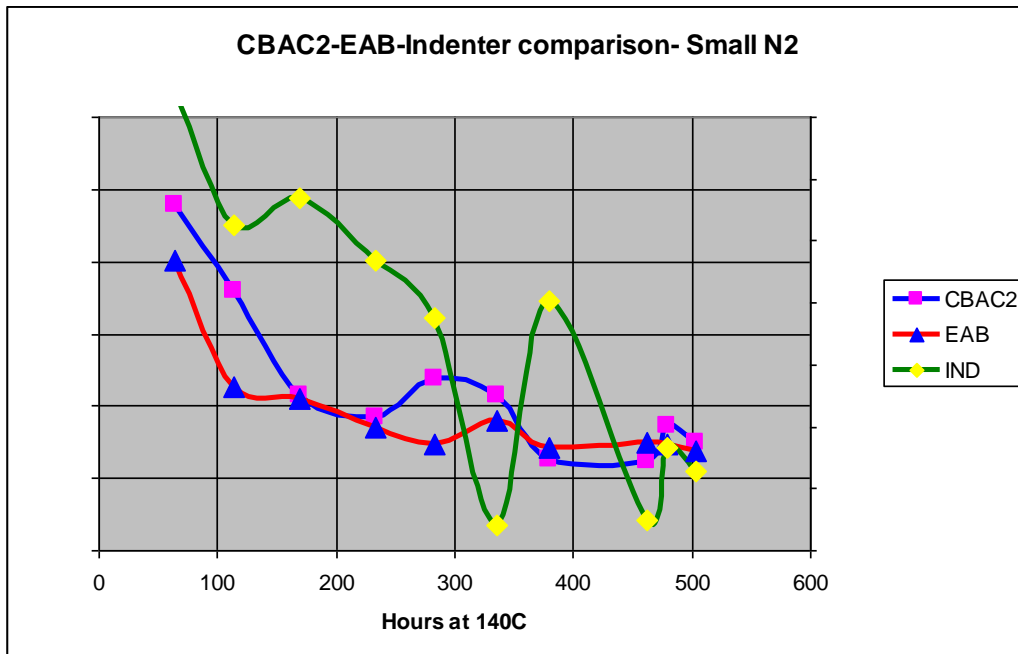
FIG. 4-51. Small type, nitrogen environment.
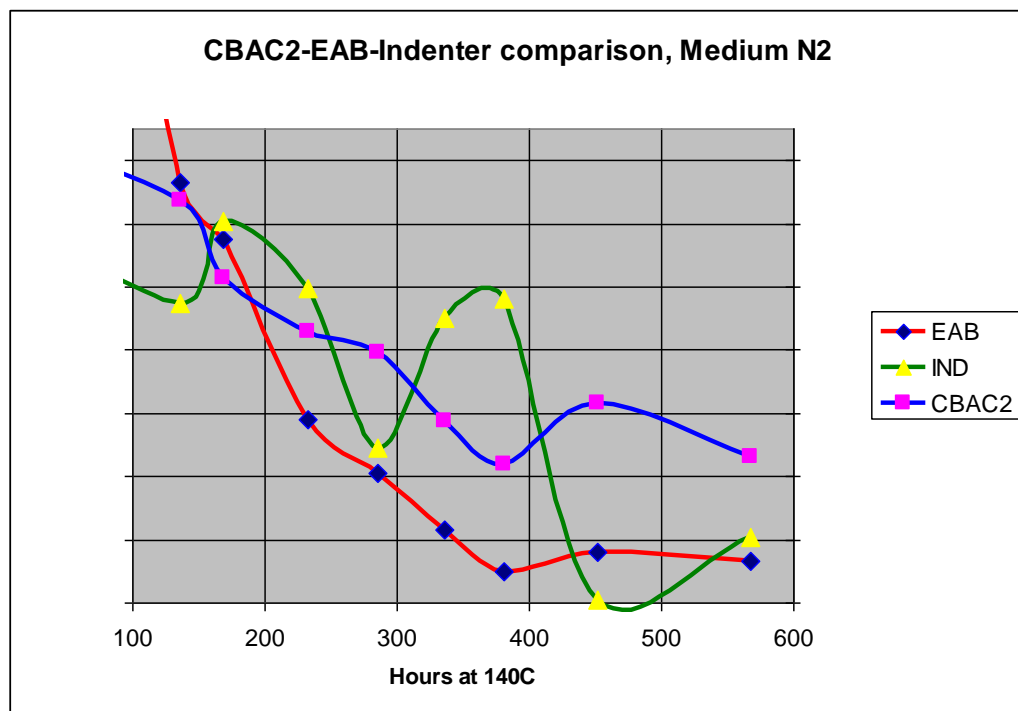
FIG. 4-52. Medium type, nitrogen environment.
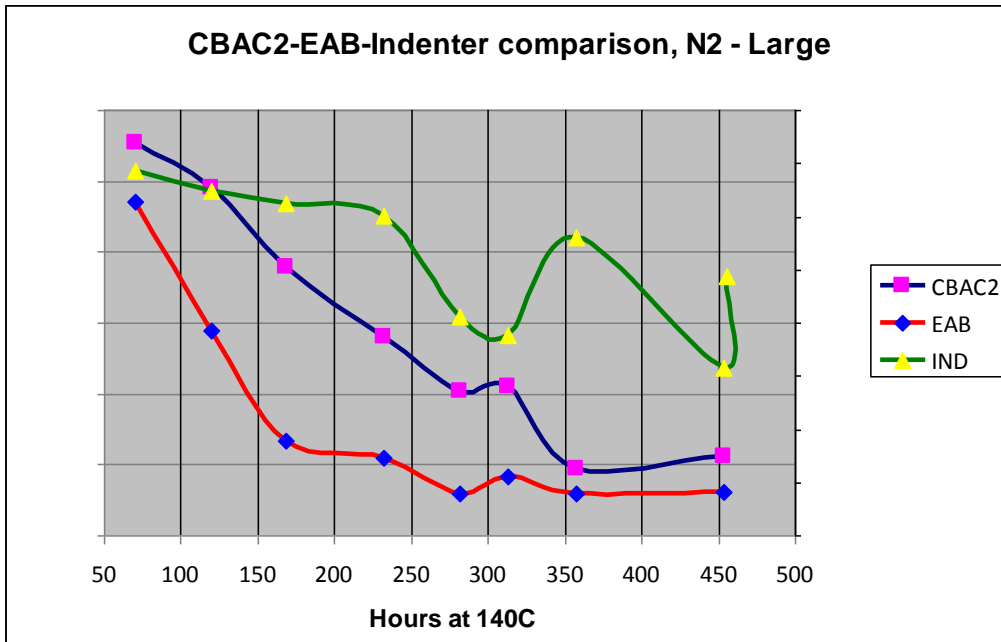
FIG. 4-53. Large type, nitrogen environment.

LIRA correlated quite well with EAB and both tend to flatten when the ageing time reaches 40 years. The only cable type that was difficult to assess for all the 3 methods was the medium type in air environment.

These tests considered only thermal ageing, up to 50 years and should be completed by considering also gamma irradiation ageing.

REFERENCES TO CHAPTER 4

[1]   MA, J., JIANG, J., Fault Detection and Identification in NPP Instruments Using Kernel Principle Component Analysis, ICONE18-28777 (2010).
[2]   ANIKANOV, S., Impact of the Advanced Monitoring and Diagnostics technology on the NPP Plant Computer Scope of Supply, ANS NPIC&HMIT (April 2009).
[3]   ANIKANOV, S., STOLYETNIY, I., SEMENOVSKIY, Y., Primary Plant Performance Evaluation and Signals, Validation, Lessons Learned, Proceeding of ANS Winter Meeting (November 2006).
[4]   ANIKANOV, S., STOLYETNIY, I., General Class of the Data Fusion Methods for NPP Control and Information Systems, NPIC&HMIT, Knoxville (2009).
[5]   FANTONI, P.F., NPP Wire System Aging Assessment and Condition Monitoring: State-Of-the-Art Report, Halden Reactor Project (HWR-746) (2004).
[6]   FANTONI, P.F., Wire System Aging Assessment and Condition Monitoring: The Line Resonance Analysis Method (LIRA), Halden Reactor Project (HWR-788) (2005).
[7]   FANTONI, P.F., TOMAN, G.J., Wire System Aging Assessment and Condition Monitoring Using Line Resonance Analysis (LIRA), Proc. NPIC&HMIT 2006, Albuquerque, NM (2006).
[8]   TOMAN, G.J., FANTONI, P.F., Cable Aging Assessment and Condition Monitoring Using Line Resonance Analysis (LIRA), ICONE17, 7-11 July 2009, Brussels (2009).
[9]   GILLEN, K.T., ASSINK, R., BERNSTEIN, R., CELINA, M., Condition monitoring methods applied to degradation of chlorosulfonated polyethylene cable jacketing materials, Polymer Degradation and Stability 91 (2006) 1273-1288.
[10]   FANTONI, P.F., Wire System Aging Assessment and Condition Monitoring: The Line Resonance Analysis Method (LIRA), Halden Reactor Project (HWR-788) (2005).
[11]   CHANG-LIAO, K.S., CHUNG, T.K., CHOU, H.P., Cable Aging Assessment by Electrical Capacitance Measuring Technique, Proc. NPIC&HMIT 2000, Washington, DC (2000).
[12]   FANTONI, P.F., TOMAN, G.J., Wire System Aging Assessment and Condition Monitoring Using Line Resonance Analysis (LIRA), Proc. NPIC&HMIT 2006, Albuquerque, NM (2006).
[13]   FANTONI, P.F., NPP Wire System Aging Assessment and Condition Monitoring: State-Of-the-Art Report, Halden Reactor Project (HWR-746) (2004).
[14]   FANTONI, P.F., TOMAN, G.J., Wire System Aging Assessment and Condition Monitoring Using Line Resonance Analysis (LIRA), Proc. NPIC&HMIT 2009, Knoxville, TN (2009).
[15]   ELECTRIC POWER RESEARCH INSTITUTE, Line Impedance Resonance Analysis (LIRA) for Detection of Cable Damage and Degradation, Topical Report (TR) 1015209, EPRI, Palo Alto, CA (2007).
[16]   TOMAN, G.J., FANTONI, P.F., Cable Aging Assessment and Condition Monitoring Using Line Resonance Analysis (LIRA), ICONE16, 11-15 May 2008, Orlando, Florida (2008).
[17]   UNITED STATES NUCLEAR REGULATORY COMMISSION, Environment Qualification of Low Voltage Instrumentation and Control Cables, USNRC, RIS 2003-09 (2003).
[18]   SANDELIN, M.J, GEDDE, U.W., Long-term performance of cables based on chlorosulphonated polyethylene. Polymer Degradation and Stability 86 (2) (2004) 331-338.